INTER

International Network on Timber Engineering Research

INTER - International Network on Timber Engineering Research

2014 the International Network on Timber Engineering Research (INTER) was founded.

Scope
Presentation, discussion and documentation of research results in timber engineering and development of application rules for timber design codes or standards related to timber engineering.

Approach
Annual meetings in different countries/places hosted by meeting participants
Presentation and discussion of papers
Peer review of the abstracts before the meeting and of the papers during the meeting
Decision of the acceptance of the abstracts before the meeting by a well-defined review process
Decision of the acceptance of the papers for the proceedings during the meeting
Publication of the papers and the discussion in proceedings

Rules
All decisions including the appointment of the chairperson or the location of annual meetings are made by the participants attending a meeting.

Membership
Persons contributing to or being interested in research related to timber engineering.

INTER PROCEEDINGS MEETING FIFTY-EIGHT 2025

MEETING FIFTY-EIGHT

ISTANBUL, TÜRKIYE

AUGUST 2025

INTER

International Network on Timber Engineering Research

Proceedings

Meeting 58

25 - 28 August 2025

Istanbul, Türkiye

Edited by Carmen Sandhaas

Timber Scientific Publishing
KIT Holzbau und Baukonstruktion
Karlsruhe, Germany
2025

Publisher:
Timber Scientific Publishing
KIT Holzbau und Baukonstruktion
Reinhard-Baumeister-Platz 1
76131 Karlsruhe
Germany
2025

ISSN 2199-9740

Table of Contents

1 List of participants

AUSTRIA	
T Demschner	Fritz Egger GmbH & Co. OG, Mistelbach
U Hübner	Association of the Austrian Wood Industries, Wien
J Lapère	Stora Enso Wood Products, Wien
CANADA	
M Bezabeh	McGill University, Montreal
G Doudak	University of Ottawa, Gatineau
F Lam	University of British Columbia, Vancouver
T Tannert	University of Northern British Columbia, Prince George
CROATIA	
N Perković	University of Zagreb
V Rajčić	University of Zagreb
ESTONIA	
A Just	Tallinn University of Technology
M Kauniste	Tallinn University of Technology
A Ollino	Tallinn University of Technology
F Tienda Resendez	Tallinn University of Technology
J L Vihmann	Tallinn University of Technology
GERMANY	
H J Blaß	Karlsruhe Institute of Technology (KIT)
T Claus	Hafencity University Hamburg
C Demirci	Eurotec GmbH, Hagen
P Dietsch	Karlsruhe Institute of Technology (KIT)
L Rauber	RWTH Aachen University
C Sandhaas	Karlsruhe Institute of Technology (KIT)
D Staiger	BE Ingenieure, Karlsruhe
O A Şişman	Eurotec GmbH, Hagen
J Töpler	Biberach University of Applied Sciences
M Westermayr	Adolf Würth GmbH & Co. KG, Künzelsau
S Winter	Technical University of Munich (TUM)
ITALY	
A Aloisio	University of L Aquila
R Scotta	University of Padova

JAPAN	
K Kobayashi	University of Tokyo
T Tsuchimoto	Building Research Institute, Tsukuba
LIECHTENSTEIN	
M Fehr	Hilti Corporation, Schaan
M Pagliarin	Hilti Corporation, Schaan
NEW ZEALAND	
P Quenneville	University of Auckland
NORWAY	
D Pasca	Treteknisk, Oslo
R Tomasi	Norwegian University of Life Science, Ås
SLOVENIA	
B Azinović	Slovenian National Building And Civil Engineering Institute
L Naumovski	Slovenian National Building And Civil Engineering Institute
SPAIN	
J M Cabrero	University of Navarra, Pamplona
N López Rodríguez	University of Navarra, Pamplona
J Riepe	Universidade Da Coruña
SWITZERLAND	
A Frangi	ETH Zürich
S Franke	ETH Zürich
L Kramer	Bern University of Applied Sciences
G Montalbetti	ETH Zürich
R Steiger	EMPA, Dübendorf

TÜRKIYE

A Ceccotti	Boğaziçi University, İstanbul
C Çelik	Öyler İnşaat, İstanbul
K D Doğan	Hsct İnşaat A.ş., İstanbul
T Dündar	İstanbul University-Cerrahpaşa
F Kurul	İstanbul University-Cerrahpaşa
A Ceylan	Yıldız Technical University, İstanbul
Z C Girgin	Yıldız Technical University, İstanbul
M Özdemir	Marmara Forestry Research Institute, İstanbul
M E Somer	Bahçeşehir University, İstanbul
İ Tuna	Marmara Forestry Research Institute, İstanbul
F Yetiş	Marmara Forestry Research Institute, Istanbul

USA

C Barnes	APA - The Engineered Wood Association, Tacoma
T Skaggs	APA - The Engineered Wood Association, Tacoma
J Smart	American Wood Council, Heathsville
B Yeh	APA - The Engineered Wood Association, Tacoma

2 Minutes of the Meeting

by F Lam, Canada

CHAIRMAN'S INTRODUCTION

The Chair opened the INTER 2025 meeting and welcomed the delegates to Istanbul. INTER 2025 is the 12th meeting of the International Network on Timber Engineering Research. In total, our group, formerly named CIB W-18, had 58 meetings in 52 years.

The Chair thanked Frank Lam, who has been a member of INTER for over 30 years, most of the time not only as a participant but also serving the INTER community in his role. The Chair also thanked Carmen Sandhaas for the preparation of proceedings, organization of reviews, provision of papers, and support for the organizers and participants.

INTER 2025 is hosted by C Girgin and her team from the Faculty of Architecture, Yildiz Technical University. The Chair thanked the organization team for their hospitality. This meeting is the first meeting of INTER or CIB W-18 respectively, in Turkey.

C Girgin welcomed the participants to the 2025 INTER meeting in Istanbul and thanked A Ceccotti for initiating the idea for having the meeting in Turkey and thanked the sponsors of the meeting. C Girgin provided a brief introduction of the history of standardization on modern timber technologies in Turkey.

INTER 2025 has 66 participants from 16 countries with especially a high participation from outside Europe indicating a strong interest in the work of the group worldwide.

INTER continues the tradition of yearly meetings to discuss research results related to timber structures with the aim of transferring them into practical applications, meaning codes and standards. INTER is an independent body with strong links to standardization, hence the Chair welcomed all colleagues who are also representing standardization committees.

25 papers were accepted for this meeting with 19 final submittals. These papers were chosen from 26 submitted abstracts, hence after some reorganization no review process had to be realized for this year’s meeting. In a review process, the papers are selected based on 4 acceptance criteria (state of the art, originality, assumed content and relation to standards or codes). The Chair thanked all authors of abstracts and papers.

The Chair commented about the late withdrawal of accepted abstracts and the logistic issues created by such actions. He asked the participants to provide suggestions on how to mitigate this problem in future. He further suggested participants to think about topics, such as publication of INTER papers and the role of INTER regarding standardization, to be discussed during the final day of the meeting.

Papers to be presented at INTER meetings shall be submitted at least one month before the meeting to enable all participants to read the papers beforehand. Papers must be presented and defended by one of the authors. The presentations were limited to a maximum of 20 minutes each in order to allow time for meaningful discussions after each presentation. The presenters were asked to relate the presentations to the objective of translating research results into design rules. All presenters were asked to conclude their presentation with a clear statement concerning the impact of the results on existing applications or future developments in codes and standards.

In INTER meetings, the delegates have the right to decide on the acceptance of the papers for the proceedings. All authors are invited to amend their papers according to the comments and recommendations of the experts in this group before final submittal for the proceedings. The proceedings will be produced by Carmen Sandhaas in Karlsruhe. Finalized papers must be sent to Carmen Sandhaas at the latest end of September this year.

The following 7 topics will be covered in this meeting:

(1) – limit state design	- 1 paper
(5) – stress grading	- 2 papers
(6) – stresses for solid timber	- 2 papers
(7) – timber joints and fasteners	- 7 papers
(15) – structural stability	- 4 papers
(16) – fire	- 2 papers
(19) – fracture mechanics	- 1 paper

There would be a possibility to present notes towards the end of the technical session. The presentation of notes is strictly limited to 10 minutes without discussion.

INFORMATION FROM OTHER ORGANIZATIONS

European standardization. The Eurocode revision is in its final stage. S Winter provided a presentation on EC 5 progress overview. The process started in 2010, the time frame for last standards to be published is Sept 30, 2027. The date of withdrawal of 1st generation of Eurocode is March 30, 2028. S Winter will step down as chair of EC 5 in 2026. P Dietsch thanked S Winter for his contribution and leadership to EC 5.

U Hübner presented information on European work on product standards in CEN/TC 124. The role of CEN is to support process between member states. Two product groups: GLT/CLT and panel products will be brought together. The CPR Acquis process is working well with European commission towards standardization requests. However new construction regulations ask for 19 environmental parameters/criteria to be provided for each product; hence, more work is needed.

G Doudak gave an update on Canadian CSA O86 code on Engineering Design in Wood with new design information on CLT floors and walls in platform construction, self-tapping screws, mechanically laminated timber, timber concrete composite, wood charring rates, and lateral torsional buckling. F Lam provided an update of the new addition of CSA O122:25 on structural glued-laminated timber with addition of new species groups (Hem-fir), manufactured laminates, and production of 1-hour and 2-hour fire-rated glulam.

J Smart of AWC provided information on updates of US codes and standards developments. In the US, the model building code (International Building Code IBC) is available which references technical information from AWC, APA, and ASTM Standards. 90% of residential construction in US is from wood. Most are light wood frame. The percentage of commercial construction in wood in the US is growing because of mass timber construction technologies. They are working on the 2027 International Code with 4 different construction types. Up to 18 stories in Type 4A without exposed timber is allowed in US. Wild fire issues are being considered in the US with the 2024 International Wildland-Urban Interface code. Interpretation of requirements for continuity for fire resistance for light wood frame platform construction has been clarified. A Frangi commented on the importance of the wild fire topic and received clarification that 2-hour fire resistance is for the inside of the building unless separation between buildings is less than ~3m.

P Quenneville provided updates on progress for NZ standards. They have issues with harmonization with the Australian code. Seismic and connection design updates are available in NZ code.

The Chair commented that INTER is a working commission, not a conference. Good quality papers are the foundation of this group but its reinforcement is the discussion process. Hence the Chair encouraged participants to speak out to continue the tradition of lively discussions in the quest for even higher quality results.

LIMIT STATE DESIGN

58-1-1 Enhancing the concept of overstrength in timber engineering: A proposal for a broader and more reliable application - B Azinović, R Brandner

Presented by B Azinović

H Blass asked whether all properties in Table 2 are considered as brittle failure (e.g. compression perpendicular to grain failures are not brittle). B Azinovic responded that these could be considered as failure modes that one wants to protect against.

P Dietsch asked why for structural timber products such as GLT, CLT and LVL in Table 2 the γ_{Rd}-values are considered without consideration of the failure modes of the strength properties such as shear or tension perp. that one wants to protect. B Azinovic agreed that this aspect could be improved. P Dietsch suggested that maybe one should consider properties that do not benefit from protection.

JM Cabrero asked why distinguish between class 2 and class 3 materials as both are brittle failure modes. B Azinovic responded that COV are different in class 2 and class 3. They further discussed differences between shear and tension perpendicular to grain failures.

R Scotta commented about their Kyoto INTER paper in 2017 which showed the type of connection is important. He asked whether the connection type should be considered. He further pointed out the overstrength factor in Eqn. 6 should be a multiplier not divider. B Azinovic responded that he is not sure about the 2017 Kyoto paper but the concept would align with current paper. He will check about the overstrength factor.

O Sisman and B Azinovic discussed the effect on different actions considered.

S Winter commented that he did not get the α-factor and different load duration situations in relation to how the overstrength factor would be changed. B Azinovic explained that α will change the shape of the distribution. S Winter further commented that Eqn. 6 is incorrect.

S Franke commented on the overstrength factor and COV as some properties have significantly less COV than the state range in the paper. B Azinovic agreed that this could be examined further.

A Ceccotti asked for a conclusive statement. B Azinovic concluded that the overstrength factor will need to be increased for unreliable properties.

P Dietsch asked for reasoning why this paper was published in the Engineering Structures Journal first, hence beneficial comments from INTER experts are missed. B Azinovic stated that this INTER paper has additional features with the intent of another publication in another journal.

STRESS GRADING

58-5-1 A binary visual-based classification model for grading reclaimed structural timber for reuse - A Aloisio, D P Pasca, Y De Santis, M Fragiacomo, H Burkart, A Øvrum

Presented by A Aloisio

F Lam asked how actual defects in reclaimed timber such as localized slope of grain, end checks be considered in the model and influence the results. A Aloisio responded that this work is a starting point and focuses on the Norwegian proposal for reclassifying recovered timber with small diameter round holes; more advanced model will be considered in future.

P Dietsch commented that the results from four-point bending tests are tied to this configuration and the member being reused in bending. A Aloisio responded that only bending strength was considered and 3 heights were studied.

P Dietsch commented that the tension strength perpendicular to grain for small clear wood of 4.5 MPa was used and asked if one should consider a lower value of say 1.0 MPa in a sensitivity study. A Aloisio responded that since a homogeneous model without defects was considered we assumed higher small tension perpendicular to grain strength.

P Dietsch commented that past research from Falk in the US suggested that holes smaller than ½ the size of the largest knots can be ignored. A Aloisio responded that a very large hole tends to drive all failures and maximum diameter does work together with the rule of sum of hole diameters in the two extreme zones.

JM Cabrero commented that the time related to the use of real beams is an important issue. A Aloisio said that the work is a starting point and the topic is complex. JM Cabrero further commented that the 4-point bending tests have a specific moment diagram which might be different from real use. A Aloisio agreed that the results depend on loading scheme, and the rule of sum of hole diameters in the two extreme zones and threshold might be adjusted for other cases.

H Blass commented that the starting point should consider realistic cases. A Aloisio responded that the starting point is related to the Norwegian standard on reclaimed wood to consider such a binary model. Selection of random parameters to generate the hole is based on experts feedback. There were discussions on closely spaced hole issues.

BJ Yeh questioned why choosing 80% as threshold. In N. America there are concerns with how to define and consider load duration issues for reclaimed wood. A Aloisio responded that the threshold is based on the Norwegian standard. It would be interesting to consider a range. He said this type of problem is multi criterion based.

A multicriteria approach is needed to consider load history and load duration issues as a separate problem.

T Demschner asked if the approach handles damages that are rectangular shape. A Aloisio responded that the model cannot handle these cases currently and will need to adjust the approach. T Demschner asked what about holes created by nails or dowels. A Aloisio responded that these cases can be handled.

S Winter questioned if comparisons were made between hole size as related to original grade. A Aloisio responded that hole size was not related to defects in the original grade. However the scatter and shape of strength distribution are similar between real timber and model.

P Dietsch commented that final editorial checks of the paper are needed before submission for the proceedings.

58-5-2 Tension strength, stiffness and visual grading of red pine structural boards in accordance with Turkish Standard TS 1265- 2012; Effect of knot diameter - F Kurul, M Özdemir, İ Tuna, T Yılmaz, M Arslan, S Ermiş, T Dündar

Presented by F Kurul

P Dietsch commented that the table listed moisture contents of 15%. Were these boards technically dried and would the results be different otherwise. F Kurul said there were no moisture adjustments for tension strength.

BJ Yeh asked if the edge and center line knots were considered differently. F Kurul said they were measured and noted but not considered in the paper.

B Azinovic commented that climatic change in Europe will lead to more availability of Mediterranean red pine species in the wood supply chain.

STRESSES FOR SOLID TIMBER

58-6-1 Deformation level and specimen geometry in compression perpendicular to the grain of solid timber, GLT and CLT timber products - D P Pasca, A Aloisio, F M Massaro, H Stamatopoulos, Y De Santis, A Øvrum

Presented by D Pasca

A Frangi commented about the calibration results showing large differences between the E_{90} chosen and the E_{90} from literature.

J Töpler asked about the possible use of the numerical model for design. D Pasca responded that the configurations covered are different and may not be applicable directly for design. J Töpler commented that numerical models involve calibration

versus verification and asked if two different data set were used. P Pasca said the data set was split such that 80% of the data were used for calibration and 20% of the data were used for verification.

R Tomasi and D Pasca discussed if the k_{mat} of case A was not of key interest but the paper focused on k_{mat} of case B matched the findings but leads to larger levels of deformation. R Tomasi asked, if the different values of h_{ef} were separated in analysis.

P Dietsch commented there are other models available and asked if the authors considered them. P Pasca responded that no as they only focused on the new Eurocode model. P Dietsch asked for any mechanistic explanation on h_{ef} = min (0.7h; 210 mm). D Pasca responded no as it was based on numerical results only. P Dietsch commented that perhaps it might be explained by compression perpendicular to grain stresses being transformed into shear stresses at this level of height.

T Tannert commented that the limit of the 210 mm seemed arbitrary. D Pasca responded that some regression work was done. He agreed this limit is a bit arbitrary and more simulations can be done in future.

P Dietsch also asked why the journal publication was realized before the INTER paper as the advantage of including suggestions from INTER experts is then missed. P Dietsch suggested that editorial checks be performed and additional references be added before submission for the proceedings.

58-6-2 Experimental study on timber compression and shear: effects of slope of grain and presence of screws - N López Rodríguez, J M Cabrero, I Arteaga Jordá, P Guindos Bretones

Presented by N López Rodríguez

H Blass pointed out that in Figure 2 the interpretation of fiber orientation was incorrect as annual ring orientation was wrongly considered as fiber orientation.

H Blass commented that the screw through the specimen at 90 degrees did not provide any reinforcement to the wood; in fact, it would weaken the specimen.

A Frangi commented that the reported shear strength more than 10 MPa as high and the generalized conclusions were too strong.

T Tannert also commented on the wording of reinforcement being confusing.

P Dietsch commented on shear tests and received clarification that different direction of fiber orientation did not cause compression rather than shear stress.

A Frangi commented that shear area decreased by 20% could potentially explain the high shear strength.

P Dietsch and N López Rodríguez discussed whether there was any need for change to standards regarding the proposal and the conclusions that reinforcement could lower the strength. P Dietsch mentioned the work of M Enders-Comberg on steel fasteners in areas of compression.

TIMBER JOINTS AND FASTENERS

58-7-1 Linear approximation of an elasto-plastic extension of the Johansen theory to predict the deformation of dowel-type fasteners - J Riepe, J Díaz, J Schänzlin

Presented by J Riepe

H Blass questioned the initial slip load slip curve shown by the model. J Riepe responded that the initial slip from the numerical model was shifted to match the initial slip from the experiment results.

H Blass commented about the angles φ_1 and φ_2 that would imply under elastic condition and the horizontal part of the dowel would also load the wood. J Riepe said some adjustments were made in the model to account for this aspect.

S Winter and H Blass discussed the shear force being zero at point of maximum moment / plastic hinge location which implies the assumed shear force and shear plane should be valid.

R Tomasi and J Riepe discussed how to implement this model into standard.

U Hübner commented that this paper is useful especially dealing with stiffness issues. Comparisons with experimental data would be useful especially dealing group effects. P Dietsch added that research on group effect was available from past research.

P Quenneville questioned why there was greater variation with modes a and b. J Riepe said there was rotation somewhere and also whether deformation of the dowel was involved would make a difference.

JM Cabrero commented that there is a need to extend the model to consider group effects and experimental verification should be done. J Riepe said the same input was used for embedment.

58-7-2 Influence of steel properties on the ductility of connections: An explorative experimental investigation - L Kramer, M Geiser, L Furrer

Presented by L Kramer

P Quenneville supports call for action on f_y values for steel.

T Tannert asked if the steel properties of the dowel were tested and suggested to add this information. L Kramer said this was tested.

C Sandhaas and L Kramer discussed the influence of production process on the dowel in relation to cold forming to the properties of the final product. C Sandhaas mentioned that does not only depend on the steel but also on the type of fastener.

58-7-3 Fatigue behaviour of threaded rods bonded into glulam for application in bridge construction - R Steiger, B Zumbrunn-Maurer, L Kramer, T Strahm, E Gehri

Presented by R Steiger

S Winter asked why parallel to grain was considered in ash but perpendicular to grain was considered in spruce. R Steiger said that budget constraints led to concentrating testing on the boundary situations to seek reduction in cost. S Winter received clarification of the stress level in the bond line.

C Demirci questioned the tolerance for this type of connections if they were made on site and asked how to ensure this work in service class 3 conditions. R Steiger replied that this type of connections needs a company with good quality control. In this case the company has more than 20 years of experience. The work was not extrapolated towards service class 3.

C Sandhaas commented on the test setup of 3 or 4 bonded-in rods and asked if the number of bonded-in rods in a connection would affect the conclusions. R Steiger agreed that this could affect the results.

H Blass commented about the statement that there is lack of guidance in the code on rolling shear failure in the perpendicular to grain cases. He said Karlsruhe Institute of Technology has worked on this topic with a proposal available. R Steiger stated that they are aware of the work but the partner company has been working on their own proposal.

P Dietsch commented that the paper indicated that a reduction to 2/3 for SC3 seems to be safe. He asked if there was any data available for justification. R Steiger agreed that they do not have test results on this.

U Hübner said high risk is associated with on-site gluing and implied that on-site gluing should generally be avoided; hence, quasi-industrial, factory made systems are needed.

58-7-4 Birch and laminated densified dowels for timber connections - an experimental study - A Aloisio, R Tomasi, Y Wang, R Crocetti

Presented by A Aloisio

F Lam received clarification from R Tomasi that the loading plates in the bending shear test setup have rounded edges.

P Dietsch commented that clamping the dowel in the test setup could cause a rope effect. A Aloisio agreed that a rope effect could exist but this was not considered in the analysis.

H Blass questioned the tensile shear test setup as the dowel could slip out under load. R Tomasi said the test set up was originally designed for screw testing. H Blass said this cannot work for dowels.

H Blass asked about the densified veneer wood dowel and whether they are considered as hardwood. A Aloisio responded that they are considered as hardwood dowels. H Blass said densified veneer wood dowels behave differently compared to hardwood dowels especially in long term behaviour.

A Aloisio and T Claus discussed rope effect mechanism as observed in the test. A Aloisio further confirmed that pull out tests were not performed.

A Frangi commented about the deformation mechanism of the dowel.

T Demschner and A Aloisio discussed about the test set up of shear/bending tests in terms of the possibility of friction and hence rope effect affecting the results.

J Smart commented that the high ductility of the birch dowel was surprising and asked what would happen if reversed cyclic loading was applied in terms of ductility. A Aloisio said high ductility of birch could be observed in other tests and they do not have information on reversed cyclic loading.

P Dietsch commented that editorial changes to the paper are needed and suggested upgrading the paper to include new information before final submission for the proceedings.

58-7-5 Resistance to brittle failure of connections with inclined STS in CLT loaded along the major strength direction - T Tannert, A Einipour, J Zhou, A Salenikovich

Presented by T Tannert

J Cabrero received clarification that the side shear failure plane was close to the screws.

A Frangi received clarification that the tests were designed to avoid screw withdrawal. T Tannert said the intent was not for designers to design these types of connectors as they are not good connections. He added that the model did not predict the failure plane.

P Dietsch commented that the paper should mention which failure mode was predicted. He asked how deep the screws need to penetrate into the longitudinal layer to be considered. T Tannert responded that they do not have information on the minimum penetration depth required.

P Dietsch agreed that we need to consider conservative models in case of lack of information. Industry however might argue that they already have good performance history hence added conservatism would not be needed. T Tannert said in Canada we do not have long history of using these large connections; hence, designers will be happy to receive guidance.

H Blass asked whether the bottom failure planes were always between two orthogonal layers. T Tannert said they were closed to the glue-line. H Blass said one should then consider the bond.

C Demirci received clarification on the difference between step and plug shear.

P Quenneville commented that the screws also pull at the glue-line.

58-7-6 Probabilistic block shear failure mode model - N López Rodríguez, R Cruz Hidalgo, J M Cabrero, P Guindos Bretones

Presented by N Lopez

P Dietsch commented that tensile stresses perpendicular to grain occur when the dowel moves into the wood; furthermore, shrinkage cracks often exit. These are not considered in analysis based on short-term testing. He commented that tensile and side plane shear resistance should not be added per points discussed previously.

C Demirci discussed parametric study where if a_4 is small one would get block shear failure. Minimum a_4 should start from a value bigger than 10 mm in the parametric study. JM Cabrero responded that they were considering plug shear in this study.

A Frangi, T Tannert and JM Cabrero discussed that the addition of resistances of different planes is incorrect.

58-7-7 Load-bearing behavior of PMPF connections with air gap between PMPF and timber - D Staiger, H J Blass

Presented by D Staiger

F Lam commented that practical adjustment factors to account for tooth embedment gap are available from N. America TPI/TPIC standard for cross reference: no adjustment for embedment gap < 0.8 mm; ineffective for embedment gap > 1.6 mm; 60% effective for embedment gas between 0.8 mm and 1.6 mm.

S Winter and D Staiger discussed the arrangement of nail plate installation procedure with the plates being slightly inclined to represent a partially withdrawn plate.

G Doudak commented about bending of teeth from shrinkage of the wood. D Staiger said that in reality the detachment was not uniform hence the test considered this fact.

G Doudak said that there is large difference between model and test results in the zero gap case. D Staiger explained that the difference is between mean vs characteristic value.

U Hübner commented that detachment of tooth plates is common and asked how would one remedy these cases. D Staiger responded that the goal of the work is to understand the phenomenon as a first step. They tried to push the plates back into the wood but it was not successful.

C Sandhaas asked would it be possible to propose considering gaps in the initial stage of design. D Staiger responded that there are other effects to be considered including plate geometry, teeth design, timber properties, etc.

S Winter commented that tooth plates with shorter nail lengths compared to the one tested are commonly used in Germany.

J Smart and D Staiger agreed that relaxation of the wood could cause further withdrawal.

D Staiger commented that manufacturers already knew about this issue.

T Tannert asked about micro teeth system which need to be compressed into the wood.

U Hübner commented that 25% of the teeth area is allowed to have gaps of 1 mm. Practical ways to consider this issue economically are needed. He commented about cyclic and drying conditions in service vs test conditions.

P Dietsch suggested to add some illustrations to the paper.

STRUCTURAL STABILITY

58-15-1 Lateral stiffness of light timber-framed shear walls with cladding - proposal for an analytical model - L Rauber, B Hoffmeister

Presented by L Rauber

A Ceccotti received confirmation that no vertical load was added. He commented that Canadian results a couple of decades ago showed gypsum system should have reduced ductility. If the strength of the cladding is reduced, the R-factor should be reduced as well.

T Skaggs questioned why OSB + cladding showed doubled capacity but not stiffness.

G Doudak asked about whether stronger hold-downs would be needed. L Rauber said the hold-down had high capacity and they also tested GTB wall alone.

R Tomasi and L Rauber discussed just using the lateral slip modulus from nails in the modeling process. R Tomasi received clarification if separate tests on staples were done. C Sandhaas commented that the test setup cannot take load in a specific direction.

S Winter commented that the doubled load capacity is due to the reduction of nail spacing. It is a plastic situation that Eurocode takes into consideration in design. In the elastic range, cladding can participate but not in the plastic range; hence, explaining the stiffness issue. He commented about fire design fixing. Tests should be conducted in density values and k_{ser} and timber properties should be measured, instead of taking properties from standards.

P Dietsch commented on the level of activation of fasteners against the stud. L Rauber said the analytical formulation considered cladding as single plate and OSB panels as second plate.

58-15-2 Experimental investigation of a two-storey full-scale CLT structure with resilient rocking walls for seismic behaviour factor determination - S R Agarwal, A Hashemi, P Quenneville

Presented by P Quenneville

T Tannert asked what is needed towards standardization of this proprietary system. P Quenneville responded that engineers have freedom to take responsibility for this system.

T Tannert asked what is needed to get a generic system into the standard with for example R=6. P Quenneville said test data would be needed.

G Doudak asked whether the R=3 is at the system level. P Quenneville responded that R=3 is based on reduction of base shear. G Doudak asked whether these systems

were designed for a specific deformation level. P Quenneville responded they were designed to remain elastic.

O Sisman asked whether overstrength factors were considered. He asked for strength limitation cases and if it would be advantageous to increase the strength of the damper without increasing the thickness of CLT. P Quenneville responded yes to both questions.

A Ceccotti commented that this system can be used for very important structures. Smaller buildings with smaller consequence classes such as two or three-storey structures do not need such sophistication. P Quenneville responded that the concept of resilient can be and should be applied to all buildings.

R Scotta and P Quenneville discussed the role of steel in friction damping.

P Dietsch commented that information on creep of post tensioned systems is available from the work of M Gräfe. He said for the system tested in this paper, a technical report should be provided as reference. P Quenneville said the work is reported in a PhD thesis.

58-15-3 Determination of Canadian seismic force modification factors for post-tensioned cross-laminated timber rocking walls - H Zhu, M A Bezabeh, A Iqbal, M Popovski, Z Chen

Presented by MA Bezabeh

G Doudak commented that this work needs to assume R_d R_o to get the archetypes and then verify the validity of the chosen R_d R_o values. He asked how would one generalize the results to other systems. MA Bezabeh said their goal was to consider as many systems as possible.

G Doudak asked how sensitive are the results to the choice of collapse criterions of 3 to 5%. MA Bezabeh responded that the choice was based on collected damage evidence.

C Demirci received clarification that the model has shear connectors and a Timoshenko beam was used to model CLT.

A Ceccotti received confirmation that the tall tested system shown had period of 2 seconds. He mentioned that wind considerations would govern the design. MA Bezabeh responded that other people had considered wind issues and agreed that base shear would be wind governed.

C Girgin and MA Bezabeh discussed differences between U shape and friction-based dampers.

P Dietsch commented that archetype ground floor layout is different from typical floors layouts of ground floors. MA Bezabeh responded that this is considered in a continuing study.

P Quenneville and MA Bezabeh discussed how tension rods can be treated if floor layouts were different between floors.

P Dietsch commented that the presentation was too long, for the INTER audience the introduction should have been shorter.

58-15-4 Studies on fluid forces acting onwood house under flood - T Tsuchimoto, S Hirano, Y Takadate

Presented by T Tsuchimoto

G Doudak commented that only one aspect ratio was considered. Was there any numerical study on the influence of aspect ratio? T Tsuchimoto responded that only one aspect ratio was tested and computer analysis will be considered in future.

T Demschner commented that the work studied slab on grade buildings only and no consideration of crawl space and basement. T Tsuchimoto responded past test results indicated crawl spaces reduced water flow.

A Frangi asked if K_{eff} can be extrapolated to other cases. T Tsuchimoto responded that this is a difficult problem.

P Dietsch asked if it would be possible to relate pressure inside the building from water to wind pressure on a building. Then information in wind codes could be applied for this topic. T Tsuchimoto responded that it would be possible.

P Dietsch commented that this paper is a reduced version of the authors' WCTE 2025 paper. He suggested to add elements to the paper to make it different from the WCTE paper, otherwise this paper could not be published as INTER paper.

FIRE

58-16-1 Performance of bond lines in different fire related small-scale tests - J L Vihmann, A Just

Presented by J Vihmann

P Dietsch asked about how was the influence of material properties excluded from the small-scale tests. JL Vihmann said density was checked.

P Dietsch received clarification that charring information was based on the company that produced this particular type of product. Also J Vihmann is working on the correlation.

S Winter received clarification that 90 min vs 120 min heating is related to GLT vs CLT. He commented that keeping Annex B and consider additional small scale test method while keeping statements in EN 18070 together.

A Frangi commented that it is good that expensive fire tests can be replaced by small scale testing. He noted adhesive 9 may have some values obtained from specifier.

T Demschner received clarification that worst case scenario being 20 mm thick laminates and fire tests will clarify possible bond line behaviour under fire.

S Winter commented that block shear tests are sensitive to wood species and asked about the amount of fiber failure under elevated temperature. J Vihmann responded that they do not have this information at hand. S Winter asked if they intend to repeat glue no. 9 tests.

J Smart commented that loading should be close to design level. J Smart and A Frangi discussed the importance of bond-line behaviour in fire and if this is a good test. A Frangi stated that tests with 40 mm laminations can't be scaled down.

58-16-2 Fire performance of hollow glue laminated timber elements - N Perković, V Rajčić, J Barbalić

Presented by N Perković

A Frangi commented that the authors encompassed too many aspects in the paper; hence, it is too complicated to make this research generally applicable for standardization, it is rather a topic for a technical approval. The authors should focus on a specific product instead. N Perkovic agreed.

A Frangi commented on charring rates for one- and three-dimensional cases with holes and that one should be careful with cases where thinner laminates are involved.

S Winter is critical of statement that intumescent paint could increase resistance to fire normally. He said in practice the intumescent paints are not effective to increase fire resistance. We want to minimize chemical treatment as this goes against green building concepts. He questioned why PUR which is a D4 class and how to control the quality of the glue. N Perkovic explained how the gluing process was conducted and different adhesives were tested before deciding on PUR.

A Just agreed with comments on standardization and received clarification about painting on three sides and which side was considered. N Perkovic further clarified definitions of some variables. A Just suggested to put recommendations in the paper. V Rajcic added the results can be applied to products for doors and windows.

P Dietsch asked about cross section width and charring rate. N Perkovic responded a higher notional charring rate was calculated; however, 0.75 mm from EC5 Part 1 and 2 was used as charring rate.

P Dietsch commented about placing mineral wool in the cavity which would reflect energy and hence increase temperature in the wood. N Perkovic agreed and saw increase in heat flux in results. He will think about alternative insulation materials.

FRACTURE MECHANICS

58-19-1 Tenon connections – Consideration of brittle failure by fracture mechanics approach - T Claus, W Seim

Presented by T Claus

S Franke asked whether mode 1+2 was considered. T Claus responded they always used a fracture energy approach. S Franke suggested to compare results with model from B Franke. T Claus responded that more tests on GL for a material model will be needed.

H Blass received clarification $h_{e,2}$ is based on height of secondary member.

S Winter asked whether impact from model results have been cross-checked for practice. T Claus responded that the model is safer: 10.6 kN vs 16 kN compared to EC model.

A Frangi received clarification that comparisons were done between mean values and probabilistic approach to achieve characteristic values.

P Dietsch commented that there are previous works on multiple tenon joints and suggested to study the influence of tolerances in the multiple tenon joints.

NOTES

Five notes were presented.

ANY OTHER BUSINESS

Open discussion of five topics was conducted related to operation of the INTER meeting.

a) C Sandhaas made a proposal on the publication of proceedings for future INTER meetings. It was agreed that the on-line version of the INTER proceedings will continue and printed versions of the proceedings will be available as print-on demand only. DOI will be given for each individual paper. For this, an abstract and

keywords for each paper will be needed. The minutes of discussion of the paper will appear before the paper which can sometimes act as warning of the content.

b) The Chair proposed that each accepted paper is reviewed by one expert on the topic. The expert will provide comments and review at the start of the meeting for the author to address. This is intended to increase the quality of the papers. The end of September will be the deadline for making changes to papers based on feedback of the review and discussion during the meeting. Participants agreed with the proposal unanimously.

c) The Chair proposed the maximum time of 20 minutes for the presentation as a hard ceiling, hence the objective should be 16-17 minutes presentation time. The Chair and Secretary will aim for 25 papers as a maximum with ~ 35 minutes per paper. Discussions of the paper involving elemental questions on methods, interpretation of findings, errors, conclusions, and concerns are of prime importance and will be issues to be included in the minutes. He asked the participants to consider this when formulating questions, some types of questions could be asked during breaks as well. Questions asked in the meeting need to be concise and clear. The Chair proposed that presentation of notes will allow some questions in case the presentation time is below 10 minutes. The total time allowed per note will remain at 10 minutes including questions to the note. Total time to be allowed for all notes will be 1 hour. The participants all agreed.

d) The Chair proposed two options to ensure INTER papers meet the traditional intent of INTER to discuss research results related to timber structures with the aim of transferring them into codes and standards. A hard option requiring each accepted abstract meeting a minimum score in the category of “relation to standards or codes” during abstract review and a soft version based on selection of papers from a threshold group with the higher score in the category of “relation to standards or codes” during abstract review. Voting on the options was very close with the soft version having one extra vote. It was suggested that the chair consider both options during the selection of abstracts during next year as this will be an evolving process.

e) L Kramer proposed to set up a shared database for timber engineering research. J Töpler commented that a modeling database is available and on-going led by FPInnovations. All participants are supportive of the proposal. The key is to find funding to support the initiative. P Dietsch asked interested parties to coordinate and plan for a short report to identify challenges. Senior members can then work together towards securing funding for this initiative.

VENUE AND PROGRAMME FOR NEXT MEETING

R Tomasi invited the participants to attend INTER 2026 at Norwegian University of Life Science in As, Norway, on August 24 to 27, 2026.

Venue in 2027: University of British Columbia, Vancouver, Canada, August 9 to 12, 2027 (a week before WCTE).

Venue for 2028 is open.

CLOSE

The host Prof C Girgin and team from Yildiz Technical University thanked the participants for coming to Türkiye for INTER 2025.

The Chair thanked the host for their hospitality. He thanked the participants, the authors, and the presenters for contributing to INTER 2025.

The Chair thanked Carmen Sandhaas for organizing the INTER proceedings and her hard work and support for INTER.

Chair thanked Frank Lam for his continued support to CIBW18 and INTER over the years.

3 INTER Papers, Istanbul 2025

Enhancing the concept of overstrength in timber engineering: A proposal for a broader and more reliable application

Boris Azinović *)
Slovenian National Building and Civil Engineering Institute (ZAG)

Reinhard Brandner *)
Graz University of Technology, Institute of Timber Engineering and Wood Technology

*) joint first authorship

Keywords: capacity-based design; overstrength; ductility; timber engineering; connections; joints; ductile failure; brittle failure; failure hierarchy

1 Introduction

1.1 Technical background and impetus for the work

Unforeseen and hardly predictable sudden collapses of structures need to be avoided. Structures that allow excessive plastic deformations as a result of local or global overloading are desirable not only to warn of an approaching collapse, but also to potentially activate less stressed components and structural areas by local stresses and global load (re)distribution in statically indeterminate structures, which could also increase their robustness (cf. Jorissen & Fragiacomo (2011)). To ensure that such plastic deformation occurs before brittle failure, a clear failure hierarchy must be followed that prioritises the yielding of the ductile regions while preventing the brittle regions from reaching their load-bearing capacity. According to the Load and Resistance Factor Design (LRFD) framework this is usually expressed by

$$R_{\mathrm{b,d}} \geq \gamma_{\mathrm{Rd}} \cdot R_{\mathrm{d,d}} \Leftrightarrow R_{\mathrm{b,k}} \cdot \frac{k_{\mathrm{mod}}}{\gamma_{\mathrm{M}}} \geq \gamma_{\mathrm{Rd}} \cdot R_{\mathrm{d,k}} \cdot \frac{k_{\mathrm{mod}}}{\gamma_{\mathrm{M}}} \quad (1)$$

where $R_{\mathrm{b,d}}$ and $R_{\mathrm{d,d}}$ are the design values of the brittle and ductile resistances, respectively, $R_{\mathrm{b,k}}$ and $R_{\mathrm{d,k}}$ are as the corresponding characteristic values, k_{mod} is the modification factor, γ_{M} is the material partial safety factor and γ_{Rd} is the so-called overstrength factor. This approach, known as capacity-based design, is based on two key concepts: the concept of overstrength design, which aims to maintain the intended failure

hierarchy, and the concept of ductility, which allows failure modes to be categorised as either brittle or ductile. While capacity-based design is widely accepted, particularly in earthquake engineering, the discussions on overstrength and ductility in timber engineering reveal ongoing uncertainties that underline the need for further development, standardisation, and regulation of these concepts.

Focusing on the concept of overstrength, there are a number of different contributions to γ_{Rd}; according to Mitchell et al. (2003) and Schick (2017), these are: (i) the use of standardised, non-optimised dimensions of components (geometry aspect), (ii) differences between characteristic (nominal) and design values (safety aspect), (iii) differences between experimental and characteristic (nominal) capacities calculated using engineering models (model aspect), (iv) material dependent activatable reserve capacities, such as strain hardening in steel (material aspect), and (v) additional capacities activated by system actions (system aspect).

In timber engineering there are even more aspects, such as equal material partial safety factors and modification factors, which are argued by ease-of-use and general conservativity in design, size and volume effects, freedom in the definition and determination of characteristic values, uncertainties caused by varying grading procedures possible for achieving the same strength class as well as limits in determining overstrength from experiments; for more details cf. Brandner & Azinović (2025). In this respect, conservatism in nominal values and engineering models must not lead to conservative design of structures in all cases, as it can be the case with overly conservative yield capacities, for example.

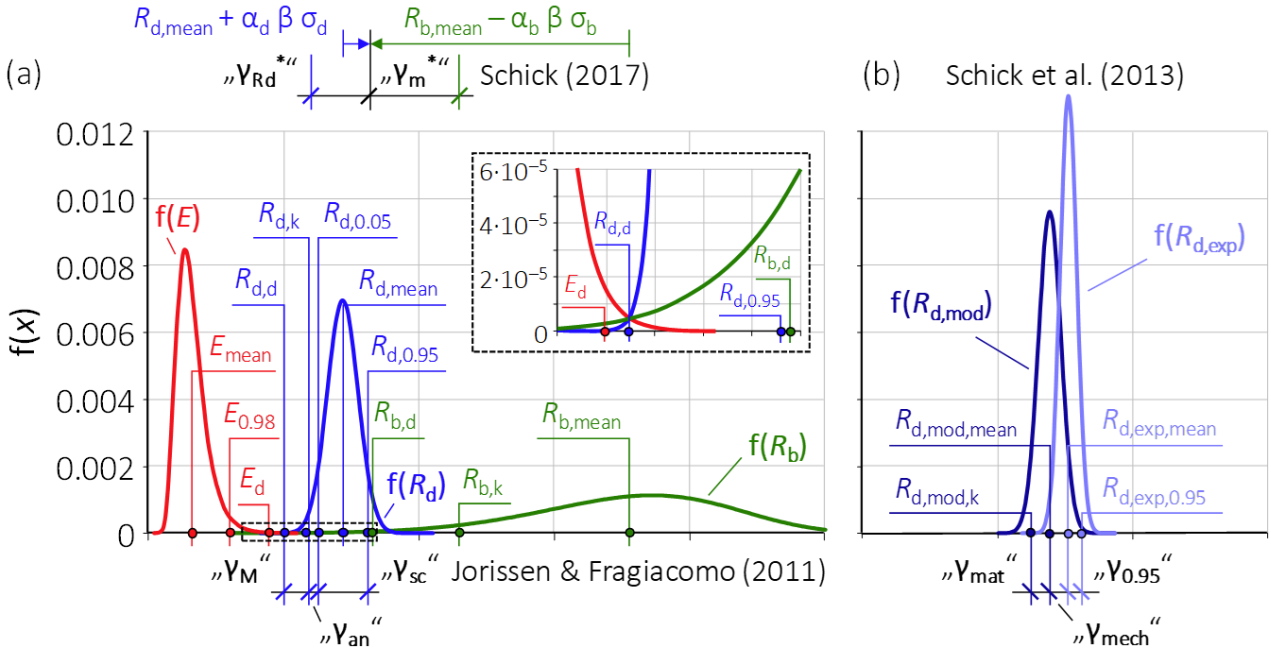

Figure 1. Definitions of the overstrength factor in the context of structural reliability analysis with action E, ductile capacity R_d and brittle capacity R_b: (a) definitions of Schick (2017) and Jorissen & Fragiacomo (2011); (b) definition of Schick et al. (2013) (please note: "…" indicates partial overstrength factors).

In the past various definitions for the overstrength factor had been developed. Related to timber engineering and with focus on earthquake design (γ_M & k_{mod} = 1.0), Mitchell et al. (2003), Jorissen & Fragiacomo (2011), Šušteršič et al. (2011), and Schick et al. (2013) (see Figure 1) defined overstrength within the LRFD framework and in principle as ratio between extreme upper and lower quantile values of the ductile resistance, with $\gamma_{Rd} = R_{d,0.95} / R_{d,d}$. These definitions involve the safety and model aspect as well as the variability of R_d and set a clear limit for the design value of the brittle resistance, with $R_{b,d} \geq R_{d,0.95}$. However, since this group of definitions only considers the ductile resistance but no interaction with the brittle resistance, there is no possibility to control the additional safety in the latter. Such a control mechanism is explicitly included in the second group of definitions, which uses the structural reliability analysis framework and treats R_d as action and R_b as resistance, with $p_{f,Rd} = P(R_b \leq R_d)$ as failure probability, i.e. the probability of brittle prior ductile failures; cf. Deam (1996), Brühl et al. (2014), Schick (2017) and Aloisio et al. (2023; 2024) (see Figure 1). However, none of these definitions allows control over the probability of failure of the brittle part and ensures that it is lower than that of the ductile part by the additional safety to be defined. This is because there is no direct control of R_b against the action E.

Studies in Brandner & Azinović (2025) clearly show that with realistic settings of the statistical distributions and parameters for E, R_d and R_b, the design of structural components according to the overstrength definitions of both groups can lead to less safety than intended and even to cases where the failure of the brittle part becomes more likely than that of the ductile part.

1.2 Objective of the study

Motivated by this, after a quick recap of past overstrength definitions for timber engineering the paper will present an alternative definition for the overstrength factor, formulated within the structural reliability analysis framework as a logical consequence of system reliability analysis in Brandner & Azinović (2025). It considers the whole system of action(s) E as well as the ductile R_d and brittle resistances R_b and directly translates the stated demand in capacity-based design that R_b needs to be overdesigned to achieve a ductile failure, which means that $p_f(R_b) < p_f(R_d) <=> P(R_b \leq E) < P(R_d \leq E)$, with $p_f(.)$ as the failure probability. This new, alternative definition is compared with the current definitions for γ_{Rd} from both previously introduced groups in frame of a parameter study, in which the statistical distribution models and its parameters are varied with focus on the variabilities of R_d and R_b.

Focusing on statistical distribution models frequently applied and recommended for representing E, R_d and R_b (c.f. JCSS (2001)) as well as realistic parameter settings (with focus on realistic ranges of variabilities), the aim is to identify possible future regulations for the overstrength factor by transferring the outcomes from structural reliability analyses into the LRFD framework. Such recommendations are considered reasonable depending on (groups of) resistances and ratios between coefficients of variation

(uncertainties) of R_b and R_d. In doing so, the authors see it as relevant to consider ductility and overstrength not only for accidental load scenarios but more generally, also for characteristic (permanent) load scenarios.

2 Assessment of overstrength factors

2.1 Review of overstrength definitions related to timber engineering

As quickly introduced in Section 1.1, past definitions of overstrength can be divided in definitions in frame of (i) the LRFD framework and (ii) structural reliability analysis.

Starting with the first group (i), the work of Jorissen & Fragiacomo (2011) need to be mentioned: They defined the overstrength factor as ratio between the 95 %-quantile and the design value of the ductile load-bearing capacity, as product of three partial factors, given as

$$\gamma_{Rd} = \frac{R_{d,0.95}}{R_{d,d}} = \frac{R_{d,0.95}}{R_{d,0.05}} \cdot \frac{R_{d,0.05}}{R_{d,k}} \cdot \frac{R_{d,k}}{R_{d,d}} = \gamma_{sc} \cdot \gamma_{an} \cdot \gamma_{M} \quad (2)$$

whereby γ_{sc} accounts for the variability within the experimentally determined ductile capacity (statistical aspect), γ_{an} for the model bias and model uncertainty at the level of 5 %-quantile values (model bias and model uncertainty aspect), and γ_M to prevent ductile failures with nominal reliability. Inserted in Eq. (1), the design requirement acc. to the LRFD framework gives $R_{b,d} \geq \gamma_{Rd} R_{d,d}$ <=> $R_{b,d} \geq R_{d,0.95}$.

Šušteršič et al. (2011) defined γ_{Rd} as the product of two partial factors, the overdesign factor $\gamma_{od} = R_{d,d} / E_d$ (= inverse of the degree of utilisation; allows explicitly to account for higher than demanded ductile capacity, which is implicitly also considered in γ_{Rd} acc. to Mitchell et al. (2003) and Schick (2017)) and the principle overstrength factor $\gamma_{Rd} = R_{d,0.95} / R_{d,d}$, with $R_{d,0.95}$ calculated directly from experiments. In seismic design (γ_M & $k_{mod} = 1$) it simplifies to $R_{d,0.95} / R_{d,0.05}$ which corresponds to γ_{sc} of Jorissen & Fragiacomo (2011).

Schick et al. (2013) defined the overstrength factor as ratio between the 95 %-quantile value of the experimental ductile capacity and the characteristic capacity estimated from engineering models, i.e. $\gamma_{Rd} = R_{d,exp,0.95} / R_{d,mod,k}$, which, in seismic design, equals again the definition of Jorissen & Fragiacomo (2011). They also divided γ_{Rd} in three, but in comparison with Jorissen & Fragiacomo (2011), differently defined partial factors, see Figure 1 (b), which are given as

$$\gamma_{Rd} = \frac{R_{d,exp,0.95}}{R_{d,mod,k}} = \frac{R_{d,mod,mean}}{R_{d,mod,k}} \cdot \frac{R_{d,exp,mean}}{R_{d,mod,mean}} \cdot \frac{R_{d,exp,0.95}}{R_{d,exp,mean}} = \gamma_{mat} \cdot \gamma_{mech} \cdot \gamma_{0.95} \quad (3)$$

whereby γ_{mech}, as model bias, is associated with mechanical effects (e.g. friction, conservatism in design rules, differences between nominal (ordered) and delivered qualities). This definition explicitly divides R_d in two density functions, one for the engineering model f($R_{d,mod}$) and one for the experiments f($R_{d,exp}$). This allows a clear definition of all measures contributing to γ_{Rd}, the model bias, model uncertainties and additional

variabilities coming from, for example, differences between samples, batches and producers.

For the second group (ii), the works of Deam (1996), Brühl et al. (2014), Schick (2017) and Aloisio et al. (2023; 2024) must be named.

Like Deam (1996) also Brühl et al. (2014) and later Brühl & Kuhlmann (2017) and Brühl (2020) deduced γ_{Rd} from structural reliability analyses with $g(\boldsymbol{X}) = R_b - \gamma_{Rd} R_d$ as limit state function, by treating R_d as action and R_b as resistance. Brühl et al. (2014) stressed the need to consider variabilities in both capacities as well as their possible correlation. This formulation has the advantage that γ_{Rd} is not only linked with the ductile capacity; however, there is still no proof that $p_f(R_b) << p_f(R_d)$. Anyway, Brühl et al. (2014) recommended to set the safety margin between R_b and R_d in relation to the consequence classes in EN 1990 (2010).

Schick (2017) and Seim & Schick (2018) defined γ_{Rd} again within the structural reliability framework by setting $p_{f,Rd} = 0.04$ ($\beta_{Rd} = 1.75$) in reference to the NZS 4203 (1992). The design point is then calculated acc. to $R_{b,d} = R_{d,d} <=> R_{b,mean} - \alpha_b \beta_{Rd} \sigma_b = R_{d,mean} + \alpha_d \beta_{Rd} \sigma_d$, with $g(\boldsymbol{X}) = R_b - R_d = 0$ and $p_{f,Rd} = P(g(\boldsymbol{X}) \leq 0)$, with α_b and α_d as sensitivity factors and σ_b and σ_d as standard deviations, respectively, for the brittle and ductile load-bearing capacities. The overstrength factor γ_{Rd} is defined as product of two partial factors γ^*_{Rd} and γ^*_m given as

$$\gamma_{Rd} = \gamma^*_{Rd} \cdot \gamma^*_m = \frac{R_{d,mean} + \alpha_d \beta_{Rd} \sigma_d}{R_{d,k}} \cdot \frac{R_{b,k}}{R_{b,mean} - \alpha_b \beta_{Rd} \sigma_b} \quad (4)$$

A similar approach was applied in Aloisio et al. (2023, 2024), who focused especially on separating bias and uncertainty in estimating the ductile capacity in aleatoric and epistemic parts.

To summarise in brief, overstrength definitions acc. to Mitchell et al. (2003), Jorissen & Fragiacomo (2011), Šušteršič et al. (2011) and Schick et al. (2013), group (i), use the LRFD framework and concentrate only on the ductile load-bearing capacity. They define γ_{Rd} as ratio between the 95 %-quantile value from experiments and the characteristic value of the ductile capacity as used in the design, so that a brittle failure prior to a ductile failure becomes unlikely. Any interactions between R_d and R_b as well as R_b and E remain unconsidered. Deam (1996), Brühl et al. (2014) and Schick (2017), group (ii), deduce the overstrength factor from structural reliability analyses on component level, with R_d as action and R_b as resistance. This allows to consider the distributions and moments of them, however, the interaction of R_b and E again remains uncontrolled. Furthermore, the presented overstrength concepts are usually formulated for specific limit states. An operational definition of overstrength which allows to apply the concept on a more general basis is still missing.

2.2 Formulation of a new concept of overstrength

Current definitions of overstrength directly / indirectly check the failure probability of the ductile part $p_f(R_d)$ and assume that placing the density function $f(R_b)$ right to $f(R_d)$

guarantees $p_f(R_b \mid E) < p_f(R_d \mid E)$, but this is not always the case, as exemplarily demonstrated in Brandner & Azinović (2025). Acc. to the presented outcomes, it is neither sufficient to set overstrength requirements by sole discussion of variability, bias and uncertainty of R_d nor by structural reliability component analysis with R_d and R_b, respectively, as action and resistance. This becomes obvious in case of $\mathrm{CoV}[R_d] << \mathrm{CoV}[R_b]$, a typical circumstance in timber engineering where ductility usually needs to be realised in steel (metal) parts, such as dowel-type fasteners and fittings, which usually feature much lower variabilities in its properties than timber products. However, it depends also on the statistical distribution models chosen for representing the action E as well the resistances R_b and R_d, especially on the tail characteristics of the distribution models, i.e. the upper tail of E and the lower tails of R_d and R_b.

To meet the target failure hierarchy that ductile prior brittle capacities are reached with set reliability and along the whole structural hierarchies (from the hierarchy of structural components, fastener and joints up to the hierarchy of the overall construction), the interactions of R_d and R_b with the action(s) E need to be considered. To account for this, a new definition of overstrength was defined within the framework of structural reliability system analysis, as published in Brandner & Azinović (2025). This approach, although deduced from structural reliability analyses at system level, is still formulated at component level. Conditioning that $p_f(R_d) = p_{f,d} \leq p_{f,0}$, with $p_{f,0}$ as the target (nominal) failure probability (e.g. $p_{f,0} = 10^{-6}$ acc. to Eurocode 0 (2010)), is ensured by the limit state function $g(\boldsymbol{X_1}) = (R_d / E) = 1.00$, with failure probability $P(g(\boldsymbol{X_1}) \leq 1.00) = P(R_d / E \leq 1.00) = p_{f,d} \leq p_{f,0}$, a second limit state function $g(\boldsymbol{X_2}) = (R_b / E) = 1.00$ is defined, with $P(g(\boldsymbol{X_2}) \leq 1.00) = P(R_b / E \leq 1.00) \leq p_{f,d}\, p_{f,Rd}$, with $p_{f,Rd}$ as probability to observe brittle before ductile failure. In doing so, the failure probability for the brittle component $p_f(R_b) = p_{f,b}$ has to fulfil $p_{f,b} \leq p_{f,d}\, p_{f,Rd}$, or in the limit case with $p_{f,d} = p_{f,0}$, the additional safety for brittle capacity is directly multiplied by the target probability required for the ductile capacity. With $p_{f,0} = 10^{-6}$ and $p_{f,Rd} = \{10^{-1}; 10^{-2}\}$, for example, the probability of brittle failures would become $p_{f,b} \leq \{10^{-7}; 10^{-8}\}$.

This new approach is a logical consequence of structural reliability system analyses of the serial chain of ductile and brittle failure modes. Piluso et al. (2019) and Maglio et al. (2024), for example, conducted parameter studies analysing the reliability of moment-resisting steel frames following the principles of the theory of plastic mechanism control in a probabilistic setting. By defining the global failure as the design target which has to be reached, e.g. in 95 % of the cases before other local failures, overstrength factors were calculated for different variabilities of yield strength as measures of aleatoric uncertainty. However, such analyses are scarce and the authors are not aware of comparable studies in timber engineering which, in contrast to steel structures, have to cope with much larger epistemic and aleatoric uncertainties.

2.3 Benchmark of the new concept with current approaches

A sort of a benchmark on a theoretical level of the new concept with current approaches was presented in Brandner & Azinović (2025). Two cases with different combinations of statistical distribution models for the action E, the ductile R_d and the brittle resistance R_b were analysed: Case (i) $\{E; R_d; R_b\}$ ~ Lognormal (LN) and Case (ii) E ~ Extreme Value type I (EV-I; Gumbel), R_d ~ Normal (N) and R_b ~ Weibull (W). The following variabilities were defined for the benchmark study: CoV[E] = 30 %, CoV[R_d] = 5–15 % and CoV[R_b] = 15–30 %. The influence of the parameters was investigated using structural reliability analysis at the component level, which means that there is only one action (one exposure scenario) and one resistance, either ductile or brittle. As will be discussed later, typical ULS scenarios usually have a range of different actions and resistances, which then require system reliability analyses.

In Case (i) (all variables distributed lognormally), only the newly proposed approach maintained a consistent reliability ratio between R_b and R_d, expressed by β_b / β_d. Depending on the ratio between CoV[R_b] and CoV[R_d] existing approaches sometimes resulted in overly conservative designs or even reliabilities below target levels. The back calculated overstrength factors γ_{Rd} which correspond to the LRFD framework differed between the new and existing approaches by up to approximately 35 %, ranging from approximately 1.0 to 1.7. In Case (ii) (mixed EV-I, N and W distributions), the newly proposed approach again ensured a constant β_b / β_d ratio, unlike existing approaches. When CoV[R_b] > CoV[R_d] the existing approaches failed to maintain ductile failure precedence. The differences between approaches are larger in Case (ii) where extremely high compensations were necessary, with overstrength factors up to ten times higher than for Case (i) demonstrating that both the variabilities and the chosen statistical distribution models strongly influence structural reliability and γ_{Rd}. The overstrength factors γ_{Rd} appeared to be extremely sensitive, ranging from approximately 0.9 to 20.0. Overall, this underlines the necessity of implementing the newly formulated approach in order to agree on the extra safety margin for brittle failures and the need for comprehensive structural reliability analyses so as to calibrate the overstrength factors accordingly to make them available for design processes within the LRFD framework.

3 Parameter study

3.1 Review on representative statistical distribution models for actions and resistances and corresponding variabilities

The decision on a statistical distribution model for representing a random variable must be made with great care and with an awareness of the fact that it might have a significant influence on the calculated probability of failure, therefore also to the calculation of the overstrength factors. Evaluation standards such as EN 14358 (2016) and ISO 12491 (1997) provide rules for common statistical distribution models but leave the choice to the user. In contrast, EN 1990 (2010) contains some recommendations for statistical distribution models, while PMC of JCSS (2001) gives more information

and detailed recommendations for statistical distribution models for a large number of action and resistance random variables.

As shown in Brandner & Azinović (2025) the statistical distribution models used to represent the action E as well the resistances R_b and R_d, can have a major influence on the calculation of overstrength, the extent of which is also shown in Section 2.3. In order to create a realistic background for the overstrength calculation with the proposed approach, it is important to use realistic parameter settings. The following bullet points provide an overview of the recommended distribution models F(X) and, if available, the typical variabilities for actions and resistances, expressed as coefficients of variation (CoV[X]), that are relevant to the topic of this paper:

- **Permanent loads:** F(X) ~ N, CoV[X] 5–10 % (Schneider & Schlatter (1996); JCSS (2001); EN 1990 (2010); ISO 2394 (2015))
- **Variable loads:** F(X) ~ {EV-I; LN; N}, CoV[X] = 15–50 % or higher (Schneider & Schlatter (1996); EN 1990 (2010); ISO 2394 (2015))
- **Snow load:** F(X) ~ {EV-I; EV-II (Fréchet)} (Schneider & Schlatter (1996); JCSS (2001))
- **Wind velocity:** F(X) ~ W ($X_{10',mean}$), CoV[X] = 20–30 %; F(X) ~ EV-I ($X_{10',mean,max}$), CoV[X] = 25–40 %; F(X) ~ EV-I (peak velocity), CoV[X] = 10 % [JCSS (2001)]
- **Spectral acceleration:** F(X) ~ LN, CoV[X] = 50–60 % or higher [Abrahamson & Silva (1997); EN 1998 (2005)]

- **Material props./resistances/model uncertainties:** F(X) ~ {LN; N; W} (EN 1990 (2010))
- **Material strengths:** F(X) ~ {N (ductile); LN (multiplicative); W (brittle)} (Sørensen (2004))
- **Structural steel:** F(X) ~ LN, CoV[X] = 4–7 % (JCSS (2001))
- **Reinforcing steel:** F(X) ~ N, CoV[X] = 5 % (JCSS (2001); ISO 2394 (2015))
- **Concrete:** F(X) ~ LN, CoV[X] = 6 % (compr.); F(X) ~ LN, CoV[X] = 30 % (tens.); F(X) ~ LN, CoV[X] = 15 % (MOE) (JCSS (2001))
- **Structural timber:** F(X) ~ N (compr. perp.; density), CoV[X] = 10 %; F(X) ~ W (tens. perp.), CoV[X] = 25 %; F(X) ~ LN (bending; shear), CoV[X] = 25 %; F(X) ~ LN (tension par.), CoV[X] = 30 %; F(X) ~ LN (compr. par.), CoV[X] = 20 %; F(X) ~ LN (elastic prop.), CoV[X] = 13 % (JCSS (2001))
- **Glulam:** F(X) ~ LN (bending strength), CoV[X] = 15 % (JCSS (2001))

- **Fatigue analysis:** F(X) ~ {N; LN; W} (Sørensen (2004))
- **Model uncertainties (general):** F(X) ~ {LN; N}, CoV[X] = 3–15 % (ISO 2394 (2015))
- **Model uncertainties (specific):** F(X) ~ LN (M & V in frames), CoV[X] = 10 %; F(X) ~ LN (steel bend. & shear), CoV[X] = 5 %; F(X) ~ LN (steel welded conn.), CoV[X] = 15 %, bias 1.15; F(X) ~ LN (steel bolted conn.), CoV[X] = 15 %, bias 1.25 (JCSS (2001))

3.2 Setting of analysed cases and applied methods

In exemplifying code calibration for structural timber, Kohler & Fink (2015) treated the resistance (CoV depending on the specific resistance variable) and model uncertainty (CoV 10 %) as lognormal variables, permanent loads as normal (CoV 10 %) and variable loads as Gumbel (EV-I) variables (CoV 40 %). Furthermore, for timber structures typical / meaningful ratios of permanent to total loads, given as $\alpha = G / (G+Q)$, were identified within 0.1 and 0.8. Kohler & Fink (2015) covered different design situations (i.e. different α_i values) by aligning to the target probability $p_{f,i} = P\{g_i(X, \hat{R}, \hat{G}, \hat{Q})\} < 0$ and by considering the following limit state equation

$$g_i(X, \hat{R}, \hat{G}, \hat{Q}) = z_i^* X\hat{R} - \alpha_i \hat{G} - (1-\alpha_i)\hat{Q} = 0 \quad (5)$$

where z_i^* are calibrated design solutions with an acceptable failure probability $p_{f,i}$, $\hat{R}$, $\hat{G}$ and $\hat{Q}$ are resistance and loads represented as random variables and normalised to a mean value of 1 and X is the model uncertainty. In this paper, Eq. (5) was used to calculate the optimal z_i^* value for designing the ductile and brittle parts to the selected target probability values of $p_{f,d} \leq 10^{-6}$ and $p_{f,b} \leq \{10^{-7}; 10^{-8}\}$.

Based on own experience in statistical analysis of experimental data and for simplification, it is suggested to represent strength, elastic properties and density of timber and timber products generally as lognormal random variables; cf. Brandner (2013). This is also true for tension perpendicular to the grain as well as compression parallel to the grain where JCSS (2001) gives also other recommendations. In general, it needs to be outlined that timber, as hierarchically organised natural material, is characterizable by quasi-brittle to ductile failure behaviour, far from ideal brittle as it is fundamental for the Weibull theory of materials; cf. Weibull (1939).

The calculation of the optimal z_i^* values in the parameter study was performed in Wolfram Mathematica v11.2 with a root-finding loop function via numerical integration for estimating the failure probability. The loop function calls calculation of failure probability while adjusting the statistical distribution parameters to find where the failure probability matches the selected target. The root-finding function uses Newton-Raphson or a hybrid secant method. The numerical integration used in Mathematica v11.2 uses adaptive numerical quadrature for simple regions, while it switches to Monte Carlo sampling for complex conditions. The overstrength factors are finally calculated by defining the quantile ratio $\gamma_{Rd} = R_{b,0.05} / R_{d,0.05}$, therefore transferring the outcomes from structural reliability analyses to the LRFD framework. The quantile values are computed analytically.

For the parameter study key sources of uncertainty and the loading ratio α where varied in the structural reliability model. Table 1 shows the analysed key parameters, which were combined to analyse altogether 60 different cases. For each case, the solution was sought by either considering the modelling uncertainties or without modelling uncertainties as well as for two different target probabilities for the brittle part (i.e.

$p_{f,b} \leq \{10^{-7}; 10^{-8}\}$). Therefore, four different solutions were calculated for each case: (i) $\gamma_{Rd,with\ X} | p_{f,b} = 10^{-7}$; (ii) $\gamma_{Rd,without\ X} | p_{f,b} = 10^{-7}$; (iii) $\gamma_{Rd,with\ X} | p_{f,b} = 10^{-8}$ and (iv) $\gamma_{Rd,without\ X} | p_{f,b} = 10^{-8}$. For the reference case the underlined parameters were selected. The model uncertainty for the brittle part (X_b) was considered as a lognormal random variable with CoV[X_b] = 10 % and a mean value of 1.0 and was not varied in this study.

This systematic variation of parameters enabled to analyse how the selected factors affect the calculated reliability for ductile and brittle failures and consequently the calculation of the required overstrength.

Table 1. Parameters and their settings as analysed by the parameter study.

parameter	variation (reference setting underlined)
CoV[G] (abbrev. "VG"); G ~ N	{<u>5</u>; 10} %
CoV[Q] (abbrev. "VQ"); Q ~ EV-I	{20; <u>30</u>; 40} %
$\alpha = G / (G + Q)$	{0.10; 0.50; <u>0.80</u>}
CoV[R_d] (abbrev. "VRd"); R_d ~ LN	{<u>5</u>; 10; 15} %
E[X_d] | CoV[X_d] = 10 % (abbrev. "Xdm"); X_d ~ LN	{<u>1.00</u>; 1.15; 1.30}
CoV[R_b] (abbrev. "VRb"); R_b ~ LN	{10; 15; 20; <u>25</u>; 30; 35} %

3.3 Results and discussion of the outcomes from the parameter study

Overstrength factors calculated from simple structural reliability analyses are presented in Figure 2. The graph shows the calculated overstrength factor variation (vertical axis) across different parameter studies (horizontal axis). The horizontal axis is divided into blocks with a different colour indicating a group of which parameters are varied — from a reference case through variations in CoV[G], CoV[Q], CoV[R_d], CoV[R_b], mean value of X_d, α and combinations of these. Different lines compare how the results change under different target failure probabilities for the brittle part ($p_{f,b} = 10^{-7}$ and 10^{-8}) and whether the modelling uncertainties of the ductile (X_d) and brittle part (X_b) are included or not.

The conclusions and observations drawn from the analysed cases are summarized in the following bullet points:

- A higher variation of G (case 2) had no influence on γ_{Rd}, as it is still much smaller than the variation of Q.
- Looking at cases {3; 4} compared to case 1, the consideration of the model bias E[X_d] > 1.00 had no effect on γ_{Rd}; this is because it was directly compensated by higher z_d-values. In common design practice, the bias coming from the models used to estimate the characteristic properties and/or from differences between the ordered and delivered product quality may not be directly taken into account; in such cases, the bias can be defined as a multiplication factor γ_{bias} applied directly to the overstrength factor, i.e. $\gamma_{bias} \cdot \gamma_{Rd}$.

- By setting the resistance part as default and just varying α and CoV[Q], it turns out that γ_{Rd} increases with increasing α and decreasing CoV[Q], i.e. in the cases analysed it is maximum at α = 0.8 and CoV[Q] = 20 %. The Increase in γ_{Rd} with increasing α is due to the circumstance that the variation of the action is decreasing but still contains a specific share of the highly variable component of the variable loads Q. Higher γ_{Rd} values at lower CoV[Q] can be explained by the fact that in these cases the distance from f(R_d) to f(E), with f(R_d) and f(E), as density functions of the ductile resistance and the action, is rather small as both have quite small variations. However, since the variation of R_b is much larger (CoV[R_b] = 25 %) compared to CoV[R_d] = 5 %, f(R_b) must lie further to the right, which leads to higher γ_{Rd} values.
- The consideration of the model uncertainty, expressed by the random variables X_d and X_b, as multipliers for the ductile and brittle resistances, leads to greater overall variability of both resistances. However, as the uncertainty is similar for both resistance parts, the effect on the overstrength factor is small. The ratio $\gamma_{Rd,without\ X}$ / $\gamma_{Rd,with\ X}$ is on average close to one (0.99 for $p_{f,b} = 10^{-7}$ and 0.98 for $p_{f,b} = 10^{-8}$) and within a range of 0.95 to 1.04. In this context it should be noted that the estimated γ_{Rd} values are also subject to some uncertainty due to the applied structural reliability approach. Nevertheless, ratios above 1.00 have in common α = 0.8, CoV[R_d] = {10; 15} % and COV[R_b] = {25; 30; 35} %, i.e. a high proportion of the permanent to total load in combination with variations of the resistances in the upper range.
- The analysis of different combinations of CoV[R_d] = {5; 10; 15} % and CoV[R_b] = {10; 15; ...; 35} % shows that the overstrength factor increases with increasing CoV[R_b] and decreasing CoV[R_d], i.e. the greater the difference between the variation of the ductile and the brittle part, the higher γ_{Rd}. However, it is also shown (case 17) that the new approach used to calculate the overstrength factor based on simple reliability analyses enables even overstrength factors < 1.00 when CoV[R_b] < CoV[R_d].
- In the last block of results (cases 33 to 60), different settings for CoV[Q], α, CoV[R_d] and CoV[R_b] were analysed. Apart from cases {53; 54} and {57; 58}, with CoV[R_d] = CoV[R_b] = 15 %, the γ_{Rd}-values for CoV[Q] = 20 % are higher than for CoV[Q] = 40 %. The reason for this has already been mentioned: < CoV[Q] consequence in a small distance between f(Q) and f(R_d) to fulfill the target failure probability of $p_{f,0} = p_{f,d} = 10^{-6}$. Because of CoV[$R_b$] > CoV[$R_d$], f($R_b$) must lie further to the right in order to also fulfill $p_{f,b} = 10^{-7}$ or 10^{-8}. This circumstance is compensated for when CoV[R_d] = CoV[R_b]. The worst combination, i.e. the settings that lead to the highest overstrength factors, is therefore an action dominated by permanent load (>> α) with small CoV[Q] (overall small CoV[E]) and CoV[R_d] << CoV[R_b].
- The overstrength factors for $p_{f,b} = 10^{-8}$ are on average 1.14-times higher than for $p_{f,b} = 10^{-7}$ (range 1.08 to 1.22). The lower values are for cases with α = 0.8 and CoV[R_b] in the lower range of {10; 15} %, whereas in the upper range the cases feature α = 0.1 and CoV[R_b] = {25; 35} %.

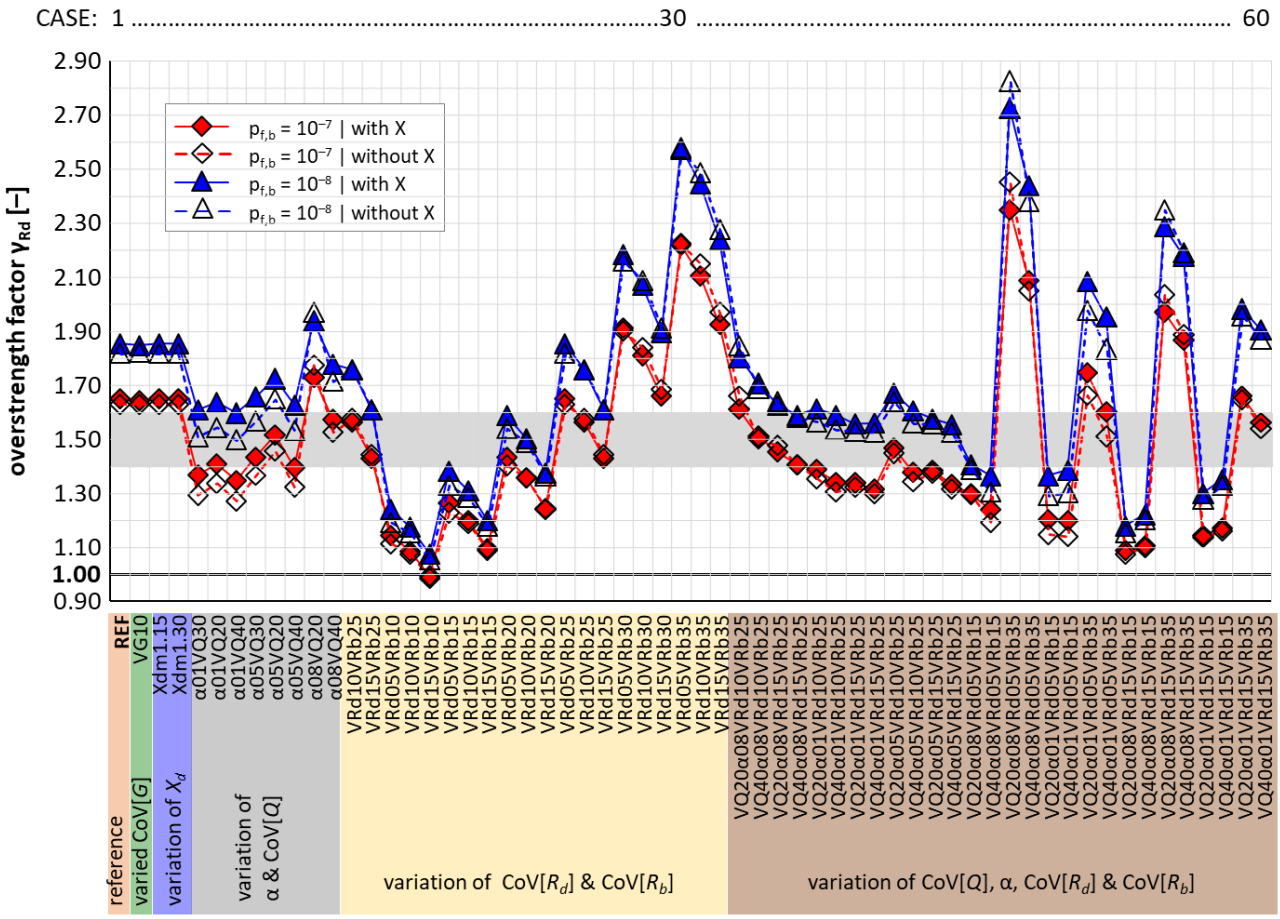

Figure 2. Overstrength factors based on simple structural reliability analyses for two different settings of the target failure probability of the brittle part ($p_{f,b} = 10^{-7}$ & 10^{-8}) and with / without consideration of the model uncertainty of the ductile(X_d) and brittle part (X_b).

4 Proposal for the regulation of overstrength factors

The need to implement the newly formulated approach to determine the overstrength factor in a way to achieve the additional safety margin and to avoid brittle failure has been emphasized in the previous chapters. In order to achieve the objective and identify possible future regulations for the overstrength factor, the results of the structural reliability analyses were transferred to the LRFD framework. Going one step further, the overstrength factors should depend on (groups of) resistances and ratios between coefficients of variation (uncertainties) of R_b and R_d to define a meaningful design proposal. Furthermore, this study highlights the importance of accounting for ductility and overstrength not just in accidental loading situations but also as a general consideration for characteristic load scenarios.

In standard design practice, the LRFD framework relies on characteristic load and resistance values, while expected values, typical coefficients of variation and statistical distribution models are usually not provided in conventional (timber) codes. To ensure the target safety / reliability levels, adjustment factors are provided to transform

characteristics properties into design properties, such as partial safety factors, material specific modification factors and others. For ease-of-use all these rules are based on a simplified and often uniform framework and overall conservatism. Therefore, it does not make sense to consider the above results from a simple reliability analysis directly in an LRFD framework. Simplifications and regulations on a conservative basis are again sought when transferring the results.

One of the first decisions to be made concerns the amount of additional safety to prevent brittle prior ductile failures. In the structural reliability analyses provided in this paper, two cases were analysed, $p_{f,b} = 10^{-7}$ and 10^{-8}, i.e. $p_{f,Rd} = 10^{-1}$ and 10^{-2}. NZS 4203 (1992), meanwhile replaced by NZS 1170.5 (2004), regulates $p_{f,Rd} = 0.04$ (permissible range 0.023–0.067) which lies in-between the analysed values in this paper. As the variabilities in timber strength properties are usually higher than for steel, $p_{f,Rd}$ in the range of 1–5 % seems to be a meaningful basis for discussion.

In addition, the regulation of overstrength factors in classes could be a simple and easily applicable approach. A corresponding proposal can be found in Table 2. The classes are defined depending on the main influencing parameter, CoV[R_b].

Table 2. Proposal for a classification of overstrength factors to be applied within the LRFD framework.

γ_{Rd} | $p_{f,Rd}$ = {0.10; 0.01}	CoV[R_b]* [%]	examples
	{< 10}	specific cases**
{1.40; 1.60}	{10 – 20}	strength graded structural timber (compression perp.) structural timber products {glulam; CLT; LVL} (strength properties) embedment strength; withdrawal strength; head pull-through strength
{1.65; 1.85}	{20 – 25}	strength graded structural timber (compression parallel) block shear; splitting; plug shear
{2.45; 2.85}	{25 – 35}	strength graded structural timber (bending; tension parallel & tension perp.)

*the CoV[R_b] here refers to the coefficient of variation of the undesired failure mode

**beneficiary low overstrength factors are possible to determine by means of structural reliability analysis

The maximum overstrength factors defined in Table 2 are exceeded in only one of the 60 cases analysed, as shown in Figure 2, which is not unrealistic in principle, i.e. practicably possible, but clearly a rare case. However, it should be noted that the presented

classification applies only to strength graded and classified timber and timber products and that the highest CoV[R_b] considered in the analysis was relatively high (35 %).

In addition to the overstrength factor in Table 2, material partial safety factors, modification factors, etc. must be taken into account for characteristic load scenarios. In general, any bias in respect to applied engineering models and bias caused by differences between ordered and delivered material quality, as often reported for steel dowel-type fasteners and fittings, especially for the lower steel classes, have to be considered too (cf. Gündel (2020)). As a result, the design value of the brittle, non-ductile part(s) need to fulfil Eq. (6).

$$R_{b,d} = R_{b,k}\frac{k_{mod,b}}{\gamma_{M,b}} \geq R_{d,d} \cdot \gamma_{Rd} \cdot \gamma_{bias} = R_{d,k}\frac{k_{mod,d}}{\gamma_{M,d}} \cdot \gamma_{Rd} \cdot \gamma_{bias} \quad (6)$$

To put the proposed overstrength classes into perspective, the values from Table 2 could be compared to the overstrength values defined by current LRFD approaches and reported in the literature. A short literature review of approximately 10 research campaigns on connections defining overstrength factors by existing LRFD approaches can be found in Ottenhaus et al. (2020). It is reported that overstrength factors for timber connections generally range from about 1.0 to 2.5, with isolated extreme cases exceeding 4.0, depending on the connection type, material, and loading direction. These published values are approximately in the range of the proposed overstrength classes, however, it needs to be noted that the values in Table 2 are without considering any bias. Further analyses should therefore be performed to define the influence of bias on the reserve capacity in timber joints.

A sort of a first estimation on the bias from the delivered steel material can be found in Ottenhaus et al. (2020), where accidental overstrength, γ_{err}, is discussed, which is introduced when materials with higher than specified (ordered) grades are supplied. In practice, this mistake often goes unnoticed since high strength steel is visually not different from mild steel and the error would only be discovered through experimental testing. Installation of the higher strength material can lead to unsafe (seismic) design since the connection may now no longer be the weakest link in the strength hierarchy. An example of large-scale hold-downs with dowels was presented and where γ_{err} reached up to 1.17. Similarly, in Blaß & Colling (2015) the dowel bending and tensile tests also revealed that actual steel strength values often show significant overstrength. Blaß & Colling (2015) showed that doweled timber connections often exceed design predictions, partly due to the inherent bias from the delivered mild steel dowels, although this is not explicitly stated.

5 Conclusions

This study reviews the existing definitions of overstrength in timber construction and shows that the current design approaches cannot always ensure a clear hierarchy between ductile and brittle failure modes. For this reason, a new reliability-based approach is proposed that explicitly takes into account the statistical distribution models and the coefficient of variations of actions and resistances. A target additional safety for brittle failure is maintained by explicit control of the ratio between the probabilities for ductile and brittle failures, thus maintaining the intended failure hierarchy.

The most important results of the study are presented in the following points:

- Firstly, the findings from Brandner & Azinović 2025 were summarised, which illustrate that conventional LRFD-based overstrength factors may be insufficient, especially when the coefficient of variation for the brittle capacity significantly exceeds that for the ductile capacity. For example, for CoV[R_b] = 30 % and CoV[R_d] = 5 %, the required overstrength factor calculated by structural reliability approach, which is back calculated to the LRFD framework, can exceed $\gamma_{Rd} > 10$, while conventional approaches would imply values closer to 1.5–2.0. Such high differences between the approaches were found when an unfavourable but still possible combination of recommended statistical distribution models (E ~ EV-I, R_d ~ N and R_b ~ W) occured.
- In Brandner and Azinović (2025), the parameter study is based on a single action (one exposure scenario) and one resistance type at the component level, whereas in this paper, the parameter study extends this by considering a combination of actions (i.e. G & Q), for a more realistic mapping of typical ULS scenarios.
- To ensure realistic, meaningful and practically relevant input data for the parameter study, a review on recommended statistical distribution models and typical CoV values for representing the random variables was carried out, since this information strongly influences the calculated overstrength factors from the proposed approach.
- The parameter study has shown that different settings for the permanent and variable loads and resistances, in particular their coefficients of variation, strongly influence the calculated overstrength factor. It was shown that the highest overstrength factors result when the permanent action dominates (high α) in combination with a low CoV[Q] and CoV[R_b] >> CoV[R_d]. This is because a small CoV[E] narrows the distance between the position of the statistical distributions of load and ductile resistance and pushes f(R_b) of the brittle resistance further to the right to maintain the target reliabilities and intended failure hierarchy.
- Practical recommendations for the classification of overstrength factors according to the variability of brittle components are given to assist designers in choosing appropriate values for realistic design scenarios. The classification of overstrength factors should at least consider the variability of the brittle components, as dominating

parameter. It is discussed that a target reliability for not observing brittle prior ductile failures should be agreed in the course of standardization. For timber structures, the probability of brittle prior ductile failures $p_{f,Rd}$ in the range of 1–5 % appears appropriate as the strength is more variable compared to steel.

- The proposed overstrength classes for a target probability $p_{f,Rd} = 10^{-1}$ range from 1.4 to 2.45. For materials and failure modes with lower scatter, such as strength properties of strength-graded structural timber in compression perpendicular to the grain, glulam, CLT, LVL, or basic connection properties (embedment; withdrawal; head pull-through), CoV[R_b] typically ranges from 10–20 %, giving a $\gamma_{Rd} = 1.4$. For strength-graded structural timber in compression parallel to the grain and for brittle joint failure modes such as block shear, splitting and plug shear, a moderate CoV[R_b] of 20–25 % suggests $\gamma_{Rd} = 1.65$. For high-scatter failure modes like bending or tension parallel or perpendicular to the grain in strength-graded structural timber, where CoV[R_b] can be 25–35 %, the required overstrength factor rises to $\gamma_{Rd} = 2.45$. For $p_{f,Rd} = 10^{-2}$ and for the same classes, $\gamma_{Rd} = \{1.60; 1.85; 2.85\}$ are proposed.
- In addition to the calculated overstrength factors, the approach in the paper is supplemented by proposing an additional bias factor γ_{bias} to account for deviations in delivered to ordered material quality (quality bias) and tested to calculated properties, latter based on engineering models (model bias), which both can significantly affect the brittle and the ductile resistance. By incorporating this additional bias factor γ_{bias} as multiplier, the overstrength factors could increase, ensuring that the intended failure hierarchy is maintained. Anyway, quality bias could be prevented if adequate quality assurance methods are applied.
- Finally, the proposed overstrength classes (without quality and model bias) were compared to LRFD-based overstrength factors determined from tests on timber connections and reported in the literature. It was shown that the values are in a similar range.

As part of future work, it is recommended to extend the considerations on ductility and overstrength beyond the scenarios for accidental to characteristic load scenarios to ensure the design of safe and robust timber structures in practice in a more general perspective. In addition, to validate the new approach, it would be necessary to generate a broader and more comprehensive set of international test data on fasteners and joints, including full background information such as test setups and load-displacement curves. Another important aspect is that joints and connections feature a number of different failure modes which, modelled as a system, all are probable to a specific level. To make the analyses presented herein more realistic this aspect needs to be taken into account and the component-wise analysis extended to system reliability analyses. In respect to the quality and model bias, which both can significantly and additionally contribute to the overall multiplier on the ductile resistance, on the one hand the establishment of adequate quality assurance measures is highly recommended (can be considered by simply adjusting γ_{bias}).

6 Acknowledgements

The financial support in the framework of the FFG BRIDGE 1 research project “CLT_joint” (No. 883672) by the Austrian Research Promotion Agency (FFG), Schmid Schrauben Hainfeld GmbH and Technowood AG is thankfully acknowledged. The financial support received from the Slovenian Research Agency (Research Core Funding No. P4-0430 and Research Project No. N2-0280) is also gratefully acknowledged. Furthermore, this article is also partly based upon the work from COST Action HELEN CA20139, supported by COST (European Cooperation in Science and Technology).

7 References

Abrahamson NA, Silva WJ (1997) Empirical response spectral attenuation relations for shallow crustal earthquakes. Seismological research letters, 68(1), 94-127.

Aloisio A et al (2023) Overstrength of CLT-to-CLT connections with inclined screws. INTER/56-7-3, Biel, Switzerland.

Blass HJ, Colling F (2015) Load carrying capacity of dowelled connections. International Network on Timber Engineering Research, INTER/48-07-03, Šibenik, Croatia.

Brandner R (2013) Stochastic System Actions and Effects in Engineered Timber Products and Structures. In: Schickhofer G, Brandner R (eds.) Timber Engineering & Technology, Vol. 2, Monographic Series TU Graz, Verlag der Technischen Universität Graz, ISBN 978-3-85125-263-7.

Brandner R, Azinović B (2025) Overstrength in timber engineering: General discussion and proposal for a more reliable and broader application. Engineering Structures, 340, 120739.

Brühl F, Schänzlin J, Kuhlmann U (2014) Ductility in timber structures: investigations on over-strength factors. In: S Aicher et al. (eds.) Materials and Joints in Timber Structures, RILEM Bookseries 9.

Deam BL (1996) The seismic design and behaviour of multi-storey plywood sheated timber-framed shearwalls. PhD Thesis, University of Canterbury, Christchurch, New Zealand.

Eurocode 0 (2010). *Basis of structural design*. EN 1990. Brussels, Belgium: European Committee for Standardization.

Eurocode 8 (2005). *Design of structures for earthquake resistance - Part 1: General rules, seismic actions and rules for buildings*. EN 1998-1. Brussels, Belgium: European Committee for Standardization.

EN 14358 (2016) *Timber structures – Calculation and verification of characteristic values*. Brussels, Belgium: European Committee for Standardization.

Gündel M (2020) Determining the overstrength factor based on statistical values of European steel grades. *Civil Engineering Design*, 2:20–28.

ISO 12491 (1997) *Statistical methods for quality control of building materials and components*. ISO.

ISO 2394 (2015) *General principles on reliability for structures*. ISO.

JCSS (2001) *Probabilistic model code. Joint committee on structural safety*, ISBN 978-3-909386-79-6, https://www.jcss-lc.org/jcss-probabilistic-model-code/.

Jorissen A, Fragiacomo M (2011) General notes on ductility in timber structures. Engineering Structures, 33(11), 2987–2997.

Kohler J, Fink G (2015) Aspect of code based design of timber structures. 12th In. Conf. On Applications of Statistics and Probability in Civil Engineering (ICASP12), Vancouver, Canada.

Mitchell D, Tremplay R, Karacabeyli E, Paultre P, Saatcioglu M, Anderson DL (2003) Seismic force modification factors for the proposed 2005 edition of the National Building Code of Canada. Canadian Journal of Civil Engineering, 30:308–327.

NZS 4203 (1992) *Code of Practice for General Structural Design and Design Loadings for Buildings*. Standards New Zealand.

NZS 1170.5 (2004) *Structural design actions – Part 5: Earthquake actions – New Zealand*. Standards New Zealand.

Ottenhaus LM, Li M, Smith T (2022) Analytical derivation and experimental verification of overstrength factors of dowel-type timber connections for capacity design. Journal of Earthquake Engineering, 26(6), 2970-2984.

Schick M (2017) Probabilistische Untersuchungen zu Überfestigkeiten von genagelten Wandelementen in Holztafel-bauweise. Schriftenreihe Bauwerkserhaltung und Holzbau, Heft 9, Universität Kassel.

Schick M, Vogt T, Seim W (2013) Connections and anchoring for wall and slab elements in seismic design. Meeting No. 46 of CIB Working Commission W18-Timber Structures, Vancouver, Canada.

Schneider J, Schlatter HP (1996) Sicherheit und Zuverlässigkeit im Bauwesen: Grundwissen für Ingenieure. 2. überarb. Aufl., Zürich, vdf Hochschulverlag ETH Zürich, Stuttgart; Teubner, ISBN 3-519-15040 (Teubner), ISBN 3-7281-2167-3 (vdf).

Šušteršič I, Fragiacomo M, Dujič B (2011) Influence of connection properties on the ductility and seismic resistance of multi-storey cross-lam buildings. International Council for Research and Innovation in Building Construction, Working Commission W18 – Timber Structures, CIB-W18/44-15-9, Alghero, Italy.

DISCUSSION

The paper was presented by B Azinović

H Blass asked whether all properties in Table 2 are considered as brittle failure (e.g. compression perpendicular to grain failures are not brittle). B Azinovic responded that these could be considered as failure modes that one wants to protect against.

P Dietsch asked why for structural timber products such as GLT, CLT and LVL in Table 2 the γ_{Rd}-values are considered without consideration of the failure modes of the strength properties such as shear or tension perp. that one wants to protect. B Azinovic agreed that this aspect could be improved. P Dietsch suggested that maybe one should consider properties that do not benefit from protection.

JM Cabrero asked why distinguish between class 2 and class 3 materials as both are brittle failure modes. B Azinovic responded that COV are different in class 2 and class 3. They further discussed differences between shear and tension perpendicular to grain failures.

R Scotta commented about their Kyoto INTER paper in 2017 which showed the type of connection is important. He asked whether the connection type should be considered. He further pointed out the overstrength factor in Eqn. 6 should be a multiplier not divider. B Azinovic responded that he is not sure about the 2017 Kyoto paper but the concept would align with current paper. He will check about the overstrength factor.

O Sisman and B Azinovic discussed the effect on different actions considered.

S Winter commented that he did not get the α-factor and different load duration situations in relation to how the overstrength factor would be changed. B Azinovic explained that α will change the shape of the distribution. S Winter further commented that Eqn. 6 is incorrect.

S Franke commented on the overstrength factor and COV as some properties have significantly less COV than the state range in the paper. B Azinovic agreed that this could be examined further.

A Ceccotti asked for a conclusive statement. B Azinovic concluded that the overstrength factor will need to be increased for unreliable properties.

P Dietsch asked for reasoning why this paper was published in the Engineering Structures Journal first, hence beneficial comments from INTER experts are missed. B Azinovic stated that this INTER paper has additional features with the intent of another publication in another journal.

A binary visual-based classification model for grading reclaimed structural timber for reuse

Angelo Aloisio, Università degli Studi dell'Aquila, Italy

Dag Pasquale Pasca, Norsk Treteknisk Institutt, Norway

Yuri De Santis, Università degli Studi dell'Aquila, Italy

Massimo Fragiacomo, Università degli Studi dell'Aquila, Italy

Hauke Burkart, Standard Norge, Oslo

Audun Øvrum, Norsk Treteknisk Institutt, Norway

Keywords: Timber Grading , Reclaimed Timber , Classification model

1 Introduction

The demolition sector generates vast amounts of waste, including wood waste, which presents significant opportunities for reuse or recycling in structural applications (*Arbelaez* et al., 2019). The repurposing of recycled construction timber is in alignment with regulatory frameworks, such as the European Union's Circular Economy Action Plan. Additionally, the increasing cost of virgin construction timber, driven by rising demand, further underscores the importance of timber recycling. However, a primary obstacle to higher recycling rates is the absence of standardized guidelines for regrading reclaimed timber, as it often contains marks and damage from prior applications.

Assessing the mechanical performance of recovered timber presents unique challenges, as traditional Visual Strength Grading (VSG) standards were designed for new timber and do not fully account for the characteristic defects of reclaimed materials. This often results in excessive downgrading (*Cruz* et al., 2015; *Arriaga* et al., 2021). Additionally, these standards are tailored for specific species and growth regions, making them less applicable to mixed-species reclaimed timber (*Smith* & *Hicks*, 2009).

Research on the mechanical behavior of recycled timber has primarily focused on evaluating stiffness (*Osuna-Sequera* et al., 2020; *Morales-Conde* & *Machado*, 2017), density (*Osuna-Sequera* et al., 2019; *Martínez* et al., 2020; *Mariño* et al., 2002; *Acuña* et al.,

2011), and strength properties (*Llana* et al., 2023). Strength assessments have been particularly concerned with the influence of irregular cross-sections and longitudinal shrinkage fissures. However, limited research exists regarding the impact of holes on the mechanical properties of reclaimed timber (*Cavalli* et al., 2016). The pioneering study by Falk et al. (*Falk* et al., 2003) demonstrated that holes with diameters up to half the allowable knot size for the assigned strength grade could be tolerated in Douglas fir. The findings highlighted that hole positioning significantly affects strength, especially when located near the tension edge of a bending member. Similar results were obtained by Crews et al. (*Crews* & *MacKenzie*, 2008), who investigated recycled hardwoods in Australia. Their work contributed to the development of an interim industry standard that permitted holes equivalent to knot sizes within a strength grade in central board regions, with stricter limitations for holes near the edges (Forest and Wood Products Australia, FWPA (2008)).

More recent investigations have prioritized non-destructive testing (NDT) to assess capacity and degradation effects associated with timber ageing (*Llana* et al., 2023). However, these studies have largely overlooked the impact of hole-induced damage. Addressing this gap, the present work introduces a classification framework for recycled timber, explicitly considering hole distribution and characteristics from prior use.

To this end, a stochastic finite element (FE) model was developed in Abaqus to conduct stress analyses of planar beams containing randomly distributed hole patterns. Dimensionless parameters derived from these simulations enabled the development of a mechanics-based methodology to estimate bending strength reduction. The generated dataset served as input for data-driven classification models, which could be seamlessly integrated into a visual grading system for recovered timber beams. The proposed binary classification approach, validated against experimental bending tests on beams with predefined hole configurations, offers a practical method for assessing the structural suitability of recycled timber. It should be noted that the experimental campaign did not account for ageing effects on mechanical properties, as newly sourced beams were used. Instead, artificial defects (i.e., holes) were introduced to simulate prior usage conditions.

2 Problem formulation

The Norwegian proposal for reclassifying recovered timber introduces a novel classification system, the R-class, which contrasts with the conventional C-class used for new structural softwood (*prNS 3691-3:2023*, 2024). The newly defined classes—R24, R18, and R14—are directly correlated with the mechanical properties of their respective C-class counterparts. According to the standard, reclaimed structural elements originally graded as C30 can be reassigned to R24, C24 to R18, and C18 to R14. The characteristic bending strength ratio between consecutive classes is approximately 80%, which serves as the threshold for determining the reduction in bending strength capacity.

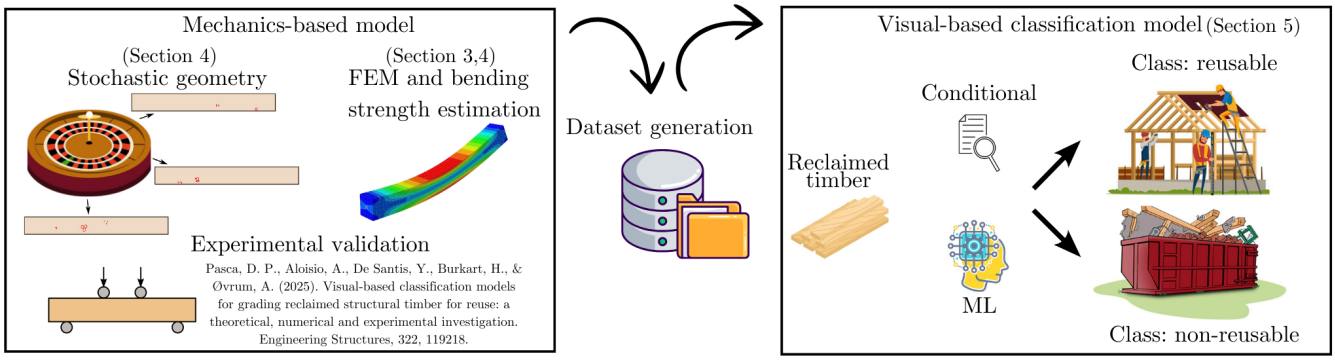

Figure 1. Illustration of the workflow of this research, starting with the mechanics-based FE model with experimental validation, used to generate a dataset for calibrating visual-based classification models of reclaimed timber, discriminating among two classes: Reusable and Non-reusable timber beams.

This study mainly focuses on developing a robust binary classification model for recovered timber beams, predicting the loss of bending capacity based on the visual assessment of artificial defects, specifically small-diameter round holes. The authors followed the subsequent logical path to achieve this, as shown in Fig. 1.

First, a stochastic finite element (FE) numerical model was developed to generate relevant configurations for training the classification model. Once the methodology was experimentally validated, as reported in (*Pasca* et al., 2025), the authors utilized Monte Carlo analysis results to predict bending strength reduction using an equivalent stress approach. Subsequently, a database was compiled, incorporating hole configurations as input and bending strength reduction as output, to develop suitable classification models. Various machine-learning classification models and simpler conditional models were compared to assess their feasibility for standard implementation in grading recovered timber.

3 Bending stregth estimation from FE model

Accurately predicting the bending capacity of timber beams containing such holes would necessitate simulating the nonlinear fracture mechanics response across numerous configurations while incorporating all potential uncertainties. Given the brittle-elastic behavior of timber under bending loads, this study proposes an alternative method that predicts the reduction in bending capacity through elastic stress analysis. This computationally efficient approach facilitates the creation of a suitable training dataset for data-driven classification models.

The classification model is built on the hypothesis that failure is linked to localized strength values around a given hole. The governing design inequalities can be formulated as:

$$\begin{cases} \sigma_{11,m} \leq f_m, \\ \sigma_{ij,h_i} \leq f_{ij}, \ \forall\{i,j\} \in \{1,2\}, \forall h_i \end{cases} \tag{1}$$

Where $\sigma_{11,m}$ is the maximum longitudinal tensile stress at the mid-span, f_m is the bending strength, σ_{ij,h_i} is the maximum stress in the *ij* direction around the *i*-th hole h_i and f_{ij} is the strength in the *ij* directions, namely 11 (parallel to the grain), 22 (perpendicular to the grain), and 12 (tangential), assuming a plane geometry of the beam and thus assuming that the perforations are through-holes. The strength value f_m is different from f_{11}. While the first is associated with the bending verification corresponding to the timber class, the second is associated with the tensile failure of the wooden fibre (*Baño* et al., 2011).

The goal is to assess the reduction of the bending capacity of the perforated beam compared to the non-perforated reference configuration, based on linear elastic analyses. Therefore, the stress verification around hole h_i is defined as an equivalent bending check, defining a bending strength associated with the effect of the perforation ($f_{m,ij}$). The following algebraic passages lead to the definition of an equivalent bending verification of a perforated beam:

$$\underbrace{\sigma_{ij,h_i} \leq f_{ij}}_{\text{Stress verification at the } h_i \text{ hole}} \rightarrow \underbrace{\sigma_{ij,h_i}\frac{\sigma_{11,m}}{\sigma_{11,m}} \leq f_{ij}\frac{f_m}{f_m}}_{\text{Algebraic manipulation}} \rightarrow \underbrace{\sigma_{11,m} \leq f_m \frac{k_{\text{strength},ij}}{k_{\text{stress},ij}} = f_{m,ij}}_{\text{Equivalent bending verification}} \tag{2}$$

where $k_{\text{strength},ij}$, $k_{\text{stress},ij}$ and $f_{m,ij}$, are defined as follows

$$k_{\text{strength},ij} = \frac{f_{ij}}{f_m} \tag{3}$$

$$k_{\text{stress},ij} = \frac{\sigma_{ij,h_i}}{\sigma_{11,m}} \tag{4}$$

$$f_{m,ij} = f_m \frac{k_{\text{strength},ij}}{k_{\text{stress},ij}} \tag{5}$$

Namely, $k_{\text{strength},ij}$ in Eq. 3 expresses the ratio between the strength along the *ij* direction (f_{ij}) and the bending strength (f_m), while $k_{\text{stress},ij}$ in Eq. 4 expresses a ratio among maximum stresses around the hole in the *ij* direction (σ_{ij,h_i}) and the maximum longitudinal tensile stress at the midspan ($\sigma_{11,m}$). Eq. 5 represents the bending capacity of the beam equivalent to the hole verification along the *ij* direction.

Eq. 2 reduces to a bending check if $k_{\text{strength},ij} = k_{\text{stress},ij} = 1$. Therefore, Eq. 2 specializes in four distinct equations in the plane case. Specifically, it reduces to a bending verification if $k_{\text{strength},ij} = k_{\text{stress},ij} = 1$ and in a verification around the generic *i*-th hole in the 11, 22, and 12 directions, knowing the strength values of the respective directions, parallel to the grain, perpendicular to the grain, and tangential, respectively. Therefore, the bending

capacity of the beam with hole ($f_{m,hi}$) can be considered as the minimum between the four, as in

$$f_{m,hi} = \min \begin{cases} f_m, \\ f_m \frac{k_{\text{stress},11}}{k_{\text{strength},11}}, \\ f_m \frac{k_{\text{stress},12}}{k_{\text{strength},12}}, \\ f_m \frac{k_{\text{stress},22}}{k_{\text{strength},22}} \end{cases} \tag{6}$$

where subscripts 11, 22, and 12 identify the directions parallel to the grain, perpendicular to the grain, and tangential.

The ultimate goal is to estimate the reduction capacity factor (k_{red}) compared to the reference configuration without holes, as reported below

$$k_{\text{red}} = \frac{R_{m,hi}}{R_m} = \frac{W f_{m,hi}}{W f_m} = \frac{f_{m,hi}}{f_m} \tag{7}$$

where $R_{m,hi}$ is the bending resistance in the perforated beam and R_m the bending resistance in the reference configuration without holes. As reported in the same equation, this expression can be written in terms of the ratio between the bending strengths, assuming the same bending modulus of resistance (W). The modulus of resistance is inherently linked to bending stiffness in the elastic phase. Experimental investigations reported in (*Pasca* et al., 2025) confirm that bending stiffness remains largely unchanged in the presence of holes. Since these holes are relatively small and comparable in scale to natural wood defects, their influence on bending stiffness and the modulus of resistance is negligible.

Using the expression in Eq. 7, derived from an elastic analysis of a perforated beam, the reduction in bending capacity can be quantified as a percentage. From a theoretical standpoint, it is important to emphasize that k_{strength} normalizes stress values relative to strength values along the grain to facilitate comparability. It is well understood that the strength perpendicular to the grain is significantly lower than that parallel to it. Consequently, even a relatively small stress in the perpendicular direction may cause bending failure, despite being lower than its parallel counterpart. Additionally, a crucial aspect to highlight is that k_{red} does not depend on the absolute stress state but rather on the relative distribution of stresses at different locations. Therefore, it can be computed by assuming any arbitrary force value in the simulation of a four-point bending test.

4 Dataset generation from stochastic FE model

The stochastic FE model was developed in three main steps: (i) generating random hole distributions, (ii) constructing a numerical model of a 2D planar beam in Abaqus and performing stress analysis under bending loads, and (iii) calculating k_{red} using Eq. 7. One

of the most challenging aspects is the random generation of hole groups. The authors selected three commonly available beam cross-sections in Norway: 50×100 mm, 50×150 mm, and 50×200 mm. In each simulation, the parameters listed in Tab. 1 were varied, including the total number of hole groups, individual hole diameters, the number of holes per group, as well as the centroid position of each group and its holes. The beam length, L, was set based on its height, H, according to the relation $L = 19H$.

Table 1. Description of the main parameters varied in the Monte Carlo simulations and the respective lower and upper bounds.

Description	Symbol	Lower bound	Upper bound
Total number of groups of holes	N_g	1	5
Diameter of each hole	d	1	30
Number of holes per group	N_h	1	5
Relative coordinates positions of the centroid of the group	$[x_C, y_C]$ [mm]	[L/19,10]	[L×18/19,H-10]
Relative coordinates of the center of each hole	$[\rho,\vartheta]$	[0,0]	[50 mm,2·π]

The generation of holes is defined in cylindrical coordinates, where ρ represents the centroid distance of the cluster of holes and the i-th hole with diameter d, and ϑ is the corresponding angle in radians. Once the beam geometry is established, the procedure begins by randomly determining the number of hole groups (N_g), the number of holes per group (N_h), their diameters (d), and their centroids (x_C, y_C), all of which are assigned randomly. Consequently, this centroid is not a geometric centroid, like the center of mass for each hole cluster, but rather a randomly defined reference point used solely to generate the subgroup of holes. The values of the variables in Tab. 1 were sampled based on a uniform probability density function within the specified bounds. These values were derived from the authors' experience and research activities conducted within the SirkTRE research project. The algorithm relies on the random generation of size, number, and position of the holes, assuming uniform probability density functions. It also includes a validation step to prevent intersections and ensure all elements remain within the beam's geometric boundaries during the generation process.

The final steps involve importing the generated geometry into Abaqus, an FE solver, to analyze the planar stress state of the randomly generated geometries. These steps are implemented using Python, which is tightly integrated with Abaqus. This approach enables the automation of geometry generation, importation into Abaqus, analysis execution, and result extraction. It is important to highlight that for stress analysis, the orthotropic nature of wood must be considered. The stiffness parameters in Tab. 2 were adopted based on the values specified in the EN 338 standard (*EN 338:2016*, 2016) for softwood solid timber with strength class C24.

To calculate k_{red}, the authors extracted the highest stress values around each group of holes and, using the relevant strength value for each stress state, estimated the reduction factors according to Eq. 7. The estimation of k_{red} required assessing the stress state in the undamaged condition for the three selected beam heights to compute k_{stress}. The values provided in Tab. 3 were then used to determine k_{strength}.

*Table 2. Mechanical parameters assumed for simulating the mechanical response of the timber beam, where **E** is the Young's modulus, **v** the Poisson ratio and **G** the shear modulus. The subscripts 1 and 2 indicate parallel and perpendicular directions to the grain, respectively(*EN 338:2016*, 2016).*

Parameter	Symbol	Value
Young's modulus parallel to grain	E_{11}	11000 MPa
Young's modulus perpendicular to grain	E_{22}	E_{11}/30 MPa
Longitudinal-radial Poisson ratio	ν_{12}	0.3
Longitudinal-tangential Poisson ratio	ν_{13}	0.036
Radial-tangential Poisson ratio	ν_{23}	0.018
Longitudinal shear modulus	G_{12}	E_{11}/16 MPa
Rolling shear modulus	G_{23}	G_{12}/10 MPa

*Table 3. Distribution, mean value (μ) and coefficient of variation assumed for the strength parameters. (*Köhler *et al., 2007;* Baño *et al., 2011)*

Property	distribution	μ [MPa]	CoV
Bending strength, f_m	Lognormal	40	0.25
Fiber strength, f_{11}	Lognormal	105	/
Tension strength perp. to the grain, $f_{t,90} = f_{22}$	2-p Weibull	4.5	0.25
Shear strength of clear wood, $f_v = f_{12}$	Lognormal	8	0.25

5 Classification model and key findings

The input features and the output k_{red}, defined in Eq. 7, were then fed to several classification algorithms. Two classes of algorithms were used: Machine Learing algorithms and a straightforward conditional model formalized below in Eq. 8 below:

$$\text{Classify}\left(k_{\text{red}}\right) = \begin{cases} k_{\text{red}} \geq 80\% & \text{if } \left(\sum_{i \in \text{Zone 1}} d_i > t_1\right) \text{ OR } \left(\sum_{i \in \text{Zone 2}} d_i > t_2\right) \\ k_{\text{red}} < 80\% & \text{otherwise} \end{cases} \tag{8}$$

where t_1 and t_2 are fixed thresholds for zones No.1 and 2. The numbering of the zones corresponds to the numbers shown in Fig. 2, where zone No. 1 identifies the two external longitudinal zones, and No. 2 refers to the inner zone.

It is important to recall the investigative process that led to defining both the sum of the hole diameters as a key feature and the specific partitioning of the beam. Regarding the sum of the diameters, the authors tested various conditional classification algorithms, but the most effective feature was the sum of the hole diameters. Other considered features included the maximum diameter, the number of holes, the average diameter, and the standard deviation of their sizes. As for the partitioning, the rational behind the division between Zone 1 and Zone 2 is evident. In the outer regions, where holes affect the fibers most stressed under bending, the impact is significantly more critical. The decision to exclude the quarters near the supports stems from the experimental campaign, which indicated that holes positioned in these regions had a negligible effect.

These observations are based on experimental configurations D, E, F, and H, which feature holes predominantly near the supports (*Pasca* et al., 2025). The results exhibit negligible reduction, with reduction factor values below 1, clearly indicating a bending capacity greater than the reference. Overall, the testing campaign demonstrates that the

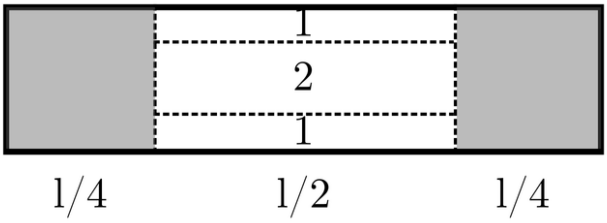

Figure 2. Beam partitioning for feature extraction.

primary factors influencing bending capacity are the hole position (significant only if near the mid-span, where the bending moment is maximal), the maximum hole diameter, and the total number of holes. Due to the lack of information on this aspect and for precautionary reasons, the quarters can be considered negligible only if the sum of hole diameters in the two extreme zones does not exceed 100 mm and the maximum hole diameter does not exceed 30 mm. Additionally, holes with diameters smaller than 3 mm are disregarded, as experimental evidence has shown them to be insignificant when equal to or below this threshold.

The purpose of machine learning models is to provide an upper accuracy limit compared to simple conditional models. This helps determine whether the increased model complexity leads to significant benefits or if it is unnecessary to go beyond the conditional model defined in Eq. 8. The authors compared a variety of ML models. Namely they trained the logistic regression (LR) (*Cramer*, 2002; *Bishop* & *Nasrabadi*, 2006), linear support vector machine (Linear SVM) (*Vapnik*, 1995), random forest (RF) (*Breiman*, 2001), and Extreme Gradient Boosting (XGBoost) (*Chen* & *Guestrin*, 2016). The calibration of the models was pursued using the k-fold method. This involves dividing the training dataset into k equally sized folds, with each fold alternately serving as the training and validation set during the k-fold cross-validation process. Prior studies have shown that stratified cross-validation with 10 folds yields a smaller bias while limiting variance, even when computational capabilities allow for more folds. Therefore, the dataset was split into 5 ($k = 5$) equal subsets, with each subset used for training and validation. In this process, one fold is selected as the validation set while the remaining $k - 1$ folds are used for training, resulting in k distinct models, each trained on a unique subset of data. To address the class imbalance issue, the authors employed the Synthetic Minority Oversampling Technique (SMOTE) algorithm (*Chawla* et al., 2002), which synthetically generates new samples in the minority class to achieve a balanced class distribution. The classification metrics from the various folds are then aggregated and averaged to get a fair comparison across different ML models. All ML algorithms were applied using their default hyperparameters provided by the Python Scikit-learn library (*Pedregosa* et al., 2011). The results of the machine learning models are not reported, as the ML models demonstrated performance metrics comparable to the conditional model. For a balanced dataset between the two classes, accuracies ranged from 85% to 90%.

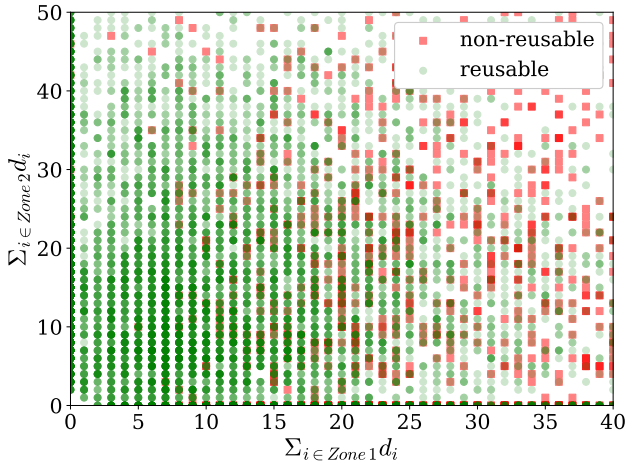

*Figure 3. Scatter plot of the data with true labels, falling in the unusable (red) or reusable (green) classes as a function of the sum of diameters in Zones 1 and 2, shown on the **x** and **y** axes, respectively.*

The conditional binary classification model in Eq. 8 relies on two thresholds, referred to as t_1 for zone No.1 and t_2 for zone No.2, as per Fig. 2. Zone one corresponds to the two areas of the beam, namely the top and bottom outer strips, each being 1/4 of the beam's height, and zone two represents the remaining central strip. Fig. 3 displays a scatter plot of Monte Carlo analysis data, with true labels distinguishing between unusable (red) and reusable (green) classifications. The sum of diameters in Zones 1 and 2 is plotted on the ***x*** and ***y*** axes, respectively. A noticeable transition between classes occurs once specific threshold values on these axes are exceeded. This transition appears to be largely independent along each axis, forming a rectangular reusability domain, where the boundaries align with the axes and extend toward an approximate separation line. While this separation is not sharply defined, a distinct transition zone is observable. To enhance visual clarity, alpha shading has been applied to overlay the Monte Carlo analysis results.

The goal of the model in Eq. 8 is to classify between reusable and non-reusable using the sum of the diameters of the holes in zones 1 and 2. The conditional model's performance metrics can be evaluated in multiple ways, tailored to reward specific aspects, such as false positives and negatives. In this model, the authors will aim to reduce the misclassification of non-reusable beams that are classified as reusable. This is indeed the worst-case scenario associated with an unsafe reuse. To this end, the metric adopted to maximize the F_1 score with $\beta = 2$ has been chosen to enphasize false negatives:

$$F_\beta = \frac{(1+\beta^2)\cdot \mathrm{TP}}{(1+\beta^2)\cdot \mathrm{TP} + \beta^2 \cdot \mathrm{FN} + \mathrm{FP}} \tag{9}$$

Where TP, FN, and FP indicate the true positives, false negatives, and false positives, respectively.

Tab.4 presents the performance metrics for the conditional models defined in Eq. 8, for both the reusable and non-reusable classes. The thresholds are selected based on

Table 4. Performance metrics of the conditional model in Eq. 8 for the usable and non-reusable classes assuming the thresholds for t_1 associated with the maximum of the F1 score and t_2 corresponding to the minimum value associated with the F1 score stabilization. The values t_1 and t_2 are in mm. B. Accuracy stands for Balanced Accuracy.

Reusable			Non-Reusable					
Precision	Recall	F1-score	Precision	Recall	F1-score	B. accuracy	Accuracy	AUC-ROC
0.97	0.79	0.87	0.34	0.82	0.48	0.80	0.79	0.80

the maximum F1 score for t_1 and the minimum value of t_2 associated with the F1 score stabilization.

The precision for the non-reusable class is notably low, indicating a high number of false positives—instances where reusable items are misclassified as non-reusable. However, the recall for this class remains consistently high, demonstrating that the models effectively capture most truly non-reusable items.

Conversely, the reusable class exhibits exceptionally high precision (0.97), accurately identifying reusable items with strong reliability. The F1 scores reflect this trend: the non-reusable class has a lower F1 score, around 0.48, emphasizing the difficulty in balancing precision and recall. In contrast, the reusable class achieves a significantly higher F1 score of approximately 0.87.

Overall, the majority of predictions across models are correct, as indicated by the consistently high AUC-ROC values. Tab. 4 highlights the model's strong ability to classify reusable items with high precision and overall accuracy. However, improving precision for the non-reusable class remains an area for enhancement to minimize false positives. Nonetheless, this limitation does not impact structural safety, as the misclassification only affects reusable items being mistakenly labeled as non-reusable.

6 Conclusions

To facilitate the reuse of structural timber recovered from existing buildings, it is essential to regrade it, assessing the impact of artificial defects such as small holes from previous applications. This study introduces a classification model to categorize beams with artificial defects as either ”reusable” or ”non-reusable,” based on whether the reduction in bending capacity remains below or exceeds 20% compared to an intact beam. To achieve this, the authors developed a stochastic finite element model (FEM) to predict the bending strength of beams containing randomly generated small holes.

The finite element model is built upon two key assumptions: the homogeneity of timber, implying the absence of natural defects, and brittle-elastic behavior. These modeling assumptions were validated against an experimental campaign reported in (*Pasca* et al., 2025). The proposed visual grading model evaluates reusability by computing the sum of hole diameters within two beam zones: Zone 1 consists of the edge strips extending

one-fourth of the beam height on each side, while Zone 2 represents the central strip.

$$\text{Classify} = \begin{cases} k_{\text{red}} \geq 80\% & \text{if } \left(\sum_{i \in \text{Zone 1}} d_i > t_1 = 12\right) \text{ OR } \left(\sum_{i \in \text{Zone 2}} d_i > t_2 = 28\right) \\ k_{\text{red}} < 80\% & \text{otherwise} \end{cases} \tag{10}$$

where k_{red}, as defined in Eq. 7, represents the reduction factor of bending capacity, d_i denotes the diameter of a given hole (excluding holes with $d_i < 3$ mm), and t_1 and t_2 are threshold values for Zones 1 and 2, respectively. The thresholds t_1 and t_2 in mm were determined to maximize the F1 score for the non-reusable class while minimizing false negatives. This approach prioritizes structural safety in classification and aligns with the conservatism principle in engineering standards. For practical application, it is recommended to disregard holes with a diameter smaller than 3 mm. Additionally, the sums of diameters should be computed along the entire beam length, excluding the quarters, provided that the maximum hole diameter does not exceed 30 mm and the total sum remains within 100 mm.

7 References

Acuña, L.; L. Basterra; M. Casado; G. López; G. Ramón-Cueto; E. Relea; C. Martínez & A. González (2011). “Application of resistograph to obtain the density and to differentiate wood species [aplicación del resistógrafo a la obtención de la densidad y la diferenciación de especies de madera].” In: *Materiales de Construccion* 61.303, pp. 451–464.

Arbelaez, R.; L. Schimleck; J. Dahlen & S. Wood (2019). “Evaluation of lumber from deconstructed Portland residential buildings.” In: *Wood and Fiber Science* 51.4, pp. 432–440.

Arriaga, F.; C. Osuna-Sequera; M. Esteban; G. Íñiguez-González & I. Bobadilla (2021). “In situ assessment of the timber structure of an 18th century building in Madrid, Spain.” In: *Construction and Building Materials* 304.

Baño, V.; F. Arriaga; A. Soilán & M. Guaita (2011). “Prediction of bending load capacity of timber beams using a finite element method simulation of knots and grain deviation.” In: *Biosystems engineering* 109.4, pp. 241–249.

Bishop, C. M. & N. M. Nasrabadi (2006). *Pattern recognition and machine learning*. Vol. 4. 4. Springer.

Breiman, L. (2001). “Random forests.” In: *Machine Learning* 45.1, pp. 5–32.

Cavalli, A.; D. Cibecchini; M. Togni & H. S. Sousa (2016). “A review on the mechanical properties of aged wood and salvaged timber.” In: *Construction and Building Materials* 114, pp. 681–687.

Chawla, N. V.; K. W. Bowyer; L. O. Hall & W. P. Kegelmeyer (2002). “SMOTE: synthetic minority over-sampling technique.” In: *Journal of artificial intelligence research* 16, pp. 321–357.

Chen, T. & C. Guestrin (2016). “Xgboost: A scalable tree boosting system.” In: *Proceedings of the 22nd acm sigkdd international conference on knowledge discovery and data mining*, pp. 785–794.

Cramer, J. S. (Dec. 2002). *The Origins of Logistic Regression*. Working Paper 2002-119/4. Tinbergen Institute.

Crews, K. I. & C. MacKenzie (2008). “Development of grading rules for re-cycled timber used in structural applications.” In: *World Conference on Timber Engineering*. World Conference on Timber Engineering (WCTE).

Cruz, H.; D. Yeomans; E. Tsakanika; N. Macchioni; A. Jorissen; M. Touza; M. Mannucci & P. Lourenço (2015). “Guidelines for on-site assessment of historic timber structures.” In: *International Journal of Architectural Heritage* 9.3, pp. 277–289.

EN 338:2016 (2016). “Structural Timber — Strength Classes.” In: *EN 338*.

Falk, R.; D. DeVisser; J. Plume & K. J. Fridley (2003). “Effect of drilled holes on the bending strength of large dimension Douglas-fir lumber.” In: *Forest products journal* 53.5, pp. 55–60.

Köhler, J.; J. D. Sørensen & M. H. Faber (2007). “Probabilistic modeling of timber structures.” In: *Structural safety* 29.4, pp. 255–267.

Llana, D. F.; G. Íñiguez-González; M. Plos & G. Turk (2023). “Grading of recovered Norway spruce (*Picea abies*) timber for structural purposes.” In: *Construction and Building Materials* 398, p. 132440.

Mariño, A.; R. Fernández & R. Fernández (2002). “Análisis comparativo de la densidad de la madera Pinus sylvestris L. mediante la utilización del Resistógrafo.” In: *Revista CIS-Madera* 9, pp. 60–70.

Martínez, R.; J.-A. Balmori; D. Llana & I. Bobadilla (2020). “Wood density determination by drilling chips extraction in ten softwood and hardwood species.” In: *Forests* 11.4.

Morales-Conde, M. & J. Machado (2017). “Evaluation of cross-sectional variation of timber bending modulus of elasticity by stress waves.” In: *Construction and Building Materials* 134, pp. 617–625.

Osuna-Sequera, C.; D. Llana; M. Esteban & F. Arriaga (2019). “Improving density estimation in large cross-section timber from existing structures optimizing the number of non-destructive measurements.” In: *Construction and Building Materials* 211, pp. 199–206.

Osuna-Sequera, C.; D. Llana; G. Íñiguez-González & F. Arriaga (2020). “The influence of cross-section variation on bending stiffness assessment in existing timber structures.” In: *Engineering Structures* 204.

Pasca, D. P.; A. Aloisio; Y. De Santis; H. Burkart & A. Øvrum (2025). “Visual-based classification models for grading reclaimed structural timber for reuse: A theoretical, numerical and experimental investigation.” In: *Engineering Structures* 322, p. 119218.

Pedregosa, F. et al. (2011). “Scikit-learn: Machine learning in Python.” In: *the Journal of Machine Learning Research* 12, pp. 2825–2830.

prNS 3691-3:2023 (2024). “Evaluation of Reclaimed Timber: Part 3 - Visual Strength Grading.” In: *prNS 3691*.

Smith, A. L. & S. J. Hicks (2009). *Design of floors for vibration: A new approach*. Tech. rep. Ascot, UK: Steel Construction Institute.

Vapnik, V. N. (1995). *The nature of statistical learning theory*. Springer Science & Business Media.

DISCUSSION

The paper was presented by A Aloisio

F Lam asked how actual defects in reclaimed timber such as localized slope of grain, end checks be considered in the model and influence the results. A Aloisio responded that this work is a starting point and focuses on the Norwegian proposal for reclassifying recovered timber with small diameter round holes; more advanced model will be considered in future.

P Dietsch commented that the results from four-point bending tests are tied to this configuration and the member being reused in bending. A Aloisio responded that only bending strength was considered and 3 heights were studied.

P Dietsch commented that the tension strength perpendicular to grain for small clear wood of 4.5 MPa was used and asked if one should consider a lower value of say 1.0 MPa in a sensitivity study. A Aloisio responded that since a homogeneous model without defects was considered we assumed higher small tension perpendicular to grain strength.

P Dietsch commented that past research from Falk in the US suggested that holes smaller than ½ the size of the largest knots can be ignored. A Aloisio responded that a very large hole tends to drive all failures and maximum diameter does work together with the rule of sum of hole diameters in the two extreme zones.

JM Cabrero commented that the time related to the use of real beams is an important issue. A Aloisio said that the work is a starting point and the topic is complex. JM Cabrero further commented that the 4-point bending tests have a specific moment diagram which might be different from real use. A Aloisio agreed that the results depend on loading scheme, and the rule of sum of hole diameters in the two extreme zones and threshold might be adjusted for other cases.

H Blass commented that the starting point should consider realistic cases. A Aloisio responded that the starting point is related to the Norwegian standard on reclaimed wood to consider such a binary model. Selection of random parameters to generate the hole is based on experts feedback. There were discussions on closely spaced hole issues.

BJ Yeh questioned why choosing 80% as threshold. In N. America there are concerns with how to define and consider load duration issues for reclaimed wood. A Aloisio responded that the threshold is based on the Norwegian standard. It would be interesting to consider a range. He said this type of problem is multi criterion based. A multicriteria approach is needed to consider load history and load duration issues as a separate problem.

T Demschner asked if the approach handles damages that are rectangular shape. A Aloisio responded that the model cannot handle these cases currently and will need to

adjust the approach. T Demschner asked what about holes created by nails or dowels. A Aloisio responded that these cases can be handled.

S Winter questioned if comparisons were made between hole size as related to original grade. A Aloisio responded that hole size was not related to defects in the original grade. However the scatter and shape of strength distribution are similar between real timber and model.

P Dietsch commented that final editorial checks of the paper are needed before submission for the proceedings.

Tension Strength, Stiffness, and Visual Grading of Red Pine Structural Boards Accordance with Turkish Standard TS 1265-2012; Effect of knot diameter

Fatih Kurul, Istanbul University-Cerrahpaşa, Faculty of Forestry

Mehmet Özdemir, General Directorate of Forestry, Marmara Forestry Research Institute.

İsmail Tuna, General Directorate of Forestry, Marmara Forestry Research Institute.

Tülay Yılmaz, General Directorate of Forestry, Marmara Forestry Research Institute.

Mehmet Arslan, General Directorate of Forestry, Marmara Forestry Research Institute.

Selim Ermiş, General Directorate of Forestry, Marmara Forestry Research Institute.

Türker Dündar, Istanbul University-Cerrahpaşa, Faculty of Forestry

Keywords: Visual grading assignment, Pinus brutia, TS 1265, Tension strength class

1 Introduction

Wood is used in many areas of life and has also been used as a building material since people settled down. In modern construction, only wood that meets a specific strength grade, as defined by each country's legal requirements, can be used. This regulation aims to ensure both structural safety and economic use of materials (Kurul and As 2023).

Structural timber is graded in two main ways: visual strength grading and machine strength grading. Visual strength grading evaluates various defects that can affect the wood's strength, including knots, fiber deviation, annual ring width, pith, and cracks (Ridley-Ellis *et al.* 2018). Each country has established its national standards for visual grading. In Türkiye, the national standard TS 1265 has been in place since 1973 for the visual grading of softwood timber used in construction, providing different classification rules for joists and boards.

Recently, there has been increasing interest in wooden structures, particularly following the earthquakes in Türkiye. This has led to demand for engineered wood materials, such as Glulam (Glue-Laminated Timber) and CLT (Cross-Laminated Timber), as well as structural timber. To meet this demand, domestic production of these materials needs to be established. Before the lamination process, boards shall be tension strength graded and declared as a tabulated strength class in accordance with EN 14080 (2013) for GLT and EN 16351 (2015) for CLT.

In 2023, a big research project, supported by the General Directorate of Forestry, was initiated to determine the tension strength classes of local softwood species corresponding to their visual grades, as specified in TS 1265 (2012). In this project, Turkish red pine (Pinus *brutia*), Anatolian black pine (Pinus *nigra*), Scots pine (Pinus *sylvestris*), fir (*Abies* spp.), spruce (Picea *orientalis*), and cedar (Cedrus *libani*) were studied as they are the most common softwood species of Türkiye (OGM 2020). The tension strength classes of six softwood species derived from this project will be submitted to the CEN TC 124/WG2/TG1 committee and included in the EN 1912 (2024) standard.

This study presents the results of the aforementioned project for Turkish red pine (*Pinus brutia*). Changes in the strength classes and grading yields were also questioned by measuring the parallel and narrow diameter of the knot, based on the ratio of the knot diameter (KDR) to twice the width.

2 Materials and Methods

2.1 Material

Turkish red pine primarily grows in the Mediterranean, Aegean, and Marmara coastal and back-coast regions, as well as locally in the Black Sea Region, as illustrated in Figure 1. This species is commonly used for structural purposes. To assess the timber sources of Turkish red pine in Türkiye, its central growing regions were first divided into four key areas: the Eastern Mediterranean, the Western Mediterranean, the South Aegean, and the North Aegean regions. In 2021, the nine Regional Directorates of Forestry in these areas produced 92% of the annual Turkish red pine sawlog output, amounting to 3.14 million cubic meters. Following this, nine "Operational Directorates of Forestry" were selected that geographically represent the Regional Directorates and had a significant sawlog sales volume in 2021, as shown in Figure 1. The nine chosen regions were then merged based on similar characteristics to create five regions. The first region was Adana, the second region was Antalya-Isparta, the third region was Çanakkale-İzmir, the fourth region was Denizli-Muğla, and the fifth region was Mersin-Maraş.

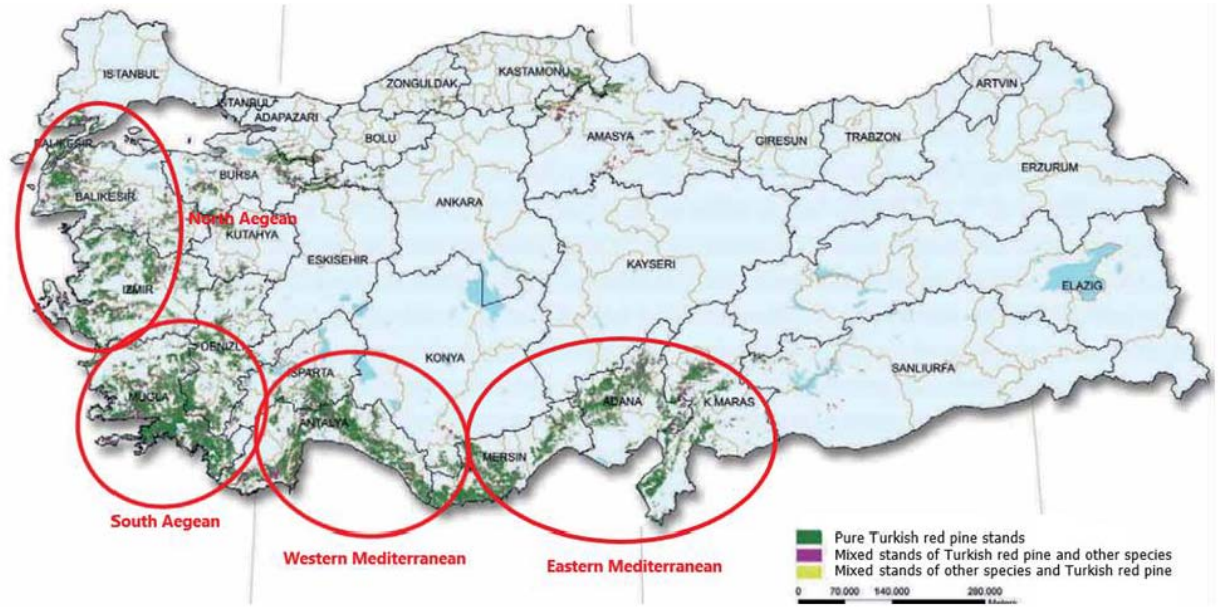

Figure 1. Sampling of Turkish red pine specimens.

A total of 1856 red pine boards, obtained from different growing regions in Türkiye, were studied with nine different cross-sections: 20×100 mm^2, 30×100 mm^2, 40×100 mm^2, 20×150 mm^2, 30×150 mm^2, 40×150 mm^2, 20×200 mm^2, 30×200 mm^2, and 40×200 mm^2 at a moisture content of 12%.

2.2 Visual Grading of the Timbers According to TS 1265 (2012)

Türkiye's national visual grading standard, TS 1265 (2012), provides the definition, classification, specifications, inspection, testing, marketing, and control rules for softwood timber manufactured from pine, fir, spruce, and cedar with a rectangular cross-section, intended for structural purposes only. Softwood timber is sorted into three classes: Class 1, Class 2, and Class 3. Measurements of features other than knots are conducted according to TS EN 1309-3 (2018). In this study, the knots were measured in two ways: parallel to the surface, as in the standards (Figure 2), and also in the narrow diameter of the knot as an alternative. Table 1 presents some of the essential visual grading rules outlined in the standard.

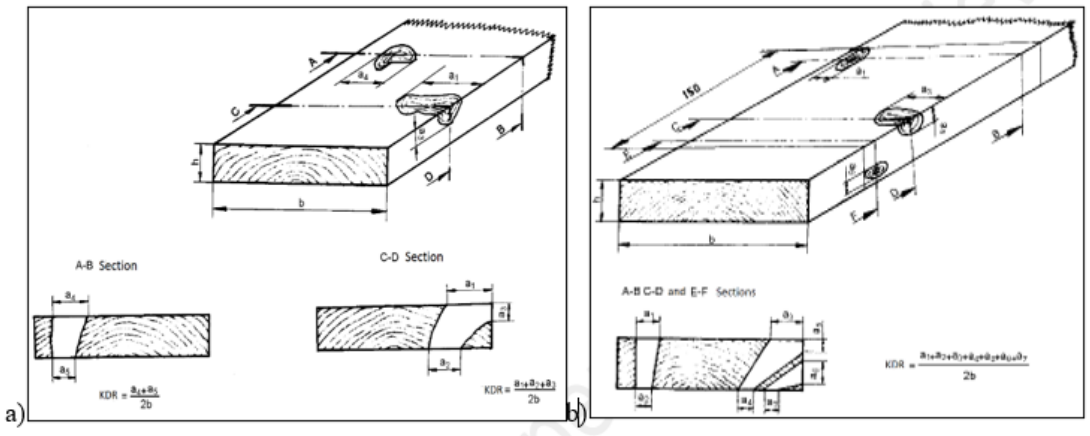

Figure 2. Measurement method of (a) single knots, (b) knot clusters for boards.

Table 1. Some of the visual grading rules in TS 1265 (2012).

Characteristics	Grades		
	High Load Bearing Capacity Class 1	Moderate Load Bearing Capacity Class 2	Low Load Bearing Capacity Class 3
Knots	The narrow diameter is no greater than 50 mm	The narrow diameter is no greater than 70 mm	No limitation
a) Single knots: - In planks, boards and laths; the ratio of the sum of the apparent dimensions of the knots on each face in the section to twice the width of the piece must be max.	0,20	0,33	0,50
b) Knot cluster: - In planks, boards, and laths; The ratio of the sum of the dimensions of the knots measured perpendicular to the timber axis, within the worst 150 mm length, to twice the width of the piece.	0,40	0,66	0,75
Slope of grain	Deviation in 1 m length is not greater than;		
a) In case of the presence of a surface fissure;	70 mm	120 mm	200 mm
b) In case of no surface fissure;	100 mm	200 mm	300 mm
Annual ring width	The area of the growth ring bigger than 4mm should not be greater than 1/2 of the whole cross-section area.	No limitation	No limitation

All criteria in the standards were checked and measured for all specimens. The biggest defect located between the machine grips was determined based on the four sides of the boards. To ensure that the biggest defect is located within the test zone, the loading points were shifted to the right or left along the specimens, which were prepared longer than required for the test. Then, the excess parts remaining at the ends of the specimens were cut.

For Turkish red pine, a total of 1856 boards were visually graded according to TS 1265 (2012), and 980 of them were selected for testing. When selecting the visual grades, the regions and cross-section dimensions of the boards were taken into account, aiming to have at least 40 specimens in each visual grade for each region. It was also considered that the selected specimens for mechanical tests were distributed as evenly as possible to each cross-section.

2.3 Mechanical Testing

The selected specimens were tested in tension to determine the modulus of elasticity in tension and the tensile strength in accordance with EN 408+A1 (2014). The test setup is shown in Figure 3.

Figure 3. Test setup for tensile test according to EN 408+A1 (2014).

The density and the moisture content of the specimens were also determined on defect-free pieces with full cross-section cuts from the specimens after the test. The moisture content of the timber was determined in accordance with EN 13183-1 (2002). The test values for the modulus of elasticity and density of specimens not tested at 12% moisture content were adjusted using the formulas given in EN 384+A1 (2020).

2.4 Derivation of Visual Grading Assignments

The method for determining characteristic values of mechanical properties and density, which indicate the strength class, for defined populations of visual grades, is given in EN 384+A1 (2020). The tension strength values of the specimens with a nominal depth of 100 mm were adjusted to a depth of 150 mm by dividing by the factor k_h as indicated in EN 384+A1 (2020).

After completing the required adjustments, the 5-percentile strength values ($f_{05,i}$), defect-free density ($\rho_{05,i}$), and the mean stiffness values were determined for each visual grade of red pine boards as stipulated in EN 14358 (2016). As an alternative, the characteristic values were also recalculated for narrow knot diameter ratio. So, how changes in KDR ratios affect the characteristic values and visual grading efficiency were analysed.

3 Results and Discussions

3.1 Mechanical Test Results

Table 2 and Table 3 present the tensile test results of Turkish red pine boards, categorized by region and visual class for parallel and narrow knot diameter ratio, respectively. As seen from the results, the mean MCs of all the specimens vary between 15,1% and 15,6%. The mean values of the modulus of elasticity in tension and tensile strength of the specimens decreased as the visual class worsened for both knot measurement methods, as expected.

Figures 4 and 5 show the correlations between the KDR and tension MoE and the tensile strength of Turkish red pine for parallel and narrow knot diameter ratios, respectively. As seen in the results, the tension MoE and tensile strength decrease as the KDR values increase. The correlations between the KDR-tension MoE are found to be moderate, and KDR-tensile strength is found to be higher than this. As can be seen, defects affect strength more than stiffness. Also, the parallel knot diameter ratio gives better correlations than the narrow knot diameter ratio. In the graphs, the KDR of 0.5 typically represents the limit value for Grade 3 timber, and points with KDR values higher than 0.5 are classified as rejected timber. However, in some specimens, this ratio can reach as high as 0.75 due to the presence of a knot cluster. This situation, combined with the presence of other defects, such as fiber deviation, causes the correlation to decrease.

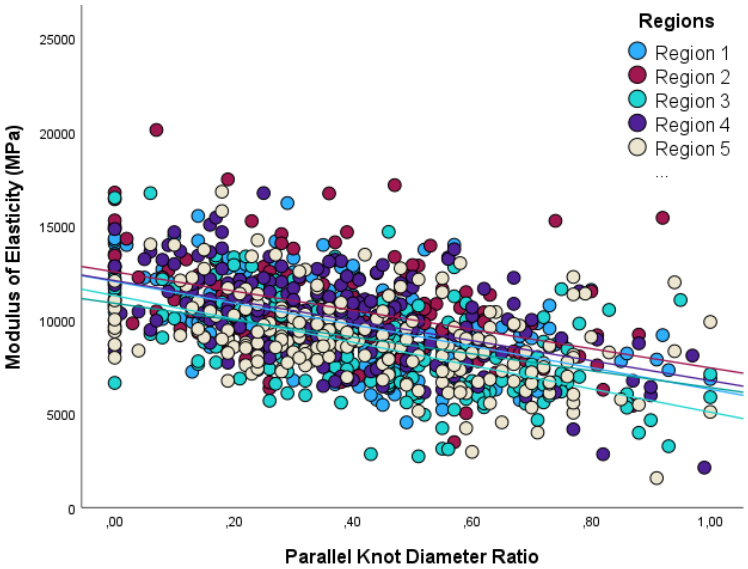

	Region 1	Region 2	Region 3	Region 4	Region 5	Total
R^2	0,278	0,164	0,309	0,250	0,210	0,245

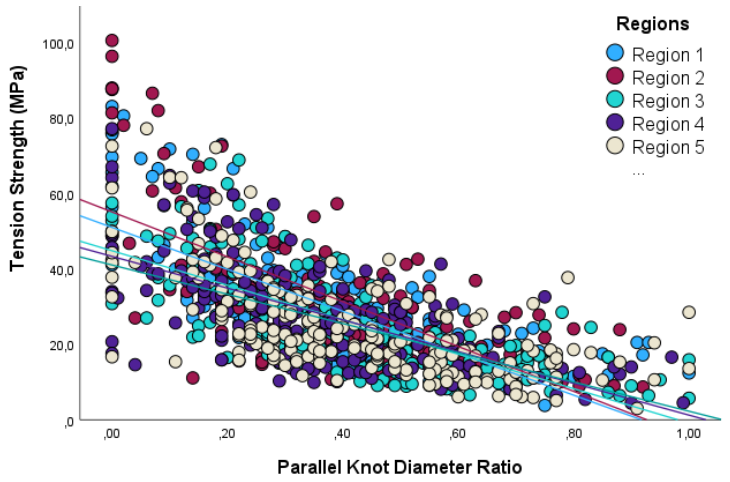

	Region 1	Region 2	Region 3	Region 4	Region 5	Total
R^2	0,518	0,444	0,530	0,416	0,420	0,454

Figure 4. The relationships between the parallel KDR-MoE and the tension strength.

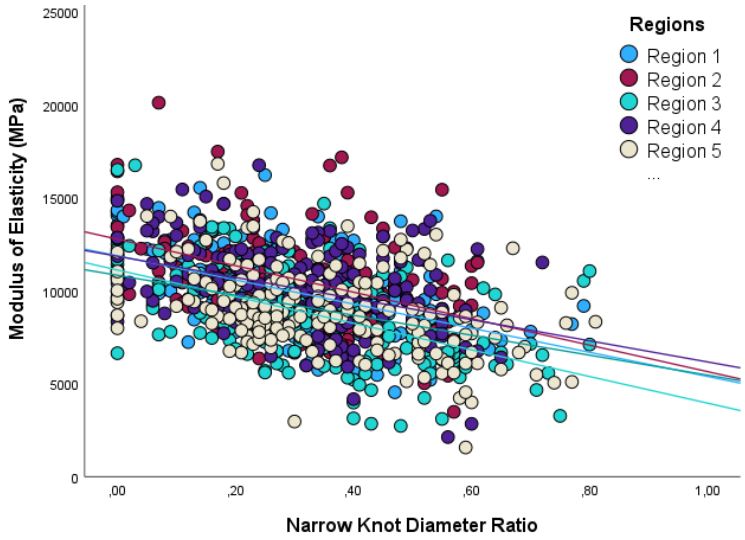

	Region 1	Region 2	Region 3	Region 4	Region 5	Total
R^2	0,230	0,173	0,259	0,162	0,188	0,208

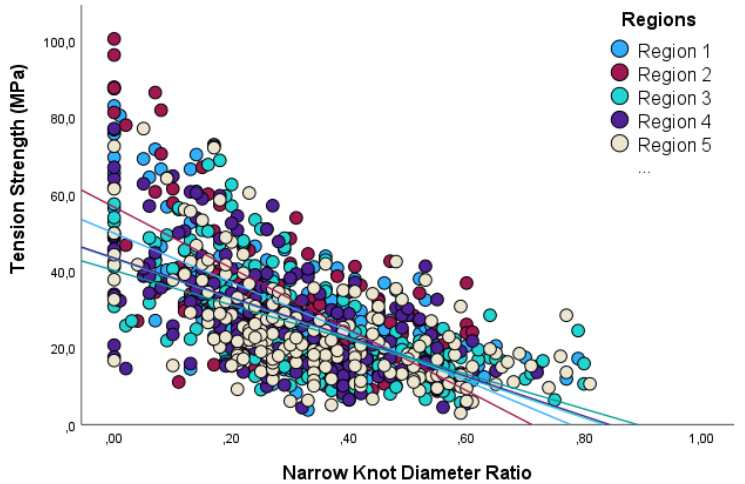

	Region 1	Region 2	Region 3	Region 4	Region 5	Total
R^2	0,448	0,435	0,430	0,354	0,354	0,394

Figure 5. The relationships between the narrow KDR-MoE and the tension strength.

Table 2. Test results of Turkish red pine boards according to the regions and the visual class for the parallel knot diameter ratio.

Sub-samples	Number of Spec.	MC (%)	$f_{t,0}$ (MPa)	$E_{t,0}$ (MPa)	Density (kg/m^3)	Number of Spec.	MC (%)	$f_{t,0}$ (MPa)	$E_{t,0}$ (MPa)	Density (kg/m^3)
	Class 1					Class 2				
Region 1	47	15,5 (6,8)	48,0 (36,9)	11487 (16,8)	571,6 (10,7)	66	15,7 (6,6)	27,3 (35,3)	9895 (18,2)	560,1 (11,1)
Region 2	40	15,7 (6,5)	51,3 (46,7)	11777 (23,4)	595,4 (9,2)	45	16,1 (6,9)	30,8 (36,0)	11058 (22,2)	584,7 (8,7)
Region 3	42	15,1 (6,6)	39,9 (34,7)	10500 (23,0)	570,9 (8,9)	69	15,3 (6,3)	30,9 (31,7)	9343 (20,6)	565,7 (9,1)
Region 4	57	15,6 (6,4)	40,1 (33,7)	11376 (16,8)	570,5 (9,8)	58	15,2 (6,7)	30,0 (37,8)	10433 (16,9)	562,3 (10,0)
Region 5	46	15,4 (5,3)	41,1 (37,3)	10418 (20,4)	515,5 (8,6)	61	15,7 (6,2)	24,6 (33,4)	9327 (17,4)	525,2 (9,4)
Total	**232**	**15,5 (6,4)**	**43,8 (39,9)**	**11119 (20,3)**	**564,2 (10,5)**	**299**	**15,6 (6,8)**	**28,6 (38,3)**	**9931 (20,3)**	**558,4 (10,2)**
	Class 3					Rejected				
Region 1	57	15,0 (5,9)	24,1 (33,8)	9171 (22,2)	564,5 (11,2)	30	15,6 (8,0)	17,4 (37,8)	8393 (21,4)	606,9 (15,2)
Region 2	46	15,8 (7,5)	23,6 (34,9)	9949 (20,6)	592,6 (10,0)	20	15,4 (8,2)	18,4 (38,4)	8678 (34,0)	636,9 (14,2)
Region 3	64	15,3 (6,0)	18,7 (36,3)	8073 (26,3)	560,6 (8,7)	44	15,3 (5,6)	14,5 (36,7)	6852 (32,7)	564,0 (11,5)
Region 4	57	15,1 (6,6)	20,6 (36,1)	9737 (21,4)	562,1 (11,8)	24	14,8 (6,5)	13,3 (46,8)	7618 (33,2)	546,8 (13,2)
Region 5	57	15,4 (6,2)	20,7 (39,1)	8754 (20,7)	528,4 (10,5)	50	15,3 (6,2)	14,7 (47,8)	7557 (32,3)	546,0 (10,1)
Total	**281**	**15,3 (6,6)**	**21,4 (37,1)**	**9078 (23,4)**	**560,4 (11,0)**	**168**	**15,3 (6,8)**	**15,4 (42,7)**	**7664 (31,6)**	**572,5 (13,7)**

The numbers in the parentheses are the coefficient of variation.

Table 3. Test results of Turkish red pine according to the regions and the visual class for the narrow knot diameter ratio.

Sub-samples	Number of Spec.	MC (%)	$f_{t,0}$ (MPa)	$E_{t,0}$ (MPa)	Density (kg/m^3)	Number of Spec.	MC (%)	$f_{t,0}$ (MPa)	$E_{t,0}$ (MPa)	Density (kg/m^3)
	Class 1					Class 2				
Region 1	77	15,6 (6,6)	38,8 (49,4)	10588 (19,8)	576,6 (11,9)	60	15,7 (6,6)	25,5 (38,2)	9681 (21,2)	559,0 (10,0)
Region 2	58	15,9 (6,8)	45,1 (51,2)	11271 (24,1)	596,6 (9,2)	50	16,0 (7,1)	26,6 (37,0)	10906 (21,4)	598,1 (10,7)
Region 3	66	15,2 (6,9)	35,2 (43,0)	9979 (23,0)	565,3 (9,3)	80	15,5 (6,1)	25,4 (51,6)	8576 (25,9)	569,5 (10,5)
Region 4	70	15,6 (6,9)	38,0 (36,9)	11051 (17,7)	571,3 (10,1)	66	15,4 (6,9)	26,4 (44,8)	10058 (20,8)	560,8 (9,7)
Region 5	67	15,5 (6,1)	35,8 (42,6)	9958 (19,8)	527,3 (10,0)	68	15,7 (5,5)	22,7 (41,4)	9083 (22,3)	521,5 (9,6)
Total	**338**	**15,6 (6,8)**	**38,4 (46,1)**	**10557 (21,3)**	**567,0 (10,9)**	**324**	**15,6 (6,5)**	**25,2 (43,8)**	**9549 (23,8)**	**560,1 (10,9)**
	Class 3					Rejected				
Region 1	53	15,0 (6,4)	23,9 (33,6)	9277 (23,2)	576,4 (13,6)	10	15,6 (9,1)	17,4 (31,7)	7962 (23,0)	572,7 (15,0)
Region 2	41	15,4 (7,3)	22,3 (38,1)	9570 (25,1)	598,2 (12,1)	2	14,3 (5,0)	16,0 (26,7)	4250 (25,6)	544,3 (2,0)
Region 3	60	15,2 (5,1)	18,1 (36,8)	7887 (29,3)	558,9 (8,3)	13	15,0 (6,1)	15,8 (29,8)	6604 (37,8)	561,8 (8,5)
Region 4	56	14,8 (4,5)	18,9 (40,4)	9315 (26,9)	555,3 (12,8)	4	14,1 (5,1)	14,6 (7,5)	8087 (29,0)	547,1 (15,6)
Region 5	62	15,3 (6,6)	17,5 (45,9)	8342 (24,9)	536,5 (9,5)	17	15,2 (5,3)	16,6 (49,2)	7229 (36,1)	536,1 (11,8)
Total	**272**	**15,1 (6,1)**	**19,9 (40,7)**	**8809 (26,8)**	**562,4 (11,8)**	**46**	**15,1 (6,9)**	**16,4 (37,1)**	**7157 (33,8)**	**552,6 (11,8)**

The numbers in the parentheses are the coefficient of variation.

3.2 Five-percentile Values

Tables 4 and 5 show the calculation of 5-percentile values of tensile strength and density, and mean values of modulus of elasticity in tension for Turkish red pine for parallel and narrow knot diameter ratios in Class 1, Class 2, and Class 3, respectively.

Table 4. The 5-percetile values of Turkish red pine for the parallel knot diameter ratio.

Source	Number of Spec.	MC (%)	Adj. $f_{t,0}$ (MPa)* Mean	$f_{05,i}$	Adj. $E_{t,0}$* ($\bar{E}_i$) (GPa)	Adj. Density (kg/m^3)* Mean	$P_{0.5,i}$
Class 1							
Region 1	47	15,6 (6,6)	46,2 (34,6)	23,4	11,9 (16,6)	561,4 (10,5)	453,9
Region 2	40	15,9 (6,8)	49,4 (45,1)	18,8	12,2 (23,1)	584,4 (9,1)	486,3
Region 3	42	15,2 (6,9)	38,4 (34,9)	18,4	10,8 (23,1)	561,8 (8,7)	472,6
Region 4	57	15,6 (6,9)	38,6 (31,9)	20,3	11,8 (16,4)	560,2 (9,8)	460,8
Region 5	46	15,5 (6,1)	39,7 (36,4)	18,3	10,8 (20,1)	506,8 (8,7)	426,4
Class 2							
Region 1	66	15,7 (6,6)	26,5 (33,8)	13,2	10,3 (19,1)	549,5 (10,9)	441,4
Region 2	45	16,0 (7,1)	30,4 (35,0)	14,6	11,5 (22,1)	572,7 (8,6)	482,2
Region 3	69	15,5 (6,1)	29,9 (40,3)	12,3	9,6 (20,3)	556,3 (9,0)	466,0
Region 4	58	15,4 (6,9)	29,1 (35,8)	13,3	10,8 (16,8)	553,2 (9,9)	454,2
Region 5	61	15,7 (5,5)	24,2 (31,8)	13,8	9,7 (17,1)	515,3 (9,3)	428,7
Class 3							
Region 1	57	15,0 (6,4)	22,7 (32,7)	11,6	9,4 (21,8)	555,9 (11,1)	444,1
Region 2	46	15,4 (7,3)	22,9 (34,7)	11,3	10,3 (20,3)	581,3 (10,0)	475,5
Region 3	64	15,2 (5,1)	18,0 (34,6)	8,7	8,3 (26,0)	551,4 (8,7)	465,2
Region 4	57	14,8 (4,5)	19,8 (35,1)	9,9	10,0 (21,3)	553,2 (11,7)	435,9
Region 5	57	15,3 (6,6)	20,0 (39,0)	9,3	9,1 (20,5)	519,3 (10,5)	421,0

Table 5. The 5-percetile values of Turkish red pine for the narrow knot diameter ratio.

Source	Number of Spec.	MC (%)	Adj. $f_{t,0}$ (MPa)* Mean	$f_{05,i}$	Adj. $E_{t,0}$* ($\bar{E}_i$) (GPa)	Adj. Density (kg/m^3) Mean	$P_{0.5,i}$
Class 1							
Region 1	77	15,6 (6,6)	37,5 (47,2)	12,7	11,0 (19,6)	566,1 (11,7)	446,7
Region 2	58	15,9 (6,8)	43,6 (49,2)	15,7	11,7 (23,7)	584,9 (9,1)	488,7
Region 3	66	15,2 (6,9)	34,0 (42,3)	13,1	10,3 (23,0)	556,2 (9,2)	464,2
Region 4	70	15,6 (6,9)	36,7 (34,9)	16,3	11,4 (17,5)	561,0 (10,1)	459,4
Region 5	67	15,5 (6,1)	34,8 (41,1)	15,5	10,3 (19,5)	518,1 (10)	424,4
Class 2							
Region 1	60	15,7 (6,6)	24,7 (36,5)	11,1	10,0 (20,9)	548,6 (9,9)	450,8
Region 2	50	16,0 (7,1)	26,3 (36,2)	12,8	11,3 (21,3)	586,0 (10,6)	473,2
Region 3	80	15,5 (6,1)	24,6 (50,3)	8,2	8,9 (25,6)	559,5 (10,4)	454,7
Region 4	66	15,4 (6,9)	25,6 (42,8)	9,8	10,4 (20,6)	551,4 (9,6)	455,5
Region 5	68	15,7 (5,5)	22,3 (40,1)	9,7	9,4 (21,9)	511,9 (9,5)	424,1
Class 3							
Region 1	53	15,0 (6,4)	22,3 (32,7)	11,6	9,5 (22,9)	567,7 (13,4)	430,0
Region 2	41	15,4 (7,3)	21,2 (37,8)	8,9	9,9 (25,2)	588,0 (12,2)	456,7
Region 3	60	15,2 (5,1)	17,2 (35,4)	8,0	8,1 (29,2)	550,0 (8,1)	474,9
Region 4	56	14,8 (4,5)	17,9 (40,1)	7,5	9,6 (26,9)	547,6 (12,8)	421,0
Region 5	62	15,3 (6,6)	16,5 (45,0)	6,3	8,6 (24,5)	527,7 (9,5)	437,1

The numbers in the parentheses are the coefficient of variation.

** Adjusted values based on the moisture contents and/or timber depths*

3.3 Derivation of Characteristic Values and Strength Classes

Following the calculation of the 5-percentile values for the regions, the characteristic values of tensile strength, modulus of elasticity in tension, and density were determined for the regions according to EN 384+A1 (2020). The characteristic values of tensile strength, modulus of elasticity in tension, and density of each visual grade and corresponding strength classes in EN 338 (2016) are given in Table 6 for parallel knot diameter ratio and in Table 7 for narrow knot diameter ratio.

As seen in Table 6, the strength classes of Class 1, Class 2, and Class 3 were found as T18, T13, and T10, respectively. In Table 7, the strength classes of Class 1 and Class 2 were found as T14,5 and T9, respectively. But for Class 3, no strength class assignment could be made. Red pine has the widest growing areas in Türkiye. In Europe, it has a limited distribution in the Mediterranean coastal zone in the Balkans and Italy. For this reason, the tension strength values of the red pine timber from any country were not assigned in the EN 1912 (2024) standard before.

When red pine is compared to other pine species in EN 1912 (2024), Scots pine boards from Austria, Germany, and Poland were assigned T22 for S13 (first grade), T14 for S10 (second grade), and T10 for S7 (third grade). So, in this study, it was found that the tension strength classes of Turkish red pine boards were slightly lower than those of similar pine species grown in Europe.

When the tension strength classes (T18-C30, T13-C22, and T10-C16) are compared to the bending strength classes for Turkish red pine (Classes 1, 2, and 3 were assigned C35, C24, and C20, respectively) in EN 1912 (2024), they are found to be lower. This is likely due to the difference in grading rules for joists and boards, as well as the fact that tensile strength is more affected by defects than bending strength.

According to Table 6, GL 28h glulam can be produced from red pine Class 1 boards, GL 22h from Class 2 boards, and GL 20h from Class 3 boards, all in accordance with the EN 14080 (2013) standard. This will pave the way for domestic manufacturers to use domestic raw materials and contribute to cost reductions.

Table 6. Derivation of characteristic values of visual grades and comparison with the requirement in EN 338 for parallel knot diameter ratio.

Grade	St. Class	Characteristic Tensile Strength (MPa)					Characteristic Modulus of Elasticity (GPa)					Characteristic Density (Kg/m^3)				
		$1{,}2f_{05,i,min}$	$\frac{\sum_{i=1}^{ns} n_i f_{05,i}}{n}$	k_n	f_k	St. class req.	$1{,}1\overline{E}_{i,min}$	$\frac{\sum_{i=1}^{ns} n_i \overline{E}_i}{n}$	k_n	$E_{0,mean,k}$	St. class req.	$1{,}1\rho_{05,i,min}$	$\frac{\sum_{i=1}^{ns} n_i \rho_{05,i}}{n}$	k_n	ρ_k	St. class req.
1	**T18**	21,9	19,9	1,0	19,9	18,0	12,5	12,1	1,0	12,1	12,0	469,0	459,1	1,0	459,1	380
2	**T13**	14,8	13,3	1,0	13,3	13,0	11,2	10,8	1,0	10,8	10,0	471,6	453,1	1,0	453,1	340
3	**T10**	10,4	10,1	1,0	10,1	10,0	9,6	9,9	1,0	9,6	8,0	463,1	447,7	1,0	447,7	310

Table 7. Derivation of characteristic values of visual grades and comparison with the requirement in EN 338 for narrow knot diameter ratio.

Grade	St. Class	Characteristic Bending Strength (MPa)					Characteristic Modulus of Elasticity (GPa)					Characteristic Density (Kg/m^3)				
		$1{,}2f_{05,i,min}$	$\frac{\sum_{i=1}^{ns} n_i f_{05,i}}{n}$	k_n	f_k	St. class req.	$1{,}1\overline{E}_{i,min}$	$\frac{\sum_{i=1}^{ns} n_i \overline{E}_i}{n}$	k_n	$E_{0,mean,k}$	St. class req.	$1{,}1\rho_{05,i,min}$	$\frac{\sum_{i=1}^{ns} n_i \rho_{05,i}}{n}$	k_n	ρ_k	St. class req.
1	**T14,5**	15,2	14,6	1,0	14,6	14,5	11,9	11,5	1,0	11,5	11,0	466,8	455,5	1,0	455,5	350
2	**T9**	9,8	10,1	1,0	10,1	9,0	10,3	10,4	1,0	10,3	7,5	466,5	450,6	1,0	450,6	300
3	-	7,6	8,3	1,0	7,6	8,0	9,4	9,5	1,0	9,4	7,0	463,1	443,7	1,0	443,7	290

4 Conclusions

The following conclusions may be drawn from the results of this research:

- In Turkish red pine boards graded in accordance with TS 1265 (2012), the strength classes corresponding to Class 1, Class 2, and Class 3 were found as T18 (C30), T13 (C22), and T10 (C16), respectively.
- In the alternative knot measuring method, the strength classes corresponding to Class 1 and Class 2 were found as T14,5 and T9, respectively. No strength class assignment for Class 3. When the knot measurement method was changed, the grading yield increased, even though lower strength classes were obtained for Classes 1, 2, and 3. Despite this, it is recommended to use the existing method in the TS 1265 standard.
- In general, the tension strength classes of red pine boards were found slightly lower than the values given in the EN 1912 standard for European-grown same or similar pine species.
- As a result, the way has been paved for the production of GLT and CLT from Turkish red pine in accordance with European standards.

5 References

EN 338 (2016): Structural timber - Strength classes. CEN.

EN 384+A1 (2020): Structural timber - Determination of characteristic values of mechanical properties and density. CEN.

EN 408+A1 (2014): Timber structures - Structural timber and glued laminated timber - Determination of some physical and mechanical properties. CEN.

EN 1309-3 (2018): Round and sawn timber-Method of measurement of features. CEN

EN 1912 (2024): Structural Timber - Strength classes - Assignment of visual grades and species. CEN.

EN 13183-1 (2012): Moisture content of a piece of sawn timber – Part 1: Determination by oven dry method. CEN.

EN 14080 (2013): Timber structures – Glued laminated timber and glued solid timber - Requirements. CEN.

EN 14358 (2016): Timber structures – Calculation and verification of characteristic values. CEN.

EN 16351 (2021): Timber structures – Cross laminated timber - Requirements. CEN.

OGM (2020): Annual Report. General Directorate of Forestry.

Kurul, F., and As, N. (2024). Visual and Machine Strength Gradings of Scots and Red Pine Structural Timber Pieces from Türkiye. BioResources, 19(3).

Ridley-Ellis, D., Stapel, P., and Baño, V. (2016). Strength grading of sawn timber in Europe: an explanation for engineers and researchers. European journal of wood and wood products, 74(3), 291-306.

TS 1265 (2012): Sawn timber (Coniferous) - For building construction. Turkish Standard Institution (TSE).

DISCUSSION

The paper was presented by F Kurul

P Dietsch commented that the table listed moisture contents of 15%. Were these boards technically dried and would the results be different otherwise. F Kurul said there were no moisture adjustments for tension strength.

BJ Yeh asked if the edge and center line knots were considered differently. F Kurul said they were measured and noted but not considered in the paper.

B Azinovic commented that climatic change in Europe will lead to more availability of Mediterranean red pine species in the wood supply chain.

Deformation level and specimen geometry in compression perpendicular to the grain of solid timber, GLT and CLT timber products

Dag Pasquale Pasca, Norsk Treteknisk Institutt, Norway

Angelo Aloisio, Università degli Studi dell'Aquila, Italy

Francesco Mirko Massaro, Norwegian University of Science and Technology (NTNU), Norway

Haris Stamatopoulos, Norwegian University of Science and Technology (NTNU), Norway

Yuri De Santis, Università degli Studi dell'Aquila, Italy

Audun Øvrum, Norsk Treteknisk Institutt, Norway

Keywords: Compression perpendicular to the grain , Deformation level , Effective height

Abstract

This study investigates the influence of deformation level and specimen geometry on the compression perpendicular to grain (CPG) behavior of solid timber, glued laminated timber (GLT), and cross-laminated timber (CLT) products. The recent inclusion of Van der Put's mechanics-based model in the Eurocode draft offers a theoretical foundation for stress dispersion. Nevertheless, critical enhancements related to deformation levels and effective height influencing stress distribution remain unaddressed. This paper extensively evaluates these enhancements through theoretical development, numerical validation using finite element modeling (FEM), and experimental validation data from two extensive testing campaigns.

1 Introduction

Timber is an orthotropic material whose mechanical behaviour depends strongly on grain orientation. Along the fibres it exhibits high strength and stiffness, whereas across the fibres its capacity is markedly lower. When loaded in compression perpendicular to the grain (CPG), collapse of the tubular wood cells governs the response and ultimate

failure *Persson*, 2000; *Swedish Wood*, 2016. Such situations frequently arise at supports *Hassan* et al., 2014 and although CPG failure seldom leads to global collapse, it could be more relevant for the Serviceability Limit State (SLS); at the Ultimate Limit State (ULS) the stresses in the members are those corresponding to an admissible deformation rather than to the intrinsic material strength.

Classical studies focused mainly on clear wood, glued laminated timber (GLT) and massive sections *Graf*, 1921; *Suenson*, 1938; *Gaber*, 1940; *Frey-Wyssling Stüssi*, 1948; *Rothmund*, 1949; *Kollmann* & *Côté*, 1968; *Gehri*, 1997; *Basta*, 2005; *Hoffmeyer* et al., 2000; *Hübner*, 2013; *Stamatopoulos* et al., 2022, while more recent investigations have extended to engineered products such as cross-laminated timber (CLT) *Brandner* et al., 2016.

Until now, European design practice *EN 1995* 2005 has relied upon the semi-empirical expressions, originating from the work of Blass *Blass* & *Goerlacher*, 2004. In the 1990s a new, plasticity-based approach was introduced by Van der Put (*Van der Put*, 1991) and subsequently refined and validated by Leijten (*Leijten*, 2016). In his comprehensive review, Leijten (*Leijten*, 2016) observed that most global bearing-capacity design models (*NEN 3852* 1978; *CIB*, 1983; *AS 1720* 1988; *NZS 3603* 1993; *DIN 1052* 1999; *EN 1995* 2005; *Van Der Put*, 2008; *Kitamori* et al., 2009; *NDS 2012* 2012; *Blass* & *Goerlacher*, 2004; *Van der Put*, 1991; *Madsen* et al., 1982) remain empirically derived and frequently lack a solid mechanical basis. After extensive debate, the forthcoming revision of Eurocode 5 has now adopted this mechanical framework.

Van der Put's formulation, rooted in plasticity theory, assumes isotropic stress spreading: compressive stresses disperse at a 1:1 angle (45°) for small deformations and at 1:1.5 (34°) when deformations reach roughly 10 %, consistent with the experimental observations of Madsen (*Madsen* et al., 1982).

Important practical questions, however, remain open. The permissible increase in strength associated with larger deformations and the effective depth over which the compressive stress is assumed to act are still determined empirically. The present study addresses these gaps. It first introduces an experimentally calibrated regression model that links the incremental CPG strength coefficient to the admissible deformation level. It then explore the maximum effective height for accurate stress distribution in deep timber elements. The findings are based on two extensive experimental campaigns on the CPG behaviour of GLT, solid timber and CLT.

2 Design Model for Compression Perpendicular to the Grain (CPG)

The draft of Eurocode 5 (prEN 1995-1-1) introduces a design-capacity model for engineered-wood members loaded in compression perpendicular to the grain, both without and with reinforcement. For unreinforced timber, the model is based on the modified Van der Put approach, comprehensively described in *Leijten*, 2016.

To verify a timber element subjected to CPG, the following design inequality shall be satisfied:

$$\sigma_{c,90,d} \leq k_{c,90}\, k_{mat}\, f_{c,90,d} \tag{1}$$

where $f_{c,90,d}$ is the design compressive strength perpendicular to the grain and $\sigma_{c,90,d}$ is the corresponding design stress, obtained by dividing the design compressive force $F_{c,90,d}$ by the contact area A: The coefficient k_{mat} reflects the material behaviour and the permissible compressive deformation, whereas $k_{c,90}$ accounts for stress redistribution within the member.

Values of k_{mat} (Table 1) were determined using the partial safety factors γ_M given in EN-1995-1-1 (*EN 1995* 2005).

According to the draft code, both $k_{c,90}$ and k_{mat} may be taken as 1.0, or they may be evaluated with Eq. (2) and Table 1, respectively:

$$k_{c,90} = \sqrt{\frac{l_{ef}}{l_{c,90}}} \leq 4.0 \tag{2}$$

Here l_{ef} is the effective stress-spreading length parallel to the grain and $l_{c,90}$ is the loaded (compressed) length in the same direction (see Fig. 1). For CPG, l_{ef} is derived from a 45° stress-spreading angle.

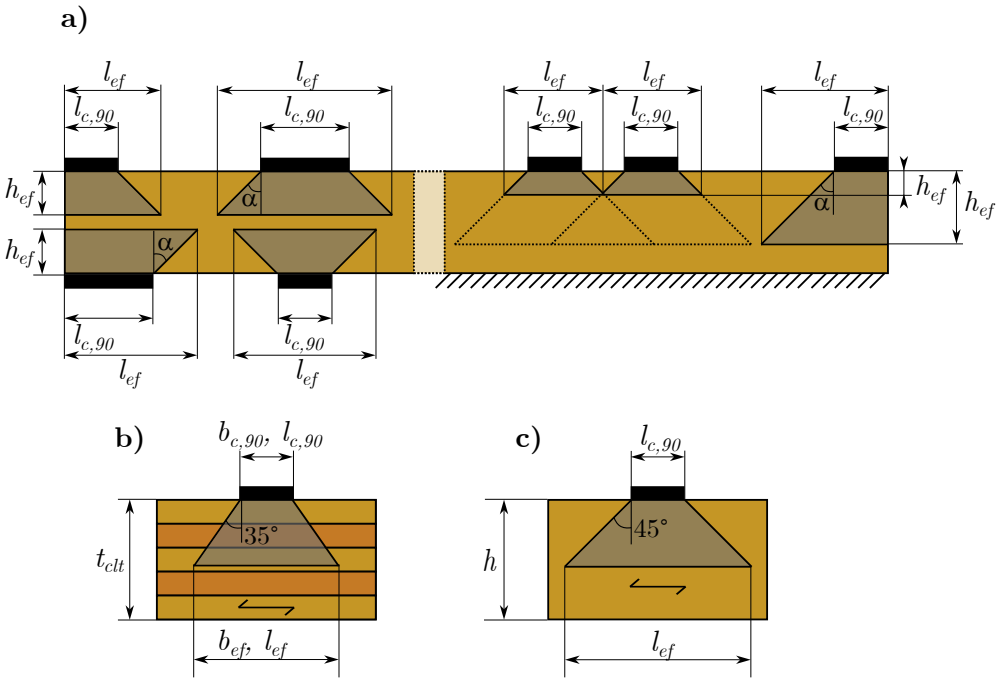

Figure 1. Typical situations used to calculate the CPG effective parameters for (a),(c) GLT and (a),(b) CLT.

Table 1. Values of the coefficients k_{mat} for different timber products.

Type of timber product	Case A		Case B		Case C	
	Strain	k_{mat}	Strain	k_{mat}	Strain	k_{mat}
Solid wood based (SWB) (see Table 5.1)	0,025	1,4	0,10	2,1	0,20	2,7
Softwood LVL and GLVL loaded edgewise	0,015	1,0	—	—	—	—
Softwood LVL and GLVL loaded flatwise	0,025	1,3[a]	0,07	1,9	0,30- 0,005h	2,5[b]
Hardwood LVL and GLVL loaded edgewise	0,015	1,0	0,035	1,2	—	—
Hardwood LVL and GLVL loaded flatwise	0,020	1,3	0,05	1,6	—	—

[a]: for $h \geq 46mm$ [b]: for $20mm \leq h < 46mm$

The strain in Table 1 is defined as total deformation divided by the effective depth h_{ef}. For members on continuous support,

$$h_{ef} = \min\{h,\ 280\ \text{mm}\}, \tag{3}$$

while for members on discrete supports and subjected to distributed and/or local CPG, h_{ef} used in Eq. (2) becomes

$$h_{ef} = \min\{0.4h,\ 140\ \text{mm}\}. \tag{4}$$

When the loaded area is non-rectangular (e.g. round washers), l_{ef} and $l_{c,90}$ in Eq. (2) may be replaced by the corresponding effective area and loaded area.

Cross-Laminated Timber (CLT). For CLT compressed perpendicular to its plane, additional mechanisms (notably the "blocking'' effect *Brandner*, 2018) result in increased capacity. The distribution factor $k_{c,90,\text{CLT}}$ can be taken as 1.0 or, where $1 \leq t_{\text{max}}/t_{\text{min}} \leq 2$, may be calculated using a 35° spreading angle:

$$k_{c,90,\text{CLT}} = \sqrt{\frac{b_{ef}\, l_{ef}}{b_{c,90}\, l_{c,90}}} \leq 4.0, \tag{5}$$

with b_{ef} the effective width perpendicular to the grain and l_{ef} the effective length parallel to the grain.

3 Experimental Campaign

Two comprehensive CPG campaigns were performed at NTI and NTNU: one on glued-laminated (GLT) and solid timber (ST) members (*Moseng* & *Hagle*, 2012), and one on cross-laminated timber (CLT) (*Troller*, 2014). An overview of the experimental series are provided in Table 2 and 3. A detailed description of the testing campaigs and its results can be found in *Pasca* et al., 2024. A short summary of the testings are hereby reported:

- GLT/ST campaign.

*Table 2. Overview of the experimental tests, where **b** and **h** are the specimen width and height, d_s is the distance from support to load plate, **l** the specimen's total length and $l_{c,90}$ the load plate length.*

Series	Plate	Spec. Geo		Length		Plate		Constraint			
	l_{c90} [mm]	b [mm]	h [mm]	d_s [mm]	l_{tot} [mm]	∧	∩	Rot	Fix	n. test	Class
A1	90	90	60		90	X			X	4	L40C
A2	90	90	90		90	X			X	5	L40C
A3	90	90	120		90	X			X	4	L40C
A4	90	90	150		90	X			X	4	L40C
B1	48	90	90		980	X			X	10	L40C
B2	48	90	90		980		X		X	15	L40C
B3	90	90	90		980		X		X	10	L40C
B4	48	90	90		980		X	X		10	L40C
B5	90	90	90		980		X	X		10	L40C
B6	48	45	90		980		X		X	10	L40C
B7	48	90	48		980		X		X	10	C24/C30
B8	90	90	405		980		X		X	10	L40C
D1	48	90	90		980		X		X	12	L40C
E1	48	90	90		980		X		X	14	L40C
F1	48	90	90		980	X			X	15	L40C
F2	48	90	90		980		X		X	15	L40C
H1	48	48	198	376	980		X		X	15	C24/C30
H2	90	90	405	605	1480		X		X	14	L40C
H3	90	90	405	605	1480		X	X		14	L40C
									Total	201	

*Table 3. Overview of the experimental tests, where **b** and **l** are the width and length, **h** the height, with subscripts specific to the load plate, specimen and support plate as done in Table ??. In and Out in the last column indicate the inner and outer lamellae.*

Series	$l_{c,90}$ [mm]	$b_{c,90}$ [mm]	l [mm]	b [mm]	h [mm]	l_s [mm]	b_s [mm]	Steel	CLT	n. test	Class
A1	50	50	50	50	100	50	50	X		9	T22 (out) T15 (in)
A2	100	100	100	100	100	100	100	X		8	T22 (out) T15 (in)
B1	50	50	400	50	100	400	50	X		5	T22 (out) T15 (in)
B2	100	100	400	100	100	400	100	X		5	T22 (out) T15 (in)
B3	100	100	400	100	100	400	100		X	5	T22 (out) T15 (in)
D1	50	50	400	50	100	50	50	X		5	T22 (out) T15 (in)
D2	100	100	400	100	100	100	100	X		5	T22 (out) T15 (in)
D3	100	100	400	100	100	100	100		X	5	T22 (out) T15 (in)
BM1	50	50	300	300	100	300	50	X		5	T22 (out) T15 (in)
BM2	100	100	300	300	100	300	100	X		5	T22 (out) T15 (in)
BM3	100	100	300	300	100	300	100		X	6	T22 (out) T15 (in)
DM1	50	50	300	300	100	50	50	X		4	T22 (out) T15 (in)
DM2	100	100	300	300	100	100	100	X		5	T22 (out) T15 (in)
DM3	100	100	300	300	100	100	100		X	6	T22 (out) T15 (in)
									Total	78	

- *Material.* Norwegian spruce GLT class L40C (≈ GL30C) and ST classes C24/C30; mean densities 454 kg/m^3 (GLT) and 412 kg/m^3 (ST) at 12% moisture content.
- *Configurations.* Seven basic layouts (A, B, D, E, F, H) with ∼ 200 tests in total. Main variables were: (i) load position (centre vs. edge), (ii) support type (continuous vs. discrete), (iii) steel plate edge (*sharp* or *smooth*), and (iv) load-transmission constraint (pinned or fixed).
- *Results.* Continuous supports yield 13–24 % higher stresses than discrete supports; edge loading reduces stresses by 21–32 %; using a 48 mm rather than a 90 mm loading plate increases stresses by 23–40 %; narrowing the specimen from 90 mm to 45 mm lowers stress by about 15 % at low strain but has little effect beyond 5 %; and the influence of plate-edge shape and rotational restraint remains within 5 %.

• CLT campaign.

- *Material.* 100 mm three-layer panels (33 mm lamellae) of Norway spruce; outer T22 / inner T15; mean density 472 kg/m^3.
- *Configurations.* Five layouts (A, B, D, BM, DM) totalling 78 tests. Key parameters varied: specimen geometry (prism, strip, plate), load area (50 × 50 or 100 × 100 mm^2), load applicator (steel plate vs. CLT block), and support scheme (continuous vs. paired loads).
- *Results.* Moving from discrete to continuous supports raises strength by 5–21 % in beam-like elements (B vs. D) and by 29–50 % in plate-like specimens (BM vs. DM). Plate-like elements also outperform beam-like ones by up to 46 % when continuously supported, whereas the advantage is limited to 8 % with discrete support. Enlarging the loading plate and specimen width decreases stresses by 14–20 % for continuous support and by up to 9 % for discrete support. Finally, replacing the steel plate with a CLT block at the load interface reduces capacity by 8–12 %.

3.1 Deformation level and k_{mat} evaluation

Two alternative definitions of deformation were evaluated. First, the **EN 408 method** (*EN 408* 2003) treats deformation as the residual value after unloading: the tangent to the initial elastic branch is translated by the target residual strain until it intersects the force–displacement curve (Fig. 2a), and the compressive strength $f_{c,90}$ is read at a residual strain of 1 %. Second, the **2.5 %ε method** regards deformation as the total strain during loading: the capacity is taken directly at a fixed total strain, here 2.5 % (Fig. 2b), a value considered roughly equivalent to 1 % residual strain in perpendicular-to-grain compression (*Leijten*, 2018). For solid timber and GLT this total-strain approach consistently underestimates strength when compared with EN 408, whereas for CLT the

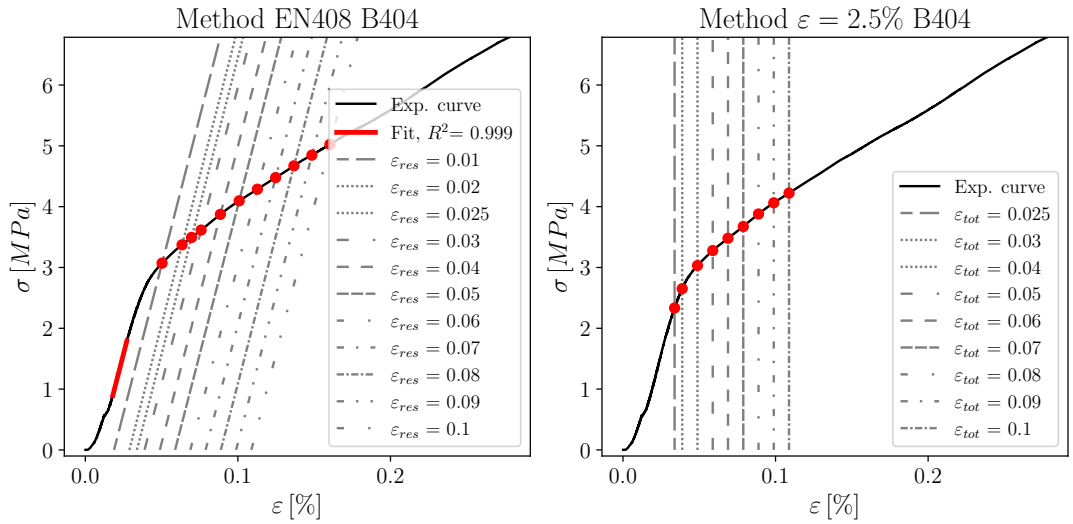

Figure 2. Procedures for assessing the capacity at several deformation levels on an experimental sample curve; (a) method based on EN408 and (b) method discussed in this research.

two procedures yield very similar results results. Consequently, EN 408 was adopted for the subsequent analysis.

The material factor k_{mat} was determined for both glue-laminated timber (GLT) and cross-laminated timber (CLT) as the ratio between the stress at a given residual strain and the stress at 1% residual strain, so that $k_{mat} = 1$ at $\varepsilon_r = 1\%$. According to the Eurocode (case B), k_{mat} is calculated as 2.1/1.4, yielding a value of 1.50 at 10% total deformation. The present experimental results indicate lower values.

For GLT, a residual deformation of 10% (corresponding to roughly 11—13% total deformation) leads to $k_{mat} = 1.46$, while at 10% total deformation the factor decreases to approximately 1.35. A linear regression of all GLT results confirms a nearly perfect linear correlation between deformation and the increase in strength, with a coefficient of determination $R^2 = 0.977$. Enforcing $\hat{k}_{mat} = 1$ at 1% strain for physical consistency, the empirical relation reads

$$\hat{k}_{mat} = 1 + 0.0522\,\varepsilon\,[\%], \tag{6}$$

where ε is the deformation level expressed in percent.

For CLT, the trend is similar but slightly less pronounced, with $k_{mat} = 1.41$ at 10% deformation. The corresponding regression, constrained to pass through $\hat{k}_{mat} = 1$ at $\varepsilon = 1\%$, exhibits an even higher coefficient of determination $R^2 = 0.985$ and is expressed as

$$\hat{k}_{mat} = 1 + 0.0461\,\varepsilon\,[\%]. \tag{7}$$

Overall, both materials exhibit an almost linear increase of k_{mat} with the deformation level, with GLT showing a marginally steeper slope than CLT. In all cases, the experimental

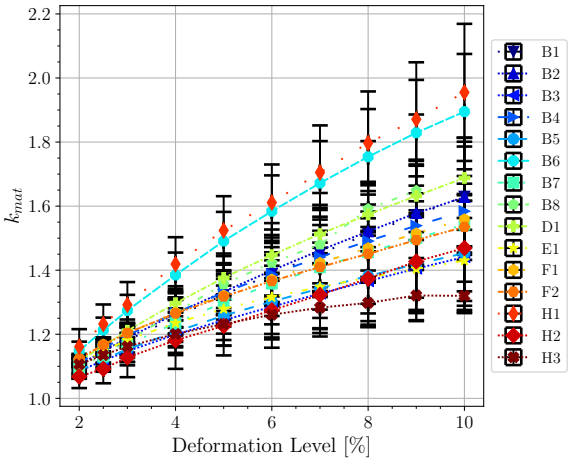

(a) Variation of the estimated k_{mat} as a function of the deformation level across the considered experimental configurations for GLT and solid timber;

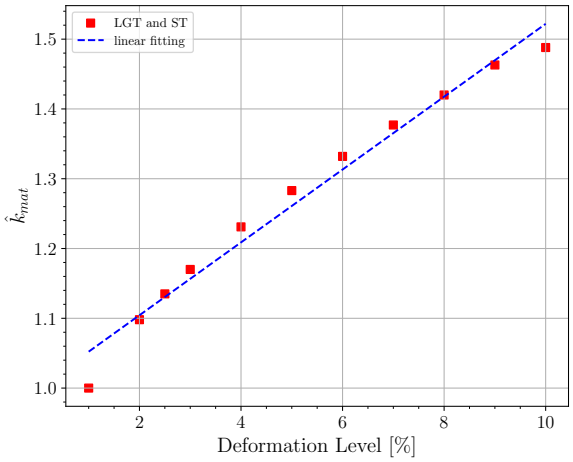

(b) linear fitting of the average k_{mat} values.

Figure 3

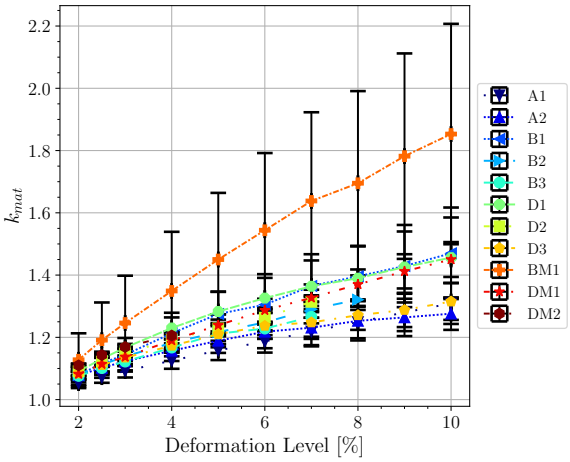

(a) Variation of the estimated k_{mat} as a function of the deformation level across the considered experimental configurations for CLT;

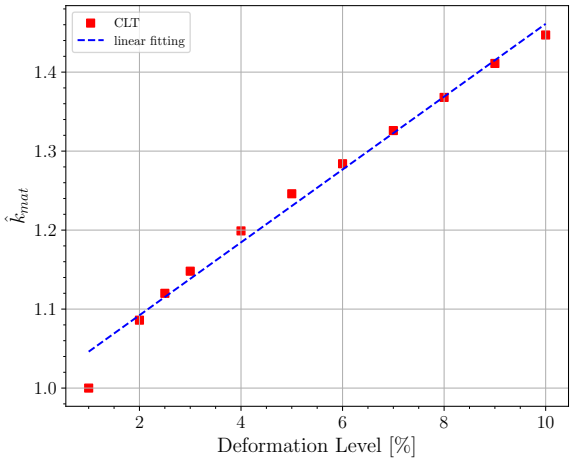

(b) linear fitting of the average k_{mat} values.

Figure 4

values remain below the Eurocode recommendation across the investigated deformation range.

3.2 Model validation

This section evaluates the predictive performance of the model presently adopted by the Eurocode, see Equation 1. The parameters k_{mat} and $f_{c,90,m}$ are taken directly from the experimental results. Specifically, $\hat{k}_{mat}$ is evaluated at the mean deformation of the glulam (GLT) and solid-timber (ST) tests, whereas $\hat{f}_{c,90,m}$ corresponds to the overall mean value of GLT+ST tests and the CLT tests at 1 % deformation. Using experimental values for k_{mat} and $f_{c,90,m}$ maximises the epistemic component of the prediction error.

$$F_{c,90,m} = k_{c,90}\,\hat{k}_{mat}\,A\,\hat{f}_{c,90,m} \tag{8}$$

Here, $F_{c,90,m}$ is the predicted mean resistance in compression perpendicular to grain (CPG), and $k_{c,90}$ is determined by Equation 2 for GLT+ST and by Equation 5 for CLT.

Figure 5 compares predicted and measured capacities for every GLT+ST configuration and deformation level. Figure 5 (a) employs the experimental mean value $\hat{f}_{c,90,m} = 3.27$ MPa, while Figure 5 (b) uses the characteristic value $\hat{f}_{c,90,k} = 1.85$ MPa obtained from a log-normal fit of the 1 %-deformation stresses in accordance with EN 408, after removing the influence of $k_{c,90}$.

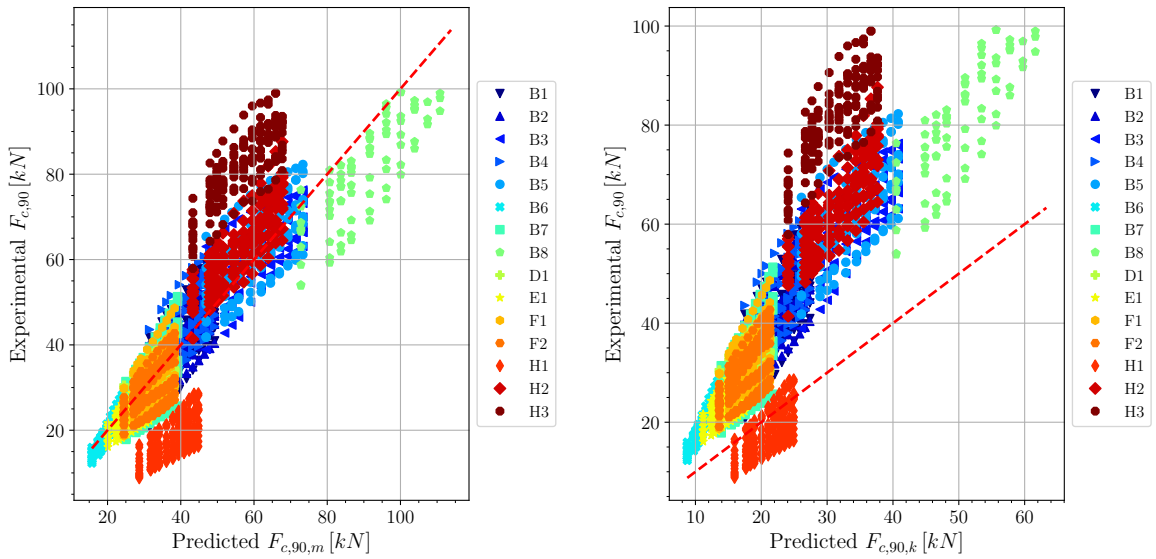

(a) prediction based on the mean CPG strength;

(b) prediction based on the characteristic CPG strength.

Figure 5. Predicted versus experimental capacities for all GLT+ST configurations and deformation levels:

The quality of the correlation varies markedly between configurations, as seen in Figure 5. Some test groups contain clear outliers, strongly over-predicting (H1) or under-predicting

(H3) the measured resistance. Table 4 quantifies these trends through the ratio of predicted to experimental forces, the standard deviation (SD) of that ratio, the mean-squared error (MSE), maximum absolute error (MAE), root-mean-squared error (RMSE), variance accounted for (VAF) and coefficient of determination (R^2).

Table 4. Error metrics of the predictive model for GLT+ST (Figure 5).

Test label	$\frac{F_{c,90,\mathrm{Pred}}}{F_{c,90,\mathrm{Exp}}}$	σ	MSE [kN^2]	RMSE [kN]	MAE [kN]	VAF [%]	R^2
B1-7	1.00	0.14	35.10	5.68	4.59	52.84	0.55
B8	1.13	0.10	144.22	12.01	10.07	67.64	0.68
D1	1.05	0.12	14.23	3.77	3.22	51.17	0.52
E1	1.13	0.11	13.92	3.73	3.17	47.31	0.56
F1-2	1.04	0.15	19.53	4.40	3.54	45.83	0.46
H1	2.25	0.42	413.71	20.34	20.04	44.27	0.55
H2	0.90	0.07	66.45	8.15	6.81	68.89	0.69
H3	0.69	0.06	646.11	25.42	24.87	62.65	0.63
H1-3	1.31	0.74	375.43	17.97	17.24	58.60	0.63
All data	1.17	0.21	115.36	10.74	7.49	73.91	0.74
All data (no H, B8)	1.03	0.15	27.50	5.24	4.10	86.53	0.87

Although individual configurations display modest R^2 values (down to 0.46 for F1-2 and averaging 0.59), the global coefficient rises to 0.74—and to 0.87 when the H series and B8 are excluded—because positive and negative errors partially cancel. On a global scale, therefore, Equation 8 provides a satisfactory prediction.

The pronounced under-prediction for B8 suggests that the assumptions regarding h_{ef} warrant reconsideration; the H series likewise merits separate scrutiny for eccentric loading at supports. Nevertheless, even with a single k_{mat} per deformation level, the formulation achieves an overall R^2 of 0.87 (excluding H and B8), a remarkably high figure in view of its simplicity. This underlines the effectiveness of Equation 1, while leaving room for refinement by allowing k_{mat} to vary with deformation.

Figure 6 presents the analogous comparison for CLT. Figure 6l (a) employs $\widehat{f}_{c,90,m} = 4.28\,\mathrm{MPa}$; Figure 6 (b) uses the characteristic value $\widehat{f}_{c,90,k} = 3.29\,\mathrm{MPa}$ obtained from a log-normal fit of the $1\,\%$-deformation stresses after removal of $k_{c,90}$.

Table 5. Error metrics of the predictive model for CLT (Figure 6).

Test label	$\frac{F_{c,90,\mathrm{Pred}}}{F_{c,90,\mathrm{Exp}}}$	σ	MSE [kN^2]	RMSE [kN]	MAE [kN]	VAF [%]	R^2
A2	1.05	0.10	5.70	2.25	1.94	49.43	0.55
B	0.86	0.12	169.16	12.13	11.00	40.76	0.42
D	0.96	0.10	80.89	7.61	6.56	49.36	0.51
BM	0.93	0.08	13.63	3.69	3.09	68.09	0.78
DM	1.16	0.16	27.32	4.99	4.70	74.06	0.82
Mean	0.99	0.15	75.44	7.04	6.28	53.22	0.57

Table 5 shows that CLT errors (MSE, RMSE, MAE) are generally smaller than for GLT+ST, though the average R^2 is lower (0.57) because the BM and DM series exhibit greater scatter. Nonetheless, the constant-k_{mat} approach again delivers acceptable accuracy.

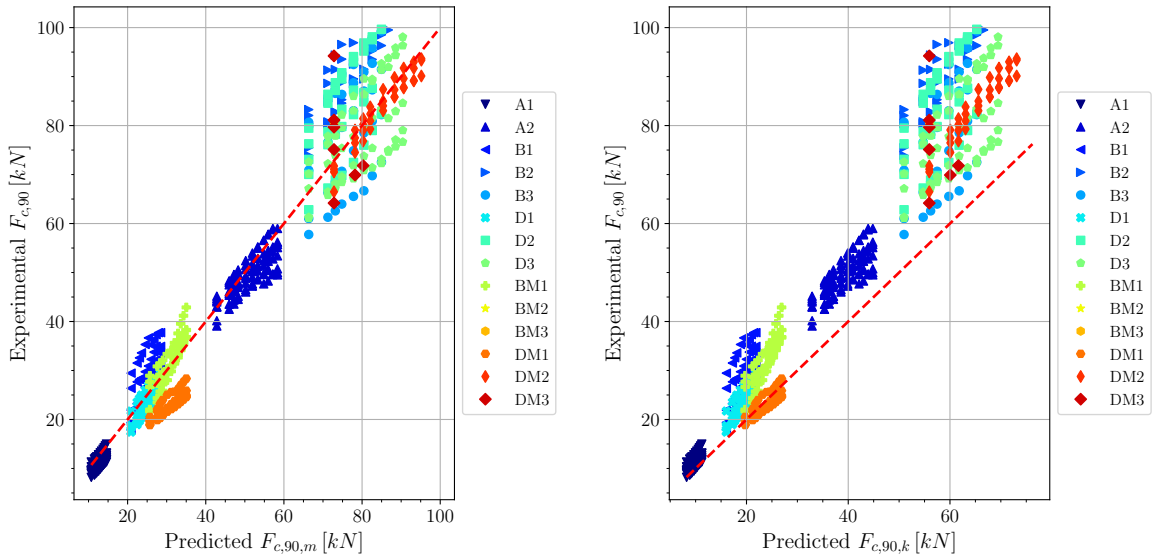

(a) prediction based on the mean CPG strength;

(b) prediction based on the characteristic CPG strength.

Figure 6. Predicted versus experimental capacities for all CLT configurations and deformation levels:

4 Effect of specimen height on the effective height

This section investigates optimal thresholds for the effective height in Equations 3 and 4 when estimating the coefficient $k_{c,90}$.

This study reveal increasing prediction errors and overestimation of capacity for specimens of greater height. This suggests that the existing limits on effective height in Equations 3 and 4 may be non-conservative for taller beams.

A calibrated finite-element (FE) model, validated against experimental capacity curves, was used for a parametric study: specimen heights h were varied from 45 mm to 750 mm across all tested configurations.

For each height, the estimated compressive strength at 1% deformation $f_{c,90,1\%}$ (per EN 408) was compared to that of reference configuration A, defining $\hat{k}_{c,90}$ as:

$$\hat{k}_{c,90} = \frac{f_{c,90,1\%}}{f_{c,90,1\%,A}} \tag{9}$$

Assuming Equation 2 holds, the effective height $\hat{h}_{ef}$ was then computed as:

$$\hat{h}_{ef} = \begin{cases} \frac{l_{c,90}(\hat{k}_{c,90}^2-1)}{2} & \text{if configuration B or D} \\ l_{c,90}(\hat{k}_{c,90}^2-1) & \text{if configuration E or F} \end{cases} \tag{10}$$

leading to the functional relationship:

$$\hat{h}_{ef} = f(h, x) \tag{11}$$

where x denotes the FE model's mechanical parameters. The goal was to identify the member height beyond which $\hat{h}_{ef}$ stabilizes, justifying a threshold in Equations 3 and 4.

4.1 Finite element model

A three-dimensional FE model in Abaqus/Standard represents GLT beams and steel plates with C3D8R hexahedral elements, using a 5 mm mesh. Symmetry reduced the simulated domain (between 1/2 and 1/8 of the geometry). Contact was modeled with hard normal behaviour and a friction coefficient $\mu = 0.3$. The contact interaction between the plates and the beam has been defined in such a way as to account for the possibility of separation, to avoid interpenetration between bodies and to reproduce friction. The steel plates were modeled as elastic-isotropic ($E = 210000\,N/mm^2$, $\nu = 0.3$). Timber was treated as homogeneous orthotropic: E_0, G_g, and G_r per EN 14080; Poisson's ratios per *Dahl*, 2009; and a bi-linear plastic law characterized by E_{90}, f_{y90} and a hardening factor $f_{100\%}/f_y$.

4.2 Model calibration

Using a genetic algorithm, the parameters $E_{90}, f_{y90}, f_{100\%}/f_y$ were optimized to minimize the RMSE:

$$\min : \Delta = \sqrt{\frac{1}{50}\sum_{p=1}^{50}(F_{M,p} - F_{E,p})^2} \tag{12}$$

with the following input parameters to optimize, defined in the domain:

$$\{30\text{ MPa}, 1\text{ MPa}, 1\} \leq \{E_{90}, f_{y90}, f_{100\%}/f_y\} \leq \{300\text{ MPa}, 10\text{ MPa}, 5\} \tag{13}$$

The calibrated averages show high variability (coefficients of variation up to 50 %, see *Pasca* et al., 2024), with mean $E_{90} = 86\text{N/mm}^2$, $f_{y90} = 2.57\text{N/mm}^2$ and hardening factor 2.03. The model's force–displacement predictions closely match experiments, and stress-diffusion patterns at 1 % displacement confirm a 45° spreading in simpler cases, with more complex shapes under boundary effects.

4.3 Results of parametric analyses

Parametric curves of $\hat{h}_{ef}$ vs. h (45–720 mm) were generated for configurations B, D, E, F and H, using both the fitted and literature parameter sets. In all cases, $\hat{h}_{ef}$ grows nearly linearly for small h but levels off as stress-spreading no longer yields full plasticization. For discrete support, $\hat{h}_{ef}$ plateaus around 150–200 mm; for continuous support, around 200–300 mm. Literature parameters slightly overestimate the threshold compared to fitted ones.

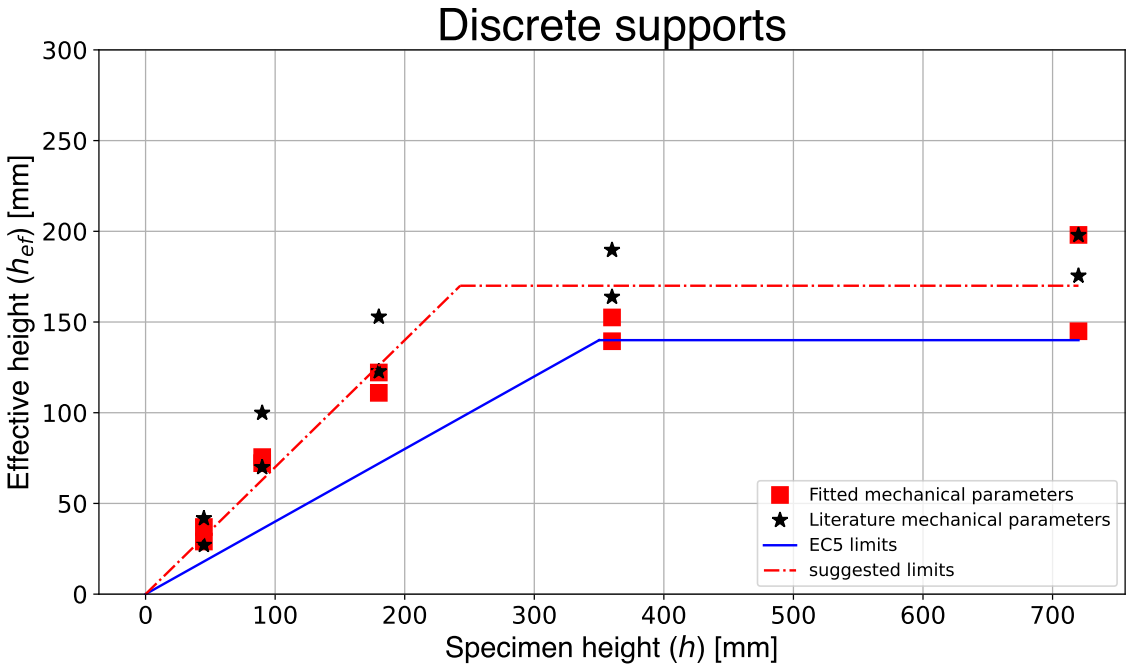

Figure 7. Variation of the effective height as a function of the specimen height for discrete support

Comparing these mean curves with existing standard thresholds shows that current limits are conservative for continuous support but non-conservative for discrete support. To reconcile this, the authors propose “suggested thresholds” that balance between the two parametric sets, rounding for practical standard use for continuous support to:

$$h_{ef} = \min\{0.7h, 210\ \text{mm}\} \tag{14}$$

and for discrete support to:

$$h_{ef} = \min\{0.7h, 170\ \text{mm}\} \tag{15}$$

These benchmarks offer a more conservative estimate for continuous supports and a more realistic one for discrete supports, aligning with the observed stabilization of effective height.

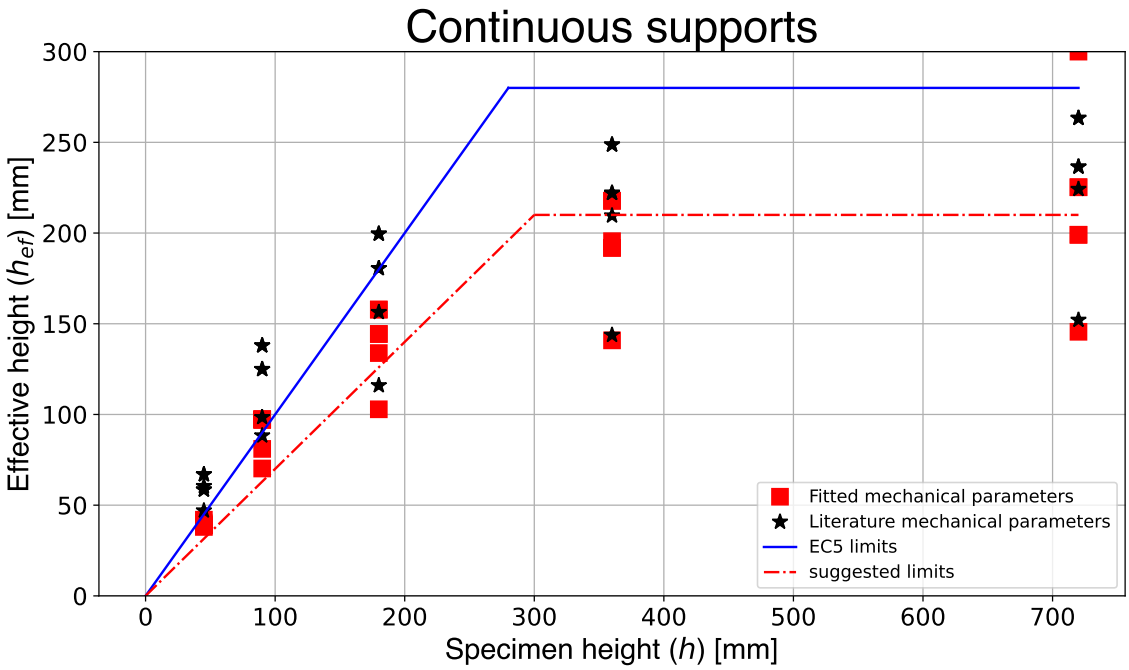

Figure 8. Variation of the effective height as a function of the specimen height for continuous support

5 Conclusions

The proposed deformation-dependent regression models for k_{mat} provide a more accurate representation of strength enhancement in CPG loading than the current Eurocode recommendation, with empirical slopes closely matching experimental behavior for both GLT/ST and CLT. Adjusting the effective depth limits to $h_{ef} = \min\{0.7h, 210\ \text{mm}\}$ for $h_{ef} = \min\{0.7h, 170\ \text{mm}\}$ continuous supports and for discrete supports yields conservative yet realistic estimates of stress redistribution. Validation against extensive testing and calibrated FEM results confirms that these modifications improve predictive capacity while maintaining simplicity.

6 References

Basta, C. (2005). In: *Characterizing Perpendicular-to-grain Compression in Wood Construction*.

Blass, H. & R. Goerlacher (2004). "Compression perpendicular to grain." In: *Proceedings of the 8th World Conference on Timber Engineering*. Lahti, Finland.

Brandner, R. (2018). "Cross laminated timber (CLT) in compression perpendicular to plane: Testing, properties, design and recommendations for harmonizing design provisions for structural timber products." In: *Engineering Structures* 171. cited By 31, pp. 944–960. DOI: 10.1016/j.engstruct.2018.02.076.

Brandner, R.; G. Flatscher; A. Ringhofer; G. Schickhofer & A. Thiel (2016). "Cross laminated timber (CLT): overview and development." In: *European Journal of Wood and Wood Products* 74.3, pp. 331–351.

CIB (1983). *Structural timber design code-edition 6*. Working Group W18- Timber Structures. CIB.

Dahl, K. B. (2009). "Mechanical properties of clear wood from Norway spruce [Doctoral thesis]." In: *Institutt for konstruksjonsteknikk, Norwegian University of Science and Technology (NTNU), Trondheim, Norway*.

EN 408 (2003). *EN 408 Timber structures — Structural timber and glued laminated timber — Determination of some physical and mechanical properties*. CEN.

DIN 1052 (1999). *Entwurf, Berechnung und Bemessung von Holzbauwerken*. Berlin: DIN.

EN 1995 (2005). *Eurocode 5 – design of timber structures – part 1–1*. Brussels: CEN.

Frey-Wyssling Stüssi, A. (1948). "Festigkeit und Vervormung von Nadelholz bei Druck quer zur faser." In: *Scheiz Z. Forstwes.* 3, pp. 106–114.

Gaber, E. (1940). "Druckversuche quer zur Faser an Nadel- und Laubhölzern." In: *Holz als Roh- und Werkstoff* 3.7-8, pp. 222–226. DOI: 10.1007/BF02717988.

Gehri, E. (1997). "Timber in compression perpendicular to grain, in IUFRO." In: *Copenhagen*.

Graf, O. (1921). "Beobachtungen über den Einfluss der Größe der Belastungsfläche auf die Widerstandsfähigkeit von Bauholz gegen Druckbelastung quer zur Faser." In: *Der Bauingenieur* 18, pp. 498–501.

Hassan, K.; T. Hussain & K. Arman (2014). "Compression perpendicular to grain in timber - Bearing strength for a sill plate." In: *Master Thesis*.

Hoffmeyer, P.; L. Damkilde & T. Pedersen (2000). "Structural timber and glulam in compression perpendicular to grain." In: *Holz als Roh - und Werkstoff* 58.1-2. cited By 30, pp. 73–80. DOI: 10.1007/s001070050390.

Hübner, U. (2013). "Mechanische Kenngröben von Buchen-, Eschen- und Robinienholz für lastabtragende Bauteile." In: *Mechanische Kenngröben von Buchen-, Eschen- und Robinienholz für Lastabtragende Bauteile*.

Kitamori, A.; T. Mori; Y. Kataoka & K. Komatsu (2009). "Effect of additional length on partial compression perpendicular to grain of wood." In: *J. Struct. Constr. Eng.* 74 (642), p. 8.

Kollmann, F. & W. Côté (1968). In: *Principles of Wood Science and Technology*.

Leijten, A. (2016). "The bearing strength capacity perpendicular to grain of norway spruce–Evaluation of three structural timber design models." In: *Construction and Building Materials* 105, pp. 528–535.

Leijten, A. (2018). "A strength and deformation model for timber loaded in compression perpendicular to grain." In: *Timber, bonds, connections, structures: Commemorative publication honoring the 65th birthday of Simon Aicher*. MPA University of Stuttgart, pp. 59–78.

Madsen, B.; R. Hooley & P. Hall (1982). "A design method for bearing stresses in wood." In: *Can. J. Civil Eng.* 9 (2), pp. 338–349.

Moseng, M. & D. Hagle (2012). "The capacity of wood for compression perpendicular to the grain." In: *Institutt for matematiske realfag og teknologi, NMBU, Oslo, Norway*.

NDS 2012 (2012). *National design specification for wood construction*. Leesburg: American Wood Council.

Pasca, D. P.; F. M. Massaro; Y. De Santis; H. Stamatopoulos; J. Ljungdahl & A. Aloisio (2024). "Deformation level and specimen geometry in compression perpendicular to the grain of solid timber, GLT and CLT timber products." In: *Engineering Structures* 321, p. 118972.

Persson, K. (2000). *Micromechanical modelling of wood and fibre properties*. Lund University, Department of Mechanics and Materials.

NEN 3852 (1978). *Regulations for the calculation of building structures– general considerations and loads TGB1972*. Delft, The Netherlands: NEN.

Rothmund, A. (1949). In: *Über Die Wiederstandsfähigkeit des Holzes Gegen Druck Quer Zur Faser*.

Stamatopoulos, H.; F. M. Massaro & J. Qazi (2022). "Mechanical properties of laterally loaded threaded rods embedded in softwood." In: *European Journal of Wood and Wood Products* 80.1, pp. 169–182.

Suenson, E. (1938). "Zulässiger Druck auf Querholz." In: *Holz als Roh- und Werkstoff: European Journal of Wood and Wood Industries* 1.6, pp. 213–216. DOI: 10.1007/BF02612242.

Swedish Wood (2016). *Design of timber structures*. vol. 1, 2nd ed. Vol. 1. Swedish Forest Industries Federation.

NZS 3603 (1993). *Timber design standard*. Standards New Zealand.

AS 1720 (1988). *Timber structures – Part 1: Design Methods*. Standards Australia.

Troller, J. B. (2014). "Compression Capacity of Timber Sills Loaded Perpendicular to the Grain: Ultimate Limit State (ULS) and Serviceability Limit State (SLS) [Master thesis]." In: *Institutt for konstruksjonsteknikk, Norwegian University of Science and Technology (NTNU), Trondheim, Norway*.

Van Der Put, T. (2008). "Derivation of the bearing strength perpendicular to the grain of locally loaded timber blocks." In: *Holz als Roh - und Werkstoff* 66.6. cited By 43, pp. 409–417. DOI: 10.1007/s00107-008-0258-0.

Van der Put, T. (1991). "Discussion of the failure criterion for combined bending and compression." In: *Meeting twenty four, International Council for Building Research Studies and Documentation Working Commission W18-Timber Structures*. Universitat Karlsruhe.

DISCUSSION

The paper was presented by D Pasca

A Frangi commented about the calibration results showing large differences between the E_{90} chosen and the E_{90} from literature.

J Töpler asked about the possible use of the numerical model for design. D Pasca responded that the configurations covered are different and may not be applicable directly for design. J Töpler commented that numerical models involve calibration versus verification and asked if two different data set were used. P Pasca said the data set was split such that 80% of the data were used for calibration and 20% of the data were used for verification.

R Tomasi and D Pasca discussed if the k_{mat} of case A was not of key interest but the paper focused on k_{mat} of case B matched the findings but leads to larger levels of deformation. R Tomasi asked, if the different values of h_{ef} were separated in analysis.

P Dietsch commented there are other models available and asked if the authors considered them. P Pasca responded that no as they only focused on the new Eurocode model. P Dietsch asked for any mechanistic explanation on h_{ef} = min (0.7h; 210 mm). D Pasca responded no as it was based on numerical results only. P Dietsch commented that perhaps it might be explained by compression perpendicular to grain stresses being transformed into shear stresses at this level of height.

T Tannert commented that the limit of the 210 mm seemed arbitrary. D Pasca responded that some regression work was done. He agreed this limit is a bit arbitrary and more simulations can be done in future.

P Dietsch also asked why the journal publication was realized before the INTER paper as the advantage of including suggestions from INTER experts is then missed. P Dietsch suggested that editorial checks be performed and additional references be added before submission for the proceedings.

Experimental study on timber compression and shear: effects of slope of grain and presence of screws

Nicol López Rodríguez, Onesta Wood Chair, University of Navarra, Pamplona, Spain;
Centro Nacional de Excelencia para la Industria de la Madera (CENAMAD),
Pontificia Universidad Católica de Chile, Santiago, Chile
nlopezrodri@unav.es

José M. Cabrero, ONESTA Wood Chair. University of Navarra, 31009 Pamplona, Spain.
jcabrero@unav.es

Ignacio Arteaga Jordá, Onesta Wood Chair, University of Navarra, Pamplona, Spain.
iarteaga@unav.es

Pablo Guindos Bretones, Faculty of Architecture and Centro de Innovación Tecnolóxica en Edificación e Enxeñería Civil (CITEEC), Universidade da Coruña, A Coruña, Spain;
Centro Nacional de Excelencia para la Industria de la Madera (CENAMAD),
Pontificia Universidad Católica de Chile, Santiago, Chile
pablo.guindos@udc.es

1 Introduction

Within the framework of the ongoing research project *Towards a Reliable and Efficient Analysis of Connections in Timber (REACT)*, several experimental campaigns have been designed to investigate the response of timber under various loading conditions and directions. Tests are planned in compression, shear, embedment, and tension, with the aim of examining the influence of anatomical singularities and effects of self-tapping screws on mechanical performance.

Previous studies have addressed off-axis compression and shear — see, for instance, *Crespo* et al. (2020), *Gupta* & *Sinha* (2012), *Hu* et al. (2021), *Liu* et al. (2019), and *Reiterer* & *Stanzl-Tschegg* (2001) for compression, and *Steiger* & *Gehri* (2011) and *Riyanto* & *Gupta* (1996) for shear. Regarding reinforcement with self-tapping screws, several works —e.g., *Bejtka* & *Blaß* (2002), *Bejtka* & *Blaß* (2005), and *Dietsch* et al. (2013)— have shown that it can improve both load-carrying capacity and ductility. Provisions for

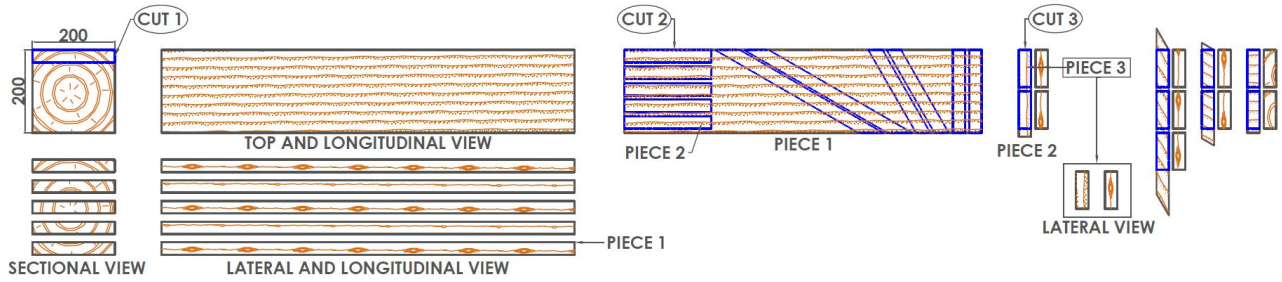

Figure 1. Cutting pattern used to obtain the samples.

reinforcement are also included in the draft version of the future Eurocode 5 (*FprEN 1995-1-1:2024*, 2024).

This paper presents the main results from the off-axis compression and shear test campaigns conducted on small-scale specimens containing natural defects. Standard testing configurations were modified when necessary, primarily for two reasons: to accommodate the screws and to maintain consistent specimen dimensions across different off-axis tests whenever possible.

2 Materials and Methods

2.1 Cutting and preparation of the samples

The samples were prepared from GL24h spruce (*Picea abies*) beams, which were sliced into 3 cm-thick layers following two distinct cutting patterns, as illustrated in Figure 1. In the first pattern, each slice contained a single lamella and is herein referred to as solid wood (S); in the second, each slice included two different lamellae with the glued interface located at mid-thickness, and is referred to as Glulam (G) for the purposes of this experimental campaign.

Each layer was subsequently cut using a CNC machine according to a predefined pattern (an example is shown in Figure 1) to produce specimens with different nominal fiber orientations.

2.2 Measurement of anatomical features

Before testing, and prior to applying the speckle pattern for photogrammetry, each specimen was photographed on all six faces. A complete geometrical and anatomical characterization was then carried out, including the recording of specimen dimensions, detailed documentation of anatomical features (e.g., slope of grain, local deviation, knots), and other relevant parameters such as moisture content, weight, and non-destructive ultrasound-based measurements of wave propagation speed.

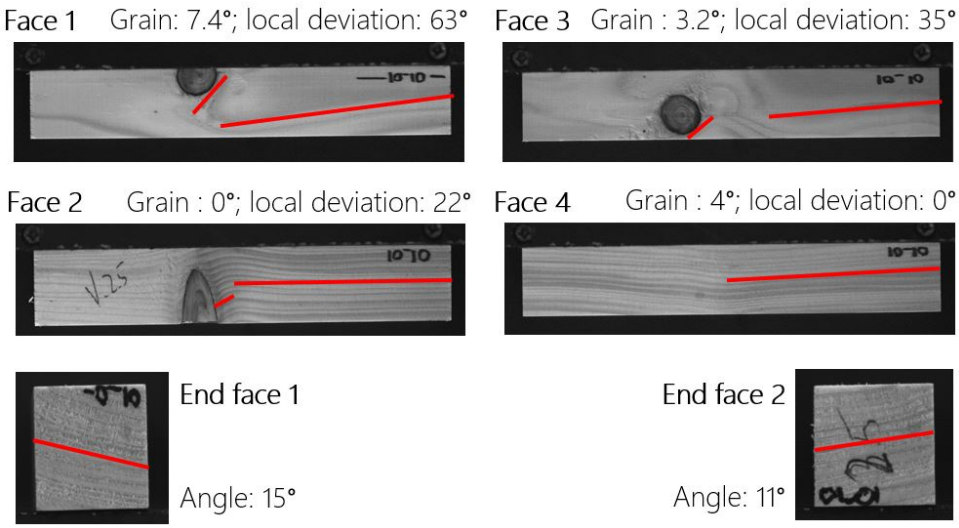

Figure 2. Measurement of face and end angles. The four side faces of a specimen with a nominal grain angle of 0° are shown. The final angles considered for this sample were: principal angle, 4° (faces 2 and 4, closer to the target angle 0°); secondary angle, 7.4° (faces 1 and 3); and local deviation, 63° (face 1).

2.2.1 Angles: principal, secondary and end grain

Each specimen was cut according to a pattern that defined a nominal slope of grain. The predominant slope of grain on the four side faces was measured, as illustrated in Figure 2, and grouped in pairs corresponding to each set of opposite faces. From each pair, the maximum value was retained. Among these, the angle closest to the nominal value was identified as the principal angle, while the angle on the orthogonal faces was defined as the secondary angle. As shown in the results, both angles influence the mechanical behavior and exhibit strong correlation.

In addition to the global slope of grain, the local slope of grain —usually associated with the presence of knots— was documented. For clarity, the term local deviation will hereafter be used to describe the local slope of grain. These were measured on all four side faces, as shown in Figure 2.

The radial or tangential orientation of each board was also characterized by an angle (see Figure 2). Values near 0° indicate tangential boards, while angles close to 45° correspond to radial orientations.

2.2.2 Knots

For knot characterization, standard criteria were followed (*EN 1309-3:2018*, 2017). The measured properties included the number of knots, their position—defined by coordinates along the longitudinal and transverse axes—and their size, expressed as the diameter in each direction.

Numerous knot-related indices have been proposed in the literature. In this study, the parameter used to characterize knot content is KAR_{eq}, defined as the ratio between the total knot area (assuming each knot to be circular) and the total area of the face.

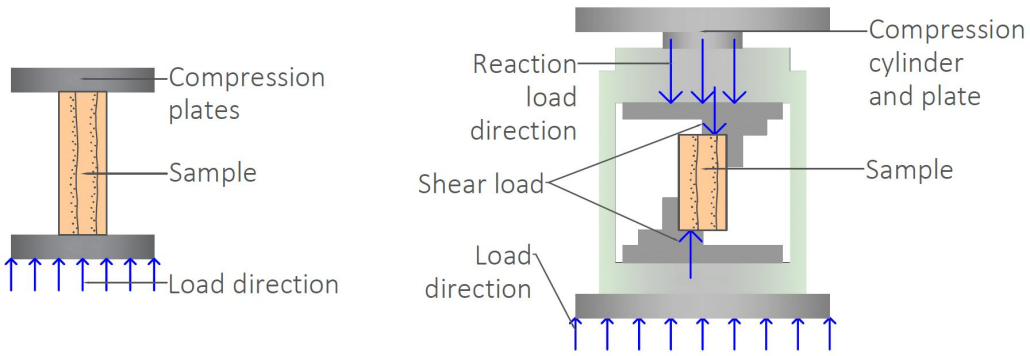

Figure 3. Test setup for compression (left) and shear (right) tests.

3 Tests

The specimens were conditioned according to *EN 408:2010+A1* (2012) to reach the reference moisture content of 12%. Strength, stiffness, and density values were subsequently corrected to this reference condition following the procedure described in *EN 384:2016+A2* (2022).

3.1 Compression tests

Compression tests were conducted following the setup described in *EN 408:2010+A1* (2012) for compression parallel to the grain, as illustrated in Figure 3 (left). In addition to standard specimens, off-axis and configurations with self-tapping screws were also tested. Specimens with dimensions of $30 \times 30 \times 180\,\text{mm}^3$ and $30 \times 30 \times 90\,\text{mm}^3$ ($b \times h \times \ell$, where b and h are the cross-sectional dimensions and ℓ is the length) were used. The variation in slenderness, from the recommended $\lambda = 6$ ($\ell = 180\,\text{mm}$) to $\lambda = 3$ ($\ell = 90\,\text{mm}$), was introduced to avoid premature buckling in off-axis specimens.

A total of twelve testing groups were defined, each comprising at least 34 specimens, and categorized according to slope of grain and the presence or absence of self-tapping screw. The studied slope of grains were 0°, 30°, 60°, and 90°. A fully threaded self-tapping screw (nominal diameter of 5.3 mm, length of 100 mm) was applied to solid wood specimens aligned parallel to the grain at angles of 30°, 45°, 60°, and 90°.

The full test campaign included 12 groups: 8 without (4 solid wood and 4 glulam) and 4 with self-tapping screws.

3.2 Shear tests

For the shear test campaign, the standard setup described in *EN 408:2010+A1* (2012) was not used, as it does not allow for the insertion of self-tapping screws. Instead, an alternative configuration was developed (Figure 3, right) to induce a shear plane along the central axis of the specimen and enable a comparative analysis between specimens with and without screw insertion.

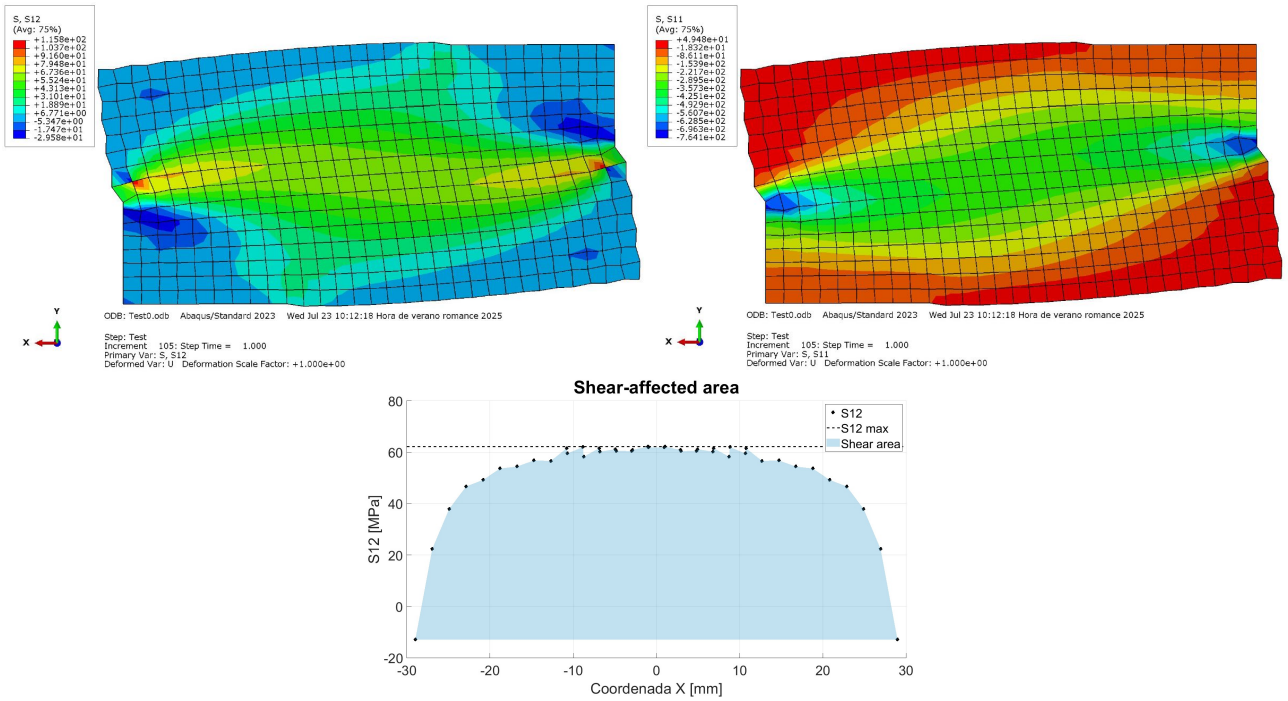

Figure 4. FEM results showing stress components and distribution: shear stress S12 (top left), and normal —compression— stress S11 distribution (top right), and the resulting shear stress distribution along the shearing section (bottom).

It is important to note that this setup, due to the presence of lateral supports to avoid overturning of the specimen, does not produce a pure shear state (as shown in Fig. 4 top); compressive stresses are also present, and thus interact with the shear stress field. A finite element model was employed to characterize the stress field and accurately determine the effective shear area (see Sect. 3.3.1).

Specimens with dimensions of $30 \times 30 \times 60\,\text{mm}^3$ ($b \times w \times h$; base, width, and height, respectively) were tested. Four groups of 30 solid timber specimens each were analyzed. All specimens had slope of grain oriented at 0° (i.e., load parallel to the grain), and three direction of screws were considered —30°, 60°, and 90°— in addition to a reference group with no screw.

3.3 Derivation of mechanical properties

3.3.1 Maximum strength

The maximum compressive strength, f_{max}, was calculated by dividing the maximum applied load, F_{max}, by the cross-sectional area ($30 \times 30\,\text{mm}^2$).

For the shear tests, a numerical model using solid elements with elastic properties was developed in ABAQUS (Figure 4) to determine the effective shear area based on the shear stress distribution $S12$ (Figure 4, bottom). The effective shear area was found to be 0.8205 bh, where b and h correspond to the nominal width (30 mm) and height (60 mm), respectively.

Due the presence of lateral supports to avoid overturning (see Fig. 3), compressive stress $S11$, which interact with the shear stress, develop (Figure 4, top right). Consequently, the calculated shear strength —obtained by dividing the maximum load by the effective area— should be cosidered as an apparent value, which nevertheless qualitatively assesses the influence of the screw presence in the shear plane response.

In cases where a plateau response was observed (off-axis compression and shear), the maximum force, F_{max}, was determined following the iterative procedure described in *EN 408:2010+A1* (2012) for compression perpendicular to the grain. This method consists of intersecting the load–deformation curve with a line shifted by $0.01h$, parallel to a reference line defined by points at 0.1 and 0.4 times an initial estimate of F_{max}.

3.3.2 Stiffness

In the compression tests, the modulus of elasticity was determined as described in *EN 408:2010+A1* (2012), based on the response between 0.1 and 0.4 times F_{max}. The deformation was measured by Digital Image Correlation (DIC) over a central segment corresponding to 67% of the specimen length, avoiding end effects due to crushing.

For shear tests, stiffness was qualitatively estimated as the ratio between the load increment, $F_2 - F_1$, measured between 0.1 and 0.4 times F_{max}, and the corresponding displacement increment, $d_2 - d_1$, recorded by the testing machine. This approximation allows for a preliminary comparison of the effect of screw presence on the mechanical response.[1]

3.3.3 Dynamic MOE

All specimens were evaluated using the *SylvaTest Trio* ultrasound device, which measures the ultrasound wave speed along the longitudinal axis of the specimen (noting that for off-axis specimens, this direction may not coincide with the fiber orientation). The dynamic modulus of elasticity (MOE_{dyn}) was calculated as $MOE_{dyn} = \rho v^2$, where ρ is the specimen density and v is the measured ultrasound wave speed (*Kasal* et al., 2010).

3.3.4 Ductility

The ductility index was determined following the definition in *EN 12512:2001* (2001) and calculated as the ratio between the ultimate slip, Δ_u, and the yield slip, Δ_y. For compression tests, Δ_u was defined as the displacement corresponding to $0.8F_{max}$, whereas for shear tests, due to their brittle behavior, Δ_u was taken at F_{max}.

[1] These are preliminary results that will be refined through a detailed assessment of the shear modulus using DIC techniques. A more comprehensive analysis of the strain distribution in the tested configuration is needed to accurately define the measurement region.

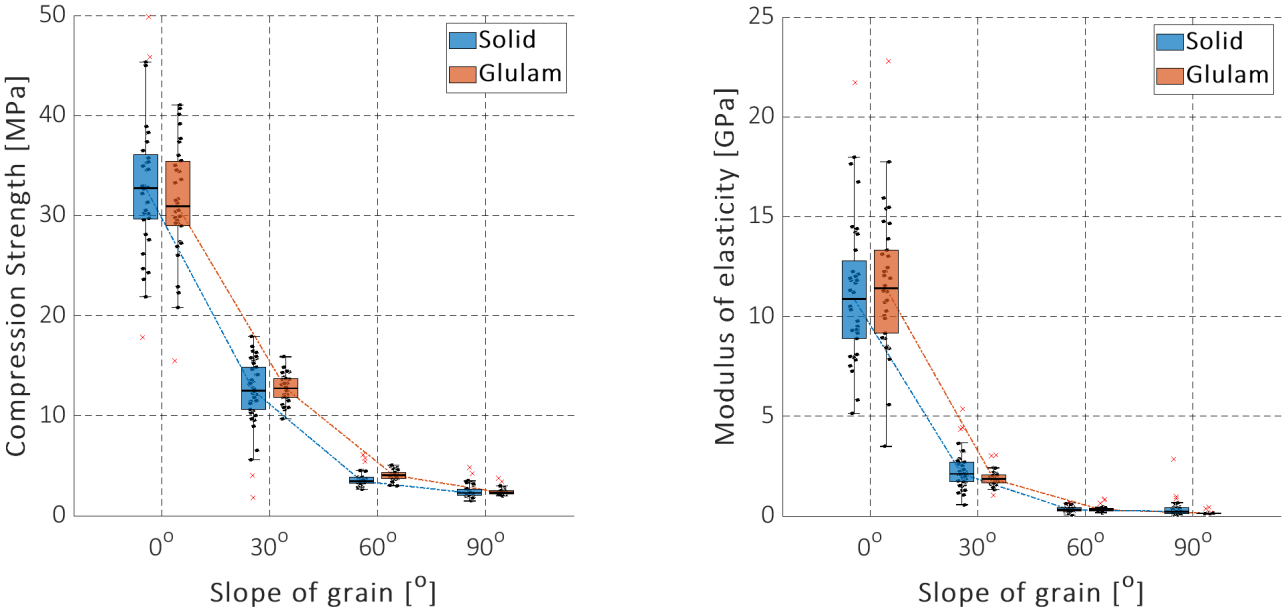

Figure 5. Compression results for off-axis tests: strength (left) and modulus of elasticity (MOE) (right).

3.3.5 Poisson's ratio

The Poisson's ratio, ν, was obtained from the DIC measurements as the ratio between the transverse strain, ε_t (radial and tangential directions were not distinguished), and the longitudinal strain.

4 Results and discusion

4.1 Compression tests

4.1.1 Mechanical properties

Table 1 presents the median values and coefficients of variation (COV) for moisture content, density, knot ratio, strength, modulus of elasticity (MOE), dynamic modulus of elasticity (MOE_{dyn}), ductility, and Poisson's ratio. Due to the high variability and presence of outliers in the experimental data, robust statistical estimators were employed, using the median as the central tendency measure and the interquartile range to assess variability.

In the groups without screw (Solid, 1–4; Glulam, 9-12), a progressive decrease in strength and stiffness with increasing slope of grain was observed, consistent with typical values reported in the literature (Figure 5). Variability tended to reduce for off-axis groups.

When applying the standard slenderness ratio ($\lambda = 6$) (*EN 408:2010+A1*, 2012) in off-axis groups, buckling was the predominant failure mode (see Figure 7). Therefore, the slenderness ratio was halved for these groups to ensure that material strength was effectively evaluated. A statistical analysis comparing results for both slenderness values showed no significant difference.

Table 1. Compression: Summary of physical and mechanical properties for all groups, showing median values and coefficients of variation. MC: moisture content; DNS: density; KR: knot ratio; STR: maximum strength; MOE: modulus of elasticity; DMOE: dynamic MOE (obtained by non-destructive techniques); DCT: ductility; ν: Poisson's ratio.

Gr.	Nom.	MC [%]	DNS [kg/m^3]	KR [%]	STR [MPa]	MOE [MPa]	DMOE [MPa]	DCT [-]	ν [-]
Solid									
1	S-00-NR-NR	11,79 (3%)	411,30 (12%)	1,40 (162%)	32,16 (15%)	10872 (26%)	11905 (26%)	2,67 (33%)	0,30 (31%)
2	S-30-NR-NR	12,03 (2%)	423,82 (12%)	0,89 (194%)	12,47 (25%)	2106 (33%)	2777 (23%)	2,56 (27%)	0,52 (84%)
3	S-60-NR-NR	11,76 (1%)	408,92 (9%)	0,87 (282%)	3,43 (13%)	326 (39%)	754 (19%)	6,18 (68%)	0,39 (101%)
4	S-90-NR-NR	11,62 (2%)	397,77 (15%)	0,81 (153%)	2,26 (19%)	226 (94%)	347 (30%)	9,40 (170%)	0,14 (269%)
Reinforced									
5	S-00-RE-30	12,08 (2%)	409,60 (13%)	1,06 (166%)	29,82 (19%)	13750 (37%)	12877 (28%)	2,01 (28%)	0,42 (26%)
6	S-00-RE-45	12,12 (2%)	436,65 (10%)	1,96 (170%)	31,63 (17%)	13041 (46%)	14584 (27%)	2,12 (30%)	0,45 (33%)
7	S-00-RE-60	11,48 (2%)	415,70 (12%)	1,90 (298%)	28,28 (20%)	12371 (43%)	12085 (24%)	3,51 (59%)	0,36 (54%)
8	S-00-RE-90	11,48 (7%)	405,27 (17%)	2,02 (165%)	29,34 (16%)	12203 (44%)	13844 (20%)	2,93 (28%)	0,42 (48%)
Glulam									
9	G-00-NR-NR	11,51 (1%)	420,79 (11%)	1,89 (236%)	30,56 (16%)	11412 (27%)	10958 (27%)	3,20 (32%)	0,33 (35%)
10	G-30-NR-NR	11,65 (7%)	384,63 (13%)	1,49 (209%)	12,56 (14%)	1852 (16%)	3357 (16%)	2,53 (49%)	0,69 (34%)
11	G-60-NR-NR	11,20 (1%)	436,52 (14%)	2,88 (131%)	3,97 (12%)	316 (34%)	1091 (28%)	10,67 (65%)	0,63 (29%)
12	G-90-NR-NR	10,98 (2%)	400,63 (16%)	1,20 (175%)	2,25 (11%)	135 (12%)	501 (31%)	10,64 (19%)	0,61 (31%)

Table 2. Shear: Summary of physical and mechanical properties for all groups, showing mean values and coefficients of variation. MC: moisture content; DNS: density; KR: knot ratio; STR: apparent maximum shear strength; STF: stiffness; DMOE: dynamic MOE (obtained by non-destructive techniques); DCT: ductility.

Nom.	MC [%]	DNS [kg/m^3]	KR [%]	STR [MPa]	STF [MPa]	DMOE [MPa]	DCT [-]
01-S-S-00-NR-NR	11.17 (2%)	473.61 (15%)	0.02 (410%)	13.92 (23%)	8442.09 (20%)	26090.38 (45%)	4.21 (20%)
05-S-S-00-RE-30	11.03 (2%)	536.21 (15%)	0.97 (279%)	14.49 (24%)	8306.29 (24%)	24858.54 (62%)	4.33 (22%)
06-S-S-00-RE-60	11.37 (2%)	449.39 (12%)	1.26 (273%)	12.7 (14%)	9700.17 (20%)	21146.02 (48%)	8.8 (19%)
07-S-S-00-RE-90	11.17 (1%)	426.14 (12%)	1.48 (291%)	13.65 (18%)	7364.16 (24%)	22888.42 (46%)	3.92 (19%)

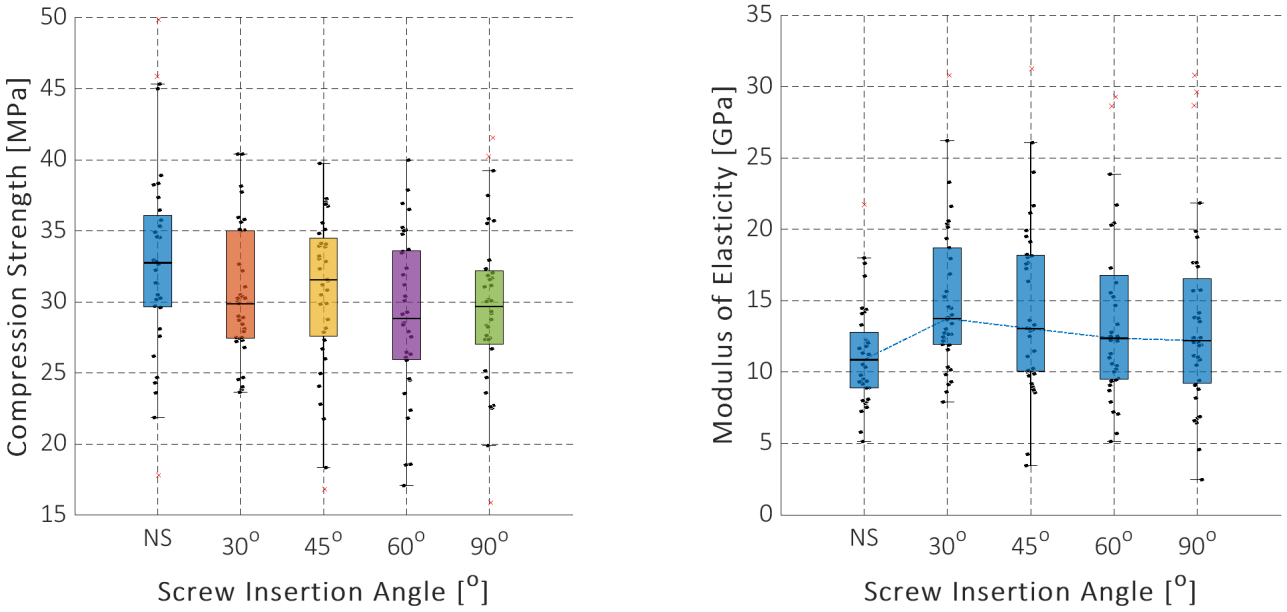

Figure 6. Compression. Groups with screw: strength (left) and modulus of elasticity (MOE) (right). The reference series (NS, no screw) is shown for comparison.

Self-tapping screws applied to specimens with slope of grain 0° did not result in a significant increase in strength (Figure 6, left), but produced a slight increase in MOE (Figure 6, right). ANOVA analysis revealed significant differences in MOE for screws inclined at 30°, 45°, and 60°, with a near-significant effect observed at 90° (p-value = 0.006).

4.1.2 Correlation between physical and mechanical properties

Table 3 presents the correlation matrix for the solid and glulam timber series without screw, illustrating the relationships between geometric features (e.g., global and local slope of grain, knot ratio) and mechanical properties (e.g., strength, modulus of elasticity, ductility, Poisson's ratio). Pearson correlation coefficients range from –1 to 1, with values closer to ±1 indicating stronger linear correlations.

4.1.2.1 Solid timber

As expected, the principal angle (PA) exhibits a strong negative correlation with maximum strength (STR) and modulus of elasticity (MOE) in both solid timber and glulam specimens without screws. No significant differences were observed between specimens composed of two lamellas (glulam) and those with a single lamella (solid). The secondary angle (SA) shows a similar, although weaker, influence on strength and MOE. Both principal and secondary angles are highly correlated, although this correlation is slightly lower in glulam due to the presence of two distinct lamellas.

The knot ratio (KR) and local deviation (LD) demonstrate a moderate positive correlation, which is expected since LD mainly corresponds to distortions occurring near knots. However, their impact on mechanical properties is less pronounced. In solid timber, KR shows negligible correlation with strength and MOE, confirming that the mere presence of knots does not significantly reduce compression properties. In glulam, a slight

Table 3. Compression. Correlation matrix between anatomical and mechanical properties. Above: glulam series; below: solid series. Key: PA: principal angle, SA: secondary angle, LD: local deviation, KR: knot ratio, EFA: end face angle, STR: maximum strength, MOE: modulus of elasticity, DMOE: non-destructive dynamic MOE, DCT: ductility, ν: Poisson's ratio.

GLULAM

		SA	KR	LD	EFA	STR	MOE	DMOE	DCT	ν	
		0.7	0.02	0.17	-0.45	-0.9	-0.8	-0.85	0.6	0.33	PA
SA	0.79		0.19	0.40	-0.12	-0.76	-0.75	-0.73	0.47	0.39	SA
KR	-0.08	0.08		0.66	0.14	-0.10	-0.12	-0.04	0.13	-0.06	KR
LD	0.18	0.31	0.65		0.11	-0.19	-0.20	-0.16	0.26	0.06	LD
EFA	-0.56	-0.44	-0.03	-0.25		0.25	0.14	0.22	-0.21	0.04	EG
STR	-0.87	-0.73	0.05	-0.14	0.33		0.95	0.96	-0.48	-0.5	STR
MOE	-0.77	-0.62	0.10	-0.09	0.28	0.92		0.97	-0.37	-0.54	MOE
DMOE	-0.82	-0.67	0.11	-0.08	0.30	0.95	0.93		-0.40	-0.52	DMOE
DCT	0.36	0.37	0.00	0.13	-0.18	-0.31	-0.24	-0.23		-0.05	DCT
ν	-0.08	-0.12	-0.12	-0.08	0.15	-0.05	-0.12	-0.06	0.03		
	PA	SA	KR	LD	EG	STR	MOE	DMOE	DCT		

SOLID

Table 4. Compression. Correlation matrix between anatomical and mechanical properties. Above: solid and glulam series without screw combined; below: with screw (0°) series. Key: PA: principal angle, SA: secondary angle, AS: angle of screw insertion, KR: knot ratio, LD: local deviation, EFA: end face angle, STR: maximum strength, MOE: modulus of elasticity, DMOE: dynamic MOE obtained by non-destructive measurement (sound speed), DCT: ductility, ν: Poisson's ratio.

SOLID+GLULAM (NO SCREW)

		SA	KR	LD	EFA	STR	MOE	DMOE	DCT	ν	
		0.72	-0.03	0.17	-0.51	-0.88	-0.79	-0.83	0.37	0.05	PA
SA	0.28		0.17	0.36	-0.28	-0.71	-0.66	-0.67	0.31	0.13	SA
KR	0.09	0.32		0.63	0.06	-0.03	-0.02	0.03	0.02	-0.03	KR
LD	0.00	0.22	0.71		-0.08	-0.16	-0.14	-0.12	0.13	-0.01	LD
EFA	-0.01	-0.11	-0.04	-0.11		0.29	0.21	0.26	-0.17	0.09	EG
STR	-0.09	-0.29	-0.57	-0.48	0.10		0.93	0.96	-0.32	-0.18	STR
MOE	-0.11	-0.11	-0.18	-0.09	0.12	0.27		0.94	-0.24	-0.24	MOE
DMOE	0.05	0.07	-0.14	-0.21	0.05	0.59	0.18		-0.25	-0.19	DMOE
DCT	0.00	0.00	0.04	0.20	0.02	-0.25	0.04	-0.32		0.00	DCT
ν	0.02	-0.14	0.04	0.05	0.15	0.16	0.18	-0.01	0.04		
	AS	SA	KR	LD	EG	STR	MOE	DMOE	DCT		

SCREW (0°)

inverse correlation between KR and mechanical properties is observed, possibly related to load eccentricity, as knots are confined to only one lamella of the cross-section.

As widely established —and forming the basis for many nondestructive mechanical and acoustic evaluation techniques— mechanical properties are strongly correlated with each other. While general trends are similar for both solid timber and glulam, correlations with ductility are notably higher in glulam, especially regarding the principal angle, where the correlation increases by an order of magnitude. Poisson's ratio shows relative weak correlations with all parameters, likely due to its sensitivity to local deformation mechanisms rather than global structural behavior.

Since statistical analysis revealed no significant differences in mechanical properties between solid timber and glulam series, the combined correlation matrix is presented in Table 4. The previously described trends persist, with most parameters behaving similarly across both groups. The most notable variation appears in the static modulus of elasticity (MOE), whose correlations with other parameters decrease when both datasets are combined.

4.1.2.2 Series with screw

The correlation matrix for specimens with self-tapping screws is presented in Table ??. In this case, the principal slope of grain is omitted because all specimens had grains oriented at 0°, parallel to the load direction. Instead, the angle of screw insertion (AS) is considered.

As expected, the insertion of the screw reduces the influence of the secondary angle. However, somewhat surprisingly, the correlations of knot ratio and slope of grain are greater in this group. As observed in failure modes (Figure 7, right), failure in specimens with screws tends to localize around the screw.

Both the dynamic and static moduli of elasticity (MOE) show a reduced correlation with strength. While strength (as shown in Table 1) did not significantly differ from the series without screw, MOE increased. This behavior likely results from the introduction of a stiffer element (the screw) in the specimen. Considering the very high correlation (0.96) between dynamic MOE and strength in the groups without screw, it is notable that the application of the screw reduces this correlation by about one third. This indicates that strength in specimens with screws is primarily influenced by the presence of the screw —rather than by the insertion angle (which shows a weak correlation)— and less so by the intrinsic mechanical properties of the timber, as reflected by the dynamic MOE.

4.2 Failure modes

Figure 7 shows representative failure modes observed in solid timber specimens, both with (left) and without screw (right).

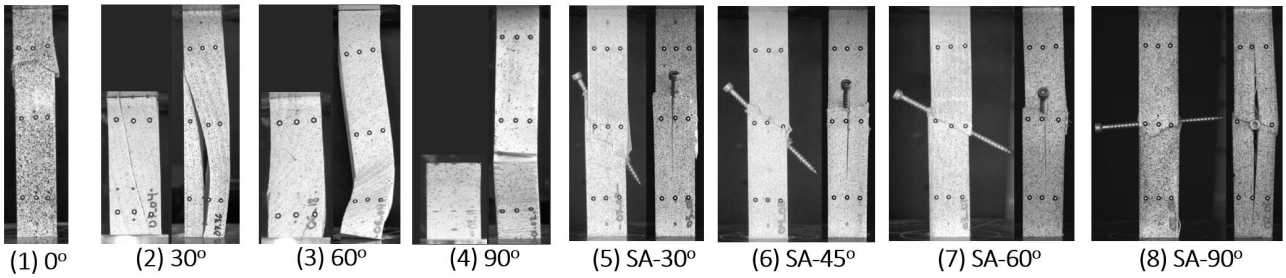

Figure 7. Failure modes of without (left, 1-4) and with screws (right, 5-6) solid timber specimens. For groups 2, 3, and 4, two specimens with different slenderness ratios are shown: specimens with the standard slenderness ratio recommended by EN 408:2010+A1 *(2012) tend to buckle, which motivated the reduction of slenderness.*

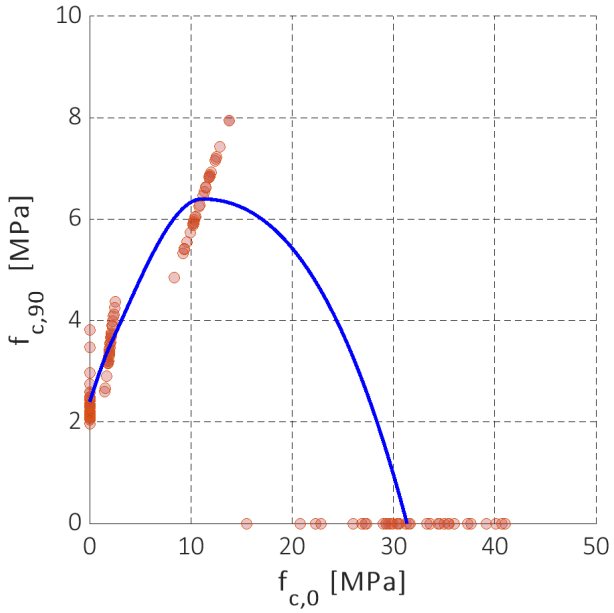

Figure 8. Compression: Interaction between longitudinal compression strength ($f_{c,0}$) and perpendicular compression strength ($f_{c,90}$). All test results are shown, with median values connected by a blue line illustrating a possible interaction envelope.

In specimens without screw, increasing slope of grain (Groups 2 to 4) leads to more ductile failure modes, such as slipping between growth rings, progressive buckling, and transverse crushing accompanied by large deformations. The parallel-to-grain group (Group 1) exhibits a localized brittle failure characterized by fiber buckling and minimal global deformation.

The four images on the right illustrate failure modes in the Groups 5 to 8 (with screws). In these groups, fractures predominantly occur near the screw, showing splitting and fiber collapse aligned with the angle of screw insertion. This behavior reflects localized load transfer and stress concentration around the screw.

4.3 Compression interaction

Figure 8 illustrates the interaction between longitudinal and perpendicular compression strengths. It can be observed that both compressive loads interact positively, with an

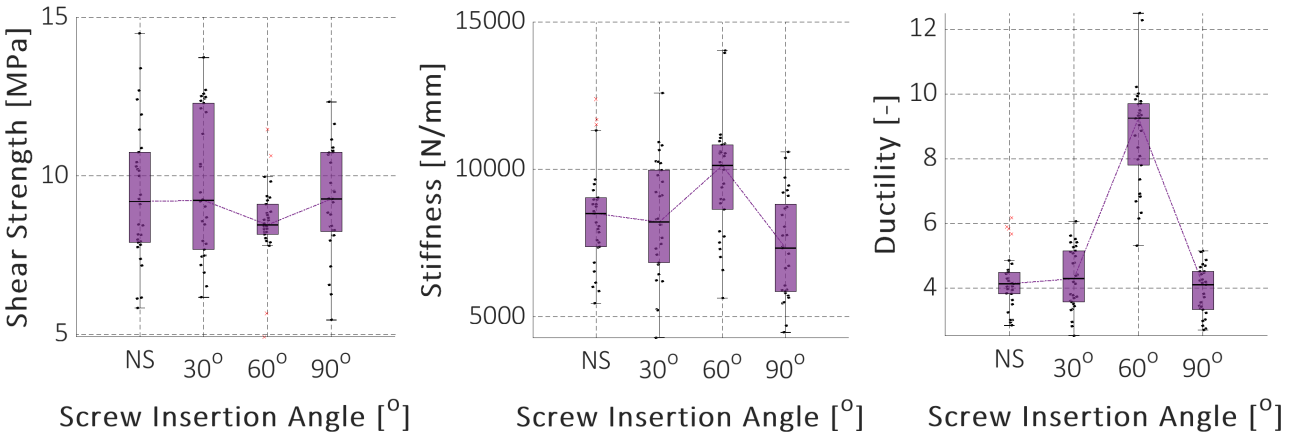

(a) Shear strength *(b) Shear stiffness* *(c) Shear ductility*

Figure 9. Shear. Experimental results: shear strength (left), stiffness (center), and ductility (right). No-screw results (NS) are shown for comparison.

increase in perpendicular strength when longitudinal compression is applied. Additional results would help refine the current polygonal interaction envelope.

5 Shear tests

5.1 Mechanical properties

Table 2 summarizes the measured mechanical and anatomical properties for each group in the shear series. Shear strength is similar across all groups (Figure 9a, left). No increase was observed in the groups without screw, while a decrease was noted for the group with a screw at 60°, accompanied by a reduction in variability. However, statistical analysis indicates no significant difference between this group and the others. The relatively high strength values observed across all groups are attributed to the influence of compression present in the test configuration, which contributes to an apparent shear responde rather than pure shear.

Specimens with screw at 60° exhibited the highest stiffness (Figure 9b, center), whereas those with screw at 90° showed the lowest stiffness; in both cases, the differences were statistically significant. Specimens with screw at 30° displayed stiffness comparable to the series without screw. All groups, except those with screw at 60°, had similar ductility indices (Figure 9c, right). The 60° screw inserted group exhibited a doubling of ductility, which was also statistically significant.

5.2 Correlation factors in shear

5.2.1 Without screw

The correlation analysis of the shear series without screw is presented in Table 5 (above). The secondary angle (SA) is strongly correlated with the principal angle (PA), reflecting the careful specimen preparation aimed at achieving a more pure inter-ring shear. Both angles exhibit a moderate negative correlation (approximately between –0.25 and

Table 5. Shear. Correlation matrix between anatomical and mechanical properties for no screw (above) and with screw specimens (0° in all cases, below). Key: PA: principal angle, SA: secondary angle, AS: angle of screw insertion, KR: knot ratio, EFA: end face angle, STR: apparent maximum shear strength, STF: stiffness, DMOE: dynamic MOE obtained by non-destructive measurement (sound speed), DCT: ductility.

NO SCREW

		SA	EFA	KR	STR	STF	DMOE	DCT	
		0.97	-0.32	0.44	-0.28	-0.33	-0.47	-0.28	PA
SA	0.91		-0.37	0.38	-0.28	-0.36	-0.52	-0.29	SA
EFA	-0.17	-0.34		-0.01	0.55	0.71	0.43	0.63	EFA
KR	0.29	0.28	-0.11		-0.24	-0.06	0.02	-0.17	KR
AS	-0.2	-0.19	-0.12	0.06		0.8	0.37	0.94	STR
STR	-0.34	-0.4	0.41	-0.25	-0.12		0.48	0.94	STF
STF	-0.29	-0.29	0.01	-0.26	-0.18	0.55		0.45	DMOE
DMOE	-0.34	-0.41	0.41	-0.3	-0.07	0.73	0.44		
DCT	-0.14	-0.13	-0.09	-0.11	-0.06	0.12	0.77	0.16	
	PA	SA	EFA	KR	AS	STR	STF	DMOE	

WITH SCREW

–0.35) with the mechanical responses analyzed, namely apparent shear strength (STR) and stiffness (STF). Note that in this series, the shear modulus is not reported; instead, a qualitative stiffness derived from load cell displacement is used.

The end face angle (EFA) indicates the radial and tangential orientation of the specimen, where low values (close to 0°) correspond to tangential boards and values approaching 45° indicate radial boards. In more tangential specimens, the shear load is likely concentrated within a single growth ring, whereas in radial specimens, several rings are affected, resulting in a slightly stronger mechanical response, as evidenced by the moderate positive correlation observed. Stiffness and ductility are notably influenced by this effect, with radial specimens tending to exhibit higher values in both properties.

The knot ratio (KR) shows limited influence on strength and ductility, although it is sometimes assumed knots may act as shear reinforcements.

The mechanical properties (strength, stiffness, and ductility) display very strong internal correlations. The dynamic modulus of elasticity (DMOE) exhibits excellent correlation with both strength and stiffness, consistent with observations from the unreinforced compression series.

5.2.2 With screw

The correlation matrix for timber specimens under shear with screw (Table 5, below) reveals a general decrease in correlation values compared to the series without screw, indicating an influence of the screw.

As expected from the results reported in Section 5.1, where a distinct response was observed only for specimens with screw at 60°, the insertion direction shows a low

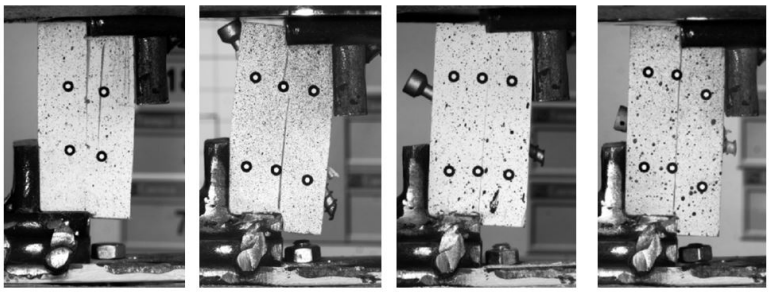

Figure 10. Failure modes in the shear tests.

correlation with mechanical properties. The consistency between stiffness and strength is reduced compared to the series without screw.

Although reduced to approximately 0.7 (compared to around 0.9 in samples without screw, the dynamic modulus of elasticity (DMOE) obtained via ultrasound speed still maintains a strong positive correlation with strength. Another high correlation is observed between ductility (DCT) and stiffness (STF).

Interestingly, the influence of the knot ratio (KR) on strength remains unchanged compared to the group without screw, while its correlation with stiffness increases. Additionally, the influence of the end face angle (EFA) increases, indicating a positive effect of the screw in connecting additional fibers for shear resistance.

5.3 Failure modes

Similar failure modes were observed across all tested groups, irrespective of the insertion self-tapping screws, as shown in Figure 10. Failure was primarily localized in a single layer, with a clear tearing between the two parts of the specimen, demonstrating the adequacy of the implemented test method.

6 Conclusions

This paper presents the results of two experimental campaigns on small timber specimens, focusing on compression and shear behavior under varying slopes of grain (compression) and presence of screw Compression tests followed slightly modified standard configurations —primarily reduced slenderness for off-axis specimens— while shear tests employed a novel setup enabling screw application. Anatomical singularities were measured for all the specimens.

In compression, slope of grain (principal and secondary angles) strongly governs mechanical response. Failure modes varied accordingly: parallel-to-grain loading induced localized crushing, whereas inclined grain produced more ductile behavior involving interlayer slip. Knot-related defects had minimal influence. An interaction was observed between compression strengths parallel and perpendicular to the grain.

The insertion of self-tapping screws (only to specimens with fibers parallel to the load) significantly increased compression stiffness across most insertion angles but did not yield a notable strength gain. Effects on ductility were inconclusive.

In shear, where grain was oriented parallel to the load, the presence of screws did not affect strength , and reduced variability for specimens with screw insertion angle at 60°. This group also exhibited the highest stiffness and ductility, with statistically significant differences. Screws at 90° resulted in the lowest stiffness, while the 30° group behaved similarly to specimens weithout screws. Shear failure localized along the midplane showed no difference between groups with and without screws.

These findings demonstrate that the application of screws, under compression and shear, primarily enhances stiffness without consistently increasing strength. Further experimental campaigns on other loading conditions (e.g., tension, embedment) are ongoing. The observed interaction between loading directions will support the development of a numerical fracture response model for timber.

Acknowledgments

The financial support provided by the Spanish Ministerio de Ciencia e Innovación and Fondo Europeo de Desarrollo Regional under contract PID2020-118569GB-C21 MINECO/FEDER UE is gratefully acknowledged. We also thank the Centro Integrado FP San Juan-Donibane for their assistance with specimen cutting and machining.

7 References

Bejtka, I. & H. J. Blaß (2002). “Joints with Inclined Screws”. In: *CIB-W18. International Council for Research and Innovation in Building and Construction. Meeting 35 (Kyoto, Japan)*. 35–7–4.

Bejtka, I. & H. J. Blaß (2005). “Self-tapping Screws as Reinforcements in Connections with Dowel-type Fasteners”. In: *CIB-W18. International Council for Research and Innovation in Building and Construction. Meeting 46 (Karlsruhe, Germany)*. 38-7-4.

Crespo, J.; A. Majano-Majano; A. J. Lara-Bocanegra & M. Guaita (2020). “Mechanical Properties of Small Clear Specimens of Eucalyptus globulus labill”. In: *Materials* 13, p. 906.

Dietsch, P.; H. Kreuzinger & S. Winter (2013). “Design of shear reinforcement for timber beams”. In: *CIB-W18. International Council for Research and Innovation in Building and Construction. Meeting 46 (Vancouver, Canada)*. 46-7-9.

EN 12512:2001 (2001). *Timber structures. Test methods. Cyclic testing of joints made with mechanical fasteners*. Comité Europèen de Normalisation (CEN).

EN 1309-3:2018 (2017). *Round and sawn timber - Methods of measurements - Part 2: Features and biological degradations*. Comité Europèen de Normalisation (CEN).

EN 384:2016+A2 (2022). *Structural timber - Determination of characteristic values of mechanical prperties and density*. Comité Europèen de Normalisation (CEN).

EN 408:2010+A1 (2012). *Timber structures - Structural timber and glued laminated timber - Determination of some physical and mechanical properties*. Comité Europèen de Normalisation (CEN).

FprEN 1995-1-1:2024 (2024). *Design of timber structures – Part 1-1: General – Common rules and rules for buildings*. Comité Européen de Normalisation (CEN).

Gupta, R. & A. Sinha (2012). "Effect of grain angle on shear strength of Douglas-fir wood". In: *Holzforschung* 66.5, pp. 655–658. ISSN: 00183830. DOI: 10.1515/hf-2011-0031.

Hu, W.; B. Chen & T. Zhang (2021). "Experimental and numerical studies on mechanical behaviors of beech wood under compressive and tensile states". In: *Wood Research* 66.1, pp. 27–38. ISSN: 13364561. DOI: 10.37763/WR.1336-4561/66.1.2738.

Kasal, B.; G. Lear & T. Tannert (2010). "In Situ Assessment of Structural Timber. State of the Art Report of the RILEM Technical Committee 215-AST". In: ed. by B. Kasal & T. Tannert. Springer. Chap. Stress waves, pp. 5–24. ISBN: 9789400705593.

Liu, F.; H. Zhang; F. Jiang; X. Wang & C. Guan (2019). "Variations in orthotropic elastic constants of green Chinese larch from pith to sapwood". In: *Forests* 10.5, pp. 1–16. ISSN: 19994907. DOI: 10.3390/f10050456.

Reiterer, A. & S. E. Stanzl-Tschegg (2001). "Compressive behaviour of softwood under uniaxial loading at different orientations to the grain". In: *Mechanics of Materials* 33.12, pp. 705–715. ISSN: 01676636. DOI: 10.1016/S0167-6636(01)00086-2.

Riyanto, D. S. & R. Gupta (1996). "Effect of ring angle on shear strength parallel to the grain of wood". In: *Forest Products Journal* 46.7-8, pp. 87–92. ISSN: 00157473.

Steiger, R. & E. Gehri (2011). "Interaction of shear stresses and stresses perpendicular to the grain". In: *CIB-W18. International Council for Research and Innovation in Building and Construction. Meeting 44 (Alghero, Italy)*. 44-6-2.

DISCUSSION

The paper was presented by N López Rodríguez

H Blass pointed out that in Figure 2 the interpretation of fiber orientation was incorrect as annual ring orientation was wrongly considered as fiber orientation.

H Blass commented that the screw through the specimen at 90 degrees did not provide any reinforcement to the wood; in fact, it would weaken the specimen.

A Frangi commented that the reported shear strength more than 10 MPa as high and the generalized conclusions were too strong.

T Tannert also commented on the wording of reinforcement being confusing.

P Dietsch commented on shear tests and received clarification that different direction of fiber orientation did not cause compression rather than shear stress.

A Frangi commented that shear area decreased by 20% could potentially explain the high shear strength.

P Dietsch and N López Rodríguez discussed whether there was any need for change to standards regarding the proposal and the conclusions that reinforcement could lower the strength. P Dietsch mentioned the work of M Enders-Comberg on steel fasteners in areas of compression.

Linear approximation of an elasto-plastic extension of the Johansen theory to predict the deformation of dowel-type fasteners

Johann Riepe, Universidade da Coruña, Center for Technological Innovation in Construction and Civil Engineering (CITEEC), Campus de Elviña, 15071, A Coruña, Spain
Jacobo Díaz, Universidade da Coruña, Center for Technological Innovation in Construction and Civil Engineering (CITEEC), Campus de Elviña, 15071, A Coruña, Spain
Jörg Schänzlin, Biberach University of Applied Sciences, Karlstraße 6-11, 88400 Biberach, Germany

Keywords: Johansen theory, Stiffness, Deformation , Beam-on-foundation method

1 Introduction

In timber structures, connections are of considerable importance in terms of the behaviour of the structural system, with regard to the distribution of forces, the deformation of the structure or the dynamic behaviour in the context of seismic resistance. In connections with dowel type fasteners (DTF), the interaction of the fastener and the timber material significantly affects the resulting stiffness. Consequently, the consideration of the deformation behaviour of a connection is given in standards. For example, *SIA265* (2021) and *DIN EN 1995-1-1* (2010) provide empirical formulae proposed by *Ehlbeck and Larsen* (1993), taking into account the density and the diameter of the fastener. However, comparing that approach with the determination of the bearing capacity, which is well described by the European Yield Model (EYM), based on *Johansen* (1949), important influencing variables are not taken into account, such as the force-fibre angle, the thickness of the cross-sections, the material properties of the fastener or the failure modes. Several studies (for example *Dorn et al.* (2013) or *Jockwer and Jorissen* (2018)) have outlined the need for further research to fill this gap. In this context, the well-established approach of a beam-on-foundation method (BOFM) should be considered, which can accurately describe the elastic-plastic behaviour of the embedded fastener

in the timber cross-section. This results in an elastic-plastic force-displacement relation which describes both the elastic stiffness of the connection at the beginning of loading and also the plasticisation, yielding at a maximum plateau, which represents the load-bearing capacity. This approach has been proved to be in good agreement with experimental data by *Lemaître et al.* (2018); *Gikonyo, Schweigler, et al.* (2024); *Gikonyo, Binder, et al.* (2023); *Gauß* (2024) and *Basterrechea-Arévalo et al.* (2023). However, this method is based on the need for finite element software and, depending on the level of detail, a high modelling and computational effort. In a standard, it may not be practical to have a procedure based on numerical software that is also highly dependent on the modelling capabilities of the designer. In *Riepe et al.* (2025), a new approach for determining the deformation of the fastener is presented based on the same theory for the determination of the bearing capacity, namely the Johansen theory. Elastic-plastic material laws are considered for the embedding behaviour of the fastener in the timber material, and also for the bending behaviour of the fastener, resulting in new extended basic equations of the original Johansen theory. With this new strategy, load-deformation curves can be obtained using numerical solvers. To further simplify the calculation procedure for engineering applications, linear approximations of the elasto-plastic extension of the Johansen theory are presented here. These approximations adequately reflect the deformation behavior of timber-timber connections with dowel-type fasteners through closed-form solutions.

2 Elasto-plastic extension and linear simplification

The consideration of elasto-plastic properties for the timber material and for the fastener of the connection results in stress distributions with linear and, depending on the load state, with plastic areas. An example of the stress distributions presented in *Riepe et al.* (2025) is shown in Fig. 1. The deformation, defining the transition from elastic to plastic bedding behaviour is provided with $w_{k,i} = f_{h,i,k}/\zeta_i$, with the embedment strength $f_{h,i,k}$ and the bedding parameter ζ_i (see section 3). Results indicate, as corroborated by several studies (e.g., *Dorn et al.* (2013)), that all force-deformation curves show similar behaviour, with elastic-plastic curves reaching an ultimate load that was already defined by the original Johansen theory.

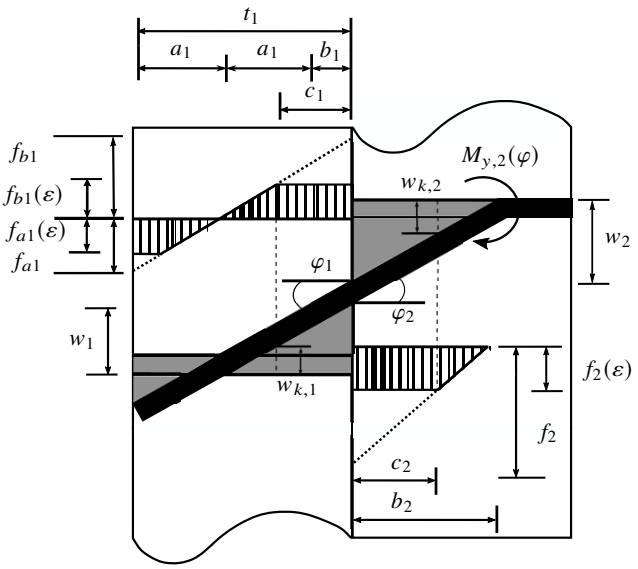

Figure 1. *Modified stress distributions for failure mode d, showing an already plasticised loadstate. A distinction between elastic and plastic areas of the stress distribution is made. Plasticised areas are indicated with c_1 and c_2 (see Riepe et al. (2025), figure 4).*

To simplify the application of the extended elasto-plastic theory, linear simplifications are presented here, defined with characteristic points of the load-deformation curve. Depending on the failure mode (FM), bilinear or, in the case of failure modes that show clear plastic behaviour, multilinear curves are obtained (see Fig. 2). In any case, at the beginning of the loading, all materials are in an elastic state. At a certain load, either the timber fibres begin to yield or, depending on the failure mode and the material properties, the fastener's bending angle is reached. With increased loading, the elastic limits of both the bedding and the fastener are reached one after the other. The plastic behaviour continues until the plastic joints of the fastener are fully developed and the plastic capacity of the contact area between the fastener and the timber material is fully exploited. The purpose of the linearised force-deformation curve is to adequately represent this characteristic behaviour.

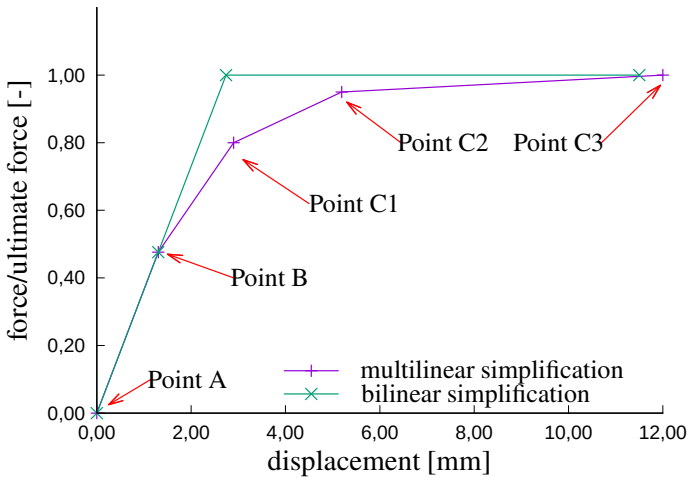

Figure 2. *Load-deformation curve. For the failure modes a, b and c, a bilinear simplification is defined by the point B, describing only the elastic stiffness. For the failure modes d, e and f, a multilinear simplification, defined by several points is provided*

Therefore, the first point of the linearised force-deformation curve (point *B* in Fig. 2) is supposed to describe the above described characteristic situation, which represents the transition from purely elastic to plastic behaviour. Since point *B* assumes different states depending on the connection configuration, i.e. elastic limit in cross-section one (CS1), elastic limit in cross-section two (CS2) or bending angle of the fastener – and in some configurations even several special cases –, the calculation is not entirely trivial and cannot be performed with a single set of formulae. If a multilinear force-deformation curve is provided (FM *d*, *e* and *f*), further points of the plastic part (points C_i) can be determined, which allows the development of a linearised elastic-plastic force-deformation relation, which in turn provides a description of the gradually flattening part.

In consequence, a clearly defined calculation procedure is required to evaluate which case occurs when determining the force-deformation relation. This procedure is illustrated in the form of flowcharts, which show the calculation process and also contain the necessary formulae (see section 8).

2.1 Description of characteristic points and special cases for failure mode *d*

A detailed description of all six failure modes and the respective points is not provided here. However, failure mode *d* will be considered in more detail. Due to its character-

istics, which are defined on the one hand by rotation of the fastener and, on the other, by the formation of a yield joint in the fastener, several failure modes can be addressed with this example: in failure mode *c*, the stress distribution in both cross-sections is similar to that in the failure mode shown here in CS1 and in failure mode *f*, the stress distributions in both cross-sections are similar to those in the example shown here in CS2 (see Fig. 1).

2.1.1 Characteristic point B

This point describes the situation in which plasticisation first occurs. When the elastic limit is reached, either the timber fibres begin to yield first, or the bending angle of the fastener is reached, depending on the embedding behaviour of the timber material and the bending angle of the fastener. As different material properties may be present in the timber cross-section, it is also necessary to distinguish in which of those the embedment resistance is reached first. For the derivation of directly calculable formulae, three different cases have to be considered.

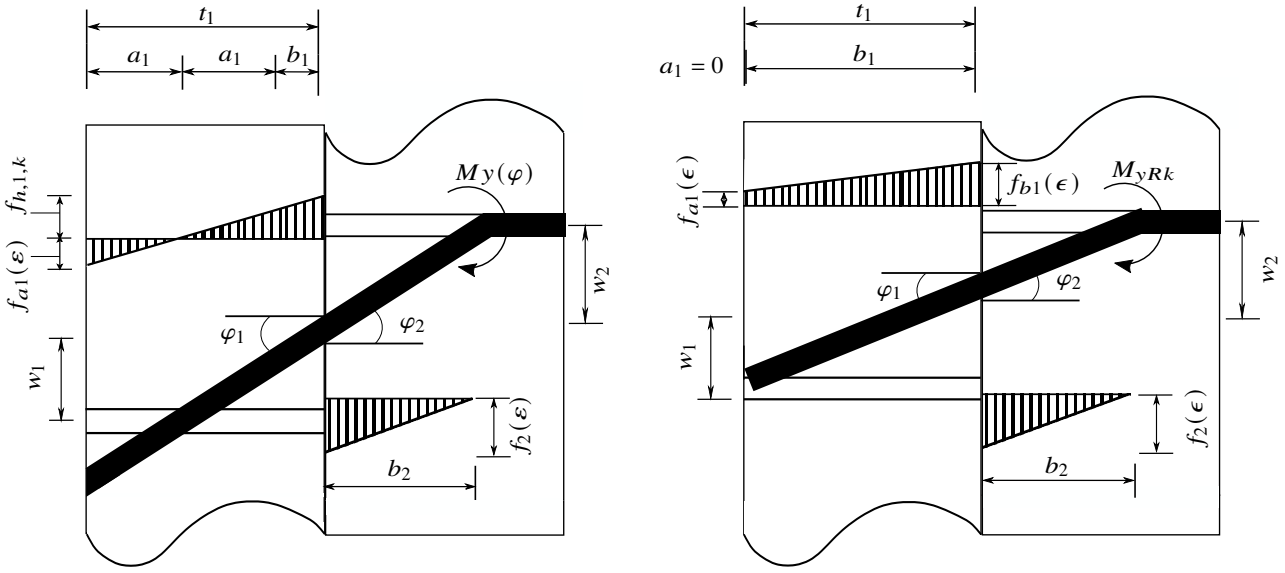

(a) *Case 1 of point B in failure mode d: elastic embedment limit reached in CS1, embedment stress in CS2 and bending moment still in elastic state.*

(b) *Special case 1 of point B in failure mode d: elastic limit of the bending moment reached with the embedding remain in elastic state.The fasteners rotation point in CS1 is located outside the CS thickness - no clamping in the area a_1 as illustrated in figure 3a.*

Figure 3. *Failure mode d: stress distribution for Case 1 (a) and Special case 1 (b).*

Fig. 3a illustrates the stress distribution that occurs when the timber material in CS 1 begins to yield. The state will be referred to as Case 1: $f_{h,1,k}$ is reached directly next to the shear plane in CS1, but the embedment limit in CS2 and the bending angle of the fastener have not yet been reached. Case 2 describes the situation in which the elastic limit is reached in CS2, while CS1 and the fastener remain in an elastic state. The stress distribution for Case 2 resembles that shown in Fig. 3a, except that $f_{h,1,k} = f_1(\varepsilon)$ (elastic) and $f_2(\varepsilon) = f_{h,2,k}$. Additionally, to describe Case 3, where the fastener shows

plastification first, Fig. 3a can be used to explain the stress distribution, when $f_{h,1,k} = f_1(\varepsilon)$ and $M_y = M_{y,Rk}$ applies. With this modification, the embedment strength is still elastic, but the plastic bending moment of the fastener would be reached.

In addition to the cases described above, three special cases were identified in this failure mode. In some connection configurations, no clear clamping of the fastener may occur at the beginning of the loading process, which is indicated by the fastener only being in contact with the timber in one direction (see Fig. 3b). The rotation point of the fastener is located outside the cross-section thickness, even though the rotation point moves with further loading into the cross-section resulting in the typical stress distribution of failure mode *d*. To address this situation, formulae for these special cases can be derived according to the stress distribution shown in Fig. 3b. Distinctions must be made here again, as plastification can first appear in either the timber material or in the fastener. Fig. 3b shows Special case 1, in which the yield joint of the fastener has been reached, but the timber is still elastic. Fig. 3b can also be used to illustrate Special cases 2 and 3, where the elastic limits in cross sections 1 or 2 have been reached, with the fastener remaining elastic with $f_b(\varepsilon) = f_{h,1,k}$ or $f_2(\varepsilon) = f_{h,2,k}$ and $M_{y,Rk} = M_y(\varphi)$. Preliminary results revealed large variation compared to a BOFM model. It is assumed that the derivation of the bending angle of the fastener for these cases needs to be revised and that the neglected deformation components have a significantly large influence. Therefore, if one of these special cases occurs, it is recommended to increase the thickness of the side member (t_1 for FM *d* or t_2 for FM *e*), so that the rotation point of the fastener is within the cross-section when the elastic limit is reached until the reason for the variations is identified.

2.1.2 Characteristic point C

With point *C*, all load states where both the timber and the fastener have already begun to yield will be described. In CS2, once plastification of the timber material has started, the stress distribution has the same appearance for all growing angles; it is only the plasticised area c_2 that increases with higher angles (see figure 1). In CS1 of the described failure mode *d*, a distinction must be made for stress distributions where c_1 is greater than or smaller than b_1. When c_1 is smaller than b_1, the stresses in area a_1 are always in an elastic state. This situation occurs in the transition between Fig. 1 and Fig. 3a. Once c_1 becomes greater than b_1, area b_1 is fully plasticised and parts of area a_1 show plastification (see Fig. 1). This requires two sets of formulae to be used. The flowchart that shows the calculation process for point *C* of failure mode *d*, provided in section 8.4.2, ensures that the relevant case can be identified. Special attention is required when calculating the situation where $c_1 < b_1$, as the derivation of the formula for the force *F* (see Eq. (44) to Eq. (46)) is based on a Taylor expansion. In most cases, using 50% of the ultimate load as the input value *x* is sufficient. However, for very good accuracy with deviations of less than 1%, the force *F* must be recalculated using the

previously calculated force F for x.

3 Input parameters

The theory presented here is derived independently of specific input parameters. Consequently, existing approaches to describing material behaviour will be considered. Theoretically, the calculation method also permits the use of multilinear moment rotation curves for the dowel-type fastener, as implemented in Riepe et al. However, for the purposes of simplicity, a bilinear approach for the bending behaviour of the DTF is employed in section 3.2. A significant limitation of the present derivation of the extended Johansen theory can be seen in the restriction to an elastic-ideal plastic approach for bedding behaviour of the timber material. Consequently, the following approach for describing the bedding behaviour of the timber material may result in the neglect of a possibly rising branch in the plasticised area.

3.1 Bedding parameter of the timber material

Various approaches have already been investigated in the literature to describe bedding behaviour. With the approach proposed by *Schweigler, Bader, Hochreiner, et al.* (2018) and *Schweigler, Bader, Bocquet, et al.* (2019) the bedding curve can be described with parametrized equations. The value $k_{f,el}$, which describes the initial slope of the bedding, will be used for the bedding value ζ in the formulas presented here. With the embedment strength $f_{h,i,k}$ according to FprEN 1995-1-1:2024, a simplified bilinear bedding curve results. In this context, it is important to note that the same bedding curve is used in the following comparison for both the extended Johansen theory and the BOFM. The present study does not permit valid conclusions to be drawn about the quality of the input values. The objective of this study is to enable a comparison between the two calculation models.

3.2 Bending angle and plastic moment of the fastener

In the numerical investigation of the basic equations in *Riepe et al.* (2025), the bending angle and bending moment were obtained from a BOFM model, since no definition of the bending angle was available. However, to address this issue, a formula for calculating the bending angle when yielding occurs in the fastener, designated as φ (equation 1), is provided below with an alternative system as described in Fig. 4. Therefore, the formula for the moment M is solved to the unknown length L and inserted into the expression for the angle φ leading to a formula depending on the diameter d, the bending stiffness EI, the plastic bending moment M_{yRk} of the DTF and the embedment strength $f_{h,i,k}$.

In a preliminary analysis described in Sec. 5, it was determined that the angle appears to be too small when the remaining length beside the plastic hinge l_{rest} is relatively small.

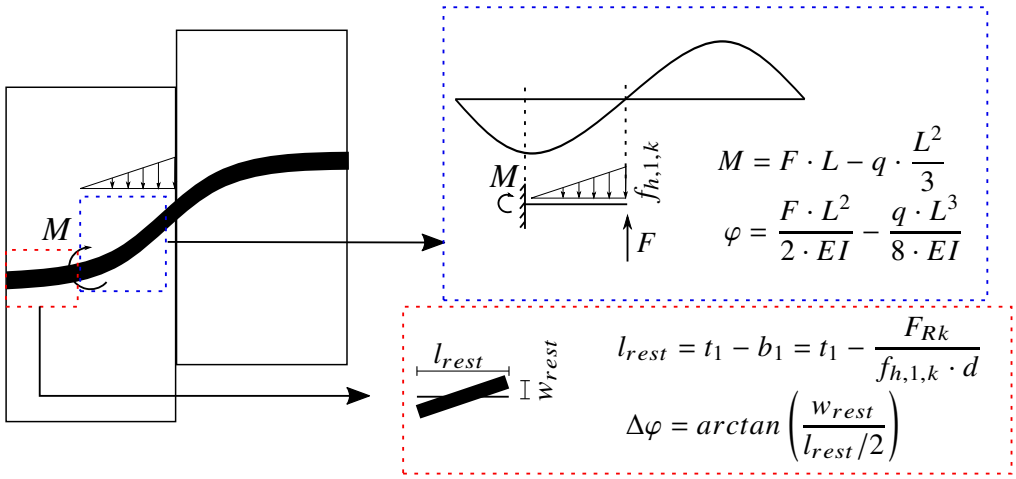

Figure 4. *Deformed dowel-type fastener when the plastic moment in the fastener is reached; the corresponding curve of the moment, and an equivalent static alternative system to derive the angle φ for the left cross-section part. A correction of the angle is required ($\Delta\varphi$), to take into account that the fastener may not be fully clamped, depending on the cross-section thickness.*

Therefore, the introduction of a $\Delta\varphi$ is required to account for this effect, allowing a deformation of $w_{rest} = f_{h,1,k}/\zeta_i$ up to elastic limit of the timber material (see figure 4). The remaining length l_{rest} can be derived with the cross-section thickness t_i and b_i, based on the ultimate force F_{Rk}. The formula for the angle $\Delta\varphi$ is provided below (see Eq. (2)). Both angles result in the modified angle φ_a, describing the transition from elastic to plastic behaviour of the DTF (see Eq. (3)).

$$\varphi = \frac{3}{4 \cdot EI} \cdot \sqrt{\frac{6 \cdot M_{yRk}^{2}}{f_{h,1,k} \cdot d}}^{3} \qquad (1)$$

correction made on 06.03.2026:
The exponent in Eqs. (1) and (3) must be 3 and not 2

$$\Delta\varphi = arctan\left(\frac{w_{rest}}{l_{rest}/2}\right) = arctan\left(\frac{2 \cdot f_{h,1,k}}{\zeta_1\left(t_1 - \frac{F_{Rk}}{f_{h,1,k} \cdot d}\right)}\right) \qquad (2)$$

$$\varphi_a = \varphi + \Delta\varphi = \frac{3}{4 \cdot EI} \cdot \sqrt{\frac{6 \cdot M_{yRk}^{2}}{f_{h,1,k} \cdot d}}^{3} + arctan\left(\frac{2 \cdot f_{h,1,k}}{\zeta_1\left(t_1 - \frac{F_{Rk}}{f_{h,1,k} \cdot d}\right)}\right) \qquad (3)$$

The plastic moment of the fastener M_{yRk} was assumed analogous to the approach recommended in *Colling et al.* (2015) (see eq. 4). With the angle φ_a and the yield moment M_{yRk}, a bilinear moment-rotation relation is provided. It should be noted that for FM f, depending on the embedment strength, bedding parameters and cross-section thickness, different bending angles may occur within a connection for the respective

cross-section.

$$M_{yRk} = \begin{cases} 0,15 \cdot \dfrac{f_y + f_u}{2} \cdot d^3 & \text{for} \quad f_u < 450\ \text{N/mm}^2 \\ 0,15 \cdot f_u \cdot d^3 & \text{for} \quad f_u > 450\ \text{N/mm}^2 \end{cases} \tag{4}$$

4 Verification

In order to verify the derived formulas, a comparison with the well-established beam-on-foundation method shall be carried out. For this purpose, a large-scale parameter study was performed, in which the points of the linearized curve according to the extended Johansen theory were recalculated using a BOFM model. The parameters were varied as shown in table 1, resulting in a total number of 23 040 different connection configurations. The materials in the cross sections correspond with the following densities: C24 (ρ = 350 kg/m^3), C30 (ρ = 380 kg/m^3), GL24h (ρ = 385 kg/m^3) and GL32h (ρ = 440 kg/m^3). The force-fibre angles α_{CS_i} take values of 0° and 90° and the diameter $\varnothing$ was varied between 6 mm and 30 mm in increments of 6 mm. The cross section thickness t_i was varied as a percentage based on t_{req}, according to *DIN EN 1995-1-1* (2010). The bedding ζ_i was determined according to *Schweigler, Bader, Bocquet, et al.* (2019), based on the density, and two steel grades were used for the DTF material.

Parameter	**Units**	**Values**
Material CS_i	–	C24, C30, GL24h, GL32h
α_{CS_i}	°	0, 90
$\varnothing$	mm	6, 12, 18, 24, 30
$\dfrac{t_i}{t_{req}}$	%	10, 25, 50, 75, 100, 150
ζ_i	%	100
f_y/f_u	N/mm^2	235/360, 355/490

Table 1. *Set of parameters for the connection configurations used for the comparison of the extended Johansen theory and K_{ser} (=K_{SLS} according to FprEN 1995-1-1:2024) with the BOFM.*

The BOFM model was generated in Sofistik using an automated Microsoft VBA script, which also returned the results of the calculation of the individual points. A relatively simple model was implemented in order to minimise the computational complexity, given the extensive number of configurations. Therefore, bilinear springs were used to model the stiffness of the timber material for the force fibre angles, with the incline defined by *Schweigler, Bader, Bocquet, et al.* (2019) and the embedment strength according to FprEN 1995-1-1:2024.

5 Results and discussion

The following comparison with the BOFM will examine the initial stiffness, as determined by the extended Johansen theory, and establish a relationship with the existing calculation method according to EC5. Therefore, the linearized curve was first determined using the extended Johansen theory, followed by the calculation of the corresponding force using BOFM for the displacement of the respective points. The initial stiffnesses were then calculated from the resulting data set using the force and the displacement of the first point (point *B*). Furthermore, K_{SLS} was calculated for the entire data set in accordance with FprEN 1995-1-1:2024. It was also compared with the stiffnesses of the BOFM. However, the consideration of the force-fibre angle for K_{SLS} in accordance with FprEN 1995-1-1:2024 remains unclear, with the proposal of a 50% reduction when the force-fibre angle is 90°. The situation in which CS1 has a force-fibre angle of 0° and CS2 has a force-fibre angle of 90° is not addressed. It has been observed that applying the reduction only for connections where both cross-sections have a force fibre angle of 90° delivers enhanced results. The comparison of K_{SLS} with the BOFM, as well as the extended Johansen theory with the BOFM, is shown separately in Fig. 5a to Fig.8b for the respective failure modes.

In figures 5a, 6a, 7a and 8a, the comparison of the stiffness according to FprEN 1995-1-1:2024 and the BOFM is illustrated. The figures clearly show that the points are widely scattered. Apart from the FM *c*, for the rest of the failure modes there is a tendency to underestimate stiffness. Proportionally, just a maximum of 19% of the stiffness values according to EC5 are within a deviation of +-10% from the stiffness values according to BOFM.

In figures 5b, 6b, 7b and 8b, the comparison of the stiffness according to the extended Johansen theory and the BOFM is illustrated. For all failure modes, a much better correlation compared to the stiffness according to EC5 can be seen. More than 80% of the connection configurations without a plastic hinge (FM *a*, *b* and *c*) show deviations less than +-10%. The failure modes with plastic hinges in the fastener cover more than 90% of configurations with a deviation of less than 10%. In FM *a* to *e*, the stiffness appears to be relatively overestimated in some configurations.

6 Conclusions

This article presents an extension of Johansen's theory that enables the determination of a linearised force-deformation relation for all six failure modes. In order to evaluate the relative capabilities of the proposed method in comparison to the well-established BOFM, a quantitative analysis was conducted. This involved the calculation of more than 23 000 connection configurations using both methods. Moreover, the proposed calculation of stiffness in accordance with FprEN 1995-1-1:2024 is to be incorporated.

In this regard, considerable discrepancies have been observed between the results ob-

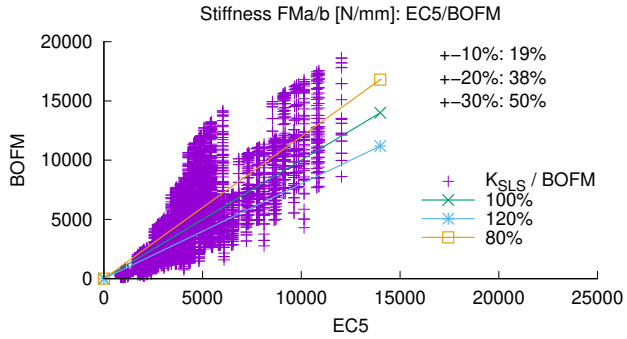

(a) *FM a/b: K_{SLS} vs. BOFM.*

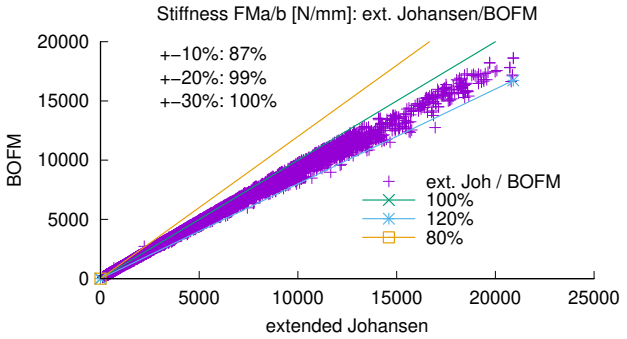

(b) *FM a/b: extended Johansen vs. BOFM.*

Figure 5. *FM a/b: K_{SLS} according to EC5 and the extended Johansen theory compared to BOFM.*

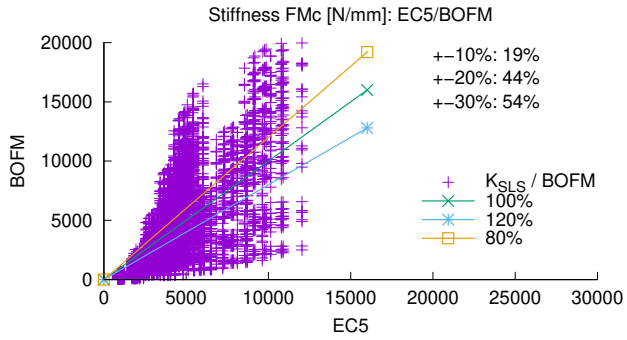

(a) *FM c: K_{SLS} vs. BOFM.*

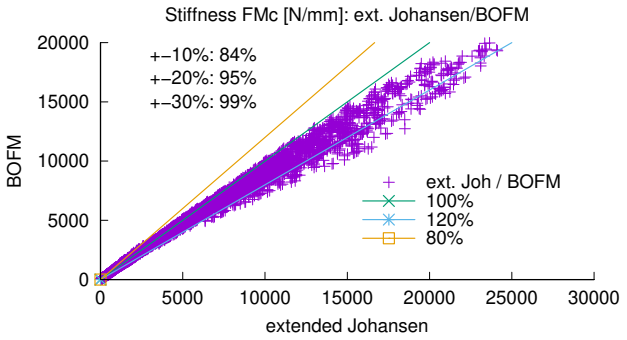

(b) *FM c: extended Johansen vs. BOFM.*

Figure 6. *FM c: K_{SLS} according to EC5 and the extended Johansen theory compared to BOFM.*

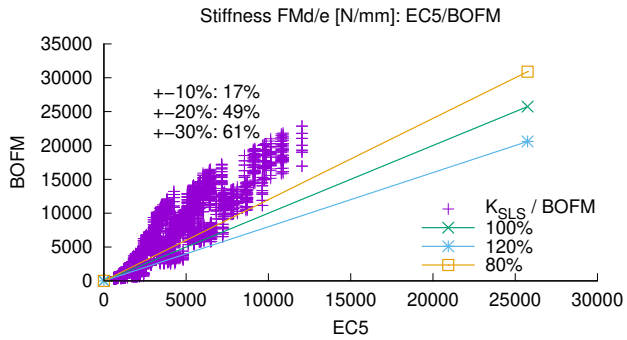

(a) *FM d/e: K_{SLS} vs. BOFM.*

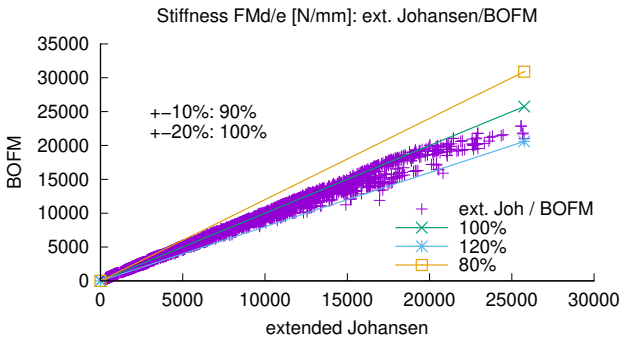

(b) *FM d/e: extended Johansen vs. BOFM.*

Figure 7. *FM d/e: K_{SLS} according to EC5 and the extended Johansen theory compared to BOFM.*

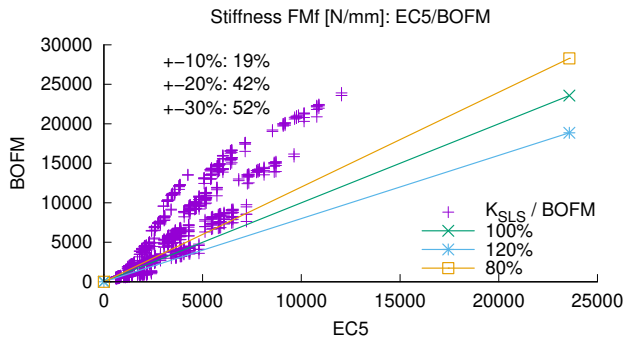

(a) *FM f: K_{SLS} vs. BOFM.*

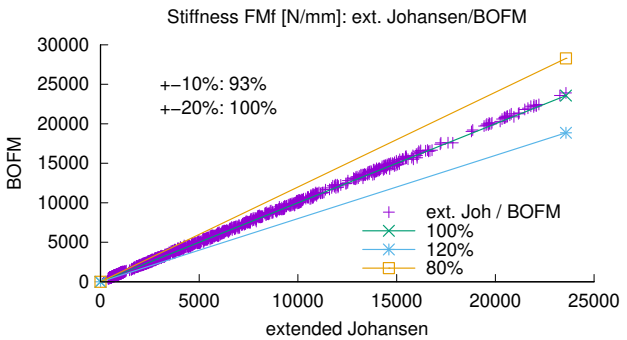

(b) *FM f: extended Johansen vs. BOFM.*

Figure 8. *FM f: K_{SLS} according to EC5 and the extended Johansen theory compared to BOFM.*

tained from K_{SLS}, according to FprEN 1995-1-1:2024, and those from the analysis by means of the BOFM. In comparison, significantly better correlations can be achieved with the extended Johansen theory, especially with failure mode *f*, where notably high levels of agreement can be achieved. The analysis of the remaining failure modes reveals a tendency towards overly rigid behaviour, which indicates that deformation components, such as the bending of the fastener, may not have been sufficiently addressed. The theoretical model of the dowel-type fastener in the Johansen Theory incorporating yield joints at one point appears to be idealised, since bending deformations apart from the yield joints are neglected. Following this, the identification and consideration of additional deformation components would be reconsidered. Additionally it is suggested that a more advanced derivation of angle φ could potentially generate improved outcomes. A notable hindrance shall be addressed, as the failure mode with only one joint (*d*/*e*) contains special cases that cannot yet be calculated with sufficient accuracy. Furthermore, these failure modes generally lead to a more complex calculation process. This in turn leads to the question of whether the focus should be set on failure mode *f*, with a concomitant effect of creating connections with clear plastic behaviour.

It should be noted that a simplified BOFM model was employed in this instance, which omitted the increasing trend of bedding behaviour for large force-fibre angles after reaching the embedding resistance. The present derivation of the extended Johansen theory similarly simplifies the bedding behaviour, solely allowing for the reflection of elastic-ideal plastic bedding behaviour. While this may not directly impact the initial stiffness, it could potentially influence the deformation behaviour within the plastic range, resulting in an underestimation of the force. A notable issue that could be raised is that the plastic moment of the fastening element was not determined in accordance with FprEN 1995-1-1:2024, but rather in accordance with *Colling et al.* (2015). The consequences of this approach remain to be fully evaluated.

Nevertheless, an alternative method for calculating stiffness is presented here, which enables the determination of both stiffness and load-bearing capacity using the same theoretical model and the same influencing factors. In addition, new information is provided that opens up additional fields of application. For example, connections that may be applied up to the elastic limit could be calculated. Since a relation has been established between the rotation of the fastener and the load on the connection, the potential of including the rope effect in the calculation arises.

The following step will be to present simplifications for steel-timber connections. These simplifications will be achieved by neglecting the deformation components of the steel part. This will result in a significant reduction in the number of formulas required and in a simplification of the calculation process.

7 References

Basterrechea-Arévalo, M., M. Schweigler, R. Lemaître, and T. K. Bader (2023). “Numerical modelling of moment-transmitting timber connections.” In: *Engineering Structures* 297, p. 116923. DOI: 10.1016/j.engstruct.2023.116923.

Colling, F., H. J. Blaß, and C. Prüfer (2015). *Tragfähigkeit von Stabdübelverbindungen*. Tech. rep. Fraunhofer IRB Verlag.

DIN EN 1995-1-1 (2010). *DIN EN 1995-1-1. Eurocode 5: Design of timber structures - Part 1-1: General Common rules and rules for buildings (includes Corrigendum AC:2006 + Amendment A1:2008)*. DIN Standards Committee Building and Civil Engineering. DOI: 10.31030/1722665.

Dorn, M., K. de Borst, and J. Eberhardsteiner (2013). “Experiments on dowel-type timber connections.” In: *Engineering Structures* 47, pp. 67–80. DOI: 10.1016/j.engstruct.2012.09.010.

Ehlbeck, J. and H. J. Larsen (1993). “Eurocode 5- Design of timber structures: Joints.” In: *International Workshop on Wood Connectors*. United States: Forest Products Society, pp. 9–23.

FprEN 1995-1-1:2024 (2024). *Eurocode 5: Design of timber structures - Part 1-1: General rules and rules for buildings*. CEN-CENELEC/TC 250.

Gauß, J. (2024). “Zum Trag- und Verformungsverhalten von Stahl-Holz- Stabdübelverbindungen- Load-bearing and deformation behaviour of steel-timber dowel connections.” Dissertation. Stuttgart : Institut für Konstruktion und Entwurf.

Gikonyo, J. W., E. Binder, M. Schweigler, and T. K. Bader (2023). “Numerical modelling of a cross-laminated timber-to-conrete dowel-type connection using the beam-on-foundation model.” In: *World Conference on Timber Engineering (WCTE 2023)*. Oslo, Norway, pp. 3101–3110. DOI: 10.52202/069179-0404.

Gikonyo, J. W., M. Schweigler, and T. K. Bader (2024). “Beam-on-Foundation modelling of dowel-type single fastener connections in cross laminated timber.” In: *Engineering Structures* 303. DOI: 10.1016/j.engstruct.2024.117519.

Jockwer, R. and A. Jorissen (2018). “Stiffness and deformation of connections with dowel-type fasteners.” In: *Design of Connections in Timber Structures: A state-of-the-art report by COST Action FP1402 / WG3*. Ed. by C. Sandhaas, J. Munch-Andersen, and P. Dietsch. Shaker Verlag Aachen, pp. 95–126.

Johansen, K. W. (1949). “Theory of timber connections.” In: *International Assoc. of Bridge and Structural Engineering Publication* 9, pp. 249–262. DOI: 10.5169/SEALS-9703.

Lemaître, R., J.-F. Bocquet, M. Schweigler, and T. K. Bader (2018). “Beam-on-foundation modelling as an alternative design method for single fastener connections.” In: *Design of Connections in Timber Structures: A state-of-the-art report by COST Action FP1402 / WG3*. Ed. by C. Sandhaas, J. Munch-Andersen, and P. Dietsch. Shaker Verlag Aachen, pp. 207–220.

Riepe, J., J. Díaz, and J. Schänzlin (2025). “An Elasto-Plastic Model for the Deformation of Dowel-Type Fasteners Based on Johansen’s Theory.” In: *Engineering Structures* 344, p. 121315. DOI: 10.1016/j.engstruct.2025.121315.

Schweigler, M., T. K. Bader, J.-F. Bocquet, R. Lemaître, and C. Sandhaas (2019). “Embedment test analysis and data in the context of phenomenological modelling for dowelled timber joint design.” In: *INTER: International Network on Timber Engineering Research: Proceedings (Meeting 52), 26-29 August 2019, Tacoma, USA, Karlsruhe, Germany. Ed.: R. Görlacher*. Vol. Meeting 52. Timber Scientific Publishing, pp. 155–172.

Schweigler, M., T. K. Bader, G. Hochreiner, and R. Lemaître (2018). “Parameterization equations for the nonlinear connection slip applied to the anisotropic embedment behavior of wood.” In: *Composites Part B: Engineering* 142, pp. 142–158. DOI: 10.1016/j.compositesb.2018.01.003.

SIA265 (2021). *SIA 265:2021 Timber Structures. SIA Swiss Society of Engineers and Architects*. Zurich, Switzerland.

8 Appendix: Flowcharts for calculation of deformation of timber-timber connections

In order to determine the stiffness of the connection, several points on the load-slip-relation are defined (see Fig. 2). The evaluation of these points is given next for the different failure modes. The first step is to determine the load capacity based on FprEN 1995-1-1:2024 by evaluating all the possible failure modes. The minimum load capacity corresponds to the critical failure mode. In the second step, only the points of the critical failure mode should be determined.

8.1 Failure mode *a*

In failure mode *a*, unlike in the original Johansen theory, both cross-sections are considered, since, depending on the thickness of the second CS, deformations also occur here which would otherwise lead to an underestimation of the deformation. Therefore, it must be checked whether the fastener remains straight or whether CS 2 is thick enough for the fastener to form a yield joint, allowing the relevant formulas to be referenced. In order to derive formulae to determine only the proportion of the second CS, the first CS was considered to be a thin steel plate, resulting in two possible failure modes in CS2, analogous to FM a and b for thin steel plates according to FprEN 1995-1-1:2024. Furthermore, it was found out that bending deformations of the fastener can have a relevant effect. Therefore, in equation 5, bending of the fastener in the left CS part (term two) and bending in the right CS part (term three) is addressed.

8.1.1 Point B

$$w_B = \frac{f_{h,1,k}}{\zeta_1} + \frac{f_{h,1,k} \cdot d \cdot {t_1}^4}{8 \cdot EI} + \frac{{F_B}^4}{3 \cdot EI \cdot {f_{h,2,k}}^3 \cdot d^3} + w_{CS2} \quad (5)$$

$$F_B = F_{Rk} \text{ acc. to Johansen, 1949 in this FM} \quad (6)$$

$$0,4 \cdot f_{h,2,k} \cdot t_2 \cdot d > \sqrt{2 \cdot M_{yRk} \cdot f_{h,2,k} \cdot d}$$

no

$$w_{CS2} = \frac{4 \cdot F_B}{d \cdot \zeta_2 \cdot t_2} + \frac{6 \cdot F_B}{d \cdot \zeta_2 \cdot {t_2}^2} \cdot t_1 \quad (7)\ (8)$$

yes

$$w_{CS2} = 2 \cdot F_B \cdot \sqrt[3]{\frac{\varphi_a}{6 \cdot d^2 \cdot {\zeta_2}^2 \cdot M_y(a)}} \quad (9)$$

$$+ F_B \cdot t_1 \cdot \sqrt[3]{\frac{\varphi_a}{6 \cdot \zeta_2^2}} \cdot \sqrt{\frac{{f_{h,2,k}}^3}{2^3 \cdot d \cdot M_y(a)^5}} \quad (10)$$

8.2 Failure mode *b*

8.2.1 Point B

In FM *b*, the same assumptions were made as those already described in FM *a*.

$$w_B = \frac{f_{h,2,k}}{\zeta_2} + \frac{f_{h,2,k} \cdot d \cdot {t_2}^4}{8 \cdot EI} + \frac{{F_B}^4}{3 \cdot EI \cdot {f_{h,1,k}}^3 \cdot d^3} + w_{CS1} \quad (11)$$

$$F_B = F_{Rk} \text{ acc. to Johansen, 1949 in this FM} \quad (12)$$

$$0,4 \cdot f_{h,1,k} \cdot t_1 \cdot d > \sqrt{2 \cdot M_{yRk} \cdot f_{h,1,k} \cdot d}$$

no

$$w_{CS1} = \frac{4 \cdot F_B}{d \cdot \zeta_1 \cdot t_1} + \frac{6 \cdot F_B}{d \cdot \zeta_1 \cdot {t_1}^2} \cdot t_2 \quad (13)\ (14)$$

yes

$$w_{CS1} = 2 \cdot F_B \cdot \sqrt[3]{\frac{\varphi_a}{6 \cdot d^2 \cdot {\zeta_1}^2 \cdot M_y(a)}} \quad (15)$$

$$+ F_B \cdot t_2 \cdot \sqrt[3]{\frac{\varphi_a}{6 \cdot \zeta_1^2}} \cdot \sqrt{\frac{{f_{h,1,k}}^3}{2^3 \cdot d \cdot M_y(a)^5}} \quad (16)$$

8.3 Failure mode *c*

8.3.1 Point B

A distinction must be made for point *B* of failure mode *c*, in order to check in which cross-section the first plastification occurs. First, F_{case1} and F_{case2} must be calculated. The smaller of these two values indicates in which cross-section plastification occurs first. The corresponding displacement can then be determined.

$$F_{case1} = \frac{d \cdot t_1 \cdot f_{h,1,k} \cdot \left(\zeta_1 \cdot t_1^3 + \zeta_2 \cdot t_2^3\right)}{4 \cdot \zeta_1 \cdot t_1^3 + 3 \cdot \zeta_1 \cdot t_1^2 \cdot t_2 + \zeta_2 \cdot t_2^3} \quad (17)$$

$$F_{case2} = \frac{d \cdot t_2 \cdot f_{h,2,k} \cdot \left(\zeta_1 \cdot t_1^3 + \zeta_2 \cdot t_2^3\right)}{4 \cdot \zeta_2 \cdot t_2^3 + 3 \cdot \zeta_2 \cdot t_2^2 \cdot t_1 + \zeta_1 \cdot t_1^3} \quad (18)$$

$F_{case1} > F_{case2}$

no

Case 1: elastic embedment limit in CS 1

$$F_B = F_{case1} \quad (19)$$

$$w_B = \frac{f_{h,1,k} \cdot \zeta_1 \cdot \zeta_2 \cdot t_1 \left(4 \cdot t_1^2 \cdot t_2 + 6 \cdot t_1 \cdot t_2^2 + 4 \cdot t_2^3\right)}{\zeta_1 \cdot \zeta_2 \cdot t_2 \cdot \left(4 \cdot \zeta_1 \cdot t_1^3 + 3 \cdot \zeta_1 \cdot t_1^2 \cdot t_2 + \zeta_2 \cdot t_2^3\right)} \quad (20)$$

$$+ \frac{f_{h,1,k} \left(\zeta_1^2 \cdot t_1^4 + \zeta_2^2 \cdot t_2^4\right)}{\zeta_1 \cdot \zeta_2 \cdot t_2 \cdot \left(4 \cdot \zeta_1 \cdot t_1^3 + 3 \cdot \zeta_1 \cdot t_1^2 \cdot t_2 + \zeta_2 \cdot t_2^3\right)} \quad (21)$$

yes

Case 2: elastic embedment limit in CS 2

$$F_B = F_{case2} \quad (22)$$

$$w_B = \frac{f_{h,2,k} \cdot \zeta_2 \cdot \zeta_1 \cdot t_2 \left(4 \cdot t_2^2 \cdot t_1 + 6 \cdot t_2 \cdot t_1^2 + 4 \cdot t_1^3\right)}{\zeta_2 \cdot \zeta_1 \cdot t_1 \cdot \left(4 \cdot \zeta_2 \cdot t_2^3 + 3 \cdot \zeta_2 \cdot t_2^2 \cdot t_1 + \zeta_1 \cdot t_1^3\right)} \quad (23)$$

$$+ \frac{f_{h,2,k} \left(\zeta_2^2 \cdot t_2^4 + \zeta_1^2 \cdot t_1^4\right)}{\zeta_2 \cdot \zeta_1 \cdot t_1 \cdot \left(4 \cdot \zeta_2 \cdot t_2^3 + 3 \cdot \zeta_2 \cdot t_2^2 \cdot t_1 + \zeta_1 \cdot t_1^3\right)} \quad (24)$$

8.3.2 Point C

For this failure mode, only a bilinear simplification is provided. Therefore the point *C* can be calculated by extrapolation of point *B*:

$$F_C = F_{Rk} \quad (25)$$

$$w_C = w_B \cdot \frac{F_{Rk}}{F_B} \quad (26)$$

8.4 Failure mode *d*

A description of the calculation procedure and it's points is provided in section 2.1.

8.4.1 Point B

$$x = \frac{2 \cdot \zeta_1}{\zeta_2} - 1 + \frac{24 \cdot M_1(\varphi_a)}{{t_1}^3 \cdot d \cdot \zeta_2 \cdot \varphi_a} \quad (27)$$

$$b_2 = \begin{cases} \text{for } x < 1 \rightarrow \cos\left(\frac{\arccos(x)}{3}\right) \cdot t_1 - \frac{t_1}{2} \\ \text{for } x > 1 \rightarrow \frac{\sqrt[3]{j^2} + 1}{2 \cdot \sqrt[3]{j}} \cdot t_1 - \frac{t_1}{2} \quad \text{with} \quad j = x + \sqrt{x^2 - 1} \end{cases} \quad (28)$$

$$k_{case1/case2} = \begin{cases} k_{case1} = \frac{2 \cdot b_2 \cdot t_1 \cdot \zeta_2}{\zeta_2 \cdot {b_2}^2 + \zeta_1 \cdot {t_1}^2} \\ k_{case2} = \frac{b_2}{2 \cdot t_1} + \frac{t_1 \cdot \zeta_1}{2 \cdot b_2 \cdot \zeta_2} \end{cases} \quad (29)$$

$k_{case1} \cdot f_{h1k} > f_{h2k}$ — no / yes

Case 1: elastic embedment limit in CS 1

$$\varphi_{BCase1} = \arctan\left(\frac{k_{Case1} \cdot f_{h,1,k}}{\zeta_2 \cdot b_2}\right) \quad (30)$$

$$a_1 + b_1 = \frac{f_{h,1,k}}{\zeta_1 \cdot \tan(\varphi_{BCase1})} \quad (31)$$

Case 2: elastic embedment limit in CS 2

$$\varphi_{BCase2} = \arctan\left(\frac{f_{h,2,k}}{\zeta_2 \cdot b_2}\right) \quad (32)$$

$$a_1 + b_1 = \frac{k_{Case2} \cdot f_{h,2,k}}{\zeta_1 \cdot \tan(\varphi_{BCase2})} \quad (33)$$

$a_1 + b_1 > t_1$ — yes → Special case 1, 2 or 3

no

$\varphi_a > \varphi_{BCase1}$ or $\varphi_a > \varphi_{BCase2}$ — yes → case 3

case 1 / no / case 2

Case 1: elastic embedment limit in CS 1

$$F_B = \frac{d \cdot b_2 \cdot k_{case1} \cdot f_{h1k}}{2} \quad (34)$$

$$w_B = \frac{f_{h1k}}{\zeta_1} + \frac{k_{case1} \cdot f_{h1k}}{\zeta_2} \quad (35)$$

Case 2: elastic embedment limit in CS 2

$$F_B = \frac{d \cdot b_2 \cdot f_{h2k}}{2} \quad (36)$$

$$w_B = \frac{k_{case2} \cdot f_{h2k}}{\zeta_1} + \frac{f_{h2k}}{\zeta_2} \quad (37)$$

Case 3: Bending angle of fastener reached

$$F_B = \frac{{b_2}^2 \cdot \tan(\varphi_a) \cdot \zeta_2 \cdot d}{2} \quad (38)$$

$$w_B = \frac{f_1(\varepsilon)}{\zeta_1} + \frac{f_2(\varepsilon)}{\zeta_2} \quad (39)$$

$$f_2(\varepsilon) = b_2 \cdot \tan(\varphi_a) \cdot \zeta_2 \quad (40)$$

$$f_1(\varepsilon) = \frac{f_2(\epsilon)}{k_{Case1}} \text{ or} \quad (41)$$

$$f_1(\varepsilon) = k_{Case2} \cdot f_2(\epsilon) \quad (42)$$

Special cases 1, 2 and 3: In the comparison of the extended theory with the BOFM (see section 5), 756 of 23 040 configurations fell into the special cases. It was observed that 65% of the special cases exhibited a stiffness that differed by more than 20% from the BOFM. Therefore, it is recommended that the connection configuration be adjusted to avoid these cases until a solution is discovered.

8.4.2 Point C

Recommendation: calculate F_T twice to increase accuracy!

F_{T1} with $x = F_{max}/2$ and F_{T2} with $x = min\{F_{T1}, F_{max}\}$

$$\varphi_C > max\left\{arctan\left(\frac{2 \cdot d \cdot f_{h,1,k}{}^2}{\zeta_1 \cdot d \cdot f_{h,1,k} \cdot t_1 + F_{max}}\right),\ arctan\left(\frac{d \cdot f_{h,2,k}{}^2}{F_{max} \cdot \zeta_2}\right)\right\} \tag{43}$$

$$a = x^2 + 2 \cdot d \cdot f_{h,2,k} \cdot \left(3 \cdot M_y(\varphi_C) - t_1 \cdot x \cdot \left(1 + \frac{2 \cdot f_{h,1,k}}{f_{h,2,k}}\right) - \frac{1}{2} \cdot d \cdot f_{h,1,k} \cdot t_1{}^2\right) \tag{44}$$

$$b = f_{h,2,k} \cdot \sqrt{d \cdot f_{h,1,k} \cdot t_1 - x} \cdot \sqrt{-(d \cdot (sin(4 \cdot \varphi_C) - 2 \cdot sin(2 \cdot \varphi_C)))} \tag{45}$$

$$F_T = \frac{x + 2 \cdot d \cdot f_{h,1,k} \cdot t_1}{3} - \frac{2 \cdot \sqrt{\zeta_1}}{3 \cdot \zeta_2{}^2} \cdot \frac{a \cdot \zeta_2{}^2 \cdot sin(\varphi_C)^2 - \frac{d^2 \cdot f_{h,2,k}{}^4 \cdot cos(\varphi_C)^2}{4}}{b - 4 \cdot \sqrt{\zeta_1} \cdot sin(\varphi_C)^2 \cdot (x + d \cdot f_{h,2,k} \cdot t_1)} \tag{46}$$

$$f_{a,1} = 2 \cdot \sqrt{\frac{\zeta_1 \cdot (d \cdot f_{h,1,k} \cdot t_1 - F_T) \cdot \left(1 - cos(\varphi_C)^2\right)}{d \cdot sin(2 \cdot \varphi_C)}} - f_{h,1,k} \tag{47}$$

$f_{a,1} < f_{h,1,k}$ — yes →

$c_1 < b_1$

$$F_C = F_T \tag{48}$$

$$w_C = tan(\varphi_{elpl}) \cdot (a_1 + b_1 + b_2) \tag{49}$$

with

$$(a_1 + b_1 + b_2) = 2 \cdot cot(\varphi) \cdot \left(\frac{f_{h,1,k}}{2 \cdot \zeta_1} + \frac{f_{h,2,k}}{4 \cdot \zeta_2}\right) + t_1 + \frac{F}{d \cdot f_{h,2,k}} - \frac{\sqrt{\zeta_1{}^3 \cdot (d \cdot f_{h,1,k} \cdot t_1 - F_C) \cdot 2 \cdot cot(\varphi)}}{\zeta_1{}^2 \cdot \sqrt{d}} \tag{50}$$

no ↓

$c_1 > b_1$

note: all following points of the force-displacement-diagramm can be calculated with this set of formulae

$$a = \frac{d \cdot f_{h,1,k}{}^3 \cdot (8 \cdot \kappa^2 \cdot (\beta + 2) + \beta^4 + 2 \cdot \beta^3)}{6 \cdot \beta \cdot \kappa^2 \cdot \zeta_1{}^2 \cdot d \cdot f_{h,1,k} \cdot tan(\varphi_C)^2} \tag{51}$$

$$F_C = \frac{d \cdot f_{h,1,k} \cdot \beta}{(\beta + 2)} \cdot \left(\sqrt{\frac{\kappa^2 \cdot \zeta_1{}^2 \cdot 12 \cdot tan(\varphi_C)^2 \cdot (d \cdot f_{h,1,k} \cdot t_1{}^2 \cdot (\beta + 1) + 2 \cdot M_{yRk} \cdot (\beta + 2))}{6 \cdot \beta \cdot \kappa^2 \cdot \zeta_1{}^2 \cdot d \cdot f_{h,1,k} \cdot tan(\varphi_C)^2}} - a - t_1\right) \tag{52}$$

$$w_C = tan(\varphi_C) \cdot \left(\frac{F_C}{d \cdot f_{h,2,k}} + \frac{F_C}{2 \cdot d \cdot f_{h,1,k}} + \frac{f_{h,2,k}}{2 \cdot \zeta_2 \cdot tan(\varphi_C)} + \frac{t_1}{2}\right) \tag{53}$$

8.5 Failure mode *e*

In FM *e*, the same calculation procedure as described for FM *d* is prescribed by switching the indices of the cross-section.

8.6 Failure mode *f*

8.6.1 Point B

$f_{h,1,k} \cdot \sqrt{\zeta_2} > f_{h,2,k} \cdot \sqrt{\zeta_1}$?

no

Case 1: elastic embedment limit in CS 1

$$\varphi_B = \frac{f_{h,1,k}}{\zeta_1} \cdot \sqrt[3]{\frac{\left(\sqrt{\zeta_1} + \sqrt{\zeta_2}\right) \cdot \zeta_1 \cdot d}{6 \cdot \sqrt{\zeta_2} \cdot \left(\frac{M_{1,y,a}}{\varphi_{1,a}} + \frac{M_{2,y,a}}{\varphi_{2,a}}\right)}} \quad (54)$$

$\varphi_B > \varphi_{1a}$ or $> \varphi_{2a}$?

yes

Case 3: bending angle of fastener reached

$\varphi_a = min\{\varphi_{1a}, \varphi_{2a}\}$

$$F_B = \frac{{b_1}^2 \cdot tan(\varphi_a) \cdot \zeta 1 \cdot d}{2} \quad , \quad b_1 = \frac{f_{h,1,k}}{\zeta_1 \cdot tan(\varphi_B)} \quad (60)$$

$$w_B = tan(\varphi_a) \cdot b_1 \cdot \left(1 + \frac{\sqrt{\zeta_1}}{\sqrt{\zeta_2}}\right) \quad (61)$$

no

Case 1: elastic embedment limit in CS 1

$$F = \varphi_B \cdot \sqrt[3]{\frac{9 \cdot \zeta_1 \cdot \zeta_2 \cdot d}{2 \cdot \left(\sqrt{\zeta_1} + \sqrt{\zeta_2}\right)^2} \cdot \left(\frac{M_{1,y,a}}{\varphi_{1,a}} + \frac{M_{2,y,a}}{\varphi_{2,a}}\right)^2} \quad (56)$$

$$w_B = \frac{f_{h,1,k}}{\zeta_1} + \frac{f_{h,1,k}}{\sqrt{\zeta_1} \cdot \sqrt{\zeta_2}} \quad (57)$$

yes

Case 2: elastic embedment limit in CS 2

$$\varphi_B = \frac{f_{h,2,k}}{\zeta_2} \cdot \sqrt[3]{\frac{\left(\sqrt{\zeta_2} + \sqrt{\zeta_1}\right) \cdot \zeta_2 \cdot d}{6 \cdot \sqrt{\zeta_1} \cdot \left(\frac{M_{1,y,a}}{\varphi_{1,a}} + \frac{M_{2,y,a}}{\varphi_{2,a}}\right)}} \quad (55)$$

$\varphi_B > \varphi_{1a}$ or $> \varphi_{2a}$?

yes

Case 3: bending angle of fastener reached.

$\varphi_a = min\{\varphi_{1a}, \varphi_{2a}\}$

$$F_B = \frac{{b_2}^2 \cdot tan(\varphi_a) \cdot \zeta 2 \cdot d}{2} \quad , \quad b_2 = \frac{f_{h,2,k}}{\zeta_2 \cdot tan(\varphi_B)} \quad (62)$$

$$w_B = tan(\varphi_a) \cdot b_2 \cdot \left(1 + \frac{\sqrt{\zeta_2}}{\sqrt{\zeta_1}}\right) \quad (63)$$

no

Case 2: elastic embedment limit in CS 2

$$F = \varphi_B \cdot \sqrt[3]{\frac{9 \cdot \zeta_1 \cdot \zeta_2 \cdot d}{2 \cdot \left(\sqrt{\zeta_1} + \sqrt{\zeta_2}\right)^2} \cdot \left(\frac{M_{1,y,a}}{\varphi_{1,a}} + \frac{M_{2,y,a}}{\varphi_{2,a}}\right)^2} \quad (58)$$

$$w_B = \frac{f_{h,2,k}}{\zeta_2} + \frac{f_{h,2,k}}{\sqrt{\zeta_2} \cdot \sqrt{\zeta_1}} \quad (59)$$

8.6.2 Point C

$$\varphi_C > max\left\{arctan\left(d \cdot {f_{h,1,k}}^2 / F_{max} / \zeta_1\right) \; , \; arctan\left(d \cdot {f_{h,2,k}}^2 / F_{max} / \zeta_2\right)\right\} \quad (64)$$

$$F_C = \frac{d \cdot {f_{h,1,k}}^2 \cdot \sqrt{\beta}}{tan(\varphi_C) \cdot \sqrt{1 + \beta}} \cdot \sqrt{\frac{2 \cdot (M_1(\varphi_C) + M_2(\varphi_C)) \cdot tan^2(\varphi_C)}{d \cdot {f_{h,1,k}}^3} - \frac{\beta^3}{12 \cdot {\zeta_2}^2} - \frac{1}{12 \cdot {\zeta_1}^2}} \quad (65)$$

$$w_C = tan(\varphi_C) \cdot \left(\frac{F_C}{d} \cdot \left(\frac{1}{f_{h,1,k}} + \frac{1}{f_{h,2,k}}\right) + \frac{1}{2 \cdot tan(\varphi_C)} \cdot \left(\frac{f_{h,1,k}}{\zeta_1} + \frac{f_{h,2,k}}{\zeta_2}\right)\right) \quad (66)$$

DISCUSSION

The paper was presented by J Riepe

H Blass questioned the initial slip load slip curve shown by the model. J Riepe responded that the initial slip from the numerical model was shifted to match the initial slip from the experiment results.

H Blass commented about the angles φ_1 and φ_2 that would imply under elastic condition and the horizontal part of the dowel would also load the wood. J Riepe said some adjustments were made in the model to account for this aspect.

S Winter and H Blass discussed the shear force being zero at point of maximum moment / plastic hinge location which implies the assumed shear force and shear plane should be valid.

R Tomasi and J Riepe discussed how to implement this model into standard.

U Hübner commented that this paper is useful especially dealing with stiffness issues. Comparisons with experimental data would be useful especially dealing group effects. P Dietsch added that research on group effect was available from past research.

P Quenneville questioned why there was greater variation with modes a and b. J Riepe said there was rotation somewhere and also whether deformation of the dowel was involved would make a difference.

JM Cabrero commented that there is a need to extend the model to consider group effects and experimental verification should be done. J Riepe said the same input was used for embedment.

Influence of steel properties on the ductility of connections: An explorative experimental investigation

Lukas Kramer Bern University of Applied Sciences, Institute of Timber Construction
Martin Geiser Bern University of Applied Sciences, Institute of Timber Construction
Lukas Furrer Bern University of Applied Sciences, Institute of Timber Construction

Keywords: Connection, Ductility, Steel properties

1 Introduction

In the design of reinforced concrete (rc) elements, the post-elastic steel properties are an important factor. This is shown by the specification of required post-elastic steel properties in SIA 262:2013 and EN 1992-1-1:2004. Furthermore, the importance was emphasized by European researchers around the year 2000 as it was found that the post-elastic steel properties drastically diminished as new production methods for reinforcement steel emerged Macchi (1996), Bachmann & Wenk (1998), Bachmann (2000). It was shown that the ductility of rc elements was substantially reduced if the steel from the new production methods was used. The characterization of post-elastic steel properties is done by strain hardening k_s as well as elongation at maximum stress A_{gt} as illustrated in Figure 1. Ductility is defined as the ratio of the ultimate displacement v_u and the yield displacement v_y.

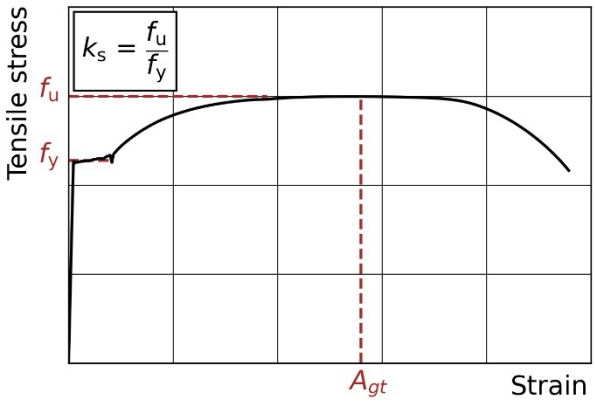

Figure 1 Definition of strain hardening k_s and elongation at maximum stress A_{gt}

Looking at the specifications in the second generation of the Eurocode regarding ductility and related connection properties, the prEN1998-1-2:2024 specifies minimum ductility levels. For framed timber shear walls (FTSW) a minimum shear wall ductility of $\mu = 3.5$ is required in the highest ductility class (DC) 3. In the dissipative design of the highest ductility class of prEN1998-1-2:2024, the sheathing to framing connection is the element responsible for dissipating energy and enabling large plastic deformations of the FTSW. Thus, for the highest ductility class DC3 of prEN1998-1-2:2024 a minimum ductility of $\mu = 5.5$ is required for the framing to sheathing connection. For braced frame structures with

dowel-type connections, a ductility of μ = 1,4 in DC2 is required for the sub-assembly. Further requirements on minimal or maximal hardening of connections are not given in prEN1998-1-2:2024. In FprEN1995-1-1:2025 minimum values for the yield strength and / or maximum strength of the steel used are provided. No specification of the relationship of the two properties are prescribed nor is any information given for the minimum strain at maximum stress. For dowel type fasteners, the low-cyclic fatigue behavior has to be evaluated according to EN 14592:2022, but no specifications regarding steel properties are given.

The evaluation of ductility in experimental timber connection studies is not straightforward. The definition of the yield displacement is a complicated matter for force-displacement curves which are strongly non-linear from the very beginning Ottenhaus et al. (2021). In research, several different procedures for defining the yield displacement have been put forth Schwendner et al. (2018), SIA 265:2021, Yasumura (1997). The definition of v_u is similarly non-trivial for static-cyclic tests.

The most common evaluation methods for the cyclic ultimate displacement $v_{u,c}$ are based on one or more criteria, of which two are illustrated in Figure 2. Both illustrated criteria are based on the load envelope curve (LEC), which is a linear interpolation between consecutive peak forces of the hysteresis for increasing displacement, as illustrated in Figure 2. Criterion *a* allows a maximal force reduction on the LEC1 of no more than α times the maximum force in this quadrant as defined in equation (1).

$$a \geq (1 - \alpha) \cdot F_{max} \quad (1)$$

Criterion *b* allows for a maximal force reduction between LEC1 and LEC3 at the same displacement *d* of β times the force on the LEC1 as defined in equation (2).

$$b(d) \geq \beta \cdot F_{LEC1}(d) \quad (2)$$

The third criterion is failure of the connection, which is not shown in the presented figures. The most common evaluation methods are defined in Table 1 and in Figure 2 or Figure 3.

The evaluation criterion may be applied to one quadrant only or to both. In scientific publications both approaches have been employed Schwendner et al. (2018), Sartori & Tomasi (2013), Germano et al. (2015), Maître et al. (2023).

Table 1 Evaluation definition for ultimate displacement of four codes

Code	*a*	*b*	Visual explanation
EN 1998:2004	0 %	20 %	Figure 2
EN 12512:2001	80 %	100 %	Figure 2
prEN1998-1-2:2024	80 %[1]	30 %	Figure 3
ASTM E2126-19	80 %	100 %	Figure 2

[1] Criteria *a* is not based on the maximum force of the quadrant but on the mean maximum force of monotonic tests according to Figure 3.

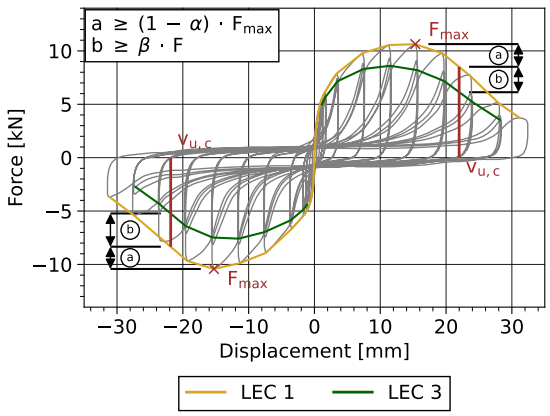

Figure 2 Visual representation of the evaluation criteria except failure

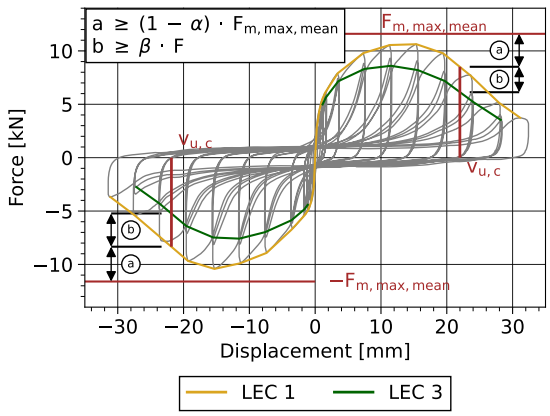

Figure 3 Visual representation of the evaluation criteria of static-cyclic test in the prEN1998-1-2:2024 except failure

The influence of the steel properties, of dowel type connections with steel dowels and slotted in plates was systematically investigated by Kramer et al. (2025). The static-cyclic tests were carried out in accordance with the complete procedure specified in EN 12512:2001/A1:2005. The yield displacement was determined based on static-monotonic tests from Bergmann (2019) and Furrer (2020) and set to v_y = 1.55 mm. The evaluation was carried out according to Figure 2 in both quadrants. The permissible force reduction on the LEC1 was a maximum of 80 % of the maximum force in the load direction under consideration. The permissible force difference between the first load envelope and the third load envelope was a maximum of 30 % at each point ($\beta \leq 0.3$). To determine the yield displacement, the stiffness was determined based on the displacement when 10 % and 40 % of the maximum force was reached on the LEC1. Since the load envelope curve is non-linear, the maximum force achieved can substantially influence the determined stiffness and thus also the determined yield displacement. Therefore, the ultimate displacement was compared.

Table 2 Specimen properties

	Serie 1	Serie 2	Serie 3	Serie 4	Serie 5	Serie 6
Timber material	GL24h			Kerto Q		
Fastener spacing [mm]	56	84		80		
Reinforcement screw	None			4 VGS 10 x 120		
Steel dowels	S355			Stainless steel 1.4307		
f_y [MPa]	722			667		
A_{gt} [%]	2.17			19.3		
k_s [-]	1.07			1.25		
Slotted in steel plate	S355		S355	DD11		DD11
f_u [MPa]	f_u = 591		f_u = 570	f_u = 492		f_u = 359
Steel plate thickness [mm]	5			10		5
Chamfered hole edges	no			yes		no
Strength ratio Steel dowel f_y / Steel plate f_u	0.82		0.79	0.74		0.54

Six test series with three test specimens each were examined. Each specimen consisted of a test connection with 6 dowels with a diameter of 8 mm, arranged in 3 rows and a mounting connection with a higher resistance and stiffness. The details of the series can be found in Table 2. The steel properties of the dowels (n = 9 for S355, n = 3 for stainless steel) as well as the steel plates (n = 3 for each plate type) were experimentally determined according to DIN EN ISO 6892-1:2019 on specimens from the same production batch. The test specimen layout is shown in Figure 4, and the test setup is shown in Figure 5.

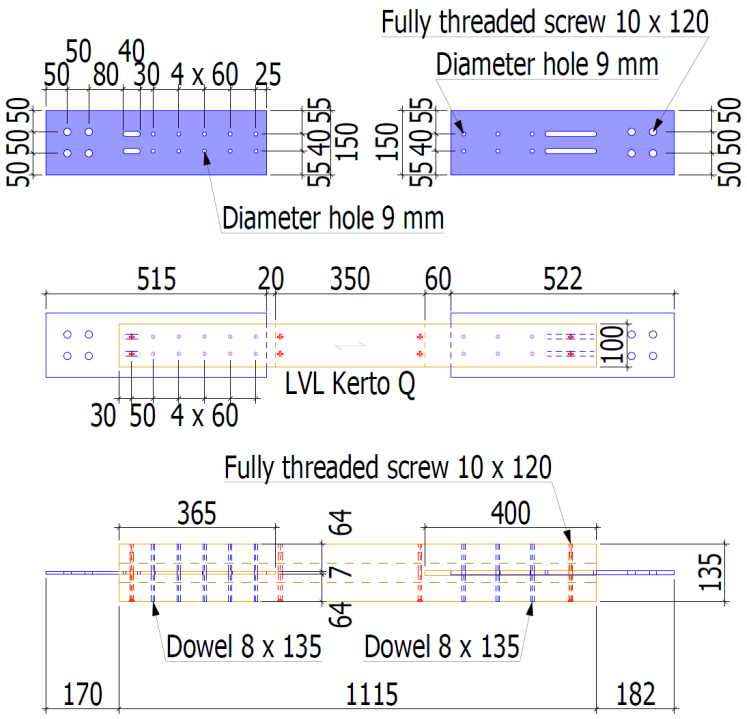

Figure 4 Test specimen plan of the static-cyclic test for the investigation of the connection ductility. On the left side is the mounting connection, which is always the same. On the right side is the test connection, with the reinforcement screws marked in red, which are only present in some test specimens. Furthermore, the distance between the steel dowels varies. Beer et al. (2022)

Figure 5 Test setup with the mounting connection at the top and the test connection at the bottom. The connection displacement of both connections was measured between the wood and the slotted plate on both sides of the test specimen. Beer et al. (2022)

The experimental investigation of the static cyclic connection properties has shown that increasing the fastener spacing in the load direction to 1.5 times the minimum spacing leads to an increase in the ultimate displacement. This can be seen from a comparison of series 1 and series 2 in Figure 6. If tearing along the load direction was prevented by using LVL-Q, the constriction of the steel dowels was reduced by using a wider slotted in plate and the splitting of the LVL-Q in the continuation of the slotted in plate was prevented by means of fully threaded screws, the ultimate displacement increases further. This effect is apparent in the comparison between series 2 and series 3 in Figure 6. A further increase in the ultimate displacement was achieved when stainless steel dowels with better post-elastic steel properties were used and

there was a lower strength ratio between the steel dowel and the slotted in plate, as illustrated by the comparison of series 3 and series 4 in Figure 6. Chamfering the edges of the holes in the slotted in plate to further reduce the notch effect caused by the slotted in plate had no influence, as indicated by the comparison of series 4 and series 5 in Figure 6. However, it was noted that this was already prevented by the strength hierarchy between the slotted in plate and the steel dowels. If this hierarchy did not exist, chamfering the hole edges could well have an influence, see Furrer (2020).

The reduction in the thickness of the slotted in plate from 10 mm to 5 mm leads to a reduction in the ultimate displacement despite the good post-elastic steel properties of the steel dowels and a hierarchy of strengths between the steel dowels and the slotted in plate. This can be seen from the comparison of series 4 and series 6 in Figure 6. It follows that the constriction or notch effect from the pressure of the slotted in plate on the steel dowels had a decisive influence on the ductility of the connection.

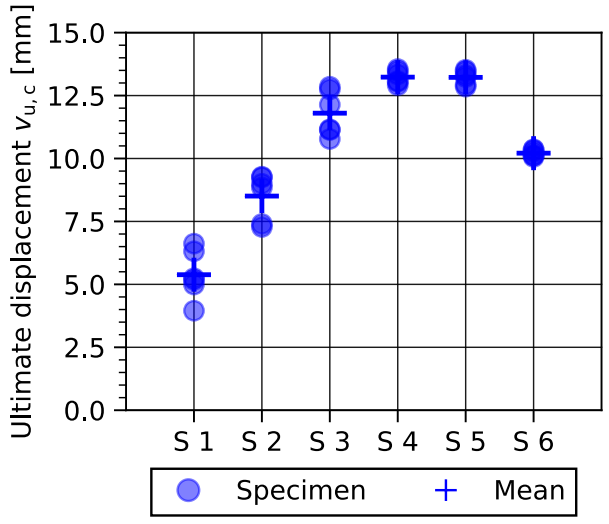

Figure 6 Ultimate displacement vu,c under static-cyclic loading

Further static-monotonic tests were performed to investigate the ductility of two serially arranged connections. As a measure of serial yielding in relation to the ultimate displacement and ductility, the ratio of the ultimate displacement of the two connections is calculated and designated UDR = $v_{u,m,1}$ / $v_{u,m,2}$ (Ultimate Displacement Ratio). By definition, $v_{u,m,1}$ is smaller than $v_{u,m,2}$. Accordingly, a UDR = 1 would hypothetically result from a test if both connections exhibited the same ultimate displacement.

The test specimens consisted of two timber beams in GL24h with dimensions 180 x 100 x 1000 mm, which were connected by two joints, each with six steel dowels with a diameter of 6 mm and two slotted in steel plates as shown in Figure 7. The steel dowels were arranged in three rows of two dowels each, the slotted in plates were 6 mm thick. A total of three series, each with three test specimens, were investigated. Due to wood defects, such as cracks present before the test, one test specimen from each series was classified as an outlier and thus was not used in the evaluation. The series differed only in the properties of the steel dowels used. The tests were carried out in accordance with EN 26891:1991. The ultimate displacement was determined in accordance with EN 12512:2001.

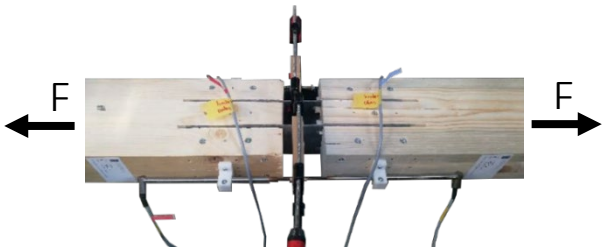

Figure 7 Connection layout and measurement setup for static monotonic tests to investigate serial yielding. However, unlike the setup shown, the connections tested were not reinforced. Bergmann (2019)

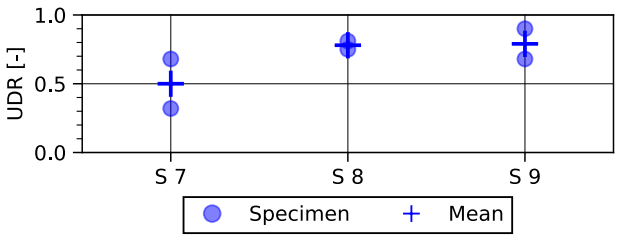

Figure 8 Ultimate displacement ratio UDR

Table 3 Properties of the steel dowels for the investigation of the serial yielding

	f_y [Mpa]	f_u [Mpa]	k_s [-]	A_{gt} [-]
Serie 7	630	650	1.03	4.2
Serie 8	512	627	1.23	12.2
Serie 9	265	386	1.46	20.7

Experimental investigations on two serially connected connections under static monotonic loading indicate that a higher strength ratio k_s of the steel dowels leads to better serial yielding. This can be seen by comparing series 7, 8 and 9 in Figure 8 and Table 3. Furthermore, the results indicate that, above a certain increase in the post-elastic steel properties, no further improvement in serial yielding occurs.

The most prevalent fasteners employed in sheathing to framing connections are staples and nails. The static-cyclic properties of such connections have been widely studied Schwendner et al. (2018), Sartori & Tomasi (2013), Germano et al. (2015), Schick (2017), Perić (2019). Staples typically have a diameter of 1.53 mm whereas nails with diameters of 2.1 mm up until 3.1 mm are most commonly used in practice. In the EN 1995:2004 nailed connections with smooth nails should have additional provisions preventing pull-out. Consequently, nails generally have ring shanks in Europe whilst smooth nails are avoided in FTSW. In the United States, smooth shanked nails are generally used Qiang et al. (2022), Seaders et al. (2009), Li et al. (2012). Consequently, the question arises as to which geometry is optimal and whether steel properties influence sheathing-to-framing connections.

The availability of different methodologies for determining $v_{u,c}$ has prompted the question of the influence that these evaluation methodologies have on $v_{u,c}$. Investigations into other types of timber fasteners have demonstrated considerable influence of steel grade and fastener geometry in order to mitigate low cycle fatigue failure. The question thus arises as to whether steel grade and geometry optimisation of nails will have a substantial effect on the static-cyclic deformation capacity of nailed sheathing to framing connections as well.

2 Material and Methods

2.1 Material Properties

The sheathing material used was OSB/3, in accordance with the specifications of EN 300:2006-09, with a nominal thickness of 15 mm. The mean density was determined to be 587 kg/m^3. The timber studs have a cross-section of 80 x 160 mm and were ordered as timber grade class C24 according to EN 14080:2013-09. The moisture content was determined in accordance with EN 13183-2:2022 immediately following the completion of the testing of the specimen. The resulting mean moisture content was 14.1 %. The mean density was determined to be 494 kg/m^3.

The investigation is based on two distinct steel grades. The two steel grades differ in their strain hardening ratio k_s and elongation at maximum stress A_{gt}. One steel grade is designated as common steel (CS) for nails. The second steel grade is a high-grade steel (HGS) with a higher k_s and high A_{gt} as shown in Table 4. The corresponding stress – strain curves are illustrated in Figure 9.

The dimensions of the nails are 3.1 x 90 mm. The investigation focused on three types of nails: Those with a smooth shaft (S), a partial ring shank (PRS) and a ring shank (RS). The specific parameter combination of the six nails under investigation is presented in Table 5. It was not possible to measure the steel properties of the PRS and RS nails, as they could not be fixed in the test setup due to the uneven surface. In the manufacturing process, the same steel was used to produce all nails with varying lengths of ring shanks.

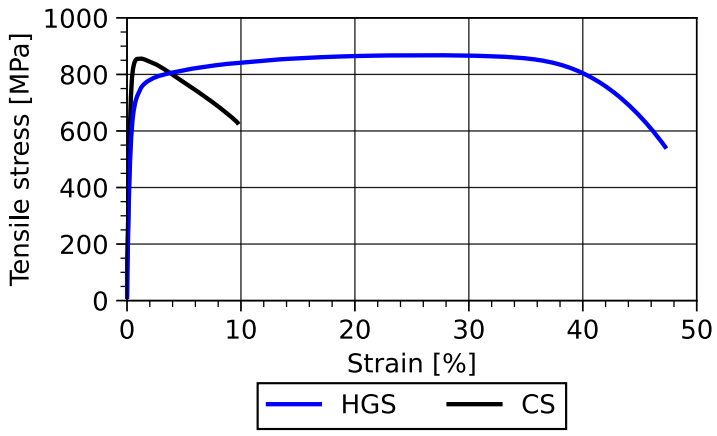

Figure 9 Stress - strain curves of CS and HGS

Table 4 Nail property specification of the 6 types of nails with a diameter of 3.1 mm and a length of 90 mm

Designation	Ring shank length	Steel grade
	[mm]	[-]
HGS_S	0	HGS
HGS_PRS	40	HGS
HGS_RS	80	HGS
CS_S	0	CS
CS_PRS	40	CS
CS_RS	80	CS

Table 5 Steel grade properties of the nails, tested according to ISO 6892-1:2019. The yield displacement was defined as $R_{p0.2}$ as no pronounced yield point was recognisable.

Designation	Ultimate stress f_u		Strain hardening k_s		Elongation at maximum stress A_{gt}	
	Mean [MPa]	CoV	Mean [-]	CoV	Mean [%]	CoV
CS (n=6)	857	0.008	1.04	0.012	1.07	0.131
HGS (n=10)	868	0.004	1.34	0.016	26.4	0.046

2.2 Specimens

The specimen comprises of two timber studs, connected on either side by OSB/3 panels. The connection between the lower timber studs and the OSB/3 panels constituted the test connection. Each panel is connected by three nails. The upper connection is necessary for the fixation of the specimen within the test rig. Consequently, a high stiffness and resistance was sought. The connection was made by screw press bonding. The screws used were 6 x 80 mm in size. The adhesive utilised was a one-component polyurethane resin (Collano Semparoc Rapid V). The specific dimensions are illustrated in Figure 10.

2.3 Test Setup

The specimens were fixed in the test rig by hydraulic clamps as illustrated in Figure 11. The clamp flanges were structured and a pressure of approximately 3 MPa was applied. The area clamped by the flanges is 12,000 mm^2.

On both sides of the test connection the relative displacement between the sheathing panel and the wood stud is measured. The measurement was made using linear variable differential transformers (LVDT).

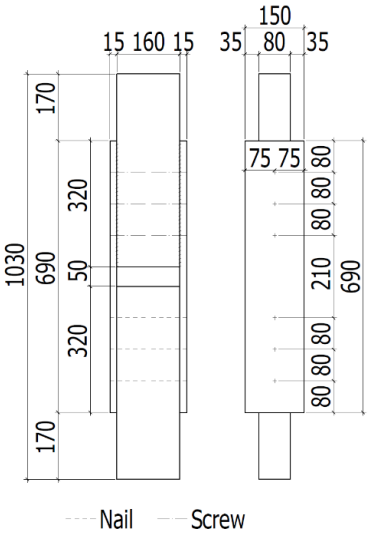

Figure 10 Plan of the specimens

Figure 11 Test setup, the test connection is on the lower side

2.4 Test Procedure and Evaluation

In order to evaluate the performance of the nailed connection under cyclic loading, tests were conducted in accordance with the full procedure of EN 12512:2001/A1:2005. The estimated yield displacement $v_{y,est}$ was determined through monotonic loading tests according to EN 26891:1991 on specimens with the exact same properties. The mean yield displacement for each nail type falls within the range of 1.22 mm to 1.92 mm. The yield displacement of $v_{y,est}$ = 1.7 mm was applied consistently across all nail types for the definition of the loading scenario of the static-cyclic test. Deviating from EN 12512:2001/A1:2005, the loading rate was set at

1.5 mm/s for the entirety of the test. The loading rate is greater than specified in the standard, resulting in an average test duration of approximately ten minutes.

Unless specified otherwise, the methodology employed to determine $v_{u,c}$ is based on the static-cyclic test as illustrated in Figure 2 with α = 80 % and β = 30 %.

Additionally, this study will demonstrate the impact of four distinct evaluation techniques on the resulting $v_{u,c}$. All methods are based on the properties of the static-cyclic test only, as illustrated in Figure 2. The parameters are listed in Table 6. This is because both the ultimate displacement evaluation method and the yield displacement evaluation method are currently under discussion, as outlined in section 1. This would result in an increased epistemic uncertainty in comparison to basing the evaluation on the ultimate displacement.

Table 6 Evaluation methods that are compared and the respective parameters

	α	β	**Code reference**
Method 1	0 %	20 %	EN 1998:2004
Method 2	80 %	20 %	EN 1998:2004 EN 12512:2001
Method 3	80 %	30 %	Adapted from prEN 1998-1-2:2024
Method 4	80 %	100 %	ASTM E2126-19

3 Results and Discussion

The displacement of the fixation side (upper side in Figure 10 and Figure 11) of the specimen is minimal. It is therefore unnecessary to discuss this further.

3.1 Comparison of different ring shank lengths and different steel grades

Based on the evaluation with α = 80 % and β = 30 %, nails with RS exhibit the shortest ultimate displacement under static-cyclic loading.

For each ring shank length, the ultimate displacement of nails in HGS is found to be substantially higher than that of nails in CS. It can be observed that none of the nails in CS reach a mean ultimate displacement of 10 mm. The mean ultimate displacement of nails in HGS and PRS or S is at least 10 mm. The results of the ultimate displacement are shown in Figure 13. The results of the ductility are shown in Figure 14.

Sartori & Tomasi (2013) also observed an increase in ductility for CS-S nails in comparison with CS-RS nails. A higher static-cyclic ultimate displacement and ductility for steel dowel connections with dowels in HGS instead of CS was observed by Kramer et al. (2025).

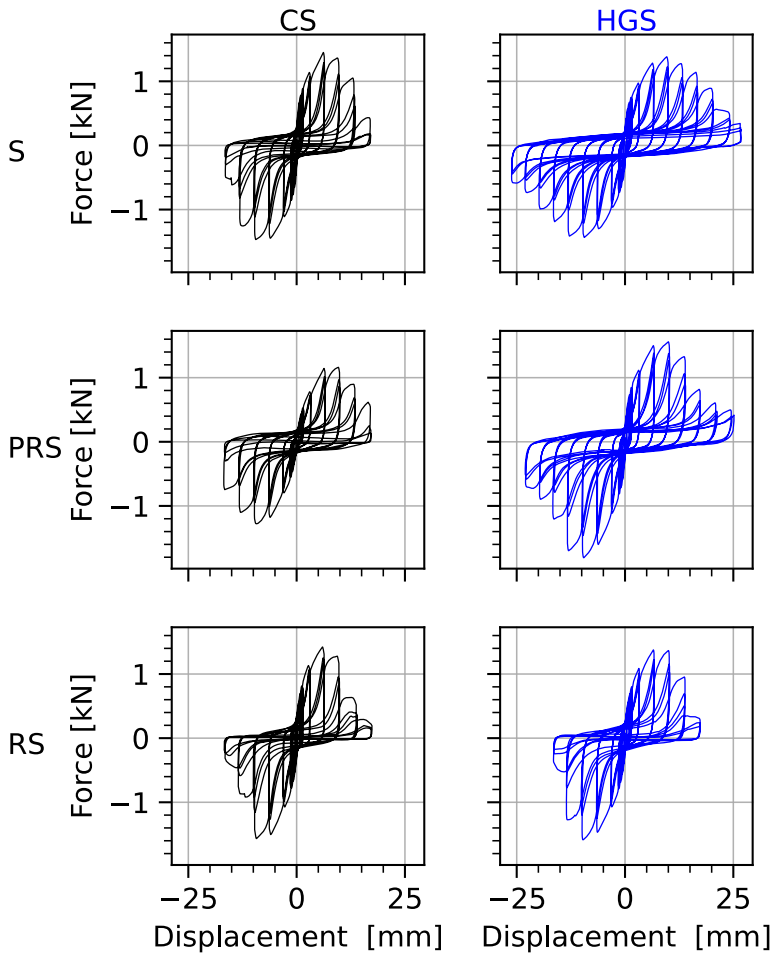

Figure 12 Exemplary hysteresis of the tested nails. The chosen specimens were CS-S Test 01, CS-PRS Test 03, CS-RS Test 02, HGS-S Test 01, HGS-PRS Test 01, HGS-RS Test 02

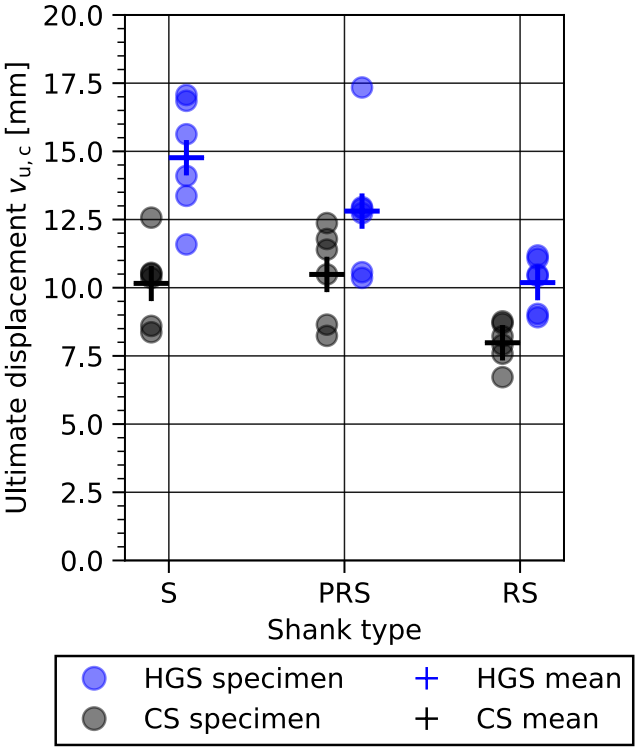

Figure 13 Ultimate displacements of nails with different ring shank lengths and both steel grades.

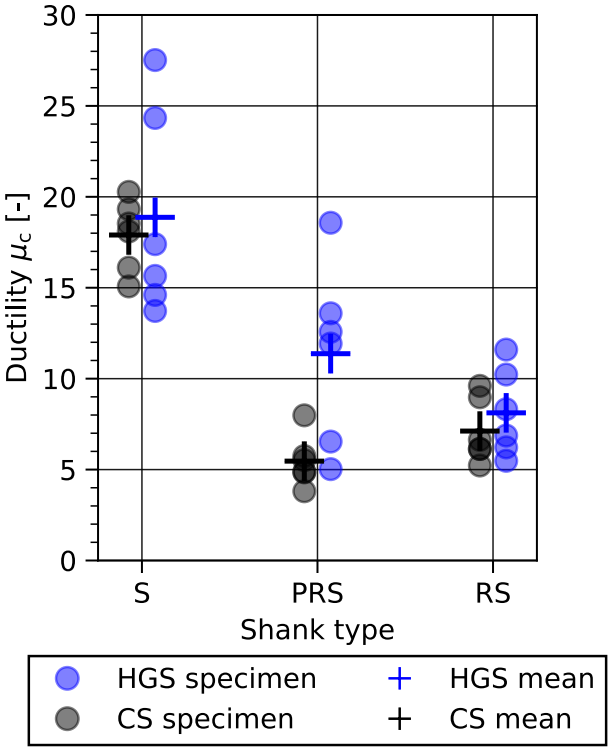

Figure 14 Ductility of nails with different ring shank lengths and both steel grades.

3.1.1 Evaluation of the failure

The failure of the nails was visually evaluated by splitting the timber after the completion of the test procedure. As illustrated in Figure 12, the maximum displacement at the conclusion of the test for the various types of nails was not constant. Nails manufactured from CS exhibited failure in low cyclic fatigue, with only a few exceptions. This phenomenon was observed for all RS nails. Figure 15 illustrates the percentage of broken and not broken nails. For nails manufactured from HGS with a S or PRS shaft, the primary failure mode is head pull-through. As illustrated in Figure 16, partial nail pull-out was observed in S nails. The low cyclic fatigue failure mode for ring shank nails in CS was also observed by Ottenhaus et al. (2021).

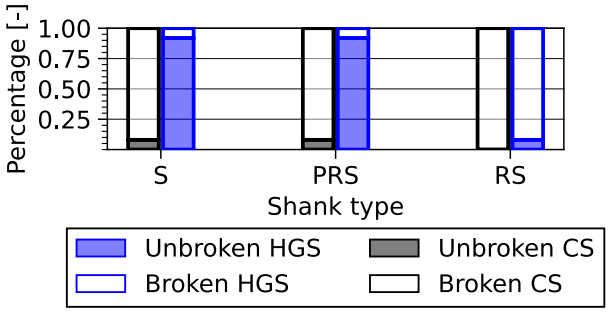

Figure 15 Proportion of broken and unbroken nails, evaluated after ending the test procedure.

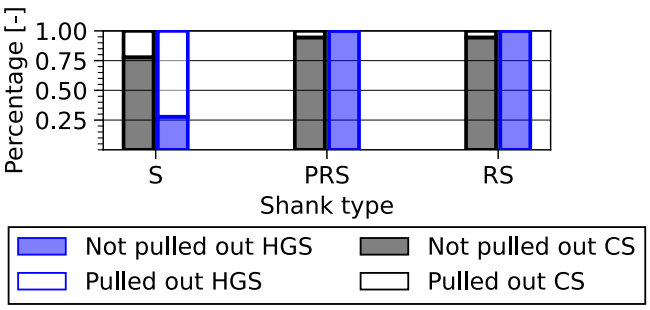

Figure 16 Comparison of nail types regarding pull out of nails based on visual inspection after ending the test procedure.

3.2 Comparison of different evaluation methods

The four evaluation methods described in Table 6 were applied to all tests. The ultimate displacement $v_{u,c}$ is illustrated in Figure 17.

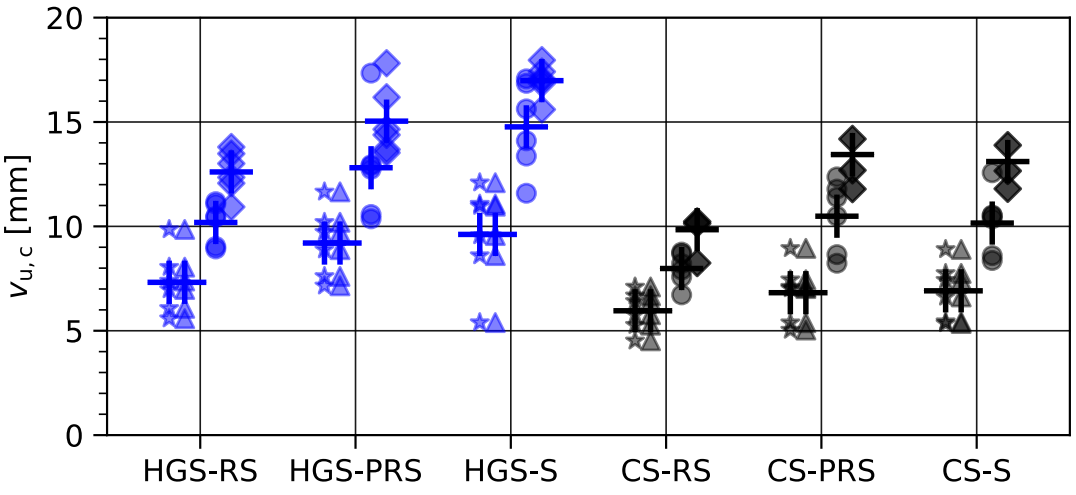

Figure 17 Ultimate displacement based on different evaluation methods.

For evaluation methods with $\beta = 20$ %, it is criterion *b* that is the determining factor for both methods. An increase in β to 30 % results in a considerable increase in the ultimate displacement, with criterion *b* remaining the decisive factor. The evaluation

with the criterion *a* only reaches slightly higher ultimate displacements. Furthermore, Figure 18 illustrates that the CoV is considerably reduced for the evaluation with criterion *a* alone. The trend of the CoV for different evaluation methods of nails with different steel properties but the same shaft specifications seem similar, as illustrated by Figure 18.

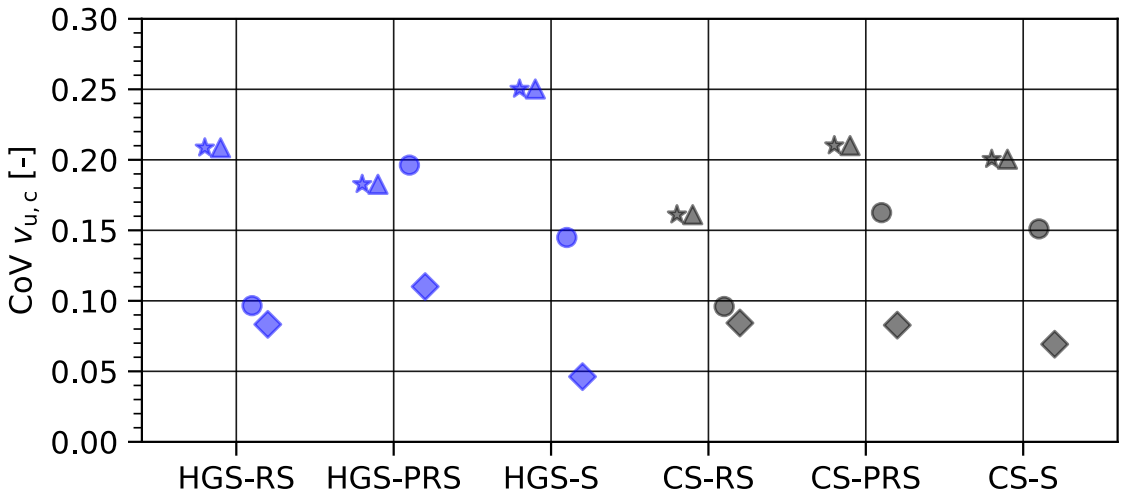

Figure 18 Coefficient of variation of the ultimate displacement

4 Conclusions

It has been shown that both post-elastic steel properties and geometric properties considerably impact static-cyclic ultimate displacement and cyclic ductility. In particular, a smooth shank surface within the range of the fastener yielding (the plastic hinges), coupled with high strain hardening and high elongation at maximum stress, is advantageous.

In light of the Eurocode, it can be concluded that HGS-PRS nails represent the optimal solution due to the need of prevented pull out of the nail. The ultimate displacement is only marginally smaller than that of HGS-S nails, but substantially larger than $v_{u,c}$ of all CS nails, as well as HGS-RS nails. From a US and Canadian perspective, HGS-S nails are the optimal choice due to their higher ultimate displacement and the acceptance of nail pull out.

For the findings of the importance of the post-elastic steel properties to be widely applicable in practice, further research is required. It is necessary to define a steel grade for dowel-type connections, analogous to the B500C class of reinforcement steel (rebars). This steel grade should include a minimal value for yield stress f_y and elongation at maximum stress A_{gt}, a range for the strain hardening ratio k_s and a maximal value for the ultimate stress f_u. However, the experimental investigation presented does not offer sufficient information to specify the proposed steel grade properties. A parametric numerical study would allow to determine the minimum and maximum mechanical fastener properties. The calibration of the numerical model on

experimental studies is strongly recommended. Moreover, further research is necessary regarding the geometric properties. In particular, the geometric optimisation of the minimal distance between the theoretically calculated yield point and the end of the ringed part of the nail would be a valuable study.

The influence of alternative assessment methodologies has revealed a reduction in variability when a criterion is employed that is based on the force reduction on the LEC1 alone. Consequently, the evaluation in accordance with ASTM E2126-19 may result in a reduction in epistemic uncertainty regarding the performance of the fastener.

5 Implications for the code development

In conclusion, the post-elastic properties of steel fasteners in timber structures are too important to be ignored in the timber design standards. It is recommended to implement a table similar to table C1 of EN 1992-1-1:2004 for connections with an increased ductility demand. No specific values are proposed as further research is needed. This article is therefore a call for action to the research community for further investigations to provide a sound basis for the specification of appropriate values.

6 Acknowledgements

The authors would like to thank Georg Disler and the df2 company for their advice on the practical application limits of the nail geometry and for providing the special nails promptly and in the desired quality. Furthermore, a big thanks goes to Raffael Schweizer who conducted the nail tests during his BSc Thesis.

7 References

Swiss Association for Standardization SNV (2013) SIA 262:2013 Concrete Structures

European Committee for Standardization CEN (2004) EN 1992-1-1:2004 Design of concrete structures - Part 1-1: General rules and rules for buildings

Macchi G., 1996, Ductility Requirements for Reinforcement under Eurocodes. Structural Engineering International p. 249-254

Bachmann H., Wenk T., 1998, Ungenügende Duktilität beim Bewehrungsstahl. Schweizer Ingenieur und Architekt 116(29). https://doi.org/10.3929/ethz-a-006297306

Bachmann H., 2000, Problems relevant to poor ductility properties of European reinforcing steel. Proceedings of the 12th World Conference of Earthquake Engineering (WCEE)

European Committee for Standardization CEN (2024) prEN 1998-1-2_FOR ENQ (working draft to CIB) Design of structures for earthquake resistance — Part 1-2: Buildings

European Committee for Standardization CEN (2025) FprEN 1995-1-1 (final draft to CIB) Design of timber structures - Part 1-1: General rules and rules for buildings

European Committee for Standardization (CEN), (2022). EN 14592. Timber Structures – Dowel-type fasteners - Requirements. Brussels, Belgium

Ottenhaus L., Jockwer R., Drimmelen D., Crews K., 2021, Designing timber connections for ductility – A review and discussions, Construction and Building Materials Vol. 304 https://doi.org/10.1016/j.conbuildmat.2021.124621

European Committee for Standardization CEN (2004) EN 1998-1:2004 Design of structures for earthquake resistance – Part 1: General rules, seismic actions and rules for buildings

European Committee for Standardization (CEN), (2005). EN 12512:2001/A1:2005. Timber Structures - Test methods - Cyclic testing of joints made with mechanical fasteners. Brussels, Belgium.

ASTM E2126-05 (2017) Standard Test Methods for Cyclic (Reversed) Load Test for Shear Resistance of Walls for Buildings, USA, DOI: 10.1520/E2126-05

Schwendner S., Seim W., Hummel J., 2018, Light-frame walls with OSB and GFB sheathing under earthquake impact – A comparative study, 2018 World Conference on Timber Engineering, Seoul, Republic of Korea

Swiss Association for Standardization SNV (2021) SIA 265:2021 Holzbau

Yasumura, M., 1997, Evaluation of wood framed shear walls subjected to lateral load. Proceedings of the 30th CIB-W18, Vancouver, Canada, https://cir.nii.ac.jp/crid/1572261550414531840

Sartori T., Tomasi R., 2013, Experimental investigation on sheathing-to-framing connections in wood shear walls, Engineering Structures, vol. 56 p. 2197-2205, http://dx.doi.org/10.1016/j.engstruct.2013.08.039

Germano F.,Metelli G., Giuriani E., 2015, Experimental results on the role of sheathing-to-frame and base connections of European timber framed shear wall, Construction and Building Materials vol. 80 p. 315-328, https://doi.org/10.1016/j.conbuildmat.2015.01.076

Maître, K., Lestuzzi, P. & Geiser M., 2023, Experimental investigations of a new highly ductile hold-down with adaptive stiffness for timber seismic bracing walls. Bulletin of Earthquake Engineering 21, 2603–2634. https://doi.org/10.1007/s10518-022-01607-5

Kramer, L., Furrer, L., Geiser, M., 2025, Stabdübelverbindungen – Einflüsse auf das plastische Verformungsvermögen, S-WIN Tagung Aus der Forschung in die Praxis, Schweiz, Biel

Bergmann M., 2019, Einfluss der Stahlqualität auf die Duktilitätseigenschaften von Holztragwerken mit Stahl-Holz-Stabdübelverbindungen, Bachelorarbeit, Berner Fachhochschule, Schweiz, Biel

Furrer L., 2020, Einfluss der Stahleigenschaften und der Detailgestaltung einer Stahl-Holz-Stabdübelverbindung auf deren Duktilität, Bachelorarbeit, Berner Fachhochschule, Schweiz, Biel

Beer S., Reber Y., Smit T., Vetter Y., Voisard J., 2022, Projektarbeit, Berner Fachhochschule, Schweiz

European Committee for Standardization (CEN), (1991). EN 26891. Timber Structures - Joints Made with Mechanical Fasteners - General Principles for the Determination of Strength and Deformation Characteristics. Brussels, Belgium

Schick, M., 2017, Probabilistische Untersuchungen zu Überfestigkeiten von genagelten Wandelementen in Holztafelbauweise. Dissertation. Kassel, Kassel University Press

Perić, L., 2019, Light Frame Timber Walls in Regions of Low to Moderate Seismicity. Dissertation. ETH Zurich. https://doi.org/10.3929/ETHZ-B-000344004

Qiang R., Zhou L., Ni C., Huang D., 2022, Seismic performance of high-capacity light wood frame shear walls with three rows of nails. Engineering Structures, 268, https://doi.org/10.1016/j.engstruct.2022.114767

Seaders P, R. Gupta R, Miller T.H., 2009, Monotonic and cyclic load testing of partially and fully anchored wood-frame shear walls Wood Fiber Science, 41, pp. 145-156

Li M., Lam F., Yeh B., Skaggs T., Rammer D., Wacker J., 2012, Modeling Force Transfer around Openings in Wood-Frame Shear Walls. Journal of Structural Engineering, *138(12), 1419–1426.* https://doi.org/10.1061/(ASCE)ST.1943-541X.0000592

European Committee for Standardization CEN (2006) EN 300: Oriented Strand Boards (OSB) - Definitions, classification and specifications

European Committee for Standardization CEN (2013) EN 14080: Timber structures - Glued laminated timber and glued laminated solid timber – Requirements

European Committee for Standardization CEN (2013) EN 13183-2: Moisture content of a piece of sawn timber - Part 2: Estimation by electrical resistance method

International Organization for Standardization ISO (2019) ISO 6892-1:2019: Metallic materials — Tensile testing Part 1: Method of test at room temperature

DISCUSSION

The paper was presented by L Kramer

P Quenneville supports call for action on f_y values for steel.

T Tannert asked if the steel properties of the dowel were tested and suggested to add this information. L Kramer said this was tested.

C Sandhaas and L Kramer discussed the influence of production process on the dowel in relation to cold forming to the properties of the final product. C Sandhaas mentioned that does not only depend on the steel but also on the type of fastener.

Fatigue behaviour of threaded rods bonded into glued-laminated timber for application in bridge construction

René Steiger, Empa – Swiss Federal Laboratories for Materials Science and Technology, Structural Engineering Research Laboratory, Dübendorf, Switzerland

Bruno Zumbrunn-Maurer, neue Holzbau AG, Lungern, Switzerland

Lukas Kramer, Empa – Swiss Federal Laboratories for Materials Science and Technology, Structural Engineering Research Laboratory, Dübendorf, Switzerland

Thomas Strahm, neue Holzbau AG, Lungern, Switzerland

Ernst Gehri, Prof. em. ETH Zürich, Dr. h. c., Rüschlikon Switzerland

Keywords: Fatigue strength, stiffness, road bridges, bonded-in threaded steel rods, Service Class 1 / 2 / 3

1 Introduction

Due to their high load-carrying capacity (resistance) and stiffness, corrosion and fire resistance as well as aesthetic advantages, connections with bonded-in threaded or ribbed steel rods (BiR) are frequently used in building construction, for example, for column anchoring, rigid connections, trusses (*Tlustochowicz et al.,* 2010) and reinforcements of various kinds (*Steiger et al.,* 2015). This very efficient type of connection can offer its advantages in bridge construction projects as well. However, timber is still used comparatively little as a building material in bridge construction, in particular for road bridges. Reasons for this are the fatigue stresses caused by traffic loads and the more difficult climatic conditions compared to the construction of buildings.

Current knowledge of the fatigue behaviour of members and connections in timber bases primarily on studies performed with metallic materials (steel, aluminium) that have been adapted for the design of timber structures. The provisions on fatigue design of timber structures in the currently still valid version of Eurocode 5-2 (*CEN,* 2004) were primarily developed for the design of structural members and they only cover selected fastener types such as nails and dowels. Despite the fatigue behaviour of BiR had been investigated, see e.g. (*Bengtsson and Johansson,* 2002), respective normative specifications for the design had been lacking in the first generation

Eurocode 5-2. In the past years, additional investigations on the fatigue resistance of BiR connections were performed (*Bletz-Mühldorfer et al.,* 2018; *Erchinger and Steurer,* 2005; *Maurer et al.,* 2022; *Molina et al.,* 2009; *Myslicki et al.,* 2019; *Myslicki et al.,* 2019); and in the Formal Vote (FV) Draft of FprEN 1995-1-1 (*CEN,* 2025), values representing the type of fatigue effect in the fatigue verification, are specified for axially loaded BiR (a_{fat} = 6.7 and β_{fat} = 1.3).

Connections with BiR are of particular interest for structures with fatigue loading, because they allow a very uniform force transfer when arranged appropriately (*Gehri,* 2000). The absence of stress peaks is generally regarded as the key to get high fatigue strength. So far, most of the experiments on fatigue strength have been carried out on connections in dry wood, i.e. in Service Class SC 1 (*CEN,* 2004)). Transferability to applications in bridge construction, where elevated moisture contents (SC 2 / SC 3) prevail, is limited. Elevated moisture content (MC or ω) significantly affects the mechanical properties of wood. This can impair the resistance, could possibly change the failure mode and reduce the fatigue strength of connections.

A research project recently conducted at Empa in collaboration with the company neue Holzbau AG (n'H) was dedicated to the determination of the fatigue strength of connections with profiled rods bonded into glulam under practical conditions with a focus on bridge construction by taking an elevated MC into account. Examples of such applications are shown in Figure 1.

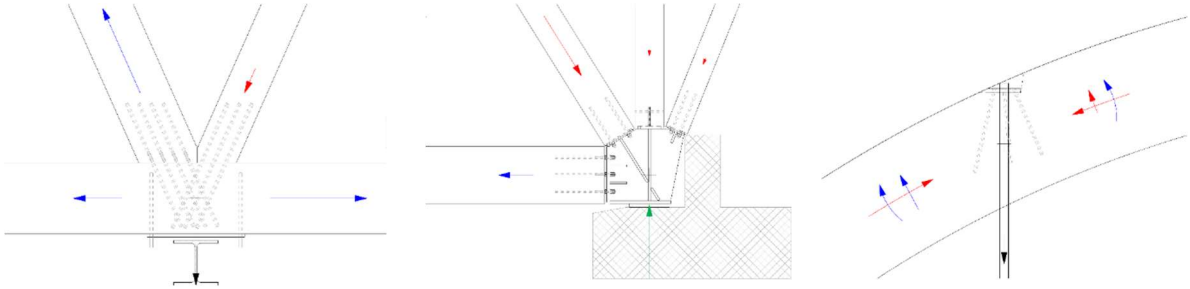

a) b) c)

Figure 1. Examples of application of BiR in bridge construction: Connections timber-to-timber (a) and steel-to-timber (b) in trusses; connections of hangers to arches (c).

2 Methodology and materials

2.1 General approach

The project focused on two configurations of BiR in relation to the grain direction of the timber (parallel ∥ and perpendicular ⊥). Fatigue tests were carried out and the mechanical properties (connection stiffness and resistance under axial tensile force) before and after passing the fatigue test in combination with the influences of the MC were investigated. In addition, the load-bearing behaviour and failure modes were compared with tests on connections subjected to static loading. Four groups of specimens (A – D) with varying type of loading and MC were subjected to testing, according to Table 1.

Table 1. Overview of the tests performed.

Group	Series	Setting of rods vs. grain direction / MC / Type of experiment	Species (GLT)
A	A1	BiR ∥ / Dry wood / Fatigue [1)]	European ash (*Fraxinus excelsior*)
	A2	BiR ∥ / Elevated MC / Static	
	A3	BiR ∥ / Elevated MC / Fatigue + Residual strength static	
B		Optimisation of test set up BiR ⊥ / Dry wood / Static	Norway spruce (*Picea abies*)
C	C1	BiR ⊥ / Dry wood / Static	Norway spruce (*Picea abies*)
	C2	BiR ⊥ / Dry wood / Fatigue + Residual strength static	
D	D1	BiR ⊥ / Elevated MC / Static	Norway spruce (*Picea abies*)
	D2	BiR ⊥ / Elevated MC / Fatigue + Residual strength static	

[1)] Test series A1 had been investigated in the course of an earlier project (*Maurer et al.,* 2022).

2.2 Shape and geometrical properties of the specimens

While it was known from previous experiments (*Maurer et al.,* 2022) that the test setup worked for the fatigue tests on BiR inserted ∥ to grain, a suitable setup first had to be developed for the tests on BiR inserted ⊥ to grain. Figure 2 and Figure 3 show the experimentally examined specimens for the series of BiR ∥ or ⊥ to grain, respectively. For the specimens with BiR ∥ to grain, hardwood was chosen because high forces can be applied here. Compared to softwood, this leads to higher stresses in the bond line. The specimens with BiR ⊥ to grain were designed with two groups of BiR (top 3 GSA in 1 row and bottom 4 GSA in 2 rows) in a way that failure in rolling shear was to be expected. In this mode, which is typical for the nodes of BiR trusses, the failure occurs in the wood between two rows of BiR crossing in the chord (see Figure 1a). Therefore, softwood glulam was chosen to allow for exploring the lower strength limit for this failure mode.

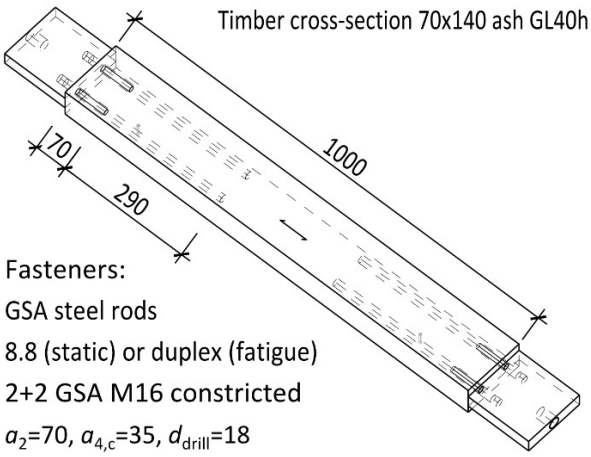

Figure 2. Specimen with 2 pairs of BiR on both sides for fatigue tests ∥ to grain in European ash glulam. All dimensions in [mm].

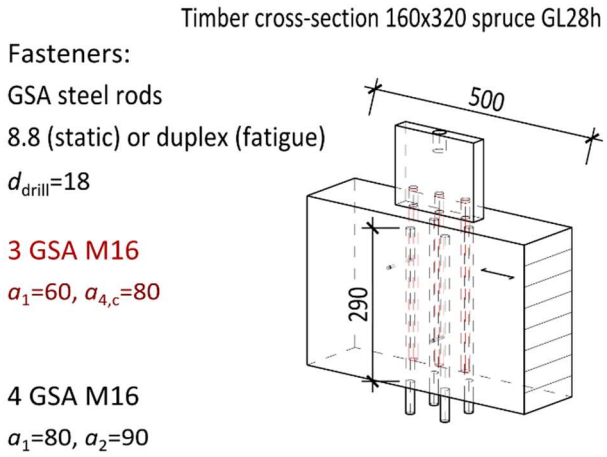

Figure 3. Specimen with 2 groups of BiR for fatigue tests ⊥ to grain in Norway spruce glulam. All dimensions in [mm].

2.3 Materials

2.3.1 Glued-laminated timber (GLT)

Glued-laminated timber (GLT) produced from the most relevant wood species (European ash, *Fraxinus excelsior*, and Norway spruce, *Picea abies*) regarding truss structures in timber dedicated to road bridge construction in Switzerland was chosen. To keep the variations of mechanical properties low, the laminations used for the GLT production were strength graded with the Timber Grader MTG (Brookhuis) into the respective T classes i.e. T18 for Norway spruce and T33 for European ash (*Arnold et al.,* 2021; *Bernasconi et al.,* 2021; *CEN,* 2016). Finally, laminations of uniform densities (groups of laminations with minimized CoV of the density) were selected.

For the series with elevated MC, conditioning of the specimens to an MC of around 20 % was essential for simulating real conditions such as those that occur in bridge structures. Hence, for the series A2, A3, D1 and D2, the laminations used to produce the GLT were stored in an environment with strongly elevated humidity of the surrounding air. A special climate box with water-tight sealing on the inside was developed, and the laminations were stored in that box above a saturated salt-water solution. After first trials with sodium chloride (NaCl), potassium chloride (KCl) was finally used to increase water uptake. The air in the box was ventilated by means of two fans. The MC achieved in the laminations was monitored by weighing them in regular intervals. After the glulam production, joinery and bonding of the rods, the climate boxes were used for further conditioning, storing and transporting the specimens ready for testing. The MC developing in the specimens was monitored indirectly by weighing reference specimens (spruce and ash members with cross-sections between 70 x 70 mm^2 and 160 x 160 mm^2), see Figure 4. The end faces of these four groups of specimens and of all reference specimens were sealed. Two layers of end grain protection from Koch & Schulte were applied with a brush.

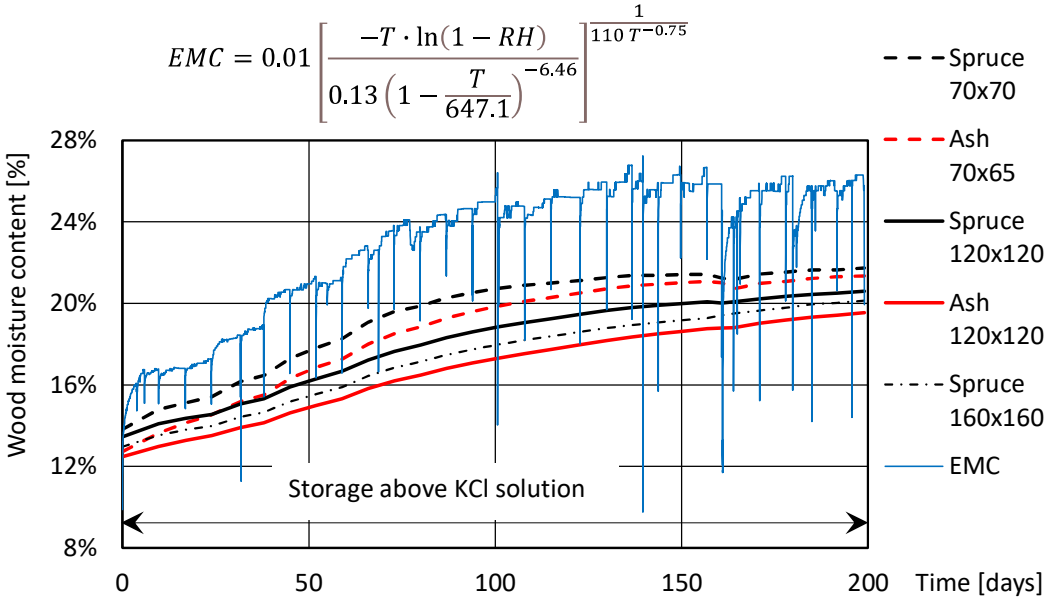

Figure 4. Development of the MC of the reference specimens (calculated equilibrium moisture content (EMC) based on the measured climate in the boxes).

The equilibrium moisture content (EMC) was calculated from the temperature *T* [K] and the relative humidity *RH* [-] according to the formula in Figure 4 (*Reichel,* 2015). The difference between this EMC model and the measured MC of the reference specimens is attributed to the size of the cross-sections. For the GLT properties determined from the tested specimens, the mean values per series are listed below, i.e. density (Table 2, Table 6) and modulus of elasticity MOE (Table 4). The individual values for each specimen are given in (*Steiger and Zumbrunn-Maurer,* 2024). The differences in MOE and density between Series A1 and A2 – A3 result from having chosen raw material from different sawmills.

Table 2. Local densities [kg/m³] at ω = 12 % of the European ash GLT specimens of group A.

Specimen	Series A1	Series A2	Series A3
Mean values	718 [1)]	644	640
		Mean value of group A	662
		CoV of group A	6 %

1) Test series A1 had been investigated in the course of an earlier project (*Maurer et al.,* 2022).

Table 3. Bulk densities [kg/m³] at ω = 12 % of the Norway spruce GLT specimens of groups B, C, D.

Specimen	Group B and Series C1	Series C2	Series D1	Series D2
Mean values	429	445	423	424
		Mean value of groups B, C and D		430
		CoV of groups B, C and D		4 %

Table 4. Modulus of elasticity [N/mm²] of the European ash GLT specimens of group A.

Specimen	Series A1	Series A2	Series A3		
Test name [1)]	Proof loading	Pull-out test	Proof loading	Preloading	Pull-out test
MC	≈ 9 %	≈ 20 %	≈ 20 %	≈ 20 %	≈ 17 %
Mean	15'500	11'900	11'300	11'500	11'900

1) The names of the static load tests are explained in 2.6.

2.3.2 Bonded-in rod connections

The tested BiR connections were of type GSA (*EOTA,* 2020), consisting of steel rods with metric thread M16 bonded into 18 mm diameter holes by means of a 2-component epoxy resin. The performance of this system is well above the minimum characteristic withdrawal strength according to the FV Draft of FprEN 1995-1-1 (*CEN,* 2025) of $f_{w,k}$ = 4 N/mm². The GSA adhesive passed tensile creep tests at 60 °C according to EN 17334 (*CEN,* 2021) loaded with a shear stress of 7 N/mm² in the bond line. For the actual specimens, the effective anchoring length (withdrawal length) of the rods was 290 mm (i.e. 16.1·d_{drill}). For group A, a recess (not bonded length) of 70 mm was applied. In this part, the thread was removed, and the rod was machined to the appropriate diameter to ensure a ductile failure in the ultimate limit state. With the partial safety factors valid in Switzerland, the design resistance as well as the forces for static proof loading and fatigue testing were calculated (Table 5).

Table 5. Calculated resistances and forces for static proof loading and fatigue testing.

Groups		A	B & C	D
Characteristic value of withdrawal resistance	R_k	200 kN	187 kN	187 kN
Partial safety factor for ductile connections [1)]	γ_M/η_M	1.5	1.5	1.5
Factor considering the influence of the MC [1)]	η_ω	1.0	1.0	0.8
Design value of withdrawal resistance	$R_d = R_k / (\gamma_M/\eta_M)$	133 kN	125 kN	99.8 kN
Conversion factor [2)]	$\gamma_Q + R \cdot \gamma_G$	1.635	1.635	1.635
Assumed variable live load [2)]	Q_k	81.5 kN	73.6 kN	61.0 kN
Chosen level of fatigue loading in tests	ΔF	90.0 kN	81.0 kN	64.8 kN
Force amplitude	F_a	±45 kN	±40.5 kN	±32.4 kN

[1)] according to the Swiss standard SIA 265 for the design of timber structures (*SIA,* 2021).

[2)] The variable live load Q_k is calculated assuming that 90 % of the maximum force acting in the case of fatigue loading (at SLS level) is caused by the fatigue-effective action. This is reflected by the chosen stress ratio R. Based on a maximum utilization in the ULS, the following equation results: $R_d = E_d = 1.35G_k + 1.5Q_k$, which for the chosen case with $G_k/Q_k = R = 0.1$ can be simplified as follows: $Q_k = R_d/1.635$.

The BiR subjected to static loading (series A2, B, C1, D1) were of steel grade 8.8. For the experiments with fatigue loading (series A1, A3, C2, D2), a duplex steel quality was chosen, as investigated in earlier experiments (*Maurer et al.,* 2022).

2.3.3 Steel parts for connecting the specimens with the testing machine

To ensure that no fatigue failure occurred in the steel connecting parts, these had to be developed and optimized regarding the steel quality and the geometric shape prior to the fatigue tests. In series A1 and A3 and for the top joint of the BiR ⊥ to grain series, 30 mm thick steel plates of grade S355J2 were used. The rod-to-plate connection detail corresponded to the design developed in 2021 (*Maurer et al.,* 2022). The other steel parts were fastened by nuts. They were tightened uniformly with a torque of 80 Nm in series A2 and 30 Nm in the bottom joint of the BiR ⊥ to grain series (for details see research report).

2.4 Connection stiffness

For comparing the measured connection stiffnesses with the specifications in the FV Draft of FprEN 1995-1-1 (*CEN,* 2025), Clause 11.3.8.3, the axial slip modulus K_{ax} [kN/mm] is modelled with 3 displacement shares (Equations 1 – 3, below). As an example, for the A2 specimens they result as follows:

Equation 1. Displacement share of the withdrawal length.

$$K_{\mathrm{ax},1} = K_{\mathrm{w}} = 460 \left(\frac{\rho_{\mathrm{mean}}}{420}\right)^{0.85} d^{0.9} {l_{\mathrm{w}}}^{0.6} = \frac{460}{1'000} \cdot \left(\frac{644}{420}\right)^{0.85} \cdot 16^{0.9} \cdot 290^{0.6} = 241$$

Equation 2. Displacement share of the constriction zone.

$$K_{\mathrm{ax},2} = K_{\mathrm{s},1} = \frac{E \cdot A}{l} = \frac{210'000 \cdot 133}{65 \cdot 1'000} = 430$$

Equation 3. Displacement share of the rod length in the steel part incl. washer & nut. (As a simplification for deformations in the threads, the entire length of the nut is considered to be free and fully loaded rod length.)

$$K_{\mathrm{ax},3} = K_{\mathrm{s},2} = \frac{E \cdot A}{l} = \frac{210'000 \cdot 157}{74 \cdot 1'000} = 446$$

Equation 4. Slip modulus for the group of 2 GSA M16.

$$K_{\mathrm{ax}} = n \cdot \frac{1}{\sum_{\mathrm{i=1}}^{\mathrm{j}} \frac{1}{K_{\mathrm{ax,i}}}} = 2 \cdot \frac{1}{\frac{1}{241} + \frac{1}{430} + \frac{1}{446}} = 229$$

where d is the diameter of the rod and l_w is the withdrawal length.

2.5 Experiments with fatigue loading

For the main set of experiments, cyclic tests at constant force amplitudes were carried out force-controlled (sinus) in pull-pull configuration (*Tlustochowicz et al.,* 2010) with a stress ratio $R = F_{min}/F_{max} = 0.1$ and frequencies of $f = 4 – 7$ Hz (Table 6). A target value of $N = 2 \cdot 10^6$ stress cycles was defined because the structural steel standards also relate their fatigue strength categories to this value. In one case, $3 \cdot 10^6$ stress cycles were applied due to the availability of the machine. A value of $R = 0.1$ was selected because this is relevant in practice for a lightweight structure with a large variable action and for comparison with results from the literature. However, the investigated stress ratio $R = 0.1$ does not cover the range of stress ratios in the design approach given in the FV Draft of FprEN 1995-1-1 (*CEN,* 2025), i.e. $-1 \leq R \leq 1$.

The temperature T in the bond lines, the machine stroke and the force F were measured continuously. Monitoring the temperature in the bond lines was important to ensure that the fatigue loading would not lead to an impermissible heating of the adhesive and thus to an influence on the load-bearing behaviour of the BiR.

Table 6. Loading parameters for the fatigue tests.

Parameter	Symbol	Series A1	Series A3	Series C2	Series D2
Number of fatigue tests	n	3	4	4	4
Minimum force	F_{min}	10 kN	10 kN [1)]	9 kN	7.2 kN [5)]
Mean force	F_m	55 kN	55 kN [2)]	49.5 kN	39.6 kN [6)]
Maximum force	F_{max}	100 kN	100 kN [3)]	90 kN	72 kN [7)]
Force amplitude	F_a	± 45 kN	± 45 kN [4)]	± 40.5 kN	± 32.4 kN [8)]
Stress ratio	$R = F_{min}/F_{max}$	0.1	0.1	0.1	0.1
Frequency	f	5 – 12 Hz	4 – 6 Hz	5.5 – 7 Hz	4 – 6.25 Hz
Wave shape	–	Sinus	Sinus	Sinus	Sinus
Control	–	Force	Force	Force	Force

Parameters for test on specimen A3-04: [1)] 14 kN [2)] 77 kN [3)] 140 kN [4)] ± 63 kN
Parameters for test on specimen D2-01: [5)] 9 kN [6)] 49.5 kN [7)] 90 kN [8)] ± 40.5 kN

In the fatigue test on specimen D2-01, cracks appeared after only 135'000 stress cycles, and it was suspected that these were initiated by the drying of the specimen. Therefore, it was decided to cover the end faces of the specimens with plastic tape for the remaining fatigue tests on specimens of series D2 in order to prevent excessive or too rapid drying out.

2.6 Experiments with static loading

The experiments with static loading were performed according to EN 26891 (*CEN,* 1991) including 1 cycle in the elastic range. At n'H, loading in pull-pull configuration was applied via hollow plunger hydraulic cylinders, operated by means of a hand pump. The load was increased incrementally, with the cylinder force (oil pressure) and the measured displacements being noted for each load step. In all static tests, the differential displacements at the BiR connections and some displacements in the timber member were measured. For parallel to grain specimens, the static MOE of the timber was determined in the central part of the member based on the deformation over a measuring length of 300 mm (*Steiger and Zumbrunn-Maurer,* 2024).

2.6.1 Proof loading and preloading prior to the fatigue tests

Static tensile proof loading and preloading was carried out on all specimens to assess their stiffness. For series A1, B, C1 and C2, the proof loading was done some days after production. The specimens of the series with elevated MC were proof loaded after conditioning. For series A2 and A3, around 166 days passed after the bonding process. Series D1 and D2 were loaded after 201 days. Proof loading ensured that no specimens were included in the fatigue tests that did not meet the quality requirements. Prior to the fatigue test, a static preloading in 5 identical cycles in pull-pull configuration was carried out on all specimens with a force level that corresponded to the maximum load of the fatigue tests F_{max}. The loading rate for the static experiments at Empa varied between 0.66 kN/s and 3 kN/s.

2.6.2 Pull-out tests after passing of fatigue tests

After the fatigue tests, static loading tests were carried out to determine the residual resistance and the residual stiffness of the BiR connections. The loading was force-controlled until reaching 1.75 times the maximum force of the fatigue tests F_{max}. Beyond, the loading was displacement-controlled with a rate of 0.012 mm/s for series A3 and 0.005 mm/s for series C2 and D2.

2.7 Investigations after testing

After completion of all tests, every specimen was disassembled and analysed in detail to identify the types of failure. Pictures of these investigations are presented in the research report (*Steiger and Zumbrunn-Maurer,* 2024).

3 Results and discussion

3.1 Temperatures in the bond lines during the fatigue tests

When testing specimen A1-01 under fatigue loading with a frequency of 12 Hz, the temperatures in the bond lines after 20'000 stress cycles (i.e. after 0.5 h of testing) reached 45 °C, and there was no indication that they would tend to increase less pronounced when continuing the test (*Maurer et al.,* 2022). Trials with lower frequencies revealed that with frequencies of 5 – 8 Hz, the temperatures in the bond lines could be kept in reasonable ranges regarding the mechanical performance of the epoxy adhesive at elevated temperatures (*Verdet et al.,* 2016). This was confirmed later when specimens of series A3 were tested with frequencies of 5 Hz and 6 Hz (Figure 5).

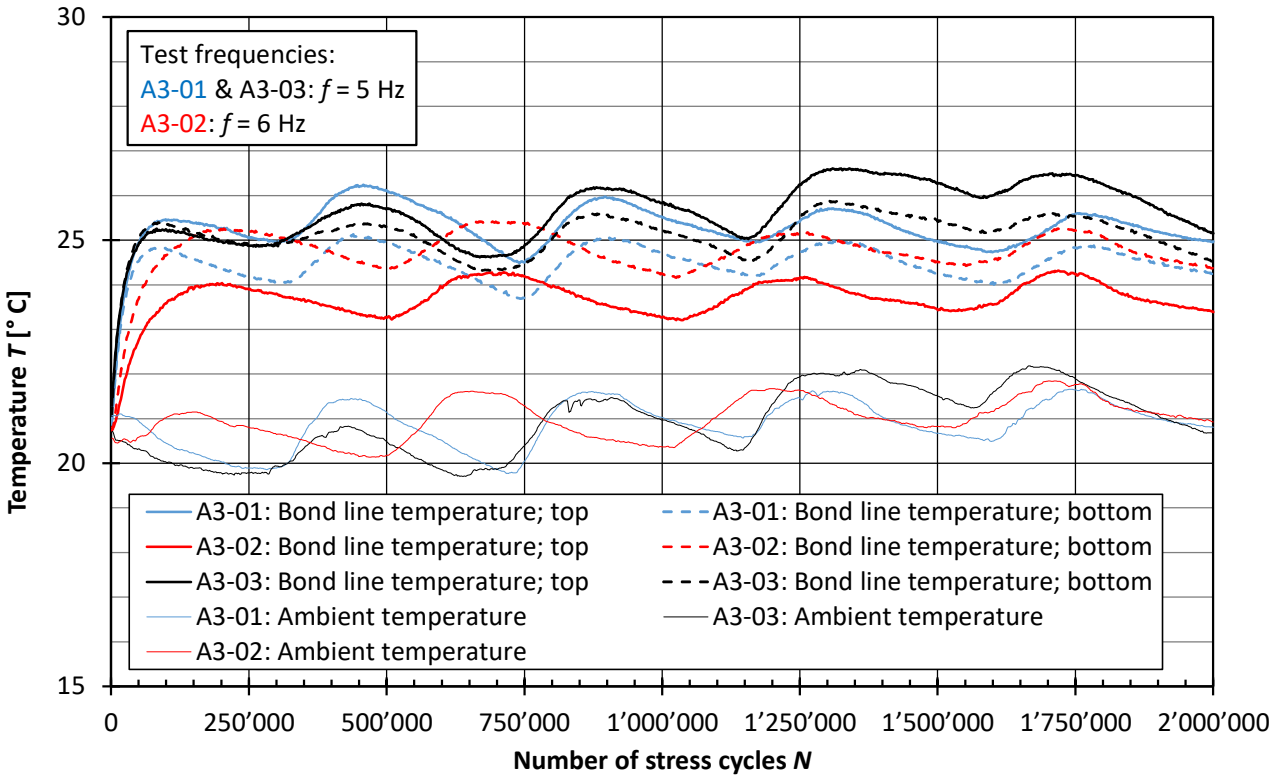

Figure 5. Development of the temperatures in the bond lines in the fatigue tests with different frequencies (BiR M16 inserted ‖ to grain in European ash GLT, 3 specimens from series A3).

3.2 BiR inserted parallel to grain in European ash GLT

The results of the tests on specimens made of European ash GLT with BiR ‖ to grain (group A) are summarized below, i.e. results of the fatigue tests (Table 7), stiffness of the BiR connections before and after fatigue loading (Table 8) and results of the pull-out tests with and without prior fatigue loading (Table 9).

In dry condition ($\omega \approx 9$ %) as well as at elevated MC ($\omega \approx 20$ %), 3 specimens passed $2 \cdot 10^6$ stress cycles (100 kN / 10 kN) without failure (Table 7). Increasing the maximum force in the fatigue test by 40 % (i.e. to the design level), led to steel failure in one of the rods after 56'000 stress cycles. The temperatures in the bond lines remain below

50 °C, if the test frequency is not higher than 6 Hz and if the chosen level of fatigue loading is in the SLS range.

Table 7. Characteristic data of the fatigue tests on the specimens with BiR inserted parallel to grain in European ash GLT (series A1 and A3).

Series A1 ($\omega \approx 9$ %)					
Specimen	Stress cycles	$\Delta\sigma_s$ [Nmm^2]	τ_{max} [N/mm^2]	Frequency [Hz]	Max. Temperature [°C] [1)]
# 1	2'054'712	287	3.4	6 – 12	55.7
# 2	2'010'000	287	3.4	8	54.2
# 3	2'010'000	287	3.4	5	48.0
Series A3 ($\omega \approx 20$ %)					
Specimen	Stress cycles	$\Delta\sigma_s$ [Nmm^2]	τ_{max} [N/mm^2]	Frequency [Hz]	Max. Temperature [°C] [1)]
# 1	2'000'486	287	3.4	5	26.2
# 2	2'000'483	287	3.4	6	25.4
# 3	2'000'486	287	3.4	5	26.6
# 4	56'175	401	4.8	5	(36.5)

[1)] Temperature in the bond line.

$\Delta\sigma_s$ Stress difference in the rods (2 GSA M16, A_s = 157 mm²).

τ_{max} Shear stress in the bond line under maximum force F_{max} (in relation to the nominal diameter of the rod and the withdrawal length).

Table 8. Connection stiffness [kN/mm] (top joint / bottom joint, respectively) determined on the specimens with BiR inserted parallel to grain in European ash GLT (group A).

Specimen	Series A1	Series A2	Series A3		
	K_{Proof} [1)]	$K_{Pull\text{-}out}$ [2)]	K_{Proof} [1)]	K_{Pre} [2)]	$K_{Pull\text{-}out}$ [2)]
	$\omega \approx 9$ %	$\omega \approx 20$ %	$\omega \approx 20$ %		$\omega \approx 17$ %
# 1, top	343	245	304	314	342
# 1, bottom	353	313	320	310	323
# 2, top	339	276	310	309	384
# 2, bottom	336	235	310	315	364
# 3, top	355	270	309	315	333
# 3, bottom	356	252	302	352	370
# 4, top	344	265	327	321	–
# 4, bottom	343	249	302	324	–
# 5, top	347	–	–	–	–
# 5, bottom	331	–	–	–	–
Mean value	**345**	**263**	**311**	**320**	**353**
CoV	2 %	9 %	3 %	4 %	7 %
K_{ax}	281	229	266	266	266
Deviation [3)]	+23 %	+15 %	+17 %	+20 %	+33 %

[1)] Connection stiffness determined during proof loading by neue Holzbau AG.

[2)] Connection stiffness determined in experiments at Empa with static preloading before the fatigue test or in pull-out tests after fatigue loading.

[3)] Relative difference of the mean value compared to K_{ax} according to the FV draft of FprEN 1995-1-1.

The comparison of connection stiffness in dry condition and at elevated MC (mean values 345 and 311 N/mm^2 in Table 8) shows a reduction of 10 % due to increased MC. Hence, for the design of a BiR connection in members with elevated MC, a reduction factor for the stiffness of η_ω = 0.9, as specified in the standard SIA 265 (*SIA,* 2021), should be applied. The 10 % increase in stiffness between preloading and pull-out test after fatigue loading (mean values 353 and 320 N/mm^2 in Table 8) is partly attributed to the decrease in MC (from around 20 % to around 17 %) and possibly to the post-curing of the adhesive during the fatigue test. Detailing of the specimens aimed at a ductile failure mode, i.e. for yielding of the rods, which is the desired failure mode in practice, and which represents the maximal performance regarding the resistance of groups of multiple BiR. However, the diameter in the constriction zone was kept larger than it would be designed in practice to prevent steel failure in the fatigue test. This was also the failure mode experienced in the static experiments (Table 9) and hence, the influence of MC on the load-bearing resistance cannot be quantified. From the experiments in Series A3, it can be concluded that exposing the BiR ∥ to grain in ash glulam to fatigue loading with 2·10^6 stress cycles and a bond line stress τ_{max} 3.4 N/mm² did not lead to a reduction of the withdrawal resistance, neither in dry condition (series A1, (*Maurer et al.,* 2022), nor at elevated MC (series A3). The differences in withdrawal resistance without and with prior fatigue loading (series A2 vs. A3) can be explained with the different steel quality of the rods, see 2.3.2.

Table 9. Withdrawal resistance [kN] and failure mode determined on the specimens with BiR inserted parallel to grain in European ash GLT (group A).

Specimen	Series A2	Series A3
	$\omega \approx 20$ %	$\omega \approx 17$ %
# 1	248	270
# 2	249	270
# 3	250	268
# 4	250	–
Mean value	249	269
Failure mode	Rod yielding	Rod yielding

3.3 BiR inserted perpendicular to grain in Norway spruce GLT

The results of the tests on Norway spruce GLT specimens with BiR ⊥ to grain (groups C & D) are reported below, i.e. for the fatigue tests (Table 10), the stiffness of the connections with 3 GSA M16 before and after fatigue loading (Table 11), and for the pull-out tests with and without prior fatigue loading (Table 12). In dry conditions (series C2), 3 specimens could be subjected to fatigue loading with 2·10^6 stress cycles at serviceability level (90 kN / 9 kN) without failure (Table 10). One specimen even passed 3·10^6 stress cycles (90 kN / 9 kN) without failure. Regarding temperatures, the tests confirmed the findings of the group A. With frequencies in the range of 4 – 7 Hz, bond lines of these series could be kept below 40 °C.

Table 10. Characteristic data of the fatigue tests on the specimens with BiR inserted perpendicular to grain in Norway spruce GLT (series C2 and D2).

Series C2 ($\omega \approx 9$ %)					
Specimen	Stress cycles	$\Delta\sigma_s$ [Nmm^2]	τ_{max} [N/mm^2]	Frequency [Hz]	Max. Temperature [°C] [1)]
# 1	2'034'359	172	2.1	5.5	32.9
# 2	1'999'998	172	2.1	5.9	30.6
# 3	1'998'521	172	2.1	6.5	31.3
# 4	2'999'801	172	2.1	7	32.1
Series D2 ($\omega \approx 20$ %)					
Specimen	Stress cycles	$\Delta\sigma_s$ [Nmm^2]	τ_{max} [N/mm^2]	Frequency [Hz]	Max. Temperature [°C] [1)]
# 1	422'834	172	2.1	6.25	(46.1)
# 2	2'000'500	138	1.6	5	30.5
# 3	2'000'500	138	1.6	5.9	33.8
# 4	2'000'500	138	1.6	4	37.6

[1)] Temperature in the bond line.

$\Delta\sigma_s$ Stress difference in the rods of the top joint (3 GSA M16, A_s = 157 mm²).

τ_{max} Shear stress in the bond line under maximum force F_{max} (in relation to the nominal diameter of the rod and the withdrawal length).

When in series D2 subjecting the same connections to fatigue loading at elevated MC with the same force parameters, fatigue failure in the wood (rolling shear) occurred after $0.4 \cdot 10^6$ stress cycles and the temperatures in the bond lines peaked to almost 50 °C. After having reduced the forces by 20 % (72 kN / 7.2 kN), 3 specimens passed $2 \cdot 10^6$ stress cycles without failure and the temperatures in the bond lines remained below 40 °C. It can be concluded that for the design of a BiR connection at elevated MC, for the strength, a reduction factor of $\eta_\omega = 0.8$, as specified in the standard SIA 265 (SIA, 2021), should be applied.

Concerning the connection stiffness (Table 11), only the values in cells shaded in grey should be compared directly, due to the displacement measurements not having been performed with the same equipment and precision. Looking at the limited number of available values, conclusions must be drawn carefully. The displacement measurements at the bottom joints were influenced by different steel parts with different nuts, depending on the series and different reference points depending on the test lab. A detailed evaluation of these results was not done yet. Therefore, no results are presented here, while the raw values could be found in the research report.

In series C2, tested in dry condition (MC ≈ 9 %), the stiffness of the top joints increased by 4 % for specimen C2-02 and decreased by 13 % for specimen C2-03, which is an indication that the fatigue loading with $2 \cdot 10^6$ stress cycles at serviceability level (90 kN / 9 kN) led to a slight reduction of the stiffness. After fatigue loading with $3 \cdot 10^6$ stress cycles, an 18 % lower stiffness was measured for specimen C2-04.

Table 11. Connection stiffness [kN/mm] determined on the specimens with BiR inserted perpendicular to grain in Norway spruce GLT (groups B, C and D) at the top joint (3 GSA M16).

Specimen	*Group B* and Series C1	Series C2			Series D1	Series D2		
	$K_{Pull-Out}$	K_{Proof}	K_{Pre}	$K_{Pull-Out}$	$K_{Pull-Out}$	K_{Proof}	K_{Pre}	$K_{Pull-Out}$
	$\omega \approx 9$ %		$\omega \approx 9$ %		$\omega \approx 20$ %	$\omega \approx 20$ %		$\omega \approx 18$ %
Testing @	n'H	n'H	Empa	Empa	n'H	n'H	Empa	Empa
# 1	*213* [1]	262	– [2]	201	188	202	212	–
# 2	*246*	264	254	263	201	188	195	46 [4]
# 3	*269*	279	256	224	212	199	182	138
# 4	250	230	210	173 [3]	–	204	185	117
# 5	263	–	–	–	–	187	–	–
# 6	274	–	–	–	–	203	–	–
Mean value	**260**		**240**	**229**	**198**		**194**	**128**
CoV	6 %		11 %	14 %	4 %		7 %	–
K_{ax}	305		310	310	299		299	299
Deviation [5]	-15 %		-23 %	-26 %	-34 %		-35 %	-57 %

[1] Value was not considered when calculating the mean value because a different reference point had been selected for measuring the joint deformation than for the other tests.

[2] Differential displacements at the BiR connections were not measured.

[3] Value was not considered when calculating the mean value because the specimen was tested after $3 \cdot 10^6$ stress cycles, whereas the other ones had been tested after $2 \cdot 10^6$ stress cycles.

[4] Although the specimen achieved $2 \cdot 10^6$ stress cycles in the fatigue test, damage appears to have occurred because of the fatigue stress. This value was not considered when calculating the mean value of joint stiffness.

[5] Relative difference of the mean value compared to K_{ax} according to the FV draft of FprEN 1995-1-1.

A clearer picture emerged from series D2 (i.e. specimens with elevated MC ≈ 18 %, tested with reduced forces 72 kN / 7.2 kN). The stiffness of specimen D2-02 after the fatigue test was 76 % lower than during preloading and the deformation at 72 kN reached almost 1.6 mm. Accounting for this and looking at the strongly reduced withdrawal resistance (37 %) of 117 kN (Table 12), it could be concluded that this specimen had suffered significant damage during the fatigue test. The BiR connections of specimens D2-03 and D2-04 were markedly less stiff after fatigue loading (24 % reduction in stiffness for specimen D2-03 and 37 % for specimen D2-04). The mean value of the stiffnesses of these two specimens (128 kN/mm) is 51 % lower than the mean value without fatigue loading in dry state (260 kN/mm).

The mean value of withdrawal resistance after fatigue loading at elevated MC (specimens D2-03 and D2-04) was 166 kN. Compared to the 5 static tensile tests in the same condition regarding MC (series D1 and specimens D2-05, D2-06), this corresponds to a reduction of 11 %. Compared to the mean value of the specimens tested in dry condition (Series B and C1), the reduction is 18 %. Hence, 20 % reduction for the strength at elevated MC ($\eta_\omega = 0.8$, as specified in the standard SIA 265 (*SIA,* 2021)) is recommended for design. Clause 10.2(4) of the FV Draft of FprEN 1995-1-1

(*CEN,* 2025) specifies that "For the calculation of the fatigue strength in SC 3, the characteristic strength f_k in Formula (10.2) should be multiplied by 2/3" and that "For connections the clause should be applied analogously."

In dry condition (series C2, MC ≈ 9%), the first 3 specimens did not show any reduction in withdrawal resistances after having been subjected to $2 \cdot 10^6$ stress cycles at serviceability level (90 kN / 9 kN). After $3 \cdot 10^6$ stress cycles, the withdrawal resistance of specimen C2-04 was 17 % lower than the mean value of the specimens in series B and C1. For the design of structures with more than $2 \cdot 10^6$ stress cycles, the fatigue strength should be confirmed with additional experiments.

For all specimens (i.e. with and without prior fatigue loading), the governing failure mode was rolling shear failure in the wood close to the BiR rows, with simultaneous cracking. Hence, this type of failure must be verified accordingly, when designing such a connection. However, despite respective research is available (e.g. (*Blass et al.,* 2019; *Meyer,* 2020)), there are no design rules available in the FV Draft of FprEN 1995-1-1 (*CEN,* 2025). There, Clause 11.6.1(7) simply states that "In addition to the splitting resistance …. for connections with more than two axially loaded fasteners in a row parallel to grain ($n_0 > 2$), the rolling shear failure should be verified along the perimeter of the group of fasteners".

Table 12. Withdrawal resistance [kN] and failure mode determined on the specimens with BiR inserted perpendicular to grain in Norway spruce GLT (groups B, C and D).

Specimen	*Group B* and Series C1	Series C2	Series *D1* and D2	Series D2
	$\omega \approx 9$ %	$\omega \approx 9$ %	$\omega \approx 20$ %	$\omega \approx 18$ %
Testing @	n'H	Empa	*n'H* / Empa	Empa
# 1	*210*	186	*200*	–
# 2	*211*	203	*179*	117 [1)]
# 3	*185*	204	*207*	181
# 4	209	167 [2)]	–	150
# 5	190	–	185	–
# 6	200	–	164	–
Mean value	**201**	**198**	**187**	**166**
Failure mode	**Rolling shear failure after formation of cracks**			

[1)] The specimen passed $2 \cdot 10^6$ stress cycles in the fatigue test. It seems that damage had occurred because of the fatigue stress. This value was not considered when calculating the mean value of withdrawal resistance.

[2)] Value not considered when calculating the mean value because the specimen was tested after having been subjected to fatigue loading with $3 \cdot 10^6$ stress cycles.

3.4 Design approach in the FV draft of FprEN 1995-1-1

In Figure 6 and Figure 7, the test results are compared with the SN-curves (Wöhler-curves) according to the FV draft of FprEN 1995-1-1. For the tested configuration and *R*°=°0.1, the design model leads to conservative numbers of stress cycles for the chosen levels of fatigue loading F_{max}.

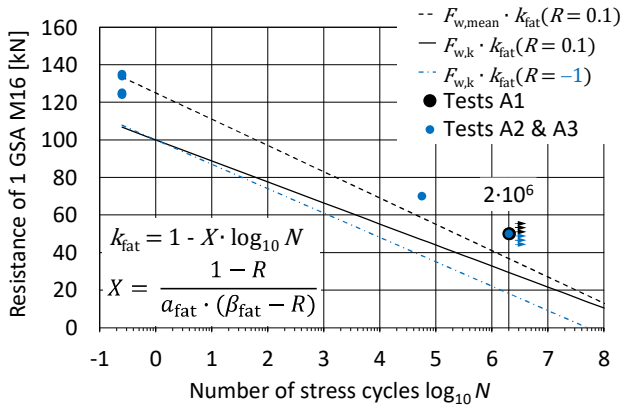

Figure 6. Experimental results of BiR ∥ to grain compared to the design model in the FV draft of FprEN 1995-1-1.

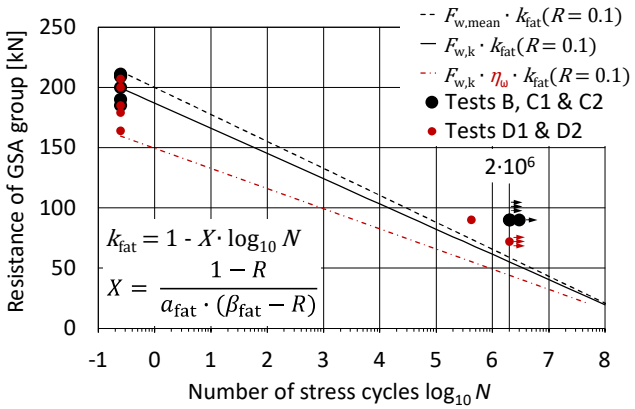

Figure 7. Experimental results of BiR ⊥ to grain compared to the design model in the FV draft of FprEN 1995-1-1.

According to the SN-curve for R = -1 (red line in Figure 6), a GSA BiR might be subjected to $2{\cdot}10^6$ fully reversed stress cycles of ±18.2 kN. The tested force amplitude of ±45 kN in the tension-tension stress range supports the expectation that the design model is conservative also for this stress ratio. However, evidence should be provided by experiments. In Figure 7, the blue SN-curve shows the proposed reduction factor for elevated MC η_ω = 0.8. This and the following proposals assume that the partial safety factor for fatigue strength is set to $\gamma_{R,fat}$ = 1.0 by the National Annexes.

4 Conclusions

From the investigations on BiR ∥ to grain in European ash GLT and BiR ⊥ to grain in Norway spruce GLT, consisting of static tests and fatigue loading with forces at SLS level and an R value of 0.1, the following conclusions can be drawn:

- The applied methodology, test setups and materialisation of specimens proved to work well for the investigation of fatigue strength of BiR at different levels of MC.
- BiR can be applied in connections subjected to fatigue loading in environment with elevated MC (e.g. to construct road bridges), provided the materials and shapes of the steel parts (rods, adapters) are optimized for fatigue loading.
- When applying high-performance BiR connections ($f_{w,k}$ > 4 N/mm²) in GLT at elevated MC (upper range of SC 2), the withdrawal resistance (for fatigue and quasi-static loading) should be reduced by 20 % in the design if the characteristic value is based on short term tests in dry conditions. This reduction would be in line with the strength reduction factor of 2/3 specified in the FV draft of FprEN 1995-1-1, Clause 10.2(4) for applications in SC 3.
- The values for the coefficients a_{fat} and β_{fat} for axially loaded BiR given in the FV draft of FprEN 1995-1-1 are considered reasonable considering the current knowledge. More tests should be performed to justify less conservative values.

- Criteria regarding the displacement increase during the fatigue test and/or regarding the residual withdrawal resistance should be defined in the standards.
- The axial slip modulus for BiR (ε = 0°) given in the FV draft of FprEN 1995-1-1 underestimates the stiffness of the tested BiR ∥ to grain configuration. For BiR ⊥ to grain with the chosen reference point on the member, the stiffness is overestimated. Assuming the reference point to be standardised and formulae for the axial slip modulus in SC 1 to be improved, the connection stiffness should be reduced by 10 % in the design for quasi-static loading at elevated MC. Stiffness reduction factors up to 0.5 should be discussed for the design of axially loaded fasteners under fatigue loading at elevated MC.
- When performing fatigue tests of BiR inserted in timber, the temperatures in the bond lines should be monitored to prevent their excessive warming. With ambient temperatures below 22 °C, test frequencies up to 6 Hz led to temperatures in the bond lines of not more than 40 °C. Respecting this limit should prevent inadmissible post-curing of the adhesives. Post-curing can lead to a beneficial behaviour of the adhesive not representing the situation in practice, where much lower frequencies of cyclic loading by vehicles occur.
- The tests on BiR ∥ to grain in European ash GLT showed that static ductility (rod yielding) can be achieved with a dedicated design, detailing and execution. Neither the fatigue loading nor the elevated MC led to questioning the provision in the FV draft of FprEN 1995-1-1, Clause 11.10.5.1(3) about ductile prior to brittle failure.
- For the specimens with BiR ⊥ to grain in Norway spruce GLT, rolling shear in the wood close to the rod rows was the governing failure mode. This was identified in the pull-out tests, for specimens with and without prior fatigue loading. Even though a respective hint can be found in the FV draft of FprEN 1995-1-1, no respective design formula is given in the standard.
- Conditioning of timber specimens to an MC to be expected in SC 2 / SC 3 takes approximately 200 days depending on the size of the specimens. Conditioning proofed to work well in a box with saturated potassium chloride (KCl) water solution and ventilation of the air in the box.
- The weighing of reference specimens with representative cross-sections showed the slower moisture uptake of lager dimensions. Their mass constancy was clearly lower than predicted by the formula for the calculated EMC. The reason for this is very likely a permanent moisture gradient which seems to establish in a timber member with dimensions as occurring in building practice.

Overall, it can be concluded that the investigation contributes to the future standardisation of fatigue and static tests on timber connections. When designing (BiR) connections for applications with elevated MC, the stiffness, withdrawal resistance and fatigue strength should be reduced. The values of the reduction factors must be aligned with the base values chosen in the standard. If a force introduced by rows of

axially loaded fasteners causes rolling shear stresses in the wood, this should be verified and hence, a suitable design approach should be added to FprEN 1995-1-1.

5 References

Arnold, M., Ehrhart, T., Lehmann, M., Strahm, T. (2021). Richtlinie zur Herstellung von verklebten Produkten aus Laubholz. Holzindustrie Schweiz, Fachgruppe Leimholz, Bern, Schweiz.

Bengtsson, C., Johansson, C.-J. (2002). GIROD – Glued-in rods for timber structures. SP Report 2002:26. Boras, Sweden.

Bernasconi, A., Ehrhart, T., Eschmann, M., Franke, S., Jockwer, R., Klippel, M., Lehmann, M., Maurer, B., Pauli, B., Ratsch, G., Schmid, H., Selter, W., Strahm, T. (2021). Verklebte Laubholzprodukte für den statischen Einsatz. Lignum – Holzwirtschaft Schweiz, Zürich.

Blass, H. J., Flaig, M., Meyer, N. (2019). Row shear and block shear failure of connections with axially loaded screws. INTER Meeting Fifty-Two. Online. Paper INTER/52-7-6:

Bletz-Mühldorfer, O., Diehl, F., Bathon, L., Myslicki, S., Walther, F., Grunwald, C., Vallée, T. (2018). Ermüdungsverhalten von eingeklebten Stäben. Bauen mit Holz 5, 30 - 35.

EN 338 (2016). Structural timber - Strength classes. CEN, Brussels, Belgium.

EN 1995-1-1 (2004). Design of timber structures, Part 1-1: General - Common rules and rules for buildings. CEN, Brussels, Belgium.EN 1995-2 (2004) Design of timber structures, Part 2: Bridges. CEN, Brussels, Belgium.

EN 1995-2 (2004) Design of timber structures, Part 2: Bridges. CEN, Brussels, Belgium.

EN 17334 (2021). Glued-in rods in glued structural timber products - Testing, requirements and bond shear strength classification. CEN, Brussels, Belgium.

EN 26891 (1991). Timber structures – Joints made with mechanical fasteners: General principles for the determination of strength and deformation characteristics. CEN, Brussels, Belgium.

FprEN 1995-1-1 (2025). Design of timber structures, Part 1-1: General – Common rules and rules for buildings. Formal Vote Draft. Doc. CEN/TC 250/SC 5/N2259. CEN, Brussels, Belgium.

Erchinger, C., Steurer, A. (2005). In Holz eingeleimte Gewindestangen – Ermüdungsverhalten. Bulletin Holzforschung Schweiz, 13(1), 12 - 13.

ETA-19/0752 (2020). Timber Structures – Glued-in rods for timber connections (GSA-Technology). EOTA, Brussels, Belgium.

Gehri, E. (2000). Klassische Verbindungen neu betrachtet. 17. Dreiländer Holztagung "Holz: Architecture - Research - Technology". Luzern, Schweiz. 43 - 50.

Maurer, B., Gehri, E., Strahm, T., Steiger, R., Affolter, C. (2022). Fatigue strength of axially loaded steel rods bonded in European ash glulam.
4th International Conference on Timber Bridges ICTB. Biel/Bienne, Switzerland.

Meyer, N. (2020). Tragfähigkeit mechanischer und geklebter Verbindungsmittel in Buchenfurnierschichtholz. PhD Thesis. Karlsruher Institut für Technologie (KIT), Karlsruhe, Germany.

Molina, J. C., Calil, C., Carreira, M. R. (2009). Pullout strength of axially loaded steel rods bonded in glulam at a 45 degrees angle to the grain.
Materials Research-Ibero-American Journal of Materials, 12(4), 427 - 432.

Myslicki, S., Bletz-Mühldorfer, O., Diehl, F., Lavarec, C., Vallée, T., Scholz, R., Walther, F. (2019). Fatigue of glued-in rods in engineered hardwood products - Part I: Experimental results. Journal of Adhesion, 95(5-7), 675-701.

Myslicki, S., Walther, F., Bletz-Mühldorfer, O., Diehl, F., Lavarec, C., Beber, V. C., Vallée, T. (2019). Fatigue of glued-in rods in engineered hardwood products – Part II: Numerical modelling. Journal of Adhesion, 95(5-7), 702 - 722.

Norm SIA 265 Holzbau (2021). Schweizerischer Ingenieur- und Architektenverein SIA, Zürich, Schweiz.

Reichel, S. (2015). Modellierung und Simulation hygro-mechanisch beanspruchter Strukturen aus Holz im Kurz- und Langzeitbereich. PhD Thesis. Technische Universität Dresden, Germany.

Steiger, R., Serrano, E., Stepinac, M., Rajcic, V., O'Neill, C., McPolin, D., Widmann, R. (2015). Strengthening of timber structures with glued-in rods.
Construction and Building Materials, 97, 90 - 105.

Steiger, R., Zumbrunn-Maurer, B. (2024). Bericht zum Projekt WHFF-CH 2022-10: Ermüdungsverhalten von in BSH eingeklebten Gewindestangen mit Einsatz im Brückenbau. https://www.aramis.admin.ch/Texte/?ProjectID=57787

Tlustochowicz, G., Serrano, E., Steiger, R. (2010). State-of-the-art review on timber connections with glued-in steel rods. Materials and Structures, 44(5), 997 - 1020.

Verdet, M., Salenikovich, A., Cointe, A., Coureau, J. L., Galimard, P., Toro, W. M., Blanchet, P., Delisee, C. (2016). Mechanical performance of polyurethane and epoxy adhesives in connections with glued-in rods at elevated temperatures. Bioresources, 11(4), 8200 - 8214.

DISCUSSION

The paper was presented by R Steiger

S Winter asked why parallel to grain was considered in ash but perpendicular to grain was considered in spruce. R Steiger said that budget constraints led to concentrating testing on the boundary situations to seek reduction in cost. S Winter received clarification of the stress level in the bond line.

C Demirci questioned the tolerance for this type of connections if they were made on site and asked how to ensure this work in service class 3 conditions. R Steiger replied that this type of connections needs a company with good quality control. In this case the company has more than 20 years of experience. The work was not extrapolated towards service class 3.

C Sandhaas commented on the test setup of 3 or 4 bonded-in rods and asked if the number of bonded-in rods in a connection would affect the conclusions. R Steiger agreed that this could affect the results.

H Blass commented about the statement that there is lack of guidance in the code on rolling shear failure in the perpendicular to grain cases. He said Karlsruhe Institute of Technology has worked on this topic with a proposal available. R Steiger stated that they are aware of the work but the partner company has been working on their own proposal.

P Dietsch commented that the paper indicated that a reduction to 2/3 for SC3 seems to be safe. He asked if there was any data available for justification. R Steiger agreed that they do not have test results on this.

U Hübner said high risk is associated with on-site gluing and implied that on-site gluing should generally be avoided; hence, quasi-industrial, factory made systems are needed.

Birch and laminated densified dowels for timber connections - an experimental study

Aloisio, Angelo University of L'Aquila, L'Aquila, Italy

Tomasi, Roberto NMBU, Ås, Norway

Wang, Yue KTH, Stockholm, Sweden

Crocetti, Roberto KTH, Stockholm, Sweden

Keywords: wooden dowels, experimental test, mechanics-based model

1 Introduction

All-wood joints without metal fasteners provide an effective and sustainable solution for structural timber applications. They can be used in frame system, or alternatively in traditional mortise-and-tenon or pegged joints, in dowel-Laminated massive panels made from softwood boards, and in hybrid system (e.g., timber–concrete composites). Fully compatible with timber, wooden dowels support circular construction by enabling easy disassembly and reuse. The possibility of real application is demonstrated by different case studies, such as the "Himmelstor" hangar in Mülheim (Germany), which used over 590 hardwood-dowel connections without requiring special approval (*Wiesenkämper* & *Berling-Hoffmann*, 2023).

The possibility to apply traditional design method for wooden dowels is still debated. The European Yield Model (EYM) provided by provided by *EN 1995-1-1* (2004) assumes that the dowel exhibits elastic-plastic behaviour, allowing it to form plastic hinges. Certain researchers have noted that the frequent yielding failure in wooden dowels is due to a mixture of bending and shear forces, leading them to suggest this mechanism as a preferable alternative to the conventional EYM to more accurately reflect the behaviour of wooden dowels (*Miller* et al., 2010). Validation of the experimental results presented in this paper will involve the application of these two alternative approaches.

1.1 Eurocode 5 proposal

The new draft of Eurocode 5 (*FprEN 1995-1-1*, 2025) include a predictive models for the capacity of connections with wooden dowels based on *Johansen* (1949). This model was originally developed for metal dowels, where plastic hinge formation in metallic fasteners (including nails, screws, or bolts) and the compression failure of wood fibers under a dowel-type connector govern the failure mode. By applying equilibrium and plasticity theories, the model estimates load-bearing capabilities under various failure conditions for both single and double shear plane connections, highlighting four primary failure modes: wood material embedment failures (mode I and mode II, exclusively for single shear connections); formation of one plastic hinge (mode III) or two plastic hinges (mode IV) within the metal dowel. The characteristic lateral resistance per shear plane $F_{v,k}$ of a single fastener is given by $F_{\mathrm{v,k}} = F_{\mathrm{D,k}} + F_{\mathrm{rp,k}}$ where $F_{D,k}$ is the characteristic dowel-effect contribution per shear plane, and $F_{rp,k}$ is the characteristic rope-effect, which is generally considered zero for wooden-dowel connections. For timber-to-timber connections using wooden dowels, including different wood products, ,the characteristic dowel-effect contribution ($F_{D,k}$) per shear plane is obtained by modifying the Johansen equations (see Eq.(1)). In this modification, the factor 1.15, originally introduced to take into consideration the differing partial safety factors and k_{mod} for steel and timber is replaced by 1.0. Although not explicitly required by *FprEN 1995-1-1* (2025), the factor of 1.05 is also adjusted to 1.0 for similar reasons. Moreover, the yield moment $M_{y,k}$ is replaced by the ultimate moment $M_{u,k}$ and the modified equations are shown below:

$$F_{\mathrm{D,k}} = \min \begin{cases} f_{h,1,k}\, t_{h1}\, d & (a) \\ f_{h,2,k}\, t_{h2}\, d & (b) \\ \frac{f_{h,1,k}\ t_{h1}\ d}{1+\beta} \left[\sqrt{\beta + 2\,\beta^2 \left[1 + \frac{t_{h2}}{t_{h1}} + \left(\frac{t_{h2}}{t_{h1}} \right)^2 \right] + \beta^3 \left(\frac{t_{h2}}{t_{h1}} \right)^2} - \beta \left(1 + \frac{t_{h2}}{t_{h1}} \right) \right] & (c) \\ \frac{f_{h,1,k}\ t_{h1}\ d}{2+\beta} \left[\sqrt{2\,\beta\,(1+\beta) + \frac{4\,\beta\,(2+\beta)\,M_{u,k}}{f_{h,1,k}\,d\,t_{h1}^2}} - \beta \right] & (d) \\ \frac{f_{h,1,k}\ t_{h2}\ d}{1+2\,\beta} \left[\sqrt{2\,\beta^2\,(1+\beta) + \frac{4\,\beta\,(1+2\,\beta)\,M_{u,k}}{f_{h,1,k}\,d\,t_{h2}^2}} - \beta \right] & (e) \\ \sqrt{\frac{2\,\beta}{1+\beta}}\ \sqrt{2\,M_{u,k}\,f_{h,1,k}\,d} & (f) \end{cases} \tag{1}$$

where $\beta = \frac{f_{h,2,k}}{f_{h,1,k}}$, $f_{h,1,k}\, f_{h,2,k}$ are the characteristic embedment strengths of members 1 and 2 respectively, $t_{h,1}$, $t_{h,2}$ are the embedment depths of members 1 and 2 respectively, $M_{u,k}$ is the characteristic ultimate moment given in equation (2), and d is the diameter of the fastener. In the case of a symmetric connection with a fastener loaded in double shear, the characteristic dowel-effect contribution is determined by considering the four possible failure modes: (a), (b), (d), and (f): mode (a) and (b) corresponding to mode

I, (d) to mode III and (f) to mode IV. The characteristic ultimate bending moment for wooden dowels, according to *FprEN 1995-1-1* (2025) is:

$$M_{u,k} = 0.75\frac{\pi}{32} f_{m,k} d^3 \quad \text{for } 12\,\text{mm} \leq d \leq 30\,\text{mm} \tag{2}$$

with $f_{m,k}$ the characteristic bending strength of the dowel. The prefactor 0.75 in Eq.(2) corresponds to a reduction factor δ introduced to account for the brittle behavior of wooden dowels (*Blaß* et al., 1999). The characteristic embedment strength $f_{h,k}$ for wooden dowels in Structural lumber (SL), parallel laminated timber (PL), and wide faces of cross-layered timber (CL), is according to *FprEN 1995-1-1* (2025).

$$f_{h,k} = 10^{-4} \rho_{\text{dowel},k} \rho_k \frac{1.1\,(1 - 0.01d)}{(3.4 - 0.045d)\sin^2\alpha + \cos^2\alpha} \tag{3}$$

where $\rho_{\text{dowel},k}$ and ρ_k are the characteristic densities of the wooden dowel and the embedment, d the diameter of the dowel and α the grain direction. The regulations for connections using wooden dowels are based on studies by *Blaß* et al. (1999). The simplified design rules are derived from the *SIA 269/5:2011* (2011) standards and adapted to characteristic values. In cases involving connections with several shear planes, the dowel-effect contribution for each fastener is calculated by adding up the contributions from each shear plane. This process takes into account the potential for failure of the shear plane due to either embedment alone or with the development of plastic hinges (as illustrated for modes C in Fig. 5).

1.2 Failure mode V according to *Miller* et al. (2010)

Unlike steel, wooden dowels exhibit mechanical properties similar to the connected timber, leading to distinct failure modes requiring specific formulations. A recurring mechanism, termed Mode V by *Miller* et al. (2010), involves combined bending, shear, and compression perpendicular to grain. Unlike cross-grain shear or central hinge formation, Mode V extends Johansen's theory by capturing this interaction. *Miller* et al. (2010) proposed a regression model linking Mode V yield capacity to the specific densities of dowel and base timber, to estimate the average shear stress at failure in the dowel as $f_v = 33.44 G_d G_m^{0.75}$, where f_v is the shear stress at failure (in N/mm^2), $G_d = \rho_d/\rho_w$ is the specific gravity of the dowel, and $G_m = \rho_m/\rho_w$ is the specific gravity of the embedding material. Here, ρ_d, ρ_m, and ρ_w denote the mass densities of the dowel, the embedding medium, and water, respectively. Since failure mode V involves multiple longitudinal shear fractures distributed across the dowel's cross-section. Thin bundles of intact longitudinal fibres remain between the fractures, which are kinked by flexure. Consequently, the yield capacity of the connection is determined by applying an average stress value to the dowel's cross-sectional area. Miller et al. also refer to this as the *effective peg shear yield mode*. Accordingly, the shear capacity is calculated as $F_v = f_v \cdot A$, where A is the dowel's shear area.

2 Experimental campaign

A testing campaign on the material properties of birch and densified wood dowels was conducted at the Norwegian University of Life Sciences in Ås, Norway (*Sæby*, 2024; *Backe*, 2023) in order to characterize the embedment strength and bending and shear strength of wooden dowels (Fig. 1a and Fig. 1b), and their application to timber to timber connections (see Fig. 1c). Birch dowels (BI) and laminated densified wood dowels (LDW) with a nominal diameter of 20 mm were used. The birch dowels were manufactured from solid timber (mean densities of 608 kg/m^3) while the LDW dowels are made from layered veneers of red beech, which are glued together using a thermosetting synthetic resin and then subjected to high pressure and heat (mean densities of 1350 kg/m^3). In a subsequent experimental campaign at KTH (*Coucher* & *Shilén*, 2024) a specific shear setup was was proposed for derive the mechanical properties of wooden dowel (see Fig. 1d). Birch dowels (birch harvested in northern Sweden, mean densities of 653 kg/m^3) and beech dowels (mean densities of 733 kg/m^3) with a nominal diameter of 20 mm and 30 mm were used.

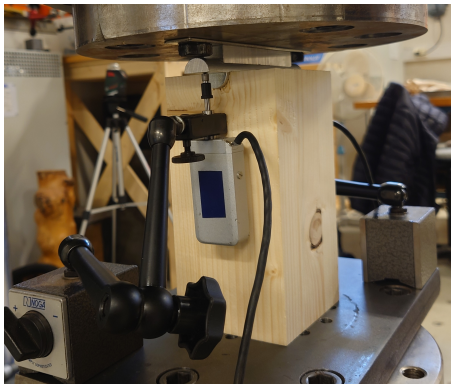

(a) Half hole setup

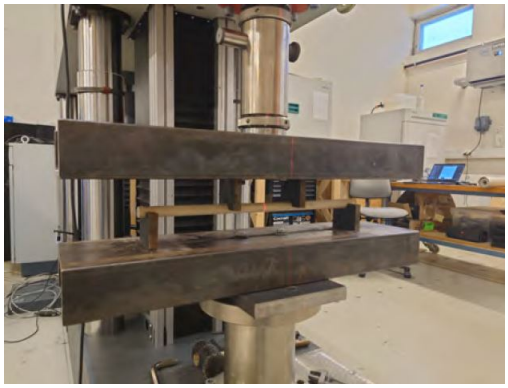

(b) Bending setup

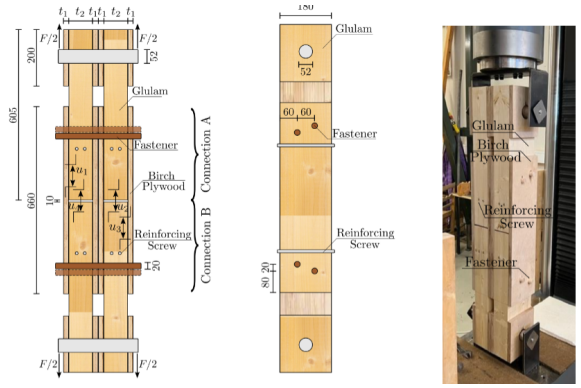

(c) Axial tension test setup

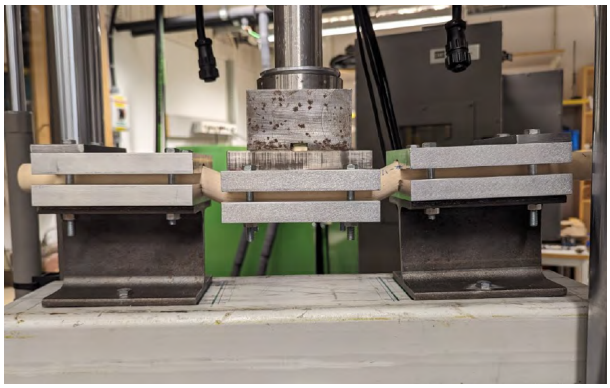

(d) Shear setup

Figure 1. Experimental assessment of embedment, bending, shear strength of wooden dowels

2.1 Bearing test on wooden dowels

The principal experimental configurations employed to assess embedment strength are the half-hole and full-hole tests. According to the European standard (*EN 383*, 2007),

the full-hole configuration is advised, while the American standard (*ASTM D5764*, 2007) outlines the designs for both configurations. Given the poorer mechanical properties of wood compared to steel, *Ottenhaus* et al. (2022) suggest the use of half-hole configurations when the embedment strength exceeds the dowel yield moment, a situation often found in engineered wood products. Therefore, the half-hole configuration of Fig. 1a was chosen since the alternative full-hole method, despite its widespread use, has been reported to trigger shear-type failures rather than pure embedment, potentially leading to misinterpretation of results. Moreover it became evident for birch dowels during testing that were prone to localized crushing, whereas laminated densified wood (LDW) dowels remained structurally intact. This raised the question of whether the observed resistance truly corresponded to embedment strength or was influenced by compressive failure of the dowel itself. *Zhang* et al. (2025) made a similar observation in case of beech dowels, and used the term ”system strength” as the this point differs from the bearing behavior between steel dowel and glulam. To clarify this issue, part of the available material was allocated to conventional embedment tests using steel dowels, which are not affected by this type of deformation and allow for a clearer interpretation of the response. A total of nine embedment test configurations were investigated using the half-hole setup shown in Fig. 1a. Three dowel materials were considered: steel, birch, and laminated densified wood (LDW). Each was tested in both glulam (parallel and perpendicular to grain) and plywood (parallel to face grain), using dowels of 20 mm diameter. The glulam specimens were 90 mm thick and the plywood specimens 61 mm thick. Each configuration is labeled as *EMB-XX-Y*, where *EMB* stands for embedment test, *XX* indicates the subgrade and load direction (*GL0* = glulam, 0°, *GL90* = glulam, 90°, *PLY* = plywood), and *Y* indicates the dowel type (*S* = steel, *BI* = birch, *LDW* = laminated densified wood). Repetitions were 3 for steel, 7 for birch, and 10 for LDW. For each test, the strength properties were determined according to EN 383 (2007), where the embedment strength is defined as $f_h = F_{max}/d \cdot t$, being F_{max} is the maximum load reached before the attainment of 5 mm of displacement excluding the test apparatus deformation, d is the dowel diameter and t is embedment length. It is interesting to observe that, in the direction parallel to the grain, steel and LDW dowels exhibit a similar two-phase response: an initial linear elastic phase followed by a plastic phase. In contrast, the response of the birch dowels exhibits a tri-linear behavior characterized by distinct hardening, which could be attributed to to the previously mention progressive crushing of the dowel material during loading. Due to the higher mechanical properties of the LDW dowels compared to birch dowels, this phenomena was not observed for these tests. In the direction perpendicular to the grain, all connectors display a clear elastoplastic response. In this case the subgrade material may yield before the crushing of the birch dowels could happen.

Plywood is characterized by significantly higher embedding strength compared to glue laminated timber loaded parallel to the grain. The most ductile behavior is obtained loading the glue laminated timber perpendicularly to the grain. However, the lowest

Table 1. Conventional embedding strength (f_h), displacement corresponding to conventional embedding strength ($u(f_h)$), Eurocode 5 predicted embedding strength ($f_{h,EC5}$) and scatter with respect to the experimental value ($S_{\%}$).

	Name	f_h (N/mm^2)	CoV (%)	$u(f_h)$ (mm)	CoV (%)	$f_{h,EC5}$ (N/mm^2)	$S_{\%}$ (%)
Birch	EMB-GL0-BI	17.8	8%	5.0	0%	25.7	45%
	EMB-GL90-BI	12.6	19%	5.0	2%	10.3	-19%
	EMB-PLY-BI	20.0	9%	5.0	0%	38.9	94%
LDW	EMB-GL0-LDW	29.9	4%	3.3	15%	49.2	65%
	EMB-GL90-LDW	16.8	29%	5.0	0%	19.7	17%
	EMB-PLY-LDW	55.5	4%	5.0	0%	74.4	34%
Steel	EMB-GL0-S	28.9	10%	2.3	9%	32.8	14%
	EMB-GL90-S	14.8	9%	4.8	6%	13.1	-11%
	EMB-PLY-S	55.1	3%	5.0	0%	49.6	-10%

Figure 2. Embedment strength: average experimental conventional values and CoV (bars), average experimental maximum values (dashed lines) and average Eurocode values according to Eq. 3 (red diamonds). The small figure in the diagram shows the typical "system failure" in the case of birch dowels.

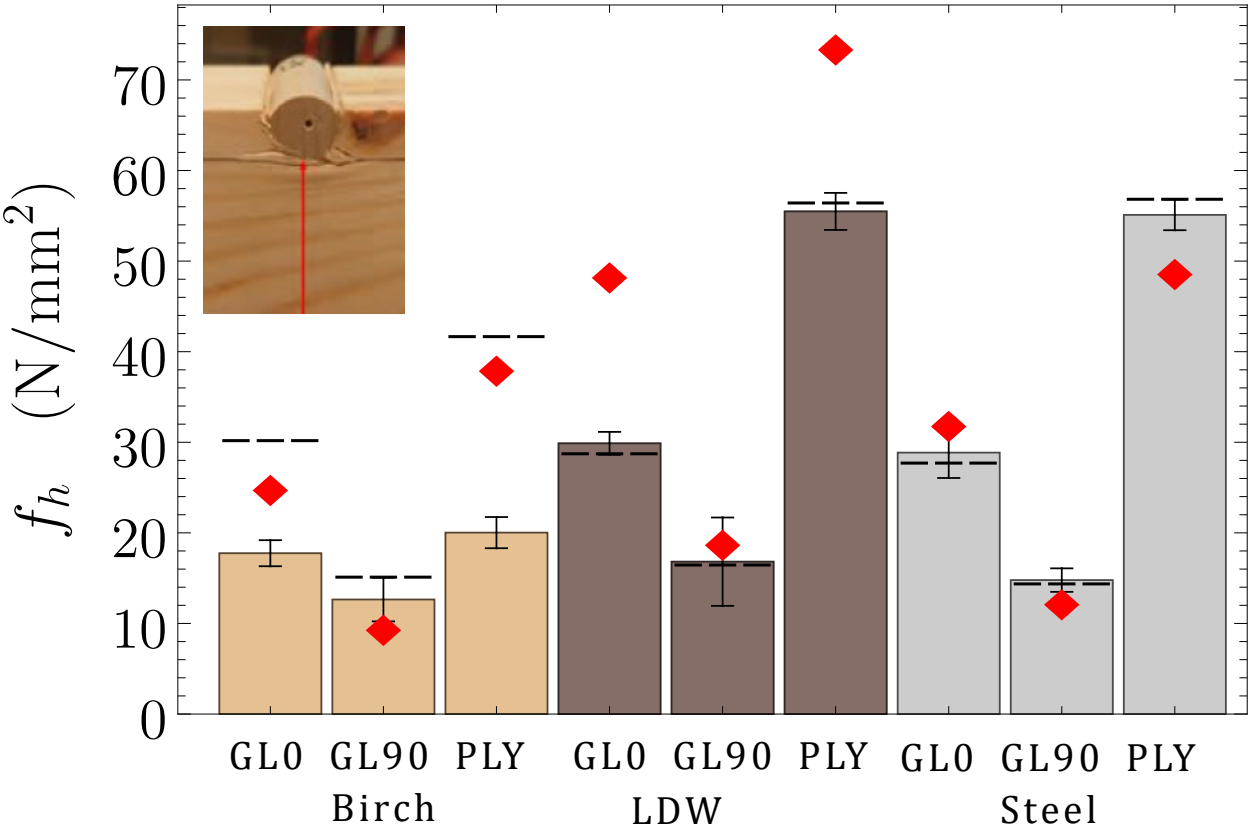

strengths are associated with this configuration. The EMB-PLY-S and EMB-PLY-LDW configurations manifest the highest embedding strength values, with steel and LDW dowels performing almost equally well. Birch dowels, on the other hand, display lower embedding strength, especially in the GL0-BI and GL90-BI configurations, which underperform compared to steel and LDW. The results are collected in Tab. 1 and in Fig. 2, compared with Eurocode 5 predictions of equation (3).

2.2 Bending test on wooden dowels

Four-point bending tests were performed to measure the shear and bending properties of the birch and laminated densified wood dowels. Ten repetitions for each configuration have been performed (see Tab. 2). The tests have been performed according to *EN 408* (2003). The load application points position has been chosen in order to reach shear and bending failure in configurations BI-D-S, LDW-D-S and BI-D-B, LDW-D-B respectively. The failure load has been determined as the maximum load reached during the tests.

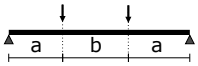

Table 2. Experimental setup for dowel shear and bending tests. Parameters include density before test (ρ), dowel diameter (d), dowel length (l), and distances a and b between support-load and application points.

Name	Dowel type	Test type	ρ (kg/m^3)	d (mm)	l (mm)	a (mm)	b (mm)	Test rep. (n°)
BI-D-S	Birch	Shear	618	20	500	70	325	10
BI-D-B	Birch	Bending	599	20	500	155	155	10
LDW-D-S	Laminated densified wood	Shear	1336	20	500	70	325	10
LDW-D-B	Laminated densified wood	Bending	1333	20	500	155	155	10

This value led to the bending moment in the central portion of the dowel at failure (M_u) and the shear in the lateral portion of the dowel at failure (T_u). The bending strength has been assumed as the bending stress at the outermost dowel fibres at dowel failure and calculated with the Navier formula $f_m = (M_u/I) \cdot (d/2)$ where M_u is the bending moment in the central portion of the dowel at failure, d is the dowel diameter and I is the second moment of area of the dowel. The shear stress at dowel failure is calculated with the well known formula $\tau_v = 1.5 \cdot T_u/A$ where T_u is the shear force at failure in the lateral portion of the dowel, and A is the section area of the dowel. The authors assumed that not all fibers in the section had been fully yielded. Therefore, it would have been too speculative to assume a uniform shear force distribution. Instead, an elastic distribution of shear stresses was considered more appropriate. Despite the two distinct test setups designed to induce both bending and shear failures, all the dowels failed due to bending, with the damage localized to the central portion of the dowel (see figures reported in Tab.3). Due to this unpredicted reason, the authors were unable to asses the shear strength of the wood dowels. Tab. 3 reports the bending strength (f_m), the corresponding shear stress at failure (τ_v), elastic modulus (E), and shear modulus (G), with coefficients of variation (CoV) reported for each, of birch dowels (BI-D) and laminated densified wood dowels (LDW-D). LDW dowels show a significantly higher

Table 3. Dowel shear and dowel bending tests results: bending strength (f_m), shear stress at failure (τ_v), elasticity modulus (E) and shear modulus (G).

Name	f_m (N/mm²)	CoV (%)	τ_v (N/mm²)	CoV (%)	E (N/mm²)	CoV (%)	G (N/mm²)	CoV (%)	Example of failure mode
BI-D-S	143.2	15%	6.8	15%	17820	11%	891	11%	
BI-D-B	132.7	11%	2.9	11%	14639	9%	732	9%	
LDW-D-S	278.0	7%	13.2	7%	35682	3%	1784	3%	
LDW-D-B	235.0	9%	5.1	9%	26580	7%	1329	7%	

bending strength compared to birch dowels. In the shear test configuration, LDW dowels reach a bending strength of 278 N/mm², almost double that of birch dowels at 143.2 N/mm². LDW dowels still exhibit a much higher value (235 N/mm²) than birch dowels (132.7 N/mm²) in the bending configuration. The elastic and shear moduli of LDW dowels are also markedly higher than birch dowels. The coefficient of variation for both types of dowels is relatively consistent, ranging from 3% to 15%, with LDW dowels characterized by lower CoV values, particularly in elasticity and shear modulus.

2.3 Test on connection with wooden dowels

In this experimental campaign each test involved a tensile test on a joint composed of two connections. Each connection included four shear planes and two fasteners. The elements are 605 mm in length, with a section height of 180 mm and a section width of 264 mm (total overall penetration thickness). The specimens consist of timber-to-timber connection with four shear planes per wooden dowel, connecting on each side two 90 mm thick glued laminated timber members (GL30c from spruce 45 mm thick lamellas) via internal and external 21 mm thick birch plywood panels. The gusset plates are made of birch plywood, consisting of 1.4 mm layers, with a mean density of $\rho_m = 680\,\mathrm{kg/m^3}$, according to *Pennala*, 1992. The gusset plates are 660 mm long and have the same height as the connected elements. Two birch or LDW dowels with the same batch of the previous tests were used per each side (see Fig. 1c). Summary of the test configuration are reported in Tab. 4. The specimen and the gusset thickness is composed of segments t_1 (Plywood), t_2 (Glulam) as indicated in Fig. 1c and Tab. 4. The wooden dowels are 300 mm long with a nominal diameter of 20 mm (Tab. 4). The dowel's diameter was chosen as the most practical standard size commonly used in timber structures, offering mechanical properties comparable to the use of screws with diameters ranging from approximately 8 to 10 mm. A hole with a diameter of 20 mm was drilled in both the gusset plates and the connected timber members, and the dowels were inserted in the beams and plates held together with clamps to align the pre-drilled holes, using rubberized hammer was used to fit in the dowels. Minimum spacings, edge and end distances for laterally-loaded dowel-type fasteners adopted were set to $a_{1,min} = 5d$, $a_{2,min} = 3d$, $a_{3,t,min} = \max(7d; 80\mathrm{mm})$, $a_{3,c,min} = 4d$, $a_{4,t,min} = 4d$, $a_{4,c,min} = 3d$. These values comply with the limits specified by *FprEN 1995-1-1* (2025) for dowels. The specimens were tested to failure using an ZwickRoell Z1200 electromechanic Universal Testing Machine with a capacity of 1200 kN.

Table 4. Fasteners properties: nominal diameter (d), inner thread diameter (d_c), length (l), overall penetration thickness (t), plate penetration thickness (t_1), connected members penetration thickness (t_2)

Configuration label	Fasteners type	Repetition	d (mm)	l (mm)	t (mm)	t_1 (mm)	t_2 (mm)
BI-D	Birch dowels	4	20	300	264	21	90
LDW-D	Laminated densified wood dowels	5	20	300	264	21	90

Force F is applied symmetrically through steel loading shoes to produce axial shear in the fasteners. The standard procedure for determining failure load R_v was determined according to *EN 26891* (1991), considering the load corresponding to the first occurrence between the absolute maximum and a relative slip of 15 mm. The associated ultimate displacement u_u was also recorded. This criterion ensures consistency across different types of connections and avoids overestimating capacity based on post-peak behaviour. The load-displacement curves of the tested specimens are presented in Fig. 3. The

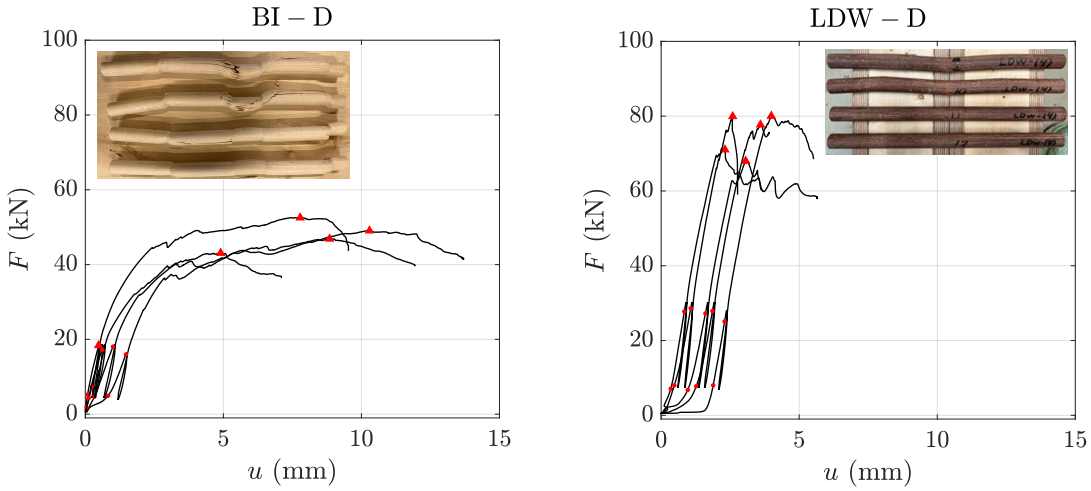

Figure 3. Force–slip response of tested connections: measured load (F) versus connection slip (u) for (BI–D) Birch dowels, (LDW–D) Laminated densified wood dowels. Red markers indicate characteristic points corresponding to the peak value, as well as 0.1 and 0.4 times the maximum load. For the birch configuration, only four curves are shown due to one excluded outlier caused by a measurement error. The images embedded in the plots illustrate the failure modes observed.

force–slip curves of birch dowels show a nearly bilinear behavior, with an initial phase of moderate stiffness, a plateau, and a final brittle failure. While LDW dowels show higher capacity compared to birch, they exhibit a clearly brittle behavior, as evident from the force–displacement curves. Ductility appears to be linked to wood density. Higher-density materials like LDW have a greater proportion of compacted cell wall substance and fewer air voids, which limits fiber mobility and energy dissipation during failure. This suggests that the densification process, while improving strength, reduces the material's ability to undergo plastic deformation. It should be remarked that the force-slip curves manifest significant variability. This variability arises from material heterogeneity typical of natural wood, including variations in density and grain orientation, and differences in moisture content across specimens. Additional sources of variability originate from

inaccuracies or variations in specimen preparation and test setups, which are challenging to completely eliminate. However, the Coefficient of Variation of the capacity is always below 30%, in a range typical of wooden connections (*Köhler* et al., 2007). The values of strength and ductility are reported in Tab. 5, which present the recorded failure load R_v and the corresponding displacement u_u for each connection. Mean values and coefficients of variation (CoV) were calculated to provide an overview of performance variability within each configuration group.

*Table 5. Failure loads (R_v), corresponding displacement (u_u), and ductility (D) of the tested connections. For BI-D-4, values marked with * refer to the last recorded point due to acquisition malfunction.*

	BI-D				LDW-D		
Config.	R_v (kN)	u_u (mm)	D	Config.	R_v (kN)	u_u (mm)	D
BI-D-1	52.5	7.8	10.0	LDW-D-1	71.0	2.3	2.0
BI-D-2	49.1	10.3	5.3	LDW-D-2	79.9	2.6	1.1
BI-D-3	46.9	8.8	7.2	LDW-D-3	80.0	4.0	1.6
BI-D-4*	18.4	0.5	–	LDW-D-4	77.7	3.6	1.2
BI-D-5	43.1	4.9	6.9	LDW-D-5	68.0	3.1	2.1
Avg.	**47.9**	**8.0**	**7.3**	Avg.	**75.3**	**3.1**	**1.6**
CoV	7%	25%	23%	CoV	7%	20%	25%

2.4 Shear test on wooden dowels

The results of previous tests indicated a predominance of type V failure mechanisms in wooden dowels. The embedment and bending tests described in Sections 2.1 and 2.2 clearly demonstrated that the traditional test configurations are inadequate for determining the material parameters required by the EYM. Several researchers have emphasized the importance of evaluating the mechanical behaviour of wooden dowels separately from the surrounding timber. This approach applies both to the assessment of embedment strength and to the evaluation of dowels subjected to combined shear and bending. In the latter case, a more reliable characterization can be achieved by isolating a single dowel using a specially designed aluminium device, as shown in Fig. 1d. Since the properties of the surrounding material, such as aluminium or steel, are well known and consistent, this configuration allows a focused investigation of the dowel's mechanical response. Similar devices have been employed in other studies, using steel plates or steel blocks with chamfered edges to prevent cutting the dowel and to provide sufficient restraint against horizontal movement (*Ceraldi* et al., 2017; *Xu* et al., 2022; *Zhang* et al., 2025). The tests conducted at KTH were organised into three main series, each corresponding to a different dowel configuration: birch dowels with a diameter of 20 mm and length of 600 mm, birch dowels with a diameter of 30 mm and length of 600 mm, and beech dowels with a diameter of 20 mm and length of 500 mm. The dowels were tested under various shear spans: no span, a span equal to half the diameter, and a span equal to the full diameter. Tests were carried out in both the tangential and radial directions relative to the grain orientation. Each specimen was identified using the format *XX-DD-S/R-D*, where *XX* indicates the wood species (BI for birch), *DD* refers to the

dowel diameter in millimetres (20 or 30), *S/R* indicates the shear span as a ratio of the diameter (0/1 for no span, 1/2 for half diameter, 1/1 for full diameter), and *D* refers to the direction of loading (T for tangential and R for radial). This coding system allowed precise classification of each test configuration, and the results are reported as mean values for each group. In Tab. 6 are reported the results, only for the birch dowels, in terms of force for the single shear plane F_{sp} and average shear stress $\tau = F_{sp}/A$. The values are expressed in term of yield value (calculated at a deformation of 5%) and ultimate value according to *EN 26891* (1991). In Fig. 4 are depicted the failure modes for birch dowels in function of the gaps.

Table 6. Shear test results for birch dowels (BI) with double shear planes

Group	$F_{sp,yield}$ (kN)	$F_{sp,ult}$ (kN)	τ_y (MPa)	τ_u (MPa)
BI-20-0/1-R	5.74	8.97	18.26	28.56
BI-20-1/2-R	4.81	6.56	15.31	20.87
BI-20-1/1-R	3.99	5.23	12.71	16.65
BI-20-0/1-T	4.41	7.75	14.04	24.68
BI-20-1/2-T	3.89	6.02	12.37	19.17
BI-20-1/1-T	3.38	5.34	10.74	16.99
BI-30-0/1-R	13.08	16.55	18.51	23.41
BI-30-1/2-R	11.68	12.36	16.52	17.48
BI-30-1/1-R	8.88	10.07	12.56	14.24
BI-30-0/1-T	9.88	16.14	13.98	22.84
BI-30-1/2-T	8.17	13.26	11.56	18.75
BI-30-1/1-T	7.09	8.27	10.03	11.70

Figure 4. Failure modes for 30 mm (first row) and 20 mm (second row) birch dowels, in function of the gaps (first column zero gap, second column half diameter, third column one diameter

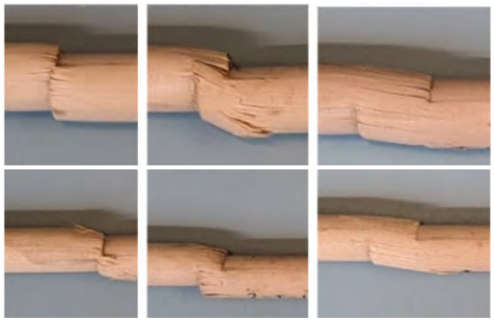

3 Discussion

Table 7 report the comparison between the predicted capacity per dowel according to the proposed model, the Eurocode 5 proposal, and the empirical equation for mode V suggested by *Miller* et al. (2010) with experimental values reported in Tab. 5, dividing the capacity R_v by the number of dowels connectors (two) and the number of shear planes (four). To predict the connection capacity using the Eurocode 5 formulation—based on the modified Johansen equations (Eq. 1), the embedment strength expression (Eq. 3), and the ultimate moment equation for wooden dowels (Eq. 2)—it is necessary to adopt mean values of the input parameters rather than characteristic ones. Specifically, in Eq. 2, the mean bending strength derived from dowel bending tests was 132.7 MPa for birch dowels (BI-D) and 235 MPa for laminated densified wood dowels (LDW-D). These values were used to calculate the ultimate moment capacity of the dowels. As for the embedment strength, both the values obtained from the Eurocode 5 expression (Eq. 3) and the experimental results were considered. The corresponding predicted capacities are reported in Table 7 as $R_{v,\mathrm{prEC5}}$ (based on calculated embedment strength) and $R_{v,\mathrm{prEC5,exp}}$ (based on experimental embedment strength). Since the Eurocode 5

Table 7. Comparison between experimental and simulated capacities per shear plane. Ultimate capacity is based on FprEN 1995-1-1 *(2025) and yielding capacity according to (*Miller *et al., 2010). Simulated values include both theoretical ($R_{v,prEC5}$) and experimental-based ($R_{v,prEC5,exp}$) predictions. Relative errors are color-shaded from green (low error) to red (high error). Values marked with * refer to last recorded points before acquisition malfunction. LDW specimens show identical yielding and ultimate values due to brittle behaviour.*

Label	$R_{v,exp}$ [kN]	$R_{v,prEC5}$ [kN]	Rel. Err. [%]	$R_{v,prEC5,exp}$ [kN]	Rel. Err. [%]	$R_{v,y,exp}$ [kN]	$R_{v,y,Miller}$ [kN]	Rel. Err. [%]	f_v [MPa]
BI-D-1	6.56	8.43	28	6.63	1	5.21	3.46	-34	15.22
BI-D-2	6.14	8.43	37	6.63	8	4.55	3.46	-24	15.22
BI-D-3	5.86	8.43	44	6.63	13	3.98	3.46	-13	15.22
BI-D-4*	2.30	8.43	267	6.63	188	4.74	3.46	-27	15.22
BI-D-5	5.39	8.43	56	6.63	23	4.56	3.46	-24	15.22
Mean BI	**5.99**	**8.43**	**42**	**6.63**	**11**	**4.61**	**3.46**	**-24**	**15.22**
LDW-D-1	8.88	16.93	91	13.08	47	8.88	7.61	-14	33.43
LDW-D-2	9.99	16.93	69	13.08	31	9.99	7.61	-24	33.43
LDW-D-3	10.00	16.93	69	13.08	31	10.00	7.61	-24	33.43
LDW-D-4	9.71	16.93	74	13.08	35	9.71	7.61	-22	33.43
LDW-D-5	8.50	16.93	99	13.08	54	8.50	7.61	-11	33.43
Mean LDW	**9.42**	**16.93**	**81**	**13.08**	**39**	**9.42**	**7.61**	**-19**	**33.43**

approach provides predictions of the ultimate load, the values obtained from FprEN 1995-1-1 were compared with the experimental ultimate shear capacities, as shown in Table 3. For all the calculated values the failure mode associated to the minimum value of Eq. 1 was always failure C according to Fig. 5. The capacity values according to Miller's model have been determined assuming the measured average density values for wooden dowels and the assigned density value for the embedment material GL30 ($\rho_m = 430\,\mathrm{kg/m^3}$). In case of birch dowels the predictions of Miller's model have been compared with the experimental yielding capacity, since the model was specifically developed for yielding. Conversely for LDW dowels, since they exhibit highly brittle behaviour, their yielding capacity has been assumed to be equal to their ultimate capacity.

On average, the new Eurocode 5 model overestimates the capacity by 42% and 81% for birch and LDW connections, respectively. However, when using experimental embedment data instead of theoretical values, the overestimation is reduced to 11% for birch and 39% for LDW dowel connections. This proves that a significant source of error lies in the Eurocode model for predicting embedment strength, which propagates through the capacity model, increasing the overall error by up to four times in the case of birch connections. For LDW dowels, using experimental embedment strength reduces the error by half, but it still leads to a significant overestimation of around 40%. Therefore, the model is not conservative, and the error increases significantly when

Figure 5. Failure modes C according to §11.2.3.7(2) and Fig. 11.8 of FprEN 1995-1-1 *(2025).*

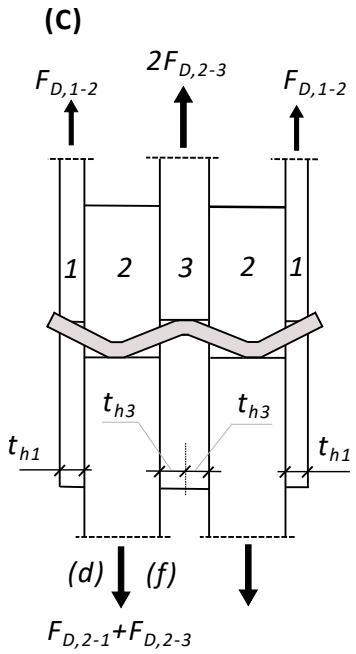

considering denser, stiffer, and more brittle dowels such as LDW. These results confirm the inadequacy of the Johansen modelling it describing the failure behaviour of wooden dowels, as it does not account for the observed failure modes. Conversely, the model in *Miller* et al. (2010) is conservative, tending to underestimate the yielding capacity by 24% for birch and 19% for LDW dowel connections. The predictive performance of Miller's model is significantly better than that of *FprEN 1995-1-1* (2025). In Table 5, the experimental yielding shear plane capacity $R_{v,\mathrm{exp}}$, when normalized by the dowel area, results in $f_{v,\mathrm{exp}} = 14.51$ MPa for Birch dowels and $f_{v,\mathrm{exp}} = 29.98$ MPa for Laminated Densified Wood (LDW) dowels (note that the theoretical predictions from the Miller model were $f_v = 10.80$ MPa for Birch dowels and $f_v = 23.71$ MPa for LDW dowels). Tab. 6 shows that the alternative shear device configuration yields results akin to those observed with the conventional setup. The data in Tab. 6 reveal that the alignment of the rings (T and R) influences the results, a conclusion corroborated by ANOVA analysis. Nevertheless, as described in section 2.3, this variable was omitted in the experiment due to the difficulties in managing it practically, and taking into account varied findings from previous studies (*Xu* et al., 2022). Shear yield stress $f_{v,y}$ was calculated assuming pure plastic shear. As differences between 20 mm and 30 mm dowels were below 5%, average values were used for each gap: $f_{v,y} = 16.20$ MPa for 0 mm (0/1), 13.94 MPa for 10–15 mm (1/2), and 11.51 MPa for 20–30 mm gaps (1/1). It is worth noting that the intermediate configuration, corresponding to a gap equal to half the dowel diameter, provides the closest match to the values obtained from traditional push-out tests. This observation suggests that a gap of this magnitude may offer a more representative reproduction of the actual embedment mechanism occurring in real connections, where partial confinement and localized deformation are typically present.

4 Conclusions

The mechanical performance and predictive modelling of wooden dowels made of birch and laminated densified wood (LDW) have been investigated in this study. The experimental campaign demonstrated that traditional methods used to determine mechanical parameters for steel connectors—such as embedment strength and yielding moment—are not entirely suitable for wooden connectors. Conversely, shear tests on individual wooden dowels using a purpose-designed setup proved to be a valid alternative to conventional push-out tests. The results confirmed that birch dowel connections exhibit a characteristically ductile load–displacement response, featuring an initial stiff phase, a plateau, and a final failure stage. This bilinear trend differs from that observed in LDW dowels, which achieved the highest load-bearing capacity—comparable to that of steel connectors—but with significantly reduced ductility. Overall, the experimental findings indicate that wooden dowels fail through mechanisms that differ substantially from those of traditional steel fasteners, particularly in terms of ductility, local embedment behaviour, and interaction with the timber substrate. The comparison with Eurocode 5 predictions presented in this work serves as an initial benchmark to assess the limitations of current analytical models, which were originally developed for steel dowel-type fasteners. The discrepancies observed between experimental and predicted values suggest that existing Eurocode 5 models are not fully adequate for capturing the mechanical behaviour of wooden dowel connections. These findings highlight the need to develop new analytical models specifically tailored to wooden dowels, supported by further experimental and numerical research.

4.1 Bending–shear interaction domain

To clarify how bending and shear combine in the Mode-V failure of wooden dowels, the KTH test results were re-cast in a non-dimensional stress plane. Each experimental point is plotted by normalising the peak shear and bending stresses at the critical section by the material strengths of the dowel, i.e. $\tau_{\max}/f_v$ (ordinate) and $\sigma_{\max}/f_m$ (abscissa). This representation makes specimens directly comparable across diameters, shear spans and loading directions.

For a solid circular dowel of diameter d and free shear span L (tested at $L/d \in \{0,\ 0.5,\ 1.0\}$), the internal actions at the failed cross-section of the rotation-restrained dowel segment are

$$M = \frac{F\,L}{4}, \qquad V = \frac{F}{2}, \tag{4}$$

with F the actuator force. From the global equilibrium, the shear reaction follows immediately. The bending field is linear,

$$M(x) = C_1 - \frac{F}{2}\,x, \tag{5}$$

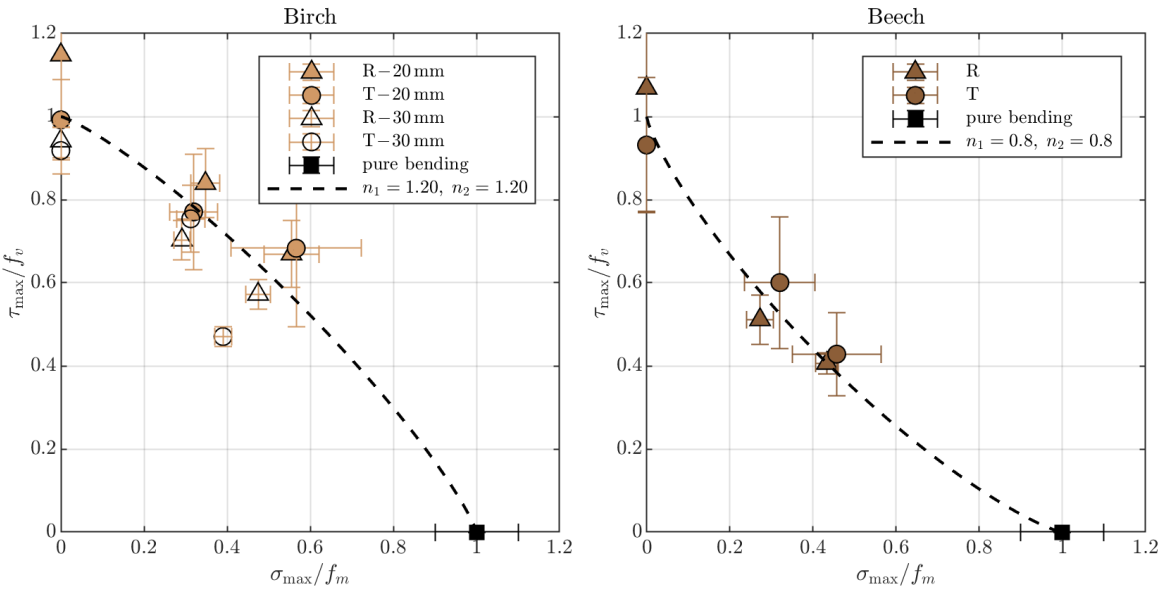

Figure 6. Mean interaction points with ±1 s.d. error bars, grouped by geometry and loading, together with fitted interaction curves from Eq. (7)*.*

where the redundant tip moment C_1 is fixed by the compatibility condition $\vartheta(L) = 0$; with either Euler–Bernoulli or Timoshenko kinematics one obtains $C_1 = FL/4$ and hence the expression for M above. Using $A = \pi d^2/4$ and $I = \pi d^4/64$, elementary beam theory TimoshenkoGere1961 gives

$$\sigma_{\max} = \frac{32M}{\pi d^3} = \frac{8FL}{\pi d^3}, \qquad \tau_{\max} = \frac{4V}{3A} = \frac{8F}{3\pi d^2}. \tag{6}$$

The data indicate that neither a pure Rankine (max-stress) nor a pure von Mises (quadratic) criterion is adequate. We therefore adopt a generalised Hill-type interaction:

$$\left(\frac{\tau_{\max}}{f_v}\right)^{n_1} + \left(\frac{\sigma_{\max}}{f_m}\right)^{n_2} = 1, \tag{7}$$

with exponents n_1, n_2 calibrated from the tests.

Figure 6 reports the mean points (with ±1 s.d.) for each configuration and the corresponding fits. Because intra-group scatter is non-negligible, precise exponent values are not the focus; instead, the following robust trends emerge. For birch, the best fits are only mildly convex, with exponents slightly above unity (average ≈ 1.2). A conservative linear envelope ($n_1 = n_2 = 1$) reproduces the data with little loss of accuracy. A weak size effect is visible: ∅20 mm birch tends towards $n \approx 1.5$, while ∅30 mm is nearly linear ($n \approx 1$). For beech, the average exponent is lower (overall ≈ 0.8), with a clear directional split: radial loading yields a visibly convex domain (≈ 0.7), whereas tangential loading is closer to linear.

Taken together, the clouds align closely with an additive bending–shear rule,

$$\frac{\tau_{\max}}{f_v} + \frac{\sigma_{\max}}{f_m} = 1, \tag{8}$$

i.e. an almost straight line in the normalised τ–σ plane.

This geometry has a clear mechanical meaning: (i) failure is brittle, with insufficient rotation capacity to form a plastic hinge; (ii) bending and shear make largely independent contributions to utilisation (no beneficial quadratic interaction); and (iii) the dowel fails when the first of the two stress ratios reaches unity, consistent with a Mode-V, parallel-to-grain shear fracture rather than a Johansen plastic-hinge mechanism. From a design standpoint, the linear envelope in Eq. (8) is both transparent and conservative for hardwood dowels within the tested range of spans and diameters.

5 References

ASTM D5764 (2007). *Standard Test Method for Evaluating Dowel-Bearing Strength of Wood and Wood-Based Products*. ASTM International.

Backe, M. (2023). “Experimental Investigations of Pure Wood Connections.” MA thesis. Ås: Norwegian University of Life Science. URL: https://hdl.handle.net/11250/3089279.

Blaß, H. J.; H. Ernst & H. Werner (1999). “Verbindungen mit Holzstiften: Untersuchungen über die Tragfähigkeit.” In: *BMH - Bauen mit Holz* 10. Sonderdruck aus bmh 10/99, pp. 1–6.

Ceraldi, C.; C. D’Ambra; M. Lippiello & A. Prota (2017). “Restoring of timber structures: connections with timber pegs.” In: *European Journal of Wood and Wood Products* 75.6, pp. 957–971. ISSN: 1436-736X. DOI: 10.1007/s00107-017-1179-6.

Coucher, I. & L. Shilén (2024). “Mechanical Characterization of Wooden Dowels With Emphasis on Shear Strength: An Experimental Study on Birch and Beech Dowels.” 30 credits. Degree project in Building Materials, Second cycle. KTH Royal Institute of Technology.

EN 1995-1-1 (2004). *Eurocode 5: Design of Timber Structures — Part 1: General — Common Rules and Rules for Buildings*. European Committee for Standardization.

EN 26891 (1991). *Timber structures. Joints made with mechanical fasteners. General principles for the determination of strength and deformation characteristics*. European Committee for Standardization.

EN 383 (2007). *Timber structures - Test methods - Determination of embedding strength and foundation values for dowel type fasteners*. European Committee for Standardization.

EN 408 (2003). *Timber structures — Structural timber and glued laminated timber — Determination of some physical and mechanical properties*. European Committee for Standardization.

FprEN 1995-1-1 (2025). *Eurocode 5: Design of timber structures. Version for formal vote*. European Committee for Standardization.

Johansen, K. (1949). "Theory of timber connections." In: *International Association of Bridge and Structural Engineering* 9:249-262. DOI: http://doi.org/10.5169/seals-9703.

Köhler, J.; J. D. Sørensen & M. H. Faber (2007). "Probabilistic modeling of timber structures." In: *Structural safety* 29.4, pp. 255–267. DOI: https://doi.org/10.1016/j.strusafe.2006.07.007.

Miller, J. F.; R. J. Schmidt & W. M. Bulleit (2010). "New Yield Model for Wood Dowel Connections." In: *Journal of Structural Engineering* 136.10, pp. 1255–1261. DOI: 10.1061/(ASCE)ST.1943-541X.0000224.

Ottenhaus, L.-M.; Z. Li & K. Crews (2022). "Half Hole and Full Hole Dowel Embedment Strength: A Review of International Developments and Recommendations for Australian Softwoods." In: *Construction and Building Materials* 344, p. 128130. ISSN: 0950-0618. DOI: 10.1016/j.conbuildmat.2022.128130.

Pennala, E. (1992). "Handbook of Finnish Plywood." English. In: *Finnish Plywood International*. Ed. by E. Pennala. Finland: Finnish Plywood International.

Sæby, V. H. (2024). "Assessing the Performance of Wooden Dowels in Pure Wood Connections." MA thesis. Ås: Norwegian University of Life Science. URL: https://hdl.handle.net/11250/3150791.

SIA 269/5:2011 (2011). *SIA 269/5:2011 – Existing Structures – Part 5: Strengthening*. Standard. Published in German, French and Italian. Zurich, Switzerland: Swiss Society of Engineers and Architects.

Wiesenkämper, T. & F. Berling-Hoffmann (2023). "Ein Himmelstor aus Holz – Neuer Hangar schafft wirkungsvollen Rahmen für ein Luftschiff in Mülheim." In: *Proceedings of the 27th Internationales Holzbau-Forum (IHF)*. In German. Innsbruck, Austria: Forum-Holzwissen, pp. 1–6.

Xu, B.-H.; S.-Y. Jiao; B.-L. Wang & A. Bouchaïr (2022). "Mechanical Performance of Timber-to-Timber Joints with Densified Wood Dowels." In: *Journal of Structural Engineering* 148.4, p. 04022023. DOI: 10.1061/(ASCE)ST.1943-541X.0003317.

Zhang, C.; H. Yang; Z. Wang; M. Wu; B. Shi; H. Tao & J. Liu (2025). "Shear characteristics of interfacial timber-to-timber joints for log-wall structures with large-diameter beech dowels: Experimental and theoretical evaluation." In: *Construction and Building Materials* 458, p. 139536.

DISCUSSION

The paper was presented by A Aloisio

F Lam received clarification from R Tomasi that the loading plates in the bending shear test setup have rounded edges.

P Dietsch commented that clamping the dowel in the test setup could cause a rope effect. A Aloisio agreed that a rope effect could exist but this was not considered in the analysis.

H Blass questioned the tensile shear test setup as the dowel could slip out under load. R Tomasi said the test set up was originally designed for screw testing. H Blass said this cannot work for dowels.

H Blass asked about the densified veneer wood dowel and whether they are considered as hardwood. A Aloisio responded that they are considered as hardwood dowels. H Blass said densified veneer wood dowels behave differently compared to hardwood dowels especially in long term behaviour.

A Aloisio and T Claus discussed rope effect mechanism as observed in the test. A Aloisio further confirmed that pull out tests were not performed.

A Frangi commented about the deformation mechanism of the dowel.

T Demschner and A Aloisio discussed about the test set up of shear/bending tests in terms of the possibility of friction and hence rope effect affecting the results.

J Smart commented that the high ductility of the birch dowel was surprising and asked what would happen if reversed cyclic loading was applied in terms of ductility. A Aloisio said high ductility of birch could be observed in other tests and they do not have information on reversed cyclic loading.

P Dietsch commented that editorial changes to the paper are needed and suggested upgrading the paper to include new information before final submission for the proceedings.

Resistance to Brittle Failure of Connections with Inclined STS in CLT Loaded along the Major Strength Direction

Thomas Tannert, School of Engineering, University of Northern British Columbia (UNBC), Prince George, Canada; thomas.tannert@unbc.ca

Amir Einipour, School of Engineering, UNBC, Prince George, Canada, einipour@unbc.ca

Jianhui Zhou, School of Engineering, UNBC, Prince George, Canada, jianhui.zhou@unbc.ca

Alexander Salenikovich, Université Laval, Quebec City, Canada, alexander.salenikovich@sbf.ulaval.ca

Keywords: Cross-laminated timber, self-tapping screws, effective depth, failure planes

1 Introduction

1.1 Background

Engineered wood products like cross-laminated timber (CLT) [1] and innovative fasteners such as self-tapping screws (STS) [2] have been drivers for the expanded use of timber in construction. Connections with laterally loaded screws exhibit low stiffness and mostly fail in ductile manner, while connections with inclined screws are stiffer, stronger, less ductile, and prone to brittle failure.

Timber connections can exhibit either ductile behaviour, characterized by wood crushing and fastener yielding, or brittle behaviour, where the wood fails in shear and/or tension with minimal plastic deformation. The ductile failure modes of connections with dowel-type fasteners are described by the European Yield Model (EYM). This model, introduced by Johansen [3] has been adopted by standards like Eurocode 5 [4] and Canadian standard for Engineering Design in Wood CSA O86 [5] for decades.

When groups of fasteners are loaded parallel to the grain, various brittle failure modes can occur depending on the member size, fastener diameter, penetration depth, and spacing. Brittle failure modes considered in design of connections of solid timber and glulam include net tension, row shear, group tear-out, plug shear, and step shear, as shown in Figure 1, adopted from [6]. Splitting is deemed prevented by using minimum spacing requirements and considering the number of effective fasteners, n_{ef}.

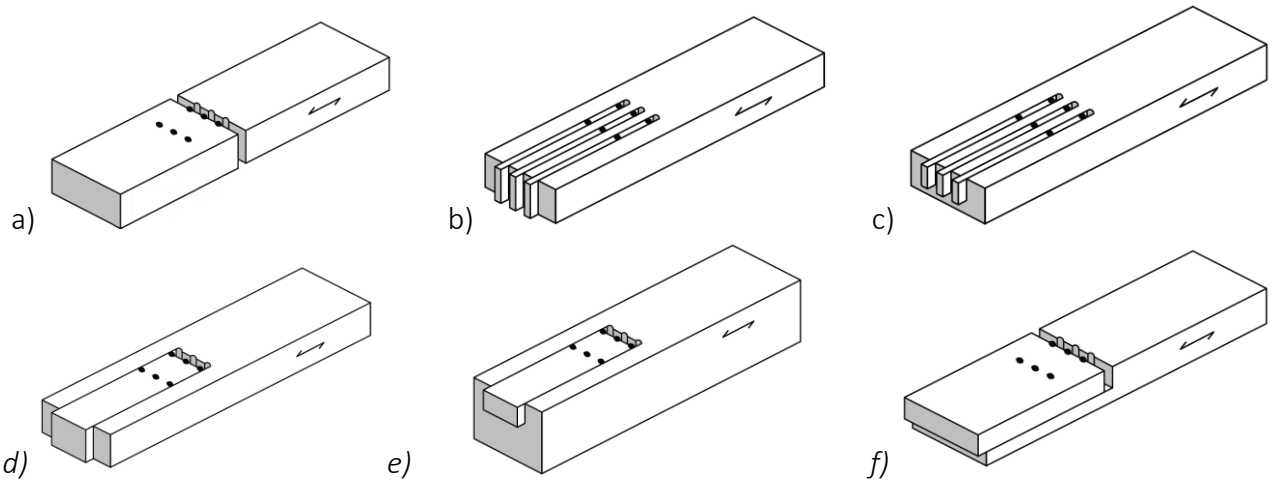

Figure 1. Brittle failure modes in connections with dowel type fasteners as depicted in CSA O86 2024 [6]: Net tension (a), row shear with full (b) and partial penetration (c), block shear or tear-out (d), plug shear (e) and step shear (f). Note: splitting is not shown.

In CLT, due to distinct major and minor strength axes, brittle failure modes are more complex [7-9], involving a compound plug and step shear failure at different depths. Herein, the classification proposed by Zarnani and Quenneville [7] was adopted, identifying possible failure modes as a function of number of activated layers, as illustrated in Figure 2a. The relevant failure planes in CLT are illustrated in Figure 2b.

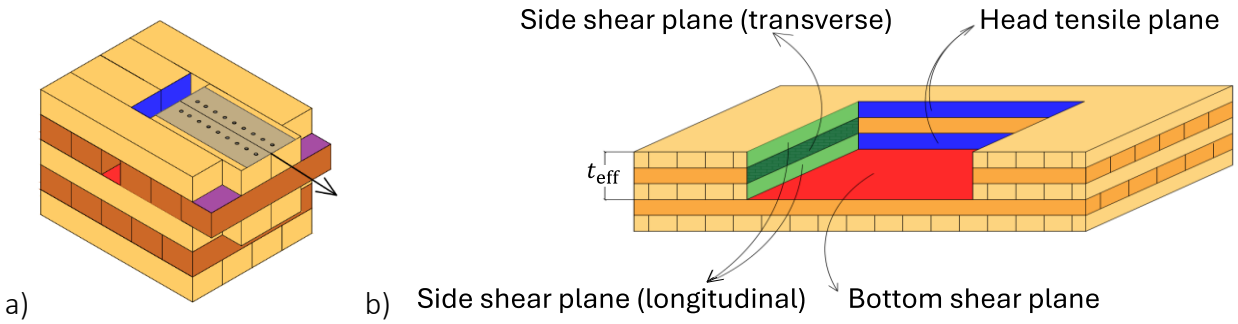

Figure 2. Brittle failure modes in CLT connections loaded along the major strength direction: plug-shear in the 2nd parallel (a), and planes resisting the load (b)

1.2 Design provisions for brittle failure modes in CSA O86

In the 2024 edition of CSA O86 [6], a new Clause 12.12 on design of connections with STS was added, including the resistance to brittle failures of wood members. For STS connections loaded parallel to the grain, the following modes are included: a) net tension resistance, $F_{t,CSA}$; b) row shear resistance, $F_{rs,CSA}$; c) group tear-out (block shear) resistance, $F_{bs,CSA}$; d) plug shear resistance, $F_{ps,CSA}$; and e) step shear resistance, $F_{ss,CSA}$.

Net tension resistance will not be further discussed herein; it is reminded that both gross and net sections of glulam members are being checked. For comparison purposes, the resistance factor ϕ_W and the load-duration factor K_D included in CSA O86 are dismissed here, and the symbols are harmonized with those used in the Eurocode

5 draft (FprEN1995) [10]. Both CSA O86 and FprEN1995 are based on the model developed by Yurrita and Cabrero, which was presented in preceding INTER meetings [11-13].

Row shear resistance, $F_{rs,CSA}$, is determined as twice the product of the minimum side shear plane resistance of a fastener row, $F_{v,sb,CSA}$, and the number of fastener rows n_{90}:

$$F_{rs,CSA} = 2 \cdot n_{90} \cdot F_{rs,j,CSA} \cdot F_{v,sb,CSA} \quad (1)$$

The block shear (group tear-out in CSA O86) resistance, $F_{bs,CSA}$, is determined as half the sum of the row shear resistance of the first, $F_{rs,1,CSA}$, and the last row, $F_{rs,nR,CSA}$, and head tensile plane resistance of the net area between the first and the last rows, $F_{t,CSA}$:

$$F_{bs,CSA} = \left[F_{t,CSA} + \left(F_{rs,1,CSA} + F_{rs,nR,CSA}\right)/2\right] \quad (2)$$

Plug shear resistance of a partially penetrated CLT member, $F_{ps,CSA}$, is determined as the sum of head tensile plane resistance, $F_{t,CSA}$, bottom shear plane resistance, $F_{v,b,CSA}$, and half the sum of the row shear resistance of the first and the last row:

$$F_{ps,CSA} = \left[F_{t,CSA} + F_{v,b,CSA} + \left(F_{rs,1,CSA} + F_{rs,nR,CSA}\right)/2\right] \quad (2)$$

Step shear resistance, $F_{ss,CSA}$, is determined as the sum of head tensile plane, $F_{t,CSA}$, and bottom shear plane resistance, $F_{v,b,CSA}$:

$$F_{ss,CSA}=\left(F_{t,CSA} + F_{v,b,CSA}\right) \quad (4)$$

The (plug) head tensile plane resistance, $F_{t,CSA}$, is determined as:

$$F_{t,CSA} = 1.25 \cdot f_t \cdot b_t \cdot t_{ef} \quad (5)$$

where f_t is the specified strength in tension parallel to grain, b_t is the critical width of head tensile plane and t_{ef} is the effective depth. For step shear, b is used instead of b_t.

The side shear plane resistance, $F_{v,sb,CSA}$, is determined as:

$$F_{v,sb,CSA} = 0.75 \cdot f_v \cdot L_s \cdot t_{ef} \quad (6)$$

where f_v is the specified longitudinal shear strength, L_s is the critical length of side shear plane and t_{ef} is the effective depth of head tensile plane, with $L_s = n_{90}\, a_{cr}$ where a_{cr} is the minimum of end distance and the spacing of fasteners in a row parallel-to-grain.

The (plug) bottom shear plane resistance, $F_{v,b,CSA}$, is determined as:

$$F_{v,b,CSA} = 0.75 \cdot f_v \cdot L_s \cdot b_{con} \quad (7)$$

where L_s is the critical length based on a_{cr}, b_{con} is the connection width, and f_v is the longitudinal shear strength, regardless of whether the bottom shear plane is located in a layer oriented parallel or perpendicular. For step shear, b is used instead of b_{con}.

For partially penetrated wood members, the effective depth t_{ef}, which is the penetration depth of the fastener considered to obtain the area of the head tensile and side shear planes, t_{ef}, see Figure 4, is determined as:

$$t_{ef} = k_{cl} \cdot \left(7t_h \,/\, (3 + t_h/d_F)\right) \leq t_h \tag{8}$$

where k_{cl} is a clamping factor taking into account the boundary conditions of the fastener in thin and thick steel side plates and in timber-to-timber connections *c.f.* Cabrero et al. [14], d_F is the fastener diameter, and t_h is the projected screw bearing length in the partially penetrated wood member, see Figure 3. For CLT, the thickness of the layers with grain direction perpendicular to the applied load shall be deducted from t_{ef}. The standard does not apply the same reduction to the side shear planes.

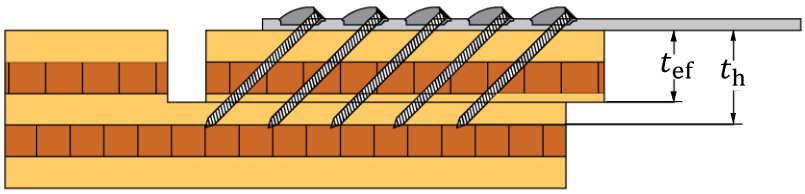

Figure 3. Definition of effective depth of the failure planes

1.3 Eurocode 5 draft

The Eurocode 5 draft [10] covers brittle failure modes of connections with dowel-type fasteners loaded parallel to grain in section 11.5. For a timber member with more than one row of fasteners, the brittle failure resistance should be determined by the minimum resistance of: a) net tensile failure (not further discussed herein); b) row shear failure; c) block shear failure (for fully penetrated members); and d) plug shear failure (for partially penetrated members).

The row shear resistance of a timber member $F_{rs,EC5}$ is taken as:

$$F_{rs,EC5} = 2 \cdot n_{90} \cdot F_{v,la,EC5} \tag{9}$$

where n_{90} is the number of fasteners in a row perpendicular to grain, and $F_{v,la,EC5}$ is the design shear resistance per side shear plane in the timber member.

The block shear resistance $F_{bs,EC5}$ for fully penetrated timber members is taken as:

$$F_{bs,EC5} = \max \begin{cases} 2 \cdot F_{v,la,EC5} \\ F_{t,EC5} \end{cases} \tag{10}$$

where $F_{t.EC5}$ is the tensile resistance parallel to grain of the head tensile plane.

The plug shear resistance $F_{ps.EC5}$ for partially penetrated timber members is taken as:

$$F_{ps,EC5} = \max\begin{cases} 2 \cdot F_{v,la,EC5} \\ F_{t,EC5} + F_{v,b,EC5} \end{cases} \quad (11)$$

where $F_{v,la.EC5}$ is the shear resistance per side shear plane; $F_{t,EC5}$ is the tensile resistance of the head plane; and $F_{v,b.EC5}$ is the shear resistance of the bottom shear plane.

The side shear plane resistance per, $F_{v,la,EC5}$ is taken as:

$$F_{v,la,EC5} = k_v \cdot t_{ef} \cdot L_{con} \cdot f_v \quad (12)$$

with $L_{con}=a_1 \cdot (n_0 - 1) + a_{3,t}$; where k_v is the adjustment factor for shear strength (varies for different products, e.g. $k_v = 0.75$ for glulam); t_{ef} is the effective depth of the plane; L_{con} is the length parallel to grain of the connection; f_v is the shear strength; a_1 is the spacing of fasteners parallel to grain; n_0 is the number of fasteners in a row parallel to grain; and $a_{3,t}$ is the loaded end distance parallel to grain.

The bottom shear plane resistance, $F_{v,b,EC5}$ is taken as:

$$F_{v,b,EC5} = k_v \cdot L_{con} \cdot b_{con} \cdot f_v \quad (13)$$

with $b_{con} = a_2 \cdot (n_{90}-1)$, where k_v, L_{con}, and f_v are as defined above; b_{con} is the width of the connection; n_{90} is the number of fasteners in a row perpendicular to grain; and a_2 is the spacing of fasteners perpendicular to grain.

The head tensile plane resistance, $F_{t,EC5}$, is taken as:

$$F_{t,EC5} = k_t \cdot b_{net} \cdot t_{ef} \cdot f_t \quad (14)$$

with $b_{net} = \left(a_2 - d_{hole,max}\right) \cdot (n_{90} - 1)$, where k_t is the increase factor for tension (varies for different products, e.g. $k_t = 1.25$ for glulam); b_{net} is the net width of area that fails in block shear; t_{ef}, a_2 and n_{90} are as defined above; f_t is the design tensile strength; $d_{hole,max}$ is the larger of the diameter of the predrilled hole and fastener diameter.

1.4 Research need

The main differences between the two standards with regards to the design of brittle failures of STS connections loaded parallel to the grain and challenges with their application towards CLT are the following:

1) Both standards assume the effective depth of failure planes, t_{ef}, for connections with inclined STS to be the same as for connections with any dowel-type fasteners installed perpendicular to the shear plane. This assumption lacks experimental proof.

2) While CSA O86 specifies that the thickness of the layers with grain direction perpendicular to the applied load shall be deducted from t_{ef} of the head tensile plane in CLT, this reduction is not applied to side shear planes. FprEN1995 does not provide guidance on how to adopt t_{ef} in CLT.

3) Neither standard provides any guidance on how to treat bottom shear planes in CLT layers perpendicular to the load. In CSA O86, the parallel to grain shear strength is applied regardless of orientation of the bottom shear plane.

4) Neither standard provides any guidance on how to treat the impact of placement of connections along the width of CLT panels, such as connections offset to one side.

5) Both standards assume a critical (effective) width of the head tensile failure plane, independent on screw installation angle. Inclined screws, however, do not necessarily weaken the entire failure plane in CLT.

6) In the calculation of the parallel-to-grain length of the side and bottom shear planes, FprEN1995 uses the actual connection length, whereas CSA O86 uses a distance based on the minimum of the parallel to grain spacing and the end distance. This approach seems unreasonably conservative when using long end distances.

7) Both standards use pre-factors for tensile and shear strength, for STS in CLT CSA O86 considers a factor of 0.75 for shear strength and a factor of 1.25 for the tensile strength. FprEN1995 provides the same factors for structural lumber and glulam.

8) The approaches differ in the calculation of the block shear (group tear-out) resistance. CSA O86 sums up the resistance of head tensile and side shear planes, while, for unreinforced connections, FprEN1995 considers the maximum of the head tensile and side shear plane resistances and does not provide specific guidance for CLT.

9) The plug shear resistance for glulam is calculated as the maximum of the side shear plane resistance and the sum of the head tensile and bottom shear plane resistances in both CSA O86 and FprEN1995. For CLT, CSA O86 sums up the resistance of head tensile, bottom shear and side shear planes, while FprEN1995 does not provide specific guidance for CLT.

10) Only CSA O86 includes step shear and row shear failure modes for STS; while the latter cannot occur in CLT, the former is possible in narrow CLT panels.

1.5 Objectives

Neither the 2024 edition of CSA O86 [6] nor the final draft of Eurocode 5, FprEN1995 [10], provide adequate design rules for the resistance to brittle failure of connections with inclined STS in CLT loaded along the major strength direction. The objectives of this work are to: i) investigate brittle failure of such connections; and ii) propose an improved model to estimate the resistance against this failure. To achieve these objectives, a comprehensive test program was conducted at the UNBC Wood Innovation Research Lab, and the results were used to evaluate the predictive capability of the existing the newly proposed design approaches.

2 Experimental work

2.1 Materials

For the experimental investigation, 3-ply, 5-ply, and 7-ply CLT panels were used. Most panels were V2 grade, composed of spruce-pine-fir (S-P-F) No.1/No.2 lumber in longitudinal and S-P-F No.3/Stud in transverse layers produced in accordance with ANSI PRG 320 [15]. One type of 5-ply CLT was manufactured using European C24 grade lumber. A summary of the CLT panel layups and grades is provided in Table 1.

Table 1. CLT layups and grades

Thickness (mm)	Thicknesses of layers [mm]	Grade
105	35-35-35	V2
100	20-20-20-20-20	C24
139	35-17-35-17-35	V2
175	35-35-35-35-35	V2
191	35-17-35-17-35-17-35	V2
245	35-35-35-35-35-35-35	V2

The STS used in this study were ASSY plus VG fully threaded carbon steel screws with a countersunk (CSK) head and a diameter of 10 mm [16]. To achieve variations in penetration depth and connection behaviour, four screw lengths (120 mm, 180 mm, 240 mm, and 280 mm) were selected. The screws were installed using 45° angle washers and pilot holes to ensure consistent alignment and accurate placement of the STS.

2.2 Specimen description

For this experimental campaign, a total of 18 test series, with six replicates each, were designed based on CSA O86, incorporating variations in screw arrangements, lengths, and CLT thicknesses to capture brittle failure. All specimens were assembled with identical 12.7 mm thick steel plates as side members on one face at both ends. The CLT specimens, as shown in Figure 4a, measured 1200 mm in length and varied between 400 mm or 600 mm in width. In each connection layout, screw spacing followed the minimum requirements specified in CSA O86 [6], with 50 mm (5d) parallel to the grain (S_p) and 40 mm (4d) perpendicular to the grain (S_q). Loaded end distances (a_L), measured from the geometric centre of the screw, varied based on screw length.

Connections were either centred or offset within the CLT, see Figure 4b. For offset connections, the unloaded edge distance (e_p) was 30 mm (3d), while in centred configurations, it depended on the specimen width, with a minimum of 120 mm (10d). The layouts of all test series are shown in Table 2, including the projected screw bearing length (t_h), the effective depth of the failure planes (t_{ef}), and the projected screw bearing length less the penetration into layer(s) perpendicular to the load direction (t_p).

Table 2. Layouts of test specimens

ID	t_{CLT} (mm)	b_{CLT} (mm)	$n_R \times n_C$	*pos*	a_L (mm)	e_P (mm)	L_{STS} (mm)	t_h (mm)	t_{ef} (mm)	t_p (mm)
S1	105	400	5 × 5	Cen	89	120	120	54	35	35
S2	105	400	5 × 5	Off	89	30	120	54	35	35
S3	100	600	5 × 5	Cen	89	220	120	54	25	34
S4	100	600	5 × 5	Off	89	30	120	54	25	34
S5	139	500	5 × 5	Cen	112	170	180	97	36	70
S6	139	500	5 × 5	Cen	89	170	120	54	28	37
S7	139	500	3 × 5	Cen	112	170	180	97	36	70
S8	139	500	5 × 5	Off	112	30	180	97	36	70
S9	175	550	5 × 5	Cen	128	195	240	139	35	70
S10	175	550	5 × 5	Off	128	30	240	139	35	70
S11	175	550	5 × 5	Cen	112	195	180	97	35	62
S12	175	550	5 × 5	Off	112	30	180	97	35	62
S13	175	550	3 × 5	Cen	128	195	240	139	35	70
S14	175	550	3 × 5	Off	128	30	240	139	35	70
S15	191	425	5 × 5	Cen	128	133	240	139	41	105
S16	191	425	5 × 5	Cen	112	133	180	97	36	70
S17	245	550	5 × 5	Cen	144	195	280	168	35	98
S18	245	550	5 × 5	Off	144	30	280	168	35	98

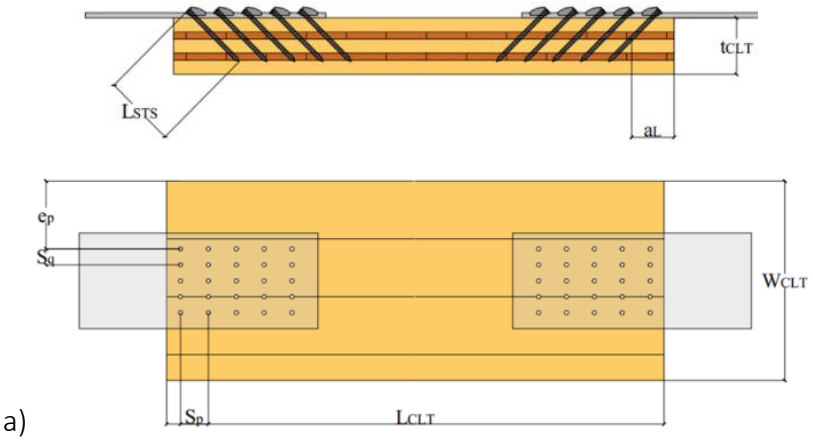

a)

b)

Figure 4. Test specimen configuration (a), and offset connection position (b)

2.3 Methods

The experimental tests were conducted at the UNBC Wood Innovation Research Laboratory in Prince George, BC, using a load frame with two hydraulic actuators providing a capacity of 1000 kN, as shown in Figure 5a. To capture the connection displacements, four string potentiometers were mounted at the CLT specimen's centre, with their other ends attached to the corners of the steel plates, see Figure 5b.

a) 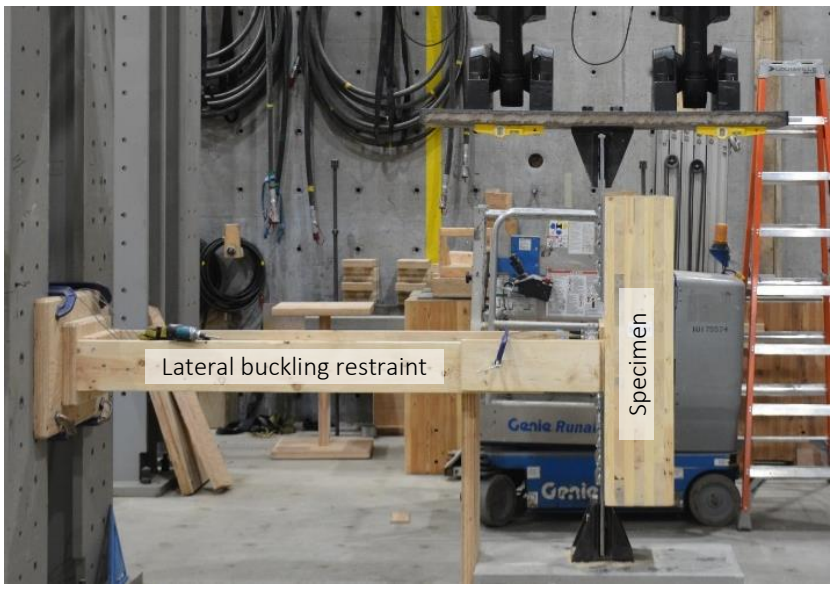

b) 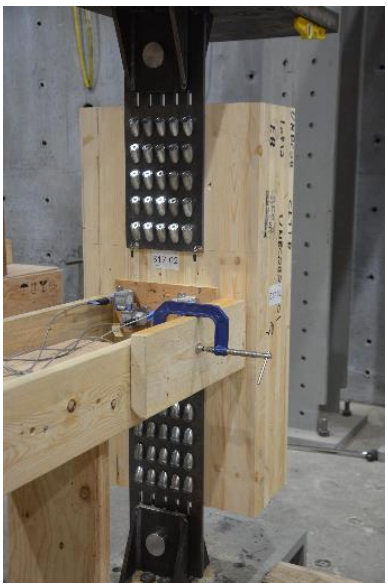

Figure 5 Test setup (a) and connection detail (b)

A quasi-static uniaxial tension load was applied following a modified ISO 6891 [9] loading protocol at a constant displacement rate of 4 mm/min until failure. The loading protocol included an initial loading up to 40% of the estimated maximum load (F_{est}) and unloading down to 10% F_{est}, followed by continuous loading until failure. The test was terminated when the post-peak load dropped below 80% of the maximum load. For each test, the applied load and the corresponding relative displacements between steel plate and CLT panel at both connections were recorded.

2.4 Load displacement behaviour and failure modes

The connections in all test series, except S6 and S7 which failed due to withdrawal of screws, exhibited quasi-linear behaviour up to the maximum load, followed by brittle failure in the CLT. The load-displacement curves for series S1 as an example are presented in Figure 6. Most failures occurred at the displacement less than 5 mm.

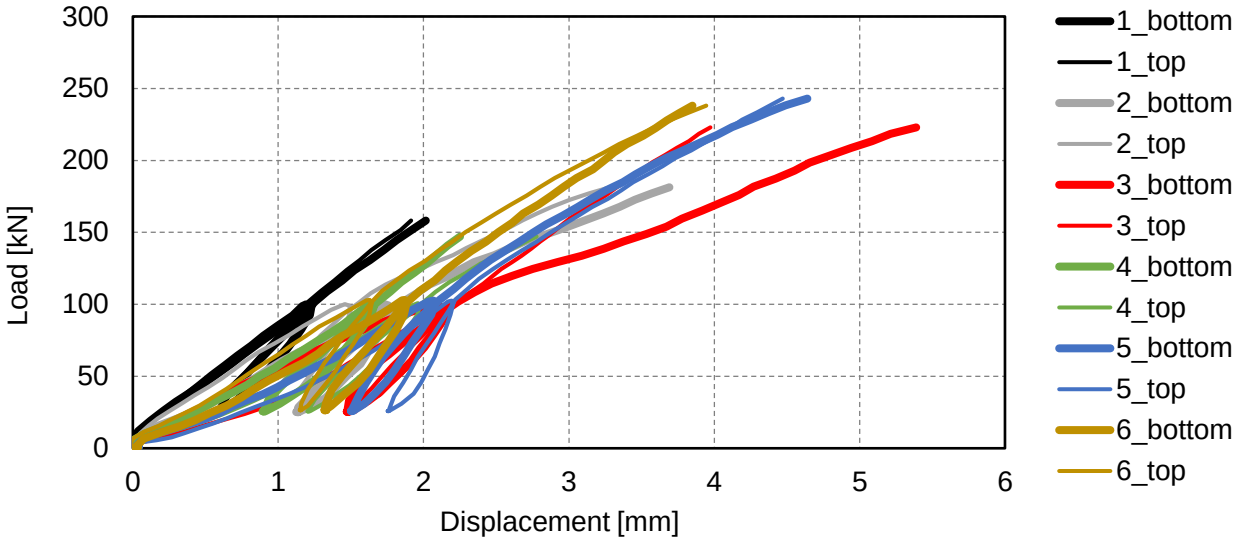

Figure 6 Load-displacement curves for tests sspecimens in series S1

The observed failure modes for each test series are illustrated in Figure 7 and summarized in Table 3 together with the observed depth of the failure plane, t_{obs}. In this experimental campaign, compound plug shear failure was the principle observed mode, occurring across multiple test series, ranging from failure in the: a) 1st parallel layer, b) 1st perpendicular layer, c) 2nd parallel layer, d) 2nd perpendicular layer, and e) 3rd parallel layer. In series S15, S17, and S18, the failure extended across the full width of the CLT specimen, akin to step shear.

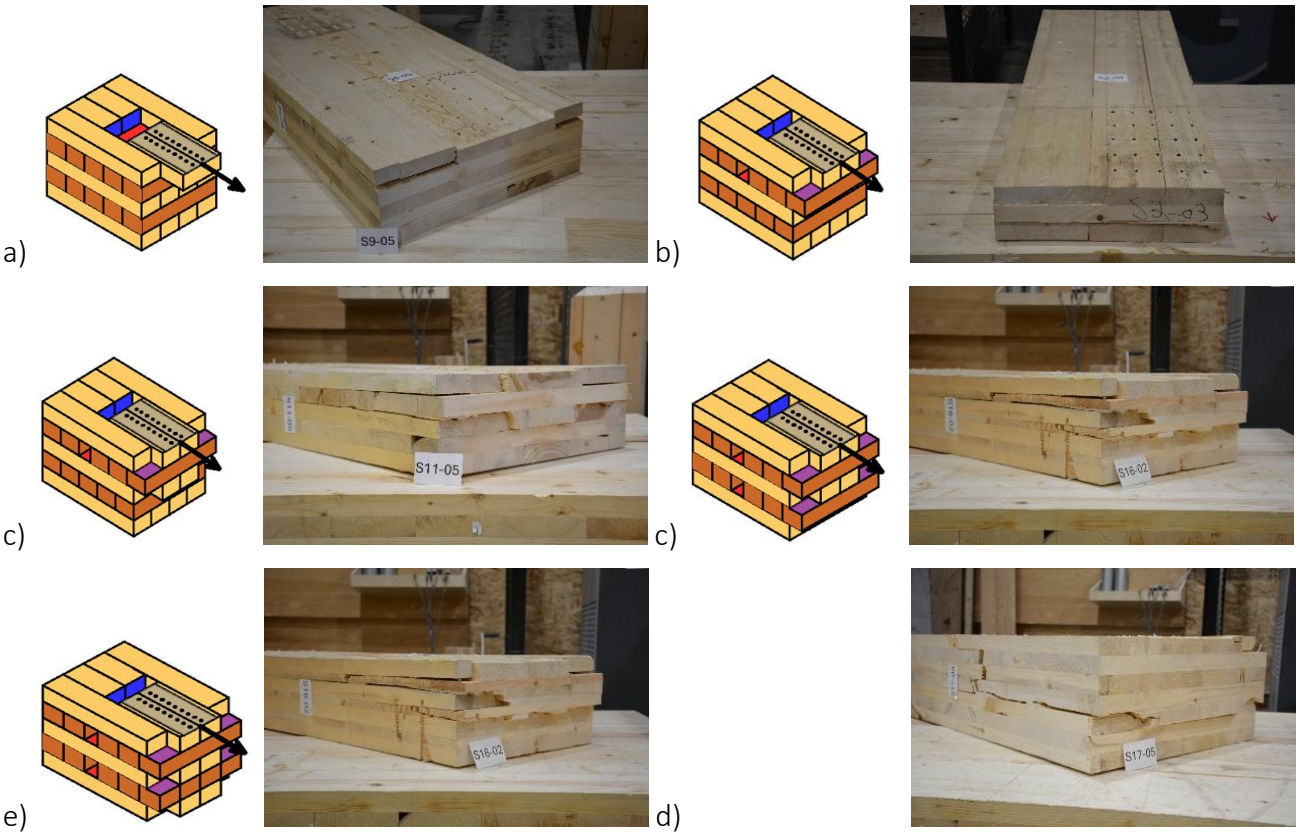

Figure 7 Compound plug shear failure mode in: 1st parallel layer (a), 1st perpendicular layer (b), 2nd parallel layer (c), 2nd perpendicular layer (d), 3rd parallel layer layer (e), and step shear (f)

2.5 Connection resistance

The summary of test results is presented in Table 3, where F_{max} is the average resistance (maximum load) for each test series, *CoV* is the coefficient of variation of F_{max}, and $u_{@Fexp}$ is the average displacement at the maximum load. The F_{max} ranged from 204 kN to 540 kN as a function of CLT layup and connection layout. The CoV, from 4% to 20%, were in the common range for brittle failure of timber. The corresponding $u_{@Fexp}$ ranged from 3.6 mm to 6.1 mm, emphasising the stiff nature of the connection.

CSA O86 [6] specifies a minimum unloaded edge distance (e_p) but does not consider the effect of exceeding this requirement. Consequently, for identical connections with different unloaded edge distances (centred vs. offset), the standard predicts the same resistance. However, the results showed that connections with larger e_p reached, on average, a 25% higher resistance, see Figure 8.

Table 3. Test series overview

ID	F_{max} (kN)	*CoV* (%)	$u_{@Fmax}$ (mm)	Dominant failure mode
S1	258	8	4.1	Plug shear in 1st perp. or 2nd par. layers
S2	204	20	3.6	Plug shear in 1st perp. or 2nd par. layers
S3	300	6	4.8	Plug shear in 2nd par. layers
S4	267	16	5.2	Plug shear in 2nd perp. or 2nd par. layers
S5	394	12	5.3	Plug shear in 2nd par. layer
S6	250	8	5.0	Screw withdrawal
S7	339	2	5.2	Screw withdrawal
S8	379	15	5.5	Plug shear in 2nd perp. layer
S9	458	7	5.1	Plug shear in 3rd par. layer
S10	305	12	4.8	Plug shear in 3rd par. layer
S11	405	12	4.0	Plug shear in 2nd par. layer
S12	328	6	4.6	Plug shear in 2nd par. layer
S13	420	10	6.1	Plug shear in 3rd par. layer
S14	239	15	6.0	Plug shear in 3rd par. layer
S15	485	12	5.3	Step shear in 2nd perp. layer
S16	475	20	6.5	Step shear or plug shear in 2nd perp. layer
S17	540	4	4.9	Step shear in 3rd par. layer
S18	480	14	5.3	Step shear in 3rd par. layer

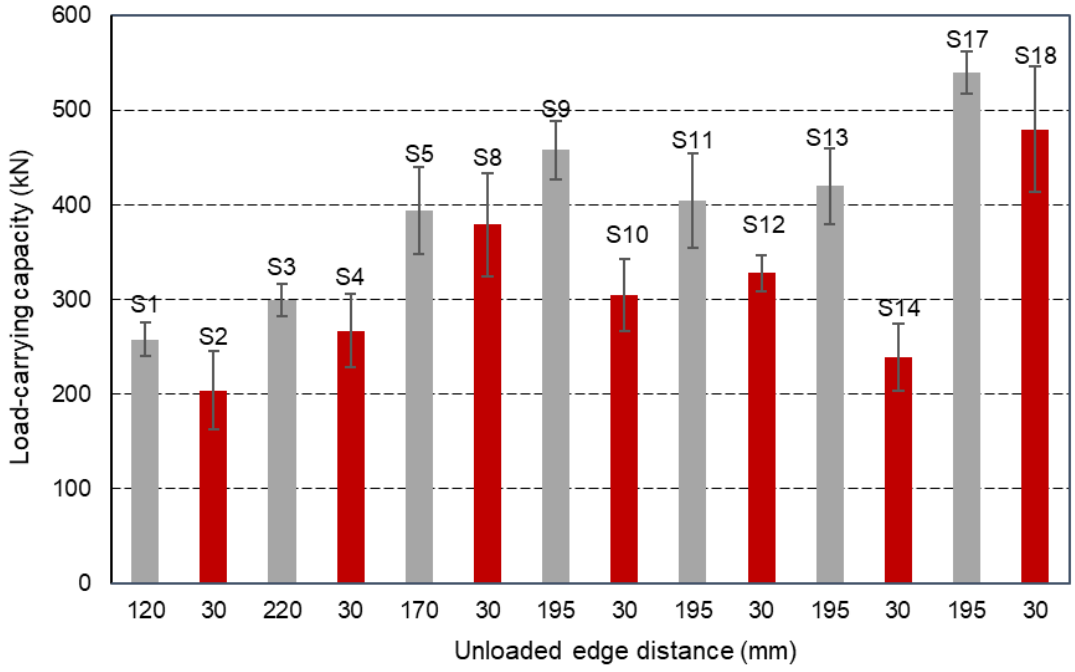

Figure 8 Effect of unloaded edge distance on connection resistance

3 Comparison of prediction models

3.1 Overview

The experimental tests were used to evaluate the predictive capability of the CSA O86 [6] design approach for STS connections inclined STS in CLT loaded along the major strength direction. Although FrpEN1995 [10] does not provide specific guidance for STS connections in CLT, the provisions were adopted herein for comparative purposes assuming the current approach as applied to glulam. Finally, based on the experimental evidence, a new model is proposed, identified by the subscript “PM”.

3.2 Assumptions of the proposed model

1) Resistance of partially penetrated CLT panels is the minimum between plug shear and step shear resistance. Row shear and group-tear out do not need to be considered. Net section tensile and ductile screw yield resistances must be checked.

2) Step shear resistance is determined as the maximum of head tensile plane and bottom shear plane resistances, both considering the full specimen width, b.

3) Plug shear resistance is determined as the maximum of head tensile plane resistance, bottom shear plane resistance, and side shear plane(s) resistance.

4) Plug shear resistance of connections offset to the edge of a CLT panel with a minimum unloaded edge distance, e_p, the resistance of only one side shear plane is considered. To account for both side shear planes, $e_p \geq 10d$ is recommended.

5) Based on the observed failure planes, the projected screw bearing length in the CLT layers parallel to the load, t_p, is used as the depth of the head-tensile failure planes.

6) In lieu of a more complex model: a) the depth of the side shear failure planes is taken as the projected screw bearing length in the CLT, t_h; and b) the parallel to grain shear strength, f_v, is used for computing the bottom shear plane resistance. This way, as done in CSA O86, the contribution of rolling shear resistance in perpendicular laminations, which are longer than the connection width, is accounted for.

7) The length of the side shear and bottom shear failure planes is the connection length as specified in FrpEN1995 and not the critical length as specified in CSA O86.

8) The width of connection with inclined STS does not need to be reduced by the holes produced by the fasteners, because the tensile failure plane is only reduced at a single point of screw penetration and not along the whole projected bearing length.

3.3 Model predictions

The evaluation was done, as in previous works [11-13], at the mean level. The specified strength in tension parallel to grain strength, f_t, and the specified longitudinal shear strength, f_v, were taken as 21.4 MPa and 5.87 MPa [17], respectively. The pre-factors (1.25 for f_t and 0.75 for f_v) were applied in all models.

Table 4 provides a summary of the predicted failure planes resistances:

$F_{t,PP,CSA}$: plug shear head-tensile plane resistance, using t_{ef} and b_{ef} (= $F_{t,PP,EC5}$)

$F_{t,PP,PM}$: plug shear head-tensile plane resistance, using t_p and b_{con}

$F_{t,PS,CSA}$: step shear head-tensile plane resistance, using t_{ef} and b (= $F_{t,PS,EC5}$)

$F_{t,PS,PM}$: step shear head-tensile plane resistance, using t_p and b

$F_{v,b,PP,CSA}$: plug shear bottom plane resistance, using b_{con} and L_S

$F_{v,b,PP,PM}$: plug shear bottom plane resistance, using b_{con} and L_{con} (= $F_{vb,PP,EC5}$)

$F_{v,b,PS,CSA}$: step shear bottom plane resistance, using b and L_S

$F_{v,b,PS,PM}$: step shear bottom plane resistance, using b and L_{con} (= $F_{vb,PP,EC5}$)

$F_{v,sb,CSA}$: side shear plane resistance, using t_{ef} and L_S

$F_{v,sb,PM}$: side shear plane resistance, using t_h and L_{con}

$F_{v,sb,EC5}$: side shear plane resistance, using t_{ef} and L_{con}

Table 4. Resistance of individual failure planes according to different models

ID	$F_{t,PP}$		$F_{t,PS}$		$F_{v,b,PP}$		$F_{v,b,PS}$		$F_{v,sb}$		
	CSA	PM	CSA	PM	CSA	PM	CSA	PM	CSA	PM	EC5
S1	126	150	345	374	247	**257**	616	643	108	155	112
S2	126	150	345	374	247	**257**	616	643	108	77	112
S3	83	120	351	450	247	**257**	925	964	71	155	74
S4	83	120	351	450	247	**257**	925	964	71	77	74
S5	128	299	446	935	247	272	770	850	110	**308**	121
S6	94	150	327	467	247	**257**	770	803	80	155	84
S7	64	150	457	935	123	136	770	850	110	308	121
S8	128	**299**	446	935	247	272	770	850	110	154	121
S9	126	299	485	1028	247	287	847	985	108	**476**	125
S10	126	**299**	485	1028	247	287	847	985	108	238	125
S11	126	237	485	816	247	272	847	935	108	**308**	119
S12	126	237	485	816	247	**272**	847	935	108	154	119
S13	63	150	497	1028	123	143	847	985	108	**476**	125
S14	63	150	497	1028	123	143	847	985	108	**238**	125
S15	145	423	422	1123	247	287	655	762	124	**476**	144
S16	128	299	374	795	247	272	655	722	110	**308**	121
S17	126	390	485	1341	247	297	847	1022	108	**599**	130
S18	126	390	485	1341	247	297	847	1022	108	**599**	130

The CSA O86 [6], FprEN1995 [10] and proposed model predictions for plug shear (PP_{rt}), which governed for all three models and every test configuration, are summarized in Table 5, including the ratios between predictions and average test result. Additional tests from a preliminary UNBC study [18] are incorporated to expand the database. The comparisons against the experimental results are further illustrated in Figure 9. The proposed model provides both the best predictions in terms of average ratio (0.96) as well as the by far smallest spread (from 0.76 to 1.25). CSA O86 and EC5 predictions are non-conservative for many connection configurations and show a much wider spread, indicating that the failure mechanisms are not adequately captured.

Table 5. Predicted connection resistance according to different models

ID	F_{max}	$PP_{rt,CSA}$	$PP_{rt,EC5}$	$PP_{rt,PM}$	CSA/Test	EC5/Test	PM/Test
S1	258	481	384	257	1.9	1.5	1.0
S2	204	481	384	257	2.4	1.9	1.3
S3	300	401	341	257	1.3	1.1	0.9
S4	267	401	341	257	1.5	1.3	1.0
S5	394	485	400	308	1.2	1.0	0.8
S6	250	421	351	257	1.7	1.4	1.0
S7	339	297	200	308	0.9	0.6	0.9
S8	379	485	400	299	1.3	1.1	0.8
S9	458	481	413	476	1.0	0.9	1.0
S10	305	481	413	299	1.6	1.4	1.0
S11	405	481	398	308	1.2	1.0	0.8
S12	328	481	398	272	1.5	1.2	0.8
S13	420	294	207	476	0.7	0.5	1.1
S14	239	294	207	238	1.2	0.9	1.0
S15	485	515	432	476	1.1	0.9	1.0
S16	475	485	400	308	1.0	0.8	0.6
S17	540	481	424	599	0.9	0.8	1.1
S18	480	481	424	599	1.0	0.9	1.2

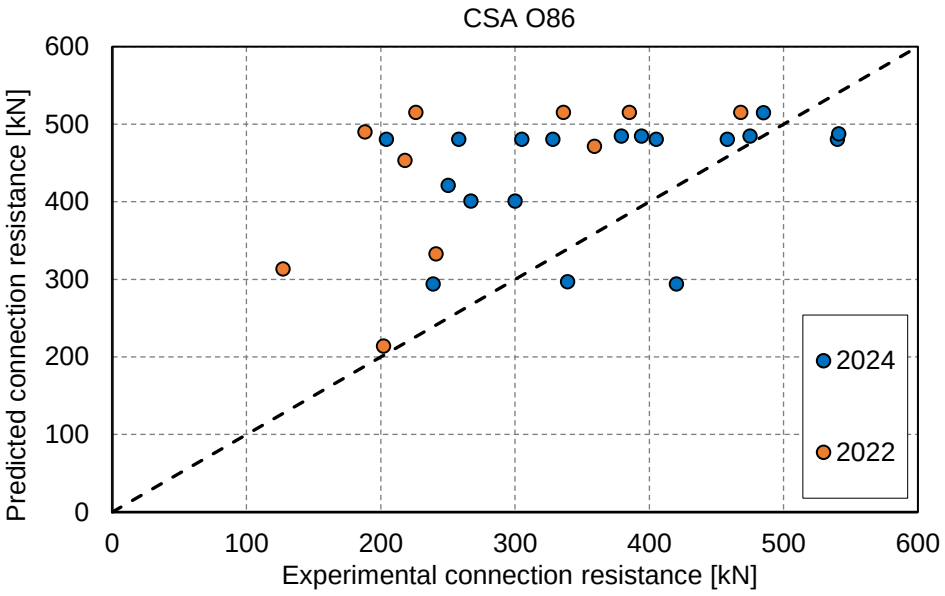

a)

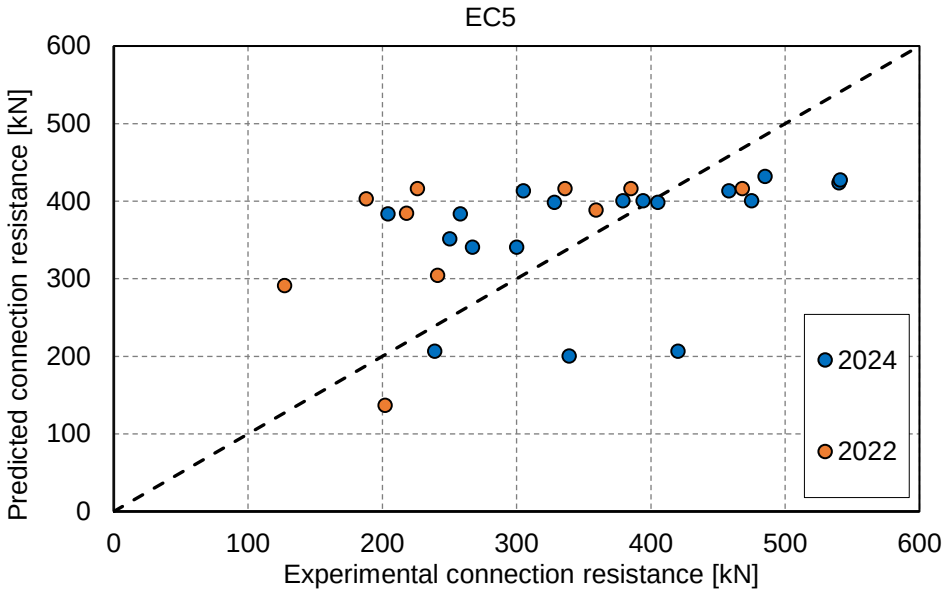

b)

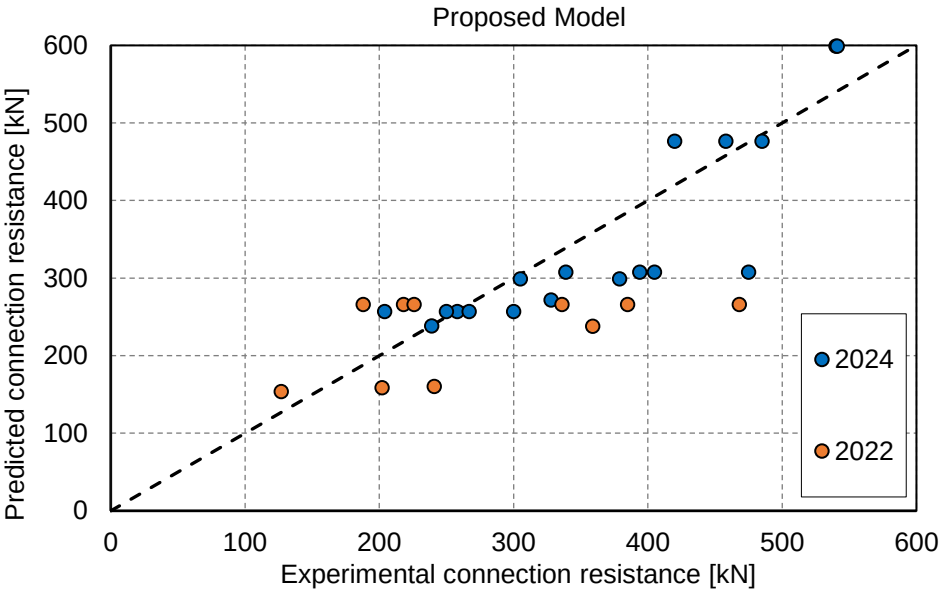

c)

Figure 9 Comparison of prediction of conenction resistance of models against experimental data: CSA O86 (a), FprEN1995 (b), and proposed model (c)

4 Conclusions

This study experimentally investigated brittle failures in CLT connections with STS installed at a 45° angle loaded along the major strength direction. Specimens included different CLT layups and various STS lengths and placement patterns to evaluate the influence of design parameters on failure modes and resistance. Several key insights emerged from the experimental campaign:

i) Brittle failure in CLT with inclined STS is more complex than in glulam and differs from failure mechanisms currently described in CSA O86. Specifically, plug shear failure did not align with CSA provisions, as failure patterns varied based on the contribution of different CLT layers.

ii) When the unloaded edge distance was increased from the minimum specified in CSA O86 by shifting STS groups away from the edge to the centre of the CLT panel, the resistance increased by 25%, on average.

iii) In test series where plug shear and step shear failures exhibited distinct failure blocks, the observed failure block depth closely corresponded to the projected bearing length of the inclined screws.

Subsequently, a new model that better accounts for the observed failure patterns was proposed. The main differences compared to the current CSA O86 approach are:

1) Plug shear and step shear resistances are determined as the maximum of the individual failure plane resistances.
2) Both side shear planes are only accounted for large unloaded edge distances.
3) The depth of the head-tensile failure planes is the projected screw bearing length in the CLT layers parallel to the load.
4) The contribution of rolling shear resistance in perpendicular laminations is accounted for by using the full projected screw bearing length in the CLT as depth of the side shear failure planes and assuming the parallel to grain shear strength.
5) The actual connection lengths and widths are used to compute failure planes.

The model predictions for the connection resistance and those using the CSA O86 [6] and the FprEN1995 [10] design approaches were compared against the experimental data. The proposed model achieved the overall best fit and smallest spread.

Future work needs to expand the investigations to connections with:

- STS installed perpendicular to the surface, where the use of t_{ef} seems appropriate.
- Two-sided STS connections, where the type of failure (plug or block shear will depend on the screw penetration).
- Wider CLT panels, where the actual resistance of the perpendicular failure planes might have to be taken into account.
- CLT panels loaded along the minor strength direction.

The proposed model will be presented to the CSA O86 technical committee for discussion to be included in the next version of the standard. The influence of the different applicable factors and design provisions and their effect on the failure mode at the characteristic and design level deserve a separate discussion. Future efforts should be aimed at international harmonization of the design approaches for brittle failure modes in CLT connections with STS.

Acknowledgments

This research was supported by the Government of British Columbia through a BC Leadership Chair. The authors extend their appreciation to UNBC lab lead Maik Gehloff, technicians Ryan Stern, James Andal, and Nathan Stern, and students Sabari, Sanya, and Jerry for their assistance during the experiments.

References

[1] R. Brandner et al. (2016) Cross laminated timber (CLT): overview and development, Eur. J. of Wood and Wood Products 74: 331–351.

[2] P. Dietsch and R. Brandner (2015) Self-tapping screws and threaded rods as reinforcement for structural timber elements—A state-of-the-art report," Construction and Building Materials, 97:78–89.

[3] K.W. Johansen (1949) Theory of timber connections. Bridge Struct Eng 9: 249–262.

[4] EN 1995-1-1 (2004) Eurocode 5. Design of timber structures - Part 1–1: General - Common rules and rules for buildings. CEN, Brussels, Belgium.

[5] CSA (2009) Engineering design in wood. CSA O86 – 2009. Canadian Standards Association, Mississauga, Ontario, Canada.

[6] CSA (2024) Engineering design in wood. CSA O86 – 2024. Canadian Standards Association, Mississauga, ON, Canada.

[7] P. Zarnani and P. Quenneville (2015) New design approach for controlling brittle failure modes of small-dowel-type connections in cross-laminated timber, Construction and Building Materials, 100: 172–182.

[8] M. Yurrita and J. M. Cabrero (2021) On the need of distinguishing ductile and brittle failure modes in timber connections with dowel-type fasteners, Engineering Structures, 242: 112496.

[9] B. Azinović et al. (2022) Brittle failure of laterally loaded self-tapping screw connections for cross-laminated timber structures, Eng Struct, 266: 114556.

[10] FprEN 1995-1-1 Eurocode 5 - Design of timber structures - part 1-1: General rules and rules for buildings, CEN, Brussels, Belgium, 2025.

[11] Yurrita M., Cabrero J. M. (2019) Effective Thickness of the Wood Member in a Timber-to-steel Connection with Large Diameter under Brittle Failure. INTER 52-7-5.

[12] Yurrita, M., Cabrero J. M. (2019) New Analytical Model for Brittle Failure in the Parallel-to-grain Direction of Timber Connections with Large Diameter Fasteners. INTER 52-7-7.

[13] Yurrita M., Cabrero J. M. (2021) New Analytical Model for Plug Shear of Timber Connections with Small Diameter Dowel-Type Fasteners in the Parallel-to-Grain Direction. INTER 54-7 10.

[14] Cabrero J. M. et al. (2024) Brittle Failure Modes of Connections with Dowel-Type Fasteners Loaded Parallel to the Grain: A Comparison between Eurocode 5 and CSA O86. INTER 57-7-9

[15] ANSI/APA PRG 320 (2025) Standard for Performance-Rated Cross-Laminated Timber. American National Standard. APA – The Engineered Wood Association, Tacoma, WA.

[16] Evaluation Report CCMC 13677-R (2023) SWG ASSY® VG Plus and SWG ASSY ® 3.0 Self-Tapping Wood Screws. Canadian Construction Materials Centre. Ottawa, ON.

[17] Jessome, A.P. (2000) Strength and Related Properties of Woods Grown in Canada. Publication SP-514E. Forintek Canada Corp. Eastern Division. Sainte Foy, QC.

[19] Armstrong G., Tannert T. (2022) Brittle Failure Modes of Connections in Cross-Laminated Timber with Self-Tapping Screws. MEng final project, UNBC, Prince George, Canada.

DISCUSSION

The paper was presented by T Tannert

J Cabrero received clarification that the side shear failure plane was close to the screws.

A Frangi received clarification that the tests were designed to avoid screw withdrawal. T Tannert said the intent was not for designers to design these types of connectors as they are not good connections. He added that the model did not predict the failure plane.

P Dietsch commented that the paper should mention which failure mode was predicted. He asked how deep the screws need to penetrate into the longitudinal layer to be considered. T Tannert responded that they do not have information on the minimum penetration depth required.

P Dietsch agreed that we need to consider conservative models in case of lack of information. Industry however might argue that they already have good performance history hence added conservatism would not be needed. T Tannert said in Canada we do not have long history of using these large connections; hence, designers will be happy to receive guidance.

H Blass asked whether the bottom failure planes were always between two orthogonal layers. T Tannert said they were closed to the glue-line. H Blass said one should then consider the bond.

C Demirci received clarification on the difference between step and plug shear.

P Quenneville commented that the screws also pull at the glue-line.

Probabilistic block shear failure mode model

Nicol López Rodríguez, Onesta Wood Chair, University of Navarra, Pamplona, Spain;
Centro Nacional de Excelencia para la Industria de la Madera (CENAMAD),
Pontificia Universidad Católica de Chile, Santiago, Chile
nlopezrodri@unav.es

Raúl Cruz Hidalgo, Department of Applied Physics and Mathematics,
University of Navarra, Pamplona, Spain
raulcruz@unav.es

José M. Cabrero, ONESTA Wood Chair. University of Navarra, 31009 Pamplona, Spain.
jcabrero@unav.es

Pablo Guindos Bretones, Faculty of Architecture and Centro de Innovación Tecnolóxica en Edificación e Enxeñería Civil (CITEEC), Universidade da Coruña, A Coruña, Spain;
Centro Nacional de Excelencia para la Industria de la Madera (CENAMAD),
Pontificia Universidad Católica de Chile, Santiago, Chile
pablo.guindos@udc.es

1 Introduction

In the design of lateral connections utilizing dowel-type fasteners, achieving ductile behaviour is a primary design objective, assumed to occur through the bending and subsequent yielding of the fasteners, coupled with the embedment of the timber. However, connections submitted to tension parallel to the grain and incorporating multiple laterally loaded dowel-type fasteners can be susceptible to premature brittle failure, such as (a) splitting; (b) row shear; (c) block shear; (d) net tensile failure; and (e) plug shear, as illustrated in Figure 1.

Previous works have addressed these brittle failure modes, from experimental testing (*Yurrita* et al., 2018; *Lemaître* et al., 2024) to the development of various analytical (*Yurrita* & *Cabrero*, 2019a,b) and numerical models (*Aquino* et al., 2024), and to the validation of models in design standards where they have been included (*Cabrero* et al., 2024).

Understanding how these brittle mechanisms affect the reliability of timber connections is of particular interest: it may not only relate to the required safety factor, but also

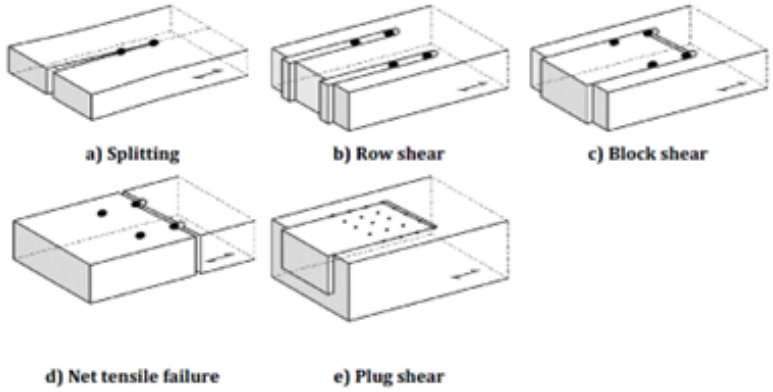

*Figure 1. Brittle failure modes in connections with dowel-type fasteners (*FprEN 1995-1-1:2024*, 2024). This paper deals only with block shear (c).*

serve as the basis for developing overstrength requirements in capacity-based design. A previous work showed the analysis of brittle failure of connections by means of a Monte Carlo analysis (*Cabrero* et al., 2019).

This study presents a statistical analysis of the block shear failure mode, grounded in the statistical definition of independent head tensile and side shear failure planes. The model makes use of typical assumptions in existing design models (i.e., definition by means of the involved failure planes, stiffness-based model for load distribution among them), and allows for a parametric analysis.

This work does not aim to provide a predictive model, but rather to analyze the inherent variation in the response associated with the block shear brittle failure mode. In the future, this approach could be extended to other failure modes, including ductile failure, to develop a more comprehensive understanding of the topic. The model provides insight into the probability distribution of resistance and, consequently, may clarify the scatter and description of the resulting failure probability distribution for this brittle failure mode.

2 Model Description

Most design models derive the block shear resistance from the resistances of the head tensile and side shear failure planes (*Cabrero* & *Yurrita*, 2018; *Marjerrison* & *Quenneville*, 2007). The probabilistic model presented in this work also makes use of these same two failure planes, as shown in Figure 2.

The probabilistic model, detailed in Section 2.1, integrates the material strengths and their associated probabilistic distributions as outlined in Section 2.2, following *JCSS* (2023). The load distribution between the involved failure planes, used in the model, is explained in Section 2.3 and is based on the stiffness-based approach developed by *Zarnani* & *Quenneville* (2012, 2013).

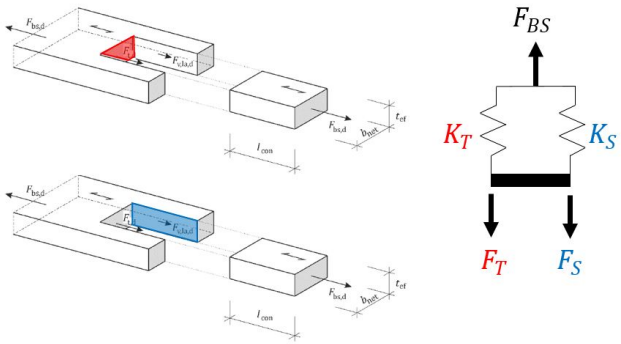

*Figure 2. Block shear failure. Involved failure planes: head tensile —red— and side shear —blue— (left); and spring model used to develop the stiffness-based approach (*Zarnani & Quenneville*, 2012) (right).*

2.1 Probabilistic framework

In a probabilistic fracture analysis, the tensile, shear, and block shear strengths can be respectively modelled as statistical variables f_T, f_S, and f_{BS} (*JCSS*, 2023). Assuming that the resistances of the planes are independent variables, the cumulative distribution of block shear failure, $P_{BS}(f_{BS})$, can be deduced in terms of the known cumulative distributions of tensile and shear strength, $P_T(f_T)$ and $P_S(f_S)$, respectively, and reads:

$$P_{BS}(f_{BS}) = 1 - (1 - P_T(f_T))(1 - P_S(f_S)). \quad (1)$$

Importantly, the above analysis may also involve the corresponding probability density functions, $p_{BS}(f_{BS})$, $p_T(f_T)$, and $p_S(f_S)$. Moreover, it incorporates the known correlation between block shear strength and the tensile and shear strengths. In this work, we assume that to relate the plane resistances to the global block shear failure mode, the load is distributed between the head and side failure planes according to their stiffness (see Section 2.3).

On the other hand, the total connection load (which at failure corresponds to the block shear resistance, F_{BS}) is obtained as the sum of the loads supported by the head tensile (F_T) and side shear (F_S) planes:

$$F_{BS} = F_T + F_S. \quad (2)$$

The load ratio for each involved failure plane may be defined as:

$$F_i = \alpha_i F_{BS}, \quad (3)$$

where α_i represents the fraction of the total load carried by the corresponding failure plane, and i refers to either the tensile (T) or shear (S) plane.

The resistance F_i can be expressed as the product of the corresponding strength f_i and area A_i, with the total block shear area A_{BS} defined as the sum of the tensile and shear

areas, i.e., $A_{BS} = A_T + A_S$. Equation (3) may then be rewritten as:

$$A_i f_i = \alpha_i A_{BS} f_{BS} \tag{3'}$$

$$f_i = \alpha_i \frac{A_{BS}}{A_i} f_{BS}. \tag{4}$$

The factor β_i may be defined to express the relation of each stress to the block shear strength as:

$$\beta_i = \alpha_i \frac{A_{BS}}{A_i}, \tag{5}$$

so that:

$$f_i = \beta_i f_{BS}, \tag{4'}$$

which allows Equation (1) to be rewritten to derive the probability distribution $p_{BS}(f_{BS})$ as:

$$p_{BS}(f_{BS}) = \beta_S(1 - (P_T(\beta_T f_{BS}))p_S(\beta_S f_{BS}) + \beta_T(1 - P_S(\beta_S f_{BS}))p_T(\beta_T f_{BS}) \tag{6}$$

Since the primary goal of this model is to analyze failure probability and the resulting statistical distributions, several simplifications have been made. Typical coefficients applied in design standards (e.g., *FprEN 1995-1-1:2024* (2024)), k_t and k_v, which account for phenomena such as uneven load distribution within the plane, are not included. Also, the effective thickness is considered to be the same for every plane (see Section 2.3).

In fact, dismissing these parameters primarily affects the quantitative resistance values. However, given that most current analytical proposals use constant values for these coefficients across all joint configurations, their omission here simply results in a uniform shift of all results. Every result is equally affected, since none of the existing proposals modify these coefficients based on connection geometry.

Consequently, the analysis of the block shear resistance parameters should be considered as qualitative. It is also worth mentioning that the block shear resistance values are not predicted as a sum or a maximum of the individual plane resistances. Instead, we examine the statistical weight of the tensile and shear modes and their interplay contributing to the block shear resistance.

2.2 Material parameters

The material description is based on the JCSS probabilistic model (*JCSS*, 2023), which specifies that the probability distributions of tensile and shear strengths follow a log-

normal distribution.

$$f(x) = \frac{1}{\sqrt{2\pi}sx} \exp\left(\frac{-\ln(x-\mu)^2}{2\sigma^2}\right) \tag{7}$$

whose parameters are derived as

$$\mu = \ln\left(\frac{f_m}{\sqrt{COV^2+1}}\right) \tag{8}$$

$$s = \sqrt{\log(COV^2+1)} \tag{9}$$

where f_m denotes the mean strength value, and COV is the coefficient of variation. It is important to note that standards such as *EN338* (2017) provide characteristic strength values; therefore, the required parameters are obtained using Equations (8) and (9).

2.3 Stiffness factors

To determine the required distribution factors, α_i, the stiffness-based model (*Zarnani* & *Quenneville*, 2012, 2013) is employed, as illustrated in Figure 2. The applied load is distributed between the planes based on their relative stiffness, and therefore

$$\alpha_T = \frac{K_T}{K_T + K_S} \tag{10}$$

$$\alpha_S = \frac{K_S}{K_T + K_S} \tag{11}$$

The tensile head plane stiffness (K_T) depends on the modulus of elasticity (E), the tensile area (A_{th}), and the connection length (L, parallel to the grain) between the first row of connectors and the loaded edge:

$$K_T = \frac{2EA_{th}}{L}. \tag{12}$$

The stiffness of the shear planes is determined based on the shear modulus (G), the total side planes area (A_{sl}), and the connection width (X_l, perpendicular to the grain) between the first and last column of fasteners. Additionally, a second component accounts for the contribution of the laterally adjacent head planes, calculated using the modulus of elasticity (E), their area (A_{tl}), and the connection length (L).

$$K_S = (1-\beta)\left(\frac{GA_{sl}}{X_l} + \frac{EA_{tl}}{10L}\right) \tag{13}$$

Table 1. Strength properties and lognormal distribution parameters for the validation tests from Hanhijärvi & Kevarinmäki *(2008).*

Strength class	$f_{t,0,m}$ [MPa]	$f_{v,m}$ [MPa]	E [MPa]	G [MPa]	μ_T	s_T	μ_S	s_S
GL28h	29	4,9	12 600	650	3,35	0,18	1,58	0,15

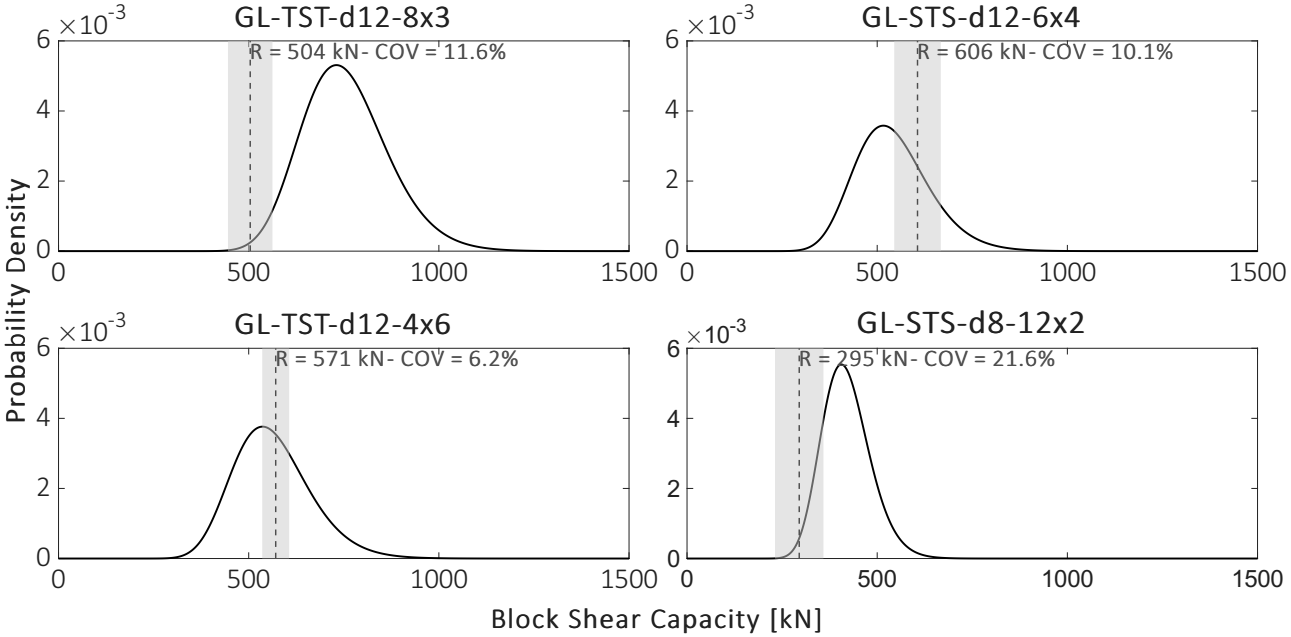

Figure 3. Distribution of block shear resistance for selected tests from Hanhijärvi & Kevarinmäki *(2008). The vertical line marks the mean experimental value and the shaded area represents the reported coefficient of variation.*

These two components are combined by weighting them according to the ratio between the unloaded edge distance (a_4) and the connection width (X_l).

$$\beta = \min\left\{0; 0,16\left(2,5 - 2\frac{a_4}{X_l}\right)^2\right\} \tag{14}$$

3 Validation

Although, as previously explained, developing a predictive model is not the objective, this section presents a preliminary validation against GL28h tests conducted by *Hanhijärvi & Kevarinmäki* (2008).

The mean strengths used—those reported in (*Hanhijärvi & Kevarinmäki*, 2008)—along with the corresponding parameters of the lognormal distribution, are summarized in Table 1. The considered coefficients of variation (COV) follow the values given for glulam in (*JCSS*, 2023): 0.15 for tension and 0.18 for shear.

The probabilistic model provides the probability density distribution of joint resistance. Four representative configurations are shown in Figure 3. Experimental results—displayed with mean values and shaded areas representing COV—fall within the predicted distribution boundaries, demonstrating the model's satisfactory qualitative performance.

Table 2. Strength properties and lognormal distribution parameters for the analysed structural timber strength classes.

Strength class	C14	GL20h	GL24h	GL32h
$f_{t,0,m}$ [MPa]	12,2	16	19,2	25,6
$f_{v,m}$ [MPa]	5	3,5	3,5	3,5
E [GPa]	7	8,4	11,5	14,2
G [GPa]	0,44	0,65	0,65	0,65
μ_T	2,46	3,07	3,25	3,54
s_T	0,29	0,18	0,18	0,18
μ_S	1,58	1,50	1,50	1,50
s_S	0,25	0,15	0,15	0,15

4 Parametric analysis

A parametric analysis is carried out by applying the developed probabilistic model to a wide range of joint dimensions, and considering a defined set of strength classes spanning from low to high values.

4.1 Geometrical parameters

The following geometrical parameters and intervals are analyzed: connection width (perpendicular to grain) between the first and last column of fasteners, X_l, spanning from 10 mm to 1 000 mm; connection length (parallel to grain) between the first row of connectors and the loaded edge, L, from 10 mm to 1 000 mm; edge distance, a_4, from 10 mm to 200 mm. Within each interval, a step size of 20 mm is applied, resulting in 11 560 analysed connection configurations.

These limit values are admittedly unrealistic and are intended solely to provide a broad overview of the trends by including extreme cases. Realistic values, obtained from a previously presented database of experimental tests (*Cabrero* et al., 2024), fall within the intervals of 17–355.6 mm for X_l, 40–1 140 mm for L, and 12–174 mm for a_4. Moreover, as results will be presented in terms of the tensile plane area ratio to the total planes area, it is noted how ratios in the same database vary between 0 and 0.4 for the tensile area ratio, *RAT*.

4.2 Mechanical properties

Four strength classes are selected: C14, GL 20h, GL 24h, and GL 32h, representing low, medium, and high strength classes, and to analyse differences among various products (solid wood and glulam). Table 2 presents the mean values of parallel tensile strength ($f_{t,0,m}$), shear strength ($f_{v,m}$), modulus of elasticity (E), and shear modulus (G) for each class, along with the required parameters for the lognormal distribution: mean value (μ) and standard deviation (s).

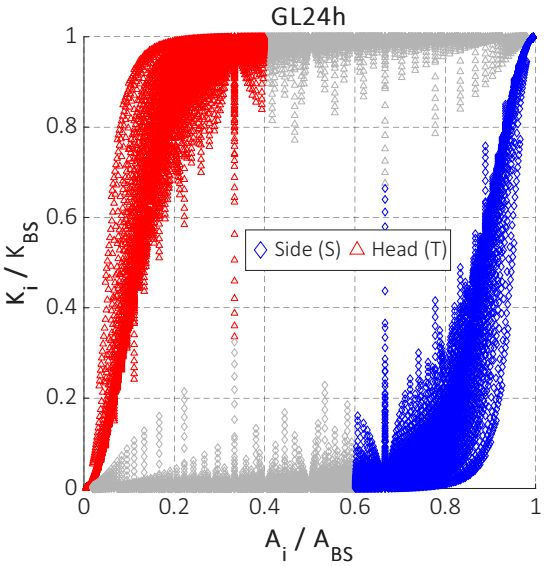

Figure 4. Relationship between plane area ratios, A_i/A_{BS}, and stiffness ratios, K_i/K_{total}. Tensile plane in red; shear planes in blue; unrealistic plane area ratios are marked in grey.

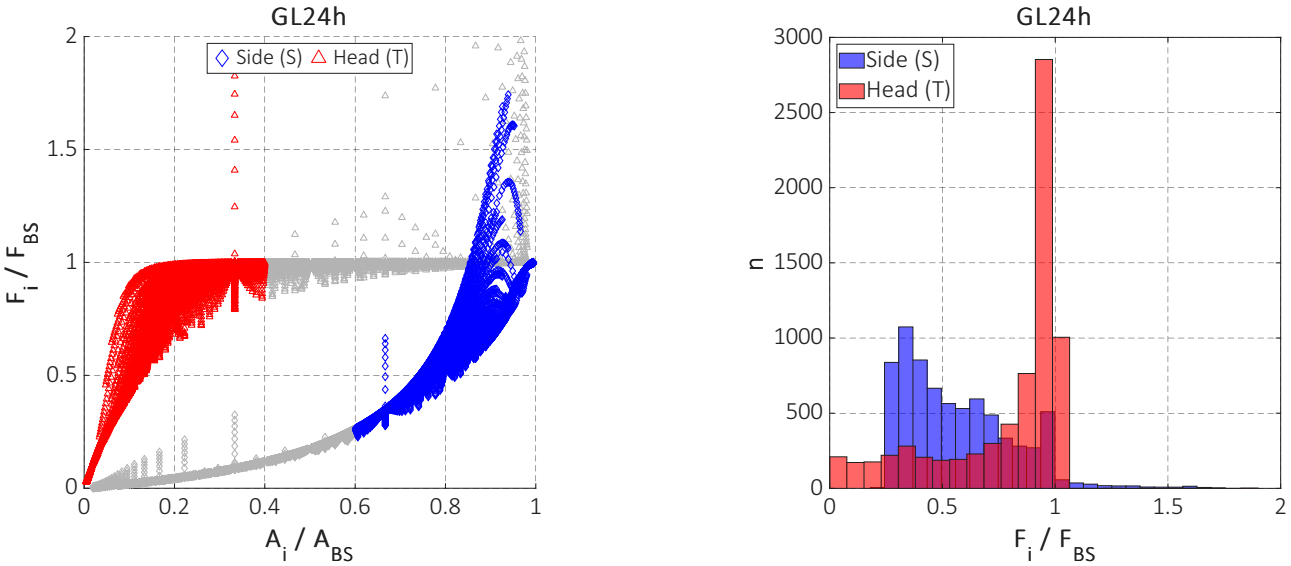

Figure 5. Resistance. Left: relationship between plane area ratios (A_i/A_{BS}) and resistance ratios (F_i/F_{BS}). Right: histogram of resistance ratios (limited to realistic area ratios). Tensile planes are shown in red, shear planes in blue, and unrealistic area ratios are marked in grey.

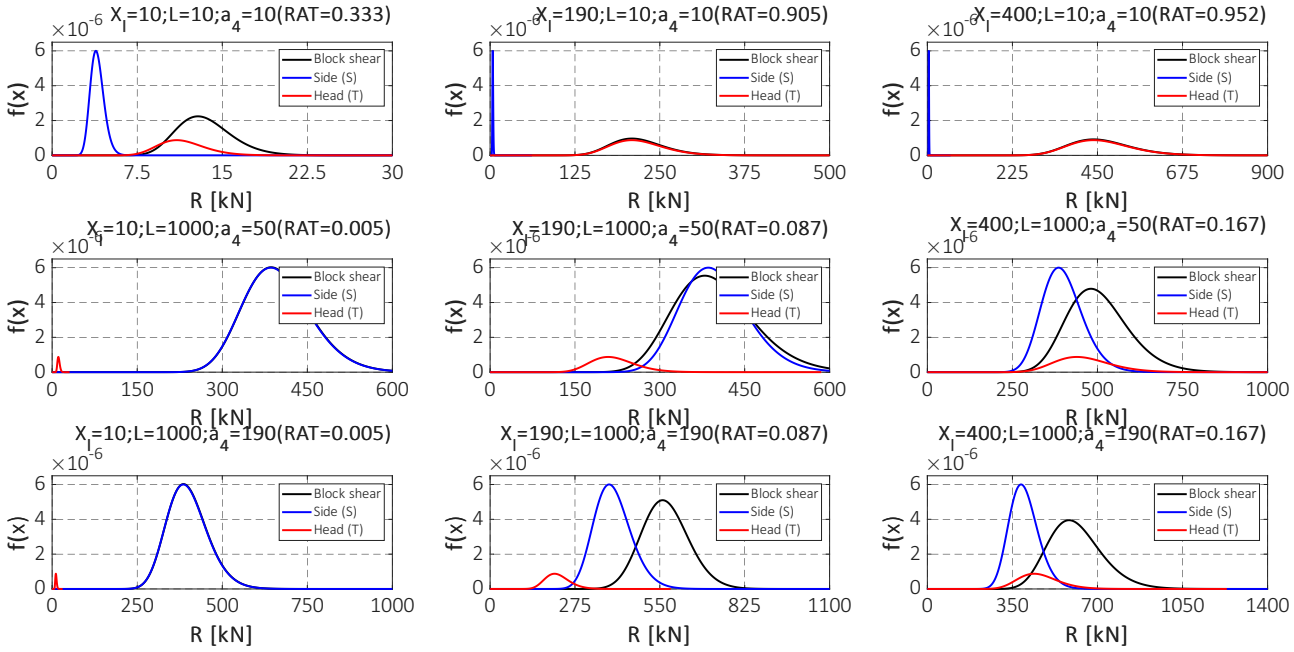

Figure 6. Relationship between the block shear (black), side shear (red) and head tensile (blue) resistances (R) for different joint geometries.

5 Results and discussion

5.1 Stiffness of the planes and load distribution

Figure 4 depicts the relationship between the area ratios of the involved planes and the resulting stiffness ratio, which controls the load distribution between the head and side planes defined by α. Each plotted point corresponds to a joint configuration within the GL24h strength class. Configurations outside the "realistic" ranges in the database are plotted in light grey. It is observed that most of the connection stiffness corresponds to the head tensile plane. The shear area ratio must increase to at least 90% to contribute to at least 50% of the overall stiffness.

Figure 5 shows the resistance ratio of each failure plane to the block shear joint resistance (mode values of the distribution are given), as well as the corresponding histogram for realistic area ratios (right). In close relation to the stiffness ratio described in Figure 4, the block shear resistance tends to be governed by the tensile plane. For joint configurations where the shear area ratio exceeds 0.8, the block shear failure tends to correspond to an interaction of both resistances (both resistance ratios lower than one). In some particular configurations with shear area ratios greater than 0.9, the resulting brittle capacity is even lower than that of the side shear planes.

5.2 Statistical distribution

The probabilistic model generates the statistical distribution of resistance for the analysed block shear failure mode, as illustrated in Figure 6, where the resulting block shear failure resistance is compared to the resistances of the involved head and side planes.

For clarity, extreme (unrealistic) cases are also presented to demonstrate how the model captures the interaction between both failure planes.

As previously shown in Figure 5, and unlike conventional design models, the resulting resistance distribution reflects a more complex interaction. The resulting resistance and its relation to the failure planes vary according to the joint geometry. In cases with reduced length and edge distance (an unrealistic 10 mm, upper row), the resistance of the side shear planes (blue) is significantly low, and the model predicts that the overall resistance mainly corresponds to the tensile one (except when the length is equally reduced—left side—where an interaction is shown).

For long connections (lower row, L = 990mm), although the resistance of the side planes increases substantially, the greater stiffness of the tensile plane still influences the resulting resistance. The interaction is evident in the plotted figures, which transition from resembling the shear resistance distribution to the tensile resistance distribution as the connection width increases (from left—reduced width—to right—medium width—in Figure 5).

5.3 Resistance

Figure 7 illustrates the general trends for the mode of the block shear resistance (black), along with the mode of the tensile (red) and shear plane (blue) resistances. The envelope of the entire parametric analysis allows describing the main patterns. The shear resistance shows a plateau up to approximately 0.4 *RAT* (the tensile area ratio, defined as $RAT = A_T/A_{BS}$), followed by a gradual decrease for higher values. Conversely, the tensile resistance increases in a quasi-linear manner from the origin.

Although similar, subtle differences emerge among the different analysed strength classes. The block shear resistance reflects the interaction between these two planes, exhibiting a local maximum at low tensile areas and a quasi-parabolic response (clearer for lower strength classes) with a local minimum around 0.1 *RAT*. Beyond this minimum, the block shear resistance increases seemingly parallel to the tensile plane resistance.

As the strength class increases, the local minimum tends to flatten into a plateau, while the shear resistance (noting that shear strength increase is relatively lower as the strength class increases) decreases. For all analysed glulam classes, the block shear resistance consistently exceeds that of the individual planes. However, for the C14 class, up to a tensile area ratio of 0.3 *RAT*, the block shear resistance is lower than the shear plane resistance. Nonetheless, the global resistance remains higher than the tensile resistance across all cases, though shaped by the contribution of the side shear planes.

Figure 8 illustrates significant configurations for strength class GL24h (similar trends observed across other strength classes) to provide broader insight into the different associated trends. As the connection width increases (Figure 8, left), so does the resistance.

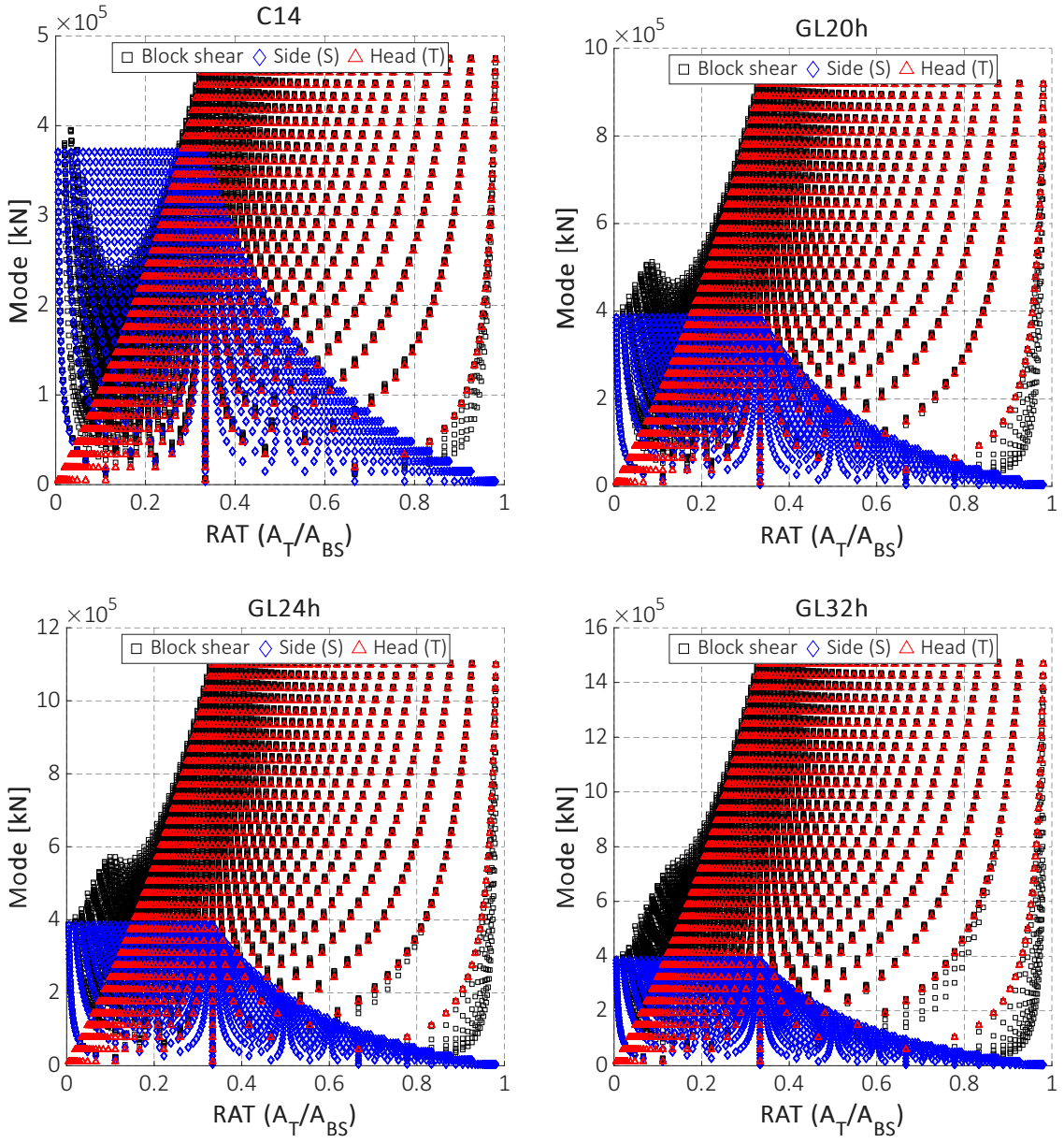

Figure 7. Resistance. Mode values for block shear (black), side shear (red) and head tensile (blue) resistances for varying tensile area ratio, RAT.

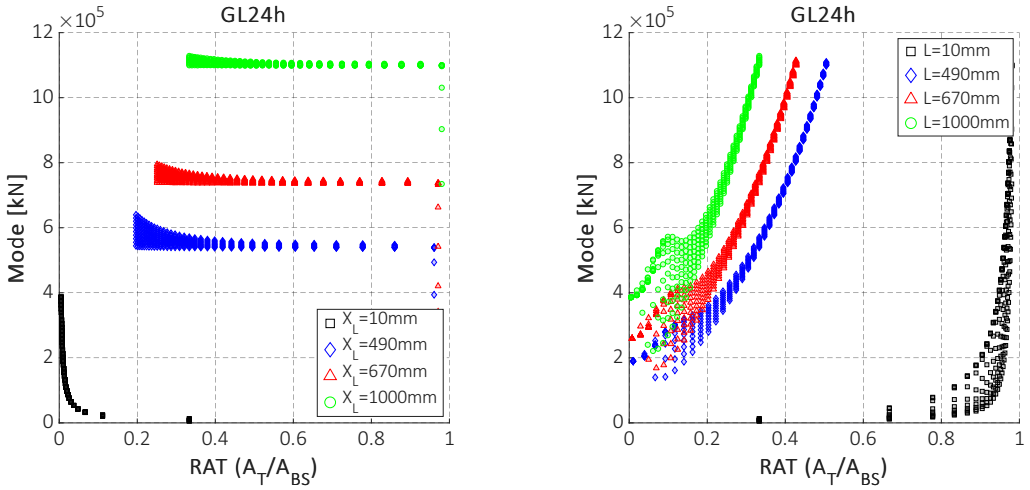

Figure 8. Resistance. Mode values variation for given connection widths (X_L, left) and lengths (L, right).

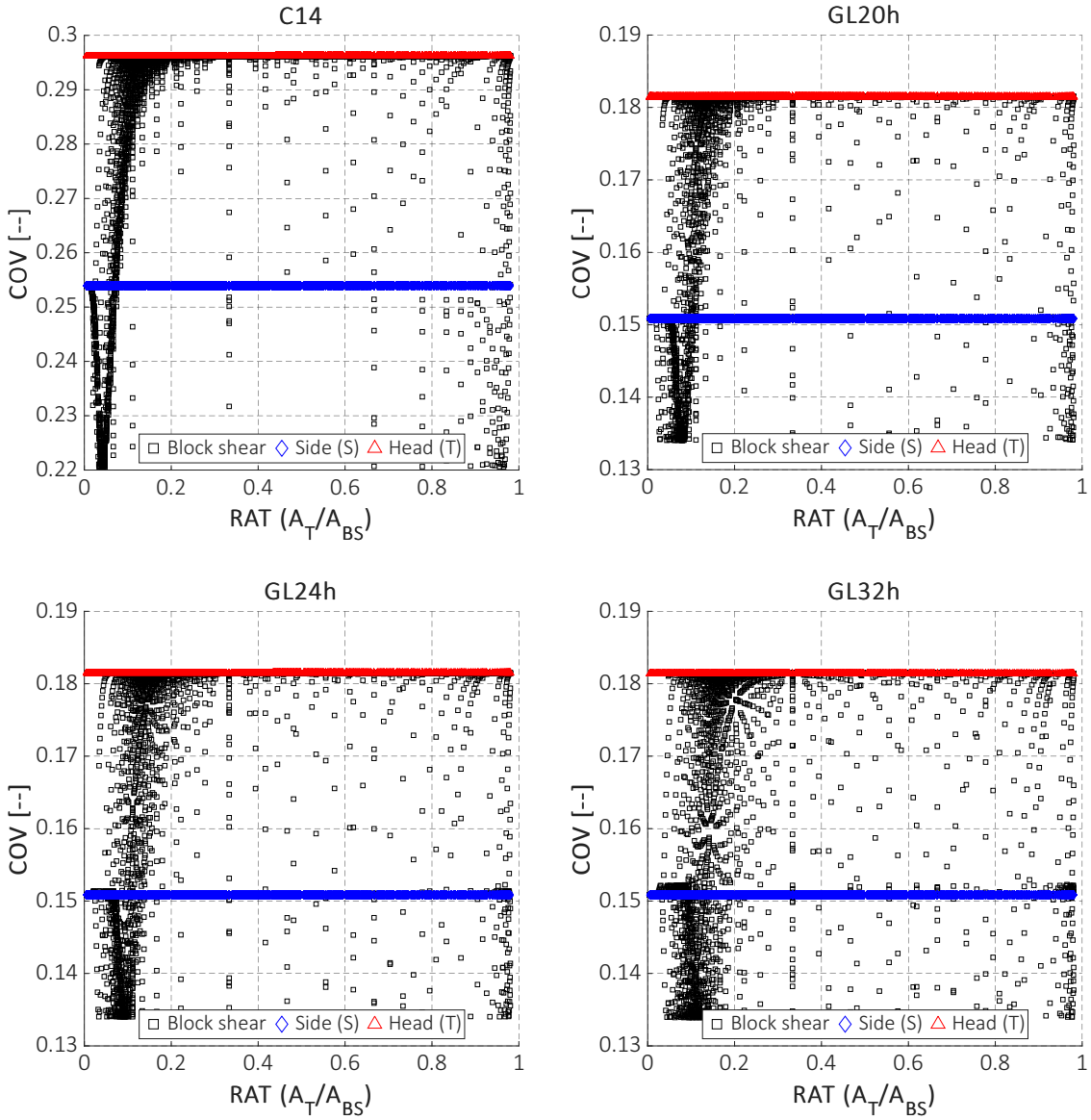

Figure 9. Coefficient of variation (COV) for block shear (black), side shear (red) and head tensile (blue) resistances for varying tensile area ratio, RAT

A vertical scatter is observed across all cases, especially at intermediate widths, diminishing with increasing width and tensile area ratio. The trend follows a hyperbolic curve with respect to tensile area, becoming less steep as width grows.

Increasing the connection length (which increases the area of the side shear planes, Figure 8, right) reveals a quasi-parabolic response. The scatter reduces as the tensile area ratio increases, with results clustering on the left side of the graph, representing more realistic area ratios.

At the characteristic resistance level (not shown), the qualitative trends remain consistent, though resistance values are lower.

5.4 Coefficient of variation (COV)

Figure 9 shows the coefficient of variation (COV) for all analyzed configurations, revealing a consistent response across the parametric analysis. The COV of the block shear

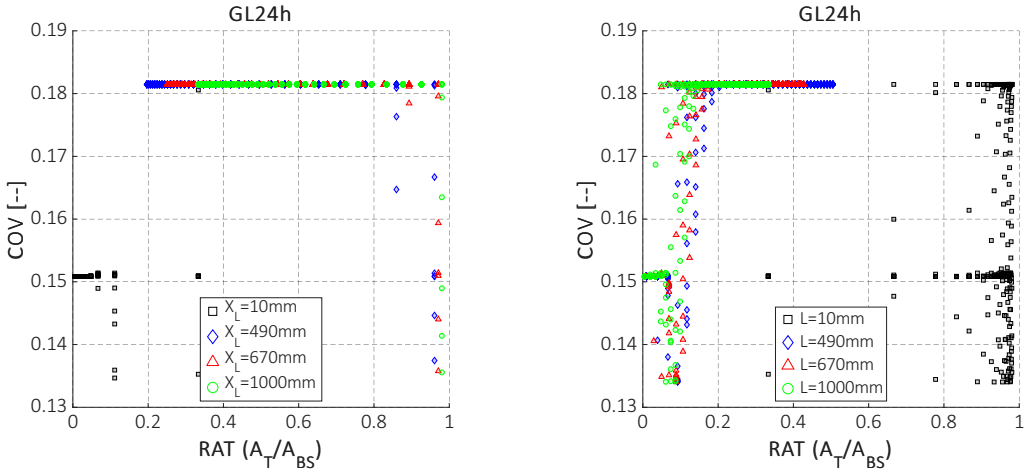

Figure 10. Coefficient of Variation (COV) values variation for given connection widths (X_L, left) and lengths (L, right).

mode tends to correspond to that of the dominant plane. Specifically, as the tensile plane resistance becomes decisive, the resulting COV aligns with the tensile plane's COV (red line). Conversely, for low tensile area ratios, it matches the shear plane's COV. Intermediate cases arise where the block shear COV is even lower than those of the individual planes. These reduced-variation zones occur within the realistic interval of the analysis.

The C14 class shows a slightly lower dispersion than the glulam classes. Moreover, the tensile area ratio at which the block shear COV shifts to that of the tensile strength is also smaller for C14, reaching a minimum around 0.05 *RAT* and matching the tensile plane's COV near 0.1 *RAT*. In the glulam classes, the minimum occurs for a slightly greater tensile area ratio (around 0.1 *RAT*), and the minimum COV region broadens as strength class increases, reflecting a greater spread in these cases.

The influence of geometric parameters is further detailed in Figure 10. For medium-wide to wide connections (some of which are already unrealistic, as the maximum realistic tensile ratio is around 0.4), the COV corresponds to that of the tensile plane. When increasing the connection length (reduced tensile area ratio, and within the realistic interval), COV may even be lower than those of the individual strength parameters. Again, these behaviours hold consistently across all strength classes analysed.

6 Conclusions

A probabilistic model for block shear brittle failure is introduced. The theoretical analysis allows examining the statistics of failure of the samples, in terms of the statistics of each failure mode, i.e., tensile and shear. The model is based on previous theoretical approaches, which deduce the load distribution among the involved failure planes (*Zarnani* & *Quenneville*, 2012, 2013), and allow access to each independent strength probability function (*JCSS*, 2023). Thus, the new probabilistic model effectively captures the combined effect of tensile and shear planes.

The results of the performed parametric analysis show how the head tensile plane tends to be the stiffest, taking most of the connection load. Conversely, the shear plane is the weakest, confirming the common tendency for failure to initiate in these side planes (most easily observed in plug shear modes). This significant influence of the tensile plane is a consequence of the stiffness model used (*Zarnani* & *Quenneville*, 2012, 2013) and the assumed parameter values. Further experimental or numerical validation of the failure evolution pattern would be beneficial.

The current model enables determination of the block shear strength distribution. The analysis shows how the resulting scatter is closely related to the material variability of the involved shear and tensile resistances. For connections with reduced tensile planes, the COV tends to correspond to that of the shear strength, while in connections governed by the tensile plane, the variability corresponds to that of the tensile plane. However, for certain (realistic) area ratios (around 0.1–0.15 *RAT*), the resulting variation may be lower than that of the individual material properties.

This study focuses exclusively on the stressed timber volume and brittle failure in isolation, specifically for block shear mode. However, it could be further expanded to include the remaining brittle and ductile failure modes to provide a comprehensive understanding of brittle failure in joints. Such future work would provide a theoretical basis to assess possible overstrength values.

Acknowledgments

The financial support provided by the Spanish Ministerio de Ciencia e Innovación and Fondo Europeo de Desarrollo Regional under contract PID2020-118569GB-C21 MINECO/FEDER UE is gratefully acknowledged.

7 References

Aquino, C. D.; M. Schweigler; L. Rodrigues; R. Lemaître; J.-F. Bocquet; J. M. Branco & T. K. Bader (2024). “The Effective Timber Thickness for Brittle Failure Assessment of Dowel-Type Connections.” In: *INTER. International Network on Timber Engineering and Research. Meeting 57 (Padova, Italy)*. 57-7-7.

Cabrero, J. M.; N. Lopez-Rodriguez; T. Tannert; A. Salenikovich & Y. H. Chui (2024). “Brittle Failure Modes of Connections with Dowel-Type Fasteners Loaded Parallel to the Grain: A Comparison Between Eurocode 5 and CSA O86.” In: *INTER. International Network on Timber Engineering and Research. Meeting 57 (Padova, Italy)*. 57-7-8.

Cabrero, J. M. & M. Yurrita (2018). “Performance of the Different Models for Brittle Failure in the Parallel-to-Grain Direction for Connections with Dowel-Type Fasteners.” In: *INTER. International Network on Timber Engineering and Research. Meeting 51 (Tallinn, Estonia)*. 51-7-12.

Cabrero, J. M.; D. Honfi; R. Jockwer & M. Yurrita (2019). “A probabilistic study of brittle failure in dowel-type timber connections with steel plates loaded parallel to the grain.” In: *Wood Material Science & Engineering* 14.5, pp. 298–311. DOI: 10.1080/17480272.2019.1645206.

EN338 (2017). *EN338. Timber structures – Strength clases*. Comité Européen de Normalisation (CEN).

FprEN 1995-1-1:2024 (2024). *Design of timber structures – Part 1-1: General – Common rules and rules for buildings*. Comité Européen de Normalisation (CEN).

Hanhijärvi, A. & A. Kevarinmäki (2008). *VTT publications 677: Timber Failure Mechanisms in High-Capacity Dowelled Connections of Timber to Steel*. Espoo: VTT. ISBN: 9789513870904.

JCSS (2023). “JCSS Probabilistic Model Code.” In: chap. 28. Properties of Timber. URL: https://jcss-pmc.github.io/.

Lemaître, R.; D. Lathuillière & J.-F. Bocquet (2024). “Design Brittle Failure Capacities of Connections with Dowel-Type Fasteners Laterally Loaded Parallel to Grain and Reinforced.” In: *INTER. International Network on Timber Engineering and Research. Meeting 57 (Padova, Italy)* 57-7-10.

Marjerrison, M. & P. Quenneville (2007). “Models for the Predictions of the Ductile and Brittle Failure Modes (Parallel-to-Grain) of Timber Rivet Connections.” In: *CIB-W18. International Council for Research and Innovation in Building and Construction. Meeting 40(Bled, Slovenia)*. 40-7-6.

Yurrita, M. & J. M. Cabrero (2019a). “Effective Thickness of the Wood Member in a Timber-to-steel Connection with Large Diameter under Brittle Failure.” In: *INTER. International Network on Timber Engineering and Research. Meeting 51 (Tacoma, USA)*. 52-7-5.

Yurrita, M. & J. M. Cabrero (2019b). “New Analytical Model for Brittle Failure in the Parallel-to-grain Direction of Timber Connections with Large Diameter Fasteners.” In: *INTER. International Network on Timber Engineering and Research. Meeting 51 (Tacoma, USA)*. 52-7-7.

Yurrita, M.; J. M. Cabrero & P. Quenneville (2018). “Multiple Shear Plane Timber Connections with Slotted-in Steel Plates and Dowel-type Fasteners: a Study of the Brittle Failure Mode in the Parallel-to-grain Direction.” In: *INTER. International Network on Timber Engineering and Research. Meeting 51 (Tallinn, Estonia)*. 51-7-10.

Zarnani, P. & P. Quenneville (2012). “A Stiffness-based Analytical Model for Wood Strength in Timber Connections loaded Parallel to Grain: Riveted Joint Capacity in Brittle and Mixed Failure.” In: *CIB-W18. International Council for Research and Innovation in Building and Construction. Meeting 45 (Växjö, Sweden)*. 45-7-1.

Zarnani, P. & P. Quenneville (2013). “Design Procedure to Determine the Capacity of Timber Connections under Potential Brittle, Mixed and Ductile Failure Modes.” In: *CIB-W18. International Council for Research and Innovation in Building and Construction. Meeting 46 (Vancouver, Canada)*. 46-7-3.

DISCUSSION

The paper was presented by N Lopez

P Dietsch commented that tensile stresses perpendicular to grain occur when the dowel moves into the wood; furthermore, shrinkage cracks often exit. These are not considered in analysis based on short-term testing. He commented that tensile and side plane shear resistance should not be added per points discussed previously.

C Demirci discussed parametric study where if a_4 is small one would get block shear failure. Minimum a_4 should start from a value bigger than 10 mm in the parametric study. JM Cabrero responded that they were considering plug shear in this study.

A Frangi, T Tannert and JM Cabrero discussed that the addition of resistances of different planes is incorrect.

Load-bearing behaviour of PMPF connections with air gap between PMPF and timber

David Staiger, BE Ingenieure GmbH, Karlsruhe, Germany

Hans Joachim Blass, BE Ingenieure GmbH, Karlsruhe, Germany

Keywords: punched metal plate fastener, PMPF, nail plate, air gap

1 Introduction

In recent years, inspections of trusses with punched metal plates fasteners (PMPF) have repeatedly revealed problems due to the PMPF detaching from the timber members (see Figure 1.1). PMPF not completely pressed in show a reduced nail load-bearing capacity. The detaching of the PMPF from the timber can therefore have a significant impact on the structural stability.

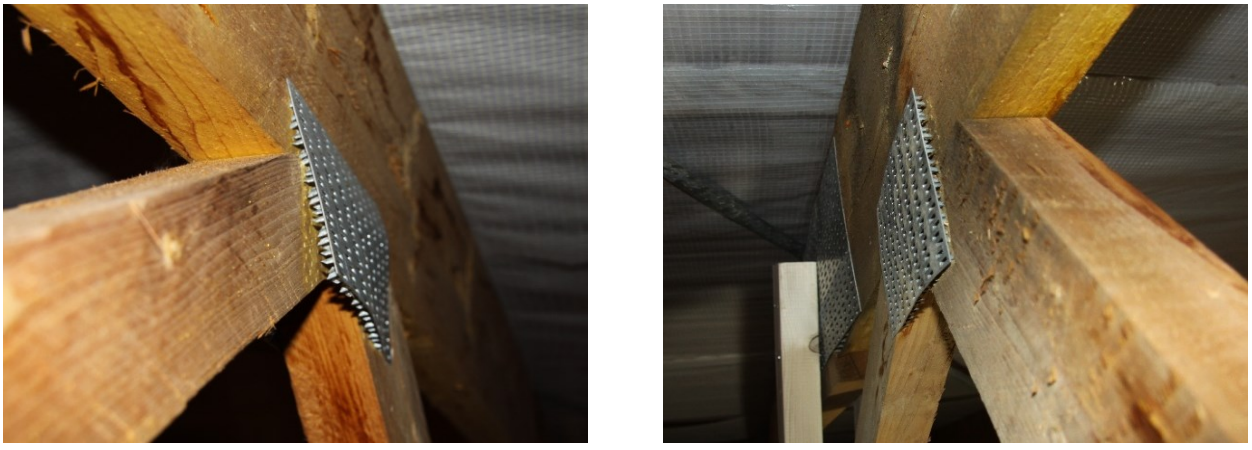

Figure 1.1. PMPF detached from the timber member

There are currently no standards or scientific studies on the load-bearing behaviour of PMPF joints with air gaps between metal plate and timber. In the literature, Paevere et al. (2009) give a general indication of a loss of the nail load-bearing capacity of more than 25 % for an air gap of 1 mm between the PMPF and the timber component. The Truss Plate Institute of Canada (2024) specifies a stepwise reduction in nail load-bearing capacity depending on the clear distance between metal plate and timber: Nails with an air gap of less than 0.8 mm are considered fully effective, nails with

an air gap between 0.8 mm and 1.6 mm are considered 60 % effective and nails with an air gap equal to or greater than 1.6 mm are considered ineffective. In EN 14250 (2010) distances between the wood surface and the metal plate of no more than 1 mm, on a maximum of 25 % on each joint area are allowed. The Expert-Commission on Building Technology of the Building Ministers in Germany (2020) recommends a static assessment of the construction as soon as the air gap between metal plate and wood component exceeds the criterion of EN 14250 (2010). However, static assessments of non-standard PMPF joints are not possible due to the lack of values for the load-bearing capacity and the stiffness for PMPF with an air gap. The characteristic values of PMPF are determined based on tests in accordance with EN 1075 (2015). Air gaps between the PMPF and the timber component are not considered in EN 1075 (2015). A mechanical model, such as the one available in Eurocode 5 (2004) to determine the load-bearing capacity of steel-timber connections with dowel-type fasteners is generally not used for PMPF joints. It is therefore not possible to apply the model for fasteners with interlayers according to Blaß and Laskewitz (2003), to mathematically capture the effects of an air layer between the PMPF and the timber member on the load-bearing capacity of the connection.

As part of a research project, tests were carried out in cooperation with Karlsruhe Institute of Technology (KIT) to determine the load-bearing capacity and stiffness of PMPF joints with air gaps between the PMPF and the wooden component. Accompanying the tests, a computational model to calculate the load-bearing capacity of (partially detached) PMPF was developed. The most important results of the research project are summarised.

2 Tests

2.1 General

The tests were carried out on the basis of EN 1075 (2015). Different angles α between force and main direction of the PMPF and angles β between force and grain direction of the timber components were considered. For each load direction test series with four different, constant air gap thicknesses between metal plate and timber component were carried out, as well as a test series with pressed-in PMPF with varying air gap. The test programme is summarized in Table 1.

Table 1. Test programme.

Test series	Angle α	Angle β	Air gaps	Number of tests
A0/0	0°	0°	0 mm, 2 mm, 4 mm, 6 mm, inclined	5 for each air gap thickness
A90/0	90°	0°	0 mm, 2 mm, 4 mm, 6 mm, inclined	5 for each air gap thickness
A0/45	0°	45°	0 mm, 2 mm, 4 mm, 6 mm, inclined	5 for each air gap thickness
A0/90	0°	90°	0 mm, 2 mm, 4 mm, 6 mm, inclined	5 for each air gap thickness
A90/90	90°	90°	0 mm, 2 mm, 4 mm, 6 mm, inclined	5 for each air gap thickness

2.2 Materials

All test specimens were manufactured with punched metal plates according to Z-9.1-855 (2023) with nail lengths of 19.5 mm. Softwood was used for the timber components. The selection of the wood for the test specimens in terms of density was made in accordance with EN 28970 (1991), method 2, based on a characteristic density of 350 kg/m^3. The surface of the timber components was planed. The timber was conditioned in service class 2 according to Eurocode 5 (2004) before the test specimens were manufactured and until the tests were carried out.

2.3 Manufacturing of the test specimens

The PMPF were pressed in by surface pressure using a testing machine of the Research Centre for Steel, Timber and Masonry, KIT. For the different constant air gaps between the metal plate and the wooden component the testing machine was operated deformation-controlled and the PMPF were pressed into the wooden components to the desired depths. For the backs of the test specimens, negative templates of the PMPF with appropriate depths were prepared. The inclined pressing-in of the PMPF was achieved by applying the pressure eccentrically to the plates. Figure 2.1 and Figure 2.2 show exemplary views of the test specimens.

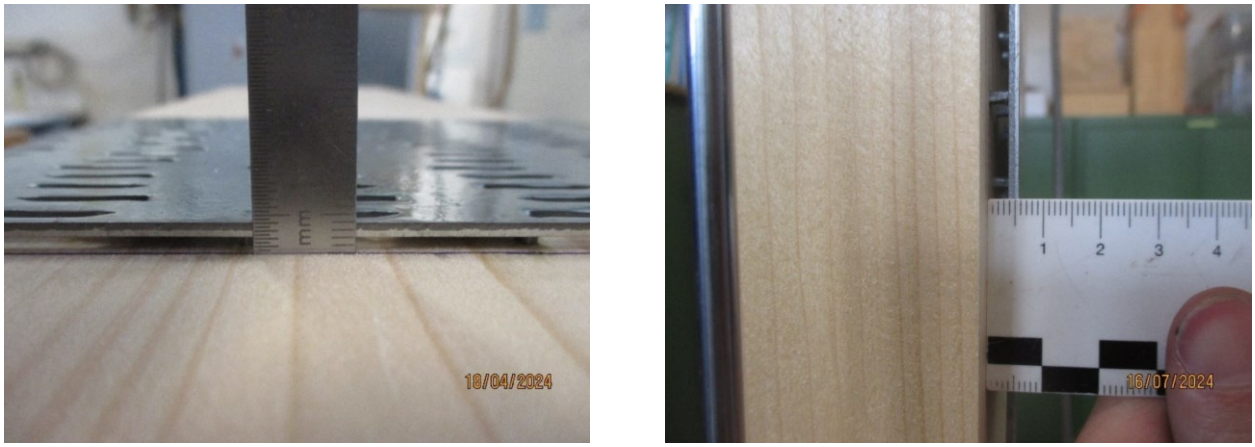

Figure 2.1. Test specimen with constant air gaps t_{air} ≈ 2 mm (left) and t_{air} ≈ 4 mm (right).

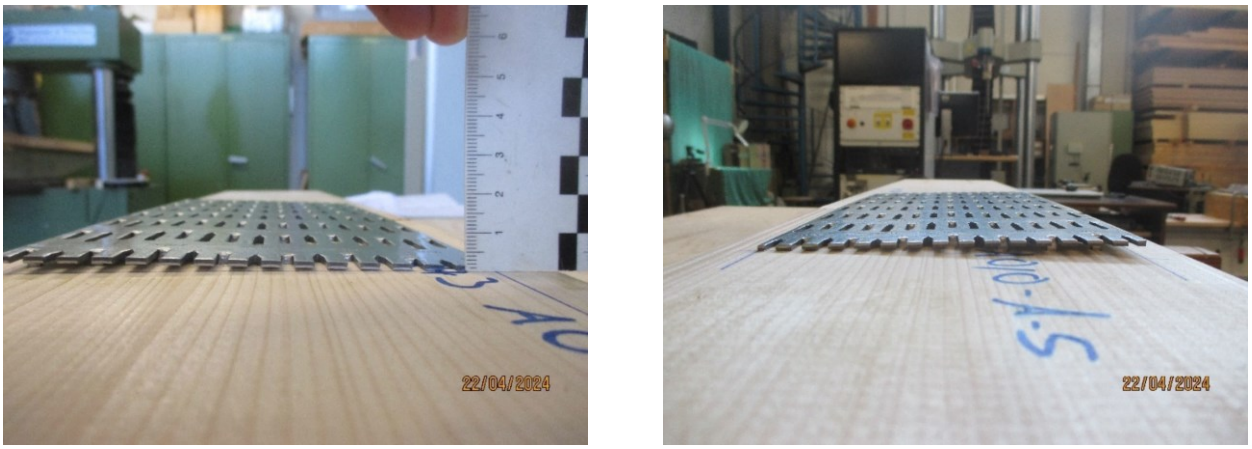

Figure 2.2. Test specimen with inclined pressed-in PMPF.

2.4 Automatic image-based recording of PMPF connections

As part of the research project, the Institute of Photogrammetry and Remote Sensing, KIT, developed an optical recording technique to automatically determine the distance between the PMPF surface and the surface of the wooden components (see Figure 2.3). This made it possible to determine the thicknesses of the air gaps between the PMPF and the timber with an accuracy of 0.01 mm for all test specimens.

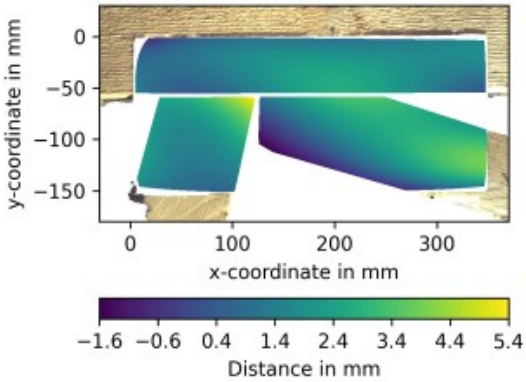

Figure 2.3. Graphical visualisation of optical detected distances between PMPF and wooden component Michel, Ulrich (2025).

2.5 Test results

2.5.1 Load-bearing capacity and stiffness for constant air gap thicknesses

Table 2. Anchorage capacities and stiffnesses for PMPF with constant air gap.

Test series	Angle α in°	Angle β in°	$t_{air,m}$ in mm	$t_{air,m,rel}$ -	$f_{a,\alpha,\beta,m}$ in MPa	$f_{a,\alpha,\beta,m,rel}$ -	$K_{s,\alpha,\beta,m}$ in N/mm^3	$K_{s,\alpha,\beta,m,rel}$ -
A0/0-X-1	0	0	0.00	0.00	2.69	1.00	3.03	1.00
A0/0-X-2	0	0	1.57	0.08	2.05	0.76	2.65	0.87
A0/0-X-3	0	0	3.38	0.17	1.65	0.61	2.14	0.71
A0/0-X-4	0	0	5.48	0.28	1.22	0.46	2.01	0.66
A90/0-X-1	90	0	0.00	0.00	2.11	1.00	6.69	1.00
A90/0-X-2	90	0	1.67	0.09	1.72	0.81	5.54	0.83
A90/0-X-3	90	0	3.56	0.18	1.34	0.64	4.95	0.74
A90/0-X-4	90	0	5.78	0.30	1.00	0.47	4.01	0.60
A0/45-X-1	0	45	0.00	0.00	2.12	1.00	3.51	1.00
A0/45-X-2	0	45	2.03	0.10	1.82	0.86	3.24	0.92
A0/45-X-3	0	45	3.91	0.20	1.48	0.70	2.72	0.77
A0/45-X-4	0	45	5.77	0.30	1.10	0.52	2.34	0.67
A0/90-X-1	0	90	0.00	0.00	1.70	1.00	5.12	1.00
A0/90-X-2	0	90	1.61	0.08	1.55	0.91	4.04	0.79
A0/90-X-3	0	90	3.75	0.19	1.31	0.77	2.93	0.57
A0/90-X-4	0	90	5.72	0.29	1.06	0.62	2.68	0.52
A90/90-X-1	90	90	0.00	0.00	1.45	1.00	11.3	1.00
A90/90-X-2	90	90	1.91	0.10	1.39	0.96	7.54	0.67
A90/90-X-3	90	90	3.95	0.20	1.26	0.87	5.06	0.45
A90/90-X-4	90	90	5.81	0.30	0.98	0.68	3.73	0.33

Table 2 contains test results for the mean anchorage capacities $f_{a,\alpha,\beta,m}$ and the mean stiffnesses $K_{s,\alpha,\beta,m}$, as well as the measured average air gap thicknesses $t_{air,m}$ per test series. The anchorage capacities were converted with reference to the characteristic density ρ_k = 350 kg/m^3 using the factor $(\rho_k/\rho)^{0,5}$. The angles α and β are indicated in each case. The air gap thicknesses are also specified in relation to the nail length with $t_{air,m,rel}$. Furthermore, the relative load-bearing capacity $f_{a,\alpha,\beta,m,rel}$ (and relative stiffness $K_{s,\alpha,\beta,m,rel}$) is specified in relation to the load-bearing capacity (and stiffness) of the respective test arrangement without air gap. The graphs in Figure 2.4 and Figure 2.5 illustrate the numerical values of Table 2. For the test series A0/0 and A90/0, with β = 0°, the reductions in load-bearing capacity due to air gaps were most pronounced. For the test series A0/45, A0/90 and A90/90, with $\beta \neq 0°$, the reduction in load-bearing capacity due to air gaps was lower. It should be noted that in the experiments with $\beta \neq 0°$ the failure of the connections was in most cases due to a combination of failure due to tension perpendicular to the grain of the wood and anchorage failure.

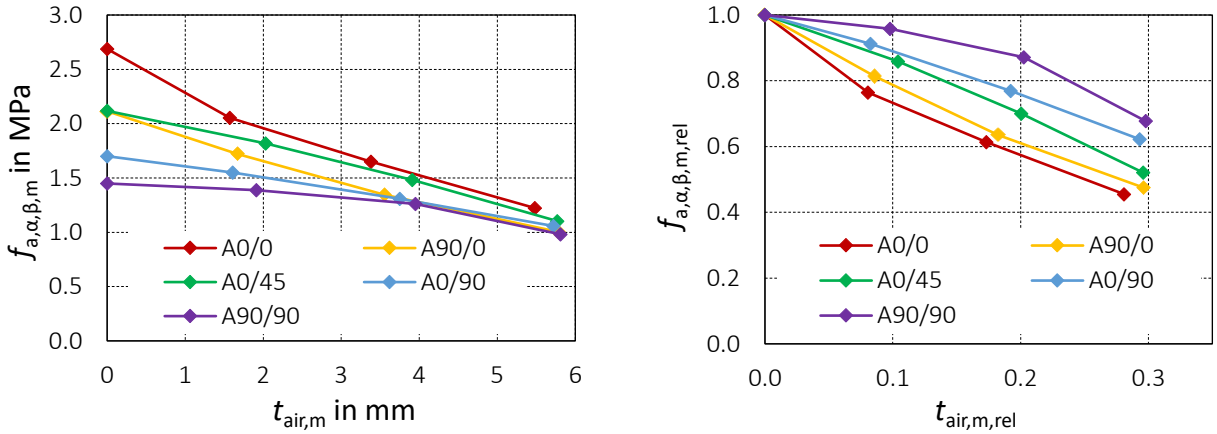

Figure 2.4. Nail load-bearing capacity $f_{a,\alpha,\beta,m}$ depending on air gap thickness $t_{air,m}$ (left) and relative nail load-bearing capacity $f_{a,\alpha,\beta,m,rel}$ depending on the relative air gap thickness $t_{air,m,rel}$ (right).

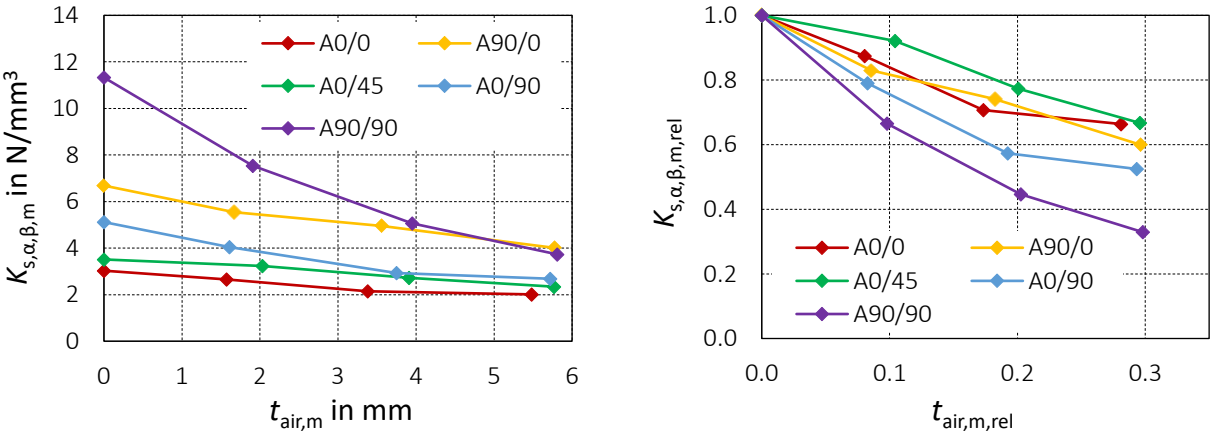

Figure 2.5. Stiffness $K_{s,\alpha,\beta,m}$ depending on air gap thickness $t_{air,m}$ (left) and relative stiffness $K_{s,\alpha,\beta,m,rel}$ depending on the relative air gap thickness $t_{air,m,rel}$ (right).

2.5.2 Load-bearing capacity and stiffness for inclined pressed-in PMPF

The results of the inclined pressed-in PMPF are compared taking their average air gap thicknesses as a reference value to the results of PMPF with a constant air gap. For

this, in Figure 2.6 the results for the inclined pressed-in PMPF are additionally entered as crosses in the graphs from Figure 2.4 and Figure 2.5 (test series "…-X-5"). The tests indicate that, by taking the average air gap thickness as a reference value, the load-bearing behaviour of the non-constant pressed-in PMPF comes close to that of PMPF with a constant air gap thickness.

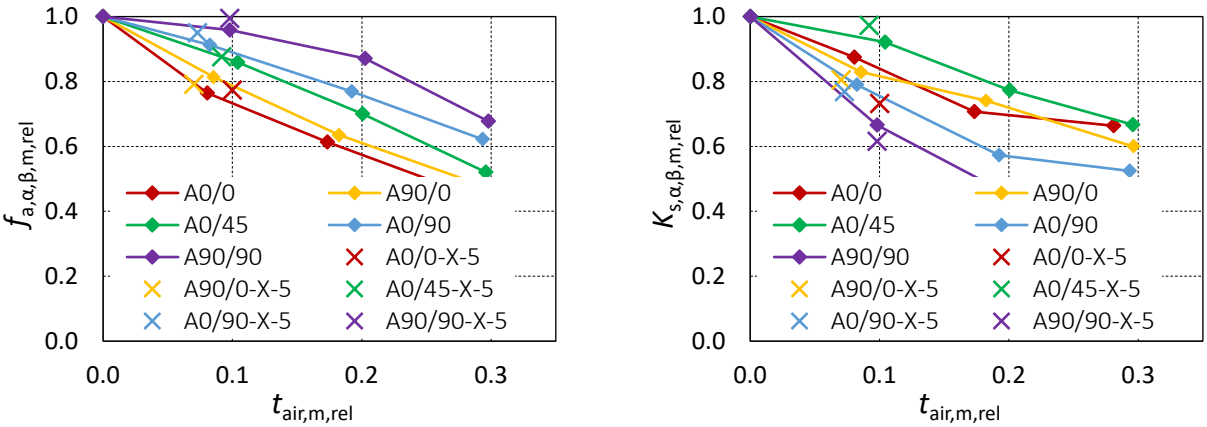

Figure 2.6. Relative load-bearing capacities $f_{\alpha,\alpha,\beta,m,rel}$ (left) and relative stiffness $K_{s,\alpha,\beta,m,rel}$ (right) depending on the relative air gap thickness $t_{air,m,rel}$ for inclined pressed-in PMPF

2.5.3 Stiffness independent of load direction

The stiffness of PMPF K_s generally used for the design of PMPF constructions is derived from the mean value of the slip moduli of all tested angles α and β. Figure 2.7 shows the change in the mean stiffness K_s (and relative stiffness $K_{s,rel}$) of all tested load directions as a function of the mean air gap thickness $t_{air,m,}$ (and relative air gap thickness $t_{air,m,rel}$) of all tested load directions.

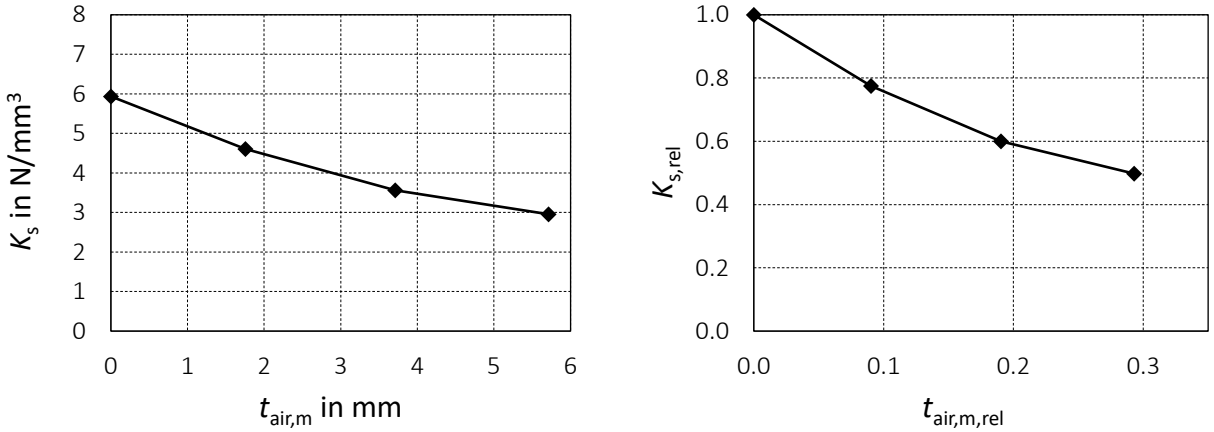

Figure 2.7. Mean total stiffness K_s as a function of the mean air gap thickness $t_{air,m}$ (left) and relative total stiffness $K_{s,rel}$ as a function of the relative air gap thickness $t_{air,rel}$ (right).

3 Computational model

3.1 General

The equations presented below for calculating the nail load-bearing capacity of PMPF are based on the design method from section 8.2 of Eurocode 5 (2004) for the load-bearing capacity of dowel-type fasteners. The equations of Eurocode 5 (2004) are

modified for the specific properties of the PMPF “Wolf 20W” according to Z-9.1-855 (2023). Additionally, the equations are extended by the method according to Blaß, Laskewitz (2003) for fasteners with interlayers.

3.2 Load-bearing capacity depending on load direction

3.2.1 Angle α between force and main direction of the PMPF

The nails of the PMPF according to Z-9.1-855 (2023) have an approximately rectangular cross section. This results in a dependence of the embedment strength and the nail’s yield moment of the angle α between the force and the main direction of the plate. The dependence of the embedment strength results from the change in the nail-width perpendicular to the direction of force with changing angle α. The dependence of the yield moment results from the change in the plastic section modulus with changing angle α. The equations therefore use the nail width d_α, which describes the nail width projected perpendicular to the direction of force, and the plastic section modulus $W_{pl,\alpha}$, which considers the change of the bending resistance of the nail, when α changes.

3.2.2 Angle β between force and grain direction

The slip of PMPF connections when reaching the maximum load, especially when loaded at right angles to the grain direction of the timber component, is usually less than 5 mm. However, the embedment strength of wood according to EN 383 (2007) is usually determined at deformations of 5 mm. From the diagrams from Yasumura and Sawata (2000) shown in Figure 3.1, it is obvious that for small deformations of e.g. 1-2 mm, the embedment stress for loads perpendicular to the grain is significantly lower than for the same deformation for loads parallel to the grain. To take this effect into account, the embedment strength for nails of PMPF is reduced according to equation (8.31) of Eurocode 5 (2004) as a function of the angle β between force and grain direction.

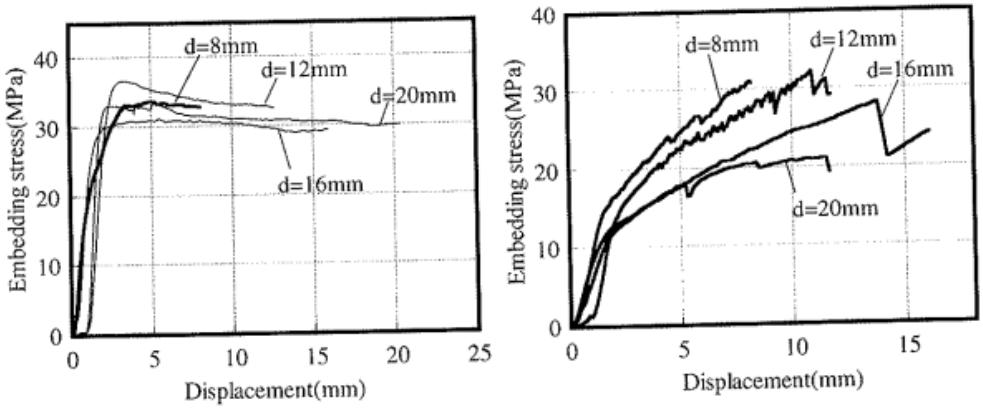

Figure 3.1. Embedding stress over the displacement in the wood for loads parallel to the grain (left) and perpendicular to the grain (right) according to Yasumura, Sawata (2000).

3.3 Position of plastic hinge

The production-related bending of the nails of PMPF leads to a hardening of the steel by cold forming close to the nail root. As a result, the yield moment for laterally loaded nails is not located directly in the shear plane between PMPF and timber, but at a distance a_y from the plate surface. This can be seen in the close-up view of the cross section of the failure points of punched metal plate nails after testing the ductility of the nail root in accordance with EN 1075 (2015), shown in Figure 3.2. Although the largest bending moment in this test occurs at the plate surface, the failure point is located at a distance from the plate surface. The failure mechanism of laterally loaded dowel type fasteners with a yield moment at a distance a_y is derived using the example of screws in Blaß et al. (2004) (see Figure 3.2) and is taken into account in the calculation model for PMPF (assumption: $a_y = 0.8 \cdot t$, where t is the thickness of the steel plate).

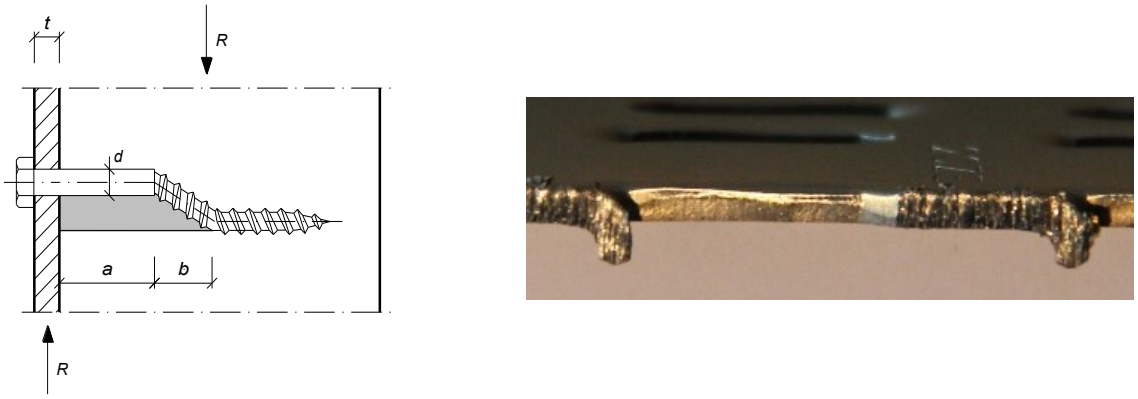

Figure 3.2. Steel wood connection with wood screw and thick steel plate, two plastic hinges in the threaded area according to Blaß et al. (2004) (left) and failure points after bending test of the nail root (right).

3.4 Rope effect

The rope effect can be considered for the nails of punched metal plates according to Z-9.1-855 (2023) by converting the value of the withdrawal parameter f_{ax} according to equation (8.25) of Eurocode 5 (2004) for a circular cross-section to a shear strength f_v for the surface of the approximately rectangular cross-section of the punched metal plate nails. The withdrawal capacity can then be calculated by multiplying the shear strength f_v with the surface of the nails. For PMPF with an air gap, the supporting effect of the rope effect is not applicable, as there is no friction between the metal plate and the timber component.

3.5 Single-shear steel-to-timber joints

In contrast to conventional steel-to-timber joints, the nails of PMPF are not driven through holes in the steel plate but are punched out of the steel plate and bent over, thus forming an integral part of the steel plate. A clamping of the nails in the steel plate is therefore assumed, regardless of the nail diameter and plate thickness. With this, the basis for calculating the load-bearing capacity for PMPF are the failure modes (c), (d), and (e) of equation (8.10) according to Eurocode 5 (2004).

Due to the plastic hinge occurring at a distance, an additional differentiation for the equations depending on the air gap thickness is introduced (see Figure 3.3). For no air gap, the embedment strength of the timber is reached in the initial area of the nail between plate surface and plastic hinge and the nail-load-bearing capacity is therefore increased (Figure 3.3, left and equation (1)). For air gaps that are smaller than the plastic hinge distance, the area with full embedment strength is reduced by the air gap but the failure mechanism is the same (Figure 3.3, centre and equation (2)). When the air gap thickness exceeds the plastic hinge distance, equations for fasteners with interlayers apply (Figure 3.3, right and equation (3)).

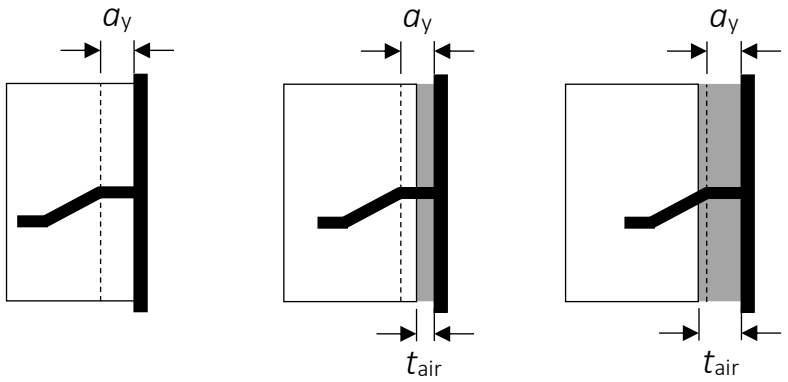

Figure 3.3. Differentiation for equations depending on air gap thickness, here for failure mode (d) (left: t_{air} = 0 mm, centre: $t_{air} \leq a_y$, right: $t_{air} > a_y$).

3.6 PMPF without air gap

Taking into account the dependence of the embedment strength and the yield moment of the direction of force (see section 3.2), the plastic hinge distance a_y according to Blaß et al. (2004) (see section 3.3) and neglecting the rope effect and the prefactor 1.15 in the failure mechanism (e), which is not mechanically determined but captures the different partial safety factors and k_{mod} values of steel and timber, equation (8.10) of Eurocode 5 (2004) becomes equation (1):

$$F_{v,Rk} = \min \begin{cases} f_{h,\alpha,\beta,k} \cdot t_1 \cdot d_\alpha & \text{(c)} \\ f_{h,\alpha,\beta} \cdot a_y \cdot d_\alpha + f_{h,\alpha,\beta,k} \cdot t_{1,net} \cdot d_\alpha \cdot \left(\sqrt{2 + \frac{4 \cdot M_{y,\alpha,Rk}}{f_{h,\alpha,\beta,k} \cdot t_{1,net}^2 \cdot d_\alpha}} - 1 \right) & \text{(d)} \\ f_{h,\alpha,\beta,k} \cdot a_y \cdot d_\alpha + \sqrt{4 \cdot M_{y,\alpha,Rk} \cdot f_{h,\alpha,\beta,k} \cdot d_\alpha} & \text{(e)} \end{cases} \quad (1)$$

Here, $F_{v,Rk}$ is the lateral load-bearing capacity per nail and shear plane in N, $f_{h,\alpha,\beta,k}$ is the embedment strength as a function of α and β in N/mm², t_1 is the penetration depth of the nail in mm, d_α is the projected nail width as a function of α in mm, a_y is the distance of the first plastic hinge from the plate surface in mm, $t_{1,net}$ is the penetration depth of the nail minus a_y in mm ($t_{1,net} = t_1 - a_y$), and $M_{y,\alpha,Rk}$ is the yield moment as a function of α in Nmm.

3.7 PMPF with air gap

The model according to Equation (1) also applies to PMPF with air gaps $t_{air} \leq a_y$. In this case, the penetration depth t_1 in (1) (c) becomes $t_{1,ef} = t_1 - t_{air}$ and a_y is reduced by t_{air}, resulting in equation (2). For air gaps $t_{air} > a_y$ the anchorage capacity of a lateral loaded nail can be calculated according to Blaß, Laskewitz (2003) and equation (3) applies.

Air gap less than or equal to plastic hinge distance, $t_{air} \leq a_y$:

$$F_{v,Rk} = \min \begin{cases} f_{h,\alpha,\beta,k} \cdot t_{1,ef} \cdot d_\alpha & \text{(c)} \\ f_{h,\alpha,\beta,k} \cdot t_{1,net} \cdot d_\alpha \left(\sqrt{2 + \frac{4 \cdot M_{y,\alpha,Rk}}{f_{h,\alpha,\beta,k} \cdot t_{1,net}^2 \cdot d_\alpha}} - 1 \right) - f_{h,\alpha,\beta,k} \cdot a \cdot d_\alpha & \text{(d)} \\ 2 \cdot \sqrt{M_{y,\alpha,Rk} \cdot f_{h,\alpha,\beta,k} \cdot d_\alpha} - f_{h,\alpha,\beta,k} \cdot a \cdot d_\alpha & \text{(e)} \end{cases} \quad (2)$$

Where $t_{1,ef} = t_1 - t_{air}$, $t_{1,net} = t_1 - a_y$ and $a = t_{air} - a_y$.

Air gap larger than plastic hinge distance, $t_{air} > a_y$:

$$F_{v,Rk} = \min \begin{cases} f_{h,\alpha,\beta,k} \cdot t_{1,ef} \cdot d_\alpha & \text{(c)} \\ f_{h,\alpha,\beta,k} \cdot t_{1,ef} \cdot d_\alpha \left[\frac{2}{t_{1,ef}} \left(\sqrt{a^2 + \frac{M_{y,\alpha,Rk}}{f_{h,\alpha,\beta,k} \cdot d_\alpha} + t_{1,ef} \cdot \left(a + 0{,}5 \cdot t_{1,ef} \right)} - a \right) - 1 \right] & \text{(d)} \\ f_{h,\alpha,\beta,k} \cdot d_\alpha \cdot \left(\sqrt{a^2 + \frac{4 \cdot M_{y,\alpha,Rk}}{f_{h,\alpha,\beta,k} \cdot d_\alpha}} - a \right) & \text{(e)} \end{cases} \quad (3)$$

Where $t_{1,ef} = t_1 - t_{air}$ and $a = t_{air} - a_y$.

3.8 Verification of the model

3.8.1 Nail load-bearing capacities of PMPF according to technical assessments and Eurocode 5

The nail load-bearing capacities of PMPF for different angles α and β are currently determined using equations (8.42), (8.43), (8.44) from Eurocode 5 (2004). The characteristic values of the equations $f_{a,0,0,k}$ and $f_{a,90,90,k}$ as well as the constants k_1, k_2 and α_0 are determined for each punched metal plate type via tests according to 1075 (2015). They are listed for each type of punched metal plate in its technical specification.

3.8.2 Comparison with values of technical assessment and variation of angles α and β

The nail load-bearing capacities calculated by equation (1) $f_{a,\alpha,\beta,calc}$ are compared with the nail load-bearing capacities according to the technical assessment Z-9.1-855 (2023) $f_{a,\alpha,\beta,TA}$. In the calculations according to equation (1) the rope effect with the minimum of $F_{v,Rk}/4$ according to the Johansen Theory and $F_{ax,Rk}/4$ is additionally

applied. The ratio $f_{a,\alpha,\beta,calc}/f_{a,\alpha,\beta,TA}$ is listed for angles $0° \le \alpha \le 90°$ and $0° \le \beta \le 90°$ in Table 3 in steps of 15°. The largest deviations are highlighted in dark, minor deviations are highlighted in light grey. With this, it can be quickly recognised that for angles $\alpha = 0°$ and $\alpha = 90°$ (first and last row) there is a very good agreement between $f_{a,\alpha,\beta,calc}$ and $f_{a,\alpha,\beta,TA}$ (maximum 9 % deviation). For $\alpha \neq 0°$ and $\alpha \neq 90°$ there is a poor agreement (maximum 38 % deviation). The variation of the angle β has no significant influence on the agreement of $f_{a,\alpha,\beta,calc}$ to $f_{a,\alpha,\beta,TA}$. One possible reason for the deviations between $f_{a,\alpha,\beta,calc}$ and $f_{a,\alpha,\beta,TA}$ derived from tests for angles $\alpha \neq 0°$ and $\alpha \neq 90°$ is seen in the moment caused by eccentric plate loading, which is due to the positioning of the PMPF in tests according to EN 1075 (2015) (e.g. for α = 60°, see Figure 3.4). This moment puts additional strain on the nails but is not included in the evaluation of the tests and the determination of the anchorage capacities.

Table 3. Ratios of calculation values $f_{a,\alpha,\beta,calc}$ to technical assessment values $f_{a,\alpha,\beta,TA}$.

	β	0°	15°	30°	45°	60°	75°	90°
α	$f_{a,\alpha,\beta}$	$f_{a,\alpha,0}$	$f_{a,\alpha,15}$	$f_{a,\alpha,30}$	$f_{a,\alpha,45}$	$f_{a,\alpha,60}$	$f_{a,\alpha,75}$	$f_{a,\alpha,90}$
0°	$f_{a,0,\beta}$	0.99	1.05	1.08	1.09	1.09	1.09	1.09
15°	$f_{a,15,\beta}$	1.19	1.12	1.15	1.16	1.13	1.21	1.16
30°	$f_{a,30,\beta}$	1.35	1.27	1.20	1.21	1.21	1.21	1.21
45°	$f_{a,45,\beta}$	1.35	1.38	1.30	1.22	1.22	1.22	1.22
60°	$f_{a,60,\beta}$	1.30	1.34	1.34	1.26	1.19	1.19	1.20
75°	$f_{a,75,\beta}$	1.19	1.23	1.24	1.22	1.15	1.11	1.11
90°	$f_{a,90,\beta}$	1.01	1.04	1.06	1.07	1.02	0.98	0.97

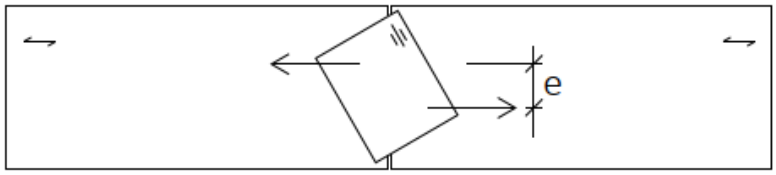

Figure 3.4. Eccentric load application in tests to determine anchorage capacity.

3.8.3 Adjustment of the calculation values

As shown in Section 3.8.2 the calculation model for anchorage capacities with $\alpha = 0°$ or $\alpha = 90°$ provides almost identical values to the characteristic load-bearing capacities given in the technical assessment Z-9.1-855 (2023). For alignment of the calculation values with the load-bearing capacities of the technical assessment for angles $\alpha \neq 0°$ and $\alpha \neq 90°$, the nail load-bearing capacities $f_{a,0,0}$ and $f_{a,90,90}$ can therefore first be calculated (with or without air gap) using the equations in section 3.6 and 3.7. In a second step it is then possible with the constants of the technical assessment k_1, k_2, α_0 and the equations (8.42), (8.43), (8.44) of Eurocode 5 (2004) to determine the anchorage capacities for all angles $0° \le \alpha \le 90°$ and $0° \le \beta \le 90°$. This procedure is analogous to EAD 130186-00-0603 (2018) for preformed three-dimensional nailing plates in the sense of "calculation assisted by testing".

3.9 Comparison of the calculated load-bearing capacities with the load-bearing capacities of the tests

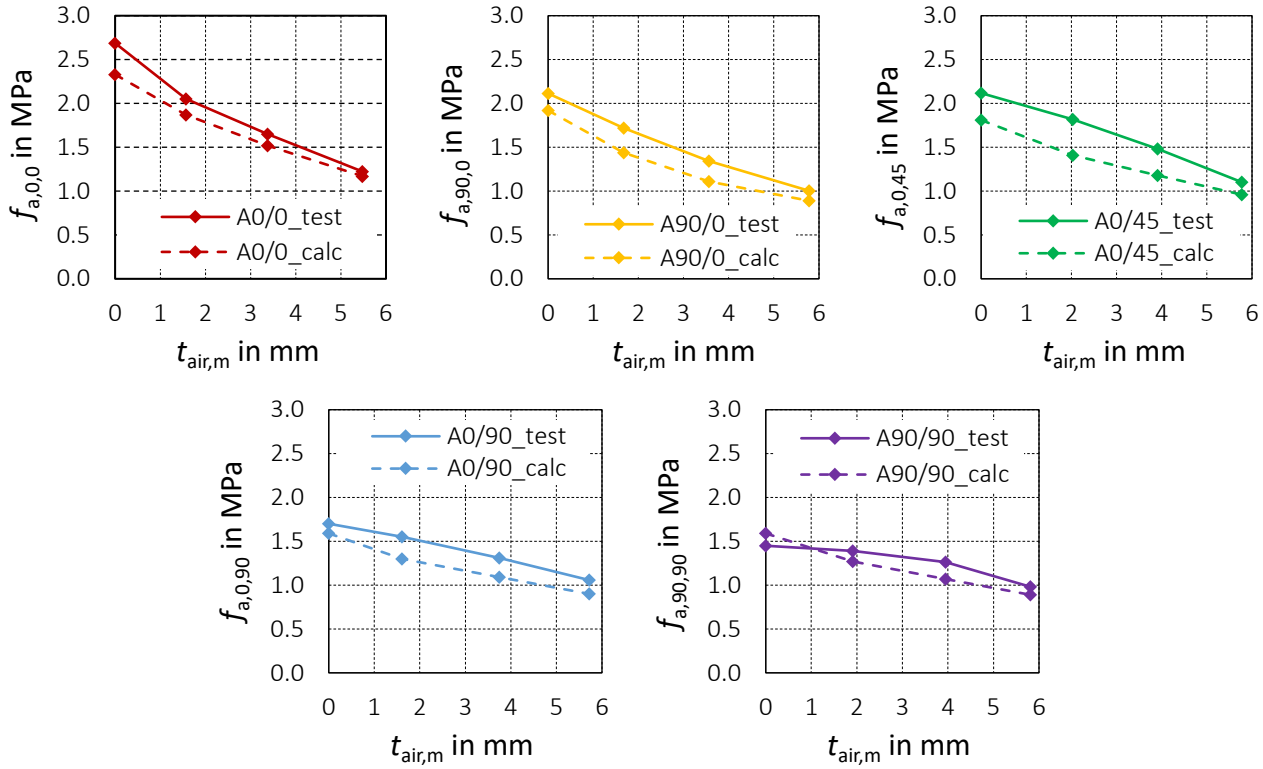

Figure 3.5. Comparison of the anchorage capacities from tests ("_test") with the calculated anchorage capacities ("_calc") as functions of the air gap thickness

The graphs in Figure 3.5 show the anchorage capacities from the test series $f_{a,test}$ together with the corresponding calculated anchorage capacities $f_{a,calc}$ according to equation (1) (without air gap) and equations (2), (3) (with air gap) in combination with section 3.8.3 as a function of the air gap thickness t_{air}. For the PMPF without air gap the rope effect was added to the calculated load-bearing capacity with the minimum of $F_{v,Rk}/4$ according to the Johansen theory and $F_{ax,Rk}/4$.

The mean ratio of all calculated nail load-bearing capacities to the nail load-bearing capacities from tests amounts to $f_{a,calc}/f_{a,test} = 0.87$. The results from the tests represent the mean values of the load-bearing capacities, while the equations of the calculation model are based on equations of Eurocode 5 (2004) for calculating characteristic values. The average underestimation for the calculated nail load-bearing capacities of 13 % of the mean nail load-bearing capacities can therefore be regarded as a good confirmation of the calculation model.

4 Discussion

4.1 Application of the equations to different types of PMPF

It is yet to be investigated to what extent the equations shown in section 3 can be used to calculate the nail load-bearing capacity of other PMPF types. In principle, a differentiated consideration of the specific material and geometric properties of the respective PMPF type is always required. For example, the nail spacing on PMPF with short nails

(e.g. 8 mm) is usually very small. To consider the splitting of the wooden components, it is probably necessary to use an effective number of nails n_{ef} for calculations. In addition, the rope effect should not be applied for short nails. Furthermore, there are punched metal plates with nails that have a cross-section that varies over their length. This influences the embedment strength and the formation of plastic hinges and must be considered in calculations.

4.2 Application of the test results to different types of PMPF

The nail lengths and nail cross-sections of different types of punched metal plates vary largely. It has not yet been clarified to what extent the test results can be transferred to other types of punched metal plates. Further experiments with different types of PMPF must be carried out, especially for PMPF with short nails.

So far, the remaining load-bearing capacities $f_{a,rel}$ for different types of PMPF can only be estimated by evaluating the graph in Figure 2.4 using the air gap thickness in relation to the nail length $t_{air,rel}$ for different nail lengths of PMPF. For various nail lengths of PMPF commonly used in construction, the remaining nail load-bearing capacities estimated on the basis of the test results are listed in Table 4 for the load direction $\alpha = \beta = 0°$ (maximum loss of load-bearing capacity) and an air gap of $t_{air} = 1$ mm.

For 8 mm and 10 mm nails, the estimated value corresponds to the loss of load-bearing capacity stated in Paevere et al. (2009) of more than 25 % for an air gap of 1 mm between the metal plate and the timber component.

Table 4. Estimated relative load-bearing capacities $f_{a,rel}$ for different nail lengths for $t_{air} = 1$ mm (load direction $\alpha = \beta = 0°$)

Nail Length	in mm	20	14	12	10	8
$t_{air,rel}$	-	0.05	0.07	0.08	0.10	0.13
$f_{a,rel}$	-	0.87	0.82	0.79	0.75	0.70

4.3 Reference to standards

4.3.1 EN 14250: 1 mm air gap on 25 % of the joint area

In EN 14250 (2010) an air gap of 1 mm on 25 % of the joint area is permitted. This equals a mean air gap of $t_{air,m} = 0{,}25$ mm for the entire joint area. In section 2.5.2 it was shown that the mean value of the air gap thickness can be used as a comparative value to the test results with constant air gap thicknesses. Analogous to section 4.2 the loss of load-bearing capacity already existing in a standard-compliant punched metal plate joint with $t_{air,m} = 0.25$ mm can thus be estimated for different nail lengths and amounts to approx. 3 % for nail length 20 mm and approx. 8 % for nail length 8 mm.

4.3.2 Material properties of steel and wood in the evaluation of tests according to EN 1075

For the steel grades S280 GD and S350 GD in accordance with EN 10346 (2015) commonly used for PMPF, a range of 140 MPa can be expected for the distribution of the

tensile strength of the steel. When evaluating the tests to determine the load-bearing capacity of nail plates in accordance with EN 1075 (2015), the actual tensile strength is not considered. Thus, the steel of the PMPF used in the tests may have a higher strength than the minimum value required for the corresponding strength class of the PMPF steel. This can lead for e.g. steel S280 GD to a ratio of the tensile strengths of (360 + 70)/ (360 - 70) = 1.48. This leads to a situation, where the yield moment of the nails is significantly overestimated.

Furthermore, the factor $(\rho_k/\rho)^c$, which considers the effect of the wood density on the nail load-bearing capacity, is no longer included in the determination of the nail load-bearing capacity according to the current EN 1075 (2015) as it was in the withdrawn EN 1075 (2000). In EN 1075 (2000) the selection of the timber for the test specimens was required to be in accordance with EN 28970 (1991), while the current EN 1075 (2015) requires the timber to be selected in accordance with EN ISO 8970 (2010). At the same time, the current EN 14545 (2009) to evaluate characteristic values of PMPF requires a selection according to EN 28970 (1991).This discrepancy between the two necessary and current standards (EN 1075 (2015) and EN 14545 (2009)) and the lack of the factor $(\rho_k/\rho)^c$ in EN 1075 (2015) means that it is no longer clearly defined to what extent the density of the timber used for the tests should be taken into account when evaluating the tests and determining the nail load-bearing capacity of PMPF.

Both the missing reference of the steel used for the tests to the required minimum strength of the steel and the missing or not clearly defined reference of the density of the timber used for the tests to the characteristic density of the timber for which the test results are to be applied can lead to an unsafe overestimation of the load-bearing capacity of PMPF.

5 Summary and recommendations

The problem of PMPF detaching from the timber components has become known in recent years and has since been observed repeatedly in existing PMPF constructions. This reveals an urgent need for standards or scientific studies on the load-bearing behaviour of PMPF with an air gap between metal plate and timber component.

With the results of the research project presented here, an initial scientific basis for the load-bearing behaviour of punched metal plates with an air gap between the metal plate and the timber component is provided. Based on tests with PMPF according to Z-9.1-855 (2023), it was shown that both the anchorage capacity and the stiffness of the PMPF decrease predictably with increasing air gap thickness. At the same time, equations to mathematically determine the load-bearing capacity of the PMPF according to Z-9.1-855 (2023) with and without air gap were introduced and confirmed by the test results. Both findings should be investigated by further experiments for PMPF with different material and geometric properties. Based on the results, a static evaluation of PMPF joints with an air gap between metal plate and

timber component would then be possible and guidelines for the inspection of existing PMPF constructions could be developed.

The effect of a possible overstrength of the steel used in tests for the determination of the load-bearing capacity should be investigated. A reduction in the load-bearing capacity of PMPF with reference to the difference between the tensile strength used in tests to the minimum tensile strength of the steel could increase the safety of punched metal plate constructions. To capture the difference between the density of the timber components used for the tests and the characteristic density of the timbers for which the test results are intended, a factor to consider the effect of the wood density on the nail load-bearing capacity should again be clearly included in respective standards as it was in EN 1075 (2000).

6 References

Blaß, H. J., Ehlbeck, J., Kreuzinger, H., Steck, G. (2004): Erläuterungen zu DIN 1052:2004-08 Entwurf, Berechnung und Bemessung von Holzbauwerken. Bruderverlag, Karlsruhe. ISBN 3-87104-152-1.

Blaß, H. J. , Laskewitz, B. (2003): Tragfähigkeit von Verbindungen mit stiftförmigen Verbindungsmitteln und Zwischenschichten. Bauen mit Holz, Band 105. Heft 1, S. 26-35.

EAD 130186-00-0603 (2018): Three-Dimensional Nailing Plates. European Assessment Document. EOTA.

EN 383 (2007): Timber Structures - Test Methods - Determination of embedment strength and foundation values for dowel type fasteners. CEN.

EN 1075 (2000) (replaced): Timber structures - Test methods - Joints made with punched metal plate fasteners. CEN.

EN 1075 (2015): Timber structures - Test methods - Joints made with punched metal plate fasteners. CEN.

EN 10346 (2015): Continuously hot-dip coated steel flat products for cold forming - Technical delivery conditions. ECISS.

EN 14250 (2010): Timber structures - Product requirements for prefabricated structural members assembled with punched metal plate fasteners. CEN.

EN 14545 (2009): Timber Structures - Connectors; Requirements. CEN.

EN 28 970 (1991): Timber structures - Testing of joints made with mechanical fasteners - Requirements for wood density. CEN. (ISO 8970: 1989).

Eurocode 5 (2004): Design of timber structures - Part 1-1: General and rules for buildings. CEN. (EN 1995-1-1).

Fachkommission Bautechnik der Bauministerkonferenz ARGEBAU (2020): Hinweise zur Untersuchung von Holzkonstruktionen in Nagelplattenbauweise auf die mögliche Gefährdung der Standsicherheit durch abstehende Nagelplatten. Fassung Sept. 2020.

Michel, C., Ulrich, M. (2025): Automatic Inspection of Punched Metal Plate Fasteners on Timber-to-Timber Joints with Image-Based 3D Reconstruction. 6th Joint international Symposium on Deformation Monitoring (JISDM). April 2025, Karlsruhe, Germany.

Paevere P., Nguyen M., Syme M., Leicester R.H., Ho K. (2009): Mechano-Sorptive Nailplate Backout in Nail-Plated Timber Trusses. PNB036-0607 Final Report & Recommendations, CSIRO Sustainable Ecosystems.

Truss Plate Institute of Canada (2024): Truss Design Procedures and Specifications for Light Metal Plate Connected Wood Trusses. TPIC 2024.

Yasumura, M. and Sawata, K. (2000); Determination of Yield Strength and Ultimate Strength of Dowel-type Timber Joints. Paper 33-7-1, Proceedings, CIB-W18 Meeting, Delft, Netherlands. ISSN 0945-6996.

Z-9.1-855 (2023): Tragende Holverbindungen unter Verwendung von Wolf-Nagelplatten Typ 20 W. Allgemeine Bauartgenehmigung. Deutsches Institut für Bautechnik, Berlin.

Acknowledgements

We would like to thank the staff of the Research Centre for Steel, Timber and Masonry, KIT, for their excellent cooperation and support in creating the test specimens and in carrying out the tests. We would also like to thank the research partner at the Institute of Photogrammetry and Remote Sensing, KIT, for the good and constructive cooperation. We would like to thank Wolf Systembau GmbH for generously providing the PMPF used for the tests.

The research project was funded by the German Federal Ministry for Economic Affairs and Climate Action.

Supported by:

Federal Ministry
for Economic Affairs
and Climate Action

on the basis of a decision
by the German Bundestag

DISCUSSION

The paper was presented by D Staiger

F Lam commented that practical adjustment factors to account for tooth embedment gap are available from N. America TPI/TPIC standard for cross reference: no adjustment for embedment gap < 0.8 mm; ineffective for embedment gap > 1.6 mm; 60% effective for embedment gas between 0.8 mm and 1.6 mm.

S Winter and D Staiger discussed the arrangement of nail plate installation procedure with the plates being slightly inclined to represent a partially withdrawn plate.

G Doudak commented about bending of teeth from shrinkage of the wood. D Staiger said that in reality the detachment was not uniform hence the test considered this fact.

G Doudak said that there is large difference between model and test results in the zero gap case. D Staiger explained that the difference is between mean vs characteristic value.

U Hübner commented that detachment of tooth plates is common and asked how would one remedy these cases. D Staiger responded that the goal of the work is to understand the phenomenon as a first step. They tried to push the plates back into the wood but it was not successful.

C Sandhaas asked would it be possible to propose considering gaps in the initial stage of design. D Staiger responded that there are other effects to be considered including plate geometry, teeth design, timber properties, etc.

S Winter commented that tooth plates with shorter nail lengths compared to the one tested are commonly used in Germany.

J Smart and D Staiger agreed that relaxation of the wood could cause further withdrawal.

D Staiger commented that manufacturers already knew about this issue.

T Tannert asked about micro teeth system which need to be compressed into the wood.

U Hübner commented that 25% of the teeth area is allowed to have gaps of 1 mm. Practical ways to consider this issue economically are needed. He commented about cyclic and drying conditions in service vs test conditions.

P Dietsch suggested to add some illustrations to the paper.

Lateral Stiffness of Light Timber-Framed Shear Walls with Cladding – Proposal for an Analytical Model

Lukas Rauber, RWTH Aachen University, Germany

Benno Hoffmeister, RWTH Aachen University, Germany

Keywords: light timber-framed walls, cladding, lateral stiffness model, test results

1 Introduction

According to *prEN 1995-1-1* (2023) the lateral stiffness of light timber-framed shear walls (LTFWs) is governed by their load-carrying components (fasteners, sheathing, framing, and anchorages). European and national regulations for fire safety of multi-storey timber buildings require additional cladding for fire protection. Fasteners of claddings are usually attached to the framing through the sheathing, which leads to additional sheathing-to-framing and cladding-to-sheathing connections (Figure 1). The contribution of cladding and its fasteners are neglected so far in the calculation models according to *EN 1995-1-1* (*EC 5*) and *prEN 1995-1-1*.

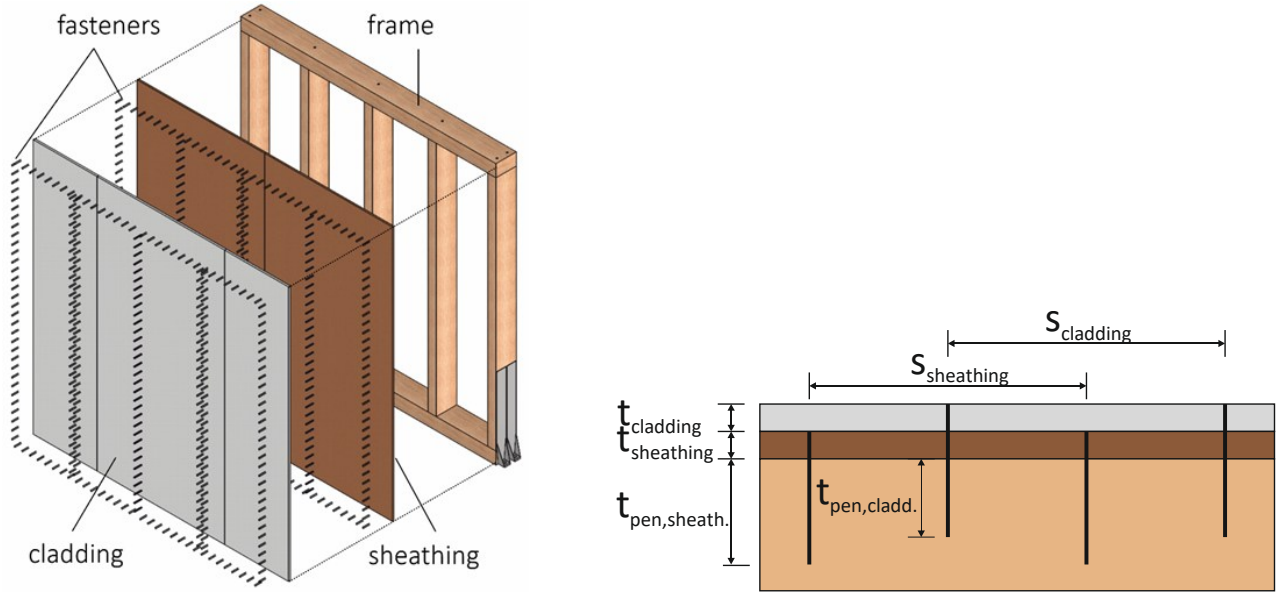

Figure 1. Components of a LTFW with cladding (left) and a detail of the sheathing-to-framing connection (right).

Neglecting claddings and their sheathing-to-framing connections is unfavourable in two respects: (i) the economic potential of the structure (increased resistance and stiffness) is not exploited and (ii) it may lead to an unsafe seismic design – since for seismic design using response spectra, the structural model requires a realistic assessment of the properties (i.e. stiffness, load-carrying capacity and ductility) of all relevant components. *Rauber et al.* (2024) showed a large increase in lateral load-carrying capacity due to staples of claddings contributing to the sheathing-to-framing connection and proposed an analytical resistance model – the stiffness was not yet addressed.

In this contribution a proposal for an analytical model to calculate the stiffness of LTFWs with cladding is presented and validated by experimental data. The influence of claddings was investigated by testing 62 LTFWs regarding the lateral load-displacement behaviour, see *Rauber et al.* (2024) and (2025). The analytical model considers the additional sheathing-to-framing and cladding-to-sheathing connections and introduces an upper and a lower bound value of the lateral stiffness.

2 State of the Art

First known experimental tests on LTFWs with cladding were performed by *Glos et al.* (1985). In the international literature tests by *Chen et al.* (2016) and *Valdivieso et al.* (2023) were found. The own test results regarding LTFWs with cladding were already presented in *Rauber et al.* (2024) and (2025). All test results confirmed a significant increase of load-carrying capacity and of stiffness for LTFWs with additional cladding in comparison to reference tests without cladding.

An analytical model for the assessment of the lateral stiffness of LTFWs with cladding or multiple sheathing layers is not known to the authors. The state-of-the-art formulas to calculate the lateral top displacement of wall diaphragms due to deformation of the individual components for LTFWs with sheathing is given in *prEN 1995-1-1*.

3 Materials and Methods

3.1 Proposed Analytical Model

The proposed analytical model for calculating the stiffness of LTFWs with claddings supplements the model provided in *prEN 1995-1-1* by three parts: (i) the strengthened sheathing-to-framing connection due to cladding fasteners; (ii) the cladding-to-sheathing connection and (iii) the shear stiffness of the cladding panels. As the test results for the stiffness vary more than the load-carrying capacity, a lower and an upper bound for the stiffness calculation are introduced. The lower bound stiffness seems sufficient for serviceability limit state (SLS) verifications. For seismic design using response spectra, an introduction of the upper bound lateral wall stiffness is reasonable, as the assessment of the seismic load depends on a realistic stiffness calculation for the walls. To this end the contributions (ii) and (iii) to the stiffness are considered only for the upper bound stiffness calculation.

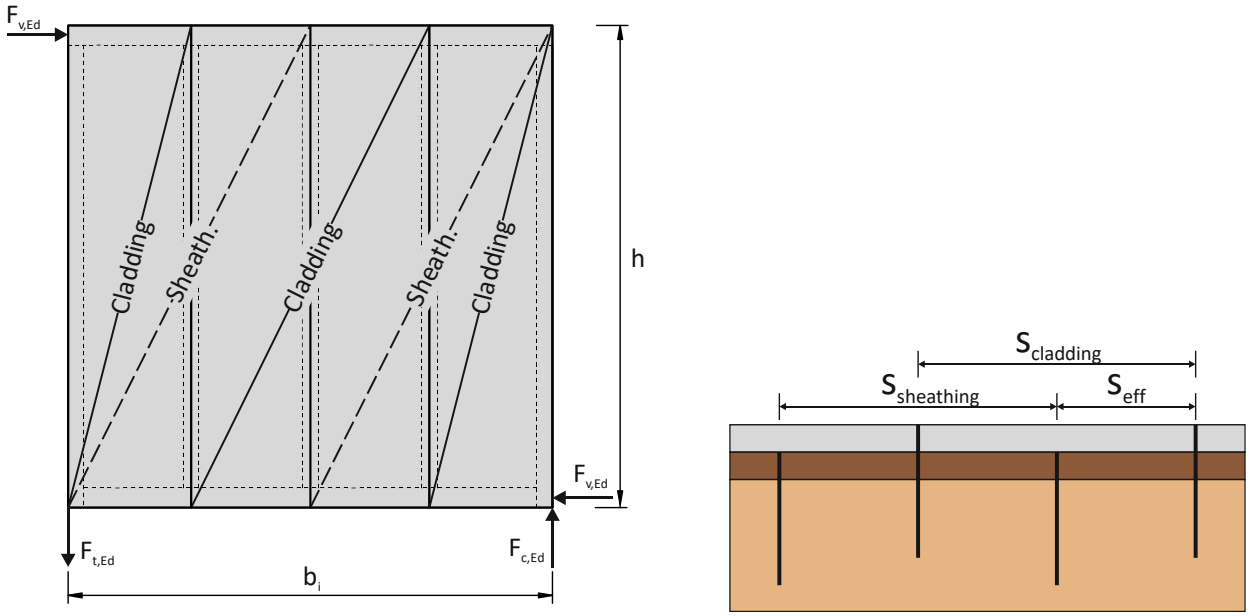

Figure 2. Structural scheme for an effective LTFW diaphragm with sheathing and cladding (left) and effective fastener spacing s_{eff} in the sheathing-to-framing connection (right).

This contribution considers only displacement components that lead to shear deformation between top and bottom rail. The considered components are the displacement u_{K} resulting from the deformation of the sheathing-to-framing connections, the displacement u_{N} resulting from the axial deformation of the framing and the displacement u_{G} resulting from the shear deformation of the sheathing (and cladding).

The shear stiffness K_{shear} of LTFW is then calculated using the following formula:

$$K_{\mathrm{shear}} = \frac{F_{\mathrm{v,Ed}}}{u_{\mathrm{K}} + u_{\mathrm{G}} + u_{\mathrm{N}}} = \frac{F_{\mathrm{v,Ed}}}{u_{shear,calc}} \qquad (1)$$

where $F_{\mathrm{v,Ed}}$ is the horizontal force acting at the top rail and $u_{shear,calc}$ is the corresponding lateral top displacement from the above-mentioned components.

3.1.1 Upper and Lower Bound Values of the Lateral Stiffness

The lower (K_{min}) and upper bound lateral stiffness (K_{max}) are elaborated hereafter and displayed in Figure 3. For the lower and upper bound all fasteners in the sheathing-to-framing connection are considered (including the ones from cladding).

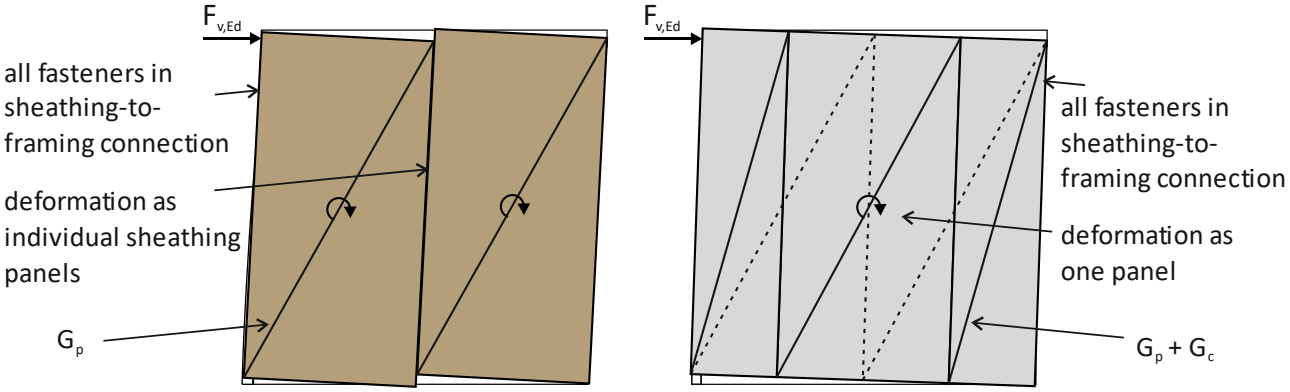

Figure 3. Scetch of the lower (left) and upper bound (right) lateral stiffness for LTFWs with cladding.

Two different displacement mechanisms of the panels are assumed: (i) for the lower bound stiffness the deformations of the fasteners at the perimeter of all individual sheathing panels are considered to calculate u_{K}; (ii) for the upper bound stiffness the deformation of the fasteners at the perimeter of a combined panel of sheathing and cladding are considered, assuming composite behaviour of the panels.

The calculation of displacements from the shear deformation of the panels u_G differs also: (i) for the lower bound only the shear moduli of the sheathing panels are considered in the calculation; (ii) for the upper bound the shear moduli of the cladding panels are added.

3.1.2 Displacement from the deformation of the sheathing-to-framing connections

The displacement u_{K} resulting from the deformation of the sheathing-to-framing connections is calculated by the following formula:

$$u_{\mathrm{K}} = \frac{F_{\mathrm{v,Ed}}/b_{\mathrm{i}}^2}{K_{\mathrm{ser},1}/s_{\mathrm{eff},1} + K_{\mathrm{ser},2}/s_{\mathrm{eff},2}} \cdot (2h \cdot n_{\mathrm{p,l}} + 2b_{\mathrm{i}} \cdot n_{\mathrm{p,h}}) \qquad (2)$$

where $F_{\mathrm{v,Ed}}$ is the horizontal force acting in the top rail, b_{i} is the length of the effective diaphragm (as in *EC 5*; l in *prEN 1995-1-1*), $K_{\mathrm{ser},1}$ and $K_{\mathrm{ser},2}$ are the slip moduli of the sheathing-to-framing fasteners on each side of the framing (renamed K_{SLS} in *prEN 1995-1-1*), $s_{\mathrm{eff},1}$ and $s_{\mathrm{eff},2}$ are the effective spacing in the sheathing-to-framing connection on each side of the framing (a_1 in *prEN 1995-1-1*), h is the height of the effective diaphragm, $n_{\mathrm{p,l}}$ is the number of consecutive sheathing panels along the length of the effective diaphragm and $n_{\mathrm{p,h}}$ is the number of panels stacked along the height of the effective diaphragm.

For the upper bound value of the lateral wall stiffness K_{max} the number of horizontal and vertical panels are taken to $n_{\mathrm{p,h}} = n_{\mathrm{p,l}} = 1$ corresponding to one large panel.

The formula for the lateral slip modulus K_{ser} (K_{SLS}) of staples has changed from *EC 5* to *prEN 1995-1-1*. Both approaches are compared within this contribution. According to *EC 5* the formula for the lateral slip modulus per staple leg K_{ser} is:

$$K_{\mathrm{ser}} = {\rho_{\mathrm{m}}}^{1,5} d^{0,8}/80 \qquad (3)$$

where ρ_{m} is the mean density in kg/m³ and d is the diameter of the fastener in mm.

According to *prEN 1995-1-1* the formula for the lateral slip modulus per staple leg for coated staples in wood-based panel to timber connections K_{SLS} is:

$$K_{\mathrm{SLS}} = {\rho_{\mathrm{mean}}}^{1,5} d/60 \qquad (4)$$

where ρ_{mean} is the mean density in kg/m³ and d the diameter of the fastener in mm. Obviously, the formula in *prEN 1995-1-1* leads to higher slip moduli.

3.1.3 Displacement from the shear deformation of sheathing and cladding

For the displacement u_G from the shear deformation of the sheathing (and cladding) panels, a distinction between the upper and lower bound stiffness is made.

For the **lower bound** stiffness of LTFWs with cladding the following formula is used for the displacement u_{G} from the shear deformation of the sheathing panels:

$$u_{\mathrm{G}} = \frac{F_{\mathrm{v,Ed}}/b_{\mathrm{i}} \cdot h}{(G_{\mathrm{p,1}} \cdot t_{\mathrm{p,1}} + G_{\mathrm{p,2}} \cdot t_{\mathrm{p,2}})} \tag{5}$$

For the **upper bound** the formula above is extended by the shear moduli of the cladding panels:

$$u_{\mathrm{G}} = \frac{F_{\mathrm{v,Ed}}/b_{\mathrm{i}} \cdot h}{(G_{\mathrm{p,1}} \cdot t_{\mathrm{p,1}} + G_{\mathrm{c,1}} \cdot t_{\mathrm{c,1}} + G_{\mathrm{p,2}} \cdot t_{\mathrm{p,2}} + G_{\mathrm{c,2}} \cdot t_{\mathrm{c,2}})} \tag{6}$$

where $F_{\mathrm{v,Ed}}$ is the horizontal force acting at the top rail, b_{i} is the length of the effective diaphragm, h is the height of the effective diaphragm, $G_{\mathrm{p,1}}$ and $G_{\mathrm{p,2}}$ are the shear moduli of the sheathing panels fixed to each side of the framing, $t_{\mathrm{p,1}}$ and $t_{\mathrm{p,2}}$ are the thicknesses of the sheathing panels fixed to each side of the framing, $G_{\mathrm{c,1}}$ and $G_{\mathrm{c,1}}$ are the shear moduli of the cladding panels fixed to each side of the framing, $t_{\mathrm{c,1}}$ and $t_{\mathrm{c,2}}$ are the thicknesses of the cladding panels fixed to each side of the framing.

3.1.4 Displacement from the axial deformation of the framing

The displacement u_{N} from the axial deformation of the framing is calculated by:

$$u_{\mathrm{N}} = \frac{2}{3} \cdot \frac{F_{\mathrm{v,Ed}}}{E_{\mathrm{0,mean}}} \cdot \left(\frac{b_{\mathrm{i}}}{A_{\mathrm{rail}}} + \frac{h^3}{A_{\mathrm{stud}} \cdot b_{\mathrm{i}}^2} \right) \tag{7}$$

where $F_{\mathrm{v,Ed}}$ is the horizontal force acting in the top rail, b_{i} is the length of the effective diaphragm, h is the height of the effective diaphragm, $E_{\mathrm{0,mean}}$ is the mean modulus of elasticity parallel to grain of the edge framing, A_{rail} is the average cross-section area of the top and bottom rails and A_{stud} is the average cross-section area of the leading and trailing studs.

3.1.5 Input Values for Model Validation

In this contribution the above-mentioned formulas are used to calculate u_{K}, u_{G} and u_{N} as well as K_{shear}. The values inserted in the equations are described hereafter. For the **frame characteristics** the mean modulus of elasticity $E_{\mathrm{0,mean}}$ parallel to grain of the framing made of structural timber and the mean density $\rho_{\mathrm{mean,frame}}$ are taken from *DIN EN 338*.

For the **panels** made of **OSB**, values provided in *DIN EN 12369-1* are used, namely the mean shear modulus $G_{\mathrm{p,OSB}}$ and the characteristic density $\rho_{\mathrm{k,OSB}}$ (the mean density ρ_{m} for panels is not available in standards). For **panels** made of **GFB**, the mean shear modulus $G_{\mathrm{p,GFB}}$ and $G_{\mathrm{c,GFB}}$ as well as the characteristic density $\rho_{\mathrm{k,GFB}}$ are taken from *ETA-03/0050*, as this GFB type was used in the tests.

As the densities of sheathing panels and framing differ, the formula $\rho_{\mathrm{m}} = \rho_{\mathrm{mean}} = \sqrt{\rho_{\mathrm{mean,frame}} \cdot \rho_{\mathrm{k,sheathing}}}$ is used to calculate the input for K_{ser} resp. K_{SLS}.

3.2 Experimental Investigations

In total 62 experimental tests on LTFWs (2.50 × 2.50 m) were performed and used to validate the analytical model. The specimens and test setup were already described in detail by *Rauber et al.* (2024) in last year's INTER meeting and in *Rauber et al.* (2025). Therefore, only a brief description of the tests is given here, focussing on the measurement of the displacements and the evaluation of the stiffness.

LTFWs with additional gypsum fibre board (GFB) cladding and reference walls with only sheathing (OSB or GFB) were tested. The tests were performed using monotonic or cyclic horizontal loading according to *ISO 21581* (2010). The individual displacements of the components were measured by transducers and an optical system. Within this contribution the values obtained by the transducers are considered.

Three displacements were investigated for the analytical model: the sheathing panel shear deformation (u_{G}), the displacement from the deformation of the sheathing-to-framing connection (u_{K}) and the displacement from the axial deformation of the framing (u_{N}). As only these displacements are considered for the stiffness calculations, rigid body translation and rotation were subtracted from the total deformation of the test specimens to get the shear displacement.

3.2.1 Materials

Structural timber of strength class C24 was used for the framing. The top and bottom rails had a cross-section of 120 × 200 mm; the studs had a cross-section of 80 × 200 mm. The sheathing consisted of OSB/3 boards (t = 15 mm), provided by Egger Holzwerkstoffe Wismar GmbH & Co. KG, or gypsum fibre boards (GFB) with a thickness of t = 12.5 or 18 mm, provided by James Hardie Europe GmbH (fermacell®). The cladding consisted of the same GFB boards. Boards of the same thickness were obtained from the same production batch. The board dimensions were 1.25 × 2.50 m.

The fasteners used were resin-coated staples, provided by ITW Befestigungssysteme GmbH (Haubold). Two types of staples were used: (i) HD 7900 with a diameter of ⌀ = 1.80 mm and a length of L = 65 mm (or L = 75 mm for the second GFB layer in wall type 07); (ii) KG 700 CDNK (divergent staples), with ⌀ = 1.53 mm and L = 35 mm for the board-to-board connection of wall type 10.

Two Simpson Strong-Tie HTT31 anchors were fully attached to each side of the wall using 41 nails (TJEP KA 40/60 mm) and four screws (CSA5.0×80).

3.2.2 Test Specimens

All test specimens had a sheathing area of 2.50 × 2.50 m (Figure 4) and a fastener spacing of s = 75 mm (so far not stated otherwise). The cladding was offset by half of the sheathing panel width and the cladding fasteners were offset by $\mathrm{s}/2$ to the sheathing ones (if not stated otherwise). The LTFW specimens were manufactured at the facilities of Adams Holzbau-Fertigbau GmbH and delivered to the lab at RWTH Aachen, where the experimental tests were performed.

Claddings were always fastened through the sheathing into the framing – except for specimen type 10, where it was fastened board-to-board with shorter and divergent staples.

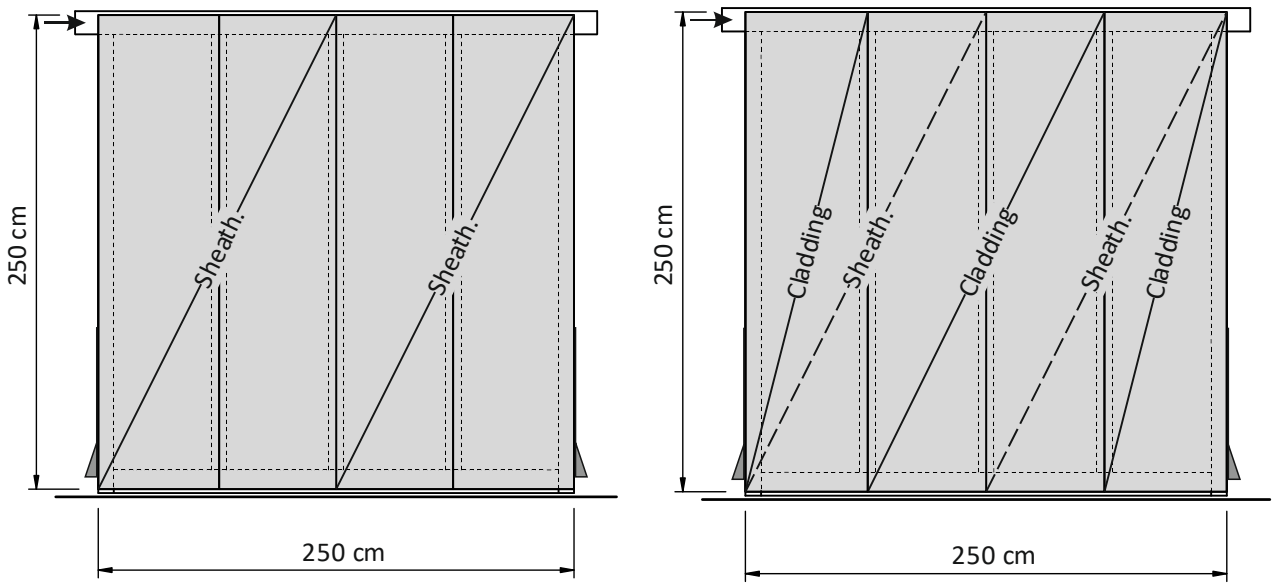

(a) Reference specimens without cladding (b) Specimens with one cladding layer

Figure 4. Dimensions and sheathing (and cladding) panel arrangement of the LTFW test specimens.

3.2.3 Tests on LTFWs with single-sided sheathing

Within the first test series the lateral load-displacement behaviour of LTFWs with and without cladding was tested with single-sided sheathing. The sheathing and cladding arrangement is shown in Figure 5. The test-specimen data for the experimental series with single-sided sheathing are shown in Table 1.

Table 1. Experimental series of LTFWs with single-sided sheathing.

Series	Type	Number		Sheathing	Cladding	Staples	Notes
[-]	[-]	m*	c*	t [mm]	t [mm]	⌀ - L [mm]	[-]
0	01	2	1	OSB 15	-	1.80 - 65	
	02	1	1	OSB 15	-	1.80 - 65	frame *not* notched
	03	2	1	GFB 12.5	-	1.80 - 65	
	04	1	1	GFB 18	-	1.80 - 65	
1	05	2	1	OSB 15	GFB 12.5	1.80 - 65	
	06	1	1	OSB 15	GFB 18	1.80 - 65	
	07	1	1	OSB 15	2 × GFB 18	1.80 - 65	2nd clad. with staples 1.80-75 and without min. spacing in sheathing
2	08	2	1	GFB 12.5	GFB 12.5	1.80 - 65	
	09	1	1	GFB 18	GFB 18	1.80 - 65	
	10	1	1	GFB 18	GFB 18	1.53 - 35	fastened board-to-board

*monotonic (m) or cyclic (c) according to *ISO 21581* (2010)

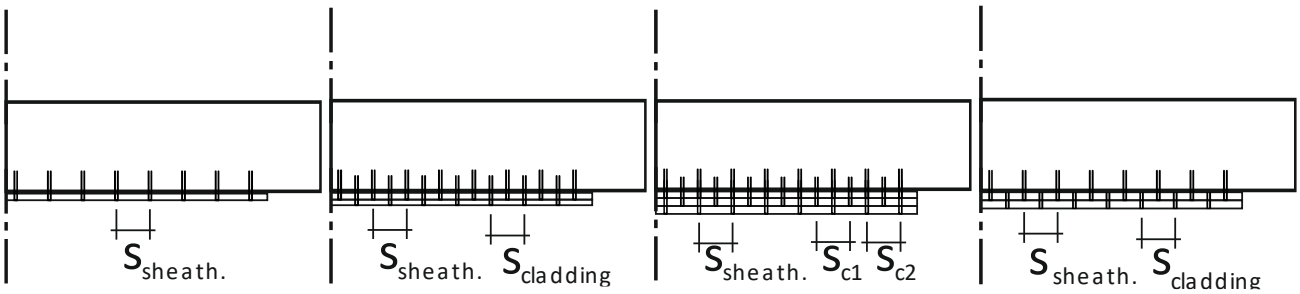

(a) Type 01, 02, 03, 04 (b) Type 05, 06, 08, 09 (c) Type 07 (d) Type 10

Figure 5. Fastener details in top rail of the test specimens with single-sided sheathing.

3.2.4 Tests on LTFWs with double-sided sheathing

Within the second test series the lateral load-carrying capacities of LTFWs with and without cladding were tested with double-sided sheathing. The sheathing and cladding arrangement is shown in Figure 6. The test-specimen data for the experimental series with double-sided sheathing are shown in Table 2.

Table 2. Experimental series of LTFWs with double-sided sheathing.

Series	Type	Number		Sheathing	Cladding	Staples	Spacing	Notes
[-]	[-]	m*	c*	t [mm]	t [mm]	ø - L [mm]	s [mm]	[-]
3	11	2	0	OSB 15	-	1.80 - 65	75	
	12	2	0	OSB 15	GFB 12.5	1.80 - 65	75	without min. spacings
4	13	4	3	OSB 15	-	1.80 - 65	75	
	14	2	1	OSB 15	-	1.80 - 65	37.5	doubled no. of staples
	15	5	3	GFB 18		1.80 - 65	86.6	
5	16	5	3	OSB 15	GFB 18	1.80 - 65	75	
	17	5	3	GFB 18	GFB 18	1.80 - 65	86.6	

*monotonic (m) or cyclic (c) according to *ISO 21581* (2010)

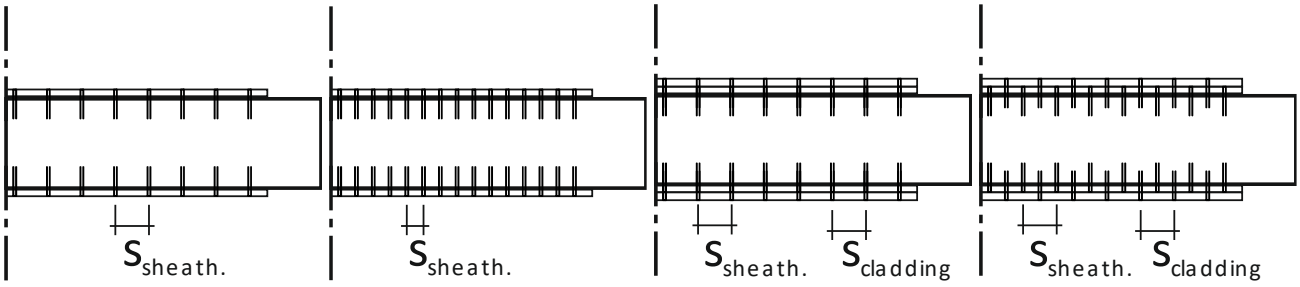

(a) Type 11, 13 and 15 (b) Type 14 (c) Type 12 (d) Type 16 and 17

Figure 6. Fastener details in the top rail of the test specimens with double-sided sheathing.

3.2.5 Evaluation of the experimental lateral stiffness

The shear deformation $u_{\text{shear,exp}}$ of the top rail was calculated by subtracting the specimen's rigid body translation and rotation with the measured displacement at the horizontal supports and vertical anchorages, as shown in formula (8):

$$u_{\text{shear,exp}} = u_{\text{h,tr}} - u_{\text{h,br}} - (u_{\text{v,A}} - u_{\text{v,B}}) \cdot \frac{h}{b_{\text{i}}} \tag{8}$$

where $u_{\text{h,tr}}$ is the horizontal displacement of the top rail, $u_{\text{h,br}}$ is the horizontal displacement of the bottom rail, $u_{\text{v,A}}$ and $u_{\text{v,B}}$ are the vertical displacements at support A and B, h is the height of the specimen and b_{i} is the length of the wall specimen.

The experimental lateral stiffness K_{exp} is then calculated for each test specimen with the shear deformation $u_{\text{shear,exp}}$ and the experimental load-carrying capacity F_{max} by:

$$K_{\text{exp}} = \frac{0{,}3F_{\text{max}}}{u_{0{,}4\text{Fmax}} - u_{0{,}1\text{Fmax}}} \tag{9}$$

where F_{max} is the lateral load-carrying capacity of the specimen, $u_{0{,}4\text{Fmax}}$ is the shear deformation $u_{\text{shear,exp}}$ at 40% of F_{max} and $u_{0{,}1\text{Fmax}}$ is $u_{\text{shear,exp}}$ at 10% of F_{max}. For the cyclic tests the first envelope curve is taken to evaluate K_{exp}.

4 Results

4.1 Experimental Results

The deformation figures at the end of the tests of a reference specimen with OSB sheathing only and a specimen with additional cladding are shown in Figure 7.

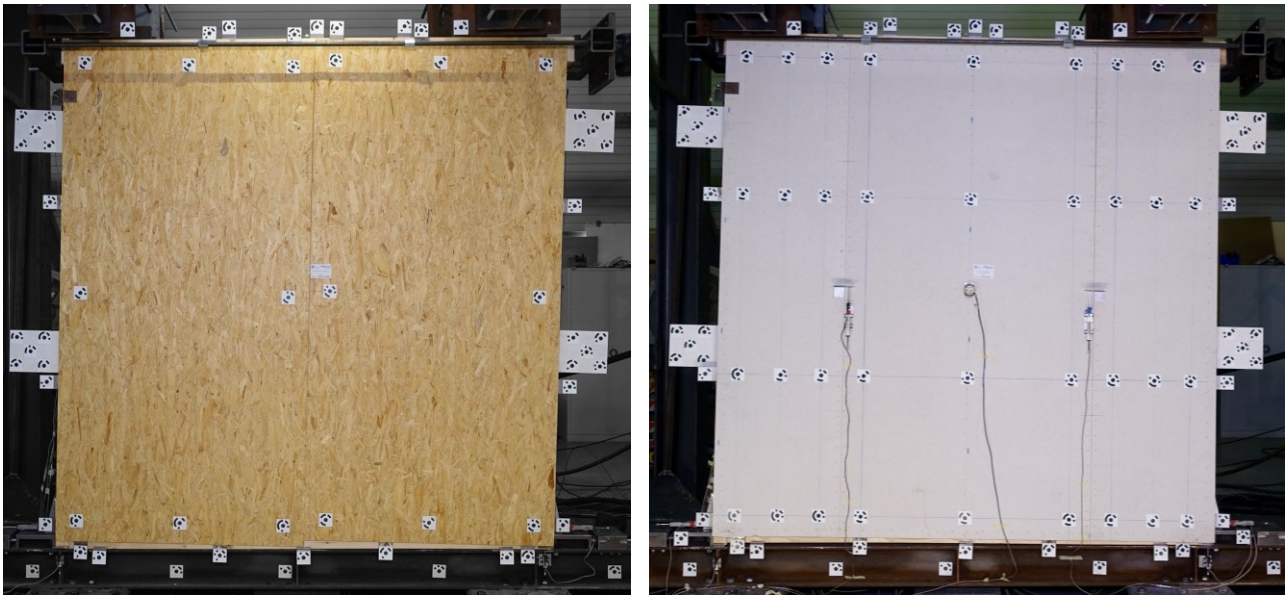

(a) Reference specimen, type 13 (b) Specimen with one cladding layer, type 16

Figure 7. Displacement figures at the test end: a) reference specimen with OSB only (displacement of individual sheathing panels); b) specimen with OSB sheathing and an additional GFB cladding layer (displacement as a composite panel of sheathing and cladding).

Although the displacements are rather small, the difference between the deformation characteristics of the reference and the cladded specimen are visible at the bottom of the specimens. While the sheathing panels of the reference tests usually rotated as individual panels (relative displacement); the panels of the specimens with additional cladding rotated as one large composite panel of sheathing and cladding.

Figure 8 shows a comparison of the experimental lateral stiffnesses K_{exp} for the specimens with double-sided sheathing (resp. cladding). The OSB sheathed tests need a closer look. Three OSB types are compared:

- **OSB** sheathing with the standard staple spacing of s = 75 mm,
- **OSB+GFB** with OSB sheathing and GFB cladding (each fastened with s = 75 mm),
- **OSB_dSt** with just OSB but the same no. of staples as OSB+GFB (s = 37,5 mm).

It can be observed that the OSB reference test has the lowest stiffness value; OSB+GFB show the highest and the OSB_dSt value is between the others.

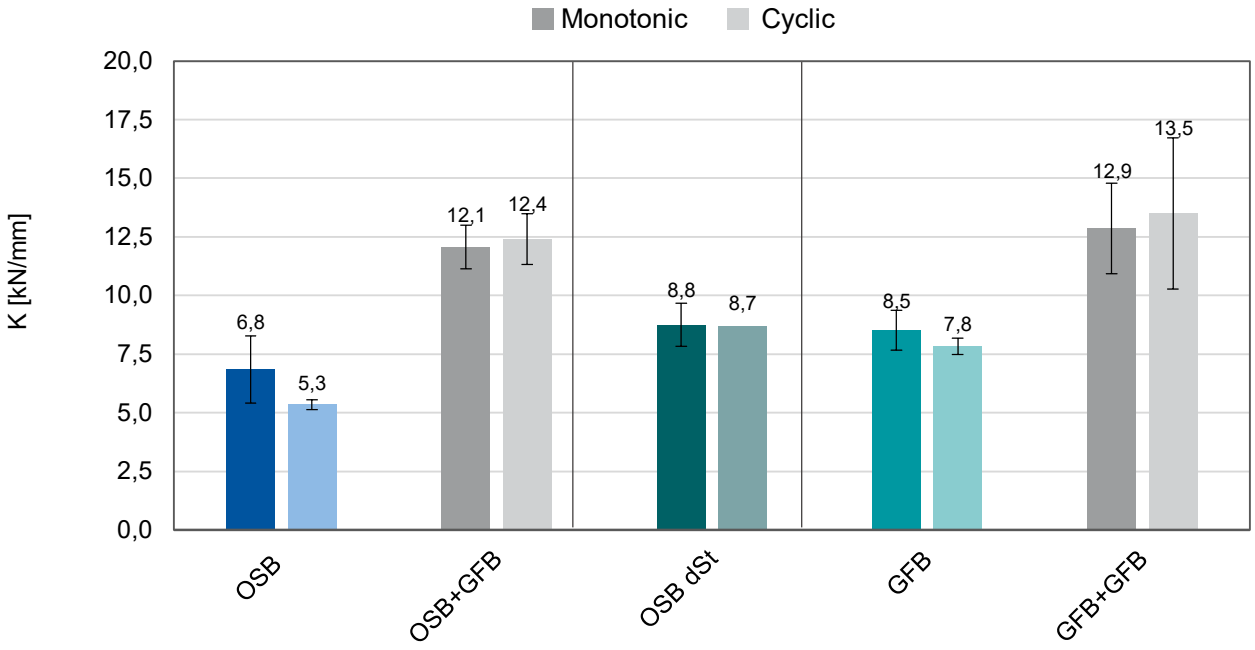

Figure 8. Bar chart of the mean experimental lateral stiffnesses K_{exp} with standard deviation for the specimen types with double-sided sheathing.

4.2 Comparison of analytical model and test results

A comparison of the stiffness calculated with the proposed model K_{shear} versus the test results K_{exp} for the different wall types is shown in the figures below. Two calculation variants are shown:

- Figure 9 shows the results using the staple slip modulus K_{ser} according to *EC 5*,
- Figure 10 shows the results using the slip modulus K_{SLS} from *prEN 1995-1-1*.

For the calculated stiffnesses a value range is provided: from the lower bound K_{min} to the upper bound K_{max}, as described in 3.1.1. The bar charts show that the calculated stiffnesses using the staple slip modulus K_{ser} (*EC 5*) are lower than using K_{SLS} (*prEN*).

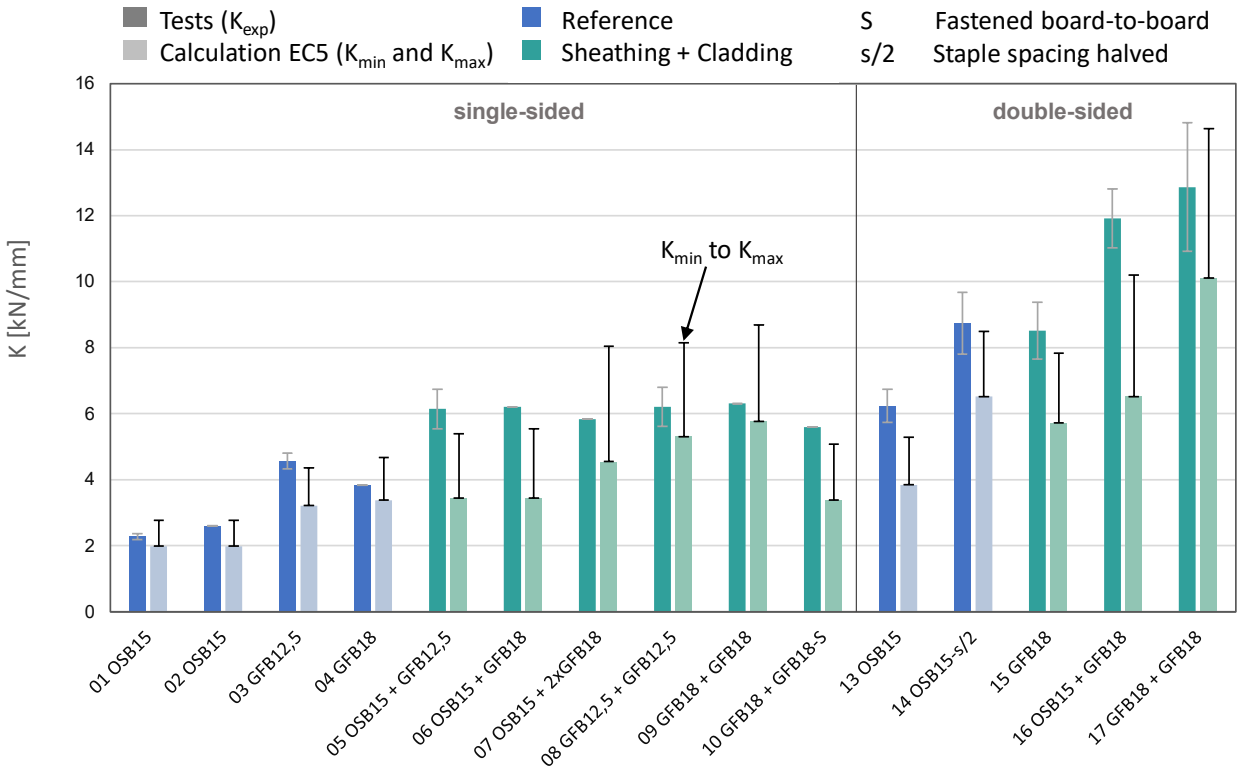

Figure 9. Bar chart comparison of stiffnesses: experimental versus calculated with K_{ser} acc. to EC 5.

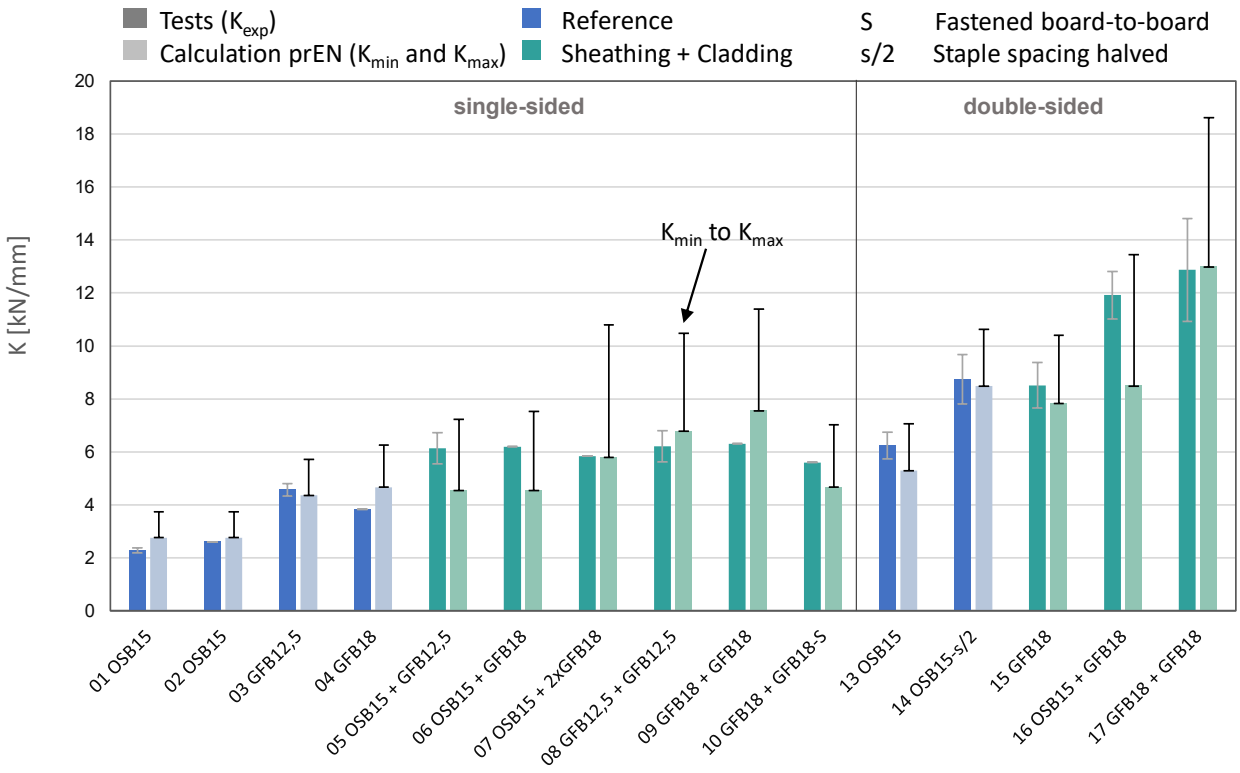

Figure 10. Bar chart comparison of stiffnesses: experimental versus calculated with K_{SLS} according to prEN 1995-1-1 (scaled differenty than Figure 9).

5 Discussion

The **experimental results** for the tested LTFWs show a large increase of the lateral stiffness due to additional claddings (and their fasteners). The comparison of the three specimen types (OSB, OSB+GFB and OSB_dSt) in Figure 8 shows that the increase of stiffness does not result from the strengthened sheathing-to-framing connection alone. The cladding-to-sheathing connection is also activated in the "linear-elastic" part of the load-displacement curve and leads to higher stiffnesses.

Rauber et al. (2024) indicated that the load-carrying capacity of LTFWs with multiple panel layers is governed by the sheathing-to-framing connection, as the total shear must be transferred through this connection's shear plane. For the stiffness, however, we assume that the cladding-to-sheathing connection is also activated and thus increases the wall's lateral stiffness. The observed displacement figures of the tests (Figure 7) support this claim, as they show sheathing and cladding acting as a composite panel. That leads to significantly lower displacements of the fasteners in the sheathing-to-framing connection at the inner studs. The composite action of sheathing and cladding also leads to lower shear deformations of the sheathing. The cladding is also activated and increases the shear modulus of the composite panel.

It could be considered that the tests were not performed under reference climate conditions and the moisture content in the timber framing was higher than 12% (on average 13,8% for the single-sided and 14,3% for the double-sided specimens). This could lead to slightly lower-than-expected stiffness values.

The **analytical stiffness model** of *prEN 1995-1-1* does not consider effects of cladding and its fasteners. The presented analytical model in this contribution gives a first approach to consider the effects of additional cladding. The model allows calculation of the increased stiffnesses for cladded LTFWs and leads to closer estimates than the current standard.

The stiffness model however does not reflect the test results as good als the model for the load-carrying capacity. This might be due to higher scattering of the stiffness values in the experimental data as well as the lack of more precise input values for the slip moduli and mean material values.

Two boundary values are introduced for the analytical stiffness, a lower and an upper bound. The introduction of the lower and upper bound seems reasonable, as the stiffness values scatter. To calculate the stiffness on the safe side by a lower bound for SLS and an upper bound for seismic loads could be an approach for the practice.

For LTFWs the calculation of the staple slip modulus has a large influence onto the calculated wall stiffness, as seen in Figure 9 and Figure 10. The slip modulus for staples in *EC 5* seems to underestimate the wall stiffness, while the slip modulus of *prEN* leads to a slight overestimation. Keeping in mind the moisture content in the tests, K_{SLS} from *prEN* might be in better agreement for standard climate conditions.

6 Summary and Outlook

Within this contribution an analytical model for the lateral stiffness of LTFWs with multiple panel layers (sheathing + cladding) is presented. The model consists of calculation formulas for the lower and upper bound stiffness. The lower bound just considers the additional cladding fasteners in the sheathing-to-framing connection. The upper bound additionally considers the cladding-to-framing connection and shear modulus of the cladding. To validate the model, test results from LTFW tests with and without cladding are used. The following conclusions can be drawn:

- The tests show that cladding and its fasteners influence the lateral stiffness of LTFWs significantly.
- The tests show that the stiffness increase results not from the strengthened sheathing-to-framing connection only, but that the cladding-to-sheathing connection and shear in the cladding are also activated.
- The proposed analytical model considers multiple panel layers and thus predicts the behaviour of cladded walls more realistically than current standards (*prEN*).
- The lower and upper bound seem a reasonable approach for practical applications.
- The slip modulus of staples in *EC 5* and *prEN 1995-1-1* differ largely. Application of *prEN* leads to higher wall stiffnesses.

The presented stiffness increase by claddings and its fasteners should be considered in future standards – especially for seismic design. This contribution provides a first analytical approach for standards to calculate the displacement and stiffness of LTFWs with multiple panel layers (of sheathing and cladding).

7 Acknowledgements

The authors gratefully acknowledge the financial support of the FNR research project HELEPOLIS funded by BMEL (FKZ 2221HV075B) and the efficient cooperation with the project partners Walter + Reif Ingenieurgesellschaft mbH and Adams Holzbau-Fertigbau GmbH.

8 References

Chen, Z.; Chui, Y.-H.; Doudak, G. et al. (2016): Contribution of Type-X Gypsum Wall Board to the Racking Performance of Light-Frame Wood Shear Walls. In: Journal of Structural Engineering 142, Issue 5.

DIN EN 12369-1 (2001): Wood-based panels - Characteristic values for structural design - Part 1: OSB, particleboards and fibreboards; German version EN 12369-1:2001. DIN.

DIN EN 1995-1-1/NA (2013): National Annex - Nationally determined parameters - Eurocode 5: Design of timber structures - Part 1-1: General - Common rules and rules for buildings. DIN.

DIN EN 338: (2016): Structural timber - Strength classes; German version EN 338:2016. DIN.

EN 1955-1-1 (2004): Eurocode 5: Design of timber structures - Part 1-1: General – Common rules and rules for buildings. CEN.

ETA-03/0050 (2023): European Technical Assessment: fermacell Gypsum fibre boards - "fermacell Gipsfaser-Platte", "fermacell Vapor", "fermacell Gipsfaser-Platte green-line". James Hardie Europe GmbH. Deutsches Institut für Bautechnik.

Glos, P.; Henrici, D.; Schmelmer, B. (1987): Festigkeit von ein- und zweiseitig beplankten Wandelementen. In: Holz als Roh- und Werkstoff 45, S. 41-48.

ISO 21581 (2010): Timber structures - Static and cyclic lateral load test methods for shear walls. International Organization for Standardization.

prEN 1995-1-1 (2023): Eurocode 5 - Design of timber structures - Part 1-1. CEN.

Rauber, L.; Hoffmeister, B. (2024): Proposal for an Analytical Model of Light Timber-Framed Shear Walls with addition-al Cladding. In: INTER Proceedings, Meeting 57, 57 - 15 - 2.

Rauber, L.; Hoffmeister, B. (2025a): Experimental Investigations of the Load-Carrying Behaviour of Light Timber-Framed Shear Walls with Cladding – Series 1 – Single-Sided Sheathing. RWTH Aachen University. DOI: 10.18154/RWTH-2025-01547

Rauber, L.; Hoffmeister, B. (2025b): Experimental Investigations of the Load-Carrying Behaviour of Light Timber-Framed Shear Walls with Cladding – Series 2 – Double-Sided Sheathing. RWTH Aachen University. DOI: 10.18154/RWTH-2025-02576

Valdivieso, D.; Guindos, P.; Montaño, J. et al. (2023): Experimental investigation of multi-layered strong wood-frame shear walls with nonstructural Type X gypsum wallboard layers under cyclic load. In: Engineering Structures 282.

DISCUSSION

The paper was presented by L Rauber

A Ceccotti received confirmation that no vertical load was added. He commented that Canadian results a couple of decades ago showed gypsum system should have reduced ductility. If the strength of the cladding is reduced, the R-factor should be reduced as well.

T Skaggs questioned why OSB + cladding showed doubled capacity but not stiffness.

G Doudak asked about whether stronger hold-downs would be needed. L Rauber said the hold-down had high capacity and they also tested GTB wall alone.

R Tomasi and L Rauber discussed just using the lateral slip modulus from nails in the modeling process. R Tomasi received clarification if separate tests on staples were done. C Sandhaas commented that the test setup cannot take load in a specific direction.

S Winter commented that the doubled load capacity is due to the reduction of nail spacing. It is a plastic situation that Eurocode takes into consideration in design. In the elastic range, cladding can participate but not in the plastic range; hence, explaining the stiffness issue. He commented about fire design fixing. Tests should be conducted in density values and k_{ser} and timber properties should be measured, instead of taking properties from standards.

P Dietsch commented on the level of activation of fasteners against the stud. L Rauber said the analytical formulation considered cladding as single plate and OSB panels as second plate.

Experimental Investigation of a Two-Storey Full-Scale CLT Structure with Resilient Rocking Walls for Seismic Behaviour Factor Determination

S.R. Agarwal, The University of Auckland, Auckland

A. Hashemi, The University of Auckland, Auckland

P. Quenneville, The University of Auckland, Auckland

Keywords: CLT, resilient rocking walls, seismic design, q-factor, low damage design, self-centering systems.

1 Introduction

Mass timber is increasingly preferred for engineered buildings due to its sustainability, lightweight properties, and efficient construction. Cross Laminated Timber (CLT), with its low cost and bidirectional properties, has been a focus of extensive research in the last two decades (Dujic, et al., 2004), (Popovski, et al., 2010) and (Lindt, et al., 2020). CLT offers integrated benefits, serving as both a primary structural component and a Lateral Load-Resisting System (LLRS), while also providing biophilic interior finishes.

As an LLRS, CLT walls behave rigidly, with ductility and damage typically concentrated at the base connections (Ceccotti, et al., 2013). Various conventional and Low Damage Design (LDD) connection options have been researched, with those most relevant to this paper discussed herein. The conventional systems include CLT walls with conventional hold-downs and couplers that are prone to damage, which results in pinched hysteresis and stiffness degradation (Ceccotti, et al., 2013), (Popovski & Gavric, 2016) and (Amini, 2018). Furthermore, these systems exhibit either rocking or sliding mechanisms, with rocking behaviour typically dominating in walls with aspect ratios designed for high ductility. Furthermore, the rocking behaviour presents

displacement compatibility challenges with connecting diaphragms (Palermo, et al., 2005).

The evolution of CLT connection research has progressed from traditional dowel-type fasteners to advanced self-centering systems. Ringhofer et al. (2018) established comprehensive design approaches for dowel-type fasteners in CLT, defining failure modes including dowel yielding, timber embedment, and brittle mechanisms such as splitting and plug shear, while Brandner et al. (2016) demonstrated the 'rope effect' in bolted connections that enhances capacity through axial force interaction. Concurrently, research has emphasized the need for connections accommodating large deformations without brittle failure (van de Kuilen et al., 2011), leading to specialized connectors designed for ductility and low-damage performance. Foundational work on inclined self-tapping screws by Uibel and Blaß (2007) demonstrated superior axial stiffness and withdrawal capacity, becoming fundamental to modern high-performance CLT connections. These connections were used in this study along with the work by Hashemi et al. (2016) to form stiffer and damage free connections. This progression from damage-prone conventional systems to advanced self-centering systems with separate energy dissipation elements represents a paradigm shift toward achieving seismically resilient structures suitable for rapid post-earthquake reoccupation

LDD concepts for CLT walls include systems with Post-tensioned (PT) cables (Sarti, et al., 2016 and Iqbal, et al., 2015) and wall systems incorporating resilient dampers and couplers (Hashemi, et al., 2016, Chan, et al., 2020 and Agarwal, et al., 2023). Several studies that have investigated rocking CLT walls with post-tensioned (PT) cables, including full-scale experimental programs include Sarti et al., 2016; Pei et al., 2012, 2018 and Blomgren et al., 2019. The NEHRI tall wood projects (Dowden et al., 2025 and Pei et al., 2024) have further contributed notably to compliant design procedures for rocking CLT walls with PT cables.

Most of these full-scale tests involved PT cables. Rocking CLT walls with PT cables require machining of the CLT panels and may need long-term monitoring of the PT force due to timber creep, potentially reducing the system's competitiveness (Blomgren, et al., 2019). Furthermore, many of these tests, including recent work by Amer et al. (2023), have indicated crushing damage at the rocking toe, leading to a loss of initial stiffness. However, the demand for higher performance, particularly in seismic regions, has driven the development beyond these conventional systems. This study investigates a non-PT alternative using resilient hold-downs, which may offer a more competitive and practical solution for a broader range of projects. Furthermore, this work provides crucial performance data, expanding the global knowledge base for diverse resilient timber systems.

This experimental work also provides the necessary data to determine and quantify the seismic behaviour factor (separate study) such as q-factor, used in European seismic design codes like Eurocode 8 (CEN, 2004). The q-factor allows for reduction of

seismic design forces based on the structure's ability to dissipate energy through ductile behaviour, overstrength, and redundancy. For novel systems like the one presented, the q-factor must be determined through extensive testing (Follesa et al., 2018).

1.1 Research Plan

To address the above discussed research gap in full-scale testing of CLT walls with self-centering hold-downs (without PT cables), this research programme investigates the holistic behaviour of a complete CLT structural system. This project involves the construction and testing of a complete full-scale CLT structure, including columns, beams, and floors (Figure 1.1).

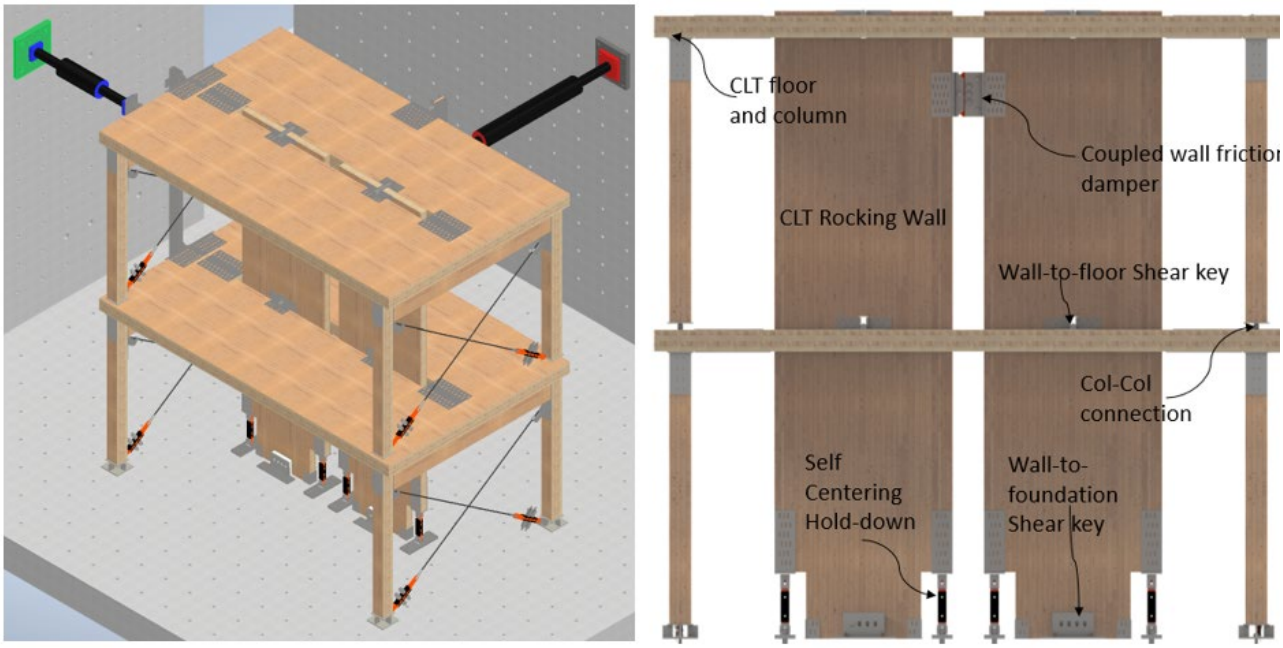

Figure 1.1. Test setup for two story full-scale CLT building.

The two-story test setup consists of two CLT walls in the longitudinal direction as the primary LLRS. Although a single CLT wall would have sufficed structurally, two walls were intentionally incorporated to investigate the coupled wall behaviour with conventional friction dampers. Tension-only X-bracing provided lateral stability in the transverse direction. The CLT walls were decoupled from the gravity system for the initial two test phases and transfer only lateral forces. The overall dimensions of the test structure are 6 meters long, 6 meters high, and 4 meters wide. The performance of various connections, including column-to-column, column-to-beam, column-to-brace, and column base connections, was evaluated under high drifts (Figure 1.2). Moreover, the structural design specifically addresses challenges identified in previous research, such as toe crushing and the associated loss of initial stiffness. The CLT walls were also tested in a coupled configuration using conventional friction dampers in combination with self-centering resilient hold-downs.

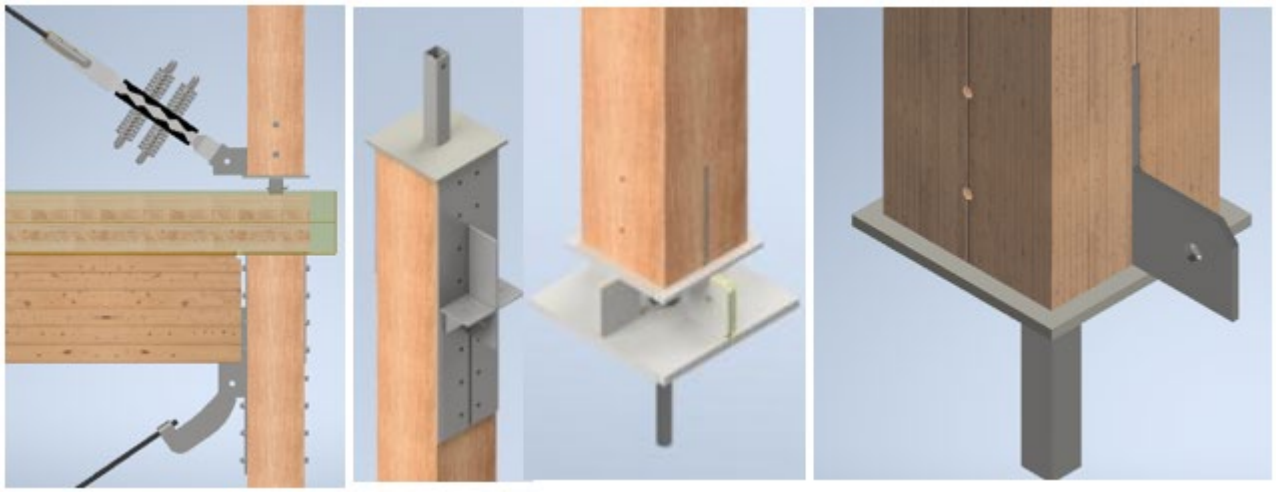

Figure 1.2. Left to right: column -column / column beam/ column brace connection, column with top connector plate, column base connection.

Quasi-static testing, using the FEMA 461 reversed cyclic loading protocol to achieve up to 4% drift was completed. Collaboration and funding are actively being sought for future shake table testing of the structure.

2 Connections for CLT Building

The connection design for the experimental setup was developed to be versatile, allowing for multiple test configurations while adhering to capacity design requirements, ensuring displacement compatibility, incorporating findings from existing research (Ringhofer, et al., 2018 and Franke & Quenneville, 2011), and complying with relevant code provisions (Eurocode 5, 2008).The inclined self-tapping screws (STS) with high axial stiffness (Uibel and Blaß, 2007) and dowel-type connections following European seismic design principles to localize ductility in steel fasteners and prevent brittle timber failure modes (Tomasi and Smith, 2015) were used, aiming for robust strength hierarchy and predictable ductile performance at drifts corresponding to collapse (4%).

The structure utilized a combination of bolted connections and inclined self-tapping screws. Column base connections employed knife plates with 12 mm diameter bolts (Figure 1.2 and Figure 2.1). A complex connection was designed at the column-to-column interface to transfer forces between columns, from the beams, and from the transverse bracing system. This connection also incorporated a mechanism to selectively disengage beam support from the CLT slab and to transfer gravity loads from the CLT wall to the gravity columns and ledge beam during later test phases. The complexity of these requirements led to the selection of external steel-plated connections over a potentially more aesthetically pleasing knife plate arrangement.

Figure 2.1. Clockwise from top left: column base connection, column beam and brace connection, rocking shear wall with shear key and rocking toes, coupling damper connection between walls.

2.1 Self-tapping screws

The capacity design was implemented using overstrength factors (OSF) of 1.35 for the hold-down connections and 1.2 for the friction couplers. Although additional screw holes were detailed to accommodate potential fastener withdrawal, none has been observed up to 2.5% drift, confirming excellent displacement compatibility (Figure 2.1). The inclined screws were installed using custom-made jigs and welding inclined cut CHS sections to connection plates, resulting in screw angles ranging from 40 to 50 degrees, thereby simulating variations likely to occur under typical site conditions.

3 CLT building testing

Following the application of the FEMA 461 reversed cyclic loading protocol up to 4.1% drift, the structure was examined for damage. The results indicate that the low-damage design performed as expected; no significant damage, screw withdrawal, or movement was observed in any connection plate. The connections between the gravity-resisting system and the LLRS exhibited synchronized behaviour, confirming full displacement compatibility. A selection of bolted base plate connections was disassembled for inspection, revealing no evidence of timber crushing.

3.1 Selected Key Results

The hysteretic behaviour of the structure, which incorporates resilient hold-downs and coupled wall dampers, is presented here (Figure 3.1).

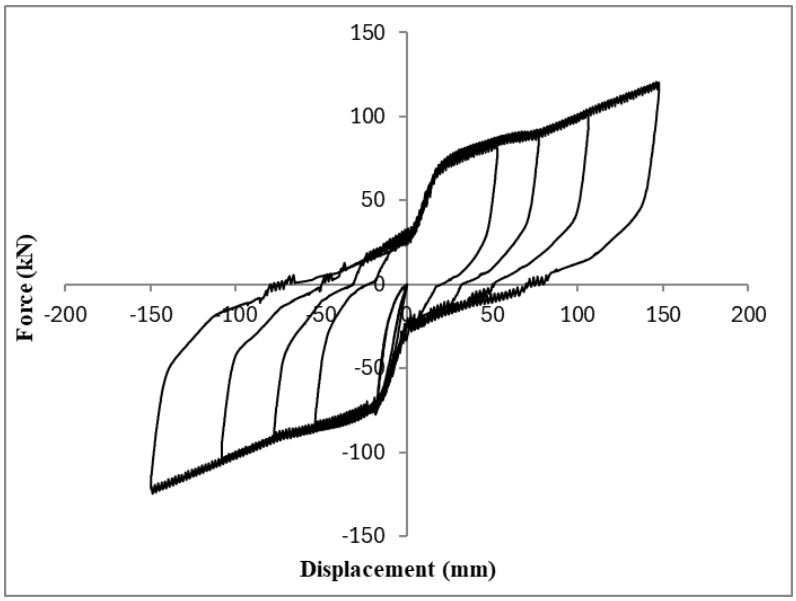

Figure 3.1 Structure hysteresis for 2 storey full scale CLT structure with coupled rocking wall with conventional friction dampers and self-centering hold-downs.

The structure achieved a displacement ductility of approximately 7.5. The hysteresis loops demonstrate no noticeable stiffness or strength degradation with repeated cycles, even up to 2.5% drift. Furthermore, the hysteresis plots reveal an increased damped response when the walls were coupled using friction dampers, with damping estimated to be in the range of 25%.

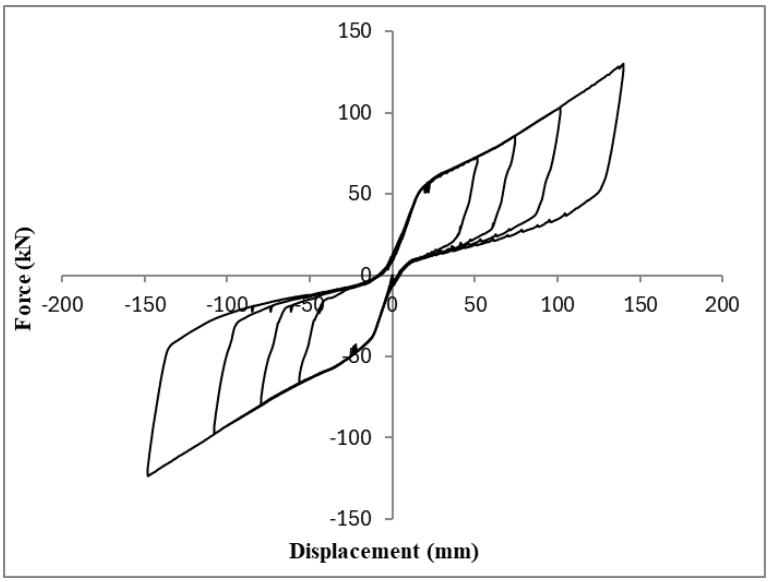

Figure 3.2 Structure hysteresis for 2 storey full-scale CLT structure with self-centering tension-only braces.

The performance of the system can be highlighted by comparing its hysteretic response to that of other CLT wall systems (as shown conceptually in Figure 3.2).

Conventional CLT walls with standard steel hold-downs and angle brackets typically exhibit a heavily 'pinched' hysteresis loop (Wright et al., 2024). This pinching, caused by timber embedment and fastener slip, results in significant stiffness degradation and lower energy dissipation capacity. In contrast, the system tested here produces stable, 'flag-shaped' loops characteristic of a well-behaved self-centering system. The wide, stable loops indicate high and repeatable energy dissipation from the friction dampers, while the unloading curve returning to near-zero force at zero displacement demonstrates the excellent recentring provided by the resilient hold-downs. This behaviour is a significant improvement over both conventional systems, which suffer from large residual drifts, and purely post-tensioned systems, which may lack sufficient energy dissipation unless paired with supplemental dampers.

To date, the structure has been subjected to more than 150 loading cycles, demonstrating the repeatability and resilience of the designed system. The hysteresis loops, characterized by low static residual force, suggest a high degree of self-centering. This self-centering capability will be thoroughly investigated in a separate, dedicated study. The transverse hysteretic behaviour of the structure is also examined (Figure 3.2). Notably, without supplemental friction dampers, the self-centering resilient brace system achieved excellent recentring capabilities even at high ductility demands ($\mu_\delta > 7.5$). The inherent damping from the bracing system was in the range of 15-17%, with the system exhibiting full repeatability and no observable damage. Finally, the tests confirm displacement compatibility between the rocking LLRS in the longitudinal direction and the resilient bracing system in the orthogonal direction. More detailed information on the testing programme will be provided in the forthcoming PhD thesis of the first author.

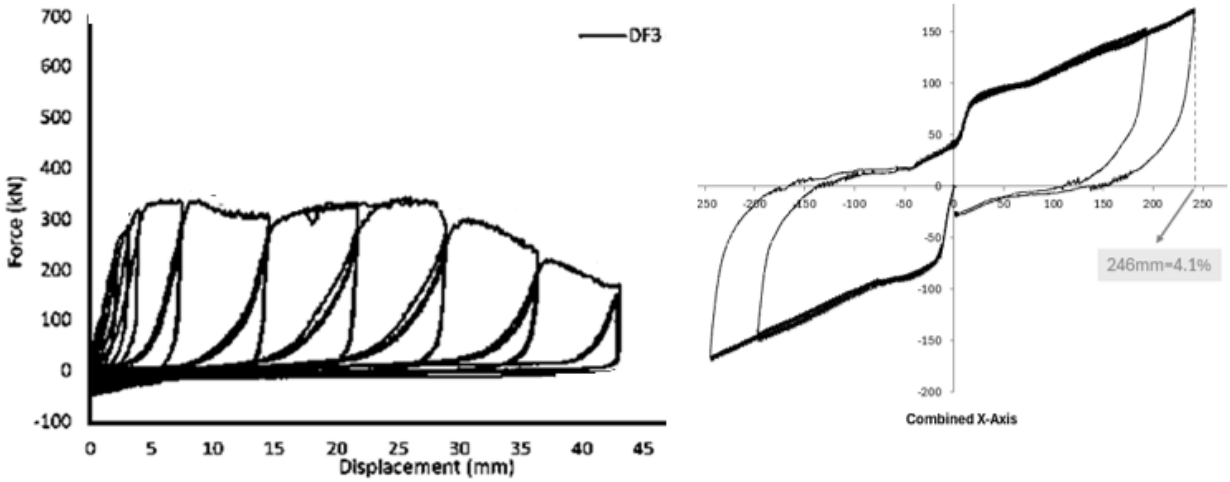

Figure 3.3 Conceptual comparison of hysteresis loops: (left) conventional CLT Wall with STS screws (Wright et al., 2024)., (right) resilient rocking wall tested in this study at 4.1%.(with additional non-self-centering dampers).

Based on the experimental results, preliminary q-factor calculations can be performed. The measured displacement ductility ($\mu_\delta = 7.5$) and overstrength factor ($\Omega \approx 1.8$, estimated from the ratio of peak to design strength) suggest significant ductility and reserve capacity. The equivalent viscous damping of 25% for the coupled system

indicates superior energy dissipation compared to conventional timber systems (typically 5-10%). Using the methodologies outlined in Follesa et al. (2018), these performance metrics suggest that a behaviour factor in the range of 4.5-6.0 could be justified for this system, representing a substantial improvement over conventional CLT wall systems (q = 2.0-3.0). However, final q-factor recommendations will require completion of the full test program, including comprehensive analysis.

4 Conclusions

This paper presents the preliminary results from an ongoing experimental programme investigating the seismic performance of a two-story, full-scale CLT structure at the University of Auckland. The structure, constructed entirely from CLT, features rocking walls with resilient hold-downs as the primary LLRS in the longitudinal direction and resilient tension-only bracing in the transverse direction. The research focuses on the seismic behaviour of the LLRS, its compatibility with the gravity system, and the performance of key connections. Initial testing, conducted up to 2.5% drift following the FEMA 461 reversed cyclic loading protocol, has demonstrated the effectiveness of the low-damage design philosophy. The structure exhibited stable hysteretic behaviour with no signs of stiffness or strength degradation, screw withdrawal, or connection damage. The connections between the gravity system and the LLRS maintained full displacement compatibility.

The results also highlight the potential of this system for achieving high displacement ductility ($\mu_\delta > 7.5$) and significant levels of supplemental damping ($\xi_{eq} \approx 25\%$). The transverse system with resilient tension-only braces also demonstrated excellent performance, achieving high ductility and inherent damping of 15-17% without supplemental devices. The successful integration of the longitudinal and transverse LLRS confirms the feasibility of this structural system for seismic applications.

These initial findings provide valuable insights for the development of seismic design guidelines for resilient mass timber structures and their behaviour factors. The demonstrated high displacement ductility, robust energy dissipation, and re-centering capability provide a strong basis for proposing a high behaviour factor (q-factor) for this structural system under codes like Eurocode 8. The lack of pinching and degradation, combined with the measured overstrength, suggests that the system can be reliably designed for reduced seismic forces while ensuring a low-damage performance objective. The ongoing research, including planned dynamic testing and shake table experiments, will further refine these recommendations and contribute to the broader adoption of sustainable and resilient mass timber construction.

5 Acknowledgement

This research was conducted at the University of Auckland, and the authors express their sincere gratitude for the use of their state-of-the-art laboratory facilities. The authors would also like to extend their appreciation to the University's staff and

technicians for their invaluable assistance and expertise throughout the experimental program. The Wide Trust of New Zealand is gratefully acknowledged for their generous financial support, which made this research possible.

6 References

Agarwal, S., Hashemi, A. & Quenneville, P. (2023): Effect of uncertainties in collapse assessment of coupled CLT walls with energy dissipators as couplers and resilient hold-downs. Auckland, New Zealand, New Zealand Society for Earthquake Engineering Annual Technical Conference.

Amer, Alia, S. & Richard (2023): Multidirectional Experimental Performance of a Seismically Resilient Self-Centering Cross-Laminated Timber Shear Wall System.

Amini, M. O. (2018): Determination of seismic performance factors for cross laminated timber shear wall system based on FEMA P695 methodology. Dept. of Civil and Environmental Engineering, Colorado State Univ.

Blomgren, H.-E. et al. (2019): Full-Scale Shake Table Testing of Cross-Laminated Timber Rocking Shear Walls with Replaceable Components. Journal of Structural Engineering, 145(10).

Brandner, R., Ringhofer, A., & Blaß, H. J. (2016): Cross laminated timber (CLT) in bending: Design of dowel-type connections. In WCTE 2016-World Conference on Timber Engineering.

Ceccotti, A. et al. (2013): SOFIE project—3D shaking table test on a seven storey full-scale cross-laminated timber building. Earthquake engineering & structural dynamics, 42(13).

CEN (2004): Eurocode 8: Design of structures for earthquake resistance - Part 1: General rules, seismic actions and rules for buildings (EN 1998-1:2004). Brussels: European Committee for Standardization.

Chan, N. et al. (2020): Pinching-Free Connector for Timber Structures. Journal of Structural Engineering, 147(5).

Dowden, et al. (2025): Shake-Table Test of a Seismically Resilient 10-Story Mass Timber Building with Supplemental Uplift Friction Dampers. J. Struct. Eng, 151(1).

Dujic, B., Pucelj, J. & Zarnic, R. (2004): Testing of racking behavior of massive wooden wall panels. Rotterdam, Netherlands., Proceedings of 37th CIB-W18 Meeting, International Council for Building Research and Innovation.

Eurocode-5 (2008): Design of timber structures. Brussels: European Committee For Standardization.

FEMA-461 (2007): Interim Testing Protocols for Determining the Seismic Performance Characteristics of Structural and Nonstructural Components. Redwood City California, Federal Emergency Management Agency.

Follesa, M., Fragiacomo, M., Casagrande, D., Tomasi, R., Piazza, M., & Vassallo, D. (2018): A state-of-the-art review on the seismic behavior of timber buildings. Engineering Structures, 171, pp. 824-848.

Franke, B. & Quenneville, P. (2011): Numerical Modeling of the Failure Behavior of Dowel Connections in Wood. Journal of Engineering Mechanics, 137(3).

Hashemi, A. et al. (2016): Ductile cross laminated timber (CLT) platform structures with passive damping. Vienna, Austria, WCTE2016.

Iqbal, A., Pampanin, S., Palermo, A. & Buchanan, A. H. (2015): Experimental performance and structural analysis of plywood-coupled LVL walls. Journal of Structural Engineering, 142(2).

Lindt, J. W. V. D. et al. (2020): Seismic Performance Factors for Cross-Laminated Timber Shear Wall Systems in the United States. Journal of Structural Engineering, 146(9).

Palermo, A., Pampanin, S., Buchanan, A. & Newcombe, M. (2005): Seismic Design of Multi-Storey Buildings using Laminated Veneer Lumber (LVL). Taupo, New Zealand, New Zealand Society for Earthquake Engineering.

Pei, et al. (2024): Shake-Table Testing of a Full-Scale 10-Story Resilient Mass Timber Building. J. Struct. Eng., 150(12).

Pei, S. et al. (2018): Full-scale shake table test of a two-story mass timber building with resilient rocking walls. Thessaloniki, Greece, 16th European Conference on Earthquake Engineering.

Pei, S., Lindt, V. d. & J.W., P. M. (2012): Approximate R-Factor for Cross Laminated Walls in Multi-Story Buildings. ASCE Journal of Architectural Engineering.

Popovski, M. & Gavric, I. (2016): Performance of a 2-Story CLT House Subjected to Lateral Loads. Journal of Structural Engineering, 142(4).

Popovski, M., Schneider, J. & Schweinsteiger (2010): Lateral Load Resistance of Cross-Laminated Wood Panels. Trento, Italy, Proceedings of World Conference on Timber Engineering, p. 20–24.

Ringhofer, A., Reinhard, B. & Blaß, H. J. (2018): Cross laminated timber (CLT): Design approaches for dowel-type fasteners and connections. Engineering Structures, 171, pp. 849-861.

Sarti, F. et al. (2016): Determination of the seismic performance factors for post-ten-sioned rocking timber wall systems. Earthquake Engineering & Structural Dynamics, pp. 181-200.

Tomasi, R., & Smith, I. (2015): A new test configuration for the characterization of connection for timber structures under cyclic load. Materials and Structures, 48(6), 1861-1878.

Uibel, T., & Blaß, H. J. (2007): Load-carrying capacity of joints with self-tapping screws in CLT. In CIB-W18 Meeting 40. Bled, Slovenia.

van de Kuilen, J. W. G., Ceccotti, A., Xia, Z., & He, M. (2011): Very tall timber buildings with cross laminated timber. Procedia Engineering, 14, pp. 1653-1659.

Wright, T., Li, M., Moroder, D., Lim, H., & Carradine, D. (2024): Cyclic behaviour of CLT shear wall hold-down connections using mixed angle self-tapping screws. Engineering Structures.

DISCUSSION

The paper was presented by P Quenneville

T Tannert asked what is needed towards standardization of this proprietary system. P Quenneville responded that engineers have freedom to take responsibility for this system.

T Tannert asked what is needed to get a generic system into the standard with for example R=6. P Quenneville said test data would be needed.

G Doudak asked whether the R=3 is at the system level. P Quenneville responded that R=3 is based on reduction of base shear. G Doudak asked whether these systems were designed for a specific deformation level. P Quenneville responded they were designed to remain elastic.

O Sisman asked whether overstrength factors were considered. He asked for strength limitation cases and if it would be advantageous to increase the strength of the damper without increasing the thickness of CLT. P Quenneville responded yes to both questions.

A Ceccotti commented that this system can be used for very important structures. Smaller buildings with smaller consequence classes such as two or three-storey structures do not need such sophistication. P Quenneville responded that the concept of resilient can be and should be applied to all buildings.

R Scotta and P Quenneville discussed the role of steel in friction damping.

P Dietsch commented that information on creep of post tensioned systems is available from the work of M Gräfe. He said for the system tested in this paper, a technical report should be provided as reference. P Quenneville said the work is reported in a PhD thesis.

Determination of Canadian Seismic Force Modification Factors for Post-Tensioned Cross-Laminated Timber Rocking Walls

Huanru Zhu, McGill University, Montreal, QC, H3A 0C3, Canada

Matiyas A. Bezabeh, McGill University, Montreal, QC, H3A 0C3, Canada

Asif Iqbal, University of Northern British Columbia, Prince George, BC, Canada

Marjan Popovski, Building Systems, FPInnovations, Vancouver, BC, Canada

Zhiyong Chen, Building Systems, FPInnovations, Vancouver, BC, Canada

Keywords:

Cross-laminated timber (CLT); Post-tensioned system; NBCC 2020; Incremental dynamic analyses; Performance margin ratio; Performance-based unified procedure; Mass-timber lateral system; Seismic force modification factors.

1 Introduction

Mass-timber buildings have gained substantial popularity over the past two decades, due to their appealing architectural aesthetics, reduced construction time, satisfactory fire resistance, and the sustainable nature of timber as a construction material. The wider adoption of mass-timber construction can help Canada achieve net-zero carbon emissions by 2050, address the housing crisis, and create employment opportunities in rural and Indigenous communities (Allan and Eaton, 2024). Given these advantages, the National Building Code of Canada (NBC) have relaxed the height limit for mass-timber construction and currently allows encapsulated mass-timber buildings up to 12 stories for office or residential occupancy. Conventional mass-timber seismic force-resisting systems (SFRSs) consist of either platform- or balloon-type Cross-Laminated Timber (CLT) shear walls. The ductility and energy dissipation of these buildings depend on the metal connectors between wood members. During seismic excitation, permanent damage to these connectors can result in significant residual drift of buildings, subsequent high repair costs, a risk of aftershock collapse, and the potential need for building demolition. To ensure post-earthquake resilience, a post-tensioned rocking wall system incorporating mass-timber panels (e.g., CLT) and replaceable energy dissipation devices (EDDs) can be utilized as SFRS in mass-timber buildings (Palermo et al. 2005; Pei et al. 2019; Chen et al. 2020). Global efforts

have been made to explore the lateral behaviour and performance of such a system. Early development and experimental tests in New Zealand focused on post-tensioned Laminated Veneer Lumber (PT-LVL) walls with EDDs (Palermo et al. 2005). Due to the relative popularity and availability of CLT, studies in North America mostly focused on PT-CLT walls (Figure 1a). These included quasi-static cyclic tests (e.g., Chen et al. 2018), multidirectional cyclic tests of PT-CLT wall-floor diaphragm sub-assemblies (Amer et al. 2024), and full-scale shaking table tests of two-story and ten-story PT-CLT rocking wall buildings (Pei et al. 2019; Pei et al. 2024). Several studies have also examined the seismic performance of PT mass timber rocking walls using numerical modelling approaches (e.g., Kovacs and Wiebe 2019; Wichman 2023; Zhu et al. 2024, 2025). All these studies demonstrated the system's adequate seismic performance and highlighted the promising applicability of the SFRS in Canada. Nonetheless, challenges remain for the practical adoption of this system in Canada due to the absence of system-specific seismic force modification factors (overstrength-related factor, R_o, and ductility-related factor, R_d) in the latest NBC (NRC 2020).

In Canada, for existing SFRSs, R_d and R_o were derived largely based on engineering judgment, limited experimental tests, and comparison of relative seismic performance among various SFRSs (Fazileh et al. 2023a). For newly developed mass-timber SFRSs, most previous studies followed FEMA P695 (FEMA 2009) to indirectly obtain or assess the validity of the proposed system-specific R_d and R_o factors. However, Fazileh et al. (2023a) identified that differences in seismic hazard, building seismic performance objectives (POs), and design requirements between Canada and the United States complicate the direct application of FEMA P695 to develop Canadian R_d and R_o factors. To address this incompatibility, efforts have been made to develop new procedures for determining R_d and R_o factors in Canada (DeVall et al., 2021; Fazileh et al., 2023a). The Canadian Construction Material Centre (CCMC) proposed evaluating R_d and R_o factors using nonlinear response history analysis (NLRHA) with ground motions scaled to 100% and 200% of the design level earthquake (DLE) (2% in 50 years) (DeVall et al., 2021). Another effort was made by the seismic resilience team at the Construction Research Centre of the National Research Council Canada (NRC-CRC), which modified FEMA P695 to develop the Performance-Based Unified (PBU) method for evaluating R_d and R_o factors. Through conducting nonlinear static analysis, NLRHA, and incremental dynamic analysis (IDA) using ground motions selected and scaled consistent with NBC, it can support the assessment of various POs such as immediate occupancy (IO), life safety (LS), and collapse prevention (CP). Hence, adopting the PBU approach can ensure that the development process considers Canadian seismicity, performance objectives, and design requirements. To facilitate practical adoption of PT-CLT walls as SFRSs in Canada, this study evaluates the R_d and R_o factors for PT-CLT rocking walls with EDDs following the PBU method. An R_o of 1.5 and R_d of 4 were initially considered. To reflect potential variability in building ge-

ometry, system configuration, and seismic hazards, 75 archetype buildings were designed. A robust multi-spring numerical modelling strategy in *OpenSeesPy* was first validated with shaking table tests and then used to model all archetype buildings. Based on the PBU procedure, nonlinear static analysis was conducted to validate the R_o factor, followed by NLRHA to assess the seismic performance of archetype buildings and identify the critical archetypes. Finally, IDA was carried out for all archetypes to validate the R_d factor by examining building performance margin ratios (PMRs).

2 SEISMIC FORCE MODIFICATION FACTOR EVALUATION FRAMEWORK

In Canada, when performing seismic design using the equivalent static force procedure (ESFP) or modal response spectrum analysis (MRSA), the product of R_d and R_o is used to reduce the elastic base shear force (NRC 2020). The R_o factor accounts for the overstrength arising from the difference between nominal and factored resistance, from conservative selection and rounding of member and element size, from the ratio of actual yield strength to the minimum specified yield strength, from overstrength due to strain hardening, and from mobilizing the full capacity of the structure until a collapse mechanism is formed (Mitchell et al. 2003). The R_d factor is used to reflect the degree of ductility of SFRSs. In this study, R_o = 1.5 was adopted, considering the upper limit for R_o as 1.7 in NBCC (Mitchell et al. 2003). R_d of 4 was initially adopted and subsequently examined.

The PBU method evaluates R_d and R_o through nonlinear analyses to determine whether designed structures meet the global PO as defined in the NBC or local limit states outlined in standards such as CSA O86 (CSA 2019). For global performance, NBC prescribed a 2.5% inter-story drift ratio (ISDR) limit under the DLE. For buildings in the normal importance category (e.g., offices or residential structures), this limit corresponds to extensive damage and aligns with performance objectives of LS (NRC 2020). Wichman (2023) used ISDRs as proxies for system limit states, recommending thresholds of 1%, 2%, and 3% ISDRs corresponding to IO, Limited Repair (LR), and CP objectives, respectively, for resilient seismic design of post-tensioned mass-timber rocking wall buildings. Previous studies (Zhu et al., 2025) further adopted a 5% ISDR as the global collapse criterion, as this value represents the maximum drift compatibility between SFRS and mass-timber gravity frames. In summary, this study identifies five POs, with the PBU method primarily focusing on assessing LS and CP. An overview of the PBU procedure is presented in Figure 1. Readers can refer to Fazileh et al. (2023a, b) for further details regarding each step within the PBU method.

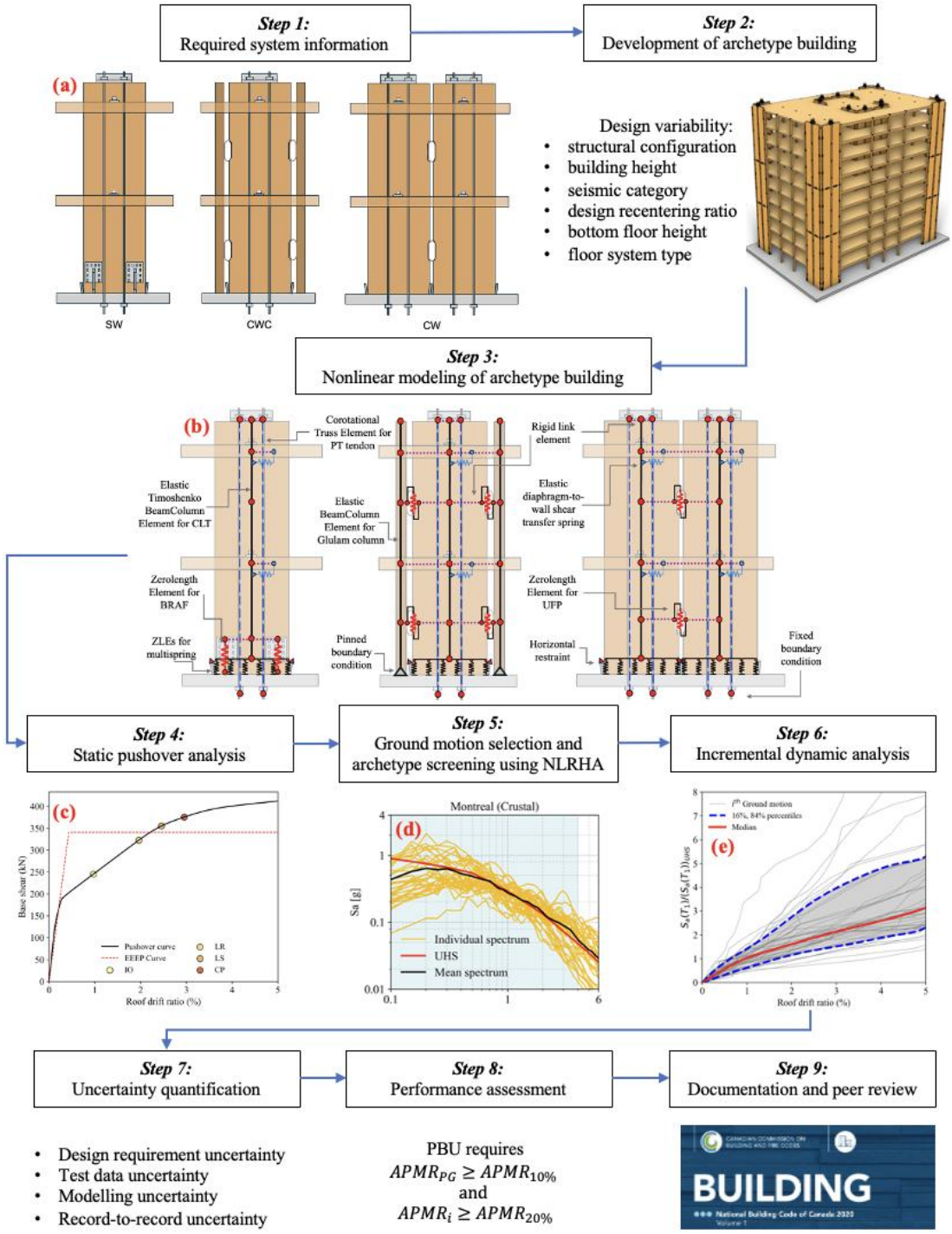

Figure 1. Seismic force modification factor evaluation framework based on the PBU method. (a) structural configurations of PT-CLT rocking walls; (b) schematics of multi-spring numerical models for PT-CLT rocking walls; (c) typical pushover curve for archetype building; (d) ground motion selected and scaled for the city of Montreal with Uniform Hazard Spectrum; (e) typical IDA curves with median, 16%, and 84% percentile statistics for archetype building.

3 ARCHETYPE BUILDINGS AND SEISMIC DESIGN

3.1 Archetype buildings

A PT-CLT rocking wall is comprised of vertically stacked CLT panels clamped by unbonded post-tensioned steel tendons from the wall top to the wall-to-foundation interface (Figure 1a). While a CLT panel can provide in-plane resistance, PT elements

will exert a restoring moment to recentre the system when elongated under lateral loading. Sliding can be prevented with shear keys. Various types of EDDs can be coupled to the system. This typically includes buckling-restrained axial fuses (BRAFs) (Zhu et al. 2024) and U-shaped flexural plates (UFPs) (Pei et al. 2024). The balloon-framing SFRS can be connected to floor diaphragms using shear keys inserted into a vertically slotted hole, as outlined in Pei et al. (2024). Based on past studies, there are three types of structural configurations for PT-CLT walls, including (a) single wall (SW), (b) column-wall-column (CWC), and (c) coupled-wall (CW) (Figure 1a).

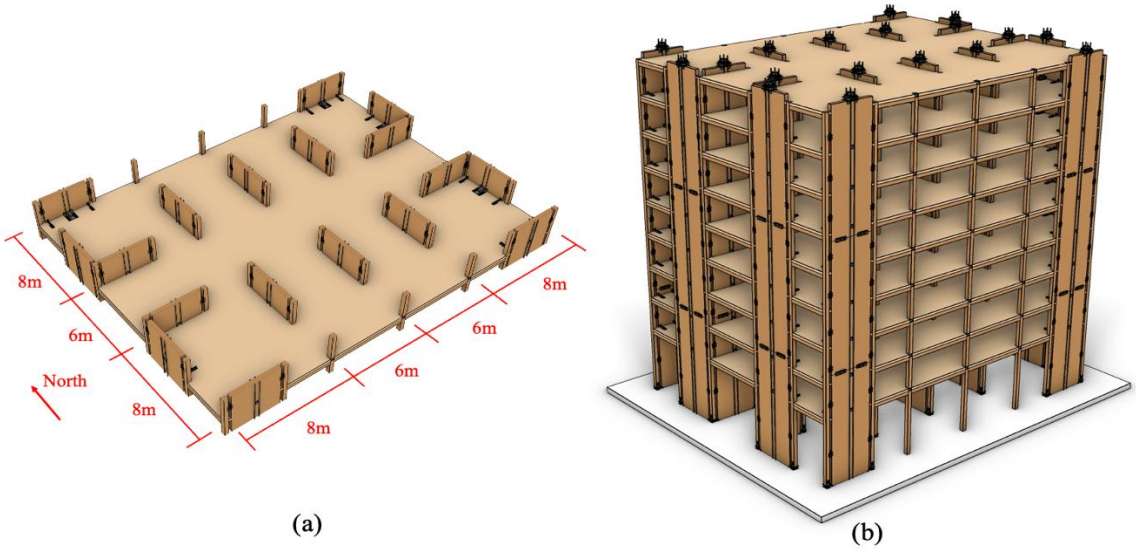

Figure 2. Details of the archetype building: (a) floor plan including wall position; (b) full building rendering.

Archetype buildings with a typical floor plan, as shown in Figure 2a, were developed in this study. The considered design variables are summarized in Figure 1 (Step 2). Each building had ten PT-CLT rocking walls positioned in the N-S direction. These buildings were designated as normal occupancy office buildings and were situated on Site Class D soil (NRC 2020). For the considered R_d of 4, 75 archetype buildings, grouped into 24 PGs, were developed. Table 1 summarizes the details of the developed archetype buildings. Using the CWC-type PT-CLT rocking wall building as an example, the archetypes in PGs 9 to 12 and 13 to 16 were hypothetically designed for Vancouver, British Columbia, and Montreal, Quebec, respectively, to represent seismic categories (SCs) 3 and 4 (moderate and high seismicity), as defined by NBC (NRC 2020). In PGs 9 and 13, the archetypes were defined with a bottom floor height of 3.6 m and a typical story height of 3.2 m, covering 3-, 6-, and 9-story building configurations. To account for potential use of the first story as an office building with commercial spaces, PGs 10 and 14 adopted a 6-m bottom-floor height. In addition, the design recentering ratio, which is the ratio of the moment resisted by PT elements to the total moment resistance of the system, was considered a variable. Whereas PGs 9, 10, 12, 13, 14, and 16 used a recentering ratio of 70%, and PGs 11 and 15 adopted a lower ratio of 60%, offering higher energy dissipation. To enhance vibration control, all these PGs (i.e., PGs 9–11 and 13–15) used timber-concrete composite floors

(TCCF), which resulted in higher seismic mass. However, PGs 12 and 16 explored an alternative floor system consisting of CLT panels only. For both seismic design and numerical modelling, the CLT-only and TCCF floor systems were assumed to behave as rigid diaphragms. Schematic representations of a 9-story CWC-type PT-CLT rocking wall building are depicted in Figure 2b. Using the same considerations, SW-type (PGs 1–8) and CW-type (PGs 17–24) PT-CLT rocking wall buildings were developed (Table 1).

Table 1. Performance groups and building archetypes information for PT-CLT rocking wall buildings.

Archetype	Structural configuration	Archetype	Structural configuration	Archetype	Structural configuration	Seismic category	Number of stories	Bottom floor height (m)	Story height (m)	Re-centering ratio	Floor system
1 (PG 1)	SW	26 (PG 9)	CWC	51 (PG 17)	CW	SC 4	3	3.6	3.2	0.7	TCCF
2 (PG 1)	SW	27 (PG 9)	CWC	52 (PG 17)	CW	SC 4	6	3.6	3.2	0.7	TCCF
3 (PG 1)	SW	28 (PG 9)	CWC	53 (PG 17)	CW	SC 4	9	3.6	3.2	0.7	TCCF
4 (PG 2)	SW	29 (PG 10)	CWC	54 (PG 18)	CW	SC 4	3	6	3.5	0.7	TCCF
5 (PG 2)	SW	30 (PG 10)	CWC	55 (PG 18)	CW	SC 4	3	6	4.2	0.7	TCCF
6 (PG 2)	SW	31 (PG 10)	CWC	56 (PG 18)	CW	SC 4	6	6	3.5	0.7	TCCF
7 (PG 3)	SW	32 (PG 11)	CWC	57 (PG 19)	CW	SC 4	3	3.6	3.2	0.6	TCCF
8 (PG 3)	SW	33 (PG 11)	CWC	58 (PG 19)	CW	SC 4	6	3.6	3.2	0.6	TCCF
9 (PG 3)	SW	34 (PG 11)	CWC	59 (PG 19)	CW	SC 4	9	3.6	3.2	0.6	TCCF
10 (PG 4)	SW	35 (PG 12)	CWC	60 (PG 20)	CW	SC 4	3	3.6	3.2	0.7	CLT
11 (PG 4)	SW	36 (PG 12)	CWC	61 (PG 20)	CW	SC 4	6	3.6	3.2	0.7	CLT
12 (PG 4)	SW	37 (PG 12)	CWC	62 (PG 20)	CW	SC 4	9	3.6	3.2	0.7	CLT
13 (PG 5)	SW	38 (PG 13)	CWC	63 (PG 21)	CW	SC 3	3	3.6	3.2	0.7	TCCF
14 (PG 5)	SW	39 (PG 13)	CWC	64 (PG 21)	CW	SC 3	6	3.6	3.2	0.7	TCCF
15 (PG 5)	SW	40 (PG 13)	CWC	65 (PG 21)	CW	SC 3	9	3.6	3.2	0.7	TCCF
16 (PG 6)	SW	41 (PG 14)	CWC	66 (PG 22)	CW	SC 3	3	6	3.5	0.7	TCCF
17 (PG 6)	SW	42 (PG 14)	CWC	67 (PG 22)	CW	SC 3	6	6	4.2	0.7	TCCF
18 (PG 6)	SW	43 (PG 14)	CWC	68 (PG 22)	CW	SC 3	9	6	3.5	0.7	TCCF
19 (PG 6)	SW	44 (PG 14)	CWC	69 (PG 22)	CW	SC 3	9	6	4.2	0.7	TCCF
20 (PG 7)	SW	45 (PG 15)	CWC	70 (PG 23)	CW	SC 3	3	3.6	3.2	0.6	TCCF
21 (PG 7)	SW	46 (PG 15)	CWC	71 (PG 23)	CW	SC 3	6	3.6	3.2	0.6	TCCF
22 (PG 7)	SW	47 (PG 15)	CWC	72 (PG 23)	CW	SC 3	9	3.6	3.2	0.6	TCCF
23 (PG 8)	SW	48 (PG 16)	CWC	73 (PG 24)	CW	SC 3	3	3.6	3.2	0.7	CLT
24 (PG 8)	SW	49 (PG 16)	CWC	74 (PG 24)	CW	SC 3	6	3.6	3.2	0.7	CLT
25 (PG 8)	SW	50 (PG 16)	CWC	75 (PG 24)	CW	SC 3	9	3.6	3.2	0.7	CLT

3.2 Prescriptive seismic design for PT-CLT rocking wall buildings

This study adopts a prescriptive design procedure for post-tensioned mass-timber rocking wall buildings, as described in Figure 3. Because the archetype building is symmetric and negligible torsion is expected, the seismic design was carried out for only one of the PT-CLT walls in the N-S direction (Figure 2a). The design framework comprised five main parts (Figure 3), which are briefly described below.

First, a conceptual structural design was developed based on the architectural layout and the characteristics of each archetype (Table 1), including CLT wall location, quantity, and dimensions. Then, a linear model was first established in *OpenSeesPy.* The model was fixed-based and excluded PT elements. CLT walls were modelled by *elastic Timoshenko beam-column* elements. Seismic mass was assigned to floor nodes. More details of linear modelling for design demand estimation can be found elsewhere (Wichman 2023). MRSA was then conducted using the design spectrum defined in NBC to obtain the elastic design base shear, which was then divided by R_dR_o and combined with the importance factor (I_E) required in NBC to derive the specified lateral earthquake force (V_d) (NRC 2020). This was further multiplied by effective height to produce the specified base overturning moment (M_d). The predicted inelastic drift ($\Delta_{inelastic}$) was obtained by multiplying the lateral deflection determined from MSRA by R_dR_o. The calculated $\Delta_{inelastic}$ must be less than the NBC 2.5% ISDR limit; otherwise, it-

erations are needed. Next, a linear static analysis was performed using the distributed story forces (F_i) determined from MRSA to calculate the panel's elastic deformation ($\Delta_{elastic}$). The rotation demand, or the maximum imposed rotation (θ_{imp}), was calculated as the difference between $\Delta_{inelastic}$ and $\Delta_{elastic}$ (Figure 3). Based on outputs from Part 2, a preliminary design was conducted. Given a system recentring ratio (β_{rc}), the design overturning moment resisted by the PT element (M_{PT}) and EDD (M_{EDD}) were initially estimated. This led to the calculation of the initial post-tensioning force in the PT elements (T_{PT}) and their sizing and detailing (e.g., cross-sectional area (A_{PT}) and number (N_{PT})). For EDDs, the initial stiffness and yield strength of a single EDD were first selected so that the required number of EDDs (N_{EDD}) was determined.

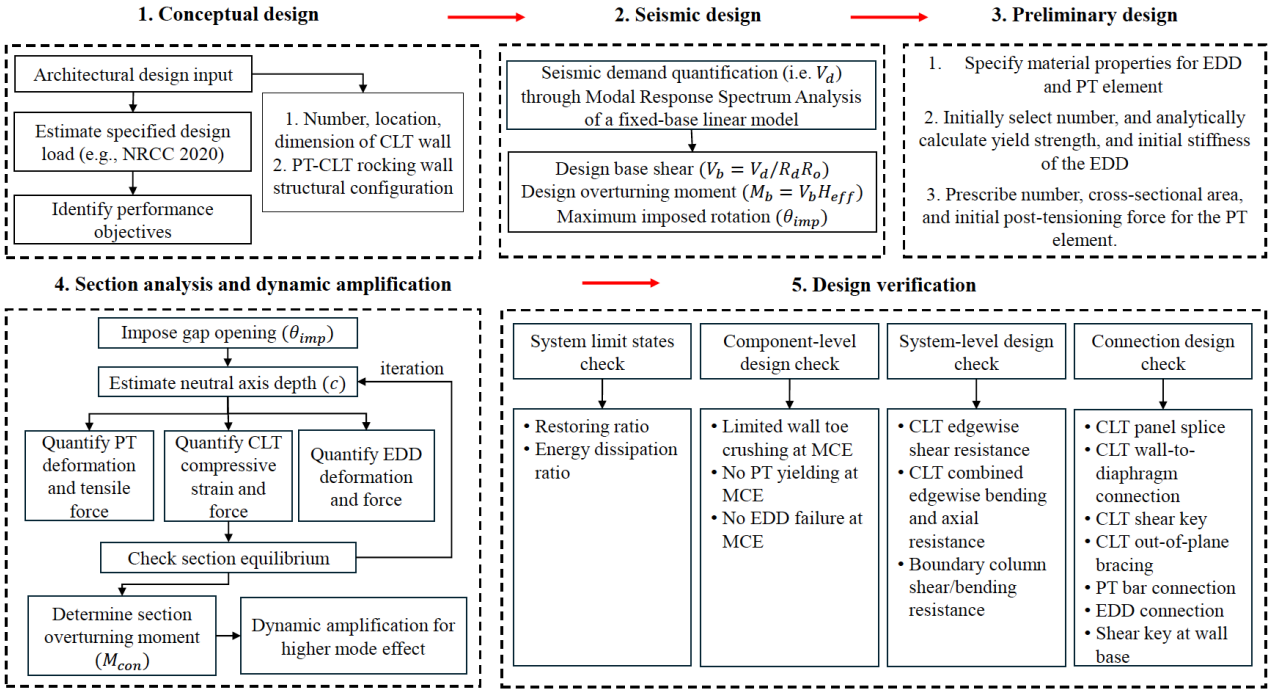

Figure 3. Force-based prescriptive design procedure for PT-CLT rocking walls.

Part 4 includes an iterative sectional analysis to validate the preliminary design (Wichman 2023; Zhu et al. 2025). Based on sectional analysis, the predicted overturning moment (M_{con}) can be estimated at θ_{imp}. Due to the distinct higher-mode effects in the rocking system, M_{con} needs to be further amplified based on the Cantilever Beam Analogy developed in the study by Wiebe and Christopoulos (2015). To validate the preliminary design, system-level limit states, including restoring force ratio and energy dissipation ratio, were first checked. At the θ_{imp}, peak component strains for the CLT compressive zone, PT elements, and EDDs were analytically derived and compared against acceptable strain limits (Wichman 2023). Global design checks then verified that the CLT wall provided sufficient in-plane shear and edgewise flexural resistance. Resistance capacities were evaluated based on manufacturer-provided CLT data where available. Furthermore, because PT forces can increase due to elongation during rocking, and additional forces could be introduced by EDDs acting at the wall rim, the combined edgewise bending and axial loading demands on

the CLT walls were also checked. To ensure satisfactory building performance, series of connection-level capacity checks were also required. Due to space constraints, readers are referred to Wichman (2023) for further details on the capacity design of individual connections. If all design checks are satisfied, the seismic design is considered complete. If any criterion is not met, design iterations are required.

4 Numerical modelling strategy and validation

To perform nonlinear static and dynamic analysis, robust numerical models are required. In this study, a multi-spring modelling strategy was adopted to develop two-dimensional models of PT-CLT walls in *OpenSeesPy*. The multi-spring model uses a series of zero-length elements (ZLEs) at the wall-to-foundation interface to capture rocking behaviour and compressive damage at the plastic zone of the CLT panel (Figure 1b). ZLEs can be distributed across the wall length using a *Labatto* Integration method. The top of each ZLE is connected to the bottom node of the CLT panel by a *rigid link* element, whereas the bottom is fully fixed. Horizontal restraint is imposed on the ZLEs at the two extreme wall edges to prevent sliding. To idealize the stress and strain relationship of the CLT, the *Concrete01* material model, which is a compression-only material with zero tensile strength, was employed to effectively capture CLT yielding, post-yielding degradation, and base uplift behaviour. The concept of contact stiffness is used to translate the CLT's stress-strain relationship into the force-deformation response of each ZLE (Wichman 2023). Above the multi-spring portion, CLT panels can be assumed to be linearly elastic and modelled by *Elastic-Timoshenko* beam elements. The PT elements are modelled by *corotational trusses* assigned with the *Giuffré-Menegotto-Pinto Model (Steel02)* material. The top of the PT tendon is connected to the upper portion of the CLT panel using *rigid elements*. Zero-length elements with calibrated uniaxial material properties in the vertical direction are used to model EDDs. At the EDD location, *zero-length elements* are rigidly connected to the nodes in CLT walls at the same height to account for the offset between the walls and the EDD. An additional gravity-leaning column representing the gravity system is modelled to capture potential P-Delta effects.

Building-level validation of the modelling strategy was performed with shaking table tests of a 10-story PT mass timber rocking wall building reported by Pei et al. (2024) to verify the model's robustness. The 34.5-meter-tall mass-timber building was tested at the world's largest outdoor shaking table facility at the University of California, San Diego (Figure 4a). The multi-phase testing program subjected the structure to a series of ground motions far exceeding those anticipated for any real building. For more information on building design, construction details, material properties, and ground motion selection and scaling, readers are directed to Wichman (2023) and Pei et al. (2024). A three-dimensional numerical model was developed for the entire structure, incorporating six gravity columns, four PT rocking timber walls, and eight associated

boundary columns (Figure 4b). The connection details and element types for wall panels, boundary columns, gravity columns, UFPs, and PT elements were identical to those described in the general modelling techniques above. Multi-spring ZLE elements were distributed in a three-dimensional regime to capture rocking in both the in-plane and out-of-plane directions (Wichman 2023). NLRHA was performed using ground motion acceleration histories obtained from shaking table tests (Pei et al. 2024a). The results were compared with post-processed structural responses from the same tests, with details of the post-processing methodology available in Wichman (2023). Time histories of floor displacements at three heights (i.e., floor levels 4, 7, and 11) of the tested structure are presented for one of the tests with seismic hazard levels corresponding to MCE_R (Figure 4c). Because the two PT-CLT walls were oriented in the east-west direction, the floor displacements presented in Figure 4c represent responses that are aligned with that axis only, even though some tests involved bidirectional seismic excitation. The results showed that the model accurately predicted displacement demands in terms of both pattern and peak values. Overall, the multi-spring model proved robust in capturing the nonlinear dynamic behaviour of PT-CLT walls, making it a reliable tool for subsequent performance assessments of archetype buildings.

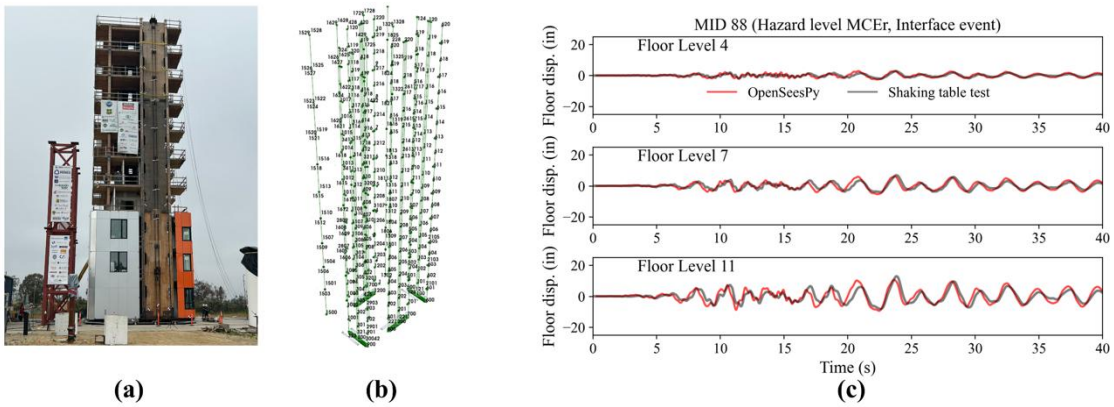

Figure 4. Numerical model validation: (a) full-scale PT mass-timber rocking wall building tested on shaking table (Picture courtesy of Matiyas A. Bezabeh); (b) numerical model in OpenSeesPy; and (c) time-history comparison between floor displacements between OpenSeesPy and shaking table test at different levels.

5 Nonlinear static and dynamic analysis

5.1 Nonlinear static analysis

PBU Step 4 applies NLSA to validate the trial R_o factor and determine period-based ductility (μ_T) at various POs (Figure 1c). In NLSA, each building was monotonically pushed, with load distribution corresponding to the first mode of the structure, using a displacement-control integrator, until a 5% roof drift (a non-simulated collapse mechanism) was triggered. Simulated collapse mechanisms applied component strain limits using the *MinMax* material in *OpenSeesPy*, where exceeding these limits triggers zero tangent stiffness to accelerate collapse. This includes a strain limit of 6% for BRAFs in the SW configuration to implicitly account for low-cycle fatigue failure and a

2% tensile strain limit for PT. Such inherent conservatism should be recognized because residual strength still remains when the aforementioned strain limits are reached.

$$R_O = V_{max}/V_d \quad (1)$$

$$\mu_T = \delta_u / \delta_{y,eff} \quad (2)$$

Based on the pushover curves (Figure 1c), R_o and μ_T were quantified for each archetype using Equations [1] and [2]. The effective yield displacement $\delta_{y,eff}$ was derived based on FEMA P695 (FEMA 2009). The R_o value for each PG was determined by averaging the R_o values of the individual archetype buildings within the group. It was found that for all PGs, the calculated R_o factors were greater than the trial value of 1.5, and this consistency is independent of structural configurations and seismic category (location). As highlighted by Morshedi et al. (2024), μ_T serves as a proxy for structural ductility and forms the basis for estimating R_d for long-period structures based on the equal displacement assumption. Notably, all PGs have average μ_T greater than the adopted R_d, which is independent of seismic category and the considered design variabilities in Table 1. These results support the validity of the assumed R_d factors. Nevertheless, the final evaluation of the trial R_d values should be carried out in PBU Step 8.

5.2 Ground motion selection

To carry out NLRHA, two distinct suites of ground motions reflecting the regional seismic characteristics of Vancouver, British Columbia, and Montreal, Quebec, Canada, were selected and scaled to each of their Uniform Hazard Spectra (UHS) (2% in 50 years at DLE). Both were recommended and provided by the NRC-CRC in the report by Fazileh et al. (2023b). The shear-wave velocity of the top 30 m of soil falls into the range between 300 m/s and 360 m/s, corresponding to a stiff soil condition (Site Class D in NBC). In Vancouver, seismic hazards are contributed from shallow crustal events, megathrust Cascadia interface earthquakes, and deep intraplate earthquakes. In contrast, a single tectonic regime of stable crust dominates the Montreal area. More information on ground motion records and scaling rationales can be found in Fazileh et al. (2023a and b).

5.3 Archetype screening using nonlinear response history analyses

With the selected and scaled ground motions, PBU Step 5 screens the archetypes using NLRHA. Throughout the entire screening process, the PO of LS (i.e., the 2.5% ISDR limit) served as a structural performance indicator. Following the PBU, NLRHA was performed using ground motion scaled to 100% DLE level to assess seismic performance. Although not shown for brevity, it is noteworthy that the mean ISDR responses for all 75 archetypes were less than 2.5% ISDR (LS PO), demonstrating the satisfactory building performance against extensive damage. Next, NLRHA was repeated using ground motions scaled to 216% and 254% DLE (APMR 10% and 6%). The detailed screening criteria introduced in Fazileh et al. (2023a, b) were used. The probability of

exceedances (PoEs) for PO of LS were quantified and compared against the outlined criteria for each individual archetype and PG. Although IDA is not required for non-critical archetypes under the PBU method, it was carried out in this study for both critical and non-critical archetypes to ensure a comprehensive assessment. Hence, the archetype screening results are not presented here for brevity; readers can refer to the IDA results in the next section.

5.4 Incremental dynamic analysis and fragility assessment

IDA was performed to assess the fragility of all archetype buildings and quantify their PMRs by scaling up each ground motion record until any one of the considered simulated and non-simulated collapse criteria was triggered. The IDA results for each archetype were used to calculate the median, 16th, and 84th percentile IDA curves (Figure 1e). Fragility assessment provides the conditional probability of exceeding a specific PO at a given intensity measurement (IM), which represents seismic hazard intensity. These probabilities can be derived from the IDA results. Assuming that the ratio of records causing exceedance to the total number of records at a specific IM level follows a lognormal distribution, fragility curves were fitted using the maximum likelihood method.

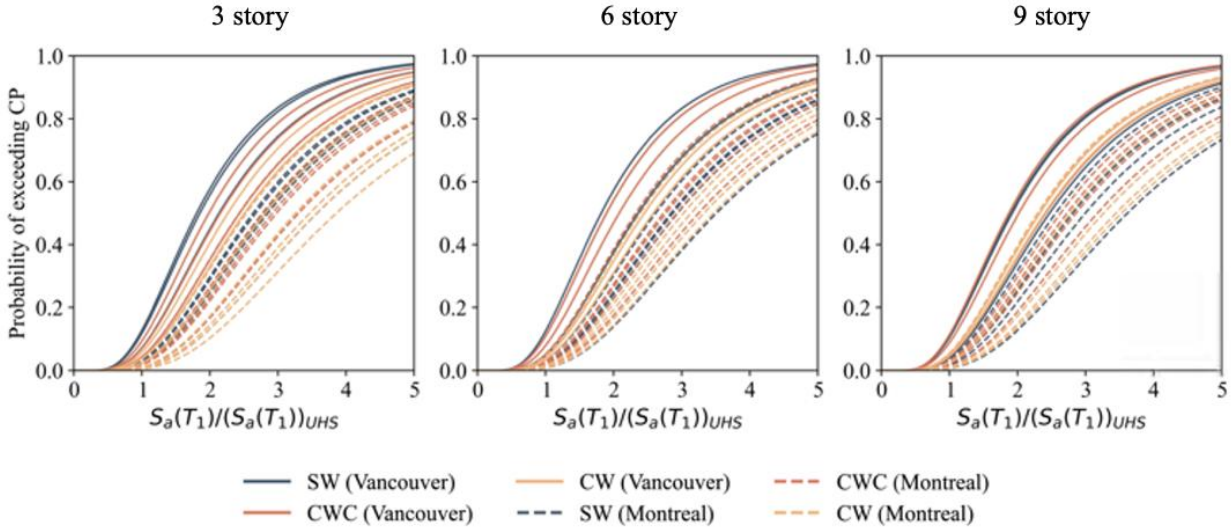

Figure 5. Collapse prevention fragilities for all archetype buildings.

Figure 5 illustrates the fragility curves for CP exceedance for buildings designed with R_d = 4. Note that these fragility curves were adjusted for total uncertainty, which is discussed in detail in the next section. The wide variation among the fragility curves in Figure 5 highlights the comprehensive consideration of various design parameters in the development of the archetypes. Note that under the 100% DLE, the highest probabilities of exceeding CP PO are 12.4%, 11.4%, and 10.9% for 3-, 6-, and 9-story archetype buildings, respectively, attesting to the satisfactory performance of these archetype buildings. The performance margin ratios (PMRs) were calculated using Equation [3], where S_{PT} is the median spectral acceleration intensity leading to exceedance of a given PO and S_{CT} is the design spectral acceleration at the fundamental period of the building. Note that in the CCMC method, archetype buildings must be

evaluated using ground motions scaled to 200% of the DLE. The system is considered to have failed if more than 50% of the ground motions result in exceeding the LS PO, which corresponds approximately to a PMR value less than 2.0. When R_d = 4 is adopted for design, the average PMR for PO of LS, CP, and collapse is 2.30, 2.70, and 4.09, respectively, based on the fragility assessment. Hence, the current PMR values under the LS possess sufficient margins to also meet the CCMC requirements.

$$PMR = S_{PT} / S_{CT} \quad (3)$$

6 Evaluation of R_d factor

6.1 Uncertainty quantification

After IDA and fragility assessment, the PBU method requires quantifying different sources of uncertainty before the final archetype assessment. The total uncertainty, β_{tot}, accounts for uncertainty in the ground motion record (β_{RTR}), system design (β_{DR}), test data (β_{TD}) and numerical modelling (β_{MDL}). The PBU method refers to the same uncertainty rating scheme as outlined in FEMA P695 (FEMA 2009). Each source is evaluated based on completeness, robustness, and confidence. Each rating category (e.g., superior, good, fair, poor) corresponds to a quantitative uncertainty value ranging from 0.10 (most certain) to 0.50 (most uncertain). In this study, β_{DR}, β_{TD}, and β_{MDL} were all set equal to 0.2, corresponding to a "good" rating. These "good" ratings were given because validation of the numerical modelling strategy based on both system- and full-scale building-level testing demonstrated that the multi-spring model can capture the structural response of PT-CLT rocking walls. Furthermore, extensive experiments on PT-CLT walls have been conducted at various scales in New Zealand, Canada, and the United States. The system is one of the most thoroughly tested among all innovative mass-timber SFRSs. The full-scale shaking table test of the 10-story post-tensioned mass-timber rocking wall building used for numerical model validation remains the largest shaking table test ever conducted at the time of writing this paper. According to PBU, β_{RTR} can be calculated at various performance objectives based on IDA results and fragility curves.

6.2 Performance assessment

PBU Step 8 suggests applying the spectral shape factor (SSF) to adjust PMRs and quantify APMRs, which accounts for the bias related to the spectral shape of the ground motion suite. For SSF quantification, this study follows the procedure applied in Morshedi et al. (2024), where readers can find more details. The final step of the PBU framework evaluates whether the adopted R_d factor can result in archetypes and PGs with adequate APMR against specified limits. As mentioned previously, the APMR evaluation considers both LS and CP according to the PBU method. Nonetheless, for brevity and conciseness, only results corresponding to the CP performance level are included. For the assessment, two acceptable thresholds outlined in the PBU procedure were considered (Figure 1). This includes an APMR for each individual archetype greater than $APMR_{20\%}$ and an APMR for each PG greater than $APMR_{10\%}$.

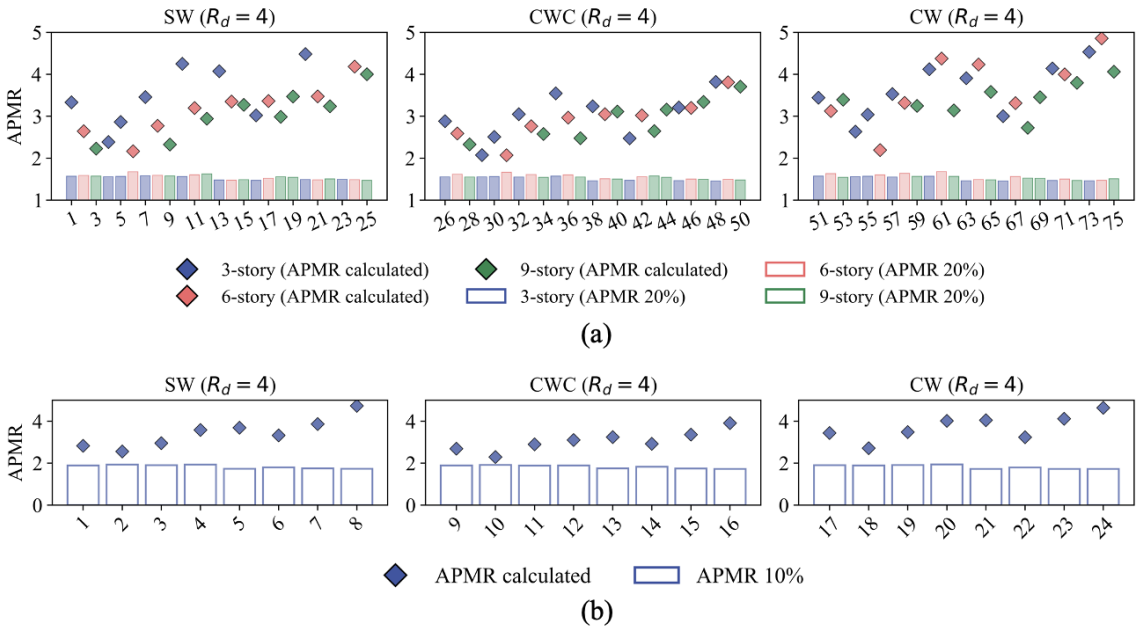

Figure 6. (a) APMR evaluation results for all archetypes considering CP PO using PBU; (b) APMR evaluation for all performance groups using PBU.

Figure 6a presents the results of the APMR evaluation for all archetypes considering CP PO. The APMRs obtained from the analysis are presented as scatter points. Based on the quantified β_{tot}, the corresponding $APMR_{20\%}$ (i.e., the acceptable threshold) for each archetype can be determined (Fazileh et al. 2023a); their values are presented using bars in the chart. Figure 6 can support a straightforward visual assessment of APMRs. For a particular archetype, if a scatter point lies above its corresponding bar in the plot, it can be concluded that the APMR is sufficient with respect to the corresponding acceptable $APMR_{20\%}$. Failure to meet the $APMR_{20\%}$ criterion is indicated when a scatter point falls within the bar. When examining the PO of CP, as shown in Figure 6, all individual archetypes designed with R_d of 4 demonstrated significantly higher APMRs than the acceptance threshold, confirming robust collapse prevention capability. Figure 6b indicates that, when designing with an R_d of 4, all PG APMRs are greater than the corresponding $APMR_{10\%}$ threshold. Overall, it can be concluded that an R_d of 4 can lead to satisfactory seismic design, with the resulting APMRs of the designed buildings being greater than the PBU acceptable threshold.

7 Conclusion

In this paper, to supplement the upcoming edition of the National Building Code of Canada (NBC), we quantified seismic force modification factors for PT-CLT walls with EDDs. The study followed the performance-based unified procedure and found that R_o = 1.5 and R_d = 4 (R_oR_d of 6) can be adopted as seismic force modification factors for PT-CLT rocking walls in Canada. It is worth mentioning that the authors of this paper are developing a comprehensive seismic design guideline considering the R_oR_d factors from this study to supplement the Canadian CSA O86, *Engineering Design in Wood*.

8 References

Allan, B., Eaton, D. (2024). The Mass Timber Roadmap: An Integrated Forest-to-Buildings Value Chain. The Transition Accelerator.

Amer, A., Sause, R., Ricles, J. (2024). Experimental response and damage of SC-CLT shear walls under multidirectional cyclic lateral loading. Journal of Structural Engineering, 150(5), 04023215. https://doi.org/10.1061/JSENDH.STENG-12576

Canadian Standards Association (CSA). (2024). *Standard CSA 086-24: Engineering Design in Wood.* Mississauga, Canada: Canadian Standards Association.

Chen, Z., Popovski, M., Iqbal, A. (2020). Structural performance of post-tensioned CLT shear walls with energy dissipators. *Journal of Structural Engineering,* 146(3), 04020035. https://doi.org/10.1061/(ASCE)ST.1943-541X.0002569

DeVall, R., Popovski, M., McFadden, J.B.W. (2021). *Technical Guide for Evaluation of Seismic Force Resisting Systems and Their Force Modification Factors for Use in the National Building Code of Canada.* National Research Council of Canada. https://doi.org/10.4224/40002658

Fazileh, F., Fathi-Fazl, R., Dolati, A., Ventura, C.E., Saatcioglu, M., Lau, D., Yang, T., Sadeghian, V., Erochko, J. (2023a). Methodology for determination of seismic force modification factors in Canada: Performance-based unified procedure. *Earthquake Spectra,* 39(1), 218–241. https://doi.org/10.1177/87552930221144325

Fazileh, F., Fathi-Fazl, R., Huang, X. (2023b). *Performance-Based Unified Procedure for Determination of Seismic Force Modification Factors R_d, R_o in NBC.* National Research Council of Canada, Construction Research Centre. https://doi.org/10.4224/40003049

FEMA (2009). *Quantification of Building Seismic Performance Factors.* FEMA P-695. Applied Technology Council for the Federal Emergency Management Agency, Washington, DC.

Mitchell, D., Paultre, P. (1994). Ductility and overstrength in seismic design of reinforced concrete structures. *Canadian Journal of Civil Engineering,* 21(6), 1049–1060. https://doi.org/10.1139/l94-109

Morshedi, E., Doudak, G., Fazileh, F., Fathi-Fazl, R. (2024). Seismic performance assessment of wood light-frame shearwalls using the performance-based unified procedure. *Journal of Structural Engineering,* 150(2), 04024172. https://doi.org/10.1061/JSENDH.STENG-13742

National Research Council of Canada (NRCC). (2020). *National Building Code of Canada 2020.* Ottawa, Canada: Canadian Commission on Building and Fire Codes.

Palermo, A., Pampanin, S., Buchanan, A., Newcombe, M. (2005). Seismic design of multi-storey buildings using laminated veneer lumber (LVL). In *Proceedings of the New Zealand Society of Earthquake Engineering Annual National Conference,* Wairakei, New Zealand.

Pei, S., Ryan, K.L., Berman, J.W., Van De Lindt, J.W., Pryor, S., Huang, D., Wichman, S., Busch, A., Roser, W., Wynn, S.L., Ji, Y., Hutchinson, T., Sorosh, S., Zimmerman, R.B., Dolan, J.D. (2024). Shake-table testing of a full-scale 10-story resilient mass timber building. *Journal of Structural Engineering,* 150(2), 04024183. https://doi.org/10.1061/JSENDH.STENG-13752

Pei, S., Van De Lindt, J.W., Barbosa, A.R., Berman, J.W., McDonnell, E., Dolan, J.D., Blomgren, H.-E., Zimmerman, R.B., Huang, D., Wichman, S. (2019). Experimental seismic response of a resilient 2-story mass-timber building with post-tensioned rocking walls. *Journal of Structural Engineering,* 145(11), 04019120. https://doi.org/10.1061/(ASCE)ST.1943-541X.0002382

Wiebe, L., Christopoulos, C. (2015). A cantilever beam analogy for quantifying higher mode effects in multistorey buildings. *Earthquake Engineering & Structural Dynamics*, 44(11), 1697–1716. https://doi.org/10.1002/eqe.2549

Zhu, H., Bezabeh, M., Iqbal, A., Popovski, M., Chen, Z. (2024). Seismic performance assessment of post-tensioned CLT shear wall buildings with buckling-restrained axial fuses. Canadian Journal of Civil Engineering, cjce-2023-0448. https://doi.org/10.1139/cjce-2023-0448

Zhu, H., Bezabeh, M.A., Iqbal, A., Popovski, M., Chen, Z., 2025. Seismic design and performance evaluation of post-tensioned CLT shear walls with coupling U-shaped flexural plates in Canada. Earthquake Spectra. https://doi.org/10.1177/87552930251316263

DISCUSSION

The paper was presented by MA Bezabeh

G Doudak commented that this work needs to assume R_d R_o to get the archetypes and then verify the validity of the chosen R_d R_o values. He asked how would one generalize the results to other systems. MA Bezabeh said their goal was to consider as many systems as possible.

G Doudak asked how sensitive are the results to the choice of collapse criterions of 3 to 5%. MA Bezabeh responded that the choice was based on collected damage evidence.

C Demirci received clarification that the model has shear connectors and a Timoshenko beam was used to model CLT.

A Ceccotti received confirmation that the tall tested system shown had period of 2 seconds. He mentioned that wind considerations would govern the design. MA Bezabeh responded that other people had considered wind issues and agreed that base shear would be wind governed.

C Girgin and MA Bezabeh discussed differences between U shape and friction-based dampers.

P Dietsch commented that archetype ground floor layout is different from typical floors layouts of ground floors. MA Bezabeh responded that this is considered in a continuing study.

P Quenneville and MA Bezabeh discussed how tension rods can be treated if floor layouts were different between floors.

P Dietsch commented that the presentation was too long, for the INTER audience the introduction should have been shorter.

Studies on fluid forces acting on wood house under flood

Takahiro TSUCHIMOTO, Building Research Institute, Japan

Shigeru HIRANO, ICHIJO Co. Ltd., Japan

Yuki TAKADATE, Building Research Institute, Japan

Please refer to the following publication for the content of this paper:

Tsuchimoto T, Hirano S, Takatake Y (2025). Consideration of fluid forces acting on parts of wood house under flood. *Proceedings of the World Conference on Timber Engineering (WCTE 2025)*, Brisbane, Australia. DOI: 10.52202/080513-0685

DISCUSSION

The paper was presented by T Tsuchimoto

G Doudak commented that only one aspect ratio was considered. Was there any numerical study on the influence of aspect ratio? T Tsuchimoto responded that only one aspect ratio was tested and computer analysis will be considered in future.

T Demschner commented that the work studied slab on grade buildings only and no consideration of crawl space and basement. T Tsuchimoto responded past test results indicated crawl spaces reduced water flow.

A Frangi asked if Keff can be extrapolated to other cases. T Tsuchimoto responded that this is a difficult problem.

P Dietsch asked if it would be possible to relate pressure inside the building from water to wind pressure on a building. Then information in wind codes could be applied for this topic. T Tsuchimoto responded that it would be possible.

P Dietsch commented that this paper is a reduced version of the authors' WCTE 2025 paper. He suggested to add elements to the paper to make it different from the WCTE paper, otherwise this paper could not be published as INTER paper.

Performance of bond lines in different fire related small-scale tests

Jane Liise Vihmann, Department of Civil Engineering and Architecture, Tallinn University of Technology, Estonia

Alar Just, Department of Civil Engineering and Architecture, Tallinn University of Technology, Estonia

Keywords: engineered wood, cone heater testing, elevated temperatures, shear testing, fire performance of bond lines

1 Introduction

The evolution of fire testing methodologies for engineered wood products is transitioning from traditional large-scale timber fire tests to more efficient and cost-effective small-scale testing techniques. So far, large-scale fire tests have been essential for evaluating the fire behaviour of timber. However, these tests are resource-intensive, time-consuming, and complex. To address these challenges, alternative approaches like shear tests at elevated temperatures or tension test under a cone heater are being investigated. This study investigates these small-scale testing methods, utilizing different adhesive families for comparison. A classification system for structural wood adhesives based on temperature resistance has been previously proposed by CEN TC193 as FprEN 18070, grounded in tests conducted at elevated temperatures. These tests (Aicher et al., 2024) demonstrated a reasonable correlation with those conducted under the cone heater and in the furnace according to Annex B in EN 1995-1-2:2025 when conducted at 270°. While the classification system may underestimate the performance of a few adhesives and gives fairly conservative results, it generally aligns with the results from the fire tests.

The fire performance of engineered wood products is crucial to ensure the safety and structural integrity of buildings in the event of a fire. The fire testing of engineered wood products is a critical aspect of ensuring their safety and performance in real-world fire scenarios. Fire performance testing involves exposing these products to flames, allowing for the observation of pyrolysis and the formation of a char layer. Engineered wood products such as cross-laminated timber (CLT), glued laminated timber (GLT), and I-joists primarily rely on adhesives to bond multiple layers of wood together. While the performance of adhesives under ambient conditions has been extensively studied, their influence on the fire performance of engineered wood products remains an area requiring further research. Studies have demonstrated that different adhesives

can significantly impact fire behaviour, with variations observed even among adhesives from the same chemical family (Vihmann et al., 2025).

Studies have shown that (phenol-)resorcinol-formaldehyde (PR/PRF) adhesives exhibit high thermal stability at elevated temperatures (Dorn & Egner, 1967; Klippel, 2014; Vihmann et al., 2025). According to EN 1995-1-2:2004 (2004), the behaviour of adhesive bond lines can be disregarded for PR/PRF adhesives and other aminoplastic type I adhesives, as specified in EN 301 (2023). Over the past decades, various other adhesives have been introduced to the market, including polyurethane adhesives (PU/PUR), melamine adhesives (MF/MUF), emulsion-polymer isocyanate adhesives (EPI), and polyvinyl acetate adhesives (PVA).

The forthcoming revision of FprEN 1995-1-2:2025 (2025) aims to introduce different design scenarios and parameters based on the behaviour of adhesive bond lines at elevated temperatures. Depending on whether the bond line can prevent or fails to prevent the detachment of the charred layer, either a linear or stepped charring model is applied.

Traditionally, large-scale fire tests have been required to assess the performance of adhesive bond lines in fire conditions. However, these tests are inherently complex, time-consuming, and costly. In response to these challenges, the field of fire testing for engineered wood products has been shifting towards more efficient model-scale and small-scale testing methods. Researchers worldwide have been working to develop small-scale testing techniques capable of providing comparable insights while significantly reducing material usage and time requirements.

1.1 FIRENWOOD

FIRENWOOD was a transnational research, development and innovation project jointly funded by national funding organizations under the ERA-NET Cofund “ForestValue – Innovating forest-based bioeconomy”. The project was coordinated by RISE Fire Research in Trondheim, Norway.

The project consortium comprised leading research institutions in this field: RISE Fire Research, MPA University of Stuttgart, Tallinn University of Technology, Technical University of Munich, and ETH Zurich. Additionally, industrial partners Moelven, Splitkon, and Masonite Beams contributed to the research and development efforts.

The project involved testing 11 different adhesives—PRF, PUR, MUF, MF, and EPI—sourced from five adhesive manufacturers under elevated temperatures and fire conditions, using a range of configurations and specimen sizes. Each individual adhesive has a unique number (1 – 12) throughout the paper. Spruce (Picea abies) timber with a strength class of T22 was utilized, with a density ranging from 430 to 480 kg/m³. The primary objective of the project was to compare testing methodologies across different scales. Tests were conducted at small-scale (Sterley et al., 2021), model-scale

(Olofsson et al., 2022; Olofsson & Sterley, 2022), and large-scale levels (Olofsson et al., 2022).

1.2 Aims and objectives

This paper examines the comparison of small-scale testing methods under elevated temperatures and fire exposure, as well as their correlation with model-scale fire tests on glued laminated timber (GLT) beams and cross-laminated timber (CLT) slabs.

2 Methods

The objective of all used methods was to record the temperature-, time-, and load-dependent thermo-mechanical behaviour of different adhesive products.

2.1 Furnace tests with glulam beams and CLT slabs

The aim of the furnace tests was to measure the mass loss and the charring depth of CLT and GLT with different types of adhesives when exposed to fire from below. It is known that heat induced delamination can occur when these products are exposed to heat or fire due to the adhesive's inability to retain its properties at higher temperatures.

The model-scale CLT specimens were composed of seven wood lamellae, each with a thickness of 30 mm. The upper and lower lamellae were oriented in the lengthwise direction of the specimen. The overall dimensions of the specimens were 2000 mm × 600 mm (length × width). The CLT specimens were tested without load and subjected to 120 minutes of fire exposure in a model-scale furnace according to Annex B in FprEN 1995-1-2:2025, following the standard fire curve. The weight of each specimen was recorded before and after the fire test. Upon cooling, charring depths were measured at six points on each specimen. One test was conducted using almost all adhesives, except for adhesives no. 4, 7, and 8.

The GLT specimens consisted of ten wood lamellae, nine of which had a thickness of 28 mm, while one, positioned at the top of the beam, had a thickness of 23 mm. The final cross-section of the specimens measured 230 mm × 275 mm. The beams were tested without load and exposed to fire for 90 minutes in a model-scale furnace, following the standard fire curve, with exposure on three sides (bottom and lateral sides). The weight of each specimen was recorded before and after the fire test. After cooling, charring depths were measured at five points on each beam. One test was conducted with each of the 11 adhesives.

A large-scale horizontal CLT specimen was prepared to test under loaded conditions in a fire furnace. The specimen's outer dimensions were 4550 mm x 2000 mm x 150 mm. The specimen consisted of five 30 mm lamellae. The test was based on EN 1365-2:2014

(*2014*) with respect to the time-temperature curve, furnace pressure and loading. The specimen was loosely mounted in a steel test frame between two aerated concrete slabs with insulation between them to prevent heat exposure on the specimen's sides. Temperatures on the unexposed surface and in the three fire-side bond lines, together with vertical deflection were measured during the test. The span was approximately 4.1 m. The specimen was loaded with 21 weights with a total weight of 1742 kg which corresponds to a load of approximately 17.09 kN or 2.08 kN/m^2. The loads were close to evenly distributed over the specimen's surface. The load was applied to the specimen at least 15 minutes before the fire test and was maintained during the whole test. The test duration was 116 minutes due to load-bearing failure.

2.2 Tests at elevated temperatures

The shear test specimens were manufactured in accordance with EN 17224 (2019) and FprEN 18070 (2025). Two types of test specimens were produced: adhesive bonded specimens and unglued solid wood specimens. The specimen geometry and dimensions are shown in Figure 1.

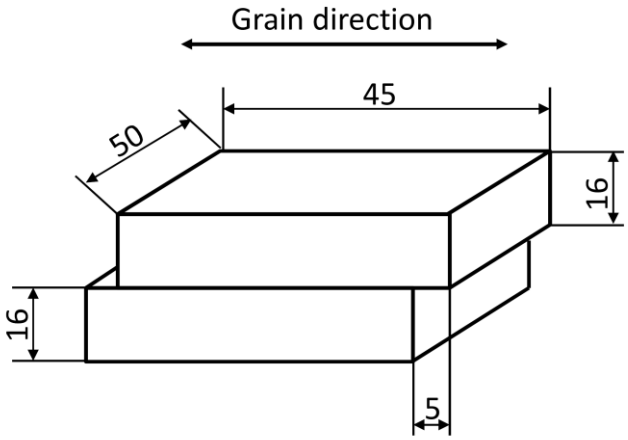

Figure 1. Block shear specimen according to FprEN 18070 (2025).

The heating process required to elevate the specimen to a higher temperature was complex. To regulate the temperature increase, the chamber temperature had to be adjusted multiple times throughout the process. The temperature of the test specimen was monitored using a thermal wire inserted into a drilled hole on one side of the specimen.

All samples were first tempered at 60℃ for a period of 48 hours and then stored in a container at 20℃ to prevent further moisture absorption until the actual temperature tests began. Before tempering the average moisture content of the samples was 11.8 ± 0.5%. After the heat treatment, the average wood moisture content was around 1.4%. No abnormalities were found in any sample after the temperature treatment. The solid wood reference samples and the glued samples were then stored unloaded in a temperature cabinet at the respective elevated temperature (70 to 270℃). After

reaching the target temperature, the test specimens were left at the respective target temperature for 15 minutes. The time from placing the test specimen in the preheated temperature cabinet until reaching the target temperature was approximately 25 – 45 minutes, depending on the target temperature. At the end of the temperature storage period, the samples were removed from the temperature cabinet, weighed and tested in the block shear test within a maximum of 60 seconds. The room temperature during the shear test was around 20 - 23℃.

2.3 Cone heater finger joint tests under tension

Knot-free spruce timber with cross-section dimensions of 50 mm x 150 mm was used for the manufacturing of finger joints. The boards had a moisture content of 12%. Finger joints were produced industrially on the Masonite Beams production line. Adhesive application was performed manually, following the specified amounts by adhesive manufacturers.

The boards, initially sized at 45 mm x 100 mm x 300 mm, were cut into strips measuring 45 mm x 10 mm x 300 mm. Holes with a 12 mm diameter were drilled into the ends of the specimen, and plywood reinforcements were glued to the ends to prevent tensile fractures at the attachment points. Bolts with a 10 mm diameter were used to apply the force. The geometry of the specimen is shown in Figure 2. The finger joint geometry is shown in Figure 3.

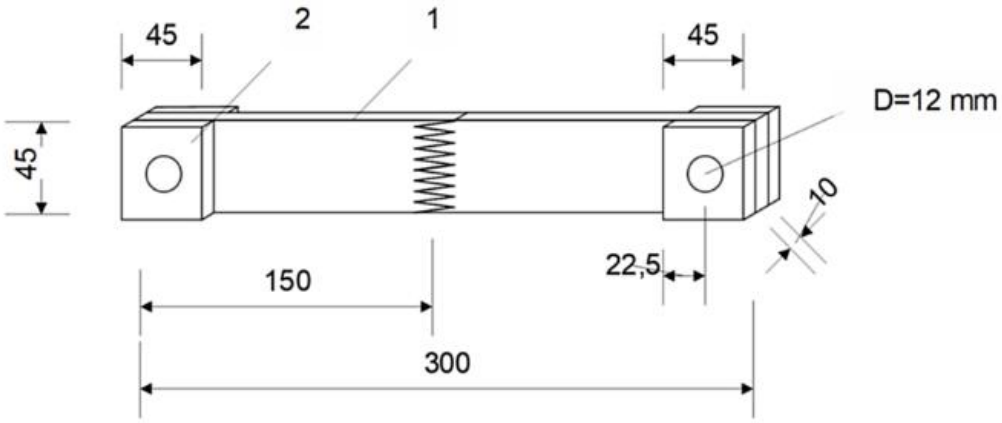

Figure 2. Finger jointed test specimen. Number 1 marks the raw specimen and number 2 marks the reinforcing plywood pieces.

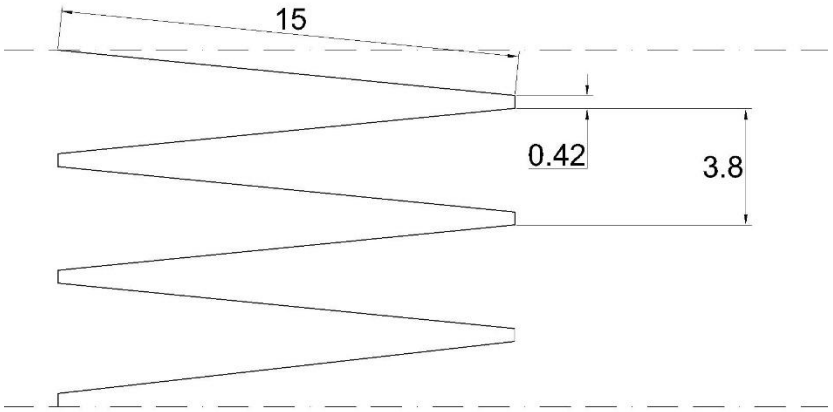

Figure 3. Finger joint geometry.

The lateral sides of the specimens were insulated with stone wool to ensure one-dimensional charring. A stainless-steel casing was used to keep the wool in place during the test as shown in Fig. 4. The chosen heat flux 25 mm from the cone (the top of the specimen) was 50 kW/m^2.

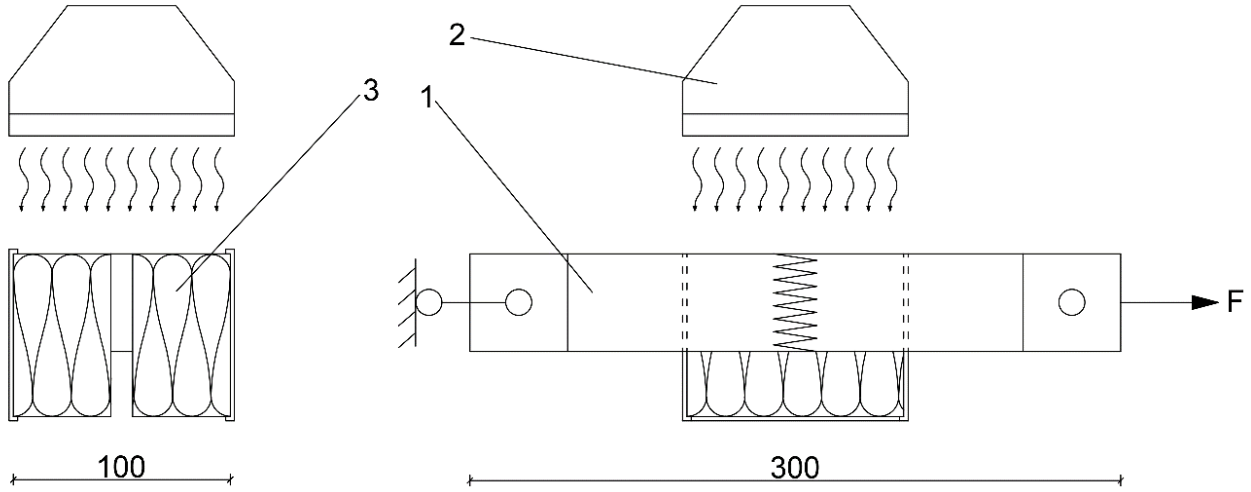

Figure 4. Specimen setup under the cone heater, where 1 marks the specimen, 2 marks the cone heater, and 3 marks the protective stone wool.

The test started when the shutter was removed from between the specimen and the cone heater. Ignition occurred within a second of plate removal. The specimen burned until rupture, after which it was removed from the cone heater and submerged in cold water to extinguish the flames and prevent further charring. Failure time and failure mode were recorded for each specimen.

The test series included a total of 61 specimens, each loaded with 100 kg, corresponding to approximately 5% of the average tensile strength of the wood. The tensile strengths were determined through tensile testing at ambient temperatures.

3 Analysis

A classification system for structural wood adhesives based on temperature resistance has been proposed in FprEN 18070, as shown in Table 1. This table is derived from single-lap compression shear block tests conducted at elevated temperatures. The classification follows the test principles of EN 17224 and ASTM D 7247 (2017), with a key deviation: the mean residual shear strength ratio of bonded samples is compared to 85% of the mean residual shear strength ratio of solid wood samples. The system consists of four adhesive classes, where higher classes (e.g. T270) fully encompass the lower classes (e.g. T232).

Table 1. Adhesive classification system

Temperature resistance class	*Temperature limit [°C]*	*Verification criteria*	*Adhesive number*	*Adhesive families*
T270	*270*	$R_{bW,Trefl80,270} \geq 0.85$	*2, 3, 6, 8, 11*	*PRF, MUF/MF*
T232	*232*	$R_{bW,Trefl80,232} \geq 0.85$	*1*	*1KPUR*
T220	*220*	$R_{bW,Trefl80,220} \geq 0.85$	*7*	*1KPUR*
T200	*200*	$R_{bW,Trefl80,200} \geq 0.85$	*4, 12, 9*	*1KPUR, MUF*

To assess the reliability of this classification system, the elevated temperature tests will be compared with small-scale cone heater tests and model-scale fire tests.

3.1 Comparison of small-scale tests

The following graph will investigate the correlations between the small-scale cone heater test method and the small-scale elevated temperature test method.

In Fig. 5, the mean shear strength of the block shear specimens tested at 270°C is compared to the mean eccentric tensile strength of the finger-jointed specimens tested under the cone heater. As observed in previous comparisons, the adhesives can be categorized into two distinct groups. Tests conducted at lower temperatures showed no clear correlations between the block shear tests and the small-scale cone heater test methods.

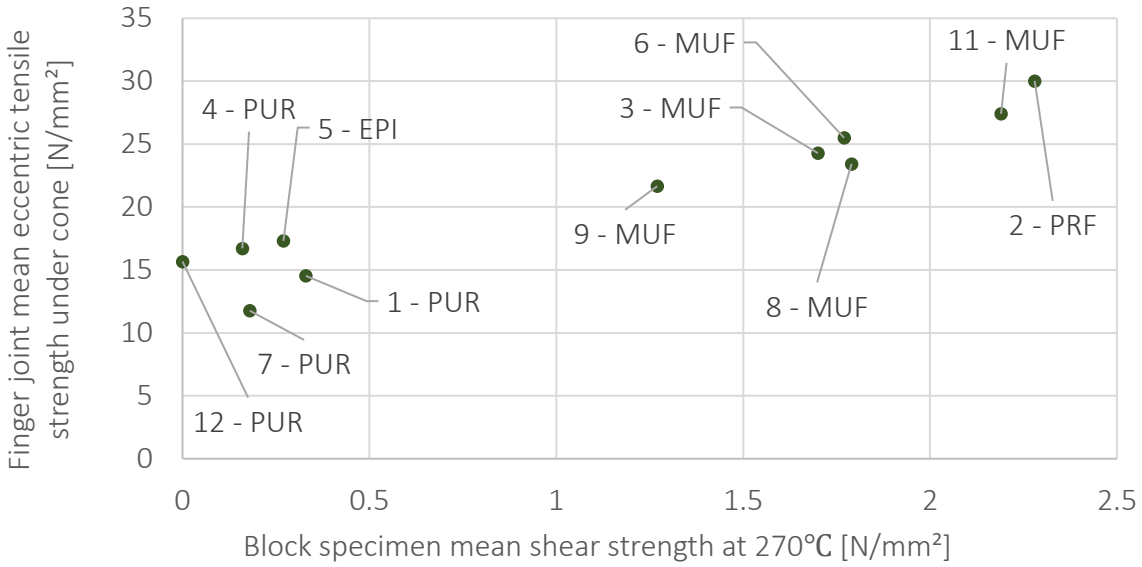

Figure 5. The block shear specimen mean shear strength at 270℃ compared to the mean eccentric tensile strength of finger jointed specimens tested under the cone heater.

3.2 Small-scale tests compared to model-scale furnace tests

The following graphs will investigate the correlations between the small-scale methods and the model-scale furnace tests. It will also be examined how the char depth of GLT beams and CLT slabs correlate with the previously proposed classification method. The charring depths of the glulam beams are shown in Figure 6 and the charring depths of the CLT slabs are shown in Figure 7. Each number on the horizontal axis represents a specific adhesive. For each beam, five thin cross-sections were cut from the beam to measure the charring depths.

In Figure 7, the charring depths for both the model-scale and the full-scale test (FST) with adhesive no. 9 are shown. The similar charring depths indicate that loading does not significantly influence charring, and that unloaded fire tests are sufficient for representing all relevant use cases.

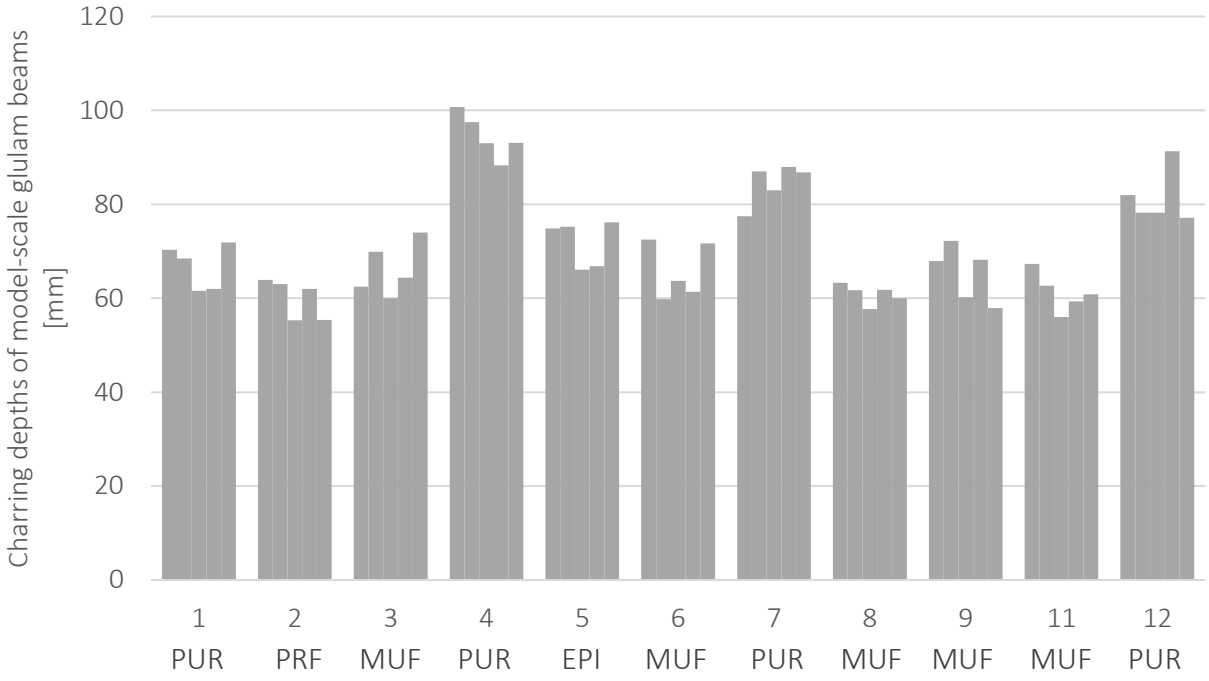

Figure 6. Charring depths on the bottom fire-exposed side of the glulam beams (90 min). Each number on the horizontal axis represents an adhesive.

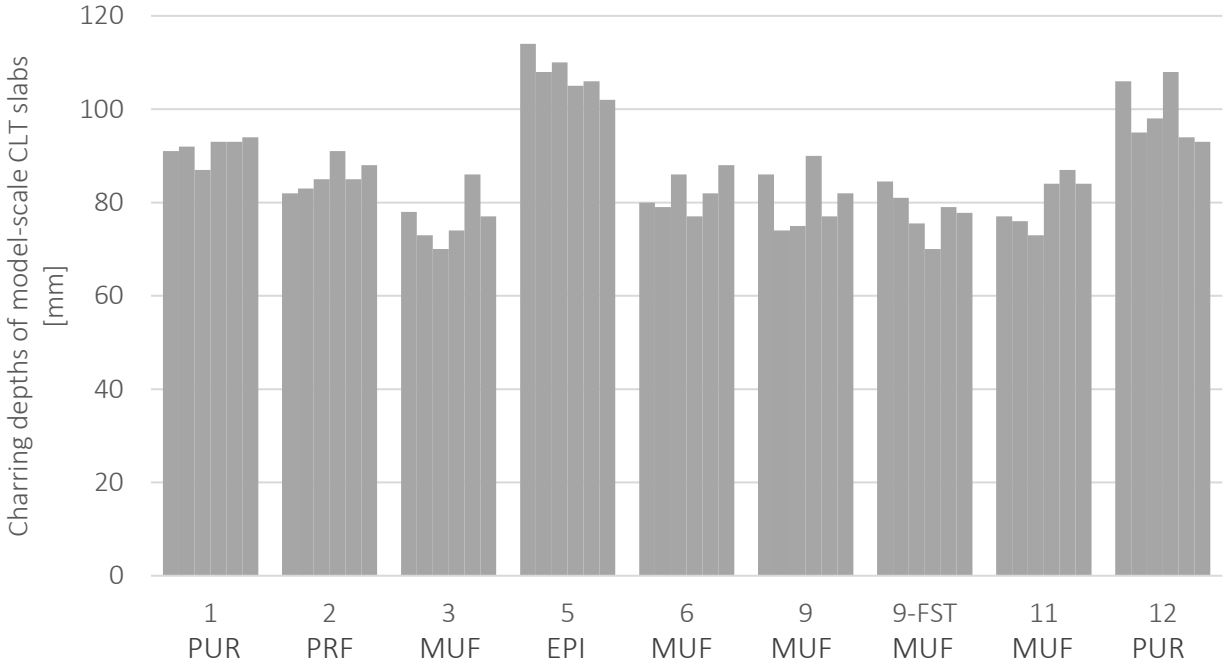

Figure 7. The average charring depths of CLT slabs (120 min). Each number on the horizontal axis represents an adhesive.

For reference, the design charring depth at 90 minutes for the charring rate of 0.65 mm/min according to the FprEN 1995-1-2:2025 is 58.5 mm. Considering the effect of corner rounding for the beams, the notional charring rate is 0.7 mm/min and the respective charring depth for 90 minutes results in 63 mm. Design charring depth for 120 minutes with charring rate of 0.65 mm/min is 78 mm.

While most of the beams showed charring depth around the mentioned values, there are quite a few that exceed this fairly. That is dependent on bond line integrity. In case

of CLT slabs the charring depths of adhesives 5 and 12 exceeds significantly the value of design charring depth.

In Figure 8, a comparison between the average charring depths of model-scale glulam beams tested in the furnace and the mean eccentric tensile strength of finger-jointed specimens tested under the cone heater is presented. The groupings observed are like those formed in the previous comparison in Figure 5. In Figure 9, similar observations are seen.

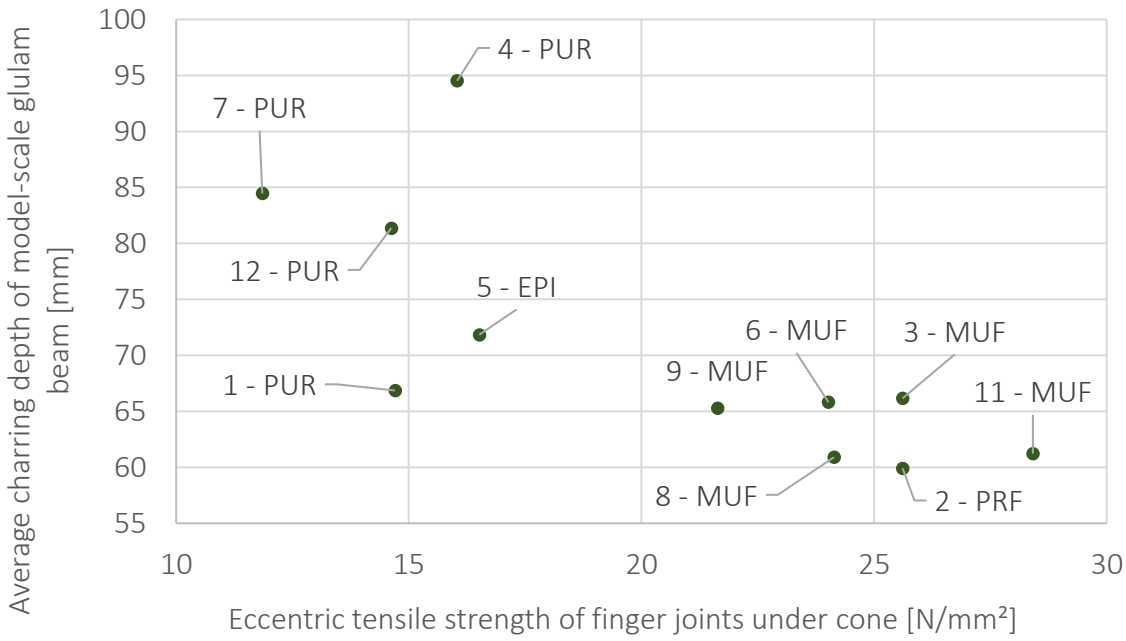

Figure 8. The mean eccentric tensile strength of finger jointed specimens tested under cone heater compared to the average charring depth of model-scale glulam beams.

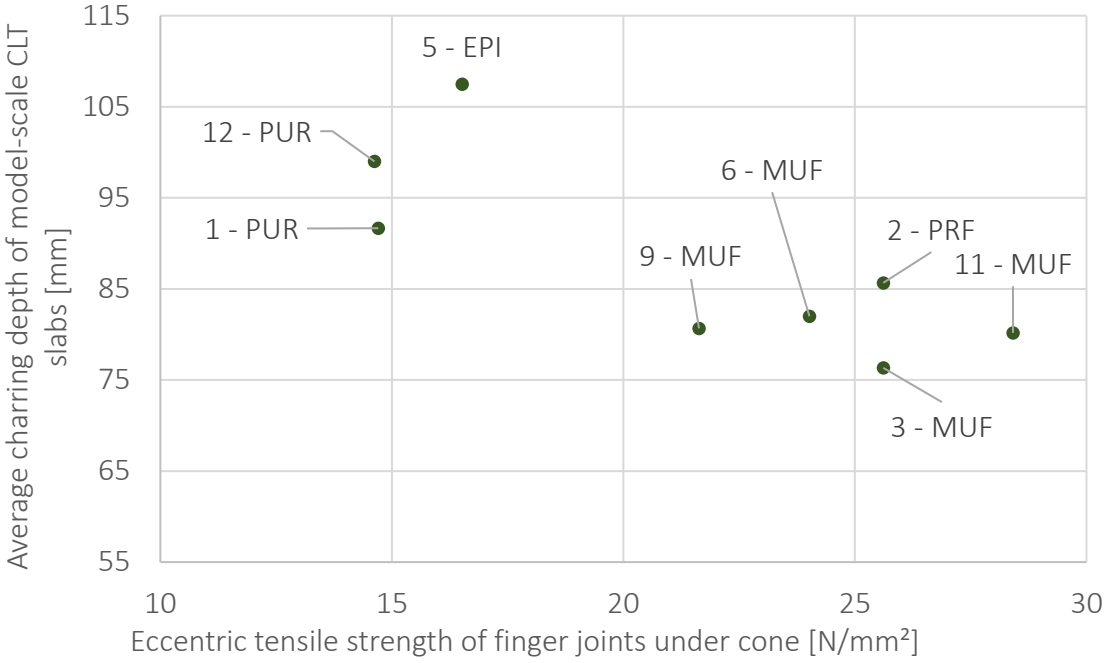

Figure 9. The mean eccentric tensile strength of finger jointed specimens tested under cone heater compared to the average charring depth of model-scale CLT slabs.

Finally, Figure 10 and Figure 11 use the charring depths of the glulam beams and CLT slabs to assess their correlation with the proposed classification system. This classification system, developed through tests conducted at elevated temperatures according to FprEN 18070:2025, aims to replace the currently used larger-scale test methods. While the classification system does not invalidate the results, it tends to be somewhat conservative for certain adhesives. For instance, adhesive no. 9 has been placed in the lowest temperature class; however, both model-scale and small-scale tests suggest it may belong in a higher temperature class. Adhesive no. 1, which exhibits variability between glulam and CLT specimens, is appropriately classified in the T232 class. While small-scale methods generally categorize adhesive no. 1 in the weaker adhesive group, model-scale tests indicate that the small-scale methods may not be the most reliable for estimating the performance of this adhesive.

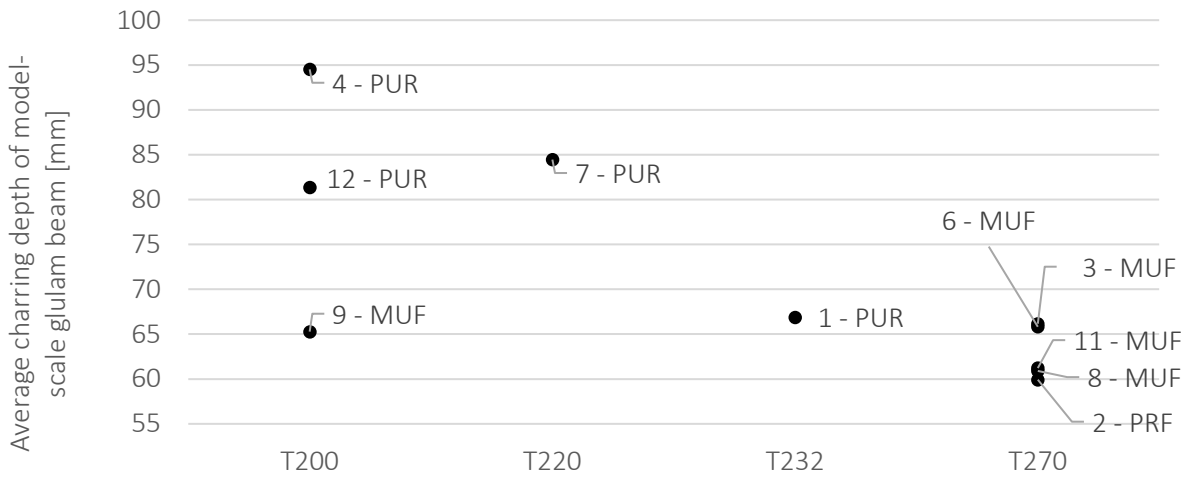

Figure 10. Charring depths of model-scale glulam beams classified according to the classification system proposed in FprEN 18070.

Figure 11. Charring depths of model-scale CLT slabs classified according to the classification system proposed in FprEN 18070.

4 Conclusions

This study investigated the performance of bond lines of engineered wood by comparing small-scale and model-scale fire testing methods. The primary objective was to evaluate the correlation between different test methods and assess the classification system for structural wood adhesives based on temperature resistance. The findings demonstrate that while small-scale test methods provide valuable insights, their ability to predict large-scale fire performance varies depending on the adhesive type and testing conditions.

In general, tests conducted at elevated temperatures yield results comparable to other fire testing methods when performed at a temperature of 270°C for single-lap compression shear block specimens. A classification system for structural wood adhesives based on temperature resistance, as outlined in FprEN 18070, was developed using

the single-lap compression shear block method. In this study, we compared this classification system to model-scale tests conducted in a furnace. In general, the classification system provides a reasonable prediction of an adhesive's fire performance and does not overestimate the performance of any adhesives. However, it underestimates the performance of one adhesive (No. 9), which, according to fire tests conducted without mechanical loading, demonstrates better fire resistance in terms of charring depth than the classification system suggests. Furthermore, a comparison between loaded and unloaded tests for this adhesive showed similar charring depths, indicating that mechanical loading had no significant effect on charring behaviour. This suggests that unloaded fire tests may be sufficient for evaluating adhesive performance in fire.

Adhering to the classification system for structural wood adhesives based on temperature resistance can provide sufficiently conservative results, as is the case with all small-scale testing methods. The advantages of the single-lap compression shear block method include its cost-effectiveness and high repeatability.

The classification system outlined in FprEN 18070 may be adopted as a general performance criterion for adhesives in fire conditions. Adhesives shall be classified into temperature classes as defined in FprEN 18070.

- Adhesives classified as temperature class T270 are permitted to follow the linear charring rate model as specified in this standard.
- Adhesives not meeting the criteria for class T270 shall default to the step model for charring behaviour unless justified according to Annex B of Eurocode 5-1-2.

For adhesives that do not qualify for the linear model under the FprEN 18070 classification, the test method in Annex B of Eurocode 5-1-2 shall remain applicable. This test allows a more refined assessment of bond line integrity. If the test results in Annex B demonstrate sufficient performance, such adhesives may be permitted to follow the linear charring model, notwithstanding their initial classification under FprEN 18070. This dual-path approach enables a balance between classification-based conformity and performance-based justification through physical testing.

5 Acknowledgements

Authors acknowledge Dr. Simon Aicher and Aaron Münzer from the Material Testing Institute of University of Stuttgart.

The research was funded by the Estonian Research Council Grant PRG2213 and by Fachagentur Nachwachsende Rohstoffe e.V. (FNR) (grant 2219NR120) with financial support by German Federal Ministry of Food and Agriculture (BMEL). The presentation is funded by Cost Action HELEN (CA20139).

6 References

Aicher, S., Henning, M., & Münzer, A. (2024). Bond line shear strength of structural wood adhesives at high temperatures up to wood carbonization – A classification approach. *Results in Engineering*, *23*, 102762. https://doi.org/10.1016/j.rineng.2024.102762

ASTM D7247-17. (n.d.). *Standard Test Method for Evaluating the Shear Strength of Adhesive Bonds in Laminated Wood Products at Elevated Temperatures*.

Dorn, H., & Egner, K. (1967). Flame tests on laminated trusses under bending load. *Holz Als Roh- Und Werkstoff*, *25*, 308–320. https://doi.org/10.1007/BF02615681

EN 301:2023. (n.d.). *Adhesives, phenolic and aminoplastic, for load-bearing timber structures—Classification and performance requirements*.

EN 1363-1 Fire resistance tests—Part 1 General requirements. Brussels European standard. Brussels: CEN European Committee for Standardization (CEN). (n.d.).

EN 1995-1-2. (n.d.). *Eurocode 5: Design of timber structures – Part 1-2: General – Structural fire design. 2004.* Brussels: European Committee for Standardization (CEN).

EN 17224:2019. (n.d.). *Determination of compressive shear strength of wood adhesives at elevated temperatures*.

FprEN 1995-1-2:2024. (n.d.). *Eurocode 5—Design of timber structures—Part 1-2: Structural fire design*.

FprEN 18070. (n.d.). *Performance of wood adhesives exposed to high temperatures with regard to behaviour of load-bearing timber structures in fire—Test method, evaluation and classification*.

Klippel, M. (2014). *Fire safety of bonded structural timber elements* [ETH-Zürich]. https://doi.org/10.3929/ethz-a-010171655

Olofsson, R., Just, A., Mäger, K. N., & Sterley, M. (2022). *Loaded fire tests with I-joists* (Nos. 978-91-89757-11-0 (ISBN); FIRENWOOD D3.2, p. 50). DiVA. http://urn.kb.se/resolve?urn=urn:nbn:se:ri:diva-61178

Olofsson, R., Mäger, K. N., Bergius, M., Persson, T., & Wikner, A. (n.d.). *Large-scale fire tests of engineered wood systems. Firenwood report D3.6*.

Olofsson, R., & Sterley, M. (n.d.). *Model scale fire tests with cross-laminated timber. Firenwood report D3.5*.

Sterley, M., Olofsson, R., Nurk, J. L., & Just, A. (2021). *Small-scale tests with adhesive bonds with CLT, GLT and finger joints. Firenwood report D3.3*.

Vihmann, J. L., Just, A., Sterley, M., Mäger, K. N., & Kers, J. (2025). The Performance of Bond Lines of Engineered Wood in Cone Heater Testing. *Fire and Materials*, fam.3295. https://doi.org/10.1002/fam.3295

DISCUSSION

The paper was presented by J Vihmann

P Dietsch asked about how was the influence of material properties excluded from the small-scale tests. JL Vihmann said density was checked.

P Dietsch received clarification that charring information was based on the company that produced this particular type of product. Also J Vihmann is working on the correlation.

S Winter received clarification that 90 min vs 120 min heating is related to GLT vs CLT. He commented that keeping Annex B and consider additional small scale test method while keeping statements in EN 18070 together.

A Frangi commented that it is good that expensive fire tests can be replaced by small scale testing. He noted adhesive 9 may have some values obtained from specifier.

T Demschner received clarification that worst case scenario being 20 mm thick laminates and fire tests will clarify possible bond line behaviour under fire.

S Winter commented that block shear tests are sensitive to wood species and asked about the amount of fiber failure under elevated temperature. J Vihmann responded that they do not have this information at hand. S Winter asked if they intend to repeat glue no. 9 tests.

J Smart commented that loading should be close to design level. J Smart and A Frangi discussed the importance of bond-line behaviour in fire and if this is a good test. A Frangi stated that tests with 40 mm laminations can't be scaled down.

Fire performance of hollow glue laminated timber elements

Nikola Perković*[1], Vlatka Rajčić[2], Jure Barbalić[3]

1 University of Zagreb, Faculty of Civil Engineering, Zagreb, Croatia nikola.perkovic@grad.unizg.hr

2 University of Zagreb, Faculty of Civil Engineering, Zagreb, Croatia vlatka.rajcic@grad.unizg.hr

2 University of Zagreb, Faculty of Civil Engineering, Zagreb, Croatia jure.barbalic@grad.unizg.hr

Keywords: timber, fire, FEM, hollow, laminated

1 Introduction

In recent years, the use of cross-laminated timber (CLT) and glued laminated timber (GLT) has seen notable expansion in the construction industry. Modern engineered wood products rely heavily on precise manufacturing processes, particularly in the bonding of lamellae. Limiting gaps between lamellae ensures fire resistance, airtightness, and visual and structural quality. Segmenting and reassembling lamellae enhances uniformity by minimizing material imperfections. Standards such as EN 16351 set strict criteria on gap dimensions, with a maximum allowed width of 6 mm [1]. Furthermore, the development of modular timber construction systems has advanced rapidly, emphasizing sustainability, efficiency, and prefabrication. Many of these systems incorporate perforated or hollow structural elements, which not only reduce material consumption but also improve thermal and structural performance. The following overview highlights several innovative modular timber systems that exemplify the integration of engineered voids and smart material use in contemporary timber construction. The LUXHOME [2] system utilizes modular "wooden bricks" and prefabricated timber components (e.g., floors, ceilings, windows) produced through automated processes, enabling precise cost and material control. This system reduces construction waste while streamlining on-site assembly and manufacturing logistics. ECOCELL [3] is a structural insulated panel (SIP) system composed of corrugated cardboard honeycomb insulation between OSB boards. Unlike typical SIPs using oil-based foams, ECOCELL employs 100% recycled paper with a mineral coating, offering a sustainable and thermally efficient solution. The Fabric Workshop [4] concept features hollow-core timber panels that reduce raw material usage by 50% and lower costs by up to 35% compared to CLT. These prefabricated elements, joined with metal connectors, achieve a high strength-to-weight ratio while simplifying on-site installation. BRIKAWOOD [5] is a timber masonry system using interlocking dovetail-jointed wooden bricks that eliminate the need for adhesives, nails, or screws. It enables rapid, dry assembly with minimal tools, making it suitable for DIY or low-tech construction

scenarios. GABLOK [6] offers modular insulated timber blocks filled with expanded polystyrene (EPS) enhanced with graphite, achieving excellent thermal performance. The lightweight, uniform block sizes (up to 90 cm long and only 7.5 kg per unit) enable crane-free installation and flexible architectural applications. STEKO [7] is a Swiss-developed modular system made from sustainably sourced timber components glued with non-toxic adhesives. Its standardized, doweled elements are applicable in buildings up to 10 storeys, as well as in temporary structures, partitions, and renovation projects. These innovative modular systems exemplify the growing potential of timber in contemporary construction, particularly in terms of sustainability, ease of assembly, and adaptability across a range of applications. However, as the use of timber expands, it becomes increasingly important to address its full environmental impact—most notably, the release of stored carbon at the end of its service life—underscoring the need for robust fire resistance strategies throughout the material's lifecycle.

To mitigate the risks associated with carbon release during combustion, it is essential to implement effective fire protection measures that enhance timber's fire performance throughout its lifecycle. In this context, fire retardants play a pivotal role, operating through various mechanisms: some promote charring, while others reduce flammability by releasing inert gases or limiting heat transfer. Fire retardants can act through different mechanisms: some promote charring, while others reduce flammability by releasing inert gases or limiting heat transfer [8,9]. High-performance adhesives are essential to maintain these qualities under both ambient and elevated temperatures. While structural failure typically occurs in the wood itself, high temperatures during fire exposure can degrade adhesives, raising concerns over bond integrity and potential delamination. Research [10,11] indicates that adhesive type plays a more significant role than lamella orientation in resisting fire-induced separation. Understanding these mechanisms is essential for advancing the design and performance of mass timber systems.

1.1 Objectives

The field of fire performance in hollow timber elements remains relatively underexplored, with only a limited number of studies addressing the structural implications of internal cavities under elevated temperatures. A relevant contribution to the fire design of timber structural systems is presented in the work [12], where the authors investigate the behaviour of hollow-core timber slabs exposed to fire. In this study, a simplified mechanical model was proposed to predict charring development and the loss of structural capacity in timber elements with internal voids. Their findings demonstrate that, despite the presence of cavities, adequate fire resistance can be achieved through proper design adjustments, particularly in estimating the effective cross-section and charring rates. The research highlights the potential for using hollow timber elements in fire-exposed applications, provided that the structural model accounts for the complex interaction between geometry, thermal degradation, and residual strength. The reviewed systems demonstrate a clear trend toward optimizing material

efficiency, structural behavior, and fire performance using modular, often perforated timber elements. Inspired by these principles, the present research explores innovative hollow glued-laminated timber beams, aiming to assess how internal cavities affect mechanical capacity and fire resistance. This concept not only reduces the amount of raw material used but also introduces opportunities for integrating fire protection strategies directly into the structural geometry. The performance of these timber components is compared against conventional solid GLT beams. This research aims to advance the understanding of the structural and fire performance of perforated glued laminated timber (GLT) elements. It focuses on how different adhesive systems affect load-bearing capacity and how elevated temperatures degrade adhesive properties, influencing overall structural behavior. The study also examines how perforation geometry impacts heat transfer and temperature distribution within the timber cross-section during fire exposure, as well as how reduced bonding surfaces increase the risk of lamella separation (debonding, delamination). Additionally, the effectiveness of passive fire protection strategies is analysed, particularly in terms of one-dimensional and effective charring rates. All findings are integrated into a modeling framework to simulate fire-structure interaction in hollow timber elements.

2 Experimental Investigation Under Fire Conditions

2.1 Timber Elements Exposed to Fire on One Side

2.1.1 Specimen Preparation

In line with the research objective—namely, to investigate the influence of elevated temperature on perforated glued-laminated timber elements—and considering certain constraints related to the dimensions of laboratory equipment (i.e., furnace size), the test specimens were adapted in both shape and size. The cross-sectional dimensions of the elements were 12 × 14 cm, with a total length of 150 cm. A total of ten specimens were tested, representing three types of configurations: solid cross-section, hollow cross-section, and a specimen with only the outer lamella left unperforated. These were further varied by the type of fire protection system and the adhesive used between the lamellae (Figure 2.1).

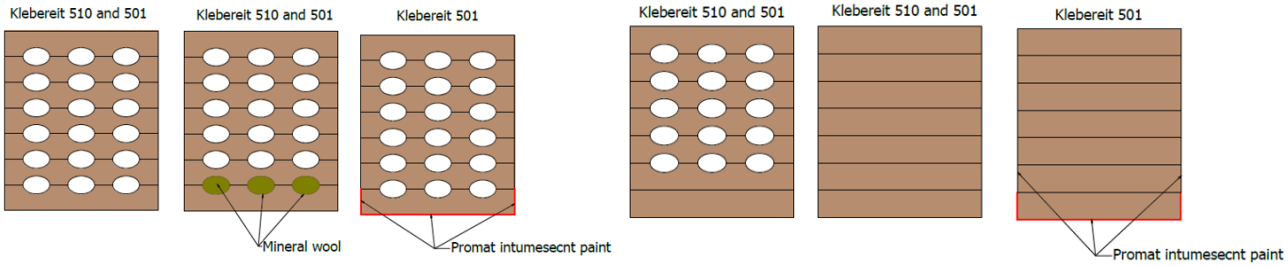

Figure 2.1 Different types of timber specimens and adhesives

The maximum perforation ratio, relative to the solid beam cross-section, was 25 %. For specimens featuring a solid outer (bottom) lamella, the perforation percentage was slightly lower, amounting to 21 %. The experimental setup and laboratory equipment [13] used for fire testing are shown in Figure 2.2.The fire tests were conducted in a

medium-scale furnace with external dimensions of 2.10 m in height, 1.35 m in width, and 1.20 m in depth. The furnace featured an open-top exposure area measuring 0.95 m × 0.80 m. The beam specimens, each 0.12 m wide, were placed over this opening. The remaining perimeter of the opening was sealed with a non-combustible thermal insulation system, consisting of metallic cladding filled with ceramic wool.

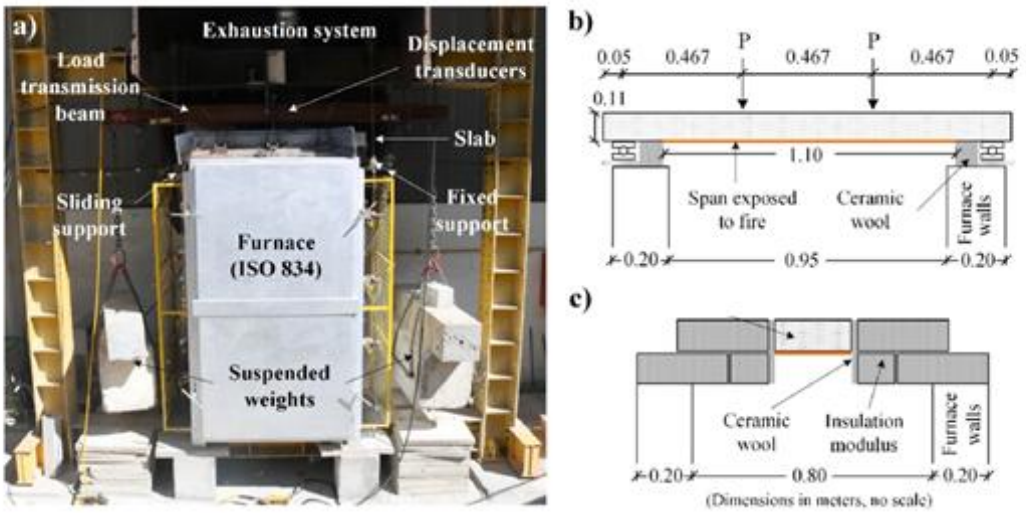

Figure 2.2 Test setup [13]

Ceramic wool strips were added near the supports and along the specimen sides to reduce lateral heat loss, while a fire-resistant textile covered the top surface to limit thermal convection. The beams were exposed to fire along the bottom face over a 1.10 m length and configured as simply supported across the furnace opening. A mechanical load was applied via suspended concrete blocks (Figure 2.2), simulating a four-point bending condition. This represents 30% of the failure load of different beams at ambient temperature [14]. The blocks were gradually positioned using a chain system and hydraulic jack to ensure controlled movement and minimize vibrations.

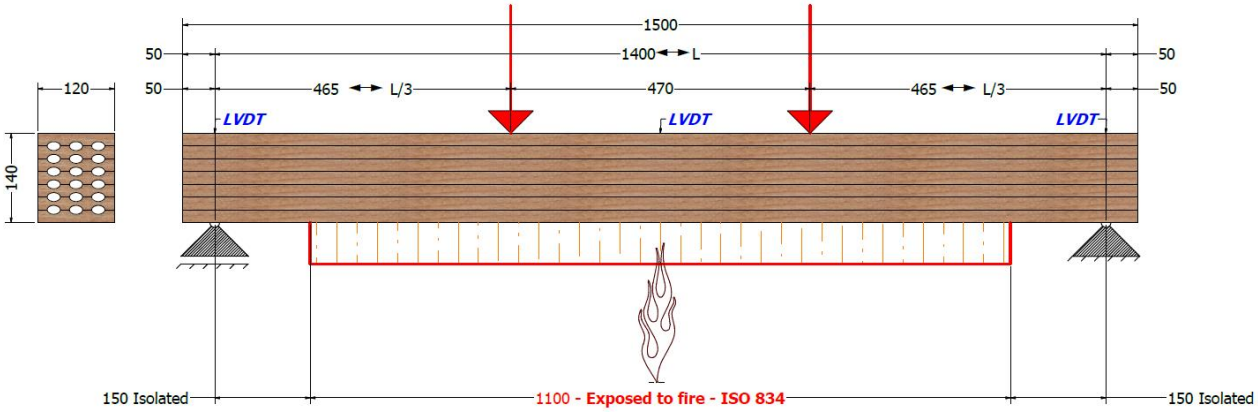

Figure 2.3 Fire test setup

Four LVDTs were employed to measure displacements—two positioned at mid-span and two at the beam supports. In addition, sixteen K-type thermocouples were embedded within each specimen to monitor the temperature evolution inside the timber element during fire exposure. To gain a detailed understanding of heat transfer

through the cross-section, thermocouples were installed both at the mid-height of each lamella and at the bond lines between adjacent lamellae (Figure 2.4).

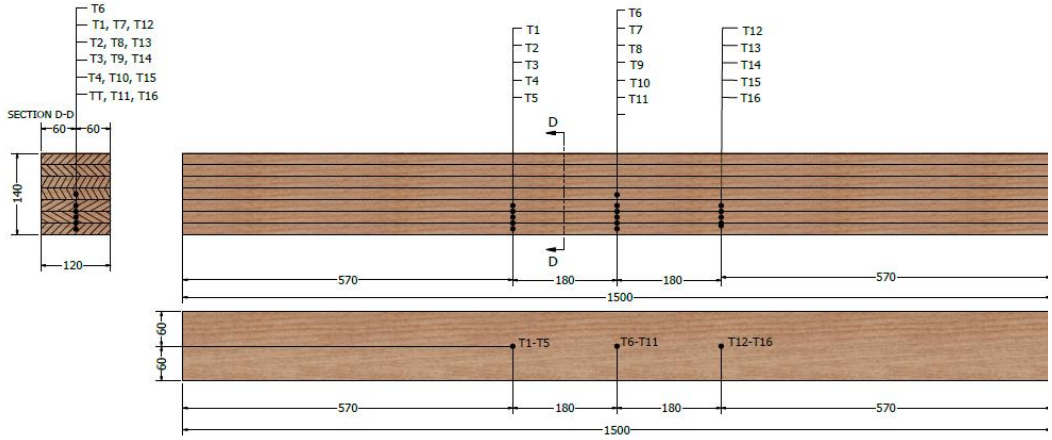

Figure 2.4 Thermocouple layout

2.1.2 Results

The primary and most indicative parameter for evaluating the influence of different cross-sectional configurations and fire protection systems is the fire resistance of the specimens—namely, the time to failure under fire exposure. Figure 2.5 represents a comparative overview of the fire resistance times recorded for all tested specimens.

Figure 2.5 Comparison of failure time

While the time to failure remains a key parameter in assessing the fire performance of timber elements, it does not fully capture the complexity of their behavior under elevated temperatures. To optimize protection strategies, it is also essential to evaluate the internal temperature development within the specimens during fire exposure. The thermocouple installed at mid-height of the second lamella (counting from the exposed side) offers the earliest indication of thermal response differences between specimens. This position is located beyond the first adhesive line and behind the first perforation, making it critical for early thermal analysis. Figure 2.6a compares temperature evolution at this position across all test specimens. The fastest temperature rise was recorded in the perforated beams, followed by those with a perforated core and a solid outer lamella. A beneficial effect was observed from the inclusion of mineral wool in the first row of voids, which helped reduce internal temperatures. The slowest

temperature increase occurred in specimens protected with an intumescent fire-resistant coating. Figure 2.6b illustrates the temperature progression at the second adhesive line. In perforated specimens, a sudden temperature spike was observed, indicating the moment flames penetrated the first row of voids. A similar phenomenon was noted in specimens with solid outer lamellae. In samples filled with mineral wool and bonded with K.501 adhesive, the wool detached during the test, while this did not occur in samples using K.510 adhesive, suggesting superior adhesion properties of the latter.

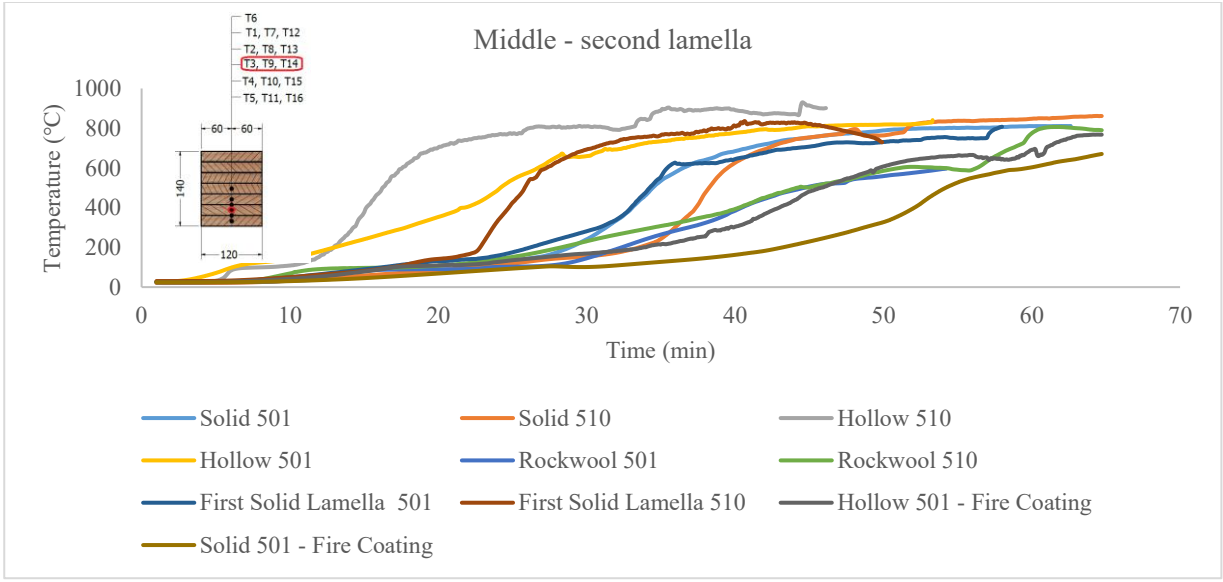

(a)

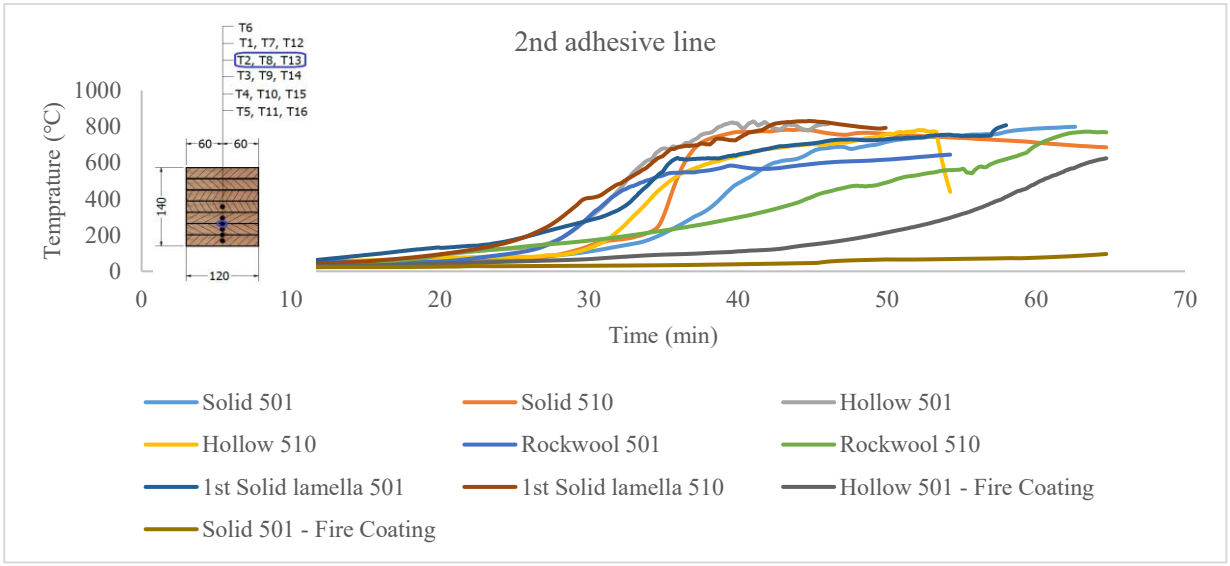

(b)

Figure 2.6 Comparison of developed temperatures: (a) 2nd bonding line; (b) middle of 2nd lamella;

2.1.3 Charring behaviour

To determine the charring rate of solid timber specimens, the beams were first cleaned after the fire tests and then cut into segments at regular intervals of 200 mm along their longitudinal axis. Each segment was carefully labelled and subsequently scanned.

The scanned files were processed and imported into a CAD environment for a detailed analysis of the charring progression (see Figure 2.7). The one-dimensional charring rate was determined to be 0.8 mm/min, which aligns with the reference values provided in EN 1995-1-2 [15].

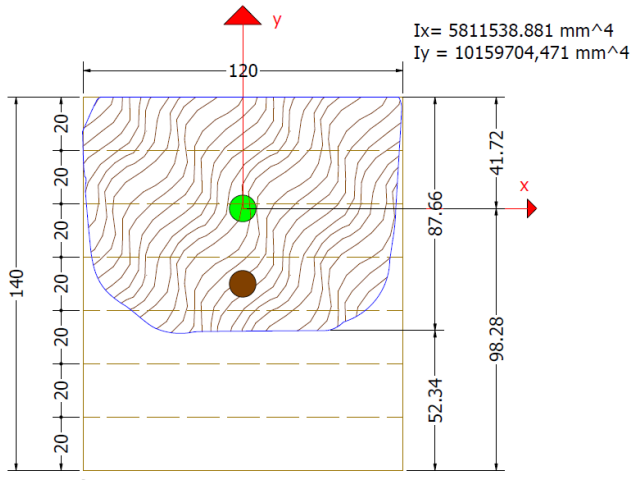

Figure 2.7 Remaining cross-section of a solid GL beam

The fire performance of perforated timber beams involves multiple charring stages. Once the first solid timber layer is fully charred and separates, the narrow vertical timber webs become exposed to fire from three sides. This leads to highly irregular residual cross-sections and greater charring depths than those observed in solid timber members (Figure 2.8).

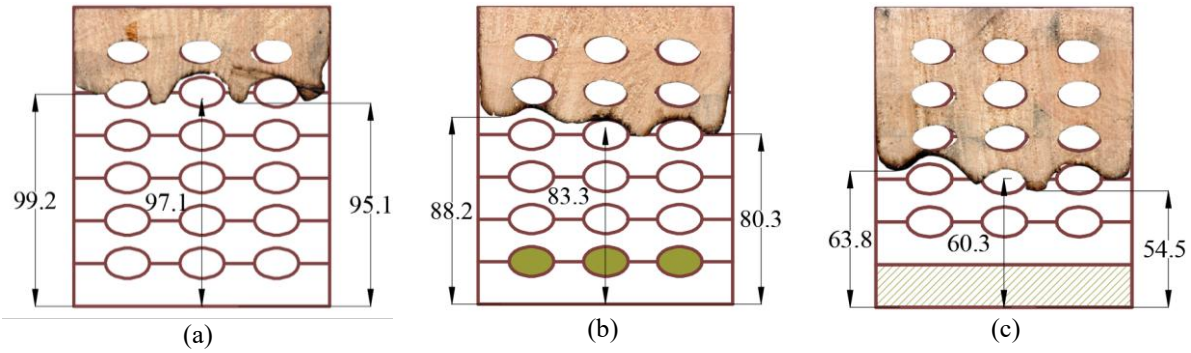

Figure 2.8 Residual cross-section of hollow timber specimens after 60 minutes of fire exposure: (a) hollow beam; (b) hollow beam with rock wool; (c) hollow beam with first solid lamella

The fire tests conducted on these elements revealed three distinct charring phases. Initially, charring occurs while the first timber layer is intact; in the second phase, fire reaches insulated cavities; and in the final stage, fire penetrates non-insulated cavities. Before the first lamella is entirely charred, the beam undergoes one-dimensional charring from a single fire-exposed surface, similar to solid timber beams. After this lamella fails, thin vertical webs become vulnerable to multi-sided exposure, compromising their integrity due to intensified thermal flow. From the standpoint of fire resistance, it is preferable that these vertical webs remain exposed to fire from one side only. This can be achieved in two ways; preventing fire intrusion into the cavities, or filling the cavities with insulating material, which protects the sides of the vertical webs after the

outer lamella fails. The first strategy is realized through fire-resistant coatings and claddings, while the second is achieved using stone wool insulation, selected for its high melting point (above 1000 °C), which ensures its presence during fire exposure. If the insulation were to melt or detach, its protective function would be compromised. Fire testing confirmed that stone wool effectively protected the lateral surfaces of the vertical webs, enabling the assumption of one-dimensional charring behavior—provided that the insulation remains in place throughout the test duration.

Three charring phases were considered, illustrated in Figure 2.9. For simplification, a linear relationship between charring depth and time was assumed for each phase.

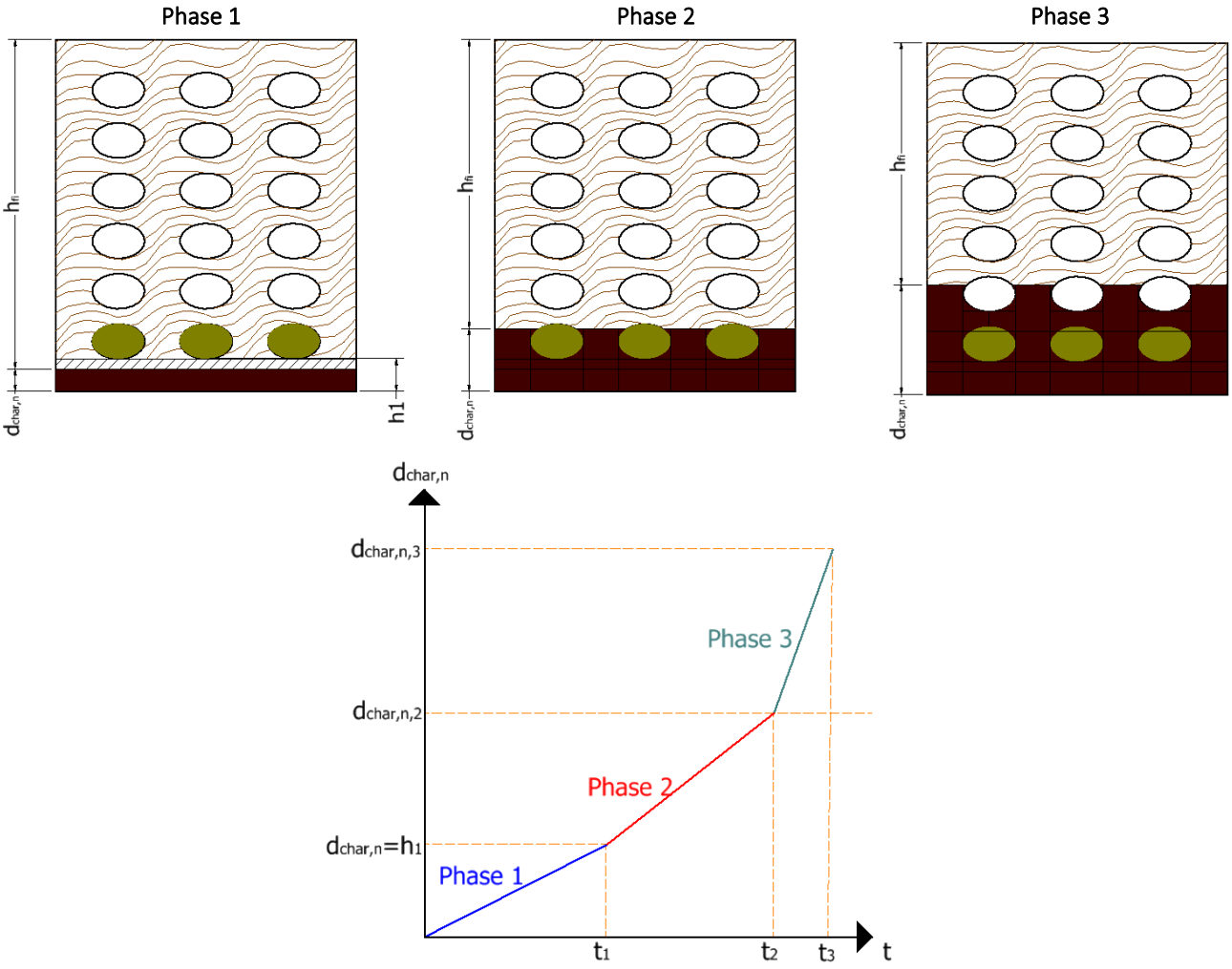

Figure 2.9 Charring stages: model for calculating the remaining cross-section of hollow elements

During the second phase, fire ingress into cavities is assumed to be prevented even after the failure of the outer lamella (h_1 in Figure 2.9). The first phase ends when the charring depth equals the thickness of the outer layer ($d_{char,n} \leq h_1$), and the corresponding charring rate $\beta_{1,n}$ is associated with one-dimensional charring. The time t_1 when this occurs is defined as:

$$t_1 = \frac{h_1}{\beta_{1,n}} \qquad (1)$$

In the second phase, vertical webs begin to char under a two-dimensional thermal flux. Due to their small thickness (23 *mm*), charring intensifies. Nominal charring depths for the first and second phases are expressed as:

$$d_{char,n} = \beta_{1,n} \cdot t_{req} \text{ for } 0 \leq t_{req} \leq t_1 \quad (2)$$

$$d_{char,n,2} = h_1 + \beta_{2,n} \cdot (t_{req} - t_1) \text{ za } t_{req} \geq t_1 \quad (3)$$

In the third phase, when fire reaches uninsulated cavities, the charring depth is:

$$d_{char,n,3} = d_{char,n,2} + \beta_{3,n} \cdot (t_{req} - t_2) \text{ za } t_{req} \geq t_2 \quad (4)$$

The effective cross-section is obtained by reducing the initial section by the effective charring depth:

$$d_{ef} = d_{char,n} + k_0 \cdot d_0 \quad (5)$$

The zero-strength layer thickness ($k_o d_o$) accounts for strength degradation at elevated temperatures. It is assumed that during the first 20 minutes, the coefficient k_o linearly increases from 0 to 1, reflecting the time needed to establish steady thermal profiles in the remaining timber. Parameters β_1, *n* and d_o for the first phase were derived from fire tests on solid and perforated timber elements. β_2, *n*, β_3, *n*, and d_o for phases two and three were established via comparisons with simplified and advanced (FE-based) models. For vertical webs (23 mm thick), the average charring rate in the second phase was β_2, *n* = 1.5 *mm/min*, based on:

$$\beta_{n,2} = k_n \cdot k_s \cdot \beta_0 \quad (6)$$

The wool insulation generally improved thermal resistance but also accelerated heating of the first layer. The measured charring rate in this configuration was β_1, *n* = 0.8 mm/min with a zero-strength layer of d_o = 7 *mm*. In the third phase, when protection detaches or cavities are uninsulated, the charring rate increases and is calculated using:

$$\beta_{n,3} = k_n \cdot k_s \cdot k_3 \cdot \beta_0 \quad (7)$$

$$k_3 = 2 \quad (8)$$

Resulting in a third-phase charring rate of β_3, *n* = 3 *mm/min*.

The complexity of the second phase stems from the multidimensional heat transfer through insulating materials, which, despite protecting the sides, can accelerate charring via lateral conduction. This phenomenon aligns with prior research on timber frame assemblies [16,17] and is accounted for in EN 1995-1-2, Annex C [15]. To correct for irregularities in the residual section, conversion factors k_s = 1.5 and k_n = 1.5 are proposed to determine the effective rectangular section under the assumption of one-dimensional charring.

2.2 Timber Elements Exposed to Fire on Three Sides

2.2.1 Specimen preparation

The specimens used in the fire resistance study had identical dimensions to those used in the mechanical testing phase investigated [18], measuring 120 × 240 × 5040 mm (width × height × length). Moisture content was measured for each specimen individually, with the average moisture determined to be 10% across all samples. Each glued-laminated timber (GLT) beam was composed of twelve lamellae, each 20 mm thick, made of softwood (fir). Bonding between the layers was achieved using a polyurethane-based structural adhesive. This PUR adhesive is certified in accordance with DIN 1052 [19] for load-bearing timber structures. To evaluate the performance of hollow GLT elements, three different beam types were tested:

- A standard GLT beam (control specimen),
- A hollow GLT beam coated with an intumescent fire-resistant paint, and
- A hollow GLT beam filled with mineral wool and coated with intumescent paint on the external surfaces.

For fire protection, the product used was PROMADUR [20]. The concept behind the hollow design was to strategically use internal cavities to inhibit the penetration of heat and flame into the core of the beam. Figure 2.10 illustrates the different cross-sectional configurations of the tested timber beams.

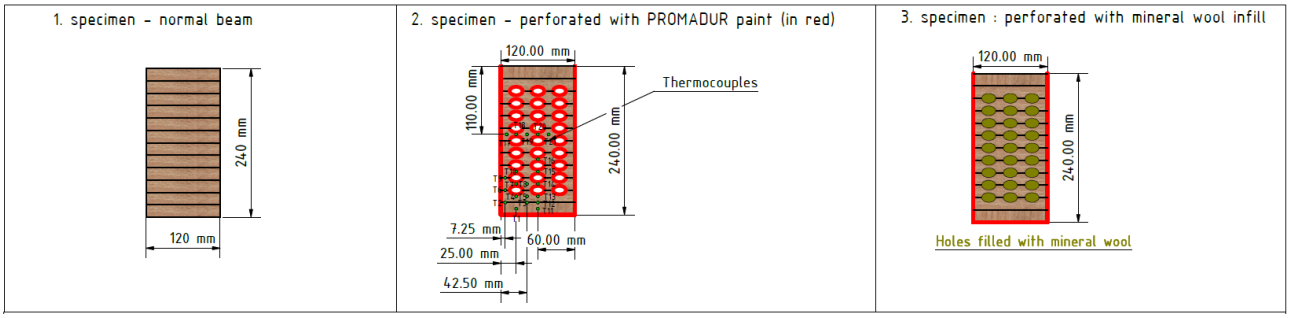

Figure 2.10 Specimen cross-section: (a) solid beam; (b) hollow with intumescent paint; (c) hollow with mineral wool infill.

The timber beam specimens were subjected to three-sided fire exposure. The specimens were mounted onto a vertical steel test frame, equipped with a hydraulic loading system to apply the required mechanical load. This represents 30 % of the failure load at ambient temperature, a load level commonly recommended in the literature [14] for simulating realistic fire conditions. The entire assembly was positioned above a horizontal fire testing furnace, ensuring that a 3000 mm-long central segment of the beam was directly exposed to fire. The beam was simply supported. The supports were placed 4320 mm apart, with both supports located outside the furnace boundaries, ensuring only the central portion experienced fire exposure. The entire experimental configuration is shown in Figure 2.11. A 40 mm-thick calcium silicate board, known for its high strength and fire resistance, was placed on top of the beam to enable load application.

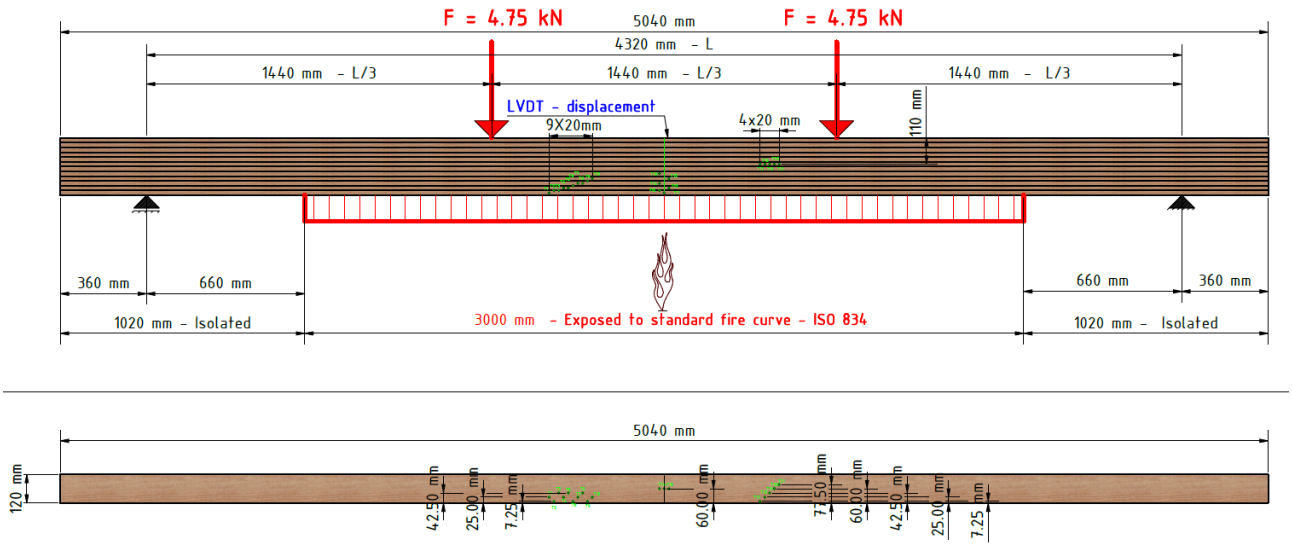

Figure 2.11 Fire test – experiment setup

Temperature development across the beam's cross-section was monitored using 21 NiCr-Ni (Type K) thermocouples, each with a wire diameter of 0.5 mm. The positioning of the thermocouples (Figure 2.11) was designed to provide comprehensive data from all sides exposed to fire. The sensors were divided into three measurement groups, each containing seven thermocouples, based on their specific locations within the beam:

- Group T11–T16 recorded temperatures induced by bottom-side fire exposure
- Group T17–T21 focused on thermal development primarily influenced by lateral fire exposure
- Group T1–T10 was arranged to monitor the notional charring rate and internal temperature progression within the cross-section.

This sensor configuration allowed for a detailed thermal profile to be captured throughout the fire exposure, facilitating subsequent analysis of charring depth, temperature gradients, and material performance.

2.2.2 Results – charring behaviour

To assess the post-fire condition of each beam, the fire-exposed specimen was cut at regular 200 mm intervals. Each resulting cross-sectional segment was labelled and scanned, after which the scanned images were processed and imported into CAD software for further geometric analysis (see Figure 2.12). Through this method, the residual cross-sectional area, moment of inertia, and section modulus were accurately determined. Subsequently, both the notional charring rate and the notional residual section were evaluated. In addition, one-dimensional charring rates (β_o) were measured individually for each lamella.

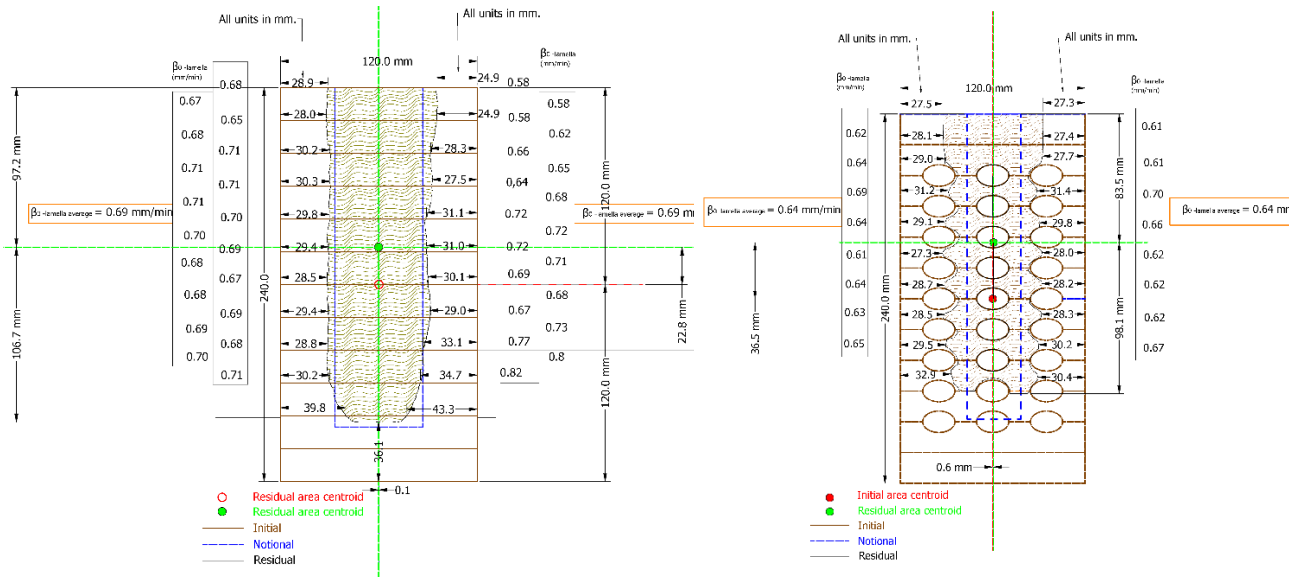

Figure 2.12 Residual cross-section analyzed with CAD software, dimensions in (mm): (a) normal GL beam; (b) hollow GL beam protected by intumescent paint.

For the standard GL beam, the average one-dimensional charring rate was 0.69 mm/min, while the notional charring rate was calculated to be 0.78 mm/min. In the case of hollow GL beams protected with intumescent paint, the fire protection system contributed to a slightly lower average one-dimensional charring rate of 0.64 mm/min. However, calculating the notional charring rate for these elements proved more complex due to the presence of internal cavities. Since the section modulus plays a significant role in determining the notional rate, and is inherently lower in hollow elements, the calculated notional charring rate was high—0.95 *mm/min*. The idealized residual cross-section geometry is illustrated with a blue dashed line in Figure 2.12.

3 Evaluation of char layer using FEM – implementation of a numerical modeling approach

In this research, a novel simulation principle for modeling the charring of timber was implemented. This method involves deactivating finite elements within the numerical model once the material temperature reaches 300 °C—reflecting the behavior of timber in accordance with EN 1995-1-2 [8], which defines this temperature as the point at which timber loses its mechanical strength and stiffness. A custom script was developed using ANSYS Parametric Design Language (APDL) [21,22] to enable this element-deactivation process (“element killing”) based on a defined thermal threshold. This marks an advancement in the fire modeling of timber elements, allowing for direct prediction of residual load-bearing capacity under fire conditions. One of the key advantages of this method is that it eliminates the need to manually extract temperatures from specific nodes within the finite element mesh. Instead, the remaining uncharred cross-section, as determined through element deactivation, is directly used in the

subsequent structural analysis to assess residual load capacity. The accuracy of the model was verified through validation against experimental tests, covering both one-dimensional and multidirectional charring scenarios. The simulations showed excellent agreement with the physical test data, confirming the robustness of the approach.

3.1 Thermal analysis – specimens exposed to fire on one side

The developed finite element model was first validated using standard solid timber beams, where a high degree of correlation was observed between the simulation results and fire test data. After 60 minutes of fire exposure, the experimentally determined char depth was 52.34 mm, while the numerical simulation using the FEM model yielded a char depth of 52 mm. Figure 3.1 illustrates the progression of the charred layer at 15, 30, and 60 minutes.

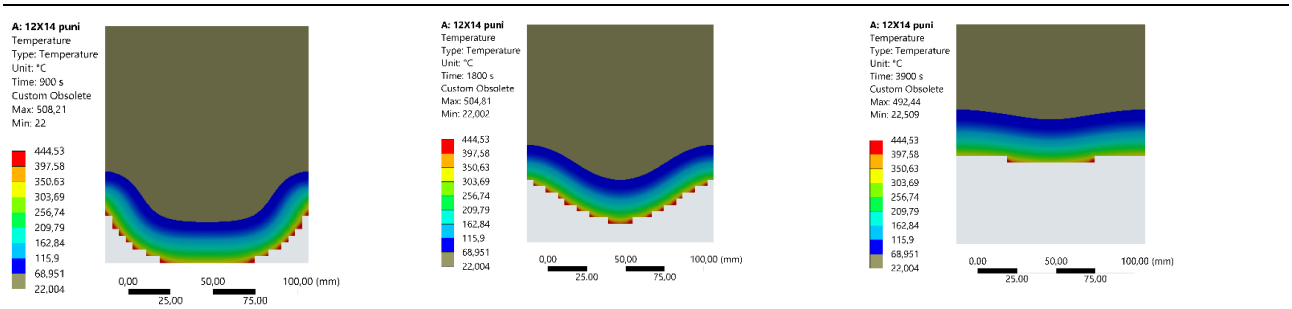

Figure 3.1 Evaluation of the char layer of a normal beam using FEM: (a) 15th minute; (b) 30th minute; (c) 60th minute

The next step involved modeling perforated beams under fire exposure. Again, the results showed excellent agreement between FEM simulations and experimental observations. After 60 minutes, the experimentally recorded char depth was 97.1 mm, while the FEM model predicted an average char depth of 99.2 mm. The temporal development of the char layer is presented in Figure 3.2.

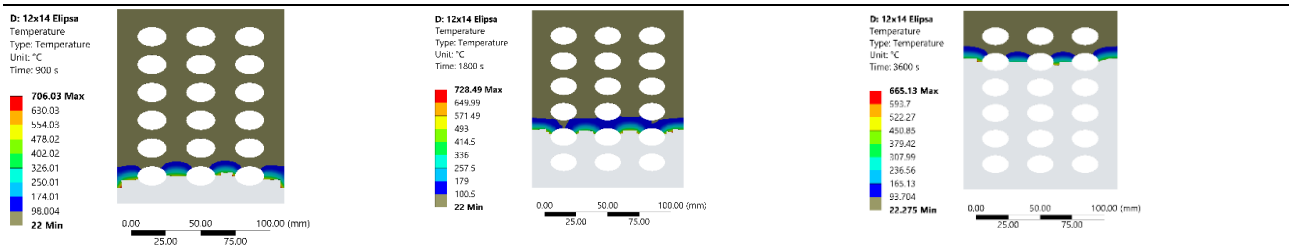

Figure 3.2 Evaluation of char layer of hollow beam using FEM: (a) 15th minute; (b) 30th minute; (c) 60th minute

To assess the influence of mineral wool placed in the first row of cavities, a numerical simulation was performed in ANSYS by incorporating elements with thermal properties matching those of mineral wool. After 60 minutes of fire exposure, the experimental char depth was measured at 83.3 mm, while the FEM simulation predicted an average char depth of 83 mm (Figure 3.3), indicating excellent agreement.

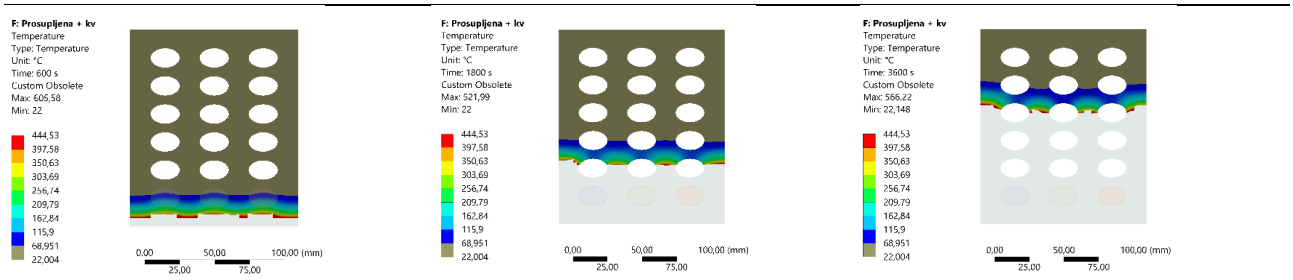

Figure 3.3 Evaluation of char layer of hollow beam with KV using FEM: (a) 10th minute; (b) 30th minute; (c) 60th minute

Building upon the previous models, a perforated beam configuration with a solid outer lamella was simulated (see *Figure 3.4*). The correlation between the experimental result (60.3 mm char depth) and the FEM-predicted value (60 mm) confirmed the robustness of the model for this complex geometry.

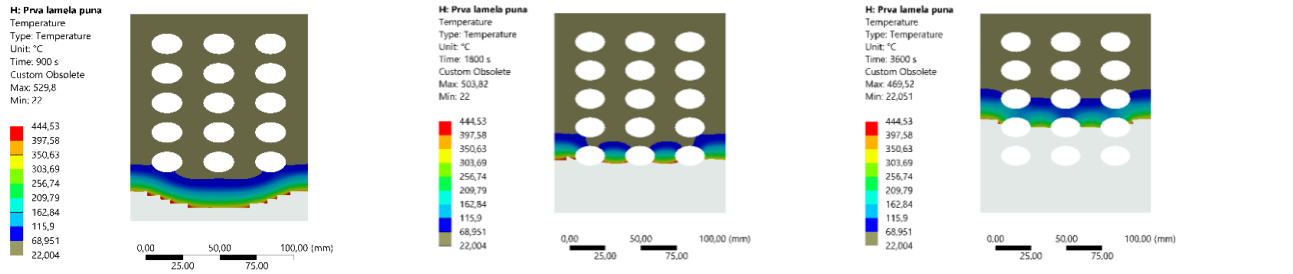

Figure 3.4 Evaluation of the char layer of a hollow beam with the first solid lamella using FEM: (a) 15th minute; (b) 30th minute; (c) 60th minute

The final set of simulations addressed beams protected with a fire-retardant coating—a considerably more complex scenario. Figure 3.5 shows the charring progression in a coated perforated coated beam. The simulations aligned well with experimental data. The average deviation between simulated and measured char depths was 3.2 mm for coated perforated beams.

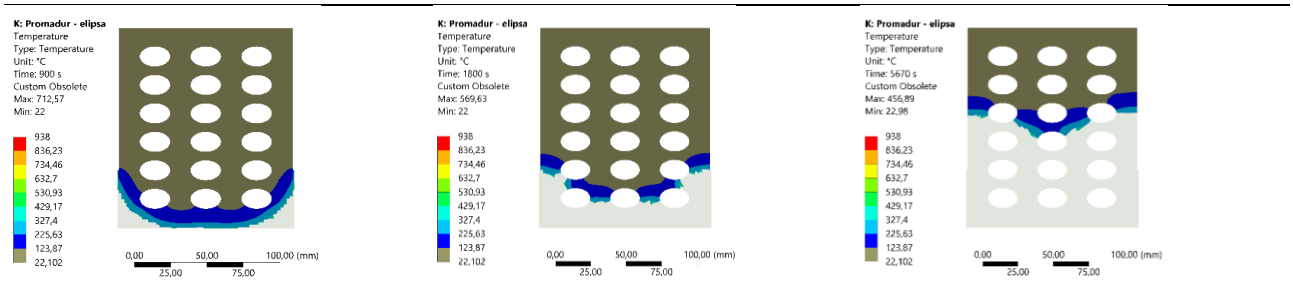

Figure 3.5 Evaluation of the charred layer of the perforated beam with fire protection coating using FEM: (a) 10th minute; (b) 30th minute; (c) 60th minute

3.2 Thermal analysis – samples exposed to fire from three sides

In line with the previous section, this part presents the results obtained using the innovative FEM-based numerical modeling approach for timber specimens exposed to fire on three sides. The char depth in a standard GLT beam at 15, 30, and 45 minutes of fire exposure is shown in Figure 3.6.

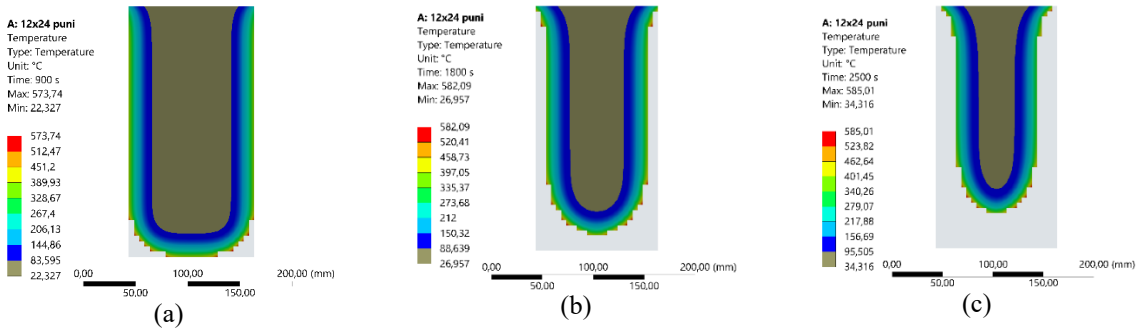

Figure 3.6 Evaluation of char depth in a solid beam exposed to fire on three sides: (a) 15 minutes; (b) 30 minutes; (c) 45 minutes

The results show strong agreement between numerical simulations and experimental fire tests. After 45 minutes of fire exposure, the only notable difference between the simulated and actual char depth appeared on the unexposed top surface, due to idealized assumptions in the model. The measured char depth on the bottom was 36.1 mm versus 35 mm in the simulation, while both lateral surfaces showed approximately 30 mm in both cases. Additional simulations on perforated beams with mineral wool infill confirmed similar accuracy, with results shown in in Figure 3.7.

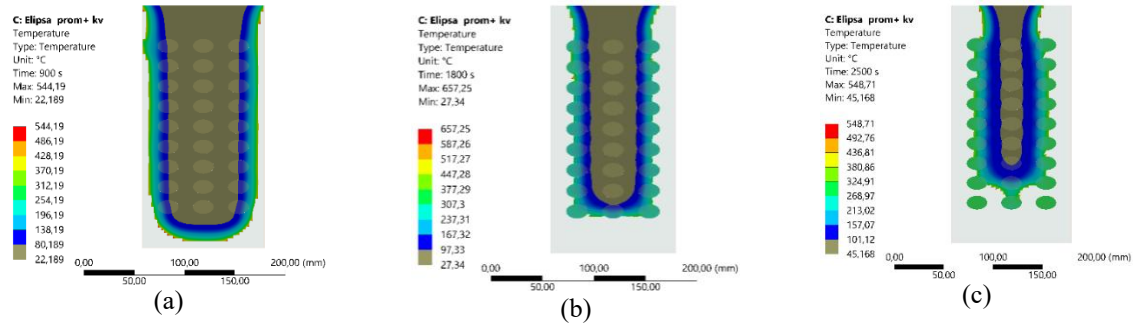

Figure 3.7 Evaluation of char depth in perforated beams with mineral wool infill, exposed to three-sided fire: (a) 15 minutes; (b) 30 minutes; (c) 45 minutes

Mineral wool was defined in the simulation as a non-combustible material (melting point of approx. 1000 °C). The average char depth measured after 45 minutes of fire exposure in these specimens was 30 mm. The FEM simulation yielded the same average value. As seen in Figure 3.7c, the only minor discrepancy was again observed near the unexposed (top) side of the specimen. Finally, the simulated temperature distribution and char depth in perforated beams protected with fire-retardant coating are presented in Figure 3.8.

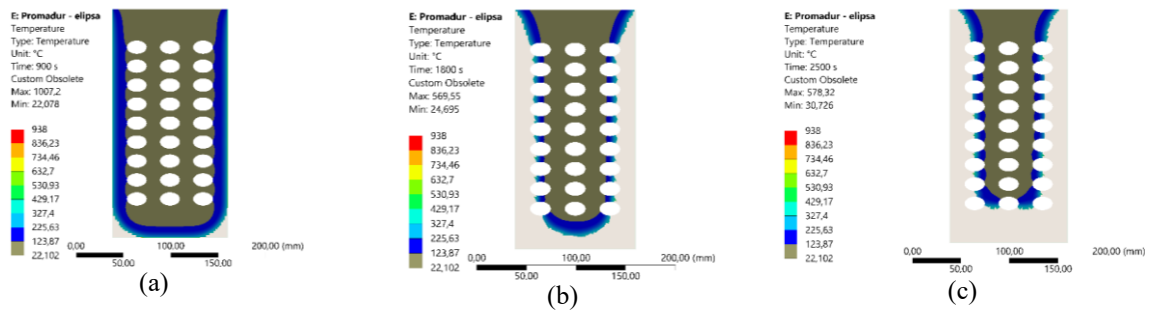

Figure 3.8 Evaluation of char depth in fire-protected perforated beams with mineral wool infill, exposed to three-sided fire: (a) 15 minutes; (b) 30 minutes; (c) 45 minutes

As shown in Figure 3.8a, the effectiveness of the fire-retardant coating is evident, as charring began only after approximately 15 minutes. The average char depth measured after 45 minutes of fire exposure in these specimens was again approximately 30 mm, which matched the result of the numerical simulation.

4 Conclusion

A comprehensive experimental and numerical investigation was conducted to evaluate the influence of internal perforations on the fire performance of glued laminated timber (GLT) elements. The study also examined the effectiveness of various passive fire protection systems in enhancing the fire resistance of both solid and perforated GLT components. The results indicated that the type of adhesive used (K.501 vs. K.510) had no significant impact on the fire resistance of solid timber elements exposed to fire from one side. However, the introduction of perforations (25 % cross-sectional reduction) led to a 23 % decrease in fire resistance. In contrast, the addition of stone wool insulation within the cavities significantly improved fire resistance by approximately 27 % compared to unprotected perforated samples. Moreover, replacing the first perforated lamella with a full lamella exposed to fire increased failure time by about 20 %. The application of intumescent fire-resistant coating further enhanced fire resistance, with improvements of 52% in solid beams and 67% in perforated beams. Debonding was observed in initially unprotected perforated GLT elements, whereas the use of a full outer lamella and/or fire protection effectively prevented this failure mode. Further analysis of specimens exposed to fire on three sides revealed that failure in perforated beams was consistently caused by debonding. However, the application of intumescent coatings and stone wool infill proved effective, yielding fire performance comparable to that of unprotected solid GLT beams. The measured one-dimensional charring rate for softwood lamellae was β_0 = 0.69 *mm/min*, in line with EN 1995-1-2, while the effective multi-dimensional charring rate for solid GLT beams was β_n = 0.78 mm/min, also consistent with normative values. In protected perforated beams, three distinct charring phases were identified, highlighting the complex thermal behavior of such systems under fire exposure. This research contributes valuable insights into the fire performance of innovative hollow timber elements, offering practical guidance for improving their resilience through targeted material choices and design strategies.

Additionally, the study confirmed that in each phase of charring, a linear relationship can be assumed between the char depth and the duration of fire exposure. For conventional (solid) glued laminated timber elements, both the one-dimensional and multi-dimensional charring rates, as well as the thickness of the zero-strength layer, align with the values prescribed by EN 1995-1-2 [15]. However, during the second charring phase of perforated elements filled with stone wool, increased charring of the vertical timber webs between the cavities was observed. This is attributed to the two-dimensional heat flow caused by thermal accumulation in the stone wool. Consequently, the zero-strength and zero-stiffness layer (d_0) should be increased as follows:

$$d_{o,eff} = d_{0,clause} + \Delta d_0,\ \Delta d_0 = \gamma \max\left(0, \frac{w_{cav}}{t_{web}} - 1\right), \quad (9)$$

Where w_{cav} – cavity width in mm, t_{web} – web thickness in mm, and γ is a calibration coefficient (dimensionless) that scales how strongly web slenderness amplifies charring. The max(0,·) keeps $\Delta d_0 = 1$ when there is no hollowing effect (i.e., $w_{cav} \leq t_{web}$) and increases it only when the cavity is wider than the thickness of web. The driver is the slenderness ratio $\psi = w_{cav}/t_{web}$. When $\psi \leq 1$ (narrow cavity, thick web), lateral flux is limited and there is no amplification. When $\psi > 1$, the web is flanked by hot cavities which means more 2D heat flow and finally faster charring. The function is continuous at $\psi = 1$ and, linear beyond it. ψ shall be validated by advanced calculation.

Finally, numerical simulations have proven to be a valuable tool for gaining deeper insights into the fire performance of perforated glued laminated timber elements. Thermo-mechanical analyses were carried out using the ANSYS software suite, with simulation results closely aligning with experimental findings. A novel numerical approach based on the finite element method was developed to evaluate the depth of the charred layer. Thermal and thermo-mechanical analyses demonstrated strong correlation between predicted and measured temperatures in timber elements exposed to standard fire conditions. The ratio of numerically predicted charring depth to the experimentally measured charring depth was found to be 1.05, indicating high accuracy with only a 5% deviation.

5 Acknowledgement

This publication is based upon work from COST Action CA20139 - HELEN, supported by COST (European Cooperation in Science and Technology).

6 References

1. EN 16351:2021 - Timber structures - Cross laminated timber - Requirements. Available https://standards.iteh.ai/catalog/standards/cen/3f9c8502-609e-4592-9cc2-219dc2ff3720/en-16351-2021 (accessed on June 23, 2025).
2. Luxhome. Available https://www.luxhome.at/ (accessed on December 11, 2024).
3. ECOCELL. Available https://ecocell.ch/en/us-building-system (accessed on December 11, 2024).
4. Fabric Workshop - Mass Timber Solutions. Available https://www.fabricws.com/building-solution (accessed on December 11, 2024).
5. Brikawood | Kits maisons bois passives écologiques, brique en bois écologique, maison BBC.”. Available https://www.brikawood-ecologie.fr/ (accessed on December 11, 2024).
6. GABLOK-Insulated formwork block for self-build project. Available https://gablok.be/en/ (accessed on December 11, 2024).
7. STEKO® Building Systems | Everybody Wins with Smart Construction. Available https://www.stekosouthamerica.com (accessed on December 11, 2024).

8. Chu, D.; Mu, J.; Avramidis, S.; Rahimi, S.; Liu, S.; Lai, Z. Functionalized Surface Layer on Poplar Wood Fabricated by Fire Retardant and Thermal Densification. Part 1: Compression Recovery and Flammability. Forests 2019, Vol. 10, Page 955, 2019, 10, 955.
9. Chu, D.; Mu, J.; Avramidis, S.; Rahimi, S.; Liu, S.; Lai, Z. Functionalized Surface Layer on Poplar Wood Fabricated by Fire Retardant and Thermal Densification. Part 2: Dynamic Wettability and Bonding Strength. Forests 2019, Vol. 10, Page 982, 2019, 10, 982.
10. Johansson, E.; Svenningsson, A. Delamination of Cross-Laminated Timber and Its Impact on Fire Development Focusing on Different Types of Adhesives; Lund, Sweden, 2018.
11. Knorz, M.; Torno, S.; van de Kuilen, J.W. Bonding Quality of Industrially Produced Cross-Laminated Timber (CLT) as Determined in Delamination Tests. Constr Build Mater, 2017, 133, 219–225.
12. Frangi, A.; Knobloch, M.; Fontana, M. Fire Design of Timber Slabs Made of Hollow Core Elements. Eng Struct, 2009, 31, 150–157.
13. Rosa, I.C.; Santos, P.; Firmo, J.P.; Correia, J.R. Fire Behaviour of Concrete Slab Strips Reinforced with Sand-Coated GFRP Bars. Compos Struct, 2020, 244.
14. Fahrni, R.; Klippel, M.; Just, A.; Ollino, A.; Frangi, A. Fire Tests on Glued-Laminated Timber Beams with Specific Local Material Properties. Fire Saf J, 2019, 107, 161–169.
15. Eurocode 5: Design of timber structures -- Part 1-2: General - Structural fire design (EN 1995-1-2:2004/A2:2014): Available https://www.phd.eng.br/wp-content/uploads/2015/12/en.1995.1.2.2004.pdf (accessed on June 27, 2024).
16. König, J. Fire Resistance of Timber Joists and Load Bearing Wall Frames. 1994.
17. König, J. Timber Frame Assemblies Exposed to Standard and Parametric Fires. Part 2 A Design Model for Standard Fire Exposure. 2000.
18. Perković, N.; Rajčić, V.; Pranjić, M. Behavioral Assessment and Evaluation of Innovative Hollow Glue-Laminated Timber Elements. Materials 2021, Vol. 14, Page 6911, 2021, 14, 6911.
19. DIN EN 1052-1 - European Standards. Available https://www.en-standard.eu/din-en-1052-1-methods-of-test-for-masonry-part-1-determination-of-compressive-strength/ (accessed on June 30, 2024).
20. PROMADUR® - Promat. Available https://www.promat.com/en/construction/products-systems/products/intumescent-paints/promadur/ (accessed on July 2, 2024).
21. ANSYS® Academic Teaching Mechanical. ANSYS Workbench User's Guide. Canonsburg: ANSYS, Inc., 2009.
22. ANSYS Mechanical APDL Basic Analysis Guide.

DISCUSSION

The paper was presented by N Perković

A Frangi commented that the authors encompassed too many aspects in the paper; hence, it is too complicated to make this research generally applicable for standardization, it is rather a topic for a technical approval. The authors should focus on a specific product instead. N Perkovic agreed.

A Frangi commented on charring rates for one- and three-dimensional cases with holes and that one should be careful with cases where thinner laminates are involved.

S Winter is critical of statement that intumescent paint could increase resistance to fire normally. He said in practice the intumescent paints are not effective to increase fire resistance. We want to minimize chemical treatment as this goes against green building concepts. He questioned why PUR which is a D4 class and how to control the quality of the glue. N Perkovic explained how the gluing process was conducted and different adhesives were tested before deciding on PUR.

A Just agreed with comments on standardization and received clarification about painting on three sides and which side was considered. N Perkovic further clarified definitions of some variables. A Just suggested to put recommendations in the paper. V Rajcic added the results can be applied to products for doors and windows.

P Dietsch asked about cross section width and charring rate. N Perkovic responded a higher notional charring rate was calculated; however, 0.75 mm from EC5 Part 1 and 2 was used as charring rate.

P Dietsch commented about placing mineral wool in the cavity which would reflect energy and hence increase temperature in the wood. N Perkovic agreed and saw increase in heat flux in results. He will think about alternative insulation materials.

Tenon connections – Consideration of brittle failure by fracture mechanics approach

Timo Claus, Timber Engineering and Building Construction,
HafenCity University Hamburg, Germany

Werner Seim, Building Rehabilitation and Timber Engineering,
Universität Kassel, Germany

Keywords: end-notched beams, tenon joints, fracture mechanics, *J*-integral

1 Introduction

Since timber constructions have been extensively planned and fabricated using digital processes, new connection types were developed for engineered timber constructions. One possibility to make more out of the precision of automated machinery is to multiply the contact surfaces in one connection. Enders-Comberg (2016) investigated the multiple-step joint and Claus & Seim (2018) conducted experimental and numerical tests on multiple tenon connections. In this context, tenons and notches are gaining new attention. The current design formulation for laterally loaded tenon connections in the second generation of Eurocode 5 (2025) is an extension of Gustafsson's (1988) approach to end-notched beams based on empirically provided factors. However, the formulation is restricted due to the limited number of experimental tests carried out in the 1980s. Consequently, modern beam geometries, materials and CNC-fabricated joint geometries have not been adequately addressed.

The following study tries to transfer the knowledge of the widely investigated end-notched beam (N) to tenon connections (T) and, finally, to multiple tenon joints (MT) with several contact surfaces and possible crack layers (Fig. 1). Additionally, the energy-based approach will be compared to experimental tests results and the results of a numerical *J*-integral model. Finally, a design formulation will be proposed for tenon and multiple tenon connections.

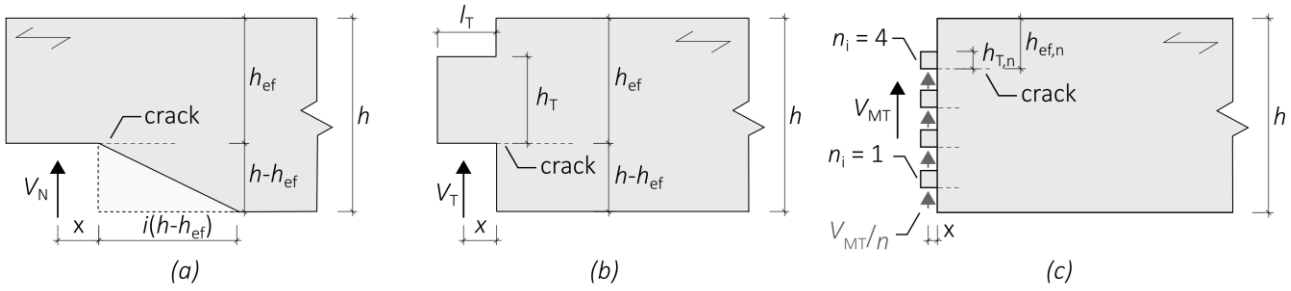

Figure 1. Geometry of different timber connections: (a) end-notched beam, (b) tenon connection and (c) tenon joint with multiple crack layers.

Table 1. Overview of the experimental test results from Schelling & Hinkes (1985) and Hinkes (1988).

test series	n_T	b	h	$l_T = 2x$	α	β	γ	$V_{T,m}$	COV	$k_s(n)$	$V_{T,k}$
	-	mm	mm	mm	-	-	-	kN	%	-	kN
Z-120	121	80	120	40	0.67	0.17	0.50	9.3	20	1.64	6.1
Z-180	93	100	180	50	0.67	0.14	0.50	16.8	32	1.64	9.3
Z-240	63	120	240	60	0.67	0.13	0.50	24.1	25	1.64	14.7
ZBH-140	3	80	140	40	0.71	0.14	0.40	13.7	4	3.15	11.9
ZBH-160	3	80	160	40	0.75	0.13	0.33	17.5	12	3.15	11.9
ZBH-180	3	80	180	40	0.78	0.11	0.29	21.2	5	3.15	18.1
ZBH-200	3	80	200	40	0.80	0.10	0.25	23.3	7	3.15	19.0
ZVO-120	3	80	120	40	0.50	0.17	0.67	8.0	39	3.15	1.8
ZVU-120	3	80	120	40	0.83	0.17	0.40	19.7	18	3.15	11.1
ZZH-180	7	100	180	50	0.78	0.14	0.29	12.8	23	2.34	7.4
ZZH-240	7	120	240	60	0.58	0.13	0.29	20.5	16	2.34	14.2

2 Experimental tests

2.1 Experimental research data of tenon connections

The experimental database for the current of Eurocode 5/NA ((2013) and Eurocode 5 (2025) formulations was provided by Schelling & Hinkes (1985) and Hinkes (1988). More than 350 tests were conducted on tenon connections with a different beam height h, location of the crack layer ($h_{ef} = \alpha h$), tenon height ($h_T = \gamma h_{ef}$) and tenon length ($l_T = 2x = 2\beta h$). The width of the tenon equals the width of the beam and was chosen between b = 80 and 120 mm. The main set-up was a tenon arranged in the centre of the cross-section with α = 2/3. Solid timber (Picea abies; ST) of quality class II, with a raw density of ρ_0 = 340 … 460 kg/m³, was used under a comparably high variation in timber humidity.

Table 1 shows the configuration of the tenon geometries for each test series, as well as the mean values of the maximum load $V_{T,m}$ and the coefficient of variation (COV) for each sampling size n. Finally, the characteristic values $V_{T,k}$ were calculated with the distribution factor $k_s(n)$, according to EN 14358 (2016).

2.2 Experimental research data of multiple tenon joints

Six different layouts of multiple tenon geometries with different beam heights were performed by Claus (2020). The number of tenons was varied between n_i = 1 and 7. The height of the tenons was chosen as h_T = 20 mm and the space in between as 30 mm for configurations of more than two tenons. The ratio of the length of the tenon to the height of the tenon l_T/h_T was chosen as 1.0. A sample size of n_{MT} = 5 or 6 was tested for each tenon configuration.

Solid timber (C24) and glued laminated timber (GLT, GL24h) was used in the main beam to secondary beam test set-up with a density between ρ_u = 430 and 470 kg/m³ and a moisture content of ω = 9.7 to 11.8 %.

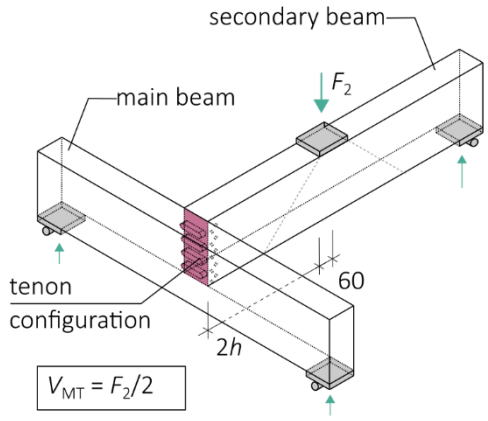

Figure 2. Test set-up of multiple tenon joints.

Table 2. Tenon configuration and experimental resistance of multiple tenon joints.

set-up	n_i	mat.	b	h	n_{MT}	$V_{MT,m}$	COV	$k_s(n)$	$V_{MT,k}$
	-	-	mm	mm	-	kN	%	-	kN
TS1	1	C24	100	240	5	13.8	20	2.46	7.2
TS2	2	C24	100	240	6	17.4	30	2.34	5.9
TS4	4	GL24h	100	240	5	37.4	6	2.46	32.4
TM2	2	GL24h	160	380	6	52.1	13	2.34	37.0
TM4	4	GL24h	160	380	6	69.4	11	2.34	52.9
TM7	7	GL24h	160	380	5	78.1	5	2.46	68.2

Table 2 shows the mean values of maximum experimental load $V_{MT,m}$ with COV, as well as the calculated characteristic values. When using more tenons and more homogeneous timber products, the load-bearing capacity of multiple tenon joints increases significantly. Connections on beams made of ST C24 results in a higher COV and lower characteristic resistance of the timber joints.

3 Application of the energy-based approach

3.1 Energy-based approach

Gustafsson (1988) developed the critical failure load for end-notched beams using the fracture mechanics approach regarding the energy balance. Therefore, the total deformation δ in the middle of the beam from shear deformation δ_v, bending deformation δ_b and rotational deformation δ_r of the beam were considered (Fig. 3a).

$$\delta = \delta_v + \delta_b + \delta_r \tag{1}$$

Due to the deformation of the beam, elastic strain energy Π^a and inner deformation energy Π^i occur. The change of crack-forming energy $\Delta\Pi^0$ related to the change of the crack area ΔA is defined as the critical energy release rate or specific fracture energy G_c.

$$\Delta(\Pi^a - \Pi^i)/\Delta A = \Delta\Pi^0/\Delta A = G_c \tag{2}$$

The change of $(\Pi^a - \Pi^i)$ can be determined by the change of the total deformation (Fig 3b).

$$\Delta\delta = \Delta\delta_v + \Delta\delta_b + \Delta\delta_r \tag{3}$$

$$= 1.2V/(G_v b)\cdot(1/\alpha - 1) + 12V/(E_x bh)\cdot(1/\alpha^3 - 1) + 24\beta V/(b\alpha^2)\cdot((1-\alpha)(1-\alpha^3)/(10\, G_v E_x))^{0.5}$$

In the next step, the potential of inner energy will be set equal to the crack-forming energy defining critical crack propagation when the critical shear force $V = V_c$ occurs:

$$\Delta\Pi^i = 1/2 V_c^2\, \Delta(\delta/V) = G_c b \Delta\beta h \tag{4}$$

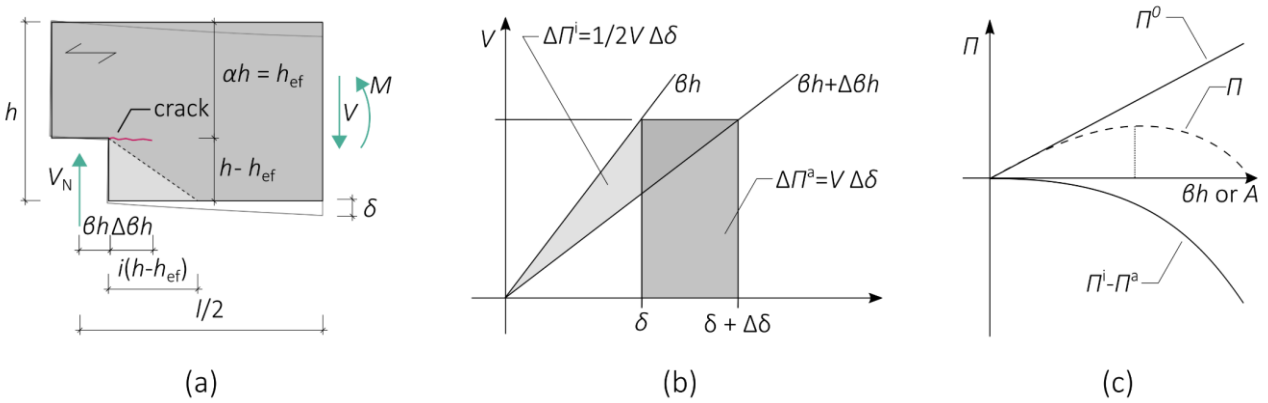

Figure 3. (a) geometry of an end-notched beam, (b) load-deformation behaviour under crack propagation and (c) energy potential under crack propagation.

The critical shear force for end-notched beams related to the remaining cross-section above the crack is

$$V_c/b\alpha h = ((2G_c/b\alpha 2h) / (\Delta(\delta/V)/\Delta\beta))^{0.5}. \quad (5)$$

Substituting expression (3) into equation (4) and then transforming the result yields the final expression

$$V_c = (b\alpha h\,(G_c/h)^{0.5}) / ((0.6\,(\alpha-\alpha^2)/G_v)^{0.5} + \beta\,(6(1/\alpha-\alpha^2)/E_x)^{0.5}). \quad (6)$$

The fracture mechanics approach, based on the energy balance, enables the fracture load to be determined as a function of the geometric dimensions and the elastic material parameters E_x and G_v, as well as the specific fracture energy G_c of the material. Calculations by Gustafsson (1988) showed good agreement between the fracture loads calculated and the experimental failure loads determined. In order to transfer the concept into a design equation, a material constant k_n was introduced so that the specific fracture energy of wood does not have to be included in Eurocode 5 (2010). Wood often exhibits pre-damage in the form of cracks, therefore, this concept can also be transferred to other problems, such as cracks developing along the fibre of cross-laminated timber (Serrano et al., 2022).

3.2 Critical fracture load of tenon joints

In terms of failure due to crack propagation, the difference in geometry between end-notched beams and tenons is the missing timber volume above the tenon. Therefore, less energy can be stored internally. As the length of the missing volume above the tenon does not increase with the crack length, solving equation (4) will not be manageable and the final design solution will differ.

Three possible solutions were analysed in Claus (2020) covering the modified geometry with the existing approach by Gustafsson (1988). Firstly, the expression (6) was applied to the tenon connection disregarding the missing volume above the tenon. In this case, the experimental failure loads were significantly lower than those obtained using the fracture mechanics approach. Secondly, the expression (6) was applied to the

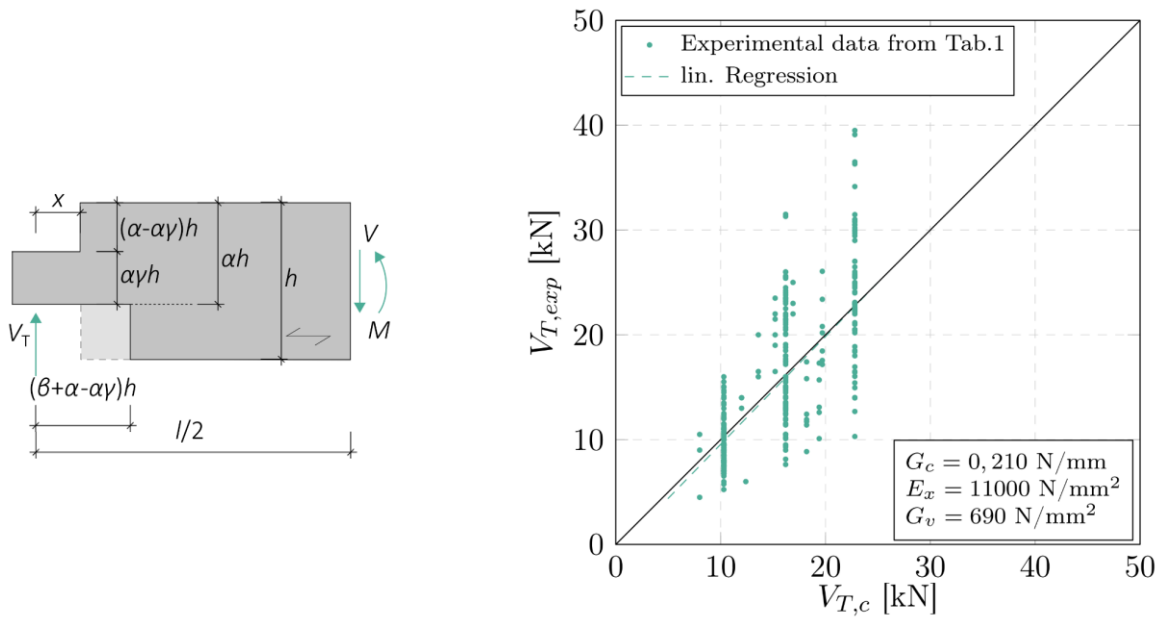

(a) *(b)*

Figure 4. (a) Geometrical definitions on tenon connections and (b) a comparison of critical failure loads $V_{T,c}$, according to eq. (7) and experimental test results $V_{T,exp}$.

tenon connection, with the height of the tenon chosen to be the height of the remaining cross-section $h_{ef} = h_T$. Due to the significant reduction of the stored energy in this approach, the mean values of the experimental failure loads were higher than in this simplified approach (Claus, 2020). Finally, as a third attempt, the height of the missing timber volume above the tenon $(\alpha-\alpha\gamma)h$ was added to the initial crack length βh. The geometry of this approach is shown in Figure 4a. A comparison made between the single experimental results $V_{T,exp}$ and the fracture mechanics approach using the following expression

$$V_{T,c} = (b\alpha h\,(G_c/h)^{0.5}) \,/\, ((0.6\,(\alpha-\alpha^2)/G_v)^{0.5} + (\beta+\alpha-\alpha\gamma)\,(6(1/\alpha-\alpha^2)/E_x)^{0.5}) \qquad (7)$$

is shown in Figure 4b. The linear regression of both values is similar to the bisecting angle, which indicates a good correlation to the mean values. The critical fracture energy of ST was assumed to be $G_c = G_C^{I+II} = 0.210$ N/mm for a combined fracture in mode I and II, according to Franke (2008).

3.3 Critical failure load of multiple tenon joints

Claus (2020) analysed three different failure modes for multiple tenon joints according to the numerical and experimental results (Claus & Seim 2018). Firstly, assuming the initial crack to be at the lowest tenon ($i = 1$) leads to significant overestimation of the experimental test results. Secondly, simultaneous cracking showed a good accordance with some of the experimental test results, but a significant overestimation for more than four tenons in one joint.

Finally, the initial crack occurring at the highest tenon ($i = n$) was analysed, as shown in Figure 5a. In this case, each underlying tenon reaches the same load $V_{MT,i} = V_{MT}/n$ and

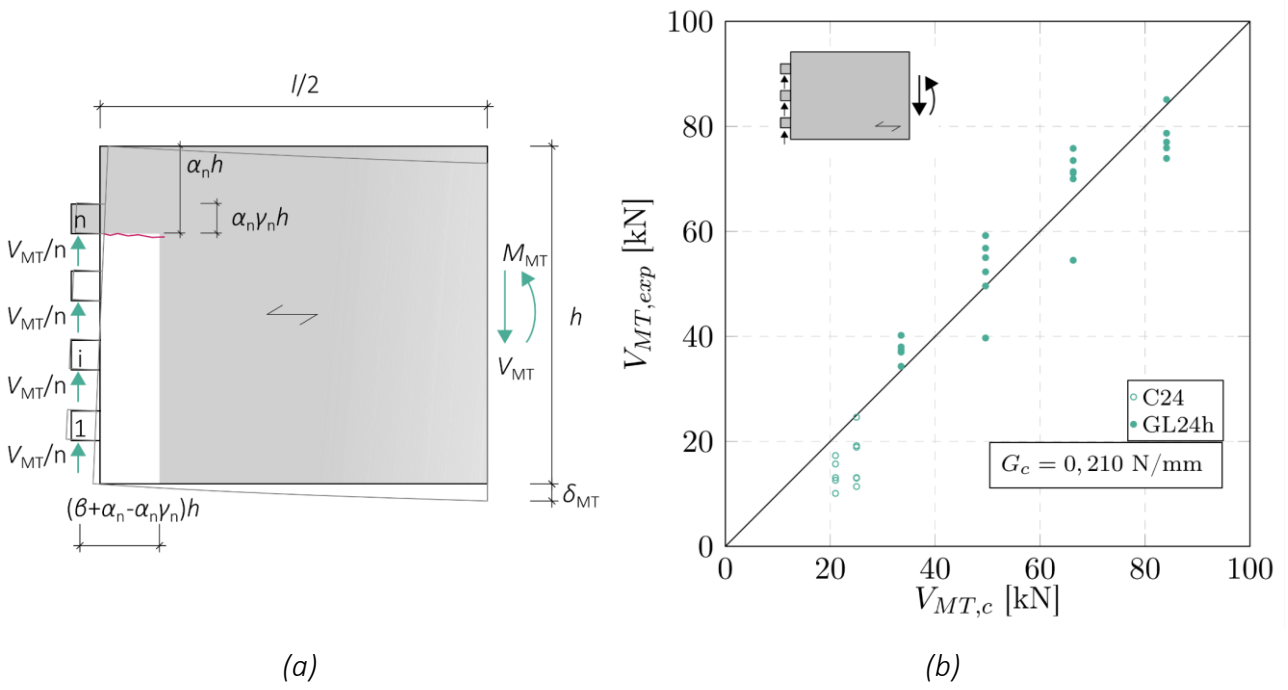

(a) (b)

Figure 5. (a) Geometrical definitions of a multiple tenon joint and (b) comparison of critical failure loads and experimental test results.

the total capacity is the product of the capacity of the highest tenon and the number of tenons:

$$V_{MT,c} = n_i \cdot V_{T(n),c} \tag{8}$$

Figure 5b shows a comparison of the experimental test data from Table 2 with the results from the fracture mechanics approach Eq. (8). The test results for glulam GL24h show good agreement with the critical failure load. Conversely, the approach overestimates the test results obtained using ST C24 with only one or two tenons. Therefore, a reliability analysis is needed to consider the model uncertainties and the variation of material parameters.

3.4 Reliability analysis related to a Eurocode 5 design proposal (Model 1)

In order to determine the statistical distribution function of the failure loads, the experimental results must be standardised for a generally valid design concept for tenon connections and multiple tenon joints. If the verification method is based on end-notched beams according to Eurocode 5 (2025), the following equation should be used for all types of geometries shown in Figure 1:

$$1.5 \cdot V_d / (n_v \cdot b \cdot k_v \cdot h_{ef}) \leq f_{v,d} \cdot k_{v,n} \tag{9}$$

with the total design shear force V_d, the number of contacts n_v, the effective width $b \cdot k_v$ the position of the crack layer h_{ef} and the design value of the shear strength $f_{v,d}$. The coefficient $k_{v,n}$ considers the fracture-mechanical behaviour. The coefficient could be calculated with the help of the normalised fracture load, according to Jockwer et al. (2011). The model uncertainty will be covered with only one parameter.

Table 3. Design parameter for end-notched beams, tenon connections and multiple tenon joints.

geometry	n_v	m	k_n	
			ST	GL
end-notched beams				
Jockwer et al. (2011)	1	β	3.0	3.9
Eurocode 5 (2025)	1	β	5.0	6.5
tenon connections (Claus, 2020)	1	$\beta + \alpha - \alpha\gamma$	2.9	-
multiple tenon joints (Claus, 2020)	≥ 2	$\beta + \alpha_n - \alpha_n\gamma_n$	1.6	5.0

The normalised fracture loads derived from the experimental tests according to Table 1 and 2 could be displayed as a log-normal distribution. The mean value, the COV and the characteristic value were calculated for this normalised distribution.

Due to the fracture load being highly dependent on specific fracture energy (Jockwer et al., 2011), it is also necessary to consider the model uncertainty. The determination of all necessary parameters depending on the partial factors γ_m and the shear strength $f_{v,k}$ are documented in Claus (2020). Regarding the proposed design model, $k_{v,n}$ can be described as follows:

$$k_{v,n} = \min \{1; k_n \cdot (1 + 1.1 \cdot i^{1.5}/h^{0.5}) / (h^{0.5} \cdot ((\alpha(1-\alpha))^{0.5} + 0.8 \cdot m \cdot (1/\alpha - \alpha^2)^{0.5}))\} \quad (10)$$

In this approach, k_n describes the model uncertainties depending on the scope of the tests performed and is, therefore, also dependent on the material parameters (Table 3). k_n increases with more homogeneous materials and the number of tests performed.

The parameter m considers the tenon geometry. Connections with multiple tenon joints should be designed with more than two tenons and a length to height ratio more than $l_T/h_T \geq 1.0$ to ensure a sufficient bending deformation and contact of tenons.

4 Application of the J-Integral model

4.1 Mechanics of the J-integral approach

Another method to describe the fracture behaviour of solids in the framework of linear elastic fracture analysis is the *J*-integral analysis. The *J*-integral is a path integral on the contour Γ around the crack tip and was discovered nearly simultaneously by Cherepanov (1967) and Rice (1968).

Only a subsystem around the crack tip needs to be analysed due to the path independency (Fig. 6a). The path encloses the area *A*. The potential of the inner energy can be expressed by the deformation energy density *U*. The latter is defined as the deformation energy per volume for an elastic material:

$$U = 1/2 \, [\sigma_x \, \partial u/\partial x + \tau_{xy} \, (\partial u/\partial y + \partial v/\partial x) + \sigma_y \, \partial v/\partial y] \quad (11)$$

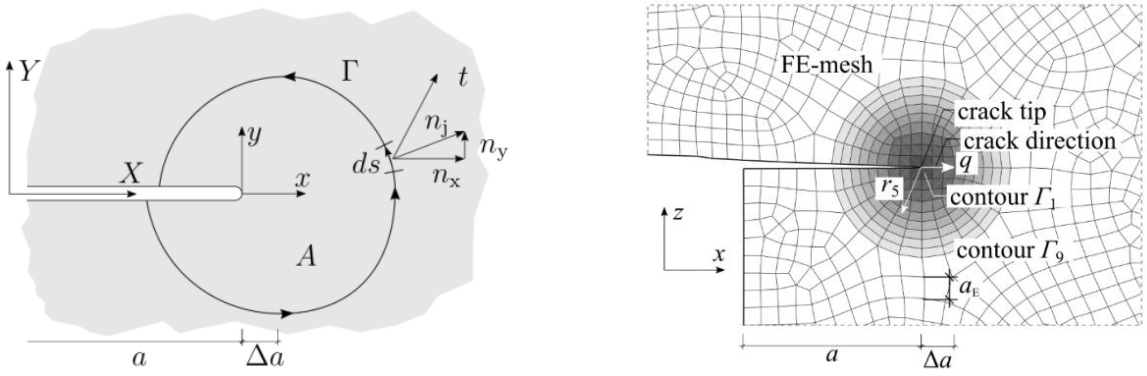

(a) *(b)*

Figure 6. (a) J-integral at the crack tip from Kuna (2013) and (b) implementation of contour integrals around the crack tip in a FE-model.

The stress tensor

$$t_i = \sigma_{ij}\, n_j \tag{12}$$

includes the stresses σ_{ij} acting from outside the area A. The vector n_j is orthogonal to the contour Γ. If no other external forces act on the subsystem and no damages or cracks occur in the enclosed area, the conservation of energy can be expressed with the path integral:

$$\int_\Gamma [U dy - t_i\, (\partial u_i/\partial x)\, ds] = 0 \tag{13}$$

The length ds describes a segment on the contour Γ. The area A moves from a to $a + \Delta a$ under crack progress in a local X-direction. The change of potential energy $d\Pi$ under crack progress Δa can be expressed comparably to the energy release rate G with the J-Integral. The following expression from Kuna (2013) can be used for a contour enclosing a crack:

$$G = -d\Pi/da = J \equiv \int_\Gamma [U dy - t_i\, (\partial u_i/\partial x)\, ds] \tag{14}$$

The critical crack progress starts when J reaches the value J_c. The fracture criteria is

$$J = J_c \leq G_c. \tag{15}$$

In order to be able to compare the multi-mode critical energy release rate G_c^{I+II}, it needs to be shown that:

$$J = J^{I+II} = J^{I} + J^{II} \tag{16}$$

It was proved that the J-integral is path independent. Thus, every path including a crack tip can be used for the determination of J. A comparison with the calculation of the energy release rate G was performed for the double cantilever beam in Claus (2020). The J-integral had already been used by other authors, for example, by Yeh and Schniewind (1992) or to determine stress intensity factors in finite element models of bolted connections (Borth et al., 2002).

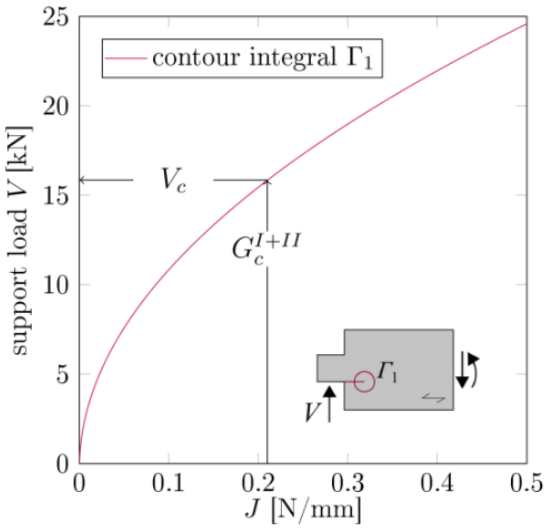

Figure 7. Non-linear relationship between support load V on the J-integral for the contour Γ_1.

Table 4. Mean values of material stiffness and fracture parameters for the finite element model.

	E_x	E_z	G_{xz}	ν_{xz}	ν_{xz}	G_c^{I+II}
	N/mm²			-		N/mm
C24	11000	370	690	0.45	0.24	0.21
GL24h	11500	300	650	0.45	0.24	0.21

The contours in the finite element model were defined automatically around the crack tip (Fig. 6b). Only 4-node elements were used for the determination of *J* in ABAQUS.

The support load *V* was determined depending on the *J*-integral (Fig. 7). The critical support load V_c was then evaluated for the critical energy release rate G_c^{I+II}.

The initial crack length *a*, the element size a_E and the distance of the contour from the crack tip r_i were investigated to check the influence of model parameters. Only minor deviations of the critical support loads were observed. The initial crack length was then fixed to a = 40 mm because of the little increase of *J* for very small values, and the element size was set to a_E = 5 mm for the model and refined to a_E = 1 mm in the area of the contours evaluated. The contour integral Γ_1 will be evaluated for the following calculations. The calculation of the *J*-integral reacts more or less insensitively when the stiffness parallel to the grain E_x and the fracture parameter G_c^{I+II} of the models are changed.

Using the material parameters from Table 4 given by the JCSS (2006), the critical support load V_c of the *J*-integral model was in good accordance with the experimental results from end-notched beams, tenon connections and multiple tenons joints, as shown in Claus (2020).

4.2 Results from the parameter study

The finite element model was applied to carve out an extensive parametric study of end-notched beams and tenon connections. In this study, the influence of the beam height, the location of the crack plane, the tenon height and length were investigated. More than 100 different geometries were analysed regarding the critical failure load. The results have already been presented and discussed in Claus & Seim (2021).

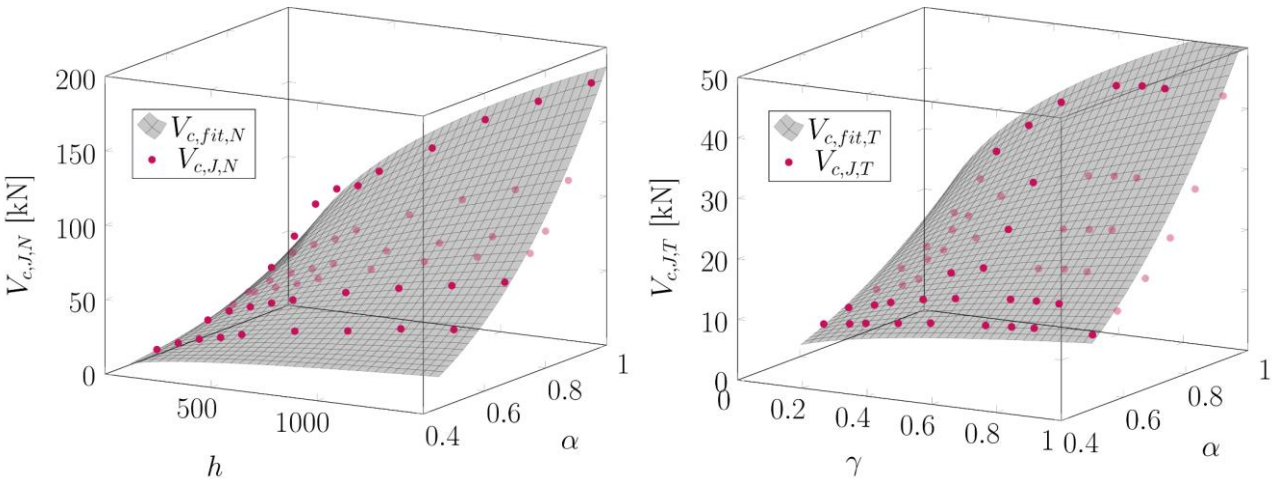

(a) *(b)*

Figure 8. Critical support load $V_{c,J}$ (dots) and equalising surface function (grey) of (a) end-notched beams and (b) tenon connections.

The failure load increases with a degressive progression while increasing the beam height and, on the other hand, the failure load increases progressively with the increasing ratio α.

Figure 8b shows the calculated failure load $V_{c,J,T}$ of tenon connections. The cross-section of the beams was fixed at b = 100 and h = 240 mm. The notch length ratio was chosen to be β = 0.1 h for all geometries of the tenons.
The results show that the critical failure load increases disproportionately with an increasing ratio α and degressively with an increase of the tenon height ratio γ. The failure loads do not increase for a tenon height ratio of $\gamma \geq 0.70$, especially for notch ratios of $\alpha > 0.67$.

4.3 Development of a simplified design model (Model 2)

The parameter study revealed a clear relationship between the failure load of the tenon connections and the position and height of the tenon. The following section will derive a simplified design model for determining the failure load from the data of the parametric study, considering the essential geometric parameters. The following procedure is used to develop the simplified design model for tenon connections and multiple tenon joints:

- setting up the theoretical resistance function;
- determining the factor k and the exponents p, q, r and s from the parametric study;
- determining the pre-factor λ_m for mean value adjustment;
- reduction of the pre-factor λ_k for the characteristic design level adjustment; and
- validation of the simplified calculation model.

The mean resistance value of all three connection types could be calculated using the following formula:

$$V_{Rm} = \lambda_m \cdot b \cdot h^p \cdot \alpha^q \cdot \gamma^r \cdot n_v^s \quad (17)$$

Here, λ is the adjustment factor for mean value correction, as described in Claus (2020)

$$\lambda = (\sum r_{e,i} \cdot r_{t,i}) / (\sum r_{t,i}^2), \quad (18)$$

with the experimental failure loads $r_{e,i}$ and the theoretical failure values $r_{t,I}$, and takes into account the material parameters. The basis of the adjustment coefficient is the pre-factor k from the parametric study. The parameters b, h, α and γ represent the geometry of the connection. The exponents p, q and r are determined by post-processing the results of the parametric study. Regarding multiple tenon joints, the number of tenons is specified as n_v, and the exponent s considers the effective number of tenons.

The characteristic value of the resistance function could then be determined based on the relationship between the mean and characteristic values, according to EN 1990 (2021)

$$\lambda_k / \lambda_m = \exp(-k_s(n) \cdot Q_r - 0.5 \cdot Q_r^2) \quad (19)$$

with the fractile value $k_s(n)$ and the standard deviation Q_r.

The equalising surface functions for end-notched beams and tenon connections were chosen as a two-parameter power function. The equalising functions shown in Figures 8a and 8b (grey surface) were created in Mathematica 8 (2010) software using 'NonlinearModelFit'. This function is limited to h = 100 … 1500 mm and $0.5 \leq \alpha < 1.0$ for notched beams, as well as $0.1 \leq \gamma \leq 1.0$ for tenon connections. Table 5 gives an overview of all necessary parameters determining the characteristic design function using the method presented.

Consequently, the following characteristic design formulation for end-notched beams, tenon connections and multiple tenons joints are as follows, using rounded values from Table 5:

$$V_{N,Rk} = 19.5 \cdot b \cdot k_v \cdot h^{0.5} \cdot \alpha^{2.5} \quad (20)$$

Table 5. Parameter of the equalisation surface function (with rounded value*) and the parameters of the characteristic resistance model.*

	b	h	k	p	q	r	s	n	λ	λ_m	$k_s(n)$	Q_r	λ_m
	mm	mm	-					-					
end-notched beams	200		29.7	0.47	2.73	-	-	27	0.96	33.6	1.87	0.27	19.5
rounded value			*35*	*0.5*	*2.5*	0.0	*0.0*						
tenon connections	100	240	34.7	-	2.31	0.37	-	309	1.37	47.8	1.64	0.30	28.0
rounded value			*35*	*0.5*	*2.5*	*0.5*	*0.0*						
Multiple tenon joints			-	-	-	-	-	33	0.94	32.9	1.87	0.24	20.3
rounded value			*35*	*0.5*	*2.5*	*0.5*	*2.5*						

for tenon connections

$$V_{T,Rk} = 28.0 \cdot b \cdot k_v \cdot h^{0.5} \cdot \alpha^{2.5} \cdot \gamma^{0.5} \quad (21)$$

and for multiple tenon joints

$$V_{MT,Rk} = 20.3 \cdot b \cdot k_v \cdot h^{0.5} \cdot \alpha^{2.5} \cdot \gamma^{0.5} \cdot n_i^{2.5} \quad (22)$$

A comparison between the mean values and the characteristic experimental test results for all three types of connections has been presented in detail by Claus (2020).

The parametric study formed the basis for the simplified design equations for end-notched beams and single and multiple tenon joints. These equations are based on key geometric parameters and consider the specific fracture energy and elastic parameters. The simplified resistance models display a high degree of correlation with experimental results for centrally placed tenons. However, their accuracy is reduced for other geometries. The model demonstrates a high degree of agreement regarding both mean and characteristic levels, particularly in the context of multiple tenon connections. The simplified approach is more effective when using GLT due to the reduced variability in fracture loads compared to solid softwood.

5 Comparison of the models

Four diagrams were created to compare the two models with the existing design formulation (Fig. 9). The cross-section in this example was chosen as GL24h with a b/h ratio of 100/240 mm. The notch length was fixed at $\beta = 0.15$ for all geometries. The second generation of the Eurocode 5 (2025) design formulation considers the material parameters with the pre-factor k_n. Jockwer et al. (2011) suggested different values based on a comprehensive reliability analysis compared to Eurocode 5 (2025) (see Table 3). The results for $k_n = 3.9$ and 6.5 are, consequently, both included in the diagrams. Regarding the performance of end-notched beams, Figure 9a shows the characteristic design resistance depending on the notch ratio $0.5 \leq \alpha \leq 1.0$ of the Eurocode and the simplified Model 2. Figure 9b illustrates the difference when analysing a higher cross-section ($h = 480$ mm). The following results are visible in the four diagrams:

- Lower values of resistance in Model 2 are caused by a comparatively low prefactor λ_k due to the limited scope of the experimental tests that were evaluated.
- Higher resistance for a higher notch ratio α could not be adequately covered from Model 2.
- The larger the cross-section, the larger the difference between the Eurocode 5 model and Model 2.

Figure 9c illustrates the performance of tenon connections dependent on $0.5 \leq \alpha \leq 1.0$ ($\gamma = 0.50$), while Figure 9d illustrates the dependence of the resistance on the tenon height ratio for $0.5 \leq \gamma \leq 1.0$ ($\alpha = 0.50$). The following results can be seen in the diagrams:

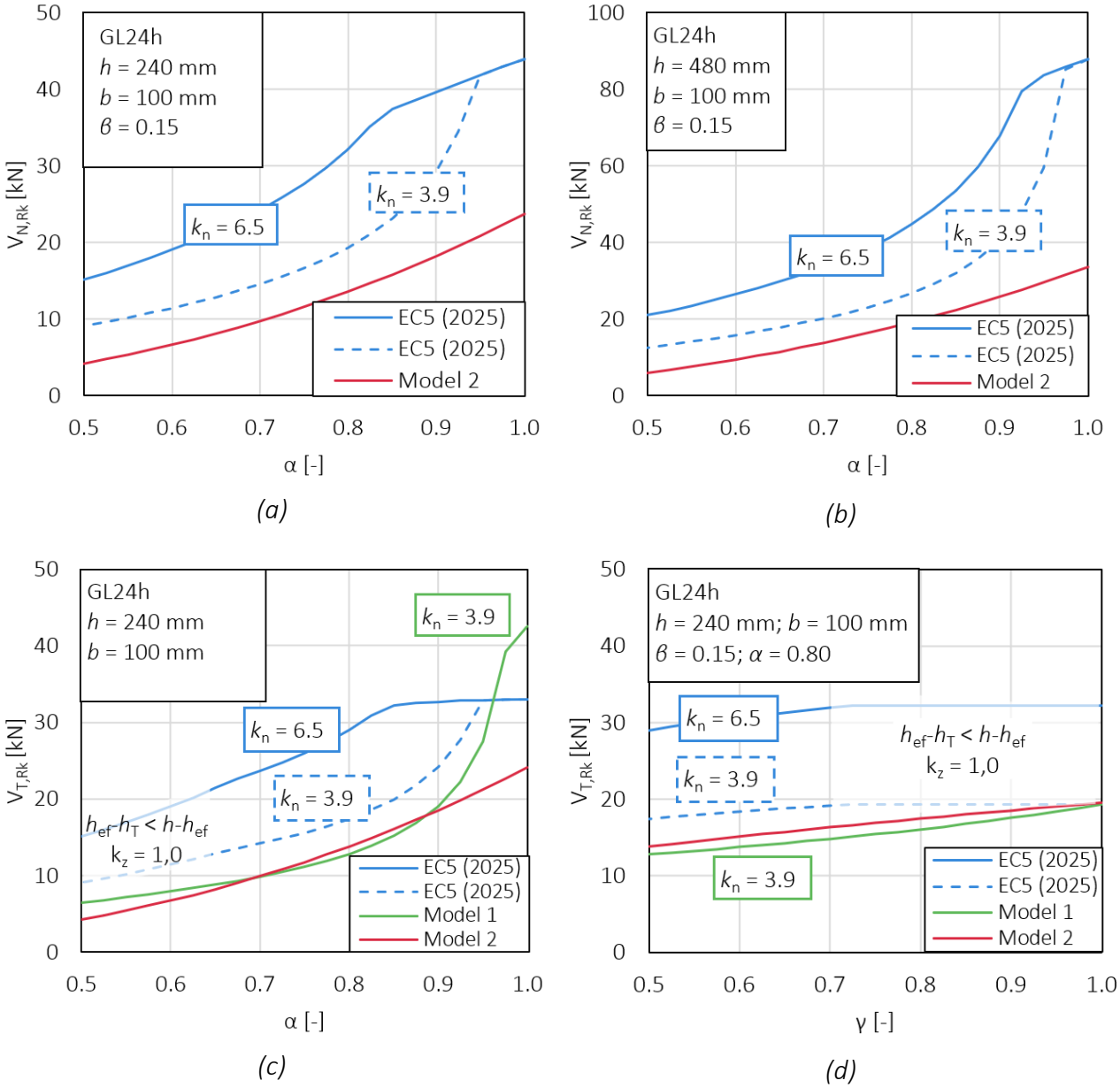

Figure 9. Design resistance of end-notched beams with (a) h = 240 mm and (b) h = 480 mm and the resistance of tenon connections depending on (c) the position of the crack layer and (d) the height of the tenon for three different design models.

- Model 1 and 2 produce comparable results for $0.5 \leq \alpha \leq 0.9$, even though the formulations' backgrounds are completely different. A higher resistance for a higher notch ratio α could not be adequately covered by Model 2.
- The Eurocode 5 model, based on experimental test results from Schelling & Hinkes (1985), shows significantly different behaviour and only covers $0.70 \leq \gamma \leq 1.0$ due to the constructive regulations.
- Regarding the dependency of the results from tenon height ratio γ, both Models 1 and 2 show similar behaviour.
- The Eurocode 5 formulation using the material parameter $k_n = 6.5$ shows significantly higher resistance, as already seen in Figures 9a and 9b.

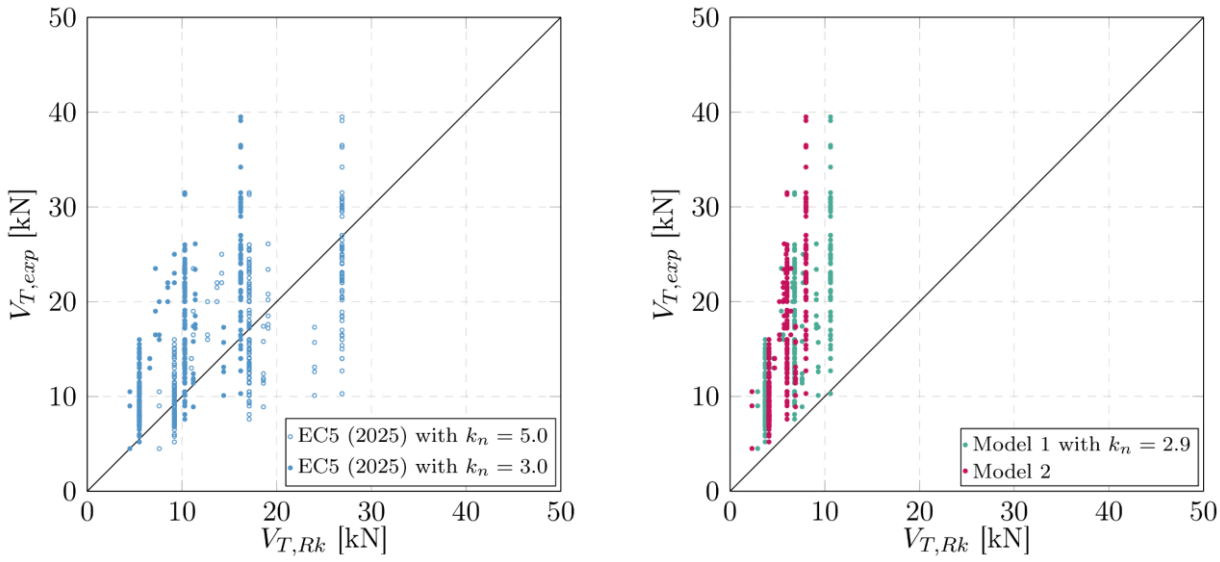

(a) *(b)*

Figure 10. Characteristic design load $V_{T,Rk}$ depending on the experimental test series from Table 1 (single values) for (a) EC5 (2025) model and (b) for model 1 and 2.

Finally, Figure 10 shows a comparison of the maximum experimental load values ($V_{T,exp}$) from Table 1 with their characteristic loads according to the Eurocode 5 (2025) model, as well as for Models 1 and 2 of this study.

Over 50 % of the test results are located below the bisecting angle for the existing model of Eurocode 5 (2025) with k_n = 5.0. Only 6 % of the experimental values are lower than the characteristic design load for the same model with k_n = 3.0.

When Model 1 is applied to the experimental test results, only one value of the characteristic design load $V_{T,RK}$ is underestimated. Model 2 shows no underestimation of the experimental results.

Conversely, the characteristic design loads of Model 1 do not exceed the limit of $V_{T,RK}$ = 10.6 kN, which is less than half the mean value of the Z-240 test series. However, the Eurocode 5 model with k_n = 3.0 reaches $V_{T,RK}$ = 16.2 kN (67 % of $V_{T,m}$).

6 Conclusion and design proposal

Two models for the calculation of the load-bearing resistance of end-notched beams, tenon connections and multiple tenon joints were developed in this study regarding the fracture mechanics behaviour due to tension stresses perpendicular to the grain. The first model is an extension of the Gustafsson (1988) model. The second, more simplified, model was derived from a comprehensive parametric analysis of all three connection types. A reliability analysis was made for both models to set up the necessary parameters for the characteristic design formulations.
All models have already been evaluated using the experimental test series and demonstrate good accordance using the parameter given in Table 3 and 5 (Claus, 2020). The

design models in this study were compared to each other as well as to the existing design formulation in the second generation of Eurocode 5 (2025).

The main results from the comparison could be summarized as follows:

- The material factor k_n for solid and GLT should be discussed in terms of reliability.
- Model 1 and 2 show much lower results in terms of the critical failure load compared to the Eurocode 5 formulation when k_n is set to 6.5 or 3.9 (glulam).
- The models presented show comparable behaviour for tenon connections for $0.5 \leq \alpha \leq 0.9$. However, Model 2 does not adequately capture the significantly better performance of connections for $0.9 \leq \alpha \leq 1.0$.
- Compared to the Eurocode 5 (2025) approach with $k_n = 3.0$, Model 1 does not account for the high performance of tenon connections with larger cross-sections.

As more simple connections become increasingly important due to the circularity of timber constructions, it will be necessary to ensure that notched connections, tenon joints and high-performance, multiple-loaded tenon joints are designed safely. Therefore, Eurocode 5 should include a harmonised design formulation for all comparable connection types using standardised materials.
Model 1, based on Gustafsson's formulation (1988), is suitable for all three types of connection presented and could easily be integrated into the existing design equation for end-notched members. More systematic experimental data is required to conclude the discussion on the design parameter k_n, particularly on tenon connections made from softwood and hardwood glulam, as no values are currently given for laminated veneer lumber. Another option is to increase the load-bearing capacity and robustness by reinforcing possible crack layers, which is an efficient solution, particularly for the occurrence of multiple cracks.

7 References

Borth, O, Schober, KU & Rautenstrauch, K (2002): Load-carrying capacity of perpendicular to the grain loaded timber joints with multiple fasteners. Proceeding of CIB W18 Meeting, 35-7-8, Kyoto, Japan.

Cherepanov, GP (1967): Crack propagation in continuous media. Journal of Applied Mathematics and Mechanics. 31 (3): 503–512.

Claus, T (2020): Design and calculation of end notched beams and tenon joints in timber constructions (in German). PhD Thesis, University of Kassel, Germany.

Claus, T & Seim, W (2018): Development of the multiple tenon timber connection based on experimental studies and FE simulation. Engineering Structures 173: 331–339.

Claus, T & Seim, W (2021): FE-Analysis of end-notched beams and tenon joints – J-integral versus cohesive zone modelling. XVI International Conference on Computational Plasticity: Fundamentals and Applications COMPLAS.

Enders-Comberg, M (2016): Multiple step joint – Efficient contact joint for compression members. Bauingenieur 89: 162–171.

EN 14358 (2016): Timber structures – Calculation and verification of characteristic values.

EN 1990 (2021): DIN EN 1990:2021-10: Basis of structural design; English version EN 1990:2002 + A1:2005 + A1:2005/AC:2010.

Eurocode 5 (2010): DIN EN 1995-1-1: Eurocode 5 – Design of timber structures – Part 1-1: General – Common rules and rules for buildings (German Version).

Eurocode 5/NA (2013): National Annex - Nationally determined parameters – Eurocode 5: Design of timber structures – Part 1-1: General – Common rules and rules for buildings (Germany). (DIN EN 1995-1-1/NA)

Eurocode 5 (2025): FprEN 1995-1-1:2025-4: Eurocode 5 – Design of timber structures – Part 1-1: General rules and rules for buildings, CEN/TC 250.

Franke, B (2008): Evaluating the load-bearing capacity of end notched beams in softwood (in German). PhD Thesis, Bauhaus University, Weimar, Germany.

Gustafsson, PJ (1988): A study of strength of notched beams. Proceedings of CIB-W18/21, Parksville, Canada.

Hinkes, F-J (1988): Experimental and theoretical investigation on the determination of load-bearing capacity of tenon joints (in German). Düsseldorf.

JCSS (2006): Joint Committee on Structural Safety (JCSS): Probabilistic Model Code Part III – Resistance Models: Timber. www.jcss-lc.org/jcss-probabilistic-model-code/

Jockwer, R, Steiger, R, Frangi, A & Köhler, J (2011): Impact of material properties on the fracture mechanics design approach for notched beams in Eurocode 5. Proceedings of CIB-W18/44, Alghero, Italy.

Kuna, M (2013): Finite elements in fracture mechanics: theory – numerics – applications. Springer.

Mathematica 8 (2010): Wolfram Research, Inc., Mathematica, Version 8.0, Champaign, Illinois, USA.

Rice, JR (1968): A path independent integral and the approximate analysis of strain concentration by notches and cracks. Journal of Applied Mechanics. 35 (2): 379–386.

Serrano, E, Jockwer, R & Danielsson, H (2022): Beams with notches or slits – Extensions of the Gustafsson approach. Proceedings of the INTER-Meeting 55 – 19 – 1, Bad Aiblingen, Germany.

Schelling, W & Hinkes, F-J (1985): Load-bearing behaviour of mortise and tenon joints (in German). IRB-Verlag. Germany.

Yeh, B & Schniewind, AP (1992): Elasto-plastic fracture mechanics of wood using the J-integral method. Wood and Fiber Science 24 (3): 364–376.

DISCUSSION

The paper was presented by T Claus

S Franke asked whether mode 1+2 was considered. T Claus responded they always used a fracture energy approach. S Franke suggested to compare results with model from B Franke. T Claus responded that more tests on GL for a material model will be needed.

H Blass received clarification $h_{e,2}$ is based on height of secondary member.

S Winter asked whether impact from model results have been cross-checked for practice. T Claus responded that the model is safer: 10.6 kN vs 16 kN compared to EC model.

A Frangi received clarification that comparisons were done between mean values and probabilistic approach to achieve characteristic values.

P Dietsch commented that there are previous works on multiple tenon joints and suggested to study the influence of tolerances in the multiple tenon joints.

4 INTER Notes, Istanbul 2025

Bracing stiffness requirements of members supported by discrete elastic supports

Haris Stamatopoulos , NTNU, Trondheim, Norway

Francesco Mirko Massaro , NTNU, Trondheim, Norway

Roberto Tomasi, NMBU, Ås, Norway

Keywords: Bracing stiffness, Critical load, Effective buckling length

1 Introduction

This note presents and discusses the analytical solution and the outcomes for a member with pinned ends under axial compression and restrained at the midspan (refer to figure 1). The problem of the elastic stability of members with discrete elastic supports under axial compression has been explored in various textbooks (e.g., *Timoshenko* & *Gere*, 1963). These sources reveal that the spring stiffness K must exceed a threshold value, specifically $K_{\text{min}} = k_{\text{min}} \cdot N_{\text{cr},a}/a$, to reach the highest buckling mode. Here, $N_{\text{cr},a} = \pi^2 EI/a^2$ signifies the critical load related to the highest buckling mode, and k_{min} is a coefficient determined by the number of spans. Theoretically, it is possible to show that the minimum factor k_{min} is 2 for a 2-span system, 3 for a 3-span system, and approaches 4 as the number of spans becomes very large. In the case of a 2-span system, a similar outcome can be achieved through simple equilibrium analysis, disregarding the member's bending stiffness (*Munch-Andersen*, 2004). For members with initial out-of-straightness, a greater minimum stiffness is expected. Consequently, the previous version of Eurocode 5 suggested k_{min} as a National Determined Parameter, ranging from 4 to 10 (*CEN*, 2004). This stiffness criterion applies specifically to the scenario where the minimum stiffness is needed to attain the maximum buckling mode. Additionally, in structures with multiple bracing elements, the minimum spring stiffness becomes significantly larger because K_{min} is inversely proportional to a^3, with a representing the span length, which diminishes as the number of bracing elements increases. Consequently, when numerous bracing components are present, achieving the necessary minimum stiffness to reach the highest buckling mode can be challenging. However, in many practical applications, achieving the highest buckling mode is not always critical for ensuring sufficient buckling resistance. Often, the member may provide adequate resistance at intermediate buckling modes.

For design verifications, this consideration can be incorporated through an effective buckling length $l_{ef}\sqrt{\pi^2 EI/N_{cr}}$, which is dependent on the critical load N_{cr} of the member based on a certain number and stiffness of springs. In such instances, a first-order analysis might suffice, as imperfections are inherently accounted for in the k_C-factors used in buckling design verifications.

2 Analytical formulation for a members with pinned ends and two spans

Let's consider a linear-elastic, homogeneous member with flexural stiffness *EI*, subjected to an axial compressive force *N*. Under the assumption of the Euler-Bernoulli beam theory, the differential equation of the elastic curve with second order effects is:

$$w''''(x) + \beta^2 \cdot w''(x) = 0 \tag{1}$$

In Eq. (1), *w* is the displacement, *x* is the coordinate along the member axis, β is defined as $\beta^2 = N/EI$ and the prime symbol indicates derivative with respect to *x*. The solution of this 4th order ordinary differential equation has the following form $w(x) = A + B \cdot x + C\cos(\beta \cdot x) + D\sin(\beta \cdot x)$, where *A*, *B*, *C*, *D* are the four unknown integration constants to be found by applying the relevant boundary conditions at the supports. For a member with two equal spans, i.e. one internal elastic support, the required boundary conditions are eight: four at the outer supports, i.e. $w_1(0) = w_2(l) = w_1'(0) = w_2''(l) = 0$ and four at the internal support, i.e. $w_1(a) = w_2(a), w_1'(a) = w_2'(a), w_1''(a) = w_2''(a)$ (continuity conditions for displacement, rotation and curvature), and $w_1'''(a) - w_2'''(a) = (K/EI)\, w_1(a)$ (shear balance at the internal support). Therefore, by applying the boundary conditions, we obtain a system of 8 equations with 8 unknowns (i.e. A_i, B_i, C_i, D_i). To obtain a non-trivial solution, the determinant of the coefficients' matrix must be zero. In the presented solutions, the bracing stiffness and the critical load are expressed in dimensionless form as respectively $\overline{K} = \frac{K \cdot a^3}{EI}$ and $z = \beta \cdot a = \sqrt{N/EI} \cdot a$. Setting the determinant of the coefficients' matrix to zero, we obtain the solution in Eq.(2):

$$\overline{K} = 2z^3 \cdot \frac{\sin(z)\cos(z)}{z\sin(z)\cos(z) - \sin^2(z)} = f_1(z) \tag{2}$$

A graphic representation of Eq. (2) and the corresponding FE solution is given in Figure 1 in terms of the dimensionless critical load (i.e. $z = \beta \cdot a$) and in terms of the dimensionless effective buckling length l_e/a. As shown in the Figure, a perfect match is obtained between the analytical and the FE result. In all plots, the buckling shape is also indicated. Note that in this Figure, estimations are also obtained by use of linear interpolation of the dimensionless critical load between the transition points of the buckling modes.

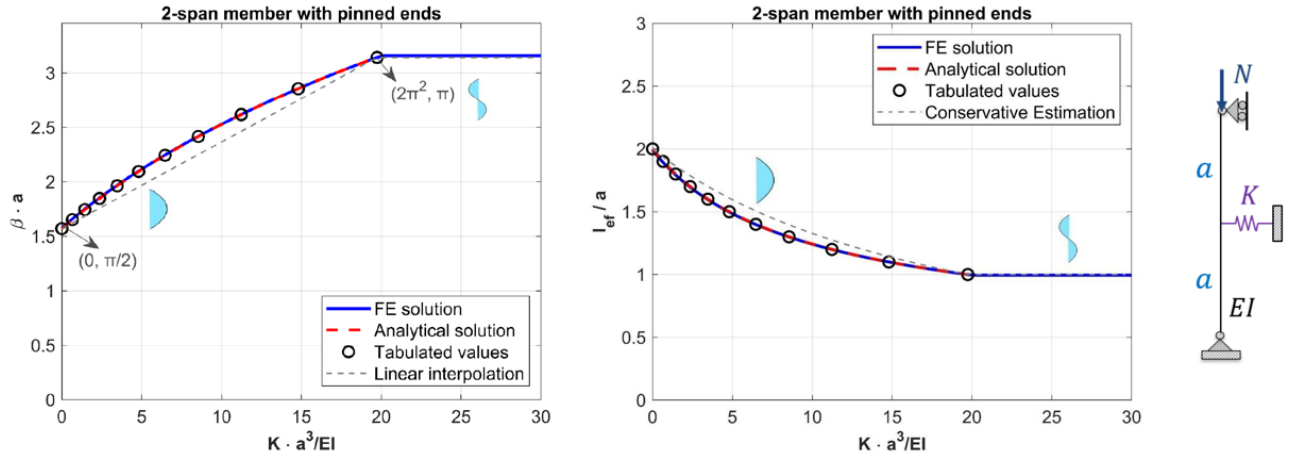

Figure 1. Dimensionless spring stiffness vs dimensionless critical load for a 2-span member with pinned ends

3 Conclusions

This note aims to determine both the critical load and the effective buckling length of braced members based on bracing stiffness, focusing on the newly proposed design strategy in the upcoming edition of Eurocode 5 for this issue (*CEN*, 2024). Although the proposed regulations offer a reasonable approximation, they tend to be overly complex for practical use and differ from the precise solutions. Consequently, this paper derives the exact analytical formulas for the critical load and the effective buckling length for a member with pinned ends and two spans under axial force. A related study, soon to be published (*Stamatopoulos* & *Massaro*, 2025), examines different scenarios, varying the number of spans from two to four as well as the type of end supports (either free or pinned), and provides more user-friendly design guidance.

4 References

CEN (2004). *EN 1995-1-1:2004 + A1:2008 + A2:2014 + NA:2010 – Eurocode 5: Design of timber structures – Part 1-1: General – Common rules and rules for buildings*. Brussels: European Committee for Standardization.

CEN (2024). *FprEN 1995-1-1:2024 – Eurocode 5: Design of timber structures – Part 1-1: General rules and rules for buildings*. Brussels: European Committee for Standardization.

Munch-Andersen, J. (2004). “Bracing of timber members in compression.” In: *Proceedings of the 37th CIB-W18 meeting*. Edinburgh, Scotland.

Stamatopoulos, H. & F. M. Massaro (2025). “Bracing stiffness requirements of members supported by discrete elastic supports.” In: *Wood Material Science & Engineering*, pp. 1–11. DOI: 10.1080/17480272.2025.2533329.

Timoshenko, S. P. & J. M. Gere (1963). *Theory of Elastic Stability*. 2nd. New York: McGraw-Hill.

Lessons learnt and proposals for further development of timber design standards focusing on connection design

José Manuel Cabrero, Ulrich Hübner, Carmen Sandhaas

1 Introduction

This note wants to initiate and provide a basis for a general discussion on how experimental validation of future design standards should look like. Furthermore, ideas on how to facilitate design model development are discussed that aim at increasing robustness of models and more straightforward model validation.
Several facts motivate this discussion:

- Code development: Ongoing debates regarding the new European timber design standard FprEN 1995-1-1 [1] – in particular brittle failure modes of connections loaded parallel-to-grain – highlight the need for better preparation for future code development.
- Harmonisation of international standards on advanced level: More and more, design standards such as European [2], Canadian [3] and New Zealand [4] standards contain comparable rules, and design gaps in one standard may be filled with rules of another standard. Therefore, there is a need for harmonisation to benefit companies, engineers, and the broader timber engineering community.
- Documentation and evaluation gaps: There is a notable discrepancy between the minimal requirements for standard tests and the potential to use such data for validating new design proposals. Furthermore, experimental evidence needed for validation of new models is the more difficult to obtain the more complex necessary testing campaigns are. Clear testing procedures agreed upon internationally and coordinated testing campaigns are needed to advance timber engineering.

The **“traditional” way to introduce a model in a design code** may be illustrated by the following example: E DIN 1052:2000 [5] contained a subclause “connections with bonded-in steel rods”, but the first attempt to introduce design rules in Eurocode 5 failed in 2004 [6]. 21 years later, FprEN 1995-1-1 [1] provides design rules and FprEN 1995-3 [7] execution rules for bonded-in rods. ISO TC165 decided in 2019 to develop a design standard for bonded-in rods, but Covid postponed physical meetings, and a first draft is based on the FprEN 1995-1-1. It will take almost 30 years to make the way from national to international rules.

The **number of scientific publications is yearly increasing by approximately 4%** [8] and more and more countries contribute to the increase in scientific knowledge in timber engineering. Overviewing and distilling the most relevant publications becomes more and more challenging. On the other hand, access to publications has become easier due to digitalisation and world-wide networks.

The education of carpenters, engineers and scientists, their knowledge and experience make progress too, but it is limited by the nature of humans and time. Human development is slower than the increase of available knowledge. This discrepancy leads to the necessity to distinguish between the front-end presented in design standards and the back-end of available knowledge, experience and advanced models. Furthermore, it is generally assumed that design standards should reflect the state of practice rather than the state of science, necessitating a lag between model development and adoption.

EN 1995-1-1:2004 + AC:2006 + A1:2008 [2] has 135 pages, and FprEN 1995-1-1 [1] has 434 pages. CSA 086:2014 [9] was printed on 128 pages and CSA O86:2024 [3] on 436 pages. It is obvious that we cannot continue to triple the number of pages in each generation of Eurocode 5 or CSA O86. Systematization and simplification are essential for a sustainable development. With regard to the necessity to reduce the negative impact of worldwide buildings to our environment rapidly we should try hard to reduce the time span for developing and implementing more efficient design models.

Conclusions after the last INTER meeting regarding brittle failure verification

The discussion at the last INTER meeting in the auditorium, but also during the lunch and coffee breaks about the verification of brittle failure modes of connections led to the following ideas:

- The models for brittle failure modes of connections included in FprEN 1995-1-1 [1] have been developed with practical application in mind and validated by benchmarking against extensive databases of existing experiments. However, these databases sometimes include connections that were either not explicitly designed for brittle failure or did not meet design requirements so to induce brittle failure.
- Evaluating existing test results is complicated due to incomplete reported data (for instance, load-carrying capacities may be determined at different deformation levels). All of this may question the applicability of literature-based databases for model validation.
- Beside the 34 CEN-members, New Zealand and Canada would also like to introduce verification of
  brittle failure modes of connections in design codes. A worldwide agreement is needed on the topic.
- However, since the work is based on publications from a single research group (2017–2021), thorough verification and additional contributions by other research groups are welcome and necessary to improve the rules.

This is just an example. The worldwide timber community faces more and more similar challenges in other fields, where cooperation and collaboration is needed to reach an

agreement and a timely incorporation into design standards. Several regions can (and should) contribute to the solutions. Worldwide cooperation is the most promising strategy to solve common problems.

2 Discussion

The previous discussion highlights several key issues. On one hand, the scientific path—driven by the pressure to publish—has led to an enormous increase in the volume of publications. Research is often conducted in isolation, primarily through nationally or privately funded projects, with limited global collaboration. On the other hand, in the realm of standardization, design codes are becoming increasingly lengthy and complex, which discourages newcomers from engaging in timber design and slows its global adoption. Furthermore, due to long revision cycles, the integration of new content into standards is extremely slow—at least in Europe.

Take, for example, the key topic of connections again: though significant progress has been made to overcome existing gaps, challenges still remain, such as stiffness, ductility, long term response, variable climate effects, or rope effect.

As previously discussed, to have a reliable model, there is a need of a consistent database. The quality and quantity of available test results and the covered connection variations determine the level and significance of the eventually proposed design model. And to have such a consistent, significant and extensive database, is not a one-man task. Therefore, internationally coordinated efforts should be undertaken to address these issues and establish a consistent set of practices (e.g., experimental testing and reporting requirements, best testing practices) to ensure robust model integration and validation in future standards.

As a start, a plausible goal would be a commonly accepted design procedure for connections of reinforced and unreinforced timber connections loaded parallel-to-grain and with dowel-type fasteners. It should cover connections with staples, nails, screws, bolts, dowels, drift pins and timber rivets. The set of required data should be discussed and defined.

For a commonly accepted database, test procedure and test plan should be developed by an international working group. If the participants of the working group represent Europe, Canada, New Zealand and other nations around the world it may be reasonable to host the group within ISO TC165 Timber structures. This would allow proper transparent documentation and support the acceptance of the results.

However, one additional challenge remains: separating model calibration and model validation is no straightforward task. This issue raises several difficulties:

- Models often incorporate multiple parameters (e.g., effective thickness, k_t- and k_v-values for brittle failure modes) that require independent validation but cannot be evaluated experimentally in isolation. Models are hence often validated on a global level only.

- Critical parameters, such as the overstrength of steel dowels or the natural variability of timber properties, significantly affect connection behaviour and may alter the response and safety level. Without experimental determination of e.g. the tensile strength of steel dowels, validation remains imprecise.

Future connection design models can be significantly strengthened through coordinated efforts to provide model developers with comprehensive validation databases. These models could be classified into two categories: advanced scientific models, which are typically complex and aimed at providing accurate physical and mechanical explanations; and design models, which are simplified, conservative, and practice-oriented. This distinction could help to address the growing complexity of design standards and facilitate a global consensus on timber engineering practices. A design standard like Eurocode 5 represents the front-end; concise and focused on general, simplified design models applicable to most practical situations. Seldom or only regionally applied design methods may be stored in a separate part of the Eurocode 5. A detailed background document should connect the front-end with the back-end, containing the sources of the given rules, but also references to advanced, detailed models. Researchers and advanced practitioners should be enabled to apply more efficient and complex engineering solutions for special applications.

3 Conclusion

This work represents an initial step in addressing existing gaps and improving current models through proposing a collaborative global effort. By presenting these preliminary ideas, the goal is to foster collective development lead by the INTER network. Coordinating research efforts would enable the harmonisation of testing procedures and a more balanced distribution of efforts, ultimately leading to a more robust validation database and improved standards.

4 References

[1] FprEN 1995-1-1:2024. Design of timber structures – Part 1-1: General – Common rules and rules for buildings. Comité Européen de Normalisation (CEN), Brussels, Belgium.

[2] EN 1995-1-1:2004 + AC:2006 + A1:2008. Design of timber structures – Part 1-1: General – Common rules and rules for buildings. Comité Européen de Normalisation (CEN), Brussels, Belgium.

[3] CSA 086:2024. Engineering Design in wood. CSA Group, Toronto, ON, Canada.

[4] NZS AS 1720.1:2022. Timber structures Part 1: Design methods. Standards New Zealand, Wellington, New Zealand.

[5] E DIN 1052:2000. Entwurf, Berechnung und Bemessung von Holzbauwerken. Allgemeine Bemessungsregeln und Bemessungsregeln für den Hochbau. DIN Deutsches Institut für Normung, Berlin.

[6] Larsen HJ, 2012. *The sad story of glued-in bolts in Eurocode 5*. CIB-W18 Timber Structures – A review of meetings 1-43, Essay 4.3. Source: https://cib-w18.com/review/ (and there *Part 6 Essays*).

[7] FprEN 1995-3:2024. Design of timber structures – Part 3: Execution. Comité Européen de Normalisation (CEN), Brussels, Belgium.

[8] Bornmann L, Haunschild R, Mutz R, 2021. Growth rates of modern science: a latent piecewise growth curve approach to model publication numbers from established and new literature databases. *Humanities and Social Science Communications* 8, 224. DOI: 10.1057/s41599-021-00903-w

[9] CSA O86:2014. Engineering design in wood. CSA Group, Toronto, ON, Canada.

Comparison of the withdrawal capacity F_{ax} of ring-shank nails and scrails in CLT

Aygül Ceylan, Faculty of Architecture, Yildiz Technical University, Istanbul, Turkiye

Z.Canan Girgin, Faculty of Architecture, Yildiz Technical University, Istanbul, Turkiye

Keywords: Withdrawal capacity F_{ax}, Ring-shank nail, Scrail, CLT, Black pine, Fir.

1 Introduction

Scrails (*SRs*) are used in CLT connections as an alternative to ring-shank nails (*RNs*), combining the installation speed of nails with the withdrawal capacity of screws, allowing rapid installation and removal after adhesive curing, with continuous quality control on the production line. Withdrawal tests are essential to assess the performance of fastener-to-timber connections. The equations to estimate the withdrawal capacity (F_{ax}) of fasteners in current standards are derived from allowable design values and regression analyses of experimental data. Studies have asserted that the equations may be inaccurate for nails with different thread geometries and coatings, as experimental results deviate from design values. Skulteti et al. (1997) and Rammer et al. (2001) reported F_{ax} values that were 34–50% higher than those prescribed by the National Design Specification. Kevarinmaki (2005) tested five types of gun-driven nails on spruce and recommended EC5 to reduce the withdrawal parameter f_{ax} at least 0.7 for profiled nails by noting hot-dip galvanized nails. Sandhaas and Görlacher (2017) emphasized quite similar results for stainless steel nails and hot-dip galvanized nails. EN 14592 specifies stainless steel and *Fe–Zn* coatings, but provides no guidance on alternative corrosion-resistant coatings; notably, Ceylan and Girgin (2020) presented the first experimental study on phosphate-coated ring-shank nails.

This paper investigates the withdrawal capacity of various coated *RNs* and the less-studied *SRs* in CLT manufactured from Turkish black pine and fir. This note examines the consistency between design equations and experimental findings as well, while ongoing work focuses on developing predictive models for the withdrawal capacity.

2 Materials, Method, and Findings

Withdrawal tests were conducted on two local CLT types (black pine and fir) through four *RN* types and two *SR* types (Table 1). *RNs* were sourced from local manufacturers with international distribution, while the *SRs* (*SR-GD-1* and *SR-GD-2*) were provided from Beck Fastener Group. Fastener lengths (80 mm) and diameters, particularly for

RNs, were closely matched to enable a valid comparison of surface coating effects. A total of 420 specimens (50×50×66 mm) were tested, comprising 35 replicates for each combination of fastener. The withdrawal tests were performed with a constant rate of loading to determine F_{max} to an accuracy of 1% according to EN 1382. In this study, withdrawal capacity (F_{ax}), withdrawal stiffness (K_{ax}), withdrawal parameter (f_{ax}), and withdrawal energy (E) characteristics were examined (Table 1). For both CLT species, *RN-PR-1* exhibited the highest F_{ax} among all fasteners, suggesting that the phosphate+resin coating enhances the withdrawal capacity of *RN*. *SR-GD* series showed higher F_{ax} than standard *RNs* (excluding *RN-PR-1*) in most cases, with *SR-GD-2* achieving 1.01 and 1.05 times greater F_{ax} than *SR-GD-1* in the black pine and fir series, respectively. Additionally, *SR-GD-1*, a plastic-striped scrail, resulted in increased wood splitting compared to *SR-GD-2*, which is wire-collated. *SRs* displayed higher K_{ax} than *RNs*, indicating a stiffer initial response during withdrawal. Among *RNs, RN-PR-1* showed the highest K_{ax} in black pine (2.91 kN/mm), highlighting the effect of coating on mechanical engagement with the CLT. Compared with *RNs, SRs* had higher f_{ax}, particularly *SR-GD-1* in black pine (0.017 kN/mm²), reflecting more efficient axial load transfer, likely due to the shank geometry. *RN-PR-1* and *RN-R* had higher withdrawal energy compared to other *RNs*, especially in fir CLT (6.43 and 5.40 kNmm, respectively). *SRs* showed moderate *E* values; *SR-GD-2* (5.30 kNmm in fir) balances high withdrawal stiffness and load. Overall, in all RN and SR test series, black pine CLT demonstrated higher F_{ax} than fir CLT, attributable to its higher specific gravity.

Table 1. Withdrawal characteristics of ring-shank nails (RNs) and scrails (SRs) in the experiments.

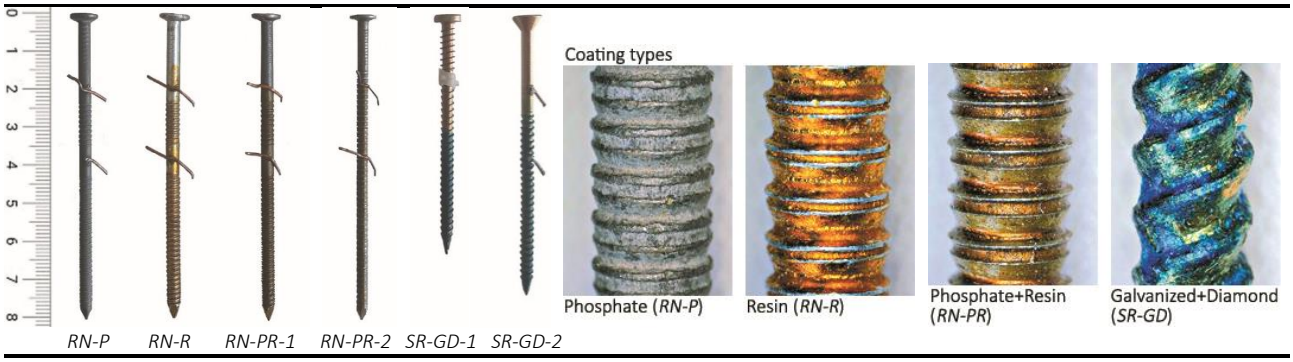

Type	d (mm)	l_d (mm)	Black Pine CLT				Fir CLT			
			F_{ax} (kN)	K_{ax} (kN/mm)	f_{ax} (kN/mm²)	E (kN.mm)	F_{ax} (kN)	K_{ax} (kN/mm)	f_{ax} (kN/mm²)	E (kN.mm)
RN-P	3.3	62.0	2.40	2.69	0.012	5.19	2.18	3.30	0.011	3.70
RN-R	3.4	62.0	2.43	3.03	0.012	4.82	2.19	2.45	0.010	5.40
RN-PR-1	3.4	62.0	2.63	2.91	0.012	5.65	2.53	2.55	0.012	6.43
RN-PR-2	2.9	62.0	2.20	2.83	0.012	3.11	2.06	2.38	0.011	2.96
SR-GD-1	3.2	45.0	2.40	3.44	0.017	4.10	2.13	2.38	0.015	4.61
SR-GD-2	3.2	57.0	2.44	3.67	0.013	4.73	2.25	3.02	0.012	5.30

Common models to predict F_{ax} of *RNs* (Table 2) were applied to *SRs* as well. Herein, the red series represents black pine CLT while the blue series displays fir CLT. Results suggest that the exponents of characteristic density and specific gravity with initial constant factors are not universal, varying with fastener type and timber interaction.

Table 2. Common models of the withdrawal capacity F_{ax} .

Source	Equation	Source	Equation	Source	Equation
Rammer et al. (2001)	$F_{ax} = 42.8\ \rho^{1.38}\ d\ l_d$	Blaß and Uibel (2007)	$F_{ax} = 0.117\ \rho_k{}^{0.8}\ d^{0.6}\ l_d$	ANSI-AWC NDS (2012)	$F_{ax} = 77.51\ \rho^2\ d\ l_d$

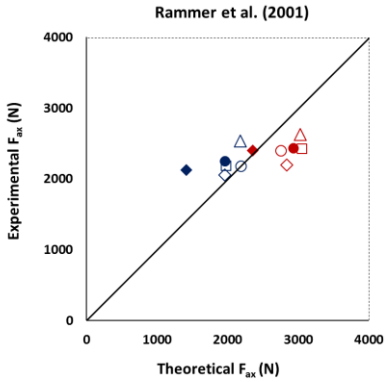

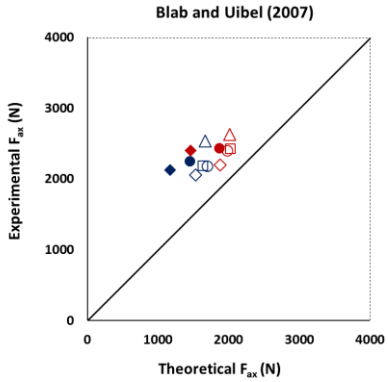

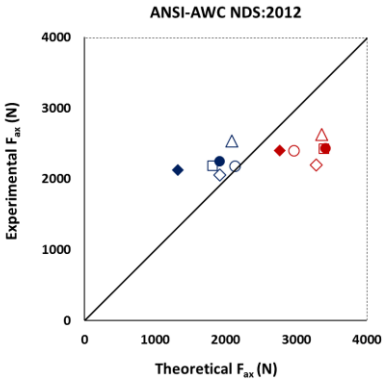

ρ_k=characteristic density (kg/m^3); ρ=specific gravity; l_d =penetration depth; d= nominal diameter of nail (mm).

3 Conclusions

The following conclusions can be drawn from this study:

- Fastener geometry and coating type strongly influence F_{ax}. Phosphate+resin coated ring-shank nail (*RN-PR-1*) has the highest F_{ax} values in black pine and fir CLT due to the enhanced mechanical friction of rough crystalline of coating.
- Scrails (*SRs*) provide higher K_{ax} and f_{ax}, while phosphate+resin coated *RNs* achieve the highest F_{ax} and E.
- Rammer et al. (2001) successfully estimate for *RNs* and *SRs* in both black pine and fir CLT.
- Ongoing research aims to develop models better matching to experimental F_{ax}. This could allow for more economical and high-performance CLT connections using local wood species.

4 Acknowledgements

This study was financially supported with Project Number FKD-2022-4892 by Research Fund of the Yildiz Technical University.

5 References

ANSI/AWC NDS.2012. National design specification for wood construction. American Wood Council, Washington, DC.

Blaß HJ, Uibel T (2007) Tragfähigkeit von stiftförmigen Verbindungsmitteln in Brettsperrholz. Universitätsverlag Karlsruhe.

Ceylan A, Girgin ZC (2020) Comparisons on withdrawal resistance of resin and phosphate coated annular ring nails in CLT specimens. Constr. Build. Mater., 238.

EN 1995-1-1.2004 (EC5). Design of timber structures - Part 1-1: General - Common rules and rules for buildings. CEN.

EN 1382. 2016. Timber Structures - Test methods - Withdrawal capacity of timber fasteners. CEN.

EN 14592. 2008. Timber structures. Dowel-type fasteners. Requirements. CEN.

Kevarinmaki A (2005) Nails in spruce splitting sensitivity, end grain joints and withdrawal strength. CIB/W18 Conf. Proc., Karlsruhe, Germany, paper 38-7-6.

Rammer DR, Winistorfer SG, Bender DA (2001) Withdrawal strength of threaded nails. J. Struct. Eng. 127 (4), 442-449.

Sandhaas C, Görlacher R (2017) Nailed joints: Investigation on parameters for Johansen model. INTER Conf. Proc., Kyoto, Japan, paper 50-7-3.

Skulteti MJ, Bender DA, Winistorfer SG, Pollock DG (1997) Withdrawal strength of ring-shank nails embedded in southern pine lumber. Trans. ASAE, 40(2), 451-456.

Rate effects of glued laminated timber beams subjected to impact loading: preliminary results

Gioele Montalbetti, Institute of Structural Engineering, ETH Zurich, Switzerland

Andrea Frangi, Institute of Structural Engineering, ETH Zurich, Switzerland

Keywords: Glued laminated timber , Impact loading , Strain rate dependency , Blast loading , Dynamic strength increase

1 Introduction

Engineered wood products used in mass timber construction, such as glued laminated timber, introduce inherent material discontinuities, which may affect their strain-rate sensitivity. Past research on glued laminated timber have focused on simulated blast (*Lacroix*, 2017) and four-point impact loading (*Wight* et al., 2024). *Lacroix* (2017) observed a ratio between the dynamic and quasi-static resistance, k_{dyn}, of 1.14 for strain rates $\dot{\varepsilon}$ between 0.14 and 0.51 s^{-1}. Further tests conducted by *Wight* et al. (2024) employed a drop-weight four-point bending test setup, yielded a slightly lower k_{dyn} of 1.13 for strain rates ranging from 0.57 to 1.05 s^{-1}. While four-point bending configurations have been used in the aforementioned studies, three-point bending tests engage a relatively small stressed volume. Consequently, both material composition and the choice of loading configuration may play a critical role in the accurate assessment of rate-dependent behaviour of glued laminated timber.

2 Material, Method and Results

The tests were conducted on the pendulum impact hammer test setup developed by *Cao* et al. (2022). 27 specimens with spans 2800, 3800, 4800 mm and heights ranging from 240 to 320 mm in 40 mm steps were tested under different impact velocities. Three further specimens were tested quasi-statically on a three-point bending setup to quantify the reference resistance. All specimens were finger-jointed GL24h glued laminated timber beams manufactured according to EN 14080:2013. Since the strain rate can be defined as $\dot{\varepsilon} = \frac{6h}{L^2}\dot{w}$, it follows that $\dot{\varepsilon} \propto 1/L^2$. Thus, varying the length L enables substantial control over the achievable strain rates. By combining the proportionality

$\dot{\varepsilon} \propto 1/L^2$ with a variation of impact velocity $v_p \approx \dot{w}$, the potential of the setup was fully exploited. The shortest specimens were subjected to the highest possible impact velocity v_p, namely a release angle ϑ_0 of 85°, and the longest specimens to the lowest safe release angle ϑ_0 of 45°.

The displacements were measured using fiducial markers (ArUco) with the setup shown in Figure 1. A precision of ±1px, equivalent to approximately ±0.90mm, was achieved and further improved by averaging eight data streams. To determine the ultimate resistance from the displacement tracking, the spring stiffness of a beam subjected to a point load at mid-span considering shear deformations:

$$k_{b,v} = \frac{1}{\frac{L^3}{48EI} + \frac{L}{4\kappa GA}}, \tag{1}$$

can be multiplied by the measured displacement w_{ArUco}, to determine the impact force $P_d = k_{b,v} w_{ArUco}$. The acting bending moment M_d can be compared to the mean bending resistance M_{Rm} of the reference specimens to determine the resulting dynamic strength increase factors k_{dyn}.

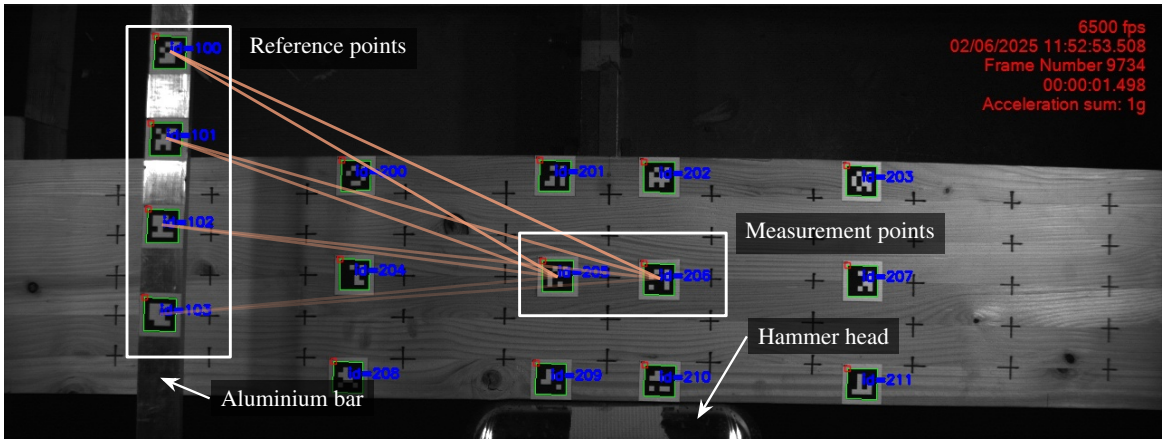

Figure 1. Displacement measurement setup for fiducial marker tracking.

As shown in Figure 2, dynamic strength increase factors k_{dyn} ranging from 0.87 to 2.20 were observed. The lowest value of 0.87 was an outlier with an early failure of a finger joint located near the centre. A Cowper–Symonds equation, which is a widely accepted model for characterizing metallic material behaviour at high strain rates, was fitted to the results. The resulting parameters for the mean value fit are c=3.1 and q=1.17 with a respective CV of 23% and 28%, and a coefficient of determination R^2 of 0.53.

When compared with the results of *Lacroix* (2017), similar dynamic strength increase factors k_{dyn} were observed for strain rates $\dot{\varepsilon}$ between 0.14 and 0.51 s^{-1}. In contrast, compared to *Wight* et al. (2024), higher strength increase factors k_{dyn} were measured in the strain rate $\dot{\varepsilon}$ range of 0.57 to 1.05 s^{-1} with an overlap for lower k_{dyn} values. Besides the known strength increase factors, a significant increase of k_{dyn} towards strain rates $\dot{\varepsilon}$ of 2.00 was observed.

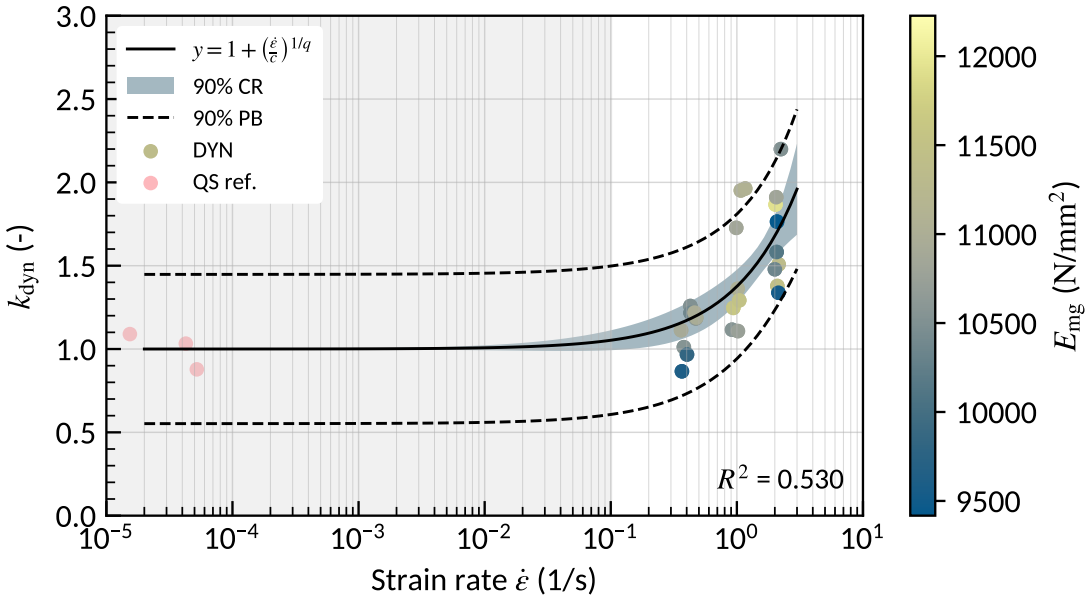

Figure 2. Dynamic strength increase factor k_{dyn} for different strain rates $\dot{\varepsilon}$. The colour bar represents the quasi-static global E-Modulus E_{mg} according to EN 408:2010.

3 Conclusion

A wide range of three-point bending tests at different strain rates $\dot{\varepsilon}$ was achieved by varying the span length L and the impact velocity v_p. In the range $\dot{\varepsilon} = 0.50$ to $0.75\ s^{-1}$, dynamic strength increases consistent with those reported in the existing literature were observed. In the range 1.00 to $2.00\ s^{-1}$, a non-linear increase in resistance was observed on the logarithmic scale, surpassing the known dynamic increase factors k_{dyn} and enlarging the dataset for strain rates $\dot{\varepsilon}$ above 2.00.

Clear limitations of this study include the lack of measured reaction and impact forces. In addition, the fitting parameters exhibit a relatively high coefficient of variation, showing that more data is required. Additional data points from existing literature could improve the fitting parameters and the coefficient of determination. Nonetheless, the findings demonstrate an evident strain-rate dependency of glued laminated timber beams subjected to impact loading.

4 References

Cao, A.; M. T. Houen; M. Lolli & A. Frangi (2022). *Pendulum impact hammer tests on glued laminated timber beams*. Report. ETH Zurich. DOI: 10.3929/ethz-b-000585619.

Lacroix, D. N. (2017). "Investigating the Behaviour of Glulam Beams and Columns Subjected to Simulated Blast Loading." PhD thesis. University of Ottawa. DOI: 10.20381/ruor-21031.

Wight, N.; C. Viau & P. Heffernan (2024). "Behaviour of glued-laminated timber beams under impact loading." In: *Canadian Journal of Civil Engineering*. DOI: 10.1139/cjce-2023-0298.

Simplified design equations for lateral slip modulus of dowel type fastener joints

Kenji Kobayashi, The University of Tokyo, Japan

Keita Ogawa, Shizuoka University, Japan

Keywords: Joint, Dowel type fastener, Slip modulus

1 Introduction

Slip modulus of the joint is important to design timber structures. In Eurocode 5 (2004), slip modulus K_{ser} is determined by simple formula with density and fastener diameter. However, this equation does not consider the effect of material thickness. In Japanese design standard (Architectural Institute of Japan (AIJ), 2006), slip modulus $k_{\mathrm{js,TBEF}}$ is determined based on theory of beam on elastic foundation (TBEF) (Kuenzi, 1955). Design equations based on TBEF contain equations involving hyperbolic and trigonometric functions (hereafter "hyperbolic parts"), thus they are too complicated and not suitable for design equations. Furthermore, in joint types that use steel plates, the slip modulus is calculated to be excessively high because the deformation of the steel plate itself is ignored.

The AIJ standard is currently scheduled for revision in 2026. One of the revisions concerns slip modulus, with the aim of creating a simplified formula based on TBEF that can calculate a value closer to the actual slip modulus. This paper introduces the simplified calculation formula for slip modulus k_{js}.

2 Proposed design equations

k_{js} for joints are determined by Equations (1) and (2).

$$k_{\mathrm{js}} = \begin{cases} C_{\mathrm{k1}} \cdot k_1 \cdot d \cdot l_{\lambda 1} & \text{(Steel-to-timber joints)} \\ (C_{\mathrm{k1}} + C_{\mathrm{k2}}) \cdot C_{\omega} \cdot k_1 \cdot d \cdot l_{\lambda 1} & \text{(Timber-to-timber joints)} \end{cases} \quad (1)$$

$$l_{\lambda i} = \left(\frac{4EI}{k_i d}\right)^{\frac{1}{4}} \quad (2)$$

where subscript i indicates main or side member (1: main member, 2: side member), $C_{\mathrm{k}i}$ is the coefficients depending on the thickness of each member, k_i is the bearing

stiffness (N/mm^3), d is the diameter of the fastener (mm), $l_{\lambda i}$ is the normalized thickness (mm), EI is bending stiffness of the fastener (Nmm^2), C_ω is the coefficient depending on the ratio of $l_{\lambda i}$.

Bearing stiffnesses parallel and perpendicular to the grain k_0, k_{90} are determined by Equation (3) (Hwang & Komatsu, 2002).

$$k_0 = \frac{E_0}{31.6+10.9d}, k_{90} = \frac{k_0}{3.4} \quad (3)$$

where E_0 is the modulus of elasticity (N/mm^2).

C_ω is determined from Equations (4) and (5).

$$C_\omega = \frac{1}{(1+\omega^2)(1+\omega)} \quad (4)$$

$$\omega = \frac{l_{\lambda 2}}{l_{\lambda 1}} \quad (5)$$

C_{k1} and C_{k2} values are shown in Table 1 and 2. $C_{\mathrm{k}i}$ is determined according to l_i / $l_{\lambda i}$.

Table 1. C_{k1} value for steel-to-timber joints

Joint type	l_1 / $l_{\lambda 1}$		
	0	1	2～
S-T-S*	0	0.8	0.8
T-S-T*	0	0.7	1.2
S-T*	0	0.2	0.4

**S: Steel member, T: Timber member*
Intermediate values are interpolated linearly

Table 2. C_{k1} and C_{k2} values for timber-to-timber joints

Joint type		$l_i/l_{\lambda i}$		
		1	2	3～
T-T-T*	C_{k1}	1.4	1.2	1
	C_{k2}	0.6	0.8	1
T-T*	C_{k1}	0.25	0.5	0.5
	C_{k2}	0.25	0.5	0.5

**T: Timber member*
Intermediate values are interpolated linearly.

In TBEF equations for timber-to-timber joints, C_{k1} represents a hyperbolic part of TBEF equations. Hyperbolic parts are replaced by simple linear lines. It also includes a reduction caused by deformation at steel part.

In TBEF equations for timber-to-timber joints, Stiffness values converge at an infinite member thickness ($k_{\mathrm{js,TBEF,inf}}$). C_ω is obtained as hyperbolic parts under infinite member thickness. $C_{k1} + C_{k2}$ values are considered as a ratio against the converged stiffness. Figure 1 shows the ratio $k_{\mathrm{js,TBEF}}/k_{\mathrm{js,TBEF,inf}}$, and Figure 2 shows an example of $C_{k1} + C_{k2}$ values in single shear timber-to-timber joints. Values in Table 2 are determined to express $k_{\mathrm{js,TBEF}}/k_{\mathrm{js,TBEF,inf}}$ ratio. The thickness of each member is limited to $l_1 \geq l_{\lambda 1}, l_2 \geq l_{\lambda 2}$, which means that the normalized thickness $l_{\lambda i}$ is also used as required minimum thickness for simplified equations.

3 Comparison with experimental values

Figure 3 shows a comparison between C_{k1}, hyperbolic parts of TBEF equation ($k_{\mathrm{js,TBEF}}$ is divided by $k_1 d l_{\lambda 1}$) and experimental values in steel-to-timber double shear joints. TBEF equations showed higher values than experiments, and C_{k1} values for simplified equations may be appropriate to estimate slip modulus for steel-to-timber joints.

A comparison between experimental and calculated values in timber-to-timber joints are shown in Figure 4. The slip modulus calculated using the proposed equations appropriately evaluates the experimental values.

4 References

Eurocode 5 (2004): Design of timber structures - Part 1-1: General and rules for buildings. CEN. (EN 1995-1-1).

Architectural Institute of Japan. (2006): Standard for Structural Design of Timber Structures (in Japanese). Maruzen, Tokyo, 231-234.

Hwang K. and Komatsu K. (2002): Bearing properties of engineered wood products I: effects of dowel diameter and loading direction. Journal of Wood Science 48, 295–301.

Kuenzi EW (1955): Theoretical design of a nailed or bolted joint under lateral load, USDA, No. D1951

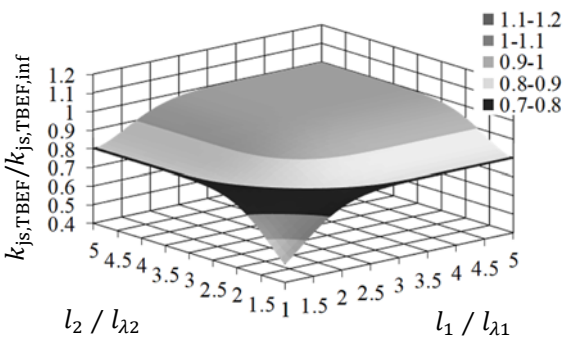

Figure 1. Relationship between member thickness and $k_{\mathrm{js,TBEF}}/k_{\mathrm{js,TBEF,inf}}$ ratio in single shear timber-to-timber joints

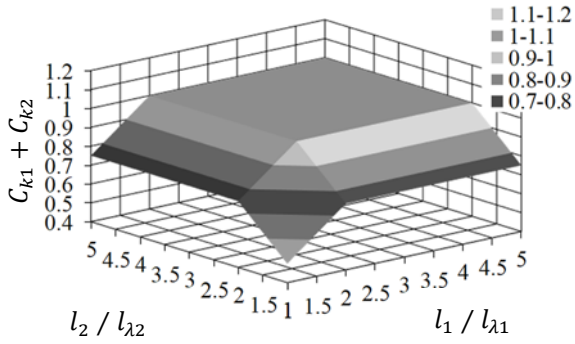

Figure 2. Relationship between member thickness and $C_{k1} + C_{k2}$ values in single shear timber-to-timber joints

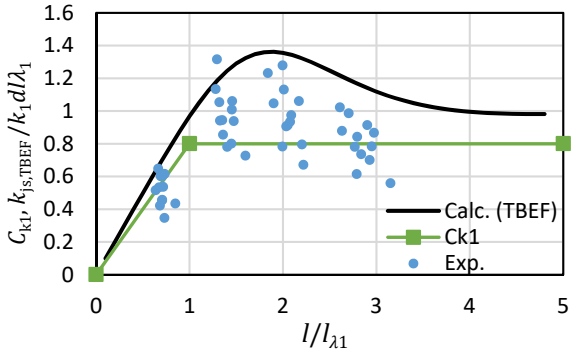

Figure 3. A comparison between C_{k1}, hyperbolic parts of TBEF equation and experimental values in steel-to-timber double shear joints

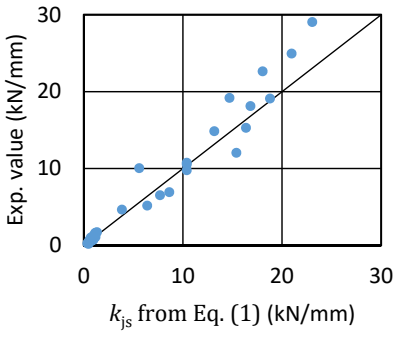

Figure 4. A comparison between experimental and calculated values in timber-to-timber joints

5 Peer review of papers for the INTER Proceedings

Experts involved:

The reviews are undertaken by long standing members of the INTER group which is a community of experts in the field of timber engineering.

Procedure of peer review

- Submission of manuscripts: all members of the INTER group attending the meeting receive the manuscripts of the papers at least four weeks before the meeting. Everyone is invited to read and review the manuscripts especially in their respective fields of competence and interest.

- Presentation of the paper during the meeting by the author

- Comments and recommendations of the experts, discussion of the paper

- Comments, discussion and recommendations of the experts are documented in the minutes of the meeting and are printed on the front page of each paper.

- Final acceptance of the paper for the proceedings with

    - no changes
    - minor changes
    - major changes
    - or reject

- Revised papers are to be sent to the editor of the proceedings and the chairman of the INTER group

- Editor and chairman check, whether the requested changes have been carried out.

6 Meetings and list of all CIB W18 and INTER Papers

CIB Meetings:

1 Princes Risborough, England; March 1973
2 Copenhagen, Denmark; October 1973
3 Delft, Netherlands; June 1974
4 Paris, France; February 1975
5 Karlsruhe, Federal Republic of Germany; October 1975
6 Aalborg, Denmark; June 1976
7 Stockholm, Sweden; February/March 1977
8 Brussels, Belgium; October 1977
9 Perth, Scotland; June 1978
10 Vancouver, Canada; August 1978
11 Vienna, Austria; March 1979
12 Bordeaux, France; October 1979
13 Otaniemi, Finland; June 1980
14 Warsaw, Poland; May 1981
15 Karlsruhe, Federal Republic of Germany; June 1982
16 Lillehammer, Norway; May/June 1983
17 Rapperswil, Switzerland; May 1984
18 Beit Oren, Israel; June 1985
19 Florence, Italy; September 1986
20 Dublin, Ireland; September 1987
21 Parksville, Canada; September 1988
22 Berlin, German Democratic Republic; September 1989
23 Lisbon, Portugal; September 1990
24 Oxford, United Kingdom; September 1991
25 Åhus, Sweden; August 1992
26 Athens, USA; August 1993
27 Sydney, Australia; July 1994
28 Copenhagen, Denmark; April 1995
29 Bordeaux, France; August 1996
30 Vancouver, Canada; August 1997
31 Savonlinna, Finland; August 1998
32 Graz, Austria; August 1999

33 Delft, The Netherlands; August 2000
34 Venice, Italy; August 2001
35 Kyoto, Japan; September 2002
36 Colorado, USA; August 2003
37 Edinburgh, Scotland; August 2004
38 Karlsruhe, Germany; August 2005
39 Florence, Italy; August 2006
40 Bled, Slovenia; August 2007
41 St. Andrews, Canada; August 2008
42 Dübendorf, Switzerland; August 2009
43 Nelson, New Zealand; August 2010
44 Alghero, Italy; August 2011
45 Växjö, Sweden; August 2012
46 Vancouver, Canada; August 2013

INTER Meetings:

47 Bath, United Kingdom; August 2014
48 Šibenik, Croatia; August 2015
49 Graz, Austria; August 2016
50 Kyoto, Japan; August 2017
51 Tallinn, Estonia; August 2018
52 Tacoma WA, USA; August 2019
53 Online Meeting; August 2020
54 Online Meeting; August 2021
55 Bad Aibling, Germany; August 2022
56 Biel/Bienne, Switzerland; August 2023
57 Padova, Italy; August 2024
58 Istanbul, Türkiye; August 2025

The titles of the CIB W 18 and INTER papers (starting from 2014) are included in the complete list of CIB/INTER papers: http://holz.vaka.kit.edu/741.php